



HAL
open science

Collisional rate coefficients of sulfur-bearing molecules induced by light and heavy colliders for interstellar and cometary applications

Amélie Godard

► **To cite this version:**

Amélie Godard. Collisional rate coefficients of sulfur-bearing molecules induced by light and heavy colliders for interstellar and cometary applications. *Astrophysics [astro-ph]*. Université de Rennes, 2024. English. NNT : 2024URENS056 . tel-04911262

HAL Id: tel-04911262

<https://theses.hal.science/tel-04911262v1>

Submitted on 24 Jan 2025

HAL is a multi-disciplinary open access archive for the deposit and dissemination of scientific research documents, whether they are published or not. The documents may come from teaching and research institutions in France or abroad, or from public or private research centers.

L'archive ouverte pluridisciplinaire **HAL**, est destinée au dépôt et à la diffusion de documents scientifiques de niveau recherche, publiés ou non, émanant des établissements d'enseignement et de recherche français ou étrangers, des laboratoires publics ou privés.

COLLEGE SCIENCES DE LA MATIERE

DOCTORAL DES MOLECULES

BRETAGNE ET MATERIAUX



Université
de Rennes

THÈSE DE DOCTORAT DE

L'UNIVERSITÉ DE RENNES

ÉCOLE DOCTORALE N° 638

Sciences de la Matière, des Molécules et Matériaux

Spécialité : *Physique*

Par

Amélie GODARD PALLUET

Collisional Rate Coefficients of Sulfur-Bearing Molecules Induced by Light and Heavy Colliders for Interstellar and Cometary Applications

Thèse présentée et soutenue à Rennes, le 2 Décembre 2024

Unité de recherche : Institut de Physique de Rennes - UMR 6251, F-35000 Rennes, France

Rapporteurs avant soutenance :

Gerrit GROENENBOOM Professeur, Université de Radboud

Jean-Christophe LOISON Directeur de recherche, CNRS, Université de Bordeaux

Composition du Jury :

Président : Ludovic BIENNIER

Examineurs : Dominique BOCKELÉE-MORVAN

Marcelino AGÚNDEZ

Tomás GONZÁLES LEZANA

Lucile RUTKOWSKI

Dir. de thèse : François LIQUE

Directeur de recherche, CNRS, Université de Rennes

Directrice de recherche, CNRS, Observatoire de Paris

Chercheur, CSIC, Instituto de Física Fundamental, Madrid

Chercheur, CSIC, Instituto de Física Fundamental, Madrid

Chargée de recherche, CNRS, HDR, Université de Rennes

Professeur, Université de Rennes

RÉSUMÉ DE LA THÈSE

L'astrochimie est un domaine relativement récent dont les principaux objectifs sont de comprendre la formation des étoiles et des planètes, ainsi que l'émergence de la vie sur Terre. Ces questions sont abordées par l'étude de la chimie et des compositions chimiques des différents milieux astrophysiques, tels que le milieu interstellaire (l'espace entre les étoiles, noté MIS), les comètes, ainsi que les régions circumstellaires et circumplanétaires.

Mes travaux de thèse portent principalement sur l'étude des nuages moléculaires, régions où se forment les étoiles et qui nous renseignent sur l'influence de la composition chimique sur ce processus. Ils concernent également l'étude des comètes, considérées comme des vestiges de la formation des planètes de notre système solaire et supposées porteuses de molécules prébiotiques, potentiellement à l'origine de la vie sur Terre.

L'étude de la composition chimique de ces milieux repose sur l'interprétation des spectres moléculaires capturés par les télescopes. Cette interprétation nécessite l'utilisation de modèles de transfert de rayonnement permettant de calculer l'intensité des raies moléculaires dans des conditions physiques spécifiques, afin de les comparer aux observations. Néanmoins, ces modèles sont souvent basés sur l'approximation de l'Équilibre Thermodynamique Local (ETL), qui suppose que les populations des niveaux d'énergie des molécules sont thermalisées et peuvent donc être simplement décrites par une distribution de Boltzmann. Cependant, il est bien établi que cette approximation est souvent invalide dans les milieux astrophysiques où la densité est insuffisante pour permettre la thermalisation des molécules. Ainsi, pour obtenir des conditions physiques précises à partir de ces modèles, il est nécessaire de réaliser un bilan détaillé de tous les processus d'excitation et de désexcitation affectant les molécules du milieu.

Ces processus peuvent être de deux natures : radiatifs ou collisionnels. Les transitions induites par absorption ou émission d'un photon sont quantifiées par les coefficients d'Einstein, qui sont connus pour toutes les molécules détectées ainsi que pour certains isotopologues. En revanche, les transitions induites par collision sont caractérisées par les taux de collisions, qui sont souvent absents de la littérature en raison de la complexité des calculs nécessaires à leur détermination. À ce jour, ces taux existent pour environ

70 molécules sur les 320 détectées en décembre 2024. Cependant, même les données disponibles ne suffisent pas à modéliser les molécules dans tous les environnements astrophysiques et à toutes les températures. L'existence de ces taux de collision représente donc un des principaux facteurs limitant pour une exploitation complète des observations et une détermination précise des abondances moléculaires dans les milieux astrophysiques.

Le calcul des taux de collision débute par la sélection d'une molécule cible, correspondant à celle observée, et d'un partenaire de collision, généralement la molécule la plus abondante dans le milieu étudié. L'interaction électronique entre ces deux espèces est évaluée en résolvant l'équation de Schrödinger électronique à l'aide de méthodes de chimie quantique, ce qui permet de construire une Surface d'Énergie Potentielle (SEP). Cette SEP est ensuite utilisée dans l'équation de Schrödinger décrivant le mouvement des noyaux afin de déterminer les sections efficaces d'excitation collisionnelle. En intégrant ces sections efficaces sur une distribution de Maxwell-Boltzmann des énergies de collision, on obtient les taux de collision. Ces données peuvent ensuite être intégrées dans des codes de transfert de rayonnement pour analyser les observations.

L'objectif de mes travaux de thèse est de calculer des taux de collision absents de la littérature, permettant ainsi de déterminer l'abondance de molécules clés dans les milieux astrophysiques. Ces études se concentrent sur des molécules soufrées afin de contribuer à la résolution du problème du soufre manquant.

L'abondance observée de cet élément dans les nuages moléculaires ne représente qu'environ un pour cent de l'abondance cosmique attendue, ce qui suggère que les principaux réservoirs de soufre restent non identifiés. Pour mieux comprendre ce problème, il est essentiel de contraindre avec précision l'abondance des principales molécules soufrées, afin d'élucider la chimie du soufre dans ces environnements.

La première partie de la thèse s'est concentrée sur la molécule CCS, omniprésente dans le MIS, avec pour objectif de modéliser son abondance ainsi que celle de quatre de ses isotopologues (^{13}CCS , C^{13}CS , CC^{34}S , et CC^{33}S) dans les nuages moléculaires, où cette molécule et ses isotopologues sont particulièrement abondants.

L'atome d'hélium (He) a été choisi comme partenaire de collision, car les taux de collision avec He peuvent être utilisés, en première approximation, pour modéliser les taux de collision avec para- H_2 ($j=0$), qui est la molécule la plus abondante dans les nuages moléculaires.

Dans un premier temps, la SEP du complexe de van der Waals CCS-He a été calculée à l'aide de la méthode de chimie quantique des Clusters-Couplés CCSD(T), et une base d'orbitale atomique aVQZ ainsi que des fonctions de liaisons grâce au logiciel MOLPRO. L'erreur de superposition des bases (ESB) a été corrigé à chaque géométrie, et un ajustement global de la SEP a été réalisé en utilisant un développement sur des polynômes de Legendre. Cette SEP a ensuite été intégrée dans le code de dynamique quantique MOLSCAT afin de résoudre les équations couplées, solution de l'équation de Schrödinger nucléaire, en utilisant la méthode « exacte », appelée Close-Coupling, tout en tenant compte de la structure fine de CCS. C'est la première fois que les taux de collision impliquant CCS ont été calculés en considérant de manière exacte sa structure interne. Par comparaison avec des études antérieures, il a été démontré qu'un traitement approximatif de la structure fine de CCS via l'approximation soudaine conduit à des différences significatives sur les taux. Ces écarts incluent une déviation globale d'un facteur 2 à 10 et des différences atteignant un facteur 100 pour certaines transitions.

Les taux de collision de quatre isotopologues (^{13}CCS , C^{13}CS , CC^{34}S et CC^{33}S) ont également été calculés, en prenant en compte la structure hyperfine pour les isotopologues contenant des atomes ayant un spin nucléaire, tels que ^{13}C ($I = 1/2$) et ^{33}S ($I = 3/2$). Pour cela, les équations couplées ont d'abord été résolues en considérant uniquement la structure fine. Les taux de collision hyperfins ont ensuite été obtenus à partir de ces calculs en appliquant une méthode de recouplage. Les données obtenues pour les différents isotopologues ont été comparées, montrant que l'effet de la substitution isotopique sur les taux de collision est faible.

Ces données ont été intégrées dans le code de transfert de rayonnement RADEX afin de tester leur impact sur l'intensité des raies observées dans les nuages moléculaires lors d'études précédentes.

Les taux de collision de CCS et de ses isotopologues ont également été utilisés pour interpréter des observations du nuage moléculaire Taurus 1, réalisées avec le télescope Yebes 40m, et pour évaluer l'abondance de CCS ainsi que celle de ses isotopologues.

Lors d'une étude précédente, il avait été constaté que les raies de C^{13}CS étaient plus intenses que celles de ^{13}CCS , ce qui avait conduit à une estimation du rapport d'abondance $[\text{C}^{13}\text{CS}]/[^{13}\text{CCS}] = 4.2 \pm 2.3$ dans cette même région du MIS. Cette anomalie peut être utilisée pour discuter des chemins de formation de la molécule.

Grâce aux nouvelles observations interprétées à l'aide des données calculées dans le cadre de ce travail de thèse, ce rapport d'abondance a été réévalué à $[\text{C}^{13}\text{CS}]/[^{13}\text{CCS}] =$

6.79 ± 0.7 , montrant que l'anomalie est en réalité plus prononcée que ce qui avait été estimé précédemment. Diverses hypothèses ont été proposées pour expliquer cette anomalie. Dans ce travail, il est suggéré que l'interconversion de ^{13}CCS en C^{13}CS constitue une explication plausible. Ce type d'anomalie a également été examiné pour d'autres molécules, et l'interconversion apparaît comme une explication raisonnable pour rendre compte de l'anomalie observée dans le cas de CCH.

La deuxième partie de cette thèse a porté sur la molécule CS, dans le but de modéliser son abondance dans les atmosphères cométaires où elle est relativement abondante.

Il existe très peu de données de collisions adaptées aux atmosphères cométaires, car les molécules les plus abondantes dans ces environnements sont CO, CO₂ et H₂O. Ces molécules possèdent beaucoup plus de niveaux d'énergie accessibles que H₂ aux mêmes températures. Le coût des calculs de dynamique quantique augmente de manière exponentielle avec le nombre d'états quantiques à prendre en compte, dépassant donc rapidement les limites actuelles des méthodes purement quantiques. Pour cette raison, des méthodes alternatives doivent être proposées, et seules quatre molécules disposent actuellement de données de collision adaptées aux comètes : CO, H₂O, HCN et HF. Cette étude novatrice propose non seulement d'ajouter la molécule CS à cette liste, mais également de développer une méthodologie viable pour le calcul de ces données dans le contexte des atmosphères cométaires.

Dans le cadre de ce travail, les systèmes CS-CO et CS-H₂O ont été étudiés, car CO et H₂O sont les molécules les plus abondantes dans les atmosphères cométaires, respectivement à grande et à courte distance du Soleil.

La SEP du complexe de van der Waals CS-CO a été calculée à l'aide de la méthode CCSD(T)-F12b avec la base d'orbitales atomiques aVTZ. La BSE a été corrigée pour chaque géométrie, et l'ajustement du potentiel a été effectué sur la base des harmoniques bisphériques, grâce à la méthode des moindres carrés mobiles avec interpolation locale. Les méthodes de dynamique quantique ne permettant pas de traiter des systèmes de cette taille, une méthode statistique nouvellement développée a été employée pour ces calculs : la méthode du modèle statistique des canaux adiabatiques (noté SACM). Cette méthode consiste à calculer les canaux adiabatiques du système par diagonalisation de l'Hamiltonien, puis à leur attribuer un poids statistique de 1 ou 0, selon s'ils sont accessible énergiquement ou non. Les canaux adiabatiques ont été obtenus avec MOLSCAT, tandis que la méthode de comptage a été implémentée dans le cadre de cette étude. La validité

de cette approche a été évaluée pour le système CS-CO, où des calculs de dynamique quantique ont également été effectués, bien que limités à l'onde partielle minimale $J = 0$. L'accord entre les taux de collisions calculés en approche Close-Coupling et avec l'approche SACM est excellent, avec une réduction du coût calculatoire d'un facteur 40 en temps et d'un facteur 7 en mémoire par rapport à la méthode quantique. Cette méthode apparaît donc comme une approche prometteuse pour les calculs de données de collisions pour des applications cométaires.

La SEP du complexe de van der Waals CS-H₂O a été obtenu avec la méthode de la théorie de la perturbation adaptée à la symétrie, couplée à la théorie de la fonctionnelle de la densité (noté SAPT-DFT), et avec une base d'orbitales aVTZ. La SEP a été développée sur des harmoniques bisphériques en utilisant une procédure d'ajustement qui repose sur un potentiel site-site. La méthode SACM a également été employée pour les calculs de dynamique. Les canaux adiabatiques ont été calculés avec HIBRIDON, et le comptage a été réalisé en adaptant le code développé lors de l'étude du système CS-CO. La précision des taux de collision ainsi obtenus n'a pas pu être évaluée, car les calculs de dynamique quantique pour ce système restent trop coûteux, même en limitant le nombre d'ondes partielles à $J = 0$.

Les taux de collisions obtenus pour CS-CO et CS-H₂O ont été utilisés dans le code de transfert de rayonnement RADEX afin d'identifier les régions des atmosphères cométaires où ces données sont nécessaires pour une évaluation précise des populations des niveaux d'énergie et, par conséquent, de l'abondance de CS. Cela a également permis d'évaluer l'impact des différents jeux de données sur les populations des niveaux d'énergies de la molécule cible. Les populations ont été impactées différemment selon que CO ou H₂O était considéré comme le principal composant du gaz, soulignant l'importance de calculer les taux de collisions avec ces deux partenaires de collision dans de futures études. De plus, il a été constaté que les données de CS-H₂, souvent utilisées pour modéliser CS dans les atmosphères cométaires par manque de données adéquates, présentaient de grandes différences par rapport aux données de CS-CO et CS-H₂O, induisant des écarts significatifs dans les populations des niveaux d'énergie de la molécule CS. Cela suggère que H₂ ne peut pas être utilisé de manière fiable pour déterminer l'abondance de CS dans les comètes.

En conclusion, ce travail de thèse a permis de déterminer des données de collision essentielles pour une interprétation fiable des observations capturées par les télescopes. Il a également conduit au développement d'une nouvelle méthodologie pour le calcul des

taux de collision dans les atmosphères cométaires, qui a montré d'excellents résultats et semble prometteuse pour de futures études. De plus, la réévaluation de l'abondance des isotopologues de CCS à base de ^{13}C a fourni de nouveaux éléments sur la chimie de cette molécule, et des résultats préliminaires suggèrent que la chimie d'autres molécules pourrait être expliquée de manière similaire.

TABLE OF CONTENTS

List of Figures	i
List of Tables	iii
1 Introduction	1
1.1 Astrochemistry: The Story Behind the Lines	1
1.1.1 Birth and Evolution of Astrochemistry	1
1.1.2 The Evolution of Matter in Space	3
1.1.3 Observing Chemistry in Space	7
1.2 Chemistry in Space	12
1.2.1 The Molecular Inventory: From Atoms to Life?	12
1.2.2 The Three Axes of Astrochemistry	13
1.3 Interpreting Observations	16
1.3.1 Beyond the LTE Approximation	16
1.3.2 State-to-state Rate Coefficients	19
1.4 Outline of the thesis	26
1.4.1 The Missing Sulfur Problem	26
1.4.2 CCS in Dark Molecular Clouds	28
1.4.3 CS in Cometary Atmospheres	30
1.4.4 Organization of the Manuscript	32
2 Theory and Methods	35
2.1 General Aspects	35
2.1.1 Molecular Hamiltonian	36
2.1.2 The Born-Oppenheimer Approximation	37
2.2 The Electronic Problem	39
2.2.1 Hartree-Fock Method	39
2.2.2 Coupled-Cluster Method	45
2.2.3 Basis Set	49
2.2.4 Analytical Representation	53

2.3	Nuclear Motion	55
2.3.1	Collisional Hamiltonian	56
2.3.2	Coordinate Systems	56
2.3.3	Quantum Approaches	58
2.3.4	Statistical Approaches	69
3	Scattering Calculations and Rate Coefficients	73
3.1	Beyond Simple Rotational Structure: CCS Isotopologues in Dark Clouds	73
3.1.1	The Peculiar Fine Structure of CCS Isotopologues	73
3.1.2	Effect of the Complex Fine Structure	86
3.1.3	Effect of the Isotopic Substitution	92
3.1.4	Nuclear Spins and Hyperfine Structure of ^{13}CCS , C^{13}CS and CC^{33}S	94
3.1.5	Discussion	99
3.2	Beyond Quantum Approaches to Study Heavy Collisional Systems: CS in Comets	101
3.2.1	The Challenge of Heavy Projectiles	101
3.2.2	The Collisional Excitation of CS Induced by CO	104
3.2.3	The Collisional Excitation of CS Induced by the H_2O Projectile	116
3.2.4	Discussion About the SACM Method	126
4	Astrophysical applications	133
4.1	Radiative Transfer	133
4.1.1	Radiative Transfer Equations	134
4.1.2	Statistical Equilibrium Equations	135
4.1.3	Escape Probability	136
4.1.4	Useful Quantities	137
4.2	The New Rate Coefficients to Study the Chemistry of CCS	138
4.2.1	CCS in Dark Molecular Clouds: Non-LTE Effects	138
4.2.2	Impact on the Brightness Temperature	145
4.2.3	Revision of CCS Abundances in TMC-1 (CP)	147
4.2.4	Impact on the Chemistry of CCS	151
4.2.5	What About Other ^{13}C -Anomaly?	158
4.3	Cometary Applications: CS in Comae	164
4.3.1	Impact of the Gas Composition	164
4.3.2	Sensitivity of Rate Coefficients to the Colliders	168

4.3.3 Sensitivity of Radiative Transfer Models to Rate Coefficients	179
Conclusion	189
Bibliography	197
A Peer-Reviewed Articles	225
A.1 Rotational Excitation of CO ₂ Induced by He: New Potential Energy Surface and Scattering Calculations	225
A.2 Fine-Structure Excitation of CCS by He: Potential Energy Surface and Scattering Calculations	237
A.3 The Effect of Isotopic Substitution on the Excitation of CCS Isotopologues in Molecular Clouds	248
A.4 Navigating in the Dark	259
A.5 BASECOL2023 Scientific Content	271

LIST OF FIGURES

1.1	The Solar System Formation	4
1.2	The Life Cycle of Stars	5
1.3	The Structure of Comets	6
1.4	Transmission of Electromagnetic Radiation of Earth's Atmosphere	8
1.5	<i>In situ</i> Measurement Missions of Comets	11
1.6	Newly Detected Molecules Over the Years	12
1.7	Abundances of Cometary Molecules Relative to Water	14
1.8	The Three Interdependent Axes of Astrochemistry	15
1.9	Energy Transfer Mechanisms Between Two Energy Levels	17
1.10	Non-LTE Modeling of Methanimine Spectra in Sgr B2	18
1.11	Experimental Integral Cross Sections vs Theoretical Predictions	24
1.12	Experimental Rate Coefficients vs Theoretical Predictions	26
1.13	Maps of HCN and CS in Comet C/2015 ER61	31
2.1	Representation of Collisional Systems in Jacobi coordinates.	53
2.2	The Space-Fixed Coordinate System	57
2.3	Convergence Test of the j_2^{MAX} Parameter	68
2.4	Adiabatic Potential Energy Curves	71
3.1	Hund's Case (a) and Hund's Case (b)	75
3.2	CCS Fine Structure Energy Levels	79
3.3	Isotopologues of CCS in Collision with He in Jacobi Coordinates	81
3.4	CCS-He Potential Energy Surface	83
3.5	CCS-He Rate Coefficients for Transitions Within Low- N_j vs High- N_j Levels	86
3.6	Accurate vs Approximate Fine-Structure Resolved Rate Coefficients	89
3.7	Rotational Rate Coefficients Computed with CCS-He PES vs OCS-H ₂ PES	91
3.8	Effect of the Isotopic Substitution on CCS-He Rate Coefficients	93
3.9	Propensity Rules of ¹³ CCS and C ¹³ CS Hyperfine Rate Coefficients	97
3.10	Propensity Rules of CC ³³ S Hyperfine Rate Coefficients	98

3.11	Comparison Between ^{13}CCS and C^{13}CS Hyperfine Rate Coefficients	99
3.12	CS-CO Collisional System in Jacobi Coordinates	105
3.13	CS-CO Potential Energy Surface	107
3.14	CS-CO Rate Coefficients Computed With Full vs Truncated Basis	109
3.15	CS-CO Adiabatic States	110
3.16	Verification of the Detailed Balance Principle for the CS-CO Rate Coefficients.	111
3.17	CC vs SACM CS-CO State-to-State Rate Coefficients	113
3.18	CC and SACM CS-CO Thermalized Rate Coefficients	114
3.19	Propensity Rules of CS-CO Rate Coefficients	115
3.20	CS-H ₂ O in Jacobi Coordinates	117
3.21	CS-H ₂ O Potential Energy Surface	120
3.22	CS-p-H ₂ O and CS-o-H ₂ O Rate Coefficients Computed with Full vs Truncated Basis	123
3.23	CS-p-H ₂ O and CS-o-H ₂ O Adiabatic States	124
3.24	Verification of the Detailed Balance Principle for CS-p-H ₂ O and CS-o-H ₂ O Rate Coefficients.	125
3.25	CS-p-H ₂ O and CS-o-H ₂ O Thermalized Rate Coefficients	126
4.1	Excitation Temperatures of CCS and CC^{34}S in Dark Molecular Clouds	141
4.2	Excitation Temperatures of ^{13}CCS and C^{13}CS in Dark Molecular Clouds	144
4.3	Brightness Temperatures of CCS in TMC-1 (CP)	146
4.4	Herschel's View of Taurus Molecular Cloud	148
4.5	^{13}CCS and C^{13}CS Emission Spectra Toward TMC-1 (CP)	153
4.6	Energetic Diagram Representing C^{13}CS and ^{13}CS	155
4.7	Schematic Representation of the Zero-Point Energy	156
4.8	Energy Profile of the $\text{CCS} + \text{H}$ Reaction	156
4.9	Observed Abundance Ratio vs Abundance Ratio Predicted From ZPE for Species Presenting a ^{13}C -Anomaly	159
4.10	^{13}C isotopologues of c-C ₃ H ₂	160
4.11	Rate Coefficients of CS-CO vs CS-o/p-H ₂ O.	165
4.12	Population of CS Energy Levels in Cometary Comae for Different Gas Composition	167
4.13	Rate Coefficients of CS Induced by Collisions with Different Projectiles.	169
4.14	Rate Coefficients of CS-CO vs CS-o/p-H ₂	171

4.15 Comparison between Rate Coefficients of CS-o/p-H ₂ O and CS-o/p-H ₂ . . .	172
4.16 Rate Coefficients of CS-CO vs CO-CO.	174
4.17 Rate Coefficients of CO-H ₂ O vs CS-H ₂ O.	175
4.18 Rate Coefficients of HCN-H ₂ O vs CS-H ₂ O.	176
4.19 Rate Coefficients of HF-H ₂ O vs CS-H ₂ O.	178
4.20 Population of CS Energy Levels in Comae using CS Rate Coefficients with Different Projectiles	180
4.21 Population of CS Energy Levels in Comae using CS-CO and CO-CO Rate Coefficients	183
4.22 Population of CS Energy Levels in Comae using CS-H ₂ O and CO-H ₂ O Rate Coefficients	184
4.23 Population of CS Energy Levels in Comae using CS-H ₂ O and HCN-H ₂ O Rate Coefficients	185

LIST OF TABLES

1.1	Sulfur-Bearing Molecules Detected in the ISM and Comae	27
3.1	Spectroscopic Constants of CCS Isotopologues	74
3.2	Fine Structure Energy Levels of CCS and Its Isotopologues	78
3.3	Energy levels of CS and CO	102
3.4	Energy Levels of H ₂ O	104
3.5	Convergence Parameters for CC calculations with MOLSCAT for the CS-CO System	112
3.6	Summary of previous studies that employed the SACM approach to treat the scattering of non-reactive systems.	131
4.1	Column Densities of CCS Isotopologues Towards TMC-1 (CP)	149

INTRODUCTION

It seems very reasonable to consider the probability of the existence of [...] polyatomic molecules as negligible and to rule out.

Eugene H. Eyster, 1937

1.1 Astrochemistry: The Story Behind the Lines

1.1.1 Birth and Evolution of Astrochemistry

Astrochemistry is a relatively young field of research that focuses on the molecular complexity in astrophysical media. Its main goals are the understanding of the formation of stars and planets, and the emergence of life on Earth. It is done through the study of the chemistry and of the chemical composition of various astrophysical environments, such as the interstellar medium (the space between stars, hereafter noted ISM), comets, circumstellar and circumplanetary regions.

The Existence of Molecules in Space: a Subject of Intense Debate

At the beginning of the 20th century, it was observed that light from distant stars was slightly attenuated as it traveled through the ISM (King, 1915). The cause of this attenuation was the subject of intense debate for decades. Observations of fixed lines in the spectra of different stars suggested that these lines originated from a diffuse gas cloud located between the observer and the stars, rather than from the stars themselves.

It was proposed to be absorption lines from molecular species, but as the existence of molecules in the ISM seemed improbable, many scientists argued that they should be artifacts (Eyster, 1937). They asserted that even if molecules did exist, they would be broken apart by the intense radiation fields emitted by stars traveling through the ISM. Given the extremely low density of this space, the probability of these atoms recombining to form new molecules was considered too low (Eddington, 1926). At that time, they did

not know the role of H₂ and dust in the shielding of UV-photons,¹ protecting molecules from dissociation.

The debate should have been settled in the late 1930s and early 1940s with the confirmed detection of CH by McKellar (1940) already suggested by Swings & Rosenfeld (1937). In their study, McKellar (1940) also reported the detection of CN. Based on new laboratory measurements, Douglas & Herzberg (1941) attributed interstellar lines observed by both Dunham (1937) and McKellar (1940) to the CH⁺ cation. Despite these three detections, the search for astromolecules was still not widespread as scientists were generally not convinced of their existence (Yamamoto, 2017).

Nearly two decades later, Townes (1957) suggested the use of microwave radiation to investigate the presence of molecules in the ISM, but his proposal initially did not receive much attention from the scientific community. However, the technological advancements in radar and radio communication during World War II significantly contributed to the development of radio astronomy. Consequently, 20 years after the first detection of a molecule in the ISM, OH, the fourth interstellar molecule, was detected by Weinreb et al. (1963) through radio observations.

The excitement about molecules in space really started with the NH₃ detection by Cheung et al. (1968), closely followed by the detection of H₂O by Cheung et al. (1969). Astronomers started to realize that very familiar molecule could be found in space. Indeed, very usual Earth species were detected, as CO (Wilson et al., 1970), H₂ (Carruthers, 1970), or NO (Liszt & Turner, 1978). The first organic molecule, H₂CO (formaldehyde), was detected by Snyder et al. (1969). A few years later, the first Complex Organic Molecule (COM) molecule, defined as a molecule containing six or more atoms including one carbon, was detected with the identification of methanol (CH₃OH) by Ball et al. (1970). With the increasing capabilities of ground- and space-based observational facilities, more and more complex chemical species were detected, and more are expected to be discovered in the future.

¹H₂ and dust will absorb and scatter UV photons, protecting the inner-layers of the clouds from UV radiation. It allows for the survival and stability of more complex molecules within molecular clouds.

1.1.2 The Evolution of Matter in Space

The Different Phases of the ISM

In our Galaxy, 90% of the visible matter is gathered in stars. Therefore, the ISM is only 10% of its mass. Despite its low fraction, this matter plays a very important role on the formation and evolution of stars. It is composed of 99% of gas, and about 1% of dust grains of about $0.1\mu\text{m}$ in size that are mostly silicates and carbonaceous compounds possibly surrounded by ice.

Hydrogen and He, which were formed a few minutes after the Big Bang, represents about 90% and 8.5% of the chemical elements, respectively. The rest is mostly second raw elements (C, N, O, F), Ne, Si, S and Fe, which abundances varies according to nucleosynthetic processes taking place in stars [Yamamoto (2017) and refs therein].

The distribution of the matter in the ISM is far from homogeneous, and is instead gathered into clumps and filaments, often referred to as clouds. The ISM is composed of several phases. First is the coronal gas phase, characterized by extremely high temperatures ranging from 10^6 to 10^7 K and extremely low density of $\sim 0.001\text{ cm}^{-3}$. In this stage, the matter is highly ionized and the principal component is H^+ .

As the coronal gas slowly cools down, electronic recombination of the chemical elements (mostly hydrogen) begins to occur, and the coronal gas transitions into an intercloud gas. In this phase, the temperature is between 10^3 and 10^4 K and the density is relatively low, ranging from a ~ 0.1 to 10 cm^{-3} .

Where most of the elements have recombined, the temperature drops to about 50 to 100 K, and the density reaches approximately 10^2 cm^{-3} , forming diffuse clouds. Within those clouds, molecular hydrogen (H_2) begins to form and coexists with hydrogen atoms. As the temperature further decreases, the density of the medium increases, gradually becoming opaque to UV radiation due to H_2 shielding² (Draine, 2011). When the molecular hydrogen density becomes higher than the atomic one, a dense molecular cloud has formed. Typical dense clouds are cold, with temperatures ranging from 5 to 50 K, and are relatively dense, between 10^3 to 10^6 cm^{-3} .

As represented in Figure 1.1, the densest cores within these clouds undergo gravitational collapse, resulting in the formation of a rotating accretion disk with a density peak

² H_2 will absorb and scatter UV photons, protecting the inner-layers of the clouds from UV radiation. It prevents excessive heating and destruction of molecular species.

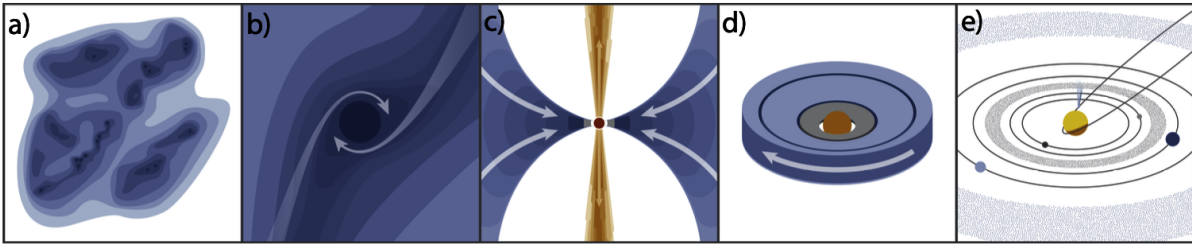


Figure 1.1: Cartoon of the different stages characterizing low-mass (Solar-like) star and planet formation taken from Öberg & Bergin (2021). (a) Dense cores of molecular clouds where star will form. (b) The dense core starts to collapse under its own gravity. (c) As the collapse proceeds, the center heats up forming a protostar. Accretion of remnant cloud material continues, funneled through a disk. (d) Once the remnants of the gas and dust cloud have dispersed, the young star, in its pre-main sequence phase, is surrounded by a circumstellar disk where planet formation takes place. (e) After gas disk dissipation and the final stages of terrestrial planet formation, a planetary system emerges. Image credit: K. Peek.

at its center, where a protostar will light up. The inner-disk will fall inward and add material onto the growing star (Draine, 2011). As the protostar evolves, it becomes a main-sequence star surrounded by a protoplanetary disk. Within this disk, dust begins to aggregate into planetesimals from which planets, asteroids, and comets eventually form.

The Life Cycle of Stars

Within the stars, hydrogen undergoes nuclear fusion, forming heavier chemical elements. After hydrogen burning is completed, the star evolves to a late-stage star. The end of a star’s life depends on its mass. For sun-like stars, their outer layers are ejected, and the star loses most of its matter, creating a planetary nebula (similar to intercloud gas), which supplies gas and dust to the ISM. The remaining core, called a white dwarf, illuminates the ejected material and will cool and fade over billions of years.

High-mass stars (at least eight times the mass of the Sun) undergo a supernova explosion, one of the most energetic processes in the Universe. The core of the star collapses, becoming either a neutron star (very compact, with a diameter of only a few kilometers) or a black hole, depending on the mass of the collapsing core during the supernova explosion. All the elements synthesized within the star, including heavier elements formed during the explosion, are ejected into the ISM. This enriches the ISM with new elements, and the gas returns to its coronal-gas stage. This cycle illustrates how matter circulates through the life cycles of stars, summarized in Figure 1.2.

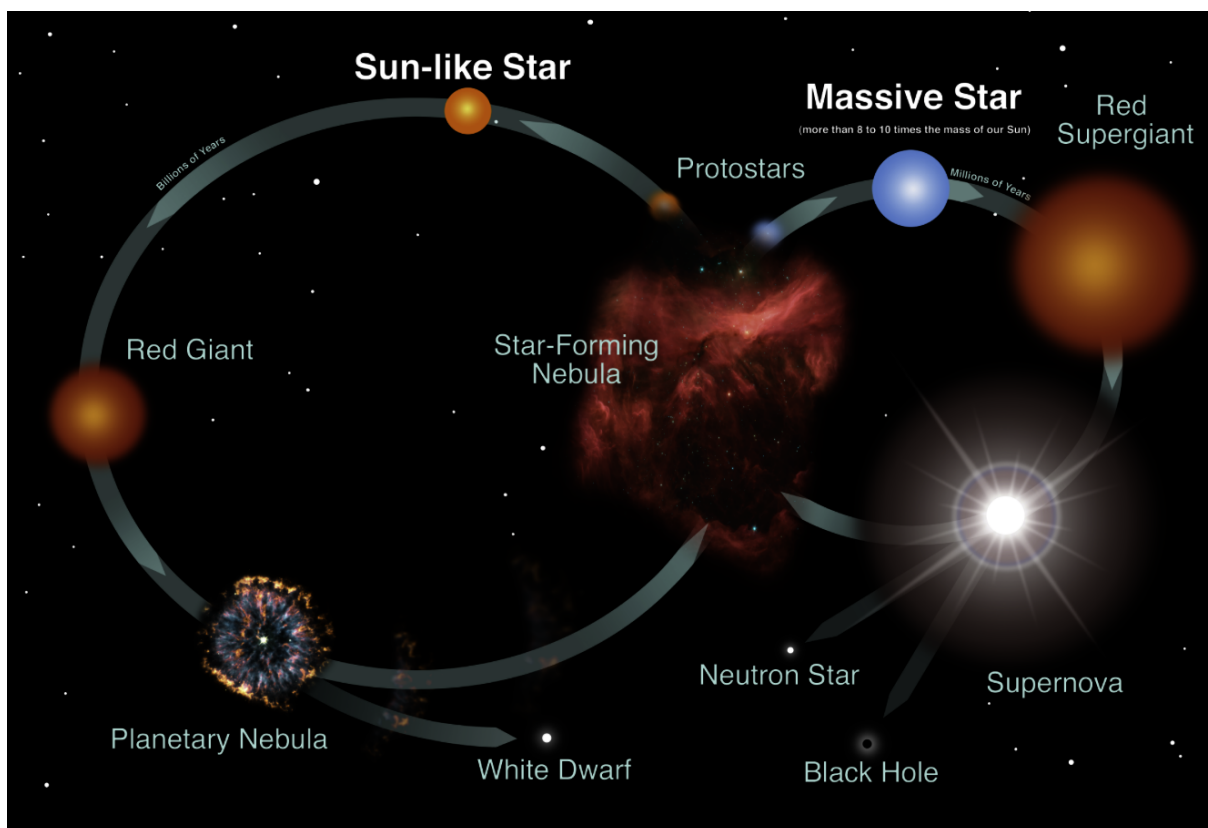


Figure 1.2: The life cycles of Sun-like and massive stars. Credits: NASA and the Night Sky Network.

Comets: The Fossils of the Solar System

The nucleus of a comet, which is few km in size, is composed of rocks (silicates and carbonaceous compounds) surrounded by ices (mainly H_2O , CO and CO_2) (Filacchione et al., 2016a; Filacchione et al., 2016b; Bockelée-Morvan & Biver, 2017)) with approximately a 1:1 mass ratio (A’Hearn, 2008). Therefore, as a comet approaches the Sun, the ices contained in its nucleus start to sublimate, forming an atmosphere surrounding the nucleus called the (cometary) coma. Closer to the Sun, dust particles are ejected, thus forming the dust tail. Ions are accelerated by the solar wind, forming the ion tail, which points in the opposite direction to the Sun. The dust tail, however, is composed of solid particles and traces a broad, gently curving path behind the comet. Cometary comae can span several hundreds of thousands of kilometers in size, and their ion tails can stretch to over an astronomical unit in some cases (Neugebauer et al., 2007).

Figure 1.3 presents both a photography of the Comet 12P/Pons-Brooks which was

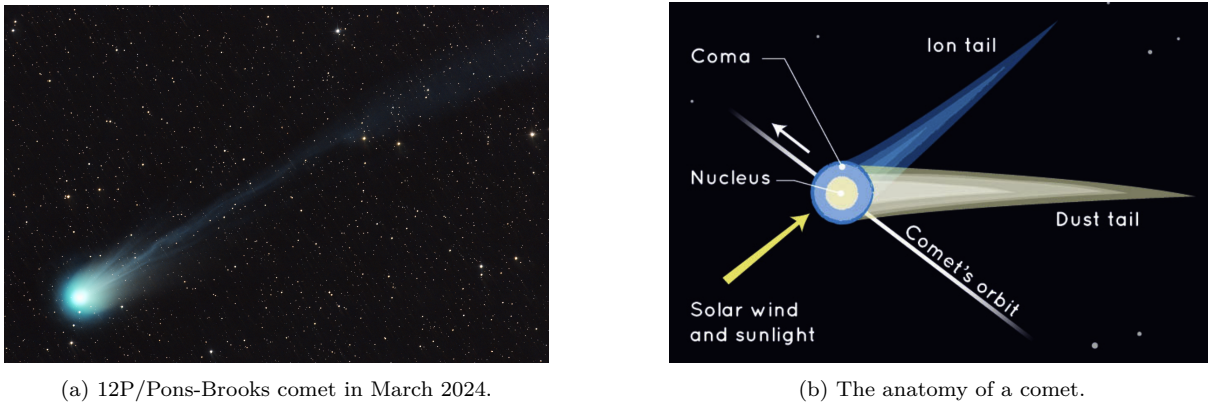


Figure 1.3: The structure of comets. Credits: (a) Nielanders via Wikimedia Commons ; (b) NASA/JPL-Caltech.

visible from Earth in March 2024 in Figure 1.3a and a schematic representation of the structure of a comet in Figure 1.3b.

The temperature in the coma decreases from approximately 200 K (the water sublimation point) to around 10 K due to the adiabatic expansion of the gas. The gas then warms up again due to photodissociation heating from solar radiation. The density within the coma strongly varies with the distance from the nucleus, ranging from 10^{12} cm^{-3} to less than 1 cm^{-3} (Despois et al., 2006). The dominant component in the coma is usually water, but CO becomes dominant for comets at large heliocentric distances $\geq 4 \text{ au}$, where the temperature is too low for water to sublime (Despois et al., 2006).

Comets in our solar system were formed from the gas, dust, and ices surrounding the Sun at its birth, approximately 4.6 billion years ago. Ejected into their reservoirs outside the solar system during planet formation, their chemical composition is expected to have remained largely unchanged since then. Consequently, they serve as excellent tracers of the chemical and isotopic composition of the solar protoplanetary disk (Mumma & Charnley, 2011). These objects are thought to play an important role in the habitability and emergence of life on Earth. One hypothesis is that they would have delivered water and other volatiles, such as amino acids, to Earth through impacts. Therefore, it is crucial to study their chemical composition, as they are not only fossils of the Early Solar System but also potential triggers for the emergence of life on Earth (Ceccarelli et al., 2014).

Comets are typically classified into three categories by their origin and orbital periods: Jupiter Family Comets (JFCs), Oort Cloud Comets (OCCs), and Halley-Type Comets (HTCs). JFCs are short-period comets (less than 20 years), thought to have formed outside Neptune's orbit and are stored in the Kuiper Belt (KB). OCCs are long-period

comets (greater than 200 years), formed in the giant-planet feeding zone and were ejected into the Oort Cloud (OC), where they are stored. HTC's are intermediate-period comets (between 20 and 200 years) and can come from either the KB or the OC.

1.1.3 Observing Chemistry in Space

Remote Observations

Besides extremely few exceptions,³ astrophysical environments are out of reach, and their chemical and physical conditions cannot be directly probed. Even in our Solar System, it takes years to reach relatively close objects. For example, the current Jupiter Icy Moons Explorer (JUICE) mission (Grasset et al., 2013), launched in April 2023, is expected to reach Venus in August 2025, and finally Jupiter in 2031. Therefore, our knowledge of the Universe relies almost exclusively on remote observations performed with ground and space-based observational facilities that capture molecular spectra from the astrophysical media they target.

Currently, ~90% of molecular detections have been made at radio, centimeter, millimeter (mm), and sub-mm wavelengths (McGuire, 2022), meaning that most molecules have been detected through rotational emission or absorption. Radio telescopes are without doubt game-changers for the study of chemistry in the ISM (Fortenberry, 2024a). The huge advantage of radio spectroscopy is that molecules can be observed in both emission or absorption against the background radiation field continuum of the media (either the Cosmological Microwave Background, or the radiation field from nearby stars). However, a major weakness is that radio telescopes are completely blind to symmetric molecules, as the strength of a rotational transition is proportional to the square of the permanent electric dipole moment of the molecule. Thus, such transitions will be invisible for highly symmetric molecules such as H₂, CO₂, or CH₄. In addition, only gas-phase molecules can be detected, as molecules in the condensed phase cannot freely rotate.

Infrared (hereafter IR) astronomy can overcome these limitations since it allows the identification of highly symmetric molecules by detecting vibrational transitions. Molecules are detected through vibrational transitions where the vibrational state breaks the symmetry of the molecule, thus inducing a dipole moment. However, as vibrational states are much higher in energy, these detections can occur only in warmer regions. In some excep-

³Planetary systems, asteroids and comets can be directly probed, e.g., JUICE, ROSETTA and OSIRIX-REx missions.

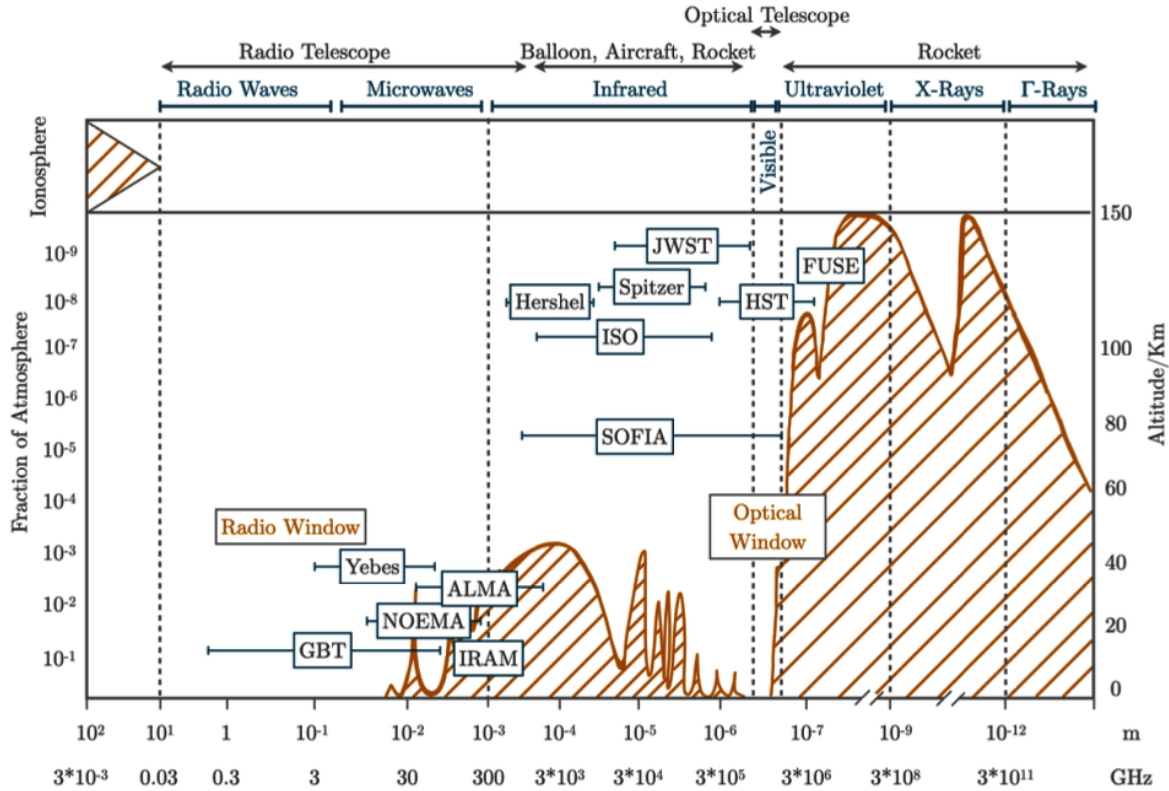


Figure 1.4: Transmission of the Earth’s atmosphere for electromagnetic radiation. The orange trace indicates the altitude at which the radiation is attenuated by 50%. This figure was taken from Tonolo (2024) adapted from Rohlfs & Wilson (2004).

tional cases, vibrationally excited molecules can be observed in cold environments, as seen with C_6H in Taurus Molecular Cloud 1 (hereafter TMC-1) (Cernicharo et al., 2023). IR astronomy also provides a unique window into the molecular content of condensed-phase materials in the ISM, as vibrational transitions are accessible in the condensed phase.

However, the Earth’s atmosphere is very opaque to sub-mm and far-IR wavelengths, as illustrated in Figure 1.4. It is due to the absorption of these wavelengths by water vapor present in the atmosphere, making ground-based observations very complex. Thus, IR observations are often space-based, as with the Herschel Space Observatory (HSO), the James Webb Space Telescope (JWST), or the Stratospheric Observatory for Infrared Astronomy (SOFIA). Although SOFIA is not space-based, it operates from a high-altitude aircraft to acquire data from above the thickest layers of Earth’s atmosphere.

The Earth’s atmosphere is strongly opaque to UV wavelengths due to ozone (O_3) and dioxygen (O_2) absorption, so space-based observatories such as the Hubble Space

Telescope (HST) and the Far Ultraviolet Spectroscopic Explorer (FUSE) are employed for UV-visible wavelengths observations.

Currently, the Yebes 40m, IRAM 30m,⁴ Nobeyama 45m, Green Bank Telescope (GBT) 100m, and the Atacama Large Millimeter/sub-millimeter Array (ALMA) are among the most widely used ground-based facilities for detecting new molecules. Unlike space-based telescopes, ground-based instruments can undergo regular maintenance and upgrades, allowing their performance to improve over time.

***In situ* Measurements**

As already mentioned, only a few types of astrophysical media can be probed by *in situ* measurements. These include planetary systems (e.g., CURIOSITY, Voyager 1 & 2, JUICE), asteroids (e.g., OSIRIS-REx, which directly sampled the Bennu asteroid), and comets. I will focus on cometary missions as part on my PhD thesis was devoted to the study of comae.

In the past, four missions have allowed for *in situ* measurements in comets: the Giotto, Deep Impact (EPOXI), Stardust, and Rosetta missions. They were probing comets 1P/Halley (hereafter Halley), 9P/Tempel and 103P/Hartley, 81P/Wild2 and 9P/Tempel again, and 67P/Churyumov-Gerasimenko (hereafter 67P), respectively.

Giotto, ESA's first deep-space mission, conducted a close fly-by of Halley's Comet's nucleus in 1986. This historic mission achieved the closest approach to any astrophysical object by a spacecraft at that time, capturing the first detailed images of a cometary nucleus. The images, shown in Figure 1.5a, are crucial as they reveal the size and shape of Halley's nucleus, providing unprecedented insights into the structure of comets.

The Deep Impact mission aimed at probing the cometary material beneath the surface of a comet. It provided an opportunity to study inner-layer material that had not been altered by thermal radiation from the Sun. The mission revealed new insights into the comet's composition, including the structure and density of its nucleus (A'Hearn et al., 2005). The spacecraft reached the comet 9P/Tempel 1 in July 2005, deploying an impactor that collided with the comet (Figure 1.5b). This collision produced an explosion equivalent to 4.7 tons of TNT and created a crater approximately 150 meters in diameter, allowing for the study of ejected material from beneath the surface.

⁴IRAM stands for Institut de Radioastronomie Millimétrique, or Institute of Millimetric Radioastronomy.

Stardust was the first mission to return samples from a comet and, more generally, from extraterrestrial objects beyond the Moon's orbit. In 2004, the spacecraft made a close flyby of comet 81P/Wild 2, collecting cometary and interstellar dust. The samples returned to Earth two years later (see Figure 1.5c) providing an unprecedented window into the composition of cometary refractory materials. They revealed a complex mixture of aromatic and aliphatic compounds similar to that found in interplanetary dust particles and meteorites. The samples also showed enrichment in deuterium and heavy nitrogen, indicating a primordial origin, as these isotopologues are favored in the cold temperatures of the solar nebula (Sandford et al., 2006). The major discovery was the first identification of $C_2H_5NO_2$, an isomer of –the simplest amino acid and a key building block of life– supporting the idea that the fundamental building blocks of life are prevalent in space (Elsila et al., 2009).

The Rosetta mission, ESA's comet chaser, was the first spacecraft to orbit a comet and fly alongside it as it headed towards the inner Solar System. It was also the first to closely examine the activity of a comet as it was warmed by the Sun, enhancing our understanding of comet dynamics. Rosetta deployed the Philae lander on the surface of comet 67P/Churyumov-Gerasimenko, providing the first images from the surface of a comet. The mission lasted almost two years before the spacecraft deliberately crashed on the comet's surface to maximize its scientific return. With this mission, 44 new cometary molecules were detected,⁵ including one isomer of glycine (Altwegg et al., 2016), thus almost doubling the number of known cometary molecules and unveiling a chemistry much more complex than what is observed from telescopes.

The future Comet Interceptor mission aims to study a comet that has never entered the inner Solar System. This will reveal the chemical composition of a comet's ices before any perturbation from the Sun's radiation since its formation and storage in its reservoirs. Its launch is planned for 2029.

In situ measurements allow to probe materials that are invisible to spectroscopic observations, as demonstrated by the Deep Impact, Stardust and Rosetta missions. Additionally, they introduce less bias in the analysis since they represent "direct" measurements. This is particularly important for comets, which are highly dynamic objects. Spectroscopy techniques capture only shots of a comet at one or a few points in time. However, strong evidence has been found on the influence of heliocentric distance on the volatile com-

⁵<http://www.astrochymist.org>, Credits: D. E. Woon.



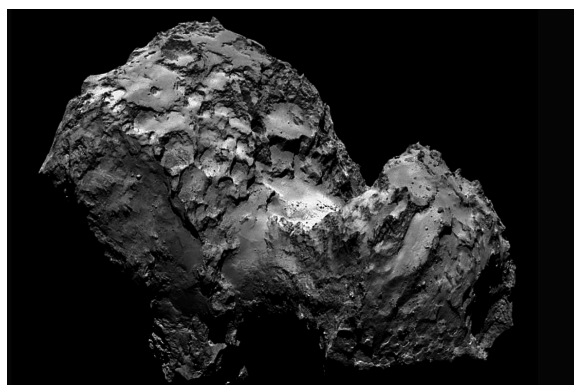
(a) Halley comet photographed by the Giotto spacecraft in 1986.



(b) 9P/Tempel 1 comet 67 seconds after Deep Impact collision on July 4, 2005.



(c) Examination of the aerogel from the Stardust mission in 2006.



(d) Photo of comet 67P taken by Rosetta on August 6, 2014.

Figure 1.5: *In situ* measurement missions for the investigation of comets in our Solar System. Credits: (a) Halley Multicolor Camera Team, Giotto Project, ESA ; (b) NASA/JPL-Caltech/UMD ; (c) NASA ; (d) ESA.

position of the coma, making it difficult to draw strong conclusions about the chemical composition of their ices (Biver et al., 2022).

The limitation of *in situ* measurements for studying molecules in comets is that mass spectrometry, the technique employed for detection, cannot differentiate between isomers. This technique works by ionizing chemical compounds to produce charged molecules or molecular fragments and then measuring their mass-to-charge ratio (m/z). While this allows for precise identification of a molecule's atomic constituents, it cannot distinguish between different isomers. For instance, the detection of 'glycine' (Elsila et al., 2009; Altwegg et al., 2016) cannot be definitively attributed to the amino acid itself, as many isomers of glycine exist, including the conformer remotely observed by Rivilla et al. (2023). Although spectroscopy has its own limitations, it is a more sensitive technique that can

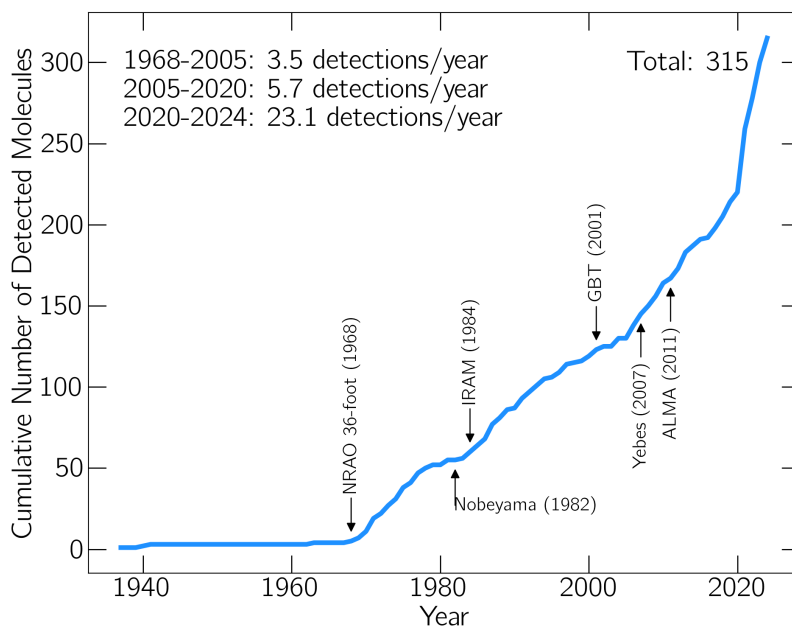


Figure 1.6: Newly detected molecules over the years. Only confirmed detections have been included. It has been updated in September 2024 from McGuire (2022) based on downloadable Python 3 package ASTROMOL (McGuire & mcguiregroup, 2021), accessible at <https://github.com/bmcguir2/astromol>.

identify specific molecules rather than just their atomic composition. Thus, these two approaches are complementary.

1.2 Chemistry in Space

1.2.1 The Molecular Inventory: From Atoms to Life?

To date, over 310 molecules have been detected in the ISM or circumstellar shells (updated in September 2024).⁵ The detection rate per year has been strongly increasing over the past four years, as seen in Figure 1.6. Currently, approximately 20 new molecules have been detected per year since 2020, with a record of 42 new detections in 2021. As of September 2024, 17 new detections have been reported for this year.

These detections include simple molecules, such as diatomic and triatomic molecules like H_2 (Carruthers, 1970), CO (Wilson et al., 1970), N_2 (Knauth et al., 2004), CO_2 (D’Hendecourt & Jourdain de Muizon, 1989), and NH_2 (van Dishoeck et al., 1993). More complex molecules are also detected including long-carbon chains such as cyanopolyynes

HC_nN (with n odd $\in [3; 11]$), Polycyclic Aromatic Hydrocarbons (PAHs) with the detection of (1 and 2)- $\text{C}_{10}\text{H}_7\text{CN}$ and C_9H_8 , fullerenes (carbon cages) with C_{60} and C_{70} (Cami et al., 2010), and C_{60}^+ (Berné et al., 2013).

Last year, the first isomer of glycine, $\text{NH}_2\text{C}(\text{O})\text{CH}_2\text{OH}$, has been detected in a star-forming region (Rivilla et al., 2023). This is so far the closest the astrochemical community has come to detect an amino acid in the ISM. This detection is significant because amino acids are considered the first building blocks of life, as they are the fundamental components of proteins, from which DNA can be built.

In cometary comae, 104 molecules have been detected through both *in situ* and remote spectroscopic observations,⁵ including hydrocarbons like CH_4 and C_2H_6 , simple organic molecules (e.g., H_2CO , H_2CS , NH_3) but also COMs (e.g., CH_3OH , HCOOCH_3 , NH_2CHO). The abundances of the most common molecules relative to water are shown in Figure 1.7. Cometary atmospheres show significant diversity in their chemical abundances relative to water. These variations could result from different formation conditions, which lead to varying chemical compositions of the ices. Alternatively, they may be due to the comets being observed at different heliocentric distances, which affect the outgassing molecules based on their different sublimation points (Biver et al., 2022).

The chemical species in cometary comae can be categorized into two groups: parent molecules, directly outgassing from the nucleus ices, and daughter species, which are products of the parent molecules. Differentiating between parent species and products is crucial for inferring the chemical composition of the ices. However, the origins of some observed molecules remain unclear (e.g., SO , CS , S_n) and, in some cases, are simply unknown (e.g., NS) (Biver et al., 2022).

1.2.2 The Three Axes of Astrochemistry

As new astromolecules were discovered, the question about the chemical processes forming/destroying these molecules emerged. Astrochemists started to build out chemical networks to match the observed molecular abundances and predict future detections. Many predicted molecules were detected, and many were not. The models are constantly refined accordingly, also fed by reference data generated by the laboratory astrophysics community.

Astrochemistry is by nature a strongly interdisciplinary field. As illustrated in Figure 1.8, it relies on three main axes:

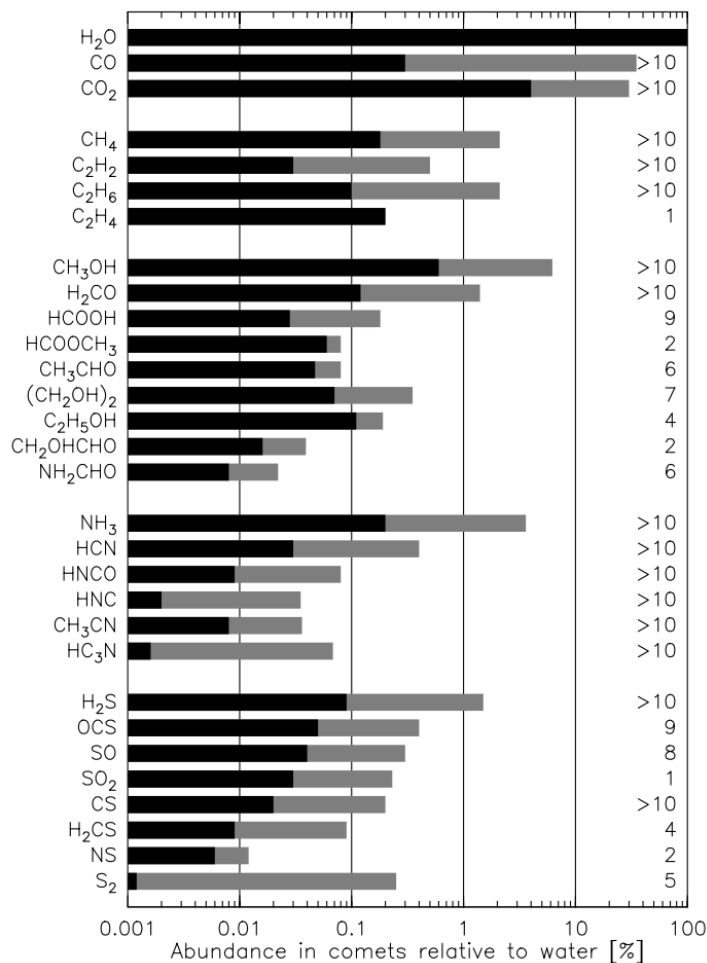


Figure 1.7: The range of abundances relative to water for commonly observed molecules in cometary comae, as detected by remote observations, is shown. The number of comets in which each molecule has been detected is indicated to the right. This Figure was taken from Biver et al. (2022).

- **Observations**, aiming at answering the questions of **which molecules** are present in space and **their respective abundances**,
- **Astrochemical modeling**, studying **how these molecules form and are destroyed** by reproducing their observed abundances,
- **Laboratory astrophysics**, which produces both **experimental and theoretical reference data** on which the previous axes rely on,

All three axes are strongly interdependent. For example, new detections must be based on comparisons with laboratory spectra. Astrochemical models require reaction rate constants for the formation and destruction of all species included in the chemical network

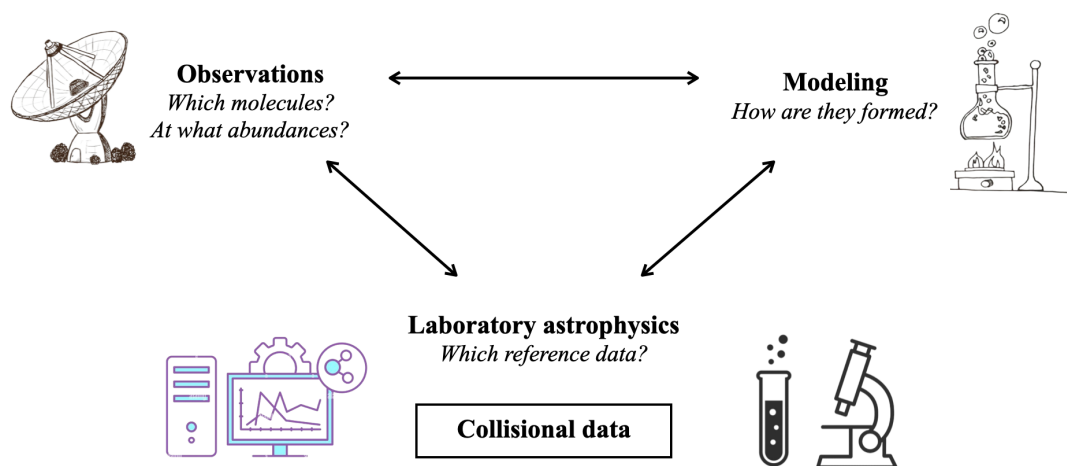


Figure 1.8: The three interdependent axes of astrochemistry.

to accurately reproduce the observed abundances of chemical species. However, a reliable determination of these abundances requires a robust interpretation of the observations using excitation models based on accurate molecular data.

This thesis focuses on this latter aspect. Accurate interpretation of observations often depends on detailed excitation models, as Local Thermodynamic Equilibrium (LTE) conditions are typically not maintained in most astrophysical environments. Therefore, determining the population of energy levels requires considering all energy transfer mechanisms, so the competition between collisional and radiative processes. However, collisional data are not available for all detected molecules, which limits the accuracy with which observations can be interpreted. This thesis aims to generate the missing collisional rate coefficients and develop new methodologies to facilitate the production of these data for future studies.

Laboratory astrophysics must respond to the needs of both observational astronomy and astrochemical models, focusing on key species since not all data can be produced as quickly as observations are made. Therefore, having a comprehensive understanding of astrochemistry is crucial for prioritizing the most significant issues, potentially unlocking multiple insights rather than just focusing on a single isolated molecule.

1.3 Interpreting Observations

Interpreting observations to determine molecular abundances is crucial for understanding the chemistry and physical conditions in astrophysical media. This process typically involves using radiative transfer models, which, based on a given set of physical conditions, calculate line intensities that can then be compared to observations.

1.3.1 Beyond the LTE Approximation

To simulate the emission or absorption lines from molecular species, the radiative transfer equations—governing how radiation propagates through a medium—must be solved. However, the interaction of molecules with radiation depends on the populations of their energy levels.

In regions where the density is high enough for Local Thermodynamic Equilibrium (LTE) conditions to prevail—where collisions dominate molecular excitation—the population of energy levels will simply follow a Maxwell-Boltzmann distribution.

However, the density in astrophysical media is generally insufficient to maintain LTE conditions. Therefore, the populations of the energy levels of molecules are determined by solving the statistical equilibrium equations. These equations describe the balance between energy transfer mechanisms based on physical conditions such as kinetic temperature, gas density, and the background radiation field.

In astrophysical media, molecules move due to the temperature and collide with each other, exchanging energy through these collisions. In addition, they can absorb photons emitted by surrounding radiation fields, originating from nearby stars, the cosmic microwave background (CMB), or emitted by other molecules. These interactions change the population of energy levels, which in turn changes the background radiation field. Therefore, these statistical equilibrium and radiative transfer sets of equations must be solved iteratively until convergence is reached.

The population of molecular levels is governed by the competition between collisional and radiative processes. These processes are illustrated in a two-level system example in Figure 1.9.

To accurately model the population of energy levels, both the Einstein coefficients B_{lu} , B_{ul} , and A_{ul} describing radiative processes, and collisional rates C_{lu} and C_{ul} , describing

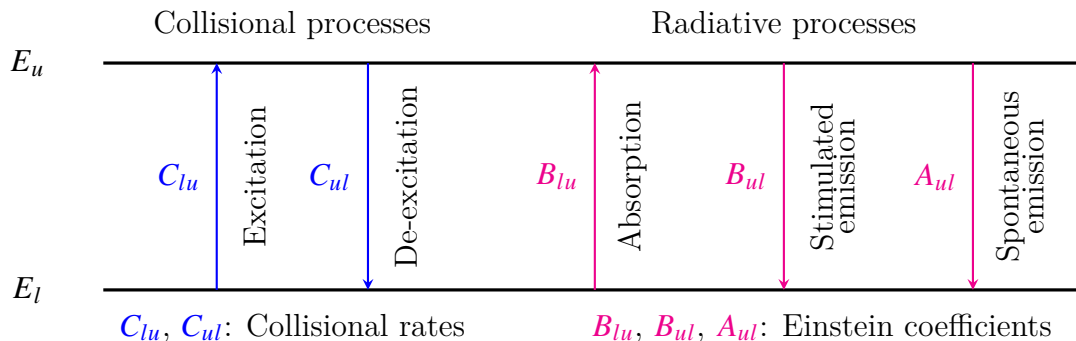


Figure 1.9: Processes involved in the distribution of population in a two-level system. B_{lu} , B_{ul} , and A_{ul} are the Einstein coefficients for absorption, stimulated emission, spontaneous emission of photons, respectively; C_{lu} and C_{ul} are the temperature-dependent collisional rates for transitions between levels l and u due to collisions with gas particles.

collisional processes, must be known.

Einstein coefficients are available for most detected molecules, including some isotopologues, in databases such as the CDMS database⁶ (Müller et al., 2001; Müller et al., 2005; Endres et al., 2016), and Jet Propulsion Laboratory (JPL) database⁷ (Pickett et al., 1998). These coefficients are often derived from experimental measurements. State-to-state rate coefficients are available for about 70 detected molecules and some of their isotopologues in databases such as BASECOL⁸ (Dubernet et al., 2024), the Leiden Atomic and Molecular Database (LAMDA)⁹ (Schöier et al., 2005), and Excitation of Molecules and Atoms for Astrophysics database (EMAA)¹⁰ (Faure et al., 2021). These datasets, however, are often incomplete in terms of collisional partners and temperature ranges.

Interpreting observations using the LTE approximation can lead to inaccurate estimates of molecular abundances. In Faure et al. (2018), the $j_{k_a k_c} = 1_{10} \rightarrow j'_{k'_a k'_c} = 1_{11}$ transition of methanimine (CH_2NH) was modeled using radiative transfer models based on detailed excitation models with accurate radiative and collisional data. The best fit was obtained for an abundance of methanimine that was four to ten times lower than what was predicted based on LTE assumptions by Halfen et al. (2013). If this accurate abundance is used, a spectrum modeled with LTE would completely fail to reproduce the observed methanimine spectrum, as shown in Figure 1.10.

⁶<https://cdms.astro.uni-koeln.de/cdms/portal/>

⁷<https://spec.jpl.nasa.gov>

⁸<https://basecol.vamdc.eu>

⁹<https://home.strw.leidenuniv.nl/~moldata/>

¹⁰<https://emaa.osug.fr/>

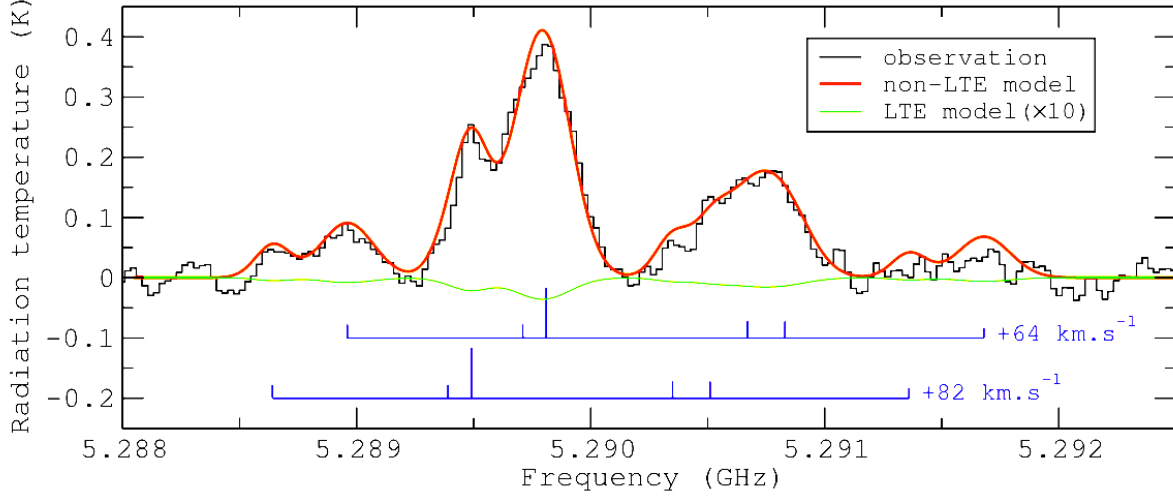


Figure 1.10: Observational and model spectra of methanimine $j_{k_a k_c} = 1_{10} \rightarrow j'_{k'_a k'_c} = 1_{11}$ transition at 5.29 GHz towards Sgr B2(N) from (Faure et al., 2018). Relative intensities of the (partially resolved) hyperfine structure in the optically thin limit are shown at the bottom (in blue). The LTE model spectrum (in green) has been multiplied by a factor of 10 for the sake of clarity.

This study clearly emphasizes the need of using non-LTE excitation models in radiative transfer calculations to accurately model the abundance of molecules in the ISM.

If molecular collisional data are not available in the literature, less robust excitation models can be used to avoid assuming LTE. One such approach, considered a pseudo-LTE method, is the Rotational Diagram method (Blake et al., 1987; Bockelee-Morvan et al., 1994). In this method, a fixed excitation temperature (T_{ex}) for all transitions is estimated based on the relative intensities of multiple lines. T_{ex} represents a fictive temperature that would reproduce the distribution of populations among energy levels.¹¹ However, in reality, each transition has its own excitation temperature, and it does not take a unique value for all transitions. Therefore, this approach is insufficient for accurately determining the populations of energy levels.

For cometary observations, where very few data are available, the impact of using robust excitation models has not been well investigated. However, applying the rotational diagram method rather than LTE assumptions led to a re-estimation of the D/H ratio by a factor of 2 in the study by Meier et al. (1998), which analyzed H₂O and HDO abundances in cometary comae. This finding suggests that cometary spectra exhibit strong

¹¹This notion will be detailed in Chapter 4

non-LTE signatures, indicating that accurate non-LTE models could significantly improve the estimation of molecular abundances in comets. Therefore, it is crucial to provide the missing collisional rate coefficients to properly interpret observations from both the ISM and cometary comae.

The accurate evaluation of molecular abundances is crucial for astrochemical models, as these models are validated by their ability to reproduce observed molecular abundances. The abundances of isotopologues are particularly important for assessing the formation and destruction pathways of molecular species. Studies by Takano et al. (1998), Sakai et al. (2007), and Taniguchi et al. (2016) have shown that the formation pathways of molecules can be inferred from the abundances of their ^{13}C isotopologues, where the ^{13}C atom can occupy different positions in the molecule, such as in XCC^{13}Y or X^{13}CCY , where X and Y stands for any atomic composition. Therefore, a reliable estimation of molecular abundances greatly benefits to astrochemical models.

1.3.2 State-to-state Rate Coefficients

State-to-state rate coefficients represent the probability that a collision between two chemical species will result in a given transition. These data are obtained for one target molecule and one colliding projectile. The target molecule is the observed molecule for which the abundance has to be determined, and the colliding partner should be the most abundant molecules in the observed medium. Therefore, for interstellar molecules, H_2 , H or He should be considered as collisional partners, while for cometary comae, H_2O , CO and CO_2 should be considered.

As most molecules are detected through rotational transitions, this work focuses on the determination of state-to-state rate coefficients involving molecules that can be considered as rigid rotors. These data will be useful for analyzing observations from all radiotelescopes mentioned in Section 1.1.3. However, with new observational facilities in the IR, such as the JWST, ro-vibrational state-to-state rate coefficients are also starting to be required by the astrophysical community.

Theoretical Studies

Rate coefficients are typically computed within the Born-Oppenheimer approximation, which allows for the decoupling of electronic and nuclear motions. First, the electronic

Schrödinger equation is solved using *ab initio* quantum chemistry methods to determine the electronic interaction energy between the colliding species. The objective is to obtain a Potential Energy Surface (PES) that accurately represents all possible configurations of the two chemical species. The gold standard for this type of calculation is the Coupled-Cluster Single, Double, and perturbative Triple excitations [CCSD(T)] method (Fortenberry, 2024b). The accuracy of the computed PESs can be assessed by comparing theoretical quantities derived from these PESs with corresponding experimental data, such as bound-state transition frequencies, Integral Cross Sections (ICS), or Pressure Broadening Cross Sections (PBCS), as these quantities are highly sensitive to the quality of the PES. Typically, the agreement between experimental and theoretical results based on these methods is very good, as demonstrated in the work of Faure et al. (2016a) and Hays et al. (2022) for example.

The numerical cost for such calculations will increase with the number of electrons in the system (it increases as n^7 for the CCSD(T) method, with n the number of correlated electrons) and with the number of degrees of freedom that describe the system (i.e., the number of points to compute). Therefore, for highly symmetric molecules composed of first and second row elements (e.g., H₂, C₂, CO₂), the calculations will be cheaper than for complex and higher-row element molecules (e.g., CS, CH₃OH). Consequently, any PES involving the He atom as a collider will be less expensive to compute than if the H₂ collider is considered, as two additional dimension will be added. If CO is considered, more points would be necessary because contrary to H₂, it is an asymmetric molecule. If H₂O is the collider, one additional dimension would be required.

Then, scattering calculations are performed by solving the coupled equations that arise from the nuclear Schrödinger equation, based on the previously computed PES. The exact solution of these equations, known as the Close-Coupling (CC) approach, was developed by Arthurs & Dalgarno (1960) for a closed-shell rigid rotor in collisions with a structureless atom. These equations can be modified to account for the collision of two rigid rotors (Davison, 1962), and the collision of a rigid rotor by an asymmetric top (Phillips et al., 1995; Valiron et al., 2008). By solving these equations, cross sections as a function of collisional energies are obtained, and by thermally averaging them, the state-to-state rate coefficients as a function of temperature are derived. The two most employed scattering code that implements the CC equations are MOLSCAT (Hutson & Green, 1994; Hutson & Le Sueur, 2019; Hutson & Green, 2022) and HIBRIDON (Alexander et al., 2023).

The excellent agreement between theoretical and experimental results for small molecular systems relevant to astrophysical applications demonstrates that this state-of-the-art quantum approach for evaluating collisional rate coefficients is highly robust (Chefdeville et al., 2015; Labiad et al., 2022). Therefore, the full CC approach is the preferred and most widely employed method due to its accuracy. It has been applied to large molecules, such as cyclopentadiene (C_5H_6) in collision with He (Demes et al., 2024), and methanol (CH_3OH) in collision with *ortho* and *para*- H_2 (Dagdikian, 2023). Full quantum approaches can also be combined with the Coupled-States (CS) approximation to handle larger molecules while maintaining good accuracy, as demonstrated with benzonitrile (C_6H_5CN) in collisions with He (Ben Khalifa & Loreau, 2023), which is, to my knowledge, the largest molecule treated with a purely quantum approach to date.

The numerical cost of scattering calculations increases with the number of quantum states N , later called channels, of the molecular system (target and projectile) during the collision that the calculation needs to account for (all open and some closed channels).¹² For full CC calculation, this numerical cost scales as N^3 for the time, and as N^2 for the memory. Therefore, the heavier the colliders are, the more quantum numbers need to be included in the calculation, and the more computationally demanding the calculation will be.

Currently, full quantum scattering approaches are limited to relatively simple molecules in collision with light collisional partners, such as He or H_2 . It remains the preferred method when feasible due to its great accuracy, especially at low temperatures where quantum effects are significant and difficult for alternative methods to account for. However, it is by far the most computationally expensive method. With the increasing availability of computational resources, rate coefficients now exist for more than 70 of the detected molecules in space. To illustrate the growth in the number of rate coefficient sets over the years, the BASECOL database included datasets for 38 detected molecules in Dubernet et al. (2013), and now includes datasets for 57 detected molecules in Dubernet et al. (2024).¹³

As increasingly complex molecules are detected in the ISM, approximate methods need to be developed to calculate rate coefficients for COMs with He and H_2 projectile, given their complex geometry and internal structure. New approaches are also required

¹²Open channels are quantum states that are energetically accessible, whereas closed channels are not.

¹³Some additional sets of rate coefficients have been recently added, and a few complementary ones are available in the EMAA database¹⁰

for studying cometary systems, where the primary colliders are H₂O, CO, and CO₂. Because these molecules are much heavier than He and H₂, quantum approaches become impractical due to the dramatic increase in the number of channels to consider, which significantly raises computational costs. Additionally, the higher temperature ranges of comae typically lead to an increased number of channels needed in calculations, as more energy levels become accessible. Therefore, full quantum approaches are often impractical.

Quantum approaches with the Coupled-States approximation have still been employed to compute collisional data for HCN in collisions with *para*-H₂O (not fully converged) by Dubernet & Quintas-Sánchez (2019) and for CO-CO by Żółtowski et al. (2022). However, these calculations were extraordinarily expensive.

Classical approaches are renowned for their efficiency, but they are expected to be more accurate at high temperatures, where quantum effects become negligible. Therefore, the Mixed Quantum/Classical Trajectory (MQCT) approach has been developed to be faster than CC calculations while improving the accuracy of Quasi-Classical Trajectory (QCT) methods. This approach allows for the computation of data for very heavy systems, such as H₂O-H₂O (Mandal & Babikov, 2023b; Mandal & Babikov, 2023a). This method has been benchmarked on systems where quantum approaches are feasible, such as the H₂O-H₂ system, and an agreement better than a factor of two at temperatures as low as 100 K has been observed (Joy et al., 2024). This suggests that it could be a promising method for cometary applications where H₂O is the dominant projectile (CO and CO₂ are dominant at larger heliocentric distances where the temperature in the coma is \lesssim 50 K).

Statistical approaches have recently emerged as another promising alternative for calculating state-to-state rate coefficients. The Statistical Adiabatic Channel Model (SACM), introduced in the 1970s by Quack & Troe (1974) and Quack & Troe (1975), relies on the statistical counting of the system's adiabatic states. This method was further refined by Loreau et al. (2018b), who used the full PES to compute the adiabatic channels, rather than considering only the isotropic potential. In their study, they compared state-to-state rate coefficients calculated using this approach with quantum calculations, demonstrating excellent agreement across temperatures ranging from 10 K to 300 K. As a result, SACM is now considered an accurate method for calculating state-to-state rate coefficients, particularly for heavy systems relevant to cometary studies. However, this method relies on the assumption that the intermediate complex lives long enough for its energy to be statistically redistributed, requiring a deep potential well to be applicable.

Fortunately, complexes involving heavy colliders, such as CO and H₂O, often meet this requirement. This method has already been applied to compute collisional data for the CO-H₂O (Loreau et al., 2018a; Faure et al., 2020) and HF-H₂O systems (Loreau et al., 2022).

In total, state-to-state rate coefficients are available for only five collisional systems of interest for cometary applications: H₂O-H₂O (Mandal & Babikov, 2023b; Mandal & Babikov, 2023a), CO-H₂O (Loreau et al., 2018a; Faure et al., 2020), HCN-H₂O (Dubernet & Quintas-Sánchez, 2019), HF-H₂O (Loreau et al., 2022), and CO-CO (Żółtowski et al., 2022). As this state-of-the-art suggests, for cometary systems it is still necessary to develop new methodologies that ensure sufficient accuracy for the reliable use of collisional data in radiative transfer models while maintaining a reasonable Central Processing Unit (CPU) usage time.

Another way to avoid the LTE assumption that is widely used for interpreting cometary observations is to use a global cross section for all collisional transitions. This method was initially employed for excitation models of H₂O-H₂O by Bockelee-Morvan (1987), using the experimental pressure broadening cross section of $5 \times 10^{-14} \text{ cm}^{-2}$ from Murphy & Boggs (1969). This value can be slightly modified for molecules with lower (or higher) dipole moments, as collisional transitions are expected to be less (or more) efficient in these molecules (Biver, 1997). However, this is a crude approximation, as cross sections are energy dependent and unique to each transition. In the work of Faure et al. (2020), the rate coefficients of CO-H₂O computed with the SACM approach have been compared to those derived by Biver et al. (1999) using this approach, and significant differences have been found. Therefore, this approach seems insufficient for the accurate determination of the population of energy levels.

Experimental studies

Experimental techniques have been developed to measure collisional data that can be compared with theoretical results. These techniques provide Differential Cross Sections (DCS), Integral Cross Sections (ICS), state-to-state rate coefficients, and Pressure Broadening Coefficients (PBC) measurements.

One of these techniques is the crossed molecular beams method, which measures DCS and/or ICS. In this technique, a single collision occurs between two crossed beams, each

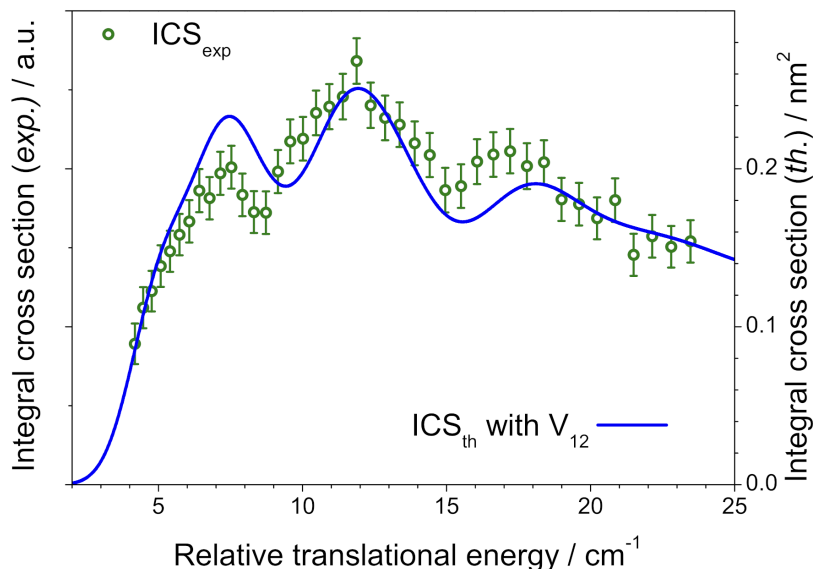


Figure 1.11: Integral Cross-Sections for the CO rotational transition $j_{\text{CO}} = 0 \rightarrow j'_{\text{CO}} = 1$ induced by *para*-H₂ as function of collision energy. The corrected experimental data (Naulin & Costes, 2014) is compared to the new theoretical ICS calculated with the CCSDT(Q) PES of Jankowski et al. (2012). This Figure was taken from Chefdeville et al. (2015).

containing either the target or the projectile. The collisional energy can be controlled by various techniques, such as varying the intersection angle between the two beams (Scharfenberg et al., 2011), using an electric field for Stark deceleration (Bethlem et al., 1999; Vogels et al., 2015), or applying an electromagnetic field for Zeeman deceleration (Vanhaecke et al., 2007).

The small-angle crossed molecular beams experiment was employed in the work of Chefdeville et al. (2015) to assess the validity of CO-*para*-H₂ theoretical scattering results and particularly the accuracy of the PES. The excellent agreement between the ICS measurements for the $j_{\text{CO}} = 0 \rightarrow j'_{\text{CO}} = 1$ transition and theoretical predictions, as shown in Figure 1.11, showed that theoretical calculations based on state-of-the-art methods were of similar accuracy than experimental results.

These experimental cross sections are relative, meaning they are a good indicator of the accuracy of theoretical cross sections only when they change rapidly with energy—typically in the low-energy range where resonances occur. In this range, theoretical cross sections are highly sensitive to the quality of the PES. Therefore, crossed-beam experiments are used to evaluate the quality of the PES, which is critical for computing inelastic cross sections and rate coefficients. Although this approach does not produce

collisional datasets for radiative transfer models, as it only provides 'relative' cross sections, it serves to validate the accuracy of theoretical predictions.

Another technique is the double-resonance experiment, which combines two sources of radiation—one for pumping, causing the populations to strongly deviate from thermal equilibrium, and one for probing the final populations. This technique was initiated by Oka and coworkers (Oka, 1968a), who studied the propensity rules in NH_3 rotational excitation induced by collisions with multiple perturbers including He and H_2 (Oka, 1968b; Daly & Oka, 1970), but also CO and H_2O (Fabris & Oka, 1983) at room temperature. To perform these measurements at interstellar temperature, this experimental set up has been coupled to the CRESU technique¹⁴ which uses the supersonic expansion of a buffer gas through convergent-divergent Laval nozzles to create a uniform supersonic flow of cold gas. This approach allow for the measurements of state-to-state rate coefficients at interstellar temperatures (down to 7 K). In the work of Labiad et al. (2022), an excellent agreement between these experimental rate coefficients and the theoretical results for the CO- H_2 collisional system from Faure et al. (2016a), as shown in Figure 1.12, demonstrated that state-of-the-art computational methods achieve similar accuracy to experimental measurements.

These comparisons are valuable, as they provide a direct comparison between experimental and theoretical state-to-state rate coefficients, allowing for an evaluation of the accuracy of the theoretical data that are directly employed in radiative transfer models.

However, these experimental approaches cannot cover all possible transitions and thus cannot provide a complete dataset for radiative transfer models. These measurements help benchmark theoretical approaches, ensuring reliable interpretation of spectra using validated rate coefficients. As ISM and cometary observations advance, new theoretical methods are being developed, making it crucial to benchmark them against experimental measurements. Thus, experimental and theoretical methods for producing state-to-state rate coefficients are complementary.

¹⁴A french acronym for Cinétique de Réaction en Ecoulement Supersonique Uniforme or Reaction Kinetics in Uniform Supersonic Flow, a technique initially developed by Rowe & Marquette (1987)

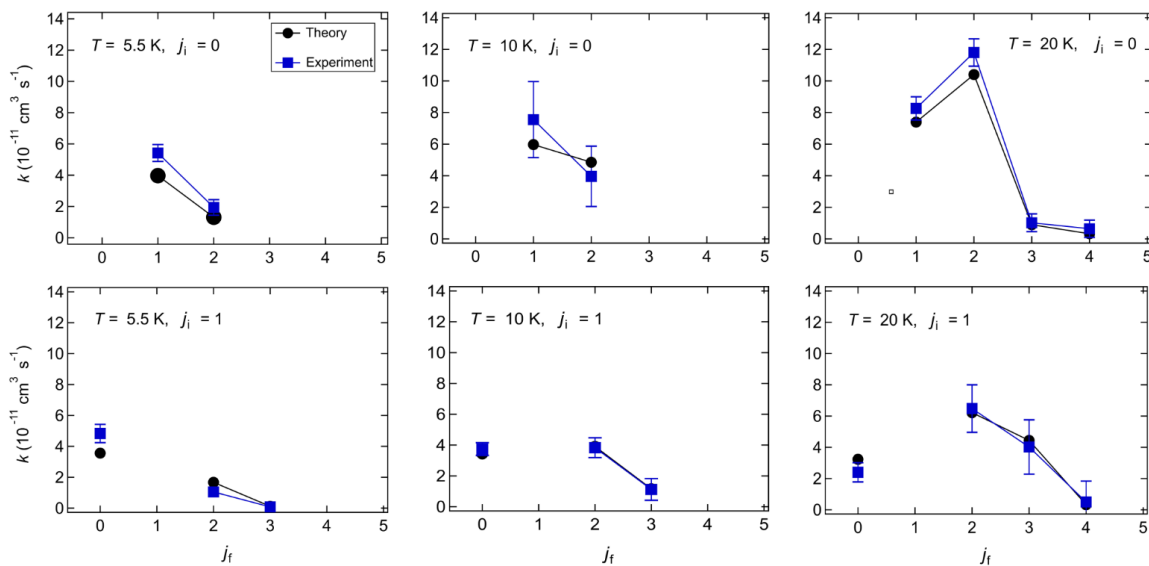


Figure 1.12: CO-H₂ measured state-to-state rate coefficients (squares) and theoretical state-to-state rate coefficients (circles), calculated using the PES of Faure et al. (2016a) for $j_i = 0 \rightarrow j_f$ and $j_i = 1 \rightarrow j_f$ at 5.5, 10 and 20 K. Error bars correspond to 2σ . This Figure was taken from Labiad et al. (2022).

1.4 Outline of the thesis

1.4.1 The Missing Sulfur Problem

Statement of the Problem

Sulfur is the 5th most abundant chemical element in astromolecules, following C, H, N, and O, respectively (McGuire, 2022). Currently, 41 sulfur-bearing molecules have been detected in molecular clouds (among more than 320 detections), and 10 have been observed by remote observations of comets (among 51 detections including tentative ones). These sulfur-bearing molecules are listed in Table 1.1.

Although the chemistry of sulfur in the dense ISM has been extensively studied, a puzzling issue known as the sulfur depletion problem persists (Ruffle et al., 1999). While sulfur’s cosmic abundance is accurately represented in diffuse clouds, which are primitive interstellar environments, it becomes significantly depleted in denser regions such as molecular clouds and star-forming regions, by two to three orders of magnitude (Jenkins, 1987; Ruffle et al., 1999; Vidal & Wakelam, 2018).

2 atoms	3 atoms	4 atoms	5 atoms	6 atoms	> 6 atoms
CS	OCS	H₂CS	HC ₃ S ⁺	CH ₃ SH	CH ₃ CH ₂ SH
SO	H₂S	HNCS	H ₂ CCS	C ₅ S	
SiS	SO₂	C ₃ S	C ₄ S	H ₂ CCCS	
NS	HCS ⁺	HSCN	CH(O)SH	HCSCCH	
S₂	H₂S⁺	HCCS	HCSCN	HC ₄ S	
SO ⁺	CCS	HCCS ⁺	NC ₃ S	NCHCCS	
SH ⁺	CS₂	HCNS	HC ₃ S		
SH	S ₂ H	HOCS ⁺			
NS ⁺	HCS	HNSO			
	HSC				
	NCS				
	HSO				

Table 1.1: Molecules in black (orange) have been detected in the ISM (comets) only. Molecules in bold font have been detected in both environments. Only remote observations are taken into account as the interpretation of remote observations is the subject of this thesis.

Where is the Missing Sulfur?

The observed depletion suggests that the primary reservoirs of sulfur remain unidentified. It could be stored either in gas-phase species that cannot be observed because they lack a dipolar momentum or because they are stuck onto grains. One of the prevailing hypothesis is that sulfur primarily exists in its atomic form, which then binds to grains and forms H₂S through hydrogenation, which is the most efficient process on grains (Garrod et al., 2007). However, H₂S has never been detected in dark cloud ices, and only upper limits have been obtained for several detections, suggesting these levels are too low to account for the missing sulfur problem. Indeed, only OCS (Palumbo et al., 1997) and SO₂ (Boogert et al., 1997) have been detected in the icy bulk of dense molecular clouds, and their total abundances have been found insufficient to explain the missing sulfur (Vidal et al., 2017).

As sulfur naturally tends to form chains and rings even at low temperatures and densities, it has been suggested that it could be stored in sulfur allotropes (S_n chains and/or rings, n ∈ [2 ; 8]). These species would form from atomic sulfur and SH (Mihelcic & Schindler, 1970) or S₂H (Sendt et al., 2002) to produce S₂, which then dimerizes to form S₄, or reacts with another sulfur atom to form S₃ etc until the formation of S₈ which is expected to be the most stable of all (Wakelam et al., 2005; Jiménez-Escobar

& Muñoz Caro, 2011; Shingledecker et al., 2020; Ferrari et al., 2024). The latter has been detected in Ryugu asteroid samples by Aponte et al. (2023), strengthening this hypothesis. However, these species are difficult to detect as they cannot be observed through rotational transitions, being homonuclear and largely stuck onto grains.

Most recently, Yang et al. (2024) suggested that sulfurated PAHs could be an important sulfur reservoir, as PAHs are known to be abundant and widespread in the Universe.

The sulfur depletion remains poorly understood, and astrochemical models struggle to reproduce it (Vidal et al., 2017). Modern astrochemical models still predicts that the bulk of sulfur resides as condensed H₂S (Vidal et al., 2017), despite this hypothesis have been questioned repeatedly (Smith, 1991; van der Tak et al., 2003; Jiménez-Escobar & Muñoz Caro, 2011; Shingledecker et al., 2020). Addressing this issue requires a strong knowledge of sulfur chemistry, which is currently poorly constrained because sulfur molecules are often unstable, making them difficult to study in the laboratory. Its network is incomplete, lacking some of the detected sulfur-bearing species, along with missing reaction pathways and significant uncertainties in reaction rate constants and branching ratios (Vidal et al., 2017; Vidal & Wakelam, 2018).

To better understand this issue, the careful determination of sulfur-bearing molecular abundances in molecular clouds must also be considered. However, these observed abundances are often derived from approximated approaches due to a lack of collisional data—data that this thesis aims to compute for dark molecular clouds.

Additionally, investigating cometary ices through the analysis of comae observations can provide insights into sulfur chemistry, as these ices are thought to behave similarly during the formation of hot cores (Irvine et al., 2000). By providing collisional data for the study of sulfur-bearing molecules in cometary comae, this work aims to offer new clues about sulfur chemistry and contribute to solving the missing sulfur problem.

1.4.2 CCS in Dark Molecular Clouds

The CCS radical is one of the dominant S-bearing molecules in the ISM and has been detected in many dark molecular clouds (Saito et al., 1987; Suzuki et al., 1992), in circumstellar envelopes (Cernicharo et al., 1987), protostellar envelope (Velusamy et al., 1995), and Bok Globules (Scappini & Codella, 1996). Its abundance is highly sensitive to the physical conditions, and it is thus expected to be a good tracer of physical conditions and evolution stages in molecular clouds (Suzuki et al., 1992; Velusamy et al., 1995;

Wolkovitch et al., 1997; Sakai et al., 2007).

For example, the distributions of CCS and NH₃ have been used to evaluate the evolutionary stage of starless cores. A large survey of 49 dense cores performed by Suzuki et al. (1992) showed that CCS tends to be depleted at the center of chemically evolved cores, whereas NH₃ becomes abundant there. CCS is expected to be easily destroyed by UV radiation from the nascent star, while NH₃ desorbs from grains due to the same radiation (Suzuki et al., 1992; Bergin & Langer, 1997; Hirota et al., 2002).

CCS is thought to be formed from S⁺ + C₂H₂ forming HCCS⁺, and finally CCS by dissociative recombination (Smith et al., 1988). However, this formation path is still under debate (Sakai et al., 2007; Furuya et al., 2011; Loison et al., 2020).

Despite CCS being an ubiquitous molecule in space, no accurate collisional rate coefficients exist for the CCS radical, so its abundance has been systematically determined using approximate approaches. This involved either assuming pseudo-LTE conditions (with a unique T_{ex}) or using rate coefficients derived from the OCS-H₂ PES and approximate scattering methods. However, these scattering methods are not suitable for molecules with large spin-orbit splitting, such as CCS, because they do not accurately account for the internal structure of such molecules (Fuente et al., 1990; Suzuki et al., 1992; Wolkovitch et al., 1997). Therefore, the derived abundance of CCS in these environments is expected to suffer from significant inaccuracies.

In addition, four isotopologues of CCS have been detected in molecular clouds: ¹³CCS, C¹³CS, CC³⁴S (Ikeda et al., 1997), and CC³³S (Fuentetaja et al., *in prep.*). It is one of the few molecules to present many observable isotopologues. The isotopic ratios (¹²C/¹³C, ³²S/³³S, ³²S/³⁴S) derived from these isotopologues are particularly useful, as they represent some of the most effective tools for tracing the chemical evolution of molecular clouds (Loison et al., 2020).

Additionally, the abundance ratios between ¹³C-bearing isotopologues are often used to constrain the formation pathways of interstellar molecules (Takano et al., 1998; Sakai et al., 2007; Taniguchi et al., 2016). In particular, the two ¹³C-bearing isotopologues of CCS exhibit strong discrepancies in their abundances, with an abundance ratio [C¹³CS]/[¹³CCS] of 4.2 ± 2.3 derived by Sakai et al. (2007), which chemical models struggle to reproduce (Furuya et al., 2011; Loison et al., 2020). This discrepancy raises questions about the

formation mechanism of CCS, suggesting that the parent molecule of CCS may not be symmetric, as previously assumed in chemical models, thereby favoring one isotopologue over the other (Sakai et al., 2007).

As the abundance ratio of CCS isotopologues has always been derived assuming the same excitation conditions, it cannot be safely concluded that the isotopic fractionation or the abundance ratio of the ^{13}C isotopologues are accurate. For the latter, the anomaly could be increased or reduced by accurate modeling of their abundances. Indeed, collisional effects could differ among the isotopologues leading to different excitation conditions, as found in the work of Dumouchel et al. (2012), Faure & Lique (2012), Flower & Lique (2015), and Navarro-Almaida et al. (2023). Therefore, the chemistry of CCS could be better understood by accurately modeling the abundance of its isotopologues.

Therefore, the collisional excitation of CCS and four of its isotopologues (namely ^{13}CCS , C^{13}CS , CC^{33}S and CC^{34}S) induced by the He atom have been studied to determine the rate coefficients necessary for the accurate modeling of these species in dark molecular clouds.

1.4.3 CS in Cometary Atmospheres

Historically, CS was first detected in comets via UV observations (Smith et al., 1980), but it is also often observed in comets through radio spectroscopy (Biver et al., 1999; Roth et al., 2021a; Biver et al., 2022; Biver et al., 2024). As sulfur presents a significant challenge in astrochemistry, which is expected to be addressed by understanding its chemistry in ices, studying sulfur-bearing molecules in cometary ices is a promising lead to address this issue.

CS is a relatively abundant cometary molecules, between 0.03 and 0.2 % of the cometary volatiles composition (Biver et al., 2022). The spatial distribution of CS clearly indicates that it is a product species originating from the inner coma. This is illustrated in Figure 1.13, which highlights the differences between the spatial distribution of a parent species, here HCN as an example (shown in Figure 1.13a), and a daughter species, CS (shown in Figure 1.13b). While the emission of HCN is concentrated around the nucleus of the comet, the emission of CS is clumpy and extends over a broader range of distances.

Daughter species are formed through the photodissociation of their parent molecules. However, the parent molecule of CS remains difficult to clearly identify (Festou et al.,

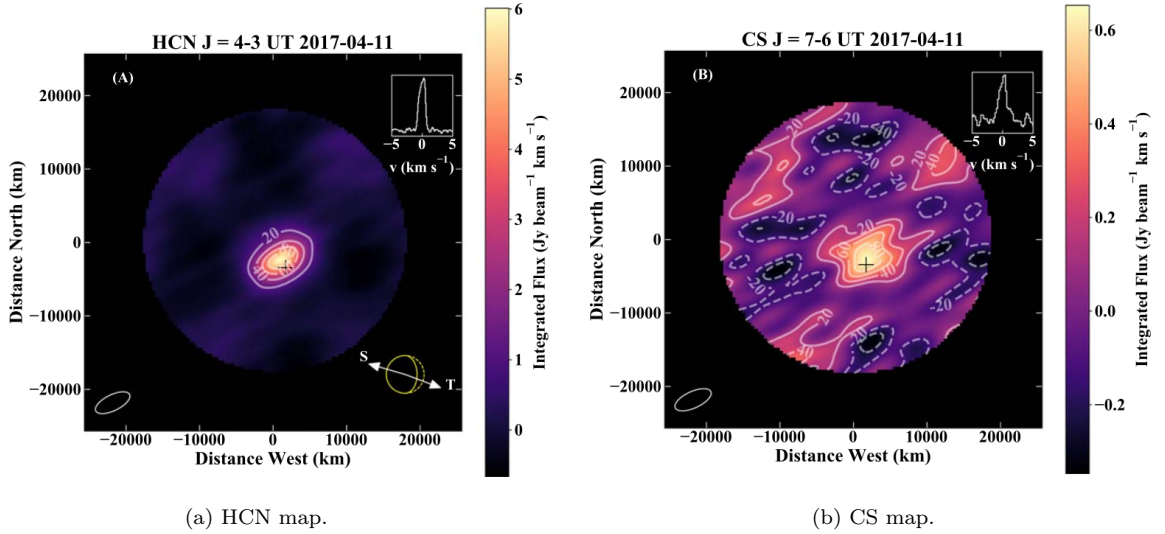


Figure 1.13: Spectrally integrated flux maps for (a) HCN, and (b) CS in Comet C/2015 ER61 on UT 2017 April 11, taken from Roth et al. (2021a).

2004; Boissier et al., 2007; Bøgelund & Hogerheijde, 2017; Roth et al., 2021a; Biver et al., 2022; Biver et al., 2024). For a long time, CS was thought to originate from the photodissociation of CS₂ ices. However, this hypothesis has been questioned by *in situ* measurements by Rosetta/Rosina, which revealed a low abundance of CS₂ in comet 67P (Calmonte et al., 2016; Rubin et al., 2019; Biver et al., 2022). Furthermore, Roth et al. (2021a) suggested that the parent molecule of CS should have a lifetime at least four times greater than that of CS₂, adding another layer of complexity to the understanding of CS formation.

Recent observations of CS by Biver et al. (2024) in the comets C/2021 A1 (Leonard) and C/2022 E3 (ZTF) have determined that the photodissociation rate of the parent molecule of CS should be approximately $4.5 \times 10^{-4} \text{ s}^{-1}$. This value is consistent with the photodissociation rate $\beta_{\text{H}_2\text{CS}} = 4.9 \times 10^{-4} \text{ s}^{-1}$ reported by Hrodmarsson & Van Dishoeck (2023), implying that H₂CS is a plausible candidate for the parent molecule of CS. However, the upper limit of the H₂CS abundance in both C/2021 A1 (Leonard) and C/2022 E3 (ZTF), as evaluated by Biver et al. (2024), is estimated to be three times lower than that of CS. This trend has also been observed in other comets, indicating that H₂CS is clearly insufficient to be the parent molecule of CS.

Evidence has also been found that the relative abundance of CS strongly varies with heliocentric distances in cometary comae (Biver et al., 2006; Biver et al., 2011), inversely proportional to the heliocentric distance. This suggests the existence of a thermal thresh-

old in the release of the parent molecule from the ices (Biver et al., 2022). Therefore, it is important to be able to model CS in comae at all heliocentric distances.

By computing the rate coefficients for CS in collisions with both CO and H₂O, the molecular spectra of CS in cometary comae can be analyzed at both large and short heliocentric distances. This will allow a comprehensive study of this molecule in cometary comae, thus revealing clues about the origin of CS and unveiling some aspects of sulfur chemistry in comets.

The challenge of identifying the parent molecule of CS implies that an unknown species may be responsible for its production, which aligns with the ongoing discussion about the missing sulfur problem. Among the molecules suggested as potential reservoirs of sulfur, none could be identified as the parent of CS. Specifically, S_n molecules cannot photodissociate to form CS, nor can H₂S. Additionally, the parent species of NS, another relatively abundant sulfure-bearing cometary species, remains unidentified, further suggesting that numerous unknown sulfur-bearing molecules may be abundant constituents of cometary ices.

Thus, many questions surround the chemistry of CS and sulfur molecules in comets in general. By accurately modeling CS in comets using the rate coefficients developed in this work, its abundance could be more effectively constrained, which could provide new insights into its origin. Unraveling the production pathway of CS may also illuminate the abundance of other sulfur molecules. Given that cometary ices are thought to offer valuable insight into the volatile composition of solar protoplanetary disks, resolving this puzzle should yield significant clues to the missing sulfur problem.

1.4.4 Organization of the Manuscript

This thesis work aimed at producing accurate collisional data for sulfur-bearing molecules in both dark molecular clouds and cometary comae. The focus was on the CCS radical, which presents a very peculiar fine structure that makes the calculation of the rate coefficients rather complex, and on the CS molecule for cometary atmospheres, where the calculations are challenging as they involved heavy collisional partners, CO and H₂O, requiring to go beyond quantum scattering approaches.

In Chapter 2, the theoretical and methodological aspects employed to study the CCS-He, CS-CO, and CS-H₂O collisional systems are described.

Chapter 3 presents the detailed work done on the collisional excitation of the molecular systems under study. Section 3.1 focuses on the study of the collisional excitation of CCS and its isotopologues (^{13}CCS , C^{13}CS , CC^{34}S , and CC^{33}S) by the He atom. For this study, the first CCS-He PES was calculated using state-of-the-art methods. The coordinates of the PES were transformed to account for the displacement of the center of mass of each isotopologue. Then, scattering calculations were performed using a quantum approach. The complexity of this study lay in accounting for the accurate structure of each isotopologues. Indeed, CCS has an electronic spin, which leads to a fine structure, and it presents an extraordinary large spin-orbit splitting. This makes approximate methods that do not account for the exact internal structure of CCS inadequate. Additionally, three of its isotopologues exhibit a hyperfine structure (^{13}CCS , C^{13}CS , and CC^{33}S), as ^{13}C and ^{33}S present nuclear spins. These hyperfine structures are resolved in the observations and thus must be considered to determine accurate collisional rate coefficients for astrophysical applications.

Next, Section 3.2 focuses on the study of the collisional excitation of CS involving heavy collisional partners CO and H₂O for cometary applications. Given the complexity of these calculations, it was necessary to move beyond quantum scattering approaches. New PESs were computed for both the CS-CO and CS-H₂O systems using state-of-the-art quantum chemistry methods, and the statistical adiabatic channel model was employed to perform the scattering calculations. The challenge was to apply this new method to study systems that had never been investigated before.

In Chapter 4, the rate coefficients produced in Chapter 3 are used in a non-LTE radiative transfer model to assess the impact of the new data on our understanding of sulfur-bearing molecules in both dark molecular clouds and cometary comae. This chapter begins with a brief introduction to radiative transfer model in Section 4.1. It is followed by Section 4.2, where the importance of using accurate data in non-LTE models of CCS isotopologues is highlighted. These new data sets have also been employed to re-evaluate the $[\text{C}^{13}\text{CS}]/[^{13}\text{CCS}]$ ratio, allowing further investigation into CCS chemistry. Finally, Section 4.3 discuss the importance of computing data for both CO and H₂O colliders, along with the sensitivity of radiative transfer models to rate coefficients in cometary systems.

Finally, conclusions are drawn, and future perspectives of this work are discussed.

THEORY AND METHODS

This chapter aims at presenting the main theories and methods used in the PhD work presented in this manuscript. It will start with a general introduction to the theory describing molecular collisions, including an overview of quantum treatment of molecular systems. It is followed by a description of the methods employed to perform electronic structure calculations. Then, the nuclear motion problem will be addressed, encompassing both the quantum and statistical treatments of the problem.

2.1 General Aspects

In this work, collisions are always considered under the impact approximation, which assumes that the collision occurs much faster than the time between two collisions. Hence, collisions will be strictly binary, corresponding to the very low density of the astrophysical media under study.

During a non-reactive collision, the two colliding species can exchange energy (either kinetic or internal energy) but the total energy of the system remains constant. If their internal energy remains unchanged before and after the collision, it is considered an elastic collision; if it changes, the collision is referred to as inelastic. To determine the probability of these two events, one needs to determine the scattering matrix, known as the S-matrix. Various observables can be derive from it, such as inelastic cross sections from which rate coefficients are finally derived (but also pressure broadening cross sections etc).

In this work, the focus will be on the study of non-reactive inelastic collisions between molecules in low energy levels (i.e. ground electronic and vibrational states) relevant to astrophysical applications.

2.1.1 Molecular Hamiltonian

To study quantum systems, the non-relativistic time-independent Schrödinger equation is employed (Schrödinger, 1926). It is expressed as

$$\hat{H}\Psi = E\Psi, \quad (2.1)$$

where \hat{H} is the Hamiltonian operator describing the molecular system, E is its energy, and Ψ is the stationary wavefunction also called eigenfunction, solution of this equation.

When direct analytical methods are not feasible, numerical approaches are used. In these cases, the Hamiltonian is represented as a matrix in a chosen basis set, and this matrix is diagonalized to obtain the eigenfunctions Ψ and the corresponding eigenvalues E . Due to the complexity of the systems under study, this work will employ such numerical techniques.

The molecular Hamiltonian for system formed by n electrons and N nuclei is defined as

$$\begin{aligned} \hat{H}_{mol} = & \underbrace{-\sum_{i=1}^n \frac{\hbar^2}{2m_e} \nabla_i^2}_{\hat{T}_e} - \underbrace{\sum_{A=1}^N \frac{\hbar^2}{2M_A} \nabla_A^2}_{\hat{T}_N} - \underbrace{\sum_{i=1}^n \sum_{A=1}^N \frac{Z_A e^2}{4\pi\epsilon_0 |r_i - R_A|}}_{\hat{V}_{eN}} \\ & + \underbrace{\sum_{i=1}^n \sum_{j<i}^n \frac{e^2}{4\pi\epsilon_0 |r_i - r_j|}}_{\hat{V}_{ee}} + \underbrace{\sum_{A=1}^N \sum_{B<A}^N \frac{Z_A Z_B e^2}{4\pi\epsilon_0 |R_A - R_B|}}_{\hat{V}_{NN}}, \end{aligned} \quad (2.2)$$

where R_A are nuclear coordinates, and r_i are electronic ones ; M_A are nuclear masses, and m_e is the mass of one electron ; Z_A are nuclear charges ; e is the elementary charge, and ϵ_0 the vacuum permittivity. \hat{T}_e and \hat{T}_N are the kinetic energy operators of the electrons and nuclei, respectively. \hat{V}_{ee} and \hat{V}_{NN} are the repulsion operator between electrons and nuclei, respectively, and \hat{V}_{eN} is the Coulomb interaction operator between electrons and nuclei.

To isolate the variables and solve the equation individually, the most famous and used approximation in quantum chemistry is the Born-Oppenheimer approximation.

2.1.2 The Born-Oppenheimer Approximation

The Born-Oppenheimer approximation (Born & Oppenheimer, 1927), fundamental in quantum chemistry, asserts that nuclei move much more slowly than electrons due to the significantly larger mass of protons compared to electrons (approximately 2000 times heavier). Hence, the electrons are treated as moving in the mean field of nuclei. From a mathematical point of view, it means that the Schrödinger equation can be solved in two steps: first, the electronic part of the Schrödinger equation is solved with the nuclei fixed, and then the nuclei are allowed to move in what they perceived as a mean field of electrons.

The molecular Hamiltonian can thus be separated into an electronic Hamiltonian \hat{H}_e , and a nuclear Hamiltonian \hat{H}_N as

$$\hat{H}_e = \hat{T}_e + \hat{V}_{int}, \quad (2.3)$$

$$\hat{H}_N = \hat{T}_{NN}, \quad (2.4)$$

where $\hat{V}_{int} = \hat{V}_{eN} + \hat{V}_{ee} + \hat{V}_{NN}$ is the interaction potential between the monomers that compose the molecular system.

The wavefunction of the total system $\Psi(\mathbf{r}, \mathbf{R})$ is thus defined as

$$\Psi(\mathbf{r}, \mathbf{R}) = \sum_k \Phi_k(\mathbf{R})\psi_k(\mathbf{r}; \mathbf{R}), \quad (2.5)$$

where \mathbf{r} and \mathbf{R} refer to the overall coordinates of electrons and nuclei, respectively; $\Phi_k(\mathbf{R})$ are the nuclear wavefunctions of the k adiabatic state for total energy of the system E . These are determined by solving the nuclear Schrödinger equation

$$(\hat{T}_N + \epsilon_k(\mathbf{R}))\Phi_k(\mathbf{R}) = E\Phi_k(\mathbf{R}), \quad (2.6)$$

where $\epsilon_k(\mathbf{R})$ is the potential created by the electrons and nuclei at a given geometry of the nucleus \mathbf{R} in the k adiabatic state. $\epsilon_k(\mathbf{R})$ are the eigenvalues of the electronic Schrödinger equation as

$$H_e\psi_k(\mathbf{r}; \mathbf{R}) = \epsilon_k(\mathbf{R})\psi_k(\mathbf{r}; \mathbf{R}), \quad (2.7)$$

where $\psi_k(\mathbf{r}; \mathbf{R})$ are the electronic wavefunctions. The latter, also called k adiabatic eigenfunctions, describe the motion of electrons for fixed positions of the nuclei; they thus depend parametrically of the position of the nuclei. Solving this equation constitutes the

electronic problem, and it will be addressed in Section 2.2.

Within the Born-Oppenheimer approximation, the Schrödinger equation can be written as

$$E\Psi(\mathbf{r}, \mathbf{R}) = \hat{H}\Psi(\mathbf{r}, \mathbf{R}) \quad (2.8)$$

$$= \sum_k \left(- \sum_A^N \frac{\hbar^2}{2M_A} \nabla_A^2 + \epsilon_k(\mathbf{R}) \right) \Phi_k(\mathbf{R}) \psi_k(\mathbf{r}; \mathbf{R}) \quad (2.9)$$

$$= \sum_k \left[\epsilon_k(\mathbf{R}) \Phi_k(\mathbf{R}) \psi_k(\mathbf{r}; \mathbf{R}) - \sum_A^N \frac{\hbar^2}{2M_A} \nabla_A^2 (\Phi_k(\mathbf{R}) \nabla_A^2 \psi_k(\mathbf{r}; \mathbf{R})) \right. \\ \left. + \psi_k(\mathbf{r}; \mathbf{R}) \nabla_A^2 \Phi_k(\mathbf{R}) + 2(\nabla_A \psi_k(\mathbf{r}; \mathbf{R})) (\nabla_A \Phi_k(\mathbf{R})) \right], \quad (2.10)$$

and by integration over electronic coordinates

$$E\Psi(\mathbf{r}, \mathbf{R}) = \epsilon_k(\mathbf{R}) \Phi_k(\mathbf{R}) - \sum_A \frac{\hbar^2}{2M_A} \nabla_A^2 \Phi_k(\mathbf{R}) \\ - \sum_A \frac{\hbar^2}{2M_A} \left[\sum_k (\Phi_k(\mathbf{R}) \langle \psi_j(\mathbf{r}; \mathbf{R}) | \nabla_A^2 | \psi_k(\mathbf{r}; \mathbf{R}) \rangle + \langle \psi_j(\mathbf{r}; \mathbf{R}) | \nabla_A | \psi_k(\mathbf{r}; \mathbf{R}) \rangle \Phi_k(\mathbf{R}) \right]. \quad (2.11)$$

The Born-Oppenheimer approximation states that electrons adjust instantaneously to nuclear motions, implying that any derivative of the electronic wavefunction with respect to nuclear coordinates should be zero. Consequently, the two last terms of Equation (2.11), called non-adiabatic coupling terms, are neglected.

To begin with, the electronic problem [Equation (2.7)] must be solved for each geometry of the nuclei $\{\mathbf{R}\}$ to obtain a Potential Energy Surface (PES) of the collisional system. This resolution can be accomplished using *ab initio* methods, as discussed in Section 2.2.

Next, the Schrödinger equation for the nuclei Equation (2.6) must be solved within the potential $\{\epsilon_k(\mathbf{R})\}$. This yields to the nuclear wavefunctions $\Phi_k(\mathbf{R})$, which describe the rotation/vibration of the monomer(s) and contain all the information about the collisions within their associated S-matrices. Based on these S-matrices, cross sections can be calculated, from which rate coefficients are derived.

In this work, we will always work within the Born-Oppenheimer approximation. This approximation remains valid as long as the electronic states of the molecular system are

well separated. However, if these states are close in energy, the non-adiabatic couplings become significant, and more complex treatments that go beyond the Born-Oppenheimer approximation are required to properly study the molecular system.

2.2 The Electronic Problem

This section is dedicated to the description of the *ab initio* methods that have been used in this work to solve Equation (2.7), enabling the computation of the electronic wavefunctions and electronic energy of a molecular system.

2.2.1 Hartree-Fock Method

The Hartree-Fock (HF) method (Hartree, 1928; Fock, 1930) is central in quantum chemistry. It approximates the electronic wavefunction as a unique Slater determinant with each electron in the mean field of the others.

Hartree-Fock Equations

In the Hartree-Fock approximation, each electron is considered to occupy strictly one spin-orbital φ_i . Consequently, the electronic wavefunction ψ_0 for a system of n -electrons is given by a single Slater determinant, a formalism that ensures the satisfaction of the Pauli exclusion principle

$$|\psi_0\rangle = |\varphi_1\varphi_2\dots\varphi_n\rangle. \quad (2.12)$$

Each electron is described by a function φ_i . It is the product of a radial function describing the orbital occupied by the electron X_i and of a spin function: α_i if the spin is up, and β_i if the spin is down.

The minimal energy of the system E_0 is then given by

$$E_0 = \langle \psi_0 | \hat{H} | \psi_0 \rangle \quad (2.13)$$

$$= \sum_{i=1}^n \hat{h}_i + \frac{1}{2} \sum_{i=1}^n \sum_{j>i}^n \underbrace{\langle \varphi_i(1) \varphi_j(2) | \frac{1}{r_{ij}} | \varphi_i(1) \varphi_j(2) \rangle}_{\hat{J}_{ij}} - \underbrace{\langle \varphi_i(1) \varphi_j(2) | \frac{1}{r_{ij}} | \varphi_j(1) \varphi_i(2) \rangle}_{\hat{K}_{ij}} \quad (2.14)$$

$$= \sum_{i=1}^n \hat{h}_i + \frac{1}{2} \sum_{i=1}^n \sum_{j>i}^n (\hat{J}_{ij} - \hat{K}_{ij}), \quad (2.15)$$

with $r_{ij} = |r_i - r_j|$ the distance between two electrons ; \hat{J}_{ij} the Coulomb operator that represents the average local potential ; \hat{K}_{ij} the exchange operator that accounts for the modification of the energy due to spin-effects. The latter arises from the antisymmetric property of the wavefunction. $\hat{h}(i)$ is the operator of a single electron in the mean field of the nuclei and is expressed as

$$\hat{h}_i = -\frac{1}{2} \nabla_i^2 - \sum_{A=1}^N \frac{Z_A}{r_{iA}}. \quad (2.16)$$

Without the Coulomb and exchange operators, the electrons would be considered to be completely independent from one another.

The Hartree-Fock equations can be solved independently for each spin-orbitals φ_i as

$$\hat{f} \varphi_i = \epsilon_i \varphi_i, \quad (2.17)$$

where ϵ_i is the energy of the electron in the φ_i spin-orbital and \hat{f} is the Fock operator defined as

$$\hat{f}(1) = \hat{h}(1) + \sum_{j=1}^n (\hat{J}_j(1) - \hat{K}_j(1)). \quad (2.18)$$

The "exact" solutions to Equation (2.17) gives the exact Hartree-Fock energy of the spin-orbitals. The spin-orbitals are described by a set of basis functions, called the basis set. The nature of these functions will be described in Section 2.2.3.

Restricted and Unrestricted Hartree-Fock

The HF method is capable of treating both closed-shell (where all electrons are paired) and open-shell (where at least one electron is unpaired) systems. Typically, for closed-shell systems, a *restricted* set of spin-orbitals is employed. The spatial orbitals X_i are the same for α and β spins, resulting in $n/2$ spatial orbitals. Within the HF framework, this approach is known as the Restricted Hartree-Fock (hereafter RHF) method. Each spin orbital can be expressed as

$$\varphi_i(x) = \begin{cases} \varphi_i(x) = X_i(r)\alpha(\omega) \\ \bar{\varphi}_i(x) = X_i(r)\beta(\omega), \end{cases} \quad (2.19)$$

and the restricted ground state wavefunction of the system is defined as follows

$$|\psi_0\rangle = |\varphi_1\varphi_2\dots\chi_n\rangle = |\varphi_1\bar{\varphi}_1\varphi_2\bar{\varphi}_2\dots\varphi_{n/2}\bar{\varphi}_{n/2}\rangle. \quad (2.20)$$

The Fock operator given in 2.18 becomes

$$\hat{f}(1) = \hat{h}(1) + \sum_{j=1}^n (2\hat{J}_j(1) - \hat{K}_j(1)), \quad (2.21)$$

and the RHF energy is given by

$$E_0 = 2 \sum_{i=1}^{n/2} \hat{h}_i + \sum_{i=1}^{n/2} \sum_{j=1}^{n/2} (2\hat{J}_{ij} - \hat{K}_{ij}). \quad (2.22)$$

The energy is calculated including only the spatial orbitals and not the spin-orbitals anymore. With an appropriate set of basis functions, this equation can be transformed into a set of algebraic equations which solutions can be found through matrix resolution. The RHF method can also be extended to open-shell systems, known as the Restricted Open-shell Hartree-Fock (hereafter ROHF) method. Simply the doubly occupied orbitals are constrained to be the same for both spins, while they differ for unpaired electrons (Jensen, 2007). The energy expression is (Roos, 1994)

$$E = 2 \sum_i^{n_{occ}^d} h_i + \sum_a^{n_{occ}^s} h_a + \sum_{i=1}^{n_{occ}^d} \sum_{j>i}^{n_{occ}^d} (2\hat{J}_{ij} - \hat{K}_{ij}) + \sum_{i=1}^{n_{occ}^d} \sum_{a=1}^{n_{occ}^s} (2\hat{J}_{ia} - \hat{K}_{ia}) + \frac{1}{2} \sum_{a=1}^{n_{occ}^s} \sum_{b>a}^{n_{occ}^s} (\hat{J}_{ab} - \hat{K}_{ab}), \quad (2.23)$$

where i, j indicate the n_{occ}^d doubly and a, b the n_{occ}^s singly occupied orbitals, respectively.

To treat open-shell systems, the Unrestricted Hartree-Fock (UHF) method uses a set of *unrestricted* spin-orbitals, where different orbitals will be used for each electron (Jensen, 2007). The spatial orbitals are then occupied by a single electron as

$$\varphi_i(x) = \begin{cases} \varphi_i^\alpha(r)\alpha(\omega) \\ \varphi_i^\beta(r)\beta(\omega), \end{cases} \quad (2.24)$$

one set of spin-orbitals describes the n_α electrons, and the other describes the n_β electrons ($n = n_\alpha + n_\beta$; $n_\alpha > n_\beta$).

The total energy of the system is then

$$E_0 = \sum_{i=1}^n h_i + \frac{1}{2} \left[\sum_{i=1}^n \sum_{j>i}^n J_{ij} - \sum_{i=1}^{n_\alpha} \sum_{j>i}^{n_\alpha} K_{ij}^\alpha - \sum_{i=1}^{n_\beta} \sum_{j>i}^{n_\beta} K_{ij}^\beta \right]. \quad (2.25)$$

Two sets of Hartree-Fock equations (one for each type of spin) can be obtained from 2.17 as

$$\hat{f}^\sigma \varphi_i^\sigma = \epsilon_i^\sigma \varphi_i^\sigma, \quad (2.26)$$

where σ indexes the spin functions α or β .

This method is significantly more computationally demanding than the RHF or ROHF methods, as it requires n sets of spatial orbitals instead of $\sim n/2$. Additionally, the UHF wavefunction is not an eigenfunction of the spin-operator \hat{S}^2 due to the independent optimization of α and β orbitals. As a consequence, the UHF method also suffers from spin-contamination meaning that the wavefunction may violate the spin-symmetry. It can lead to an inadequate description of the spin correlation.

Self-Consistent Field (SCF) Procedure

In the HF method, each electron is considered in the mean field of others, a field which is determined from their spin-orbitals. Hence, HF equations are non-linear and must be solved iteratively with the so-called Self-Consistent-Field (SCF) procedure.

To describe the molecular orbitals, the Linear Combination of Atomic Orbitals (LCAO) model is employed. In this model, each molecular orbital X_i is constructed as the linear combination of M atomic orbitals ϕ_k from the constituent atoms within the molecule.

$$X_i = \sum_{k=1}^M c_{ik} \phi_k. \quad (2.27)$$

The choice of a basis functions to describe the atomic orbitals ϕ_k will be discussed in Section 2.2.3. Yet, we will only assume that $\{\phi_k\}$ is a set of known functions.

The HF equations can be written as

$$\hat{F} \sum_{k=1}^M c_{ik} \phi_k = \epsilon_i \sum_{k=1}^M c_{ik} \phi_k. \quad (2.28)$$

The HF method respects the variational principle, so the SCF procedure iteratively minimizes the energy by modification of the c_{ik} coefficients. The accuracy of the results increases with the number of atomic orbitals used, but at the expense of the computational cost.

Within the Born-Oppenheimer approximation, the procedure determines the electronic ground state wavefunction ψ_0 and its corresponding electronic energy E_0 for a system of n electrons in the mean field of the N nuclei.

In practice, the first step is to specify the nuclear coordinates of the molecular system $\{\mathbf{R}_A\}$ the atomic numbers of the nuclei $\{Z_A\}$, and a basis set $\{\phi_k\}$. By computing this energy for several set of nuclear coordinates $\{\mathbf{R}_A\}$, the potential energy surface (PES) of the system can be explored.

Limit of the Hartree-Fock Method: the Correlation Energy

The HF method relies on a single Slater determinant, treating each electrons in the mean field of the others neglecting instantaneous interactions between the electrons. As a result, the HF energy is overestimated compared to the real energy of the system as it does not include the correlation energy arising from electron-electron interactions.

The correlation energy is defined as the energy difference between the exact solution to the electronic non-relativistic Schrödinger equation and the HF limit, which represents the lowest energy achievable with an HF calculation.

$$E_{corr} = E_{exact} - E_0^{HF \text{ limit}}. \quad (2.29)$$

The exact electronic wavefunction cannot be expressed as a single Slater determinant because each electron exists in a superposition of multiple orbitals simultaneously.

Methods that overcome this limitation are called post-HF methods.

Post-Hartree-Fock Methods

Ideally, the wavefunction of the system would consider all ground and excited Slater determinants to account for any distribution of the n electrons among the $2K$ available spin-orbitals, with K the number of molecular orbitals X_i .

The Configuration Interaction (CI) methods, introduced by Coulson & Fischer (1949), are promoting electron(s) from occupied to virtual orbitals to generate singly, doubly, triply etc., excited Slater determinants. The resulting wavefunction is expressed as the linear combination of all Slater determinants created, including the reference wavefunction as

$$|\psi_{CI}\rangle = c_0|\psi_0\rangle + \sum_a \sum_r |\psi_a^r\rangle + \sum_{a<b} \sum_{r<s} |\psi_{ab}^{rs}\rangle + \sum_{a<b<c} \sum_{r<s<t} |\psi_{abc}^{rst}\rangle + \dots, \quad (2.30)$$

where $|\psi_a^r\rangle$, $|\psi_{ab}^{rs}\rangle$ and $|\psi_{abc}^{rst}\rangle$ are a singly, doubly and triply excited determinants, respectively. They are generated from the promotion of electron(s) from occupied orbitals (a, b, c, \dots) to virtual ones (r, s, t, \dots). For example, $|\psi_a^r\rangle$ is generated by the promotion of one electron from the occupied spin-orbital φ_a to the virtual one φ_r . The c coefficients ($c_0, c_a^r, c_{ab}^{rs}, c_{abc}^{rst}$, etc.) are the amplitudes of the respective determinants and need to be determined.

If the total wavefunction was including all excited determinants, it would represent the exact wavefunction. In combination with a complete basis (i.e., an infinite number of basis function describing each spin-orbital), the exact energy of the system would be recovered. Consequently, Full Configuration Interaction (FCI) calculations are used as benchmark results. However, due to the enormous number of excited determinants generated, such calculations are computationally unfeasible for almost all polyatomic molecules. Therefore, alternative post-HF methods have been developed to address this challenge by selecting a subset of Slater determinants, thereby reducing the computational effort.

With the CI approach, the excited determinants are generated from a single configuration, typically represented by the HF wavefunction. However, when the molecular system is described by multiple configurations (i.e., when it is multiconfigurational), the CI method becomes inadequate because it relies on a single reference configuration.

For such multiconfigurational systems, Multi-Configurational SCF (MC-SCF) methods are required. These methods build the reference wavefunction by combining mul-

tiple configurations, including excited determinants, and simultaneously optimize both the weights of these configurations (c_i) and the molecular orbitals. A common MC-SCF method is the Complete Active Space SCF (CAS-SCF) method (Hegarty & Robb, 1979). In this approach, a subset of orbitals, known as the *active space*, is selected for electron promotion, typically including the frontier orbitals (the last occupied and first unoccupied orbitals). The molecular orbitals and their coefficients are then optimized through an SCF procedure, similar to that used in the HF method.

Further excited determinants can be included using the Multi-Configurational CI (MRCI) method, which generates additional excited determinants based on the CAS-SCF reference wavefunction. Unlike traditional CI methods, which generate excited determinants from a single reference configuration, MRCI uses the multiconfigurational reference, involving at least two Slater determinants, to capture a more accurate description of the system.

2.2.2 Coupled-Cluster Method

In this work, all systems under study are monoconfigurational and one of the most efficient methods to compute the correlation energy for such systems are the Coupled-Cluster methods. The coupled-cluster method is a post-HF method developed by Čížek (1966) and Čížek (1969). The general idea is to include *all corrections of a given type to infinite order*.

The Coupled-Cluster Operator

The electrons are promoted from occupied orbitals φ_a to virtual ones φ_r by the excitation operator \mathbf{T}

$$\mathbf{T} = T_1 + T_2 + T_3 + \dots + T_n, \quad (2.31)$$

where T_i converts the reference Slater determinant of the reference wavefunction ψ_0 into a linear combination of all i^{th} excited Slater determinant by promoting i electron(s) from

occupied spin-orbitals (a, b, c, \dots) to virtual ones (r, s, t, \dots).

$$T_1\psi_0 = \sum_a^{\text{occ}} \sum_r^{\text{vir}} t_a^r \varphi_a^r, \quad (2.32)$$

$$T_2\psi_0 = \sum_{a<b}^{\text{occ}} \sum_{r<s}^{\text{vir}} t_{ab}^{rs} \varphi_{ab}^{rs}, \quad (2.33)$$

\vdots

$$T_n\psi_0 = \sum_{a<b<c<\dots}^{\text{occ}} \sum_{r<s<t<\dots}^{\text{vir}} t_{abc\dots}^{rst\dots} \varphi_{abc\dots}^{rst\dots}, \quad (2.34)$$

where t_a^r are the amplitudes of the φ_a^r determinants.

In our work, the reference wavefunction ψ_0 will always be an HF wavefunction (restricted or not). The coupled cluster wavefunction is defined as

$$\psi_{CC} = e^T \psi_0, \quad (2.35)$$

where the exponential operator is developed following a Taylor-series expansion

$$e^T = 1 + T + \frac{1}{2}T^2 + \frac{1}{6}T^3 + \dots + \frac{1}{n!}T^n = \sum_{k=0}^{\infty} \frac{1}{k!}T^k \quad (2.36)$$

$$\begin{aligned} &= 1 + T_1 + \left(T_2 + \frac{T_1^2}{2}\right) + \left(T_3 + T_2T_1 + \frac{T_1^3}{6}\right) \\ &\quad + \left(T_4 + T_3T_1 + \frac{T_2^2}{2} + \frac{T_2T_1^2}{2} + \frac{T_1^4}{24}\right) + \dots \end{aligned} \quad (2.37)$$

The electronic Schrödinger equation becomes

$$\hat{H}_e e^T \psi_0 = E e^T \psi_0. \quad (2.38)$$

The coupled-cluster energy is expressed as

$$E_{CC} = \langle \psi_0 | \hat{H}_e e^T | \psi_0 \rangle. \quad (2.39)$$

According to the expansion of the excitation operator in 2.36, the calculation of the energy of the system will quickly become manageable only for the smallest system. By taking into account all excitation operators up to T_n , all possible excited Slater deter-

minants will be constructed. The resulting wavefunction is then equivalent to the FCI wavefunction.

The great description of the electronic correlation is enabled by the exponential form of the cluster operator. Through the Taylor-series expansion, higher-order correlation effect can be accounted for, such as those captured by the T_2^2 operator. These effects can be important and would be missed with a restriction to the T_2 operator only (Jensen & Bunker, 2000; Shavitt & Bartlett, 2009).

One limitation of the CC method is its monoconfigurational nature, since it relies on a single Slater determinant. To assess the validity of this restriction, the T_1 diagnosis evaluates the extent of single excitation contributions to the wavefunction

$$T_1 = \frac{\sqrt{(t_i^r)^2 + (t_j^s)^2 + \dots + (t_k^t)^2 + \dots}}{\sqrt{n}}, \quad (2.40)$$

which must be < 0.02 for closed-shell system, and < 0.04 for open-shell system. This diagnosis tool is implemented in MOLPRO V15.1 to provide an insight into the monoconfigurational assumption.

Truncated Coupled-Cluster Method

In practice, the CC method is employed with a truncated excitation operator \hat{T} to limit the computational cost of the calculation.

In the CCSD method, the excitation operator is restricted to single (S) and double (D) excitations only, represented as $T = T_1 + T_2$. This method typically recovers 95% of the correlation energy (Purvis & Bartlett, 1982), and its computational cost scales as K^6 , with K the number of orbitals (Jensen & Bunker, 2000; Jensen, 2007).

The CCSDT method includes triple (T) excitations in addition to single and double excitations. This method recovers 99% of the correlation energy (Noga & Bartlett, 1987; Noga & Bartlett, 1988) and its computational cost scales as K^8 (Jensen, 2007).

To improve efficiency, some methods have been developed to compute high-order CC terms using perturbative theories (less expensive than variational ones), as these are the most computationally expensive terms. The most significant technique is CCSD(T) (Raghavachari et al., 1989) which includes a non-iterative, perturbative correction for the effect connected to triple excitation (thus parenthesis). Its computational cost scales as K^7 (Jensen, 2007). Referred to as the "gold-standard" method, CCSD(T) is often used to

benchmark more approximate methods.

Restricted and Unrestricted Coupled-Cluster

To treat open-shell systems using CC methods, adjustments are necessary from the treatment described above. The simplest approach to treat open-shell molecules at the CC level is to use a UHF wavefunction as the reference wavefunction, but it is computationally expensive. The CC method typically scales as $K^6 - K^8$, and using a UHF wavefunction doubles the number of required orbitals K .

An unrestricted approach also exists for the CCSD(T) method, known as UCCSD(T), where the wavefunction is not required to be an eigenfunction of \hat{S}^2 , so α and β orbitals are optimized independently as for the UHF method (Section 2.2.1), so the computational cost is much larger.

Knowles et al. (1993) introduced a partially spin-restricted approach to the CCSD(T) method, denoted RCCSD(T). This method requires the wavefunction to be an eigenfunction of \hat{S}^2 , resulting in a reduced spin-contamination and more accurate description of the electronic structure. In their study, they demonstrated that RCCSD(T) results were very similar to those of UCCSD(T), with a computational time reduced by a factor of 3.

In MOLPRO V2015.1, both RCCSD(T) and UCCSD(T) are implemented as described in Knowles et al. (1993) and Knowles et al. (2000). However, only a preliminary implementation of the ROHF-RCCSD(T) is available yet, no CPU time is saved by using RCCSD(T) compared to UCCSD(T). In both cases, the calculations is based on ROHF calculation described in Section 2.2.1.

Explicitly Correlated Approaches

The challenge of accurately describing electrons arises from the electron-electron repulsion operator $1/r_{12}$, where the motion of electrons becomes correlated. If this correlation could be ignored, the Schrödinger equation could be solved with a single Slater determinant composed of orbitals.

This operator becomes infinite when $r_{12} = 0$ resulting in a cusp in the wavefunction. The convergence in this region is challenging due to the discontinuous derivative. To improve the description of this cusp, an explicit dependence on the electron-electron distance can be included in the electronic wavefunction, leading to explicitly correlated methods. Therefore, computationally expansive calculations at short distances are reduced.

For the R12 methods, a linear form is used for the dependence of the electronic distance (Jensen, 2007)

$$\psi(r_{12}) = A + \frac{1}{2}r_{12}, \quad (2.41)$$

where A is a constant. However, some more sophisticated form can be used.

A more convenient approach is to consider the correlation factor \hat{F}_{12} as a Slater function, known to describe accurately the wavefunction at short distances, as suggested by Ten-no (2004). The CCSD(T)-F12 methods have been developed for closed (Adler et al., 2007) and open-shell molecules (Knizia et al., 2009) with the correlation factor defined as

$$\hat{F}(r_{12}) = -\frac{1}{\gamma} \exp(-\gamma r_{12}) \approx \sum_i c_i \exp(-\alpha_i r_{12}^2), \quad (2.42)$$

where γ has an optimum value for each molecules and basis set. In practice, Slater functions are inferred by a linear combination of Gaussians, as indicated by right term of the equation.

Some benchmark calculations performed by Adler et al. (2007) and Knizia et al. (2009) with the CCSD(T)-F12 approximation exhibited better accuracy for computational times reduced by two to three orders compared to CCSD(T) with a large basis set. This allows to compute better results with smaller basis, thus drastically reducing computational time. However, there is a risk of overestimating the interaction energy, and thus its use must be benchmarked and restricted to a rather small basis set. CCSD(T)-F12, RCCSD(T)-F12 and UCCSD(T)-F12 are implemented in MOLPRO V15.1 (Werner et al., 2012).

2.2.3 Basis Set

To solve the electronic Schrödinger equation, a set of basis functions to describe the molecular orbitals of the system must be chosen. These are atom-centered functions used to describe the atomic orbitals, and the basis set is the collection of these functions.

Molecular Orbitals (MO)

As presented in Equation (2.27), the MO are linear combination of M atomic orbitals. In principle, M should be infinite to exactly describe the molecular orbitals and reach the "exact" energy within the limit of the computational method employed. Including more functions in the basis improves the accuracy of the calculation, but this number needs to

remain appropriate so the computational cost stays reasonable. Therefore, the choice of a basis set is critical step toward electronic structure calculations.

Expanding the basis set involves calculating integrals over this set. In practice, the methods to calculate these integrals depends on the nature of the orbitals. Therefore, the efficiency of a calculation can be enhanced by a wise choice of functions. Various type of functions have been developed to meet that need.

Nature of the Basis Functions

There are two main types of orbitals: Slater-type orbitals (STO) and Gaussian-type orbitals (GTO). STOs are expressed as follows (Slater, 1930)

$$\chi_{\zeta,n,l,m}(r, \theta, \varphi) = NY_{l,m}(\theta, \varphi)r^{n-1}e^{-\zeta r}, \quad (2.43)$$

where N is a normalization factor, $Y_{l,m}$ represents spherical harmonic functions and ζ are numerical coefficients that determines the spatial extension of the orbital.

The radial dependence $e^{-\zeta r}$ factor mimics the behavior of the exact hydrogen orbitals as the distance between the nucleus and electrons varies, ensuring a good representation of the electrons at short distances. However, electron integrals involving three or four centers cannot be solved analytically with this description, leading to the replacement of STOs with GTOs.

GTO are defined as follow (Boys, 1950)

$$\chi_{\zeta,n,l,m}(r, \theta, \varphi) = NY_{l,m}(\theta, \varphi)r^{2n-2-l}e^{-\zeta r^2}. \quad (2.44)$$

GTO integrals are relatively easy to compute, but the description of the electron's radial behavior is less accurate. GTOs do not exhibit a cusp at short distances as they should, and they decrease too rapidly with increasing distance r . Therefore, to properly describe electron behavior, multiple Gaussian functions must be combined. However, adding more functions increases computational time and memory requirements, making the switch from STOs to GTOs less advantageous.

To overcome this problem, *contracted* GTOs, hereafter noted CGTOs, have been developed. CGTO are linear combination of primitive GTO (hereafter PGTO).

$$\chi(r) = \sum_{i=1}^k c_i x^{\beta_i} y^{\gamma_i} z^{\delta_i} e^{-\alpha_i r^2}, \quad (2.45)$$

where c_i are contraction coefficients that are optimized to reproduce STOs as much as possible ; β_i , γ_i , δ_i are positive integers that depends of the symmetry of the orbital (s, p, d) and α_i a positive real number. The contraction degree k represents the number of PGTO used for each CGTO.

Different type of functions to enhance some properties of the basis can be included:

- Polarization functions: they describe orbitals of angular quantum l greater than the largest value of valence orbitals. They are empty orbitals that polarize occupied orbitals.
- Diffuse functions: they describe the electron density far from its maximum (Kendall et al., 1992). They have the same angular momentum l as valence orbital, and a small radial exponent to make them more diffuse at longer distances. Diffuse functions are crucial because the outer part of the electron density is the most affected by polarization. Basis sets that include diffuse functions are denoted with the *aug-* prefix.
- Correlation-consistent functions can also be included to improve the description of electronic-correlation effects (Dunning, 1989). This basis set is denoted with the *cc-* prefix for *correlation consistent*.

Basis Set of Common Use

Among the most commonly used basis sets are the ones denoted as STO- n G basis sets, where n contracted Gaussian-type orbitals (CGTOs) are used to approximate Slater-type orbitals (STOs). The STO-3G basis set for instance employs 3 CGTOs to mimic one STO orbital.

Pople basis sets are also widely employed, denoted as X - YZG , where X indicates the number of PGTOs used to construct each CGTO of core orbitals, and Y and Z indicate the number of PGTOs used for each valence CGTO. Additional diffuse functions are indicated by "+" or "++" if they are added to only heavy atoms ($> H, He$) or all atoms, respectively. Similarly, polarization functions are denoted by "*" and "***" if they are added to only heavy atoms or all atoms.

Among the most commonly used basis sets are Dunning cc - $pVXZ$ basis sets (Dunning, 1989; Woon & Dunning, 1993; Kendall et al., 1992). These are *correlation-consistent* (cc) basis sets that include *polarization* (p) functions and use X basis functions to describe the

valence zeta orbitals. These basis sets can also include diffuse functions, denoted by the *aug-* prefix, leading to well-known *aVXZ* basis sets.

Mid-Bond Functions

Mid-bond functions are atomic orbitals centered between the nuclei of atoms within a molecule. They were originally suggested by Rothenberg & Schaefer (1971) to replace additional polarization functions centered on atoms, i.e. a larger basis set, since they greatly describe polarization effects. As a result, the convergence of the calculations is faster compared to the use of a larger basis set that would include more polarization functions and give similar results. It is then possible to save computational time while the accuracy is maintained. However, these functions do not have physical meaning and can lead to an overestimation of the correlation energy; thus, they must be used with a limited basis set to avoid this problem. The energy obtained using an aVTZ basis with mid-bond functions is often comparable to the energy obtained through basis set extrapolation (Lique et al., 2005).

Several sets of mid-bond functions were developed, including a set by Cybulski & Toczyłowski (1999) employed in this work. These functions, established through van der Waals complex interaction energy calculations, demonstrated an accuracy within 1% compared to experimental values.

Basis Set Superposition Error (BSSE)

When dealing with interaction energy calculations, the basis set superposition error (BSSE) must be considered.

The issue arises because in the calculations of the $A + B$ system, the orbitals of A can be used to minimize the energy of B , leading to an overestimation of the energy of the monomer B , and vice versa. As a consequence, the computed energies are lower than the "true" values of the calculations due to this numerical artifact.

To address that problem, Boys & Bernardi (1970) suggested a counter procedure to minimize this error. The principle is simple: to obtain the correct interaction energy, the energy of the individual monomers must be computed with the full basis set $E_{A+B}(A)$ and $E_{A+B}(B)$. These energies are then subtracted from the total energy of the system in the full basis set, denoted as $E_{A+B}(A + B)$

$$V(A + B) = E_{A+B}(A + B) - E_{A+B}(A) - E_{A+B}(B). \quad (2.46)$$

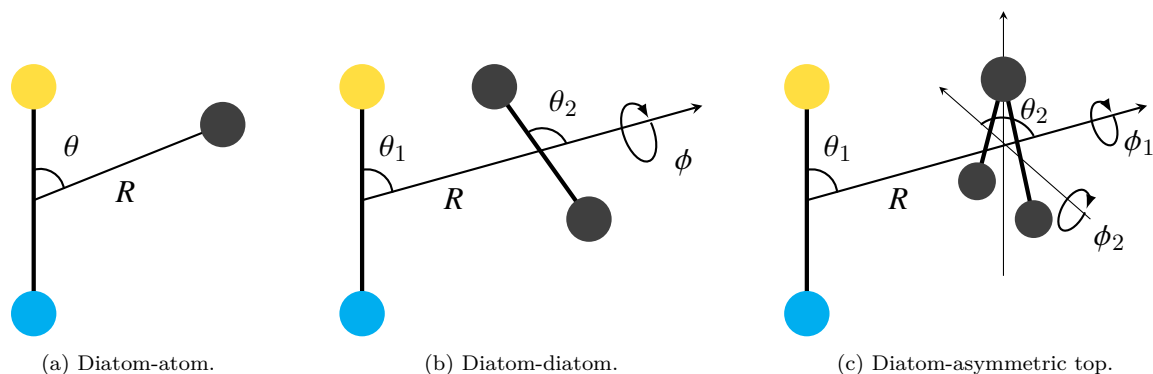


Figure 2.1: Representation of Jacobi coordinates for atom-linear molecule (left), linear-linear molecules (center), and asymmetric top-linear molecule (right).

This procedure should be applied on all computed points. The BSSE is greater for a limited basis set, but also depends on the method employed. The correction of such errors increases computational time as the energy of each monomers must be computed with a full basis set at each geometry.

2.2.4 Analytical Representation

Fitting Procedure

The interaction energy between the two colliding species must be evaluated for a grid of *ab initio* points that must be carefully chosen to efficiently capture interaction between the two colliding species and build up the PES.

Typically, the relative orientations of the non-reactive colliding species are expressed in Jacobi coordinates, as represented in Figure 2.1. In this frame, the origin is fixed on the center of mass of the target molecule. The distance separating the centers of mass of the two colliding species is denoted by R , while θ ($\equiv \theta_1$) represents the angle between the internuclear axis of the target molecule and R , describing the orientation of the target molecule with respect to its collider. If the collider is a linear molecule (center panel), θ_2 represents the angle between the internuclear axis of the collider and R , and ϕ ($\equiv \phi_1$) describes the rotation of the collider around the R axis. Additional orientation can be considered for more complex colliders, such as asymmetric-top molecule (right panel) where the ϕ_2 angle is introduced to describe the rotation of the asymmetric-top around an inertia axis.

The interaction between species can be divided into three main regions. First, the

short-range where the two species are very close resulting in a high interaction energy due to strong nuclear repulsion. Second, the intermediate region, characterized by the stabilization of the van der Waals complex, that typically exhibits global and local(s) minima in the PES. Last, the long-range of interaction, where the distance R increases until a zero interaction energy is reached. It is important not to neglect the accuracy of the long-range region, as the S-matrix is evaluated based on the asymptotic behavior of the total wavefunction of the system.

Once all *ab initio* points describing the interaction potential between the two colliding species are obtained using the chosen method and basis set, it becomes necessary to create an analytical function capable of reproducing not only all computed points but also additional points through a fitting procedure. A typical course of action is to fit the data to a “model” dependent on adjustable parameters. The model could be just a convenient class of flexible functions (such as Gaussians, or polynomials) and the fit only provides the optimal values of the flexible coefficients. The approach is similar in most cases: one designs (or simply chooses) a “merit function” that quantifies how close the agreement is between the data and the model with a particular set of parameters. The merit function is defined such that small values represent close agreement. The parameters of the model are then adjusted to achieve a minimum in the merit function, obtaining the best-fit parameters as a result (Dawes & Quintas-Sánchez, 2018).

The fitting procedure for van der Waals (vdW) systems is especially difficult because a large region of configuration space with multiple local minima is accessible. The full range of angular coordinates must be described, and the variation along the R coordinates is of large amplitude.

Typically, the convergence criterion is set to a few percent for all *ab initio* points, and the root-mean-square value must be minimized. It is a very important step of the work since the quality of the fit will impact the accuracy of the collisional data computed as described in Section 2.3.

Expansion in Functions

In most numerical code, the PES is implemented through a potential expansion of the following form

$$V(R, \alpha) = \sum_{\lambda} v_{\lambda}(R) f_{\lambda}(\alpha), \quad (2.47)$$

where α is a set of angular coordinates describing the monomers; $v_{\lambda}(R)$ are radial coeffi-

cients, and $f_\lambda(\alpha)$ are functions describing the angular part of the potential expression.

In this thesis work, I produced one PES for an atom-linear molecule system, for which the general analytical representation of the potential is given by an expansion over λ Legendre polynomials $P_\lambda(\cos \theta)$ as given in the procedure suggested by Werner et al. (1989)

$$V(R, \theta) = \sum_{\lambda} v_{\lambda}(R) P_{\lambda}(\cos \theta), \quad (2.48)$$

where λ is determined based on the number of θ angles chosen in the potential description. It can be constrained to even values if the molecule exhibits a symmetry according to its center of mass.

The $v_{\lambda}(R)$ radial coefficients represents the behavior of the potential as a function of R , with a distinct expression for each set of Jacobi angles. For a neutral species colliding with a rare-gas atom, these coefficients are fitted to the following functional form

$$v_{\lambda}(R) = e^{-a_1^\lambda R} (a_2^\lambda + a_3^\lambda R + a_4^\lambda R^2 + a_5^\lambda R^3) - \frac{1}{2} \left[1 + \tanh \left(\frac{R}{R_{ref}} \right) \right] \left(\frac{C_6^\lambda}{R^6} + \frac{C_8^\lambda}{R^8} + \frac{C_{10}^\lambda}{R^{10}} \right), \quad (2.49)$$

where a_n^λ are the expansion coefficients, and the coefficients of the R^{-n} terms are denoted by C_n^λ . These coefficients are used for the long-range extrapolation. The hyperbolic tangent factor provides a smooth transition between the short-range ($\theta < R < R_{ref}$) and the long-range regions ($R > R_{ref}$). The value of R_{ref} depends on λ and is optimized along with other fitting parameters.

The number of coefficients λ used in the expansion must be chosen to be sufficiently large so the PES is correctly reproduced, but as small as possible because the computational cost, both memory and CPU time, will increase with it.

2.3 Nuclear Motion

Now that the electronic problem is solved, the PES obtained through the methods discussed in the previous section can be employed to solve the nuclear Schrödinger equation. From the nuclear wavefunction obtained through this resolution, we will be able to derive S-matrices, and thus, calculate cross sections and rate coefficients.

2.3.1 Collisional Hamiltonian

The general expression of the Hamiltonian for two monomers in collision is

$$\hat{H} = -\frac{\hbar^2}{2M_1}\nabla_1^2 - \frac{\hbar^2}{2M_2}\nabla_2^2 + \hat{H}_1 + \hat{H}_2 + V_{\text{int}}(\mathbf{R}, \alpha), \quad (2.50)$$

where $\frac{\hbar^2}{2M_1}\nabla_1^2$, $\frac{\hbar^2}{2M_2}\nabla_2^2$ are the kinetic operators of the monomers with M_1 , M_2 the mass of the monomers; \hat{H}_1 , \hat{H}_2 are their internal Hamiltonian; $V_{\text{int}}(\mathbf{R}, \alpha)$ in the interaction potential between the two colliding species calculated with the methodology described in Section 2.2.

The complexity of H_i varies depending on the internal structure of the species under consideration. Each monomer can range from a structureless atom with no internal Hamiltonian to a vibrating or rotating molecule with electronic and/or nuclear spins. During this thesis work, we neglected vibrational effects and focused solely on rotational, fine, and hyperfine excitations. The complexity of these structures can also vary depending on the molecule's complexity, such as whether it is a linear molecule or an asymmetric top. While we will address briefly each specific case through the manuscript, general equations will be presented for collisions between two linear molecules.

If we consider that the two colliding systems are two closed-shell rigid linear molecules, the Hamiltonian of Equation (2.50) becomes

$$\hat{H} = -\frac{\hbar^2}{2M_1}\nabla_1^2 - \frac{\hbar^2}{2M_2}\nabla_2^2 + \frac{\hat{j}_1^2}{2I_1} + \frac{\hat{j}_2^2}{2I_2} + V_{\text{int}}(\mathbf{R}, \alpha), \quad (2.51)$$

where α would refer to $(\theta_1, \theta_2, \phi)$ angles in the center panel of Figure 2.1 ; \hat{j}_1, \hat{j}_2 are the rotational operators of monomer (1) and (2), respectively ; $I_i = \mu_i r_i^2$ is the principal inertia axis of the molecule i that depends on its reduced mass μ_i and equilibrium bond length r_i .

2.3.2 Coordinate Systems

In Section 2.2.4, the position of the colliders was introduced in Jacobi coordinates, which belong to the Body-Fixed (BF) coordinate system. This frame is more natural to describe the electronic interaction between the two monomers and the PESs are generally computed in this coordinate system. However, it does not allow the direct calculation of the S-matrices from the nuclear wavefunction since it does not have the proper asymp-

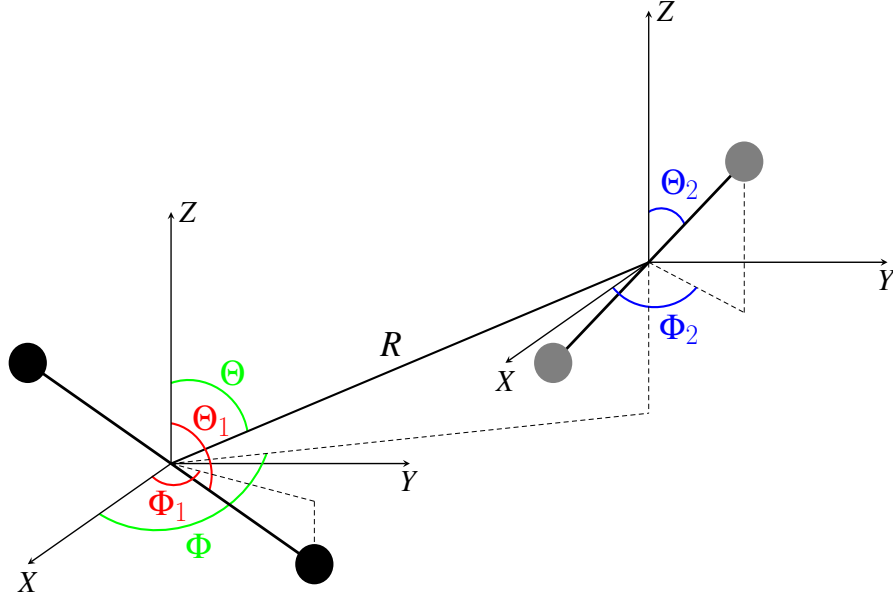


Figure 2.2: Two rigid rotor in the space-fixed (X,Y,Z) coordinate system.

otic behavior. Therefore, the Space-Fixed (SF) coordinate system (X, Y, Z) must be introduced.

In the SF coordinate system represented in Figure 2.2, the origin is placed at the center of mass of the target molecule just as in the BF frame. The coordinates of the target molecule [monomer (1)] will be given by $\boldsymbol{\rho}_1 \equiv (\Theta_1, \Phi_1)$ and the colliding monomers [monomer (2)] coordinates are given by $\boldsymbol{\rho}_2 \equiv (\Theta_2, \Phi_2)$, and their relative motion is given by $\mathbf{R} \equiv (R, \Theta, \Phi)$.

The kinetic energy operator of the collisional system is given by

$$\hat{T}(\boldsymbol{\rho}_1, \boldsymbol{\rho}_2) = \frac{\hbar^2}{2M_1} \nabla_1^2 - \frac{\hbar^2}{2M_2} \nabla_2^2. \quad (2.52)$$

If the frame is placed to the relative motion of the two monomers, the expression becomes

$$\hat{T}(\mathbf{R}_{\text{com}}, \mathbf{R}) = \frac{\hbar^2}{2M} \nabla_{\mathbf{R}_{\text{com}}}^2 - \frac{\hbar^2}{2M} \nabla_{\mathbf{R}}^2, \quad (2.53)$$

where $M = M_1 + M_2$, $\mu = (M_1 M_2) / (M_1 + M_2)$ are the total and the reduced mass of the collisional system, respectively ; \mathbf{R} represents the relative position of the monomers, and $\mathbf{R}_{\text{com}} = (M_1 \mathbf{R}_1 + M_2 \mathbf{R}_2) / M$ represents the position of the center of mass (referred as com) of the collisional system. In the SF frame, the translational energy of the collisional

system is neglected, so the kinetic operator becomes

$$\hat{T}(\mathbf{R}) = -\frac{\hbar^2}{2M} \nabla_{\mathbf{R}}^2 \quad (2.54)$$

$$= -\frac{1}{2\mu} \frac{1}{R} \frac{\partial^2}{\partial R^2} R + \frac{\hat{l}^2}{2\mu R^2}, \quad (2.55)$$

where \hat{l} is the angular momentum between the two colliders.

Therefore, the collisional Hamiltonian Equation (2.51) becomes

$$\hat{H} = -\frac{\hbar^2}{2\mu} \frac{\partial^2}{\partial R^2} + \frac{\hat{l}^2}{2\mu R^2} + \frac{\hat{j}_1^2}{2I_1} + \frac{\hat{j}_2^2}{2I_2} + V_{\text{int}}(R, \alpha). \quad (2.56)$$

To solve the Schrödinger equation with the collisional Hamiltonian (2.56), different approaches can be employed. In this work, we focused on well-known quantum approaches (detailed in Section 2.3.3) and explored statistical approaches (discussed in Section 2.3.4) to address this problem.

2.3.3 Quantum Approaches

Given the low temperatures of the media under consideration, quantum effects play a significant role. Therefore, despite their considerable computational complexity and cost compared to (semi)classical and statistical approaches, quantum methods are more suitable.

The Coupled Equations

The formal equations to the partial waves were originally developed by Percival & Seaton (1957) for the $\text{H} + e^-$ collision in the perspective of new computational developments enabling intensive calculations. Building on this foundation, Arthurs & Dalgarno (1960) developed similar formal equations to treat collisions between an atom and a rigid linear molecule. Later, Davison (1962) and Green (1975) presented a straight forward extension of these equations to address inelastic collision between two rigid rotors.

The equations are developed in a SF frame, so the eigenfunctions of the rotational

operators \hat{j}_i^2 are spherical harmonics $Y_{j_i m_{j_i}}(\hat{\rho}_i)$ like

$$\hat{j}_1^2 Y_{j_1 m_{j_1}}(\hat{\rho}_1) = \hbar^2 j_1(j_1 + 1) Y_{j_1 m_{j_1}}(\hat{\rho}_1), \quad (2.57)$$

$$\hat{j}_2^2 Y_{j_2 m_{j_2}}(\hat{\rho}_2) = \hbar^2 j_2(j_2 + 1) Y_{j_2 m_{j_2}}(\hat{\rho}_2), \quad (2.58)$$

where $\rho_1 \equiv \rho_1(\Theta_1, \Phi_1)$; $\rho_2 \equiv \rho_2(\Theta_2, \Phi_2)$ specify the orientation of the internuclear axis of the molecules with respect to axis in the SF frame ; j_1, j_2 are the rotational quantum number of molecule (1) and (2) and m_{j_1}, m_{j_2} are their respective projections along the Z axis of the SF frame. The expression of the spherical harmonics are given by

$$Y_{j_i m_{j_i}}(\hat{\rho}_i) = (-1)^{m_{j_i}} \left[\frac{(2j_i + 1)(l_i - m_{j_i})!}{4\pi(l_i + m_{j_i})} \right]^{1/2} P_{j_i}^{m_{j_i}}(\cos \Theta_i) e^{im_{j_i} \Phi_i}, \quad (2.59)$$

where $i = 1, 2$; $P_{j_i}^{m_{j_i}}(\cos \Theta_i)$ is an associated Legendre polynomial ; l_i the individual angular momentum of each molecules.

By including the spherical harmonics of the whole complex Y_{lm_l} , the angular solutions $\mathcal{Y}_\gamma^{JM}(\hat{\mathbf{R}}, \hat{\rho}_1, \hat{\rho}_2)$ of the collisional Hamiltonian (2.51) are

$$\mathcal{Y}_\gamma^{JM}(\hat{\mathbf{R}}, \hat{\rho}_1, \hat{\rho}_2) = \sum_{m_1 m_2 m_{12} m_l} C_{j_1 m_1 j_2 m_2}^{j_{12} m_{12}} C_{j_{12} m_{12} l m_l}^{JM} Y_{j_1 m_{j_1}}(\hat{\rho}_1) Y_{j_2 m_{j_2}}(\hat{\rho}_2) Y_{l m_l}(\hat{\mathbf{R}}), \quad (2.60)$$

where $\gamma \equiv j_1 j_2 j_{12} l$; l the relative angular momentum of the molecules and m_l its projection of the Z -axis of the SF frame ; j_{12} takes all integer values between $|j_1 - j_2|$ and $j_1 + j_2$ the rotational angular momentum of both molecules ; $m_{12} = m_1 + m_2$; $M = m_{12} + m_l$; $C_{j_1 m_1 j_2 m_2}^{j_{12} m_{12}}$ and $C_{j_{12} m_{12} l m_l}^{JM}$ are Clebsh-Gordan coefficients.

Therefore, $\mathcal{Y}_\gamma^{JM}(\hat{\mathbf{R}}, \hat{\rho}_1, \hat{\rho}_2)$ are eigenfunctions of all angular operators, namely \hat{j}_1, \hat{j}_2 and \hat{l} , so they satisfy Equations (2.57), (2.58), and

$$\hat{l}^2 \mathcal{Y}_\gamma^{JM}(\hat{\mathbf{R}}, \hat{\rho}_1, \hat{\rho}_2) = \hbar^2 l(l + 1) \mathcal{Y}_\gamma^{JM}(\hat{\mathbf{R}}, \hat{\rho}_1, \hat{\rho}_2). \quad (2.61)$$

This wavefunction describes a system of total angular momentum J that will take all integer values between $|j_{12} - l|$ up to $j_{12} + l$ and which is conserved during the collision. The projection of J along the Z -axis of the SF frame is noted M . This wavefunction encompasses the complete angular dependence of both colliding molecules and is relatively straightforward to construct as it relies on well-established spherical harmonics and Clebsch-Gordan coefficients derived from Wigner's symbols.

The total solution of the collisional Schrödinger equation $\Phi_\gamma^{JM}(\hat{\mathbf{R}}, \hat{\rho}_1, \hat{\rho}_2)$ must also include a radial dependence $\mathcal{U}_{\gamma';\gamma}^J(R)$ and is given by

$$\Phi_\gamma^{JM}(\hat{\mathbf{R}}, \hat{\rho}_1, \hat{\rho}_2) = \frac{1}{R} \sum_{\gamma'} \mathcal{U}_{\gamma';\gamma}^J(R) \mathcal{Y}_{\gamma'}^{JM}(\hat{\mathbf{R}}, \hat{\rho}_1, \hat{\rho}_2). \quad (2.62)$$

Each column of the $\mathcal{U}_{\gamma';\gamma}^J(R)$ matrix defines the expansion coefficients for collisions in which the colliding partners are in a given initial state whose index corresponds to the selected column. Therefore, all channels γ' are connected to all other possible γ channels. The solutions $\Phi_\gamma^{JM}(\hat{\mathbf{R}}, \hat{\rho}_1, \hat{\rho}_2)$ are called partial-waves since they correspond to a solution at a given value of the total angular momentum J and for a given parity of the wavefunction $\epsilon = (-1)^{J+l} = \pm 1$. The parity is a good quantum number that ensures that the inversion of the coordinates of all particles in the SF coordinate systems leaves the Hamiltonian invariant.

By substitution of the suitable total wavefunction (2.62), Hamiltonian (2.56), using Equation (2.57), Equation (2.58) and Equation (2.61), the Schrödinger equation becomes

$$\left[-\frac{\hbar^2}{2\mu} \frac{\partial^2}{\partial R^2} + \frac{\hbar^2 l'(l'+1)}{2\mu R^2} + \frac{\hbar^2 j'_1(j'_1+1)}{2I_1} + \frac{\hbar^2 j'_2(j'_2+1)}{2I_2} + V_{\text{int}}(R, \alpha) \right] \Phi_\gamma^{JM}(\hat{\mathbf{R}}, \hat{\rho}_1, \hat{\rho}_2) = E \Phi_\gamma^{JM}(\hat{\mathbf{R}}, \hat{\rho}_1, \hat{\rho}_2), \quad (2.63)$$

which can be simplified to

$$\left[-\frac{\hbar^2}{2\mu} \frac{\partial^2}{\partial R^2} + \frac{\hbar^2 l'(l'+1)}{2\mu R^2} - k_{j'_1 j'_2}^2 + V_{\text{int}}(R, \alpha) \right] \Phi_\gamma^{JM}(\hat{\mathbf{R}}, \hat{\rho}_1, \hat{\rho}_2) = 0, \quad (2.64)$$

with $k_{j'_1 j'_2}^2$ the wavenumber, defined as

$$k_{j'_1 j'_2}^2 = \frac{2\mu}{\hbar^2} (E - B_1 j'_1(j'_1+1) - B_2 j'_2(j'_2+1)) \quad (2.65)$$

$$= \frac{2\mu}{\hbar^2} (E - E_{j'_1} - E_{j'_2}), \quad (2.66)$$

where $B_i = \frac{\hbar^2}{2I_i}$ are the rotational constants of the monomers.

Equation (2.64) is reduced by using the orthonormality properties of the basis functions

$\mathcal{Y}_{\gamma'}^{JM*}(\hat{\mathbf{R}}, \hat{\rho}_1, \hat{\rho}_2)$ as

$$\iiint \mathcal{Y}_{\gamma'}^{JM*}(\hat{\mathbf{R}}, \hat{\rho}_1, \hat{\rho}_2) \left[-\frac{\hbar^2}{2\mu} \frac{\partial^2}{\partial R^2} + \frac{\hbar^2 l'(l'+1)}{2\mu R^2} - k_{j_1 j_2}^2 + V_{\text{int}}(R, \alpha) \right] \times \Phi_{\gamma}^{JM}(\hat{\mathbf{R}}, \hat{\rho}_1, \hat{\rho}_2) d\hat{\mathbf{R}} d\hat{\rho}_1 d\hat{\rho}_2 \quad (2.67)$$

$$= \left[-\frac{\hbar^2}{2\mu} \frac{\partial^2}{\partial R^2} + \frac{\hbar^2 l'(l'+1)}{2\mu R^2} - k_{j_1 j_2}^2 \right] \mathcal{U}_{\gamma';\gamma}^J(R) + \sum_{\gamma''} \mathcal{U}_{\gamma'';\gamma'}^J(R) \iiint \mathcal{Y}_{\gamma'}^{JM*}(\hat{\mathbf{R}}, \hat{\rho}_1, \hat{\rho}_2) V_{\text{int}}(R, \alpha) \mathcal{Y}_{\gamma''}^{JM*}(\hat{\mathbf{R}}, \hat{\rho}_1, \hat{\rho}_2) d\hat{\mathbf{R}} d\hat{\rho}_1 d\hat{\rho}_2 = 0. \quad (2.68)$$

The notation of the coupling elements of the potential are simplified as

$$\langle \gamma' J | V_{\text{int}} | \gamma'' J \rangle = \iiint \mathcal{Y}_{\gamma'}^{JM*}(\hat{\mathbf{R}}, \hat{\rho}_1, \hat{\rho}_2) V_{\text{int}}(R, \alpha) \mathcal{Y}_{\gamma''}^{JM*}(\hat{\mathbf{R}}, \hat{\rho}_1, \hat{\rho}_2) d\hat{\mathbf{R}} d\hat{\rho}_1 d\hat{\rho}_2, \quad (2.69)$$

so Equation (2.68) becomes the set of coupled equations:

$$\frac{\hbar^2}{2\mu} \left(\frac{\partial^2}{\partial R^2} - \frac{l'(l'+1)}{R^2} + k_{\gamma';\gamma}^2 \right) \mathcal{U}_{\gamma';\gamma}^J(R) = \sum_{\gamma''} \langle \gamma' J | V_{\text{int}} | \gamma'' J \rangle \mathcal{U}_{\gamma'';\gamma'}^J(R). \quad (2.70)$$

Solving the scattering problem involves solving Equation (2.70) for each set of $\{\epsilon JM\}$. To accomplish this task, powerful numerical techniques have been developed and implemented in various computational packages. Currently, two of the most widely used packages are MOLSCAT (Hutson & Green, 1994; Hutson & Le Sueur, 2019; Hutson & Green, 2022) and HIBRIDON (Alexander et al., 2023), both used during my thesis work. In the following sections, different quantum approaches to solve these sets of coupled equations will be presented.

Close-Coupling (CC) Approach

The close-coupling approach is the most exact approach to solve the coupled equations (2.70). The S-matrices are obtained from the asymptotic behavior of the radial part $\mathcal{U}_{\gamma';\gamma}^J(R)$ of the solutions. Indeed, the wavefunction should vanish when $R \rightarrow 0$ so

$$\lim_{R \rightarrow 0} \mathcal{U}_{\gamma';\gamma}^J(R) = 0, \quad (2.71)$$

and for the total wavefunction (2.62) to represent the scattering of an incoming spherical wave, the radial functions must respect the following asymptotic behavior

$$\lim_{R \rightarrow +\infty} \mathcal{U}_{\gamma'; \gamma}^J(R) = \delta_{\gamma\gamma'} e^{-ik_\gamma R} - i^{-l-l'} \sqrt{\frac{k_\gamma}{k_{\gamma'}}} S^J(\gamma; \gamma') e^{ik_{\gamma'} R}, \quad (2.72)$$

where $S^J(\gamma; \gamma')$ are elements of the complex scattering matrix that provide all information necessary for a complete description of the collision. $S^J(\gamma; \gamma')$ is diagonal in J , and independent of M .

While this approach is the most precise, it is also the most expensive one. Its cost scales as N^3 in CPU time and N^2 in memory, where N represents the number of channels. Typically, the maximum number of channels for close-coupling calculations is around 10,000. To reduced the computational cost of quantum approaches, the idea is to use approximations that will reduce the number of channels involve in the calculations.

Coupled-States Approximation (CS)

The centrifugal decoupling approximation has thus been introduced simultaneously by Pack (1974) and McGuire & Kouri (1974). The idea is that

$$\frac{\hat{l}^2}{2\mu R^2} = \frac{l(l+1)}{2\mu R^2} \hbar^2, \quad (2.73)$$

and all $l(l+1)$ terms are then approximated by $J(J+1)$ in Pack (1974) so the collisional Hamiltonian (2.51) becomes

$$\hat{H} = -\frac{\hbar^2}{2\mu} \frac{\partial^2}{\partial R^2} + \frac{J(J+1)}{2\mu R^2} \hbar^2 + \frac{\hat{j}_1^2}{2I_1} + \frac{\hat{j}_2^2}{2I_2} + V_{\text{int}}(R, \alpha). \quad (2.74)$$

With this approximation, the couplings between j_{12} and l are completely neglected and thus, the number of channels will not increase with the total angular momentum J , but remains the same J when it explodes with the CC approach. For small J collisions, the CPU time saved is already of about two orders of magnitude (Pack, 1974), and is supposed to be better and better when large J systems are considered. It is also worth to notice that this approximation is much more adapted to the BF formalism, saving about two orders of magnitude of CPU time when CS is implemented in the BF formalism compared to SF due to the size that the matrix to diagonalize (Pack, 1974).

By definition, this approximation is expected to work better for heavy collisional system where the coupling between the relative motion of the monomers and their own

rotation will be weak. It is also expected to work better at high collisional energies.

Infinite-Order-Sudden Approximation (IOS)

The approximation have been introduced by Goldflam et al. (1977). The CS approximation neglects the coupling the internal angular momenta of the monomers (j_{12}) and their relative orbital momentum l , i.e. the centrifugal coupling. The Infinite-Order-Sudden (IOS) approximation goes even further by neglecting the angular motion of the monomers. Thus, the wavenumber is given by

$$k_{j_1 j_2}^2 = 2\mu [E - E_{j_1} - E_{j_2}] \sim 2\mu E, \quad (2.75)$$

so the collision Hamiltonian (2.51) becomes

$$\hat{H} = -\frac{\hbar^2}{2\mu} \frac{\partial^2}{\partial R^2} + \frac{l(l+1)}{2\mu R^2} \hbar^2 + V_{\text{int}}(R, \alpha). \quad (2.76)$$

The set of coupled equations (2.70) becomes a set of fully uncoupled equations

$$\frac{\hbar^2}{2\mu} \left(\frac{\partial^2}{\partial R^2} - \frac{\hbar^2 l'(l'+1)}{R^2} + k_{\gamma'}^2 \right) \mathcal{U}_{\gamma; \gamma'}^J(R) = V_{\text{int}}(R, \alpha) \mathcal{U}_{\gamma; \gamma'}^J(R). \quad (2.77)$$

To hold, this approximation must be applied when the collisional energy is greater than the relative energy spacing between the two monomers energetic structure. As for the CS approximation, the larger the energy is, the better the approximation is expected to work. Therefore, along the quantum approaches, only the CC approach is valid at low energy.

Cross Sections and Rate Coefficients

Once the coupled-equations are solved, the S-matrices are obtained for all set of $\{\epsilon JM\}$ quantum numbers and collisional data, as cross sections and rate coefficients, can finally be calculated.

State-to-state integral cross sections are computed as the sum of the partial-waves

$$\sigma_{j_1 j_2 \rightarrow j'_1 j'_2} = \frac{\pi}{g_1 g_2 k_{j_1 j_2}^2} \sum_J (2J+1) \sum_{l'l'} |\delta_{\gamma\gamma'} - S^J(\gamma; \gamma')|^2, \quad (2.78)$$

with $g_i = 2j_i + 1$ the degeneracy of the rotational level of monomer i .

The inelastic state-to-state rate coefficients at a given temperature T are obtained by calculating the thermal average of the cross sections over kinetic energies

$$k_{j_1 j_2 \rightarrow j'_1 j'_2}(T_k) = \sqrt{\frac{8}{\pi \mu k_B^3 T_k^3}} \int_0^\infty \sigma_{j_1 j_2 \rightarrow j'_1 j'_2}(E_k) E_k \exp\left(\frac{-E_k}{k_B T_k}\right) dE_k, \quad (2.79)$$

where $E_k = E - E_{j_1} - E_{j_2}$ is the kinetic energy of the transition, and T_k is the kinetic energy of the media.

The state-to-state rate coefficients defined in Equation (2.79) must follow the detailed balance principle as

$$k_{j_1 j_2 \rightarrow j'_1 j'_2}(T_k) = \frac{g'_1 g'_2}{g_1 g_2} \exp\left(\frac{\Delta E}{k_B T_k}\right) k_{j'_1 j'_2 \rightarrow j_1 j_2}(T_k), \quad (2.80)$$

with $\Delta E = E_{j_1 j_2} - E_{j'_1 j'_2}$ the difference in energy between the initial and final levels involve in the transition.

The state-to-state rate coefficients thus obtained are required to evaluate the competition between radiative and collisional processes, thus deriving the population of energy levels in radiative transfer models. Once the population of energy levels is known, theoretical spectra of molecules can be obtained and compared to observations to derive physical conditions of the media and abundance of molecules.

Propagators

To numerically solve the coupled-equations (2.70), the wavefunctions are propagated along the R coordinate, which represents the distance between the two monomers. Over the years, several propagators have been developed for this purpose. A good propagator must possess two key qualities: numerical stability, ensuring that errors are not amplified during solution propagation, and efficiency in terms of CPU time.

In its matrix form, the coupled-equations (2.70) can be represented as

$$\psi''(R) + \mathbf{W}(R)\psi(R) = 0, \quad (2.81)$$

where

$$\begin{aligned}\mathbf{W}(R) &= \frac{2\mu}{\hbar^2}V(R) - k^2, \\ \psi''(R) &= \frac{\partial^2}{\partial R^2}\psi(R),\end{aligned}\tag{2.82}$$

where $V(R)$ is the potential matrix including the centrifugal term $\frac{l'(l'+1)}{R^2}$; μ is the reduced mass of the system; k is a diagonal matrix of asymptotic channel wave number and $\psi(R)$ is a square matrix containing each linear independent solutions of the problem in each column.

Johnson (1973) introduced a log-derivative propagator, which propagates a log-derivative matrix instead of the matrix of solutions $\psi(R)$. This approach exhibited better efficiency and numerical stability, so it is now a commonly used approach for propagators. The log-derivative matrix $\mathbf{Y}(R)$ is define as

$$\mathbf{Y}(R) = \psi'(R)\psi^{-1}(R).\tag{2.83}$$

The integration of $\mathbf{Y}(R)$ at certain value of R might be impossible due to its possible divergence for certain values of R . Indeed, as $R \rightarrow 0$, $\psi(R)$ must tend to 0, and the only restriction on $\psi'(R)$ at these distances is that it must lead to linear independent solutions. Therefore, $\mathbf{Y}(R)$ can diverge in the classically forbidden region. However, this issue can be easily avoided by propagating $\mathbf{Y}(R)$ using an invariant embedding (Johnson, 1973). The embedding propagator $\mathcal{Y}(R)$ on an interval $[R', R'']$ is defined as

$$\begin{pmatrix} \psi'(R') \\ \psi'(R'') \end{pmatrix} = \begin{pmatrix} \mathcal{Y}_1(R', R'') & \mathcal{Y}_2(R', R'') \\ \mathcal{Y}_3(R', R'') & \mathcal{Y}_4(R', R'') \end{pmatrix} \begin{pmatrix} -\psi'(R') \\ \psi'(R'') \end{pmatrix}.$$

The propagator matrix may also be undefined on certain $[R', R'']$ intervals. However, contrary to the propagation of $\mathbf{Y}(R)$, it does not cause any stability problem because the propagator matrix is defined at the ends of the interval. Thus, it will not be affected by any singularity present in $\mathbf{Y}(R)$ within the $[R', R'']$ interval.

The integration range will be split into $[R', R'']$ intervals called sectors. The propagation matrix $\mathcal{Y}(R)$ will be constructed for each sector and the log-derivative of matrix is propagated through the following recursion relation

$$\mathbf{Y}(R'') = \frac{\mathcal{Y}_4(R', R'') - \mathcal{Y}_3(R', R'')}{\mathbf{Y}(R') + \mathcal{Y}_1(R', R'')} \mathcal{Y}_2(R', R'').\tag{2.84}$$

The two most used log-derivative propagators are the locally adiabatic Airy propagator (hereafter denoted as the Airy propagator) and the log-derivative diabatic modified propagator (hereafter LDMD).

The Airy propagator, initially introduced by Gordon (1969) and modified by Alexander (1984) and Alexander & Manolopoulos (1987) to accommodate the log-derivative propagation, uses a potential-following method. It is specifically designed to handle long-range integration, where the potential matrix $\mathbf{W}(\mathbf{R})$ varies slowly. At each midpoint within the interval, the potential matrix $\mathbf{W}(\mathbf{R})$ is diagonalized using a transformation matrix \mathbf{T}_n , where n represents the number of intervals. As a result, the states in this region become locally quasiadiabatic. One advantage of the Airy propagator is its ability to efficiently handle long-range distances, allowing for a rapid increase in step size with separation.

The LDMD propagator, developed by Manolopoulos (1986), employs a solution-following using a reference potential $\mathbf{W}_{\text{ref}}(\mathbf{R})$, which is constructed as the diagonal part of the interaction matrix $\mathbf{W}(\mathbf{R})$ defined at the mid-position of each sector. Unlike other propagators, LDMD does not require diagonalization of $\mathbf{W}(\mathbf{R})$ at each step, making it highly efficient. However, its effectiveness is contingent upon keeping the sectors relatively small compared to the local wavelength, rendering it less suitable for long-range interactions.

In both the works of Manolopoulos (1986) and Alexander & Manolopoulos (1987), the authors suggested to use an hybrid propagator using LDMD propagator in the short-range of interactions and the Airy propagator in the long-range of interactions. As a result, these complementary propagators are often employed together as a hybrid approach.

Both of the Airy and LDMD propagators are implemented in MOLSCAT (Hutson & Green, 2022) and HIBRIDON (Alexander et al., 2023).

Propagation Parameters

The numerical resolution of the coupled-equations (2.70) involves a propagation of the wavefunction from a minimal distance R_{MIN} to a maximum distance R_{MAX} with a propagation step p .

The grid of total energy E for which the scattering calculations are performed is usually an irregular grid. It is very narrow at low energy when channels opens to properly describe the resonances, and it can be increased at higher energies where cross sections exhibit a flatter behavior.

The best sets of these propagation parameters $\{R_{\text{MIN}}, R_{\text{MAX}}, p\}$ must be determined through convergence tests. The objective is to identify the least computationally expensive

values for these parameters without sacrificing the accuracy. The convergence test for each parameter is performed at each energy range.

While R_{MIN} is typically set at the shortest distance for which the potential is defined, R_{MAX} is determined separately for each energy range. R_{MAX} should correspond to the distance at which the potential couplings become sufficiently small, such that the channels are no longer coupled.

The step of propagation p should be as large as allowed by the converge. In HIBRIDON (Alexander et al., 2023), p is directly fixed. However, in MOLSCAT (Hutson & Green, 2022), p is defined by the number of intervals STEPS as

$$\frac{\pi\sqrt{\hbar}}{\sqrt{2\mu E_k} \text{ STEPS}}, \quad (2.85)$$

where the STEPS parameter must be fixed by the user. As the step of propagation p varies at the inverse of the square-root of the E , the STEPS parameter, also evaluated through convergence tests, can be lowered at higher energies.

Basis Parameters

Matrix operations, including inversion, scalar products, but mainly diagonalization, are responsible for the high cost of coupled-equations resolution. Consequently, CPU time increases proportionally to N^3 , where N represents the number of channels included in the calculations. These channels can be classified as either open or closed, depending on whether their energy is higher or lower than the total energy of the system E .

It is important to notice that in quantum approaches, even closed channels must be accounted for to ensure a proper convergence of the results, as they are coupled to open channels through the potential matrix elements.

In practice, N will be reduced to include only channels that are of interest, or to the number that can be possibly taken into account due to numerical limitations. The size of N is fixed by the basis set, so the number of rotational levels included for each monomers (fixed by j_1^{MAX} and j_2^{MAX}) and by the total angular momentum J over which the S-matrices are summed to obtain cross sections.

As for propagation parameters, convergence tests can be performed to reduce j_1^{MAX} and j_2^{MAX} without loss of accuracy at each energy range. At higher energies, more channels are open, so the basis should be larger. Also, the size of the basis depends on the well-depth since more closed channels will coupled with the open ones in the potential well.

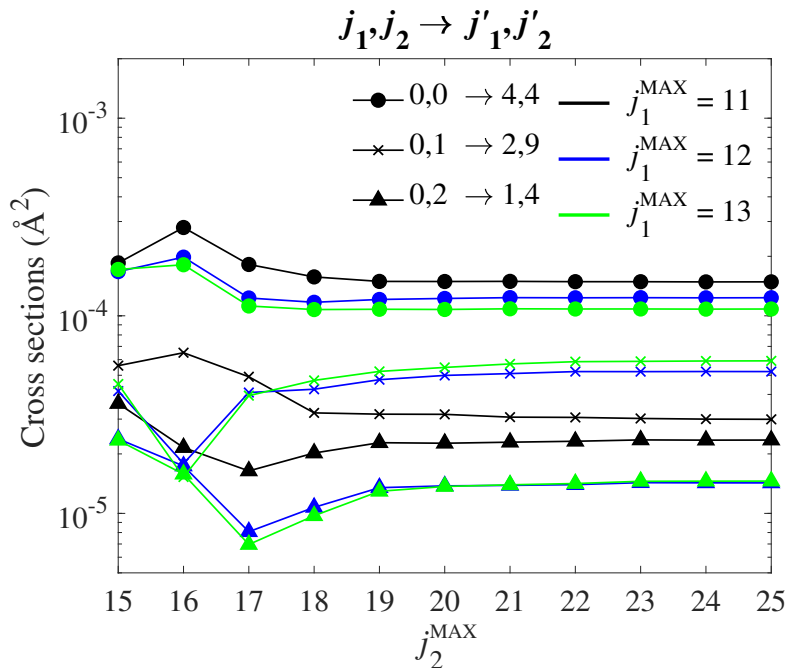


Figure 2.3: Representation of a convergence test of the j_2^{MAX} parameter for few $j_1, j_2 \rightarrow j'_1, j'_2$ cross sections at $E = 150 \text{ cm}^{-1}$ and for $J = 0$, with CO as monomer 1, and CS as monomer 2.

The deeper the potential well is, the larger the rotational basis needs to be to converge the calculation. Figure 2.3 illustrates the evolution of CS-CO cross sections with the value of the j_2^{MAX} parameter which corresponds to the highest rotational state of CS to include in the basis. The convergence is reached for $j_2^{\text{MAX}} = 22$.

In principle, to compute cross sections, an infinite number of partial waves J should be included in the sum of Equation (2.78). However, in practice, this number is truncated to a maximum value J^{MAX} , that corresponds to the most significant partial waves. J^{MAX} is also determined through convergence tests to minimize the computational cost without loss of accuracy. As the energy E increases, J^{MAX} also increases. It is because, at higher energies, the centrifugal barrier (associated with the angular momentum l) needs to be larger for channels to close.

In MOLSCAT, the maximum total angular momentum JTOT ($\equiv J^{\text{MAX}}$) taken into account is converged automatically by the software and the convergence criteria are chosen by the user with DTOL and OTOL, indicating the maximum deviation of elastic and inelastic transitions, respectively, compared to the reference cross sections in Å^2 .

The numerical parameters we want to optimize to reduce the computational cost

$(p, R_{\text{MAX}}, j_1^{\text{MAX}}, j_2^{\text{MAX}}, J^{\text{MAX}})$ are mostly independent of each other. It means that when conducting convergence test for one parameter, other parameter can be set to a minimal values. However, this minimal value should still capture the essential physics of the system. For example, the convergence tests for propagation parameters should be performed with the minimum basis, ensuring that all open channels at the given energy are included.

2.3.4 Statistical Approaches

When dealing with heavy molecular systems that involve heavy collisional partners like CO, CO₂ or H₂O, the number of channels can quickly escalate, easily exceeding the 10,000 channels limit of quantum approaches. This presents a significant challenge not only in terms of CPU time but also memory usage; so other approaches must be employed.

Typically, when quantum approaches cannot be employed, (semi)classical methods are considered. However, these methods are generally restricted to high temperatures, where quantum effects become less pronounced and mostly negligible. As a result, they might not be suitable to treat heavy systems at low temperature. To overcome this limitation, statistical approaches have been developed. Both approaches are complementary, since statistical methods provide a more accurate representations of some quantum effects (not all, resonances for example cannot be accounted for), making them suitable for low-temperature conditions.

In statistical approaches, it is assumed that the intermediate complex formed by the colliders lives enough for the energy to be statistically redistributed within the complex. Therefore, the limitation of this method is that it can work only on strongly bond systems.

Statistical Adiabatic Channel Model (SACM)

This method, initially proposed by Quack & Troe (1974) to address reactive collisions and produce reactive state-to-state rate coefficients, was later extended to include inelastic collisions by Quack & Troe (1975). The goal of their series of papers was to develop a statistical approach capable of treating inelastic and reactive scattering processes involving strongly bound intermediate complexes.

It is assumed that the complex forms and stabilizes within the minima of an adiabatic curve. Then, the energy within the complex is redistributed, causing it to lose memory of its entrance channel. Finally, the complex dissociates into any energetically accessible

(open) channel. Consequently, the final states of the colliding species are independent of their initial states. However, for this assumption to hold, the interaction between the colliding species must be strong enough to ensure a sufficiently long lifetime for proper energy redistribution. Hence, this method will perform better as the strength of the interaction increases and the collisional energy decreases, as it will maximize the lifetime of the complex.

The SACM model operates under the straightforward assumption that all open channels have equal probabilities, while closed channels have zero probability. The probability of any channel $P_{\gamma''}^{JM}(E)$ (with $\gamma'' \equiv j''_1 j''_2 l''$) is expressed as

$$P_{\gamma''}^{JM}(E) = \begin{cases} 0, & \text{for closed channels} \\ \frac{1}{N(E,J,M)}, & \text{for open channels,} \end{cases} \quad (2.86)$$

where $N(E, J, M)$ is the total number of open channels given by

$$N(E, J, M) = \sum_{\gamma''} P_{\gamma''}^{JM}(E). \quad (2.87)$$

An open channel is defined as a channel that exhibits a minimum along its adiabatic curve $V(R)$ (see Figure 2.4), and where the energy between this minimum and its asymptotic value is always lower than the total energy E of the collision. Conversely, a closed channel is one that fails to meet one of these requirements; either it lacks a minimum, or its centrifugal barrier or asymptotic value exceeds E .

The probability of the transition from $(j_1, j_2) \rightarrow (j'_1, j'_2)$ is the square modulus of the corresponding S-matrix element and is expressed as

$$|S_{\gamma, \gamma'}^{JM}(E)|^2 = \frac{P_{\gamma}^{JM}(E) P_{\gamma'}^{JM}(E)}{\sum_{\gamma''} P_{\gamma''}^{JM}(E)} \equiv P_{\gamma, \gamma'}^{JM}(E). \quad (2.88)$$

According to the definition of the S-matrix in the SACM model (2.88), the cross

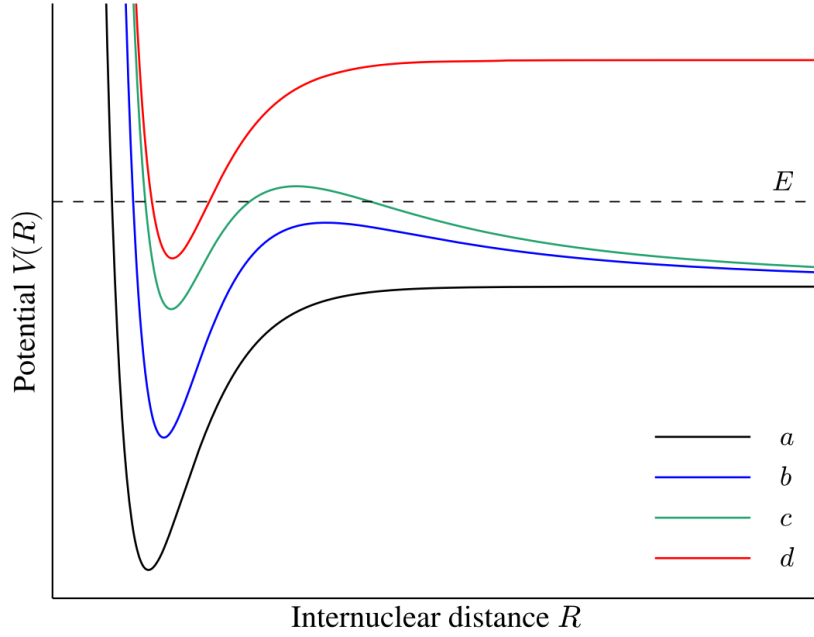


Figure 2.4: Representation of the potential energy $V(R)$ of the adiabatic curves as a function of the R distance between the monomers. At the total energy E , a, b channels are open, and c, d channels are closed.

sections (2.78) are then computed as

$$\sigma_{j_1 j_2 \rightarrow j'_1 j'_2}(E) = \frac{\pi}{g_1 g_2 k_{j_1 j_2}} \sum_J (2J+1) \sum_{l'l''} \frac{P_\gamma^{JM}(E) P_{\gamma'}^{JM}(E)}{\sum_{\gamma''} P_{\gamma''}^{JM}(E)} \quad (2.89)$$

$$= \frac{\pi}{g_1 g_2 k_{j_1 j_2}} \sum_J (2J+1) \frac{N(E, J, j_1, j_2) N(E, J, j'_1, j'_2)}{N(E, J)}, \quad (2.90)$$

with $N(E, J, j''_1, j''_2) = \sum_{l''} P_{\gamma''}^{JM}(E)$.

In their work, Quack & Troe (1974) and Quack & Troe (1975) employed analytical formula to generate the adiabatic curves. Inspired by their work, Loreau et al. (2018b) applied this statistical method but employing accurate potential adiabatic curves that are obtained from diagonalization of the $\mathbf{W}(R)$ matrix defined in Equation (2.81) between R_{MIN} and R_{MAX} , which includes the matrix elements of the potential and the centrifugal barrier. Huge amount of computational effort is then saved, since the wavefunction is propagated only once (and not at each energy) and with less closed-channels. Then, the S-matrices are constructed by attribution of a statistical weight to each channels.

The significant advantage of this statistical method over approximate semi- or quasi-classical approaches is its effectiveness at low temperatures, where these methods would fail (this statement is also true with approximated quantum as CS and IOS). Therefore, it offers a valuable tool for studying strongly-bound systems at low temperatures, where neither quantum nor semi/quasi-classical approaches are suitable.

The adiabatic states (sometimes referred as *adiabats*) can be generated with HIBRIDON by a simple specification on the input, and with MOLSCAT by a slight modification of the backbone code. The counting part, which involves assigning the statistical weight to each channel, has been implemented in a script.

SCATTERING CALCULATIONS AND RATE COEFFICIENTS

This chapter aims at presenting the scattering calculations performed to obtain rate coefficients for the sulfur-bearing molecules of interest in this work. The first part of the chapter is devoted to the case of the CCS radical and its isotopologues in collision with He, for which state-of-the-art full quantum approaches were used. The second part focuses on the study of CS in collision with both CO and H₂O. These latter studies are pioneering in scattering calculations of collisional systems for cometary systems.

3.1 Beyond Simple Rotational Structure: CCS Isotopologues in Dark Clouds

3.1.1 The Peculiar Fine Structure of CCS Isotopologues

Rotational Spectroscopy

CCS is a linear open-shell molecule (also known as a radical) whose ground electronic structure is given by (Xie & Schaefer, 1992)

$$1\sigma^2 2\sigma^2 3\sigma^2 4\sigma^2 5\sigma^2 1\pi^4 6\sigma^2 7\sigma^2 2\pi^4 8\sigma^2 9\sigma^2 3\pi^2. \quad (3.1)$$

As the isotopic substitution of either the ¹²C, or ³²S is not affecting the electronic ground state, all the following description holds for all CCS isotopologues studied in this work, namely ¹²C¹²C³²S, ¹³C¹²C³²S, ¹²C¹³C³²S, ¹²C¹²C³³S, and ¹²C¹²C³⁴S. Hereafter, these isotopologues are noted CCS, ¹³CCS, C¹³CS, CC³³S, and CC³⁴S, respectively.

The CCS radical has a total electronic angular momentum $S = 1$, and its orbital angular momentum $\Lambda = 0$. Therefore, the molecular spectroscopic term for describing

Spectr. const.	CCS	¹³ CCS	C ¹³ CS	CC ³⁴ S	CC ³³ S
B	0.2160745	0.2064124	0.2150476	0.2113423	0.213630
$D \times 10^8$	5.7610	5.2436	5.7103	5.5182	[5.763988]
$\gamma_0 \times 10^4$	-4.9071	-4.690	-4.880	-4.7987	[-4.9157]
λ_0	3.2420979	3.24238	3.24313	3.24208	3.24293
$b_F \times 10^4$	–	6.20	-6.40	–	7.91
$c \times 10^4$	–	-17	-5.3	–	-21.5
$eQq \times 10^4$	–	–	–	–	-1.7169

Table 3.1: Spectroscopic constants of CCS isotopologues from McGuire et al. (2018) for CCS, ¹³CCS, C¹³CS and CC³⁴S, and from Fuentetaja et al. (in prep.) for the CC³³S isotopologue. The values in brackets are theoretical values.

this system is ³Σ. Due to the coupling between the electronic spin S and the rotational quantum number N , the total angular momentum j is given by

$$\hat{j} = \hat{N} + \hat{S}, \quad (3.2)$$

with $|N - S| \leq j \leq N + S$. Consequently, all rotational levels of CCS are split into three fine structure levels for $j \geq 1$. The Hamiltonian of the molecule \hat{H}_{mol} is given by

$$\hat{H}_{mol} = \hat{H}_{rot} + \hat{H}_{sr} + \hat{H}_{ss}, \quad (3.3)$$

where \hat{H}_{rot} , \hat{H}_{sr} , and \hat{H}_{ss} denote respectively for the rotational, spin-rotation, and spin-spin terms of this Hamiltonian. They are expressed as

$$\hat{H}_{rot} = B\hat{N}^2 - D\hat{N}^4, \quad (3.4)$$

$$\hat{H}_{sr} = \gamma_0(\hat{N} \cdot \hat{S}), \quad (3.5)$$

$$\hat{H}_{ss} = \frac{2}{3}\lambda_0(3\hat{S}_z^2 - \hat{S}^2), \quad (3.6)$$

where B is the rotational constant, D is the centrifugal distortion constant, γ_0 is the spin-rotation interaction constant, and λ_0 is the spin-spin interaction constant given in Table 3.1 for each CCS isotopologues.

The fine structure of linear molecules are treated according to Hund's classification, which is based on five idealized molecular models, denoted as Hund's cases (a) through (e),

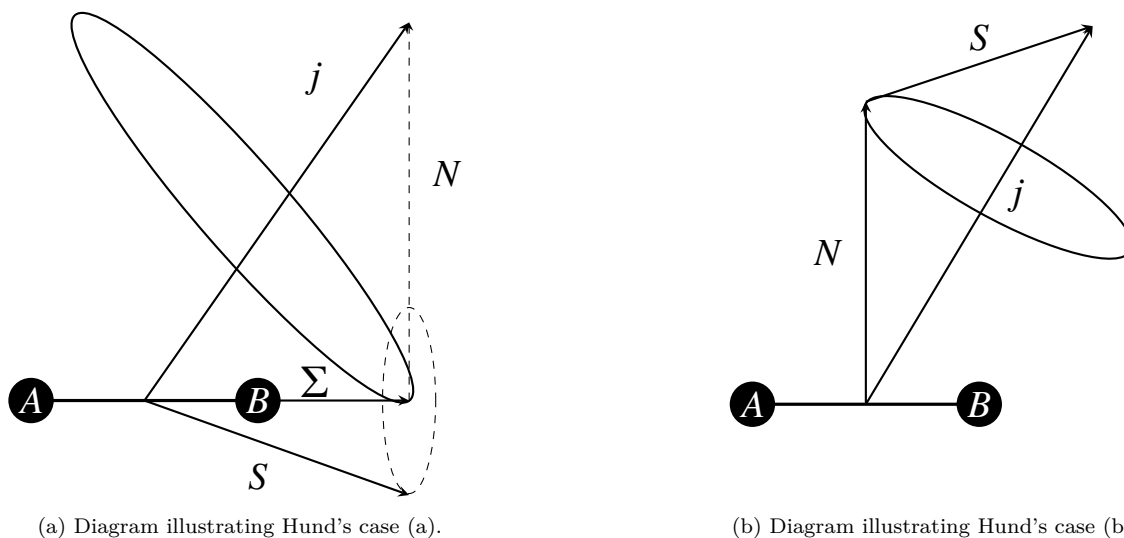


Figure 3.1: Representation of the coupling between the electronic spin S , the rotational angular momentum N , the angular momentum of the molecule L and the internuclear axis of a $2S+1\Sigma$ molecule in (a) Hund's case (a) and (b) Hund's case (b).

depending on the strength of the coupling between the electronic spin S , the rotational angular momentum N , the angular momentum of the molecule L and the internuclear axis of the molecule. A general description of Hund's cases can be found in Townes & Schawlow (1975).

In Hund's case (a), the strongest coupling is between the electronic spin S and the internuclear axis of the molecule. The total angular momentum j is then the vectorial sum of Σ , the projection of S over the internuclear axis, and the rotational angular momentum N , as illustrated in Figure 3.1a.

In Hund's case (b), the strongest coupling is between S and N . The addition of these two vectors yields the total angular momentum j , as illustrated in Figure 3.1b.

For high values of N , the coupling between N and S is predominant, so the fine structure of CCS radical can be accurately described by a pure Hund's case (b). However, for low N values, this coupling is comparable to the coupling between S and the internuclear axis. Therefore, the description of the fine structure of CCS radicals over all N values must be done by accounting for both Hund's case (a) and (b), which is called the intermediate coupling scheme. The rotational wave function of CCS for $j \geq 1$ is thus expressed as (Tatum & Watson, 1971; Alexander & Dagdigian, 1983)

$$\begin{aligned}
 |F_1jm\rangle &= \cos \alpha |N = j - 1, Sjm\rangle + \sin \alpha |N = j + 1, Sjm\rangle, \\
 |F_2jm\rangle &= |N = j, S, jm\rangle, \\
 |F_3jm\rangle &= -\sin \alpha |N = j - 1, Sjm\rangle + \cos \alpha |N = j + 1, Sjm\rangle,
 \end{aligned} \tag{3.7}$$

where $|N, Sjm\rangle$ denotes pure Hund's case (b) basis functions, and α is the mixing angle. This angle is obtained by diagonalization of the molecular Hamiltonian. It depends on j , B_0 , γ_0 , and λ_0 .

In a pure Hund's case (b), \hat{H}_{rot} and \hat{H}_{sr} are diagonal as (Corey et al., 1986)

$$\langle N'Sj'm' | B\hat{N}^2 + \gamma_0(\hat{N} \cdot \hat{S}) | NSjm \rangle = \delta_{NN'}\delta_{jj'}\delta_{mm'} \{ BN(N+1) \tag{3.8}$$

$$+ \left(\frac{\gamma_0}{2} \right) [j(j+1) - S(S+1) - N(N+1)], \tag{3.9}$$

and the pseudo-spin-dipolar \hat{H}_{ss} term mixes the states

$$\begin{aligned}
 \langle N'Sj'm' | 3\hat{S}_z^2 - \hat{S}^2 | NSjm \rangle &= \delta_{jj'}\delta_{mm'} (-1)^{j+S} [3(2N+1)(2N'+1)]^{1/2} \\
 &\times S(S+1)(2S+1) \begin{Bmatrix} N & 2 & N' \\ 0 & 0 & 0 \end{Bmatrix} \begin{Bmatrix} S & S & 1 \\ 2 & 1 & S \end{Bmatrix} \begin{Bmatrix} j' & N' & S \\ 2 & S & N \end{Bmatrix}, \tag{3.10}
 \end{aligned}$$

where $\begin{Bmatrix} \dots \\ \dots \end{Bmatrix}$ denotes Wigner 6-j symbols.

The energy of the fine structure levels of CCS isotopologues within the intermediate coupling scheme are thus calculated as

$$E_{F_1} = \frac{1}{2}(C + E) + \frac{1}{2}\sqrt{(C - E)^2 + 4F^2}, \tag{3.11}$$

$$E_{F_2} = Bj(j+1) - Dj^2(j+1)^2 - \gamma_0 + \frac{2}{3}\lambda_0, \tag{3.12}$$

$$E_{F_3} = \frac{1}{2}(C + E) - \frac{1}{2}\sqrt{(C - E)^2 + 4F^2}, \tag{3.13}$$

where F_1 , F_2 , and F_3 label fine-structure levels, and

$$C = Bj(j-1) - Dj^2(j-1)^2 - \gamma_0(j-1) + \left(\frac{2}{3} - \frac{2j}{2j+1}\right)\lambda_0, \quad (3.14)$$

$$E = Bj(j+1)(j+2) - D(j+1)^2(j+2)^2 - \gamma_0(j+2) + \left(\frac{2}{3} - \frac{2(j+1)}{2j+1}\right)\lambda_0, \quad (3.15)$$

$$F = 2\frac{\sqrt{j(j+1)}}{2j+1}\lambda_0, \quad (3.16)$$

with B , D , λ_0 , and γ_0 the spectroscopic constants in Table 3.1.

In a pure Hund's case (b) limit, $\alpha \rightarrow 0$, and the F_1 , F_2 , F_3 levels correspond to $N = j-1$, $N = j$, and $N = j+1$ levels, respectively. The first 31 N_j fine structure levels of all five CCS isotopologues can be found in Table 3.2, where they have been labeled with the N_j labeling, as if they were pure Hund's case (b) levels.

The strength of the mixing between Hund's case (a) and (b) representation as a function of the rotational quantum number N is illustrated by the 1, F_1 , the 5, F_1 and 10, F_1 levels. Their rotational wavefunctions are described by

$$\begin{aligned} 1_2 \equiv 1, |F_1jm\rangle &= 0.75 |N = j-1, Sjm\rangle + 0.66 |N = j+1, Sjm\rangle, \\ 5_6 \equiv 5, |F_1jm\rangle &= 0.90 |N = j-1, Sjm\rangle - 0.44 |N = j+1, Sjm\rangle, \\ 10_{11} \equiv 10, |F_1jm\rangle &= 0.96 |N = j-1, Sjm\rangle - 0.29 |N = j+1, Sjm\rangle, \end{aligned} \quad (3.17)$$

for which the mixing angle α values are of 41° , 26° , and 17° , respectively. This shows that at low N levels, the mixing between two pure Hund's case (b) are strong, as their weights are almost equal. At $N = 10$, a pure Hund's case (b) representation is almost reached.

The strength of the intermediate coupling scheme in the CCS radicals is due to the fact that the spin-spin spectroscopic constant λ_0 is approximately one order of magnitude larger than the rotational constant B of the radicals. Therefore, the energy levels are not grouped strictly by N values, but are mixed up to $N \leq 9$, as shown in Figure 3.2. This is different from typical $^3\Sigma$, where B is usually one order of magnitude larger than λ_0 (e.g., NH). This behavior has also been observed, to a lesser extent, for the SO molecule, where the "classical" structure is reached for $N > 5$ (Lique et al., 2005).

The difficulties arising from the nature of this internal structure in scattering calcula-

Label N_j	Energy (cm^{-1})				
	CCS	^{13}CCS	C^{13}CS	CC^{34}S	CC^{33}S
1 ₀	0.00000	0.00000	0.00000	0.00000	0.00000
0 ₁	0.37091	0.35707	0.36947	0.36416	0.36744
1 ₂	1.11623	1.07412	1.11184	1.09569	1.10568
2 ₃	2.24206	2.15627	2.23310	2.20018	2.22054
3 ₄	3.75575	3.60982	3.74048	3.68447	3.71909
4 ₅	5.66471	5.44124	5.64128	5.555450	5.60851
1 ₁	6.48371	6.48429	6.48579	6.48368	6.48537
2 ₁	6.54495	6.54005	6.54640	6.54220	6.54518
2 ₂	7.34800	7.30994	7.34596	7.32905	7.33989
3 ₂	7.52821	7.47429	7.52440	7.50141	7.51598
5 ₆	7.97569	7.65656	7.94216	7.81965	7.89535
3 ₃	8.64444	8.54841	8.63624	8.59710	8.62166
4 ₃	8.99526	8.86907	8.98369	8.93300	8.96466
4 ₄	10.3730	10.1997	10.3566	10.2878	10.3307
6 ₇	10.6944	10.2610	10.6488	10.4824	10.5852
5 ₄	10.9387	10.7181	10.9170	10.8302	10.8842
5 ₅	12.5337	12.2638	12.5071	12.4012	12.4670
6 ₅	13.3512	13.0149	13.3171	13.1859	13.2673
7 ₈	13.8256	13.2589	13.7659	13.5483	13.6827
6 ₆	15.1266	14.7407	15.0876	14.9373	15.0305
7 ₆	16.2259	15.7533	16.1773	15.9939	16.1074
8 ₉	17.3730	16.6538	17.2971	17.0211	17.1916
7 ₇	18.1515	17.6304	18.0982	17.8960	18.0212
8 ₇	19.5571	18.9283	19.4918	19.2485	19.3991
9 ₁₀	21.3396	20.4486	21.2455	20.9035	21.1147
8 ₈	21.6086	20.9329	21.5388	21.2774	21.4392
9 ₈	23.3400	22.5354	23.2560	22.9453	23.1375
9 ₉	25.4978	24.6482	25.4095	25.0814	25.2843
10 ₁₁	25.7277	24.6456	25.6133	25.1980	25.4545
10 ₉	27.5710	26.5710	27.4662	27.0806	27.3190
10 ₁₀	29.8191	28.7762	29.7102	29.3080	29.5567

Table 3.2: List of fine structure energy levels of the CCS, ^{13}CCS , C^{13}CS , and CC^{34}S isotopologues, based on the spectroscopic constants from McGuire et al. (2018), and of CC^{33}S from Fuentetaja et al. (in prep.), as exhibited in Table 3.1

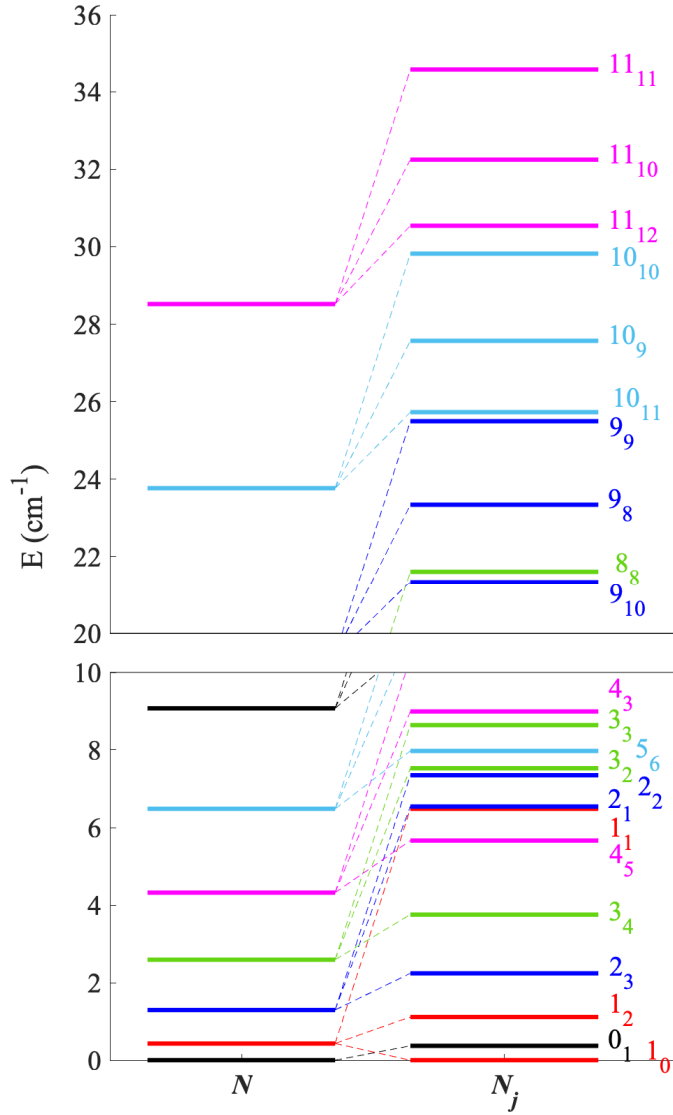


Figure 3.2: Purely rotational (left) and fine structure (right) energy levels of the CCS radical. It can be observed that for low N_j levels, the fine structure levels are not grouped by N values, whereas they are grouped for $N_j \geq 10$.

tions are of two natures: first, the equations need to be adapted to fit this new structure and account for the intermediate coupling scheme; second, the computational cost of the scattering calculations increases as the number of levels is approximately tripled (only the ground rotational level is not split). To limit the increasing CPU cost, approximate approaches (including the the IOS approximation described in Section 2.3.3) have been

employed in previous work (Fuentes et al., 1990; Suzuki et al., 1992; Wolkovitch et al., 1997) to evaluate the rate coefficients for CCS in collisions with a spherical $\text{H}_2(j = 0)$.

However, Lique et al. (2005) found in their work about the SO-He collisional system that the IOS approximation fails to produce accurate collisional data because it intrinsically assumes a pure Hund's case (b) fine structure, which is not valid for any SO level with $N < 5$ and for any of the CCS levels with $N < 10$. Additionally, by assuming a pure Hund's case (b) fine structure, many excitation transitions are incorrectly considered as de-excitation transitions (and vice-versa). Specifically, transitions from $N_j \rightarrow N'_j$, with $N > N'$ should be de-excitation transitions in a pure Hund's case (b) limit. However, due to the entanglement of energy levels, this is not the case for many transitions. For example, the transitions $1_0 \rightarrow 0_1$, $2_3 \rightarrow 1_1$, $3_4 \rightarrow 1_1$, $4_5 \rightarrow 1_1$, etc., should be de-excitations, but they are actually excitations. Therefore, only the CC approach (or another approach that exactly accounts for the energetic structure of CCS such as the Coupled-States approach) can be employed to produce accurate state-to-state rate coefficients for CCS isotopologues at low temperatures.

PES of the CCS-He Complex

The separation between electronic states of the CCS-He complex is expected to be large enough that only the ground electronic state needs to be considered in the evaluation of the electronic interaction. According to the work of Murakami (1990) and Xie & Schaefer (1992), the most stable geometry of the complex is linear (rather than cyclic), and it is also the detected structural isomer of CCS (Saito et al., 1987). The potential energy surface (PES) for the CCS-He complex was computed within the Born-Oppenheimer approximation. The He atom is a structureless atom, and the CCS molecule was approximated as a rigid rotor, despite the presence of a low-lying doubly-degenerate bending mode at $\nu_2 = 134 \text{ cm}^{-1}$ (McGuire et al., 2018).

The internuclear distances of CCS were set as $r_{C-S} = 2.96a_0$ and $r_{C-C} = 2.47a_0$, based on experimental measurements of Yamamoto et al. (1990). The interaction potential between CCS and He was described using Jacobi coordinates (R, θ) , where R represents the distance between the CCS center of mass and the helium atom, and θ describes the angle between R and CCS internuclear axis. The CCS-He collisional system in Jacobi coordinates is shown in Figure 3.3.

The PES was computed with the partially spin-restricted Hartree-Fock and spin-unrestricted coupled-cluster single double and perturbational triple excitations *ab initio*

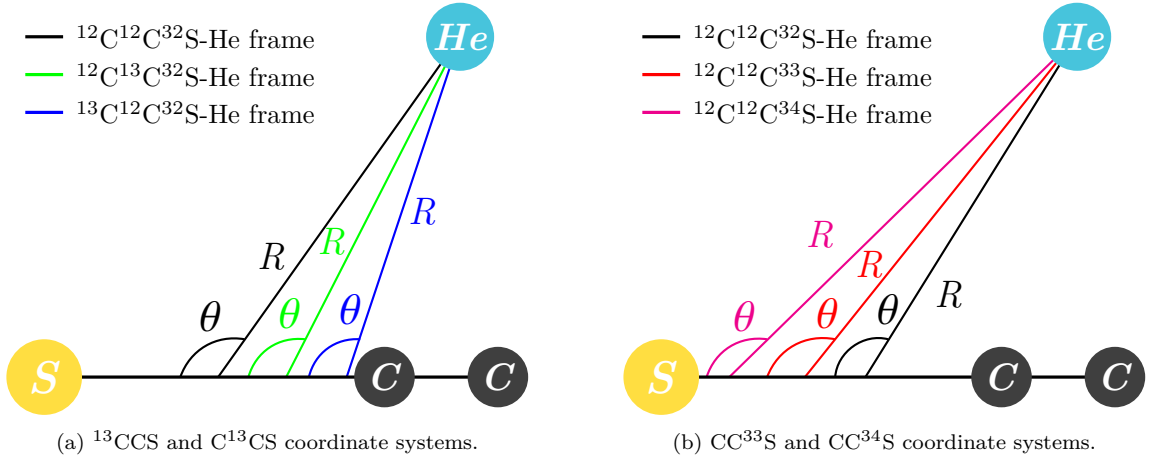


Figure 3.3: Schematic representation of the $^{12}\text{C}^{12}\text{C}^{32}\text{S}$ -He (black), $^{12}\text{C}^{13}\text{C}^{32}\text{S}$ -He (green), $^{12}\text{C}^{13}\text{C}^{32}\text{S}$ -He (blue), $^{12}\text{C}^{12}\text{C}^{33}\text{S}$ -He (red) and $^{12}\text{C}^{12}\text{C}^{34}\text{S}$ -He (pink) collisional systems in Jacobi coordinates. The isotopologues have been separated into isotopic substitution of (a) ^{12}C and (b) ^{32}S for the sake of clarity. The displacement of center of mass have been exaggerated for the sake of clarity.

method [RHF-UCCSD(T)] (Knowles et al., 1993; Knowles et al., 2000) with the augmented correlation consistent quadruple-zeta basis set of Woon & Dunning (1993) (hereafter aVQZ) and additional mid-bond functions of Cybulski & Toczyłowski (1999). All *ab initio* points were computed with MOLPRO 2010 package (Werner et al., 2012).

Calculations have been performed for 44 values of R that have been chosen to accurately describe all ranges of interactions: $R \in [4.5, 30]a_0$ with a step of $0.25a_0$ for $R \in [4.5, 13]a_0$, a step of $0.5a_0$ for $R \in [13, 15]a_0$, a step of $2a_0$ between 16 and $20a_0$, and finally, a step of $5a_0$ between 20 and $30a_0$. θ was taken $\in [0, 180]^\circ$ with a regular step of 5° . The Basis Set Superposition Error (BSSE) have been corrected at each geometry $\mathbf{R} \equiv R, \theta$ according to Equation (2.46), following the procedure of Boys & Bernardi (1970). The average CPU time required for each point was approximately 5,600 seconds, leading to a total of 2,532 CPU hours for the entire PES calculation.

Only 1,351 *ab initio* points were included in the fitting procedure out of the 1,628 computed. Indeed, to get rid of Gibbs oscillations (numerical artifacts that manifest as non-physical oscillations in the potential between *ab initio* points), θ angles were selected as a 10° increment $\in [0 ; 20]$, and $\in [140 ; 170]$, and with a 5° increment $\in [25 ; 135]$ and $\in [175 ; 180]$. Additionally, at short distances where the potential is high, a few points did not converge properly due to the presence of an electronic state. The $^1\Delta$ excited electronic state of CCS, predicted by Xie & Schaefer (1992) to lie at approximately

4,000 cm⁻¹, interfered with these calculations. Therefore, *ab initio* points with a T₁ diagnostic value below the threshold of 0.04 were retained. Since the UCCSD(T) method is monoconfigurational and cannot handle excited states, 57 points with convergence issues due to the excited state were manually excluded from the grid.

The global fit of the potential was performed using an expansion over Legendre polynomials $P_\lambda(\cos \theta)$ as

$$V(R, \theta) = \sum_{\lambda=0}^{\lambda_{max}} v_\lambda(R) P_\lambda(\cos \theta), \quad (3.18)$$

where λ_{max} was taken equal to 31 according to the numbers of θ angles chosen for the fit. The radial coefficients $v_\lambda(R)$, that defines the dependence of the potential as a function of R , have been fitted for each set of Jacobi angles according to the procedure of Werner et al. (1988) as

$$v_\lambda(R) = e^{-a_1^\lambda R} (a_2^\lambda + a_3^\lambda R + a_4^\lambda R^2 + a_5^\lambda R^3) - \frac{1}{2} \left[1 + \tanh \left(\frac{R}{R_{ref}} \right) \right] \left(\frac{C_6^\lambda}{R^6} + \frac{C_8^\lambda}{R^8} + \frac{C_{10}^\lambda}{R^{10}} \right), \quad (3.19)$$

where a_n^λ are the expansion coefficients, and the coefficients of the R^{-n} terms are denoted by C_n^λ . These coefficients are used for the long-range extrapolation. The hyperbolic tangent factor provides a smooth transition between the short-range ($0 < R < R_{ref}$) and the long-range regions ($R > R_{ref}$). The value of R_{ref} , which lies in the range [7.77 ; 12.3]a₀, depends on λ and is optimized along with other fitting parameters.

The fitted potential reproduces all of our *ab initio* points at better than 2%. The root-mean-square (hereafter RMS) deviation is 3.513 cm⁻¹ but is mostly due to the deviation at short distances for angles between 140 and 180°. The RMS is about 0.016 cm⁻¹ in the potential well region [$V(R, \theta) < -1$ cm⁻¹], and about 9.3×10^{-4} in the long-range of interactions [$0 \leq V(R, \theta) \leq -1$ cm⁻¹]. The minimum distance for which the PES is defined is 4.36a₀, making the PES valid for a scattering energy $E \leq 1,500$ cm⁻¹, which corresponds to the lowest value of the potential at this distance.

The isocontours and 3D representation of the PES computed in this work at the RHF-UCCSD(T)/aVQZ level of theory with additional mid-bond functions are presented in Figure 3.4. The PES has a global minimum of $V = -37.12$ cm⁻¹ for the T-shape complex ($\theta = 97.72^\circ$) at $R = 6.70a_0$, and one local minimum of $V = -31.85$ cm⁻¹ for the

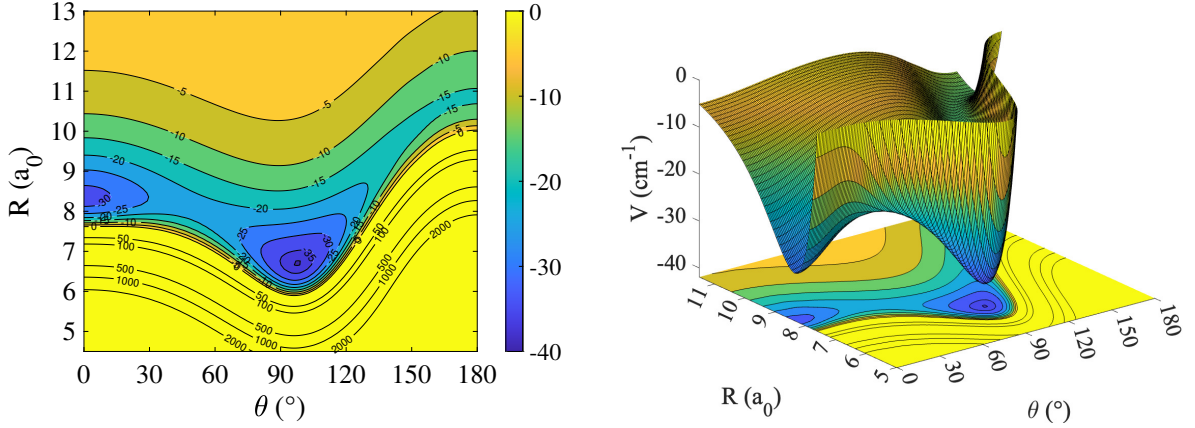


Figure 3.4: Isocontours (left panel) and 3D representation (right panel) of the PES for the CCS-He van der Waals complex.

linear-shape complex, with the He atom facing the sulfur of the CCS radical ($\theta = 0^\circ$) at $R = 8.35a_0$. These two minima are separated by a low barrier of about 16 cm^{-1} with respect to the global minimum. Additional details about the topology of the PES can be found in Godard Palluet & Lique (2023a) presented in Appendix A.2.

As the PES is computed within the Born-Oppenheimer approximation, the electronic PES can be used for all CCS isotopologues. However, a correction of the coordinates is needed to account for the displacement of the center of mass, δr , which is illustrated in Figure 3.3 for each isotopologue. The new coordinates (R' , θ') for the PES of each isotopologue were adjusted to account for the shift in the center of mass according to the following formula

$$R' = \sqrt{R^2 + \delta r^2 - 2R\delta r \cos \theta}, \quad (3.20)$$

$$\theta' = \sin^{-1} \left(\frac{R \sin \theta}{R'} \right), \quad (3.21)$$

with $\delta r = r_{\text{CCS}}^{\text{main}} - r_{\text{CCS}}^{\text{iso}}$ denotes the difference in the position of the center of mass along the CCS internuclear axis between the main isotopologue ($^{12}\text{C}^{12}\text{C}^{32}\text{S}$) and the secondary isotopologue of CCS (any CCS isotopologue where one of the atom of the main isotopologue have been substituted by one rarer isotope as ^{13}C , ^{33}S or ^{34}S), respectively.

These adjusted coordinates (R' , θ') are directly applied in the PES (VRTP) routine of MOLSCAT for implementing the potential for the scattering calculations.

Scattering Calculations

As the temperature will determine how the scattering calculations are performed, the astrophysical environments of interest for this study must be defined. CCS isotopologues have primarily been detected in dark molecular clouds, where the temperature can vary from a few Kelvin to around a dozen Kelvin. The main isotopologue of CCS has also been detected in warmer environments, such as the core of B335—a typical example of a young protostellar region—and the outer part of the circumstellar envelope of IRC+10216. In these environments, the temperatures are typically around 25 K for B335 and 50 K for the outer part of the circumstellar envelope of IRC+10216.

Therefore, fine structure levels with energies $\leq 100 \text{ cm}^{-1}$ must be included in the scattering calculations to produce rate coefficients applicable for astrophysical media up to 50 K. Consequently, levels up to $N_j = 20_{20}$ are considered, which is approximately at 95 cm^{-1} for all isotopologues. This results in a total of 61 energy levels that need to be accounted for in the scattering calculations.

The eigenfunctions $|F_i j l J M\rangle$ of the total angular momentum J in the intermediate coupling scheme are defined as

$$|F_i j l J M\rangle = \sum_{m m_l} \langle j l m m_l | J M \rangle |F_i j m\rangle, \quad (3.22)$$

where $|F_i j m\rangle$ are the rotational wavefunction within the intermediate coupling scheme, as defined in Equation (3.7); $\langle j l m m_l | J M \rangle$ are the Clebsh-Gordan coefficients; l is the relative angular momentum, and m_l its projection on the z -axis of the Space-Fixed frame defined in Section 2.3.2.

Thus, the total wavefunction of the collisional system $\Phi_{F_i j l J M}^{J M}(\mathbf{R})$ is given by

$$\Phi_{F_i j l J M}^{J M}(\mathbf{R}) = \frac{1}{R} \sum_{F'_i j' l'} \mathcal{U}_{F'_i j' l'; F_i j l}(\mathbf{R}) |F'_i j' l' J M\rangle. \quad (3.23)$$

With the CC approach, described in Section 2.3.3, the S-matrices $S^J(j F_i l ; j' j F'_i l')$ are obtained from the boundary conditions on the wavefunction components $\mathcal{U}_{F_i j l; F'_i j' l'}(\mathbf{R})$, according to Equation (2.72). The components $\mathcal{U}_{F_i j l; F'_i j' l'}(\mathbf{R})$ are obtained by solving the set of coupled differential equations given in Equation (2.70), using the appropriate total wave function $\Phi_{F_i j l J M}^{J M}(\mathbf{R})$, as detailed in Orlikowski (1985).

The inelastic cross sections between fine structure levels N_j were computed as (Or-

likowski, 1985)

$$\sigma_{jF_i \rightarrow j'F'_i} = \frac{\pi}{(2j+1)k_{jF_i}^2} \sum_{Jl'l'} (2J+1) |\delta_{NN'} \delta_{jj'} \delta_{ll'} - S^J(jF_i l ; j'F'_i l')|^2. \quad (3.24)$$

The scattering calculations were performed using the CC approach, implemented through a modified version of the MOLSCAT code. This modified version allows for the scattering calculation of a $^3\Sigma$ molecule, with a description of the fine structure with the intermediate coupling scheme, in collisions with a structureless atom. Currently, no open-source codes account for the scattering of a $^3\Sigma$ molecule by a 1S atom. The calculations were performed similarly for all five CCS isotopologues.

The calculations were conducted for total energy E ranging from 0.5 to 600 cm^{-1} , with varying energy steps to accurately capture the resonances in the cross sections. The propagation parameters R^{MAX} , STEPS, and the basis parameter N^{MAX} (referred as j^{MAX} in Section 2.3.3) were optimized to ensure that the inelastic cross sections converged to better than 2% at all energies. More details about the scattering calculations (e.g., propagation parameters) can be found in Godard Palluet & Lique (2023a) presented in Appendix A.2.

From the computed cross sections, the rate coefficients were obtained by averaging over collisional energies assumed to follow a Maxwell-Boltzmann distribution of kinetic energies

$$k_{N_j \rightarrow N'_j}(T) = \left(\frac{8k_B T}{\pi \mu} \right)^{1/2} \left(\frac{1}{k_B T} \right)^2 \int_0^\infty \sigma_{N_j \rightarrow N'_j}(E_k) E_k \exp\left(\frac{-E_k}{k_B T} \right) dE_k, \quad (3.25)$$

with k_B the Boltzmann constant.

For these scattering calculations, the highest number of channels considered was 2,379 and 2,418 channels for parities $\epsilon = -1, 1$, respectively, which were reached from $J = 39$ when the largest rotational basis was employed, corresponding to $N^{\text{MAX}} = 39$. These calculations, which are the most computationally expensive, required approximately 300 MB of memory and less than 2 CPU hours per core per calculation. Therefore, a total of approximately 30,000 CPU hours was needed to generate rate coefficients for the 5–50 K temperature range for one CCS isotopologue in collision with a He atom. It therefore a total of 150,000 CPU hours to generate the fine-structure resolved sets of rate coefficients for all five CCS isotopologues in collision with He for the 5-50 K temperature range.

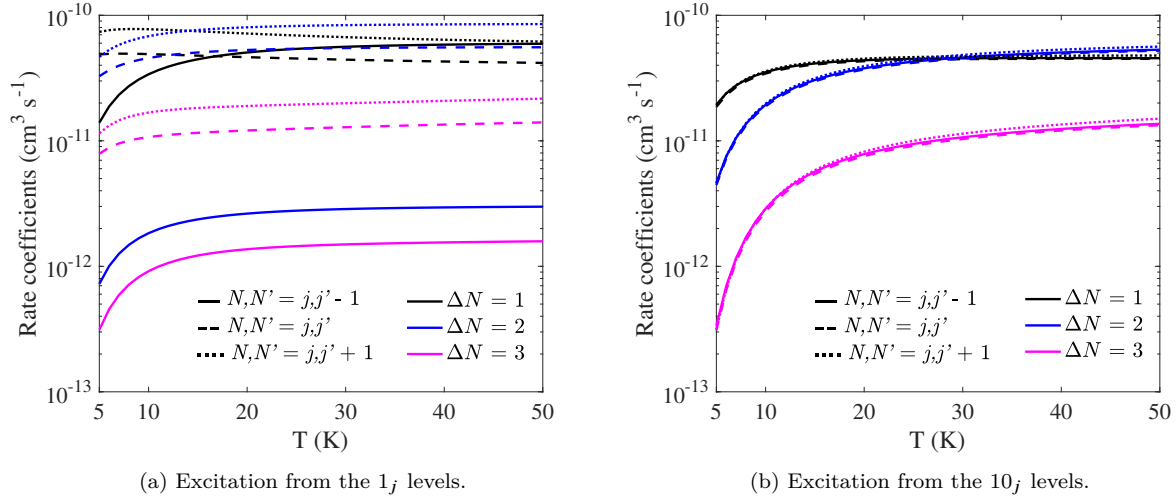


Figure 3.5: Excitation rate coefficients (in $\text{cm}^3 \text{s}^{-1}$) as a function of temperature (in K) for $\Delta N = \Delta j = 1$ (black), 2 (blue), 3 (magenta) transitions from the (a) 1_j levels and (b) 10_j levels.

3.1.2 Effect of the Complex Fine Structure

As the nature of the fine-structure levels evolves with the rotational quantum number N , the behavior of the rate coefficients is expected to vary according to the N values of the levels involved. To discuss the impact of the structure, it is important to examine the behavior of the rate coefficients for similar types of transitions within two distinct regimes: the lowest N_j levels, which need to be described by an intermediate coupling scheme, and higher $N_j \geq 10_j$ levels, for which a pure Hund's case (b) representation would have been sufficient.

The dominant transitions are within levels of the same nature, i.e. within F_1 levels (or within F_2 or F_3 levels). These type of transitions are called F_i -conserving transitions. If the fine structure levels are labeled using Hund's case (b) notations, these transitions occur within levels where $N, N' = j, j' - 1$, $N, N' = j, j'$, and $N, N' = j, j' + 1$. Consequently, for this type of transitions, $\Delta N = N' - N = \Delta j = j' - j$.

The rate coefficients as a function of temperature for the dominant transitions, where $\Delta N = \Delta j$ (F_i -conserving transitions) are represented in Figure 3.5. Specifically, the transitions within the lowest N_j levels are depicted in Figure 3.5a, and those within $N_j \geq 10_j$ levels are also illustrated in Figure 3.5b.

By comparing these rate coefficients, it is observed that their behavior varies significantly depending on the nature of the N_j levels within which the transitions occur. For transitions within the lowest N_j levels (Figure 3.5a), the behavior of $\Delta N = \Delta j$ transitions

differs significantly if $N = j - 1$ (F_1 -conserving), $N = j$ (F_2 -conserving), or $N = j + 1$ (F_3 -conserving). In other words, F_1 -conserving, F_2 -conserving and F_3 -conserving transitions exhibit distinct behaviors and values.

In contrast, when transitions occur within $N_j \geq 10_{j'}$ levels (Figure 3.5b), the behavior and values of the rate coefficients for $N = j - 1$ (F_1 -conserving), $N = j$ (F_2 -conserving), and $N = j + 1$ (F_3 -conserving) transitions become nearly identical across the full temperature range.

From this analysis, it can be concluded that the nature of the N_j levels involved in the transitions significantly impacts the behavior of the rate coefficients. However, as previously noted, the unique fine structure of CCS has never been accurately accounted for in producing CCS rate coefficients. Further discussion about the influence of the fine-structure on the propensity rules can be found in Godard Palluet & Lique (2023a) (see Appendix A.2).

To date, three sets of approximated rate coefficients have been produced for the CCS radical in the studies by Fuente et al. (1990), Suzuki et al. (1992), and Wolkovitch et al. (1997).

Fuente et al. (1990) used the purely rotational (spin-free) rate coefficients calculated with the Coupled-States approximation by Green (1978) for the OCS-H₂ collisional system. They incorporated spin-dependence to generate fine-structure-resolved rate coefficients using the IOS approximation, as presented by Alexander & Dagdigian (1983) assuming a pure Hund's case (b) for the description of the fine structure levels of CCS. The exact same methodology was employed by Suzuki et al. (1992).

Within the IOS approximation, the spin-dependent cross sections $\sigma_{N_j \rightarrow N_{j'}}$, are described by (Corey & McCourt, 1983)

$$\sigma_{N_j \rightarrow N_{j'}}(E_k) = \frac{k_0^2}{k_{N_j}^2} \sum_{\lambda} (2N + 1)(2N' + 1)(2j' + 1) \quad (3.26)$$

$$\times \begin{Bmatrix} N' & N & \lambda \\ 0 & 0 & 0 \end{Bmatrix}^2 \begin{Bmatrix} \lambda & j & j' \\ S & N' & N \end{Bmatrix}^2 \sigma_{0 \rightarrow \lambda}(E_k), \quad (3.27)$$

where $\sigma_{0 \rightarrow \lambda}$ are the rotational cross sections out of the fundamental rotational level $N = 0$. Therefore, within the IOS approximation, the cross sections are independent of the energy of the initial state, except for the factor $\frac{k_0^2}{k_{N_j}^2}$. As a result, the IOS approximation

is expected to poorly reproduce cross sections near the level threshold, particularly for strongly mixed energy levels.

The IOS approximation is generally applicable when the collisional energy is large compared to the level spacing, and the closed channels do not play a significant role (Corey & McCourt, 1983). However, CCS isotopologues have been detected in low-temperature environments, where the energies involved cannot be strictly considered "large" compared to the energy level spacings. Moreover, if only quantum numbers are considered, some transitions might be incorrectly classified as excitations when they are, in fact, de-excitations, and vice versa. This misclassification is expected to have a significant impact on the rate coefficients, as their behavior will be different if they are excitation or de-excitation.

The most sophisticated set of approximated rate coefficients was produced by Wolkovitch et al. (1997). They employed the OCS-H₂ PES computed by Green (1978) and calculated rotational rate coefficients for the CCS-H₂ system using the CC approach. Their results differed by approximately 10% compared to the OCS-H₂ rate coefficients provided by Green (1978). Based on the spin-free set of CCS-H₂ rate coefficients, Wolkovitch et al. (1997) applied the IOS approximation to incorporate the spin-dependence using the Hund's case (b) coupling scheme for the fine-structure levels, due to difficulties in implementing the intermediate coupling scheme. They provided a set of approximated fine-structure rate coefficients at 10 K and 20 K for the CCS-H₂ system for transitions within the $N_j \leq 12_j$ levels that they validated by reproducing Suzuki et al. (1992) interpretation of observations.

It is important to note that in these studies, H₂ was consistently treated as a structureless particle. Additionally, in the work of Green (1978), on which all these studies are based, the PES was computed for the OCS-He complex, with only the long-range interactions being considered with the H₂ molecule as a projectile.

To discuss the validity of the IOS approximation for systems with a large spin-spin interaction, such as CCS, a comparison between the rate coefficients produced by Wolkovitch et al. (1997) and those obtained in this work is presented in Figure 3.6.

To assess whether the deviations could significantly impact non-LTE models where these data will be employed, the Weighted Mean Error Factor (WMEF), as defined in Equation (3.28), has been evaluated by considering de-excitation rate coefficients of transitions between all 61 fine-structure levels included in the scattering calculations. The WMEF represents the deviation between the CC rate coefficients computed in this work

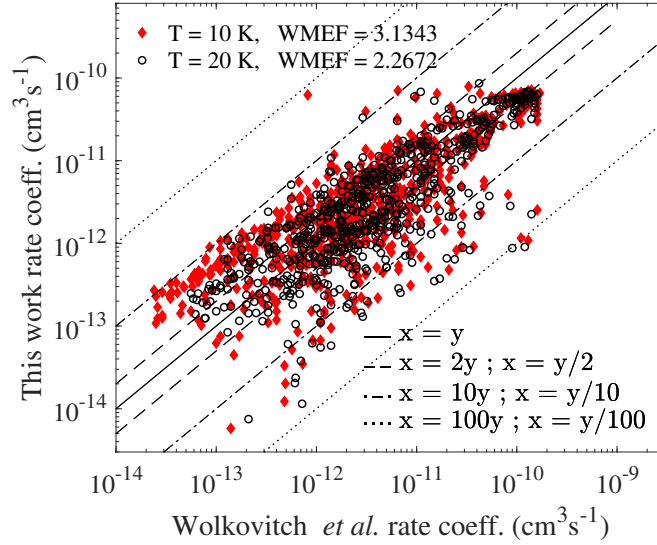


Figure 3.6: Systematic comparison between the fine-structure resolved rate coefficients produced by Wolkovitch et al. (1997) (x-axis) and those obtained in this work (y-axis) at 10 K (red diamonds) and 20 K (black circles). The solid line represents perfect agreement between the two sets of data ($x = y$); the dashed, dashed-dotted, and dotted lines delimit the regions where the rate coefficients differ by less than a factor of two, 10, and 100, respectively.

and the IOS rate coefficients computed by Wolkovitch et al. (1997), weighted by the highest rate coefficients.

$$\text{WMEF} = \frac{\sum_i k_i^{\text{REF}} r_i}{\sum_i k_i^{\text{REF}}}, \quad (3.28)$$

where $r_i = \max(k_i^{\text{REF}}/k_i, k_i/k_i^{\text{REF}}) \geq 1$, where k_i^{REF} and k_i are the rate coefficients for the i^{th} transition computed with the CC approach in this work (considered as the reference), and with the IOS approximation by Wolkovitch et al. (1997), respectively. Therefore, $k_i^{\text{REF}} \equiv k_i^{\text{CC}}$ and $k_i \equiv k_i^{\text{IOS}}$.

A large deviation between the two sets of rate coefficients is observed at both temperatures. The rate coefficients are sparsely distributed around the $x = y$ axis, and they tend to be slightly larger in the work of Wolkovitch et al. (1997) than the ones computed in this work. Most of the rate coefficients agree within a factor of 10, although for some transitions, the deviation can be as large as two orders of magnitude. The agreement for dominant transitions is slightly better; however, the WMEF still indicates a global deviation of a factor 3.13 and 2.27 at 10 K and 20 K, respectively. The agreement improves at

20 K compared to 10 K, suggesting that at higher temperatures, the IOS approximation aligns better with the CC results; nevertheless, the deviations remain significant.

The largest deviations are coming from F_1-F_3 transitions that are generally underestimated by the IOS approximation, for which the WMEF is as high as 5.28 and 4.24 at 10 K and 20 K, respectively. Fuente et al. (1990) predicted that using a Hund’s case (b) description of the fine structure would overestimate that the rate coefficients for F_1-F_2 transitions due to Equation (3.26). These rate coefficients are also overestimated by the IOS approximation, and a large WMEF is also exhibited, with a value of 3.39 and 3.68 at 10 K and 20 K, respectively. These are the only type of transitions for which the WMEF increase with temperature, suggesting the overestimation of F_1-F_2 transitions will not get better at higher temperature, where the IOS approximation is expected to work better. Such large deviations in the rate coefficients are expected to impact the modeling of CCS spectra in dark molecular clouds, where the temperature ranges from about 10 to 20 K. Indeed, the sensitivity threshold of such models for interstellar applications have been estimated by Roueff & Lique (2013) at a factor of two on the rate coefficients, which is greatly exceeded here.

As the large deviation could originate from differences in the spin-free rate coefficients rather than from the IOS approximation itself, spin-free (purely rotational) rate coefficients were computed in this work based on the CCS-He PES calculated here, providing rotational rate coefficients at 10 K and 20 K. These spin-free rate coefficients were compared to the CCS-H₂ spin-free rate coefficients from Wolkovitch et al. (1997). These rate coefficients were computed as

$$k_{N \rightarrow N'}(T) = \sum_{jj'} k_{N_j \rightarrow N'_{j'}}(T), \quad (3.29)$$

where $k_{N_j \rightarrow N'_{j'}}(T)$ are the spin-dependent rate coefficients, which are available in the paper of Wolkovitch et al. (1997).

A systematic comparison of the two sets of data for transitions from the ground state $N = 0$ is shown in Figure 3.7, as the IOS spin-dependent cross sections are constructed from the cross sections out of the fundamental rotational level $N = 0$ according to Equation (3.26).

The agreement between the two sets of rotational rate coefficients is generally good, with most of the rate coefficients agreeing within a factor of two. The WMEF is of

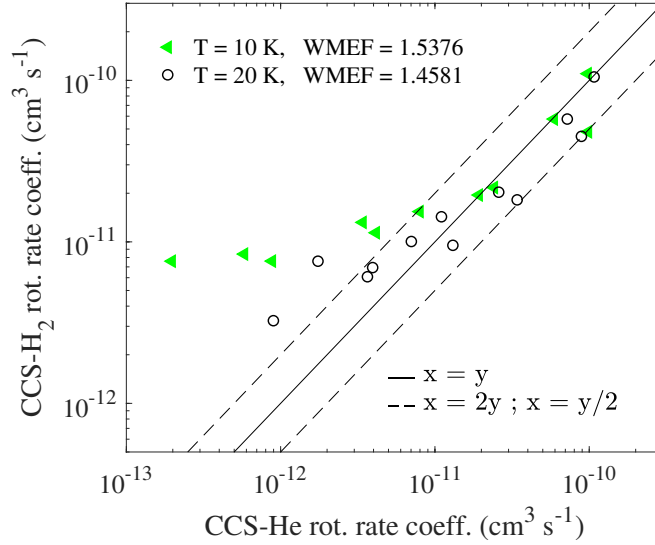


Figure 3.7: Systematic comparison between excitation the spin-free rate coefficients $k_{0 \rightarrow N'}$ of CCS-He computed in this work (x-axis) and for the CCS-H₂ computed by Wolkovitch et al. (1997) (y-axis) at 10 K (green triangles), and 20 K (black circles).

1.54 and 1.46 at 10 K and 20 K, respectively, which is significantly lower than the WMEF observed when comparing the rate coefficients computed using the CC and IOS approaches in Figure 3.6. Additionally, the WMEF decreases less with temperature compared to the trend observed in the previous comparison. Therefore, the large deviation observed between the rate coefficients from Wolkovitch et al. (1997) and those computed in this work can be attributed to the IOS approach.

The limitations of the IOS approximation for systems with fine-structure levels that have large spin-spin interaction were previously noted by Lique et al. (2005) in their study of SO ($^3\Sigma$) excitation induced by He atoms at low temperatures. This issue arises because the IOS approximation assumes a pure Hund’s case (b), which poorly describes the low-lying N_j levels of molecules with large spin-spin interaction, such as SO and CCS. This inaccurate representation not only leads to an incorrect evaluation of the wavefunctions of the states involved but also mischaracterizes the nature of the transitions. As previously mentioned, by neglecting the intermediate coupling between Hund’s cases (b) levels, some transitions within the low-lying levels may be incorrectly classified as excitations when they are actually de-excitations, and vice versa, thus introducing significant errors into the rate coefficients.

Therefore, only the CC approach (or the Coupled-States approach), which accounts for

the intermediate coupling scheme, can be used to accurately determine the rate coefficients of CCS and its isotopologues.

3.1.3 Effect of the Isotopic Substitution

In radiative transfer models, the excitation conditions of isotopologues are often assumed to be identical. To evaluate the validity of this assumption for CCS isotopologues, the effect of isotopic substitution on the rate coefficients is investigated.

To study this effect, a systematic comparison of the fine-structure resolved rate coefficients for CCS isotopologues has been performed, as shown in Figure 3.8a for the isotopic substitution of one of the ^{12}C atoms by ^{13}C , and in Figure 3.8b for the isotopic substitution of ^{32}S by ^{33}S or ^{34}S . Only de-excitation transitions between the first 31 fine-structure levels are represented for clarity.

The WMEF, as defined in Equation (3.28), was calculated to evaluate the impact of the deviations on the non-LTE modeling of CCS isotopologues, where dominant transitions have a greater influence. The rate coefficients of the secondary isotopologues are compared to the ones of the main isotopologue, considered as the reference. Therefore, $k_i^{\text{REF}} \equiv k_i^{\text{MAIN}}$ and $k_i \equiv k_i^{\text{SEC}}$.

For the isotopic substitution of one ^{12}C by ^{13}C , the sets of fine-structure resolved rate coefficients of both C^{13}CS and ^{13}CCS agree very well with the set of CCS rate coefficients at both 10 K and 50 K. The global deviation, indicated by the WMEF, is lower than a factor 1.01 for C^{13}CS , and lower than a factor 1.03 for ^{13}CCS at both temperatures, and slightly decreases with increasing temperatures. As the temperature increases, the threshold effect, or the influence of the energy of the fine-structure levels, becomes less significant. The features of the PES will also have a reduced influence on the cross-sections. Since the differences between the collisional systems of the two isotopologues arise from the shift in the PES ($\delta r_{\text{C}^{13}\text{CS}} = 0.0205a_0$ and $\delta r_{^{13}\text{CCS}} = 0.0640a_0$) and differences in the spectroscopic constants (by a few percent), it is not surprising that the isotopic substitution of one ^{12}C does not have a strong effect on the rate coefficients.

It is noteworthy that the deviation is greater for the comparison between CCS and ^{13}CCS rate coefficients compared to the comparison between CCS and C^{13}CS , which can be simply explained by a larger shift of the center of mass. A larger shift of the center of mass will affect more the moments of inertia, which modifies the spectroscopic constants, leading to greater differences in the energy levels. A larger shift also implies more changes

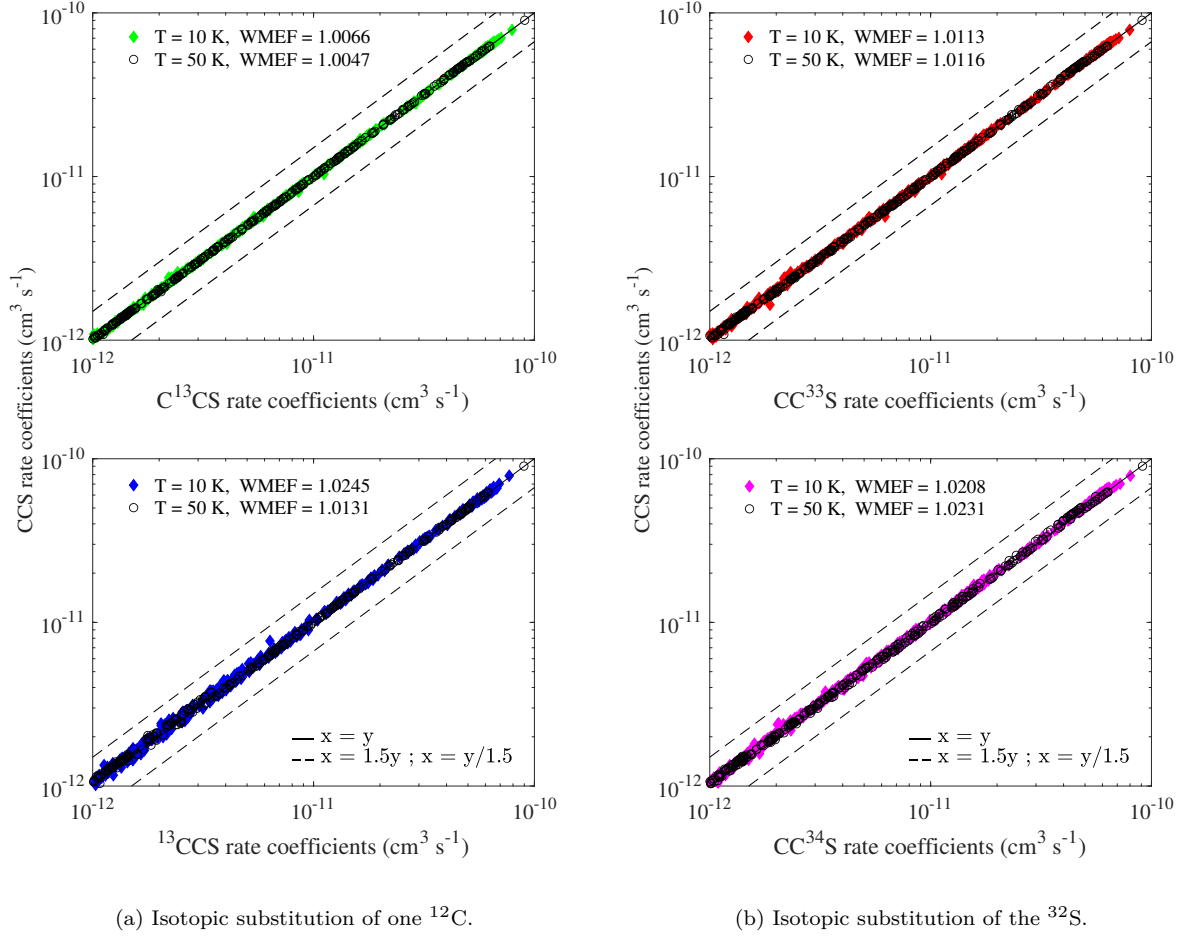


Figure 3.8: Systematic comparison of the de-excitation rate coefficients (in $\text{cm}^3 \text{s}^{-1}$) of the CCS-He collisional system and rate coefficients of (a) C^{13}CS -He (upper panel) and ^{13}CCS -He (lower panel); (b) CC^{33}S -He (upper panel) and CC^{34}S -He (lower panel) collisional systems, at 10 K (colored diamonds) and 50 K (black circles).

in the PES. Therefore, this explains why the deviation is slightly larger for ^{13}CCS than for C^{13}CS .

For the isotopic substitution of ^{32}S by either ^{33}S or ^{34}S , the deviation in the rate coefficients is also small, with a WMEF lower than 1.02 for CC^{33}S , and lower than 1.03 for CC^{34}S at both temperatures. Similar to the isotopic substitution of ^{12}C , the larger the shift of the center of mass, the greater the deviation (although it remains small). However, in contrast to the WMEF calculated for the isotopic substitution of ^{12}C , the WMEF increases with temperature. Nonetheless, the changes are minimal and could be considered potential numerical artifacts.

For all sets of rate coefficients at all temperatures, the WMEF is always lower than 1.05 for all isotopologues at both 10 K and 50 K. This indicates that the effect of isotopic substitution of either ^{12}C or ^{32}S leads to a global deviation of less than a factor 1.05 on the fine-structure resolved rate coefficients.

From this comparison, it can be concluded that the sets of rate coefficients are very similar for all CCS isotopologues. Therefore, for future studies, restricting the calculations to only one isotopologue should be sufficient, allowing for a significant reduction in computational effort while ensuring high accuracy in the non-LTE modeling of CCS isotopologues. Further details about the effect of isotopic substitution on the rate coefficients of CCS isotopologues can be found in Godard Palluet & Lique (2023b) presented in Appendix A.3.

3.1.4 Nuclear Spins and Hyperfine Structure of ^{13}CCS , C^{13}CS and CC^{33}S

Rotational Spectroscopy

When a molecule contains atoms with non-zero nuclear spin, a coupling between this nuclear spin I and the nuclear spin-free total angular momentum j occurs. As a result, each fine-structure level is split into hyperfine structure levels. The appropriate quantum number to describe these levels is F , which is defined as

$$\hat{F} = \hat{j} + \hat{I}, \quad (3.30)$$

with $|j - I| \leq F \leq j + I$.

In this work, two types of isotopic substitutions involve isotopes with non-zero nuclear spins: ^{13}C ($I = 1/2$) and ^{33}S ($I = 3/2$). Consequently, each fine-structure level of ^{13}C -bearing isotopologues is split into two hyperfine levels for $j \geq 1$, and into four hyperfine levels for $j \geq 2$ in ^{33}S -bearing isotopologues (for the latter, only three hyperfine levels arise from fine-structure levels with $j = 1$).

The molecular Hamiltonian \hat{H}_{mol} is then defined as

$$\hat{H}_{mol} = \hat{H}_{fine} + \hat{H}_{hfs}, \quad (3.31)$$

with $\hat{H}_{fine} = \hat{H}_{rot} + \hat{H}_{sr} + \hat{H}_{ss}$ defined in Equations (3.4) to (3.6); \hat{H}_{hfs} represents the hyperfine structure Hamiltonian, defined as the sum of \hat{H}_Q (the quadrupole interac-

tion Hamiltonian), $\hat{H}_{\hat{I},\hat{j}}$ (the magnetic hyperfine interaction Hamiltonian), and $\hat{H}_{\hat{S},\hat{I}}$ (the spin-spin interaction Hamiltonian, also known as the Fermi contact interaction). These Hamiltonians are expressed as

$$\hat{H}_Q = \frac{eQq}{2I(2I-1)j(2j-1)} \left[3(\hat{I} \cdot \hat{j})^2 + \frac{3}{2}(\hat{I} \cdot \hat{j}) - \hat{I}^2 \cdot \hat{j}^2 \right], \quad (3.32)$$

$$\hat{H}_{\hat{I},\hat{j}} = c(\hat{I} \cdot \hat{j}), \quad (3.33)$$

$$\hat{H}_{\hat{S},\hat{I}} = b_F(\hat{I} \cdot \hat{j}), \quad (3.34)$$

where c , b_F , and eQq are the nuclear spin-rotation, Fermi contact, and quadrupolar coupling constants, respectively. The quadrupolar coupling constant is non-zero only for $I \geq 1$, hence only $eQq(\text{CC}^{33}\text{S}) \neq 0$. The values of these constants can be found in Table 3.1.

Scattering Calculations

To account for the hyperfine structure of ^{13}CCS , C^{13}CS , and CC^{33}S in the scattering calculations and to produce hyperfine-structure resolved rate coefficients, the recoupling method was employed.

Since the potential is independent of the nuclear spin involved in the collision, I can be considered a spectator in the collision process. This approximation is considered valid due to the weak coupling between the different angular momenta, which results in small hyperfine splittings between hyperfine structure levels. Typically, the energy difference between two hyperfine levels within the same fine-structure level is approximately 10^{-3} cm^{-1} . Therefore, it is assumed that the energy differences between the hyperfine levels involved will not play a significant role in the collision, so that this approximation will not significantly affect the rate coefficients.

In the recoupling approach, which is the most accurate method aside from the full CC approach, the hyperfine cross sections are inferred from the nuclear spin-free S-matrix $S^J(jF_i l ; j'F'_i l')$ obtained using the full CC approach as described in Alexander & Dagdigan (1985)

$$\sigma_{jF_i, F \rightarrow j'F'_i, F'}(E_k) = \frac{\pi}{k_{jF_i}^2} (2F' + 1) \sum_K \left\{ \begin{matrix} j & j' & K \\ F' & F & I \end{matrix} \right\}^2 P^K(jF_i \rightarrow j'F'_i), \quad (3.35)$$

with

$$P^K(jF_i \rightarrow j'F'_i) = \frac{1}{2K+1} \sum_{l'l'} |T^K(jF_i l ; j'F'_i l')|^2, \quad (3.36)$$

and

$$T^K(jF_i l ; j'F'_i l') = (-1)^{-j-l'} (2K+1) \sum_J (-1)^J (2J+1) \quad (3.37)$$

$$\times \begin{Bmatrix} l' & j' & J \\ j & l & K \end{Bmatrix} [\delta_{FF'} \delta_{jj'} \delta_{ll'} - S^J(jF_i l ; j'F'_i l')], \quad (3.38)$$

with $|F - F'| \leq K \leq F + F'$.

Within this approximation, the hyperfine-structure levels jF_i, F are assumed to be degenerate and have the same energy than the corresponding fine-structure level jF_i . Consequently, the kinetic energy for the cross sections integration is computed as $E_k = E - E_{jF_i}$.

Since the ^{13}CCS , C^{13}CS , and CC^{33}S isotopologues have been detected only in dark molecular clouds, it was decided to restrict the calculation of hyperfine rate coefficients to the 5–15 K temperature range to limit the computational cost. Therefore, hyperfine levels up to $N_j, F \leq 10_{10}, F$ were considered, which includes all hyperfine levels with internal energies lower than approximately 30 cm^{-1} . Cross sections were computed using the recoupling approach for total energies $\leq 120 \text{ cm}^{-1}$. By integrating over the kinetic energies, the hyperfine-structure resolved rate coefficients for the 5–15 K temperature range were obtained for the ^{13}CCS , C^{13}CS , and CC^{33}S isotopologues.

Propensity Rules

To study the propensity rules induced by the hyperfine structure, Figure 3.9 presents the hyperfine-structure resolved de-excitation rate coefficients of ^{13}CCS (blue) and C^{13}CS (green) as a function of ΔN at 10 K for various transitions out of the $4_5, F$ hyperfine levels. Since the rate coefficients have been computed based on the fine-structure resolved S-matrices $S^J(jF_i l ; j'F'_i l')$, only the propensity rules regarding the hyperfine quantum number F will be discussed here.

The rate coefficients for both isotopologues appear to follow the same propensity rules, so all following conclusions hold for both isotopologues. Also, these propensity rules are shown at 10 K, but are generally respected over the whole range of temperatures.

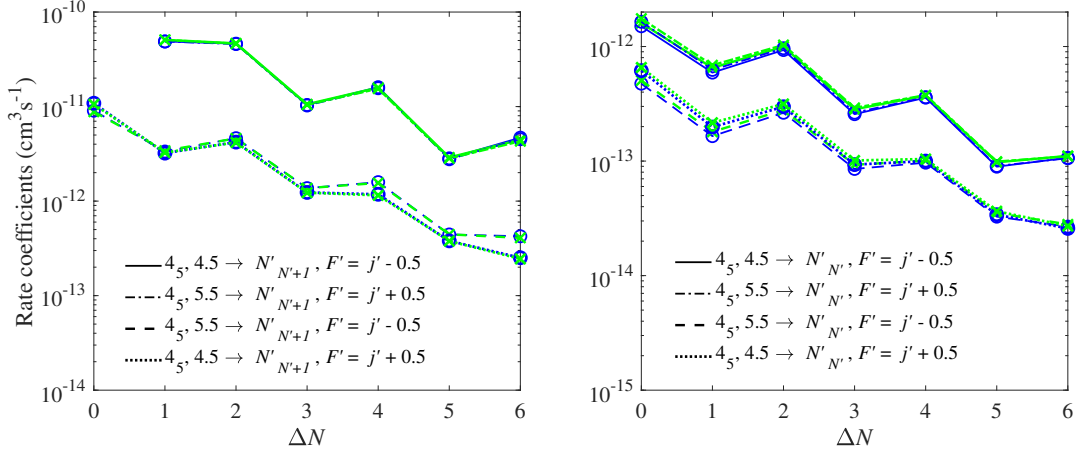


Figure 3.9: Propensity rules for hyperfine-structure resolved excitation rate coefficients at 10 K for ^{13}CCS (blue) and C^{13}CS (green) isotopologues from the $4_5, F$ hyperfine-structure levels as a functions of $\Delta N = N' - N$. Rate coefficients for $\Delta N = \Delta j$ (F_i -conserving, left panel) and $\Delta N \neq \Delta j$ (F_i -changing, right panel) transitions.

For $\Delta N = \Delta j$ (F_i -conserving, left panel) transitions and $\Delta N \neq \Delta j$ (F_i -changing, right panel) transitions, a propensity rule in favor of $\Delta j = \Delta F$ transitions (solid and dashed-dotted lines) is observed, which is typical of systems with hyperfine structure due to the Wigner 6- j symbol. These rules were predicted by Dixon & Field (1979) and Alexander & Dagdigan (1985) and confirmed experimentally by Alexander & Dagdigan (1985). This behavior has also been observed in other systems (Daniel et al., 2004; Dumouchel et al., 2012; Kalugina et al., 2012; Buffa, 2012; Lique et al., 2016; Dumouchel et al., 2017; Dagdigan, 2018; Ndaw et al., 2021; Pirlot Jankowiak et al., 2023b; Pirlot Jankowiak et al., 2023a). However, $\Delta N = \Delta j = \Delta F$ transitions are favored over $\Delta N \neq \Delta j = \Delta F$ transitions. For the $\Delta j = \Delta F$ propensity rule, the values of F and F' do not significantly matter, and rate coefficients are nearly identical for $F, F' = j, j' - 0.5$ (solid lines) and $F, F' = j, j' + 0.5$ (dashed-dotted lines) across both $\Delta N = \Delta j$ (left panel) and $\Delta N \neq \Delta j$ (right panel) for the entire range of ΔN .

Transitions with $\Delta j \neq \Delta F$ lead to similar hyperfine-structure resolved rate coefficients for $\Delta N = \Delta j$ (left panel) and $\Delta N \neq \Delta j$ (right panel) transitions. However, hyperfine rate coefficients with $F = j + 0.5$ and $F' = j' - 0.5$ (dotted lines) are slightly dominant compared to those with $F = j - 0.5$ and $F' = j' + 0.5$ (dashed lines) for $\Delta N = \Delta j$ transitions, and the opposite behavior is observed for $\Delta N \neq \Delta j$ transitions.

For $\Delta N \neq \Delta j$ transitions, the deviation between the rate coefficients of ^{13}CCS and C^{13}CS is slightly larger compared to $\Delta N = \Delta j$ transitions. However, the differences

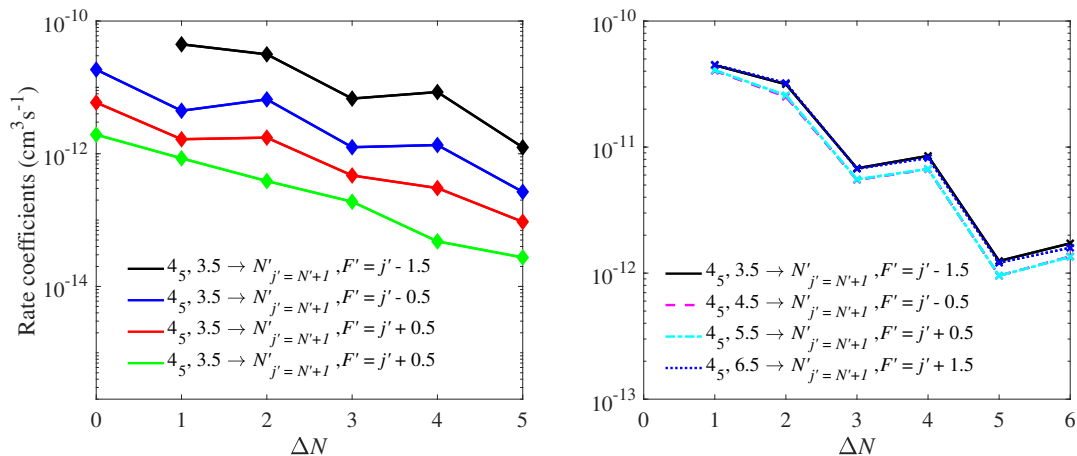


Figure 3.10: Propensity rules for hyperfine-structure resolved rate coefficients of CC^{33}S isotopologue at 10 K from the 4_5 , F levels. Rate coefficients for $\Delta N = \Delta j$ (right panel) and $\Delta j = \Delta F$ (right panel) transitions are investigated.

remain reasonable.

The rate coefficients seem to favor even $\Delta N = \Delta j = \Delta F$ over odd $\Delta N = \Delta j = \Delta F$, but this behavior appears to originate from the PES rather than from the quantum number F , so it will not be further discussed here.

The hyperfine-structure excitation rate coefficients of the CC^{33}S isotopologue from the 4_5 , F hyperfine levels at 10 K are presented in Figure 3.10. The left panel discusses the impact of ΔF on $\Delta N = \Delta j$ transitions, while the right panel examines the impact of F , F' values on $\Delta j = \Delta F$ transitions.

Similar to ^{13}CCS and C^{13}CS , the dominant transitions in CC^{33}S are those for which $\Delta j = \Delta F$, with $\Delta N = \Delta j = \Delta F$ (black lines) transitions being the most prominent.

Due to the larger nuclear spin of CC^{33}S ($I(^{33}\text{S}) = 3/2 > I(^{13}\text{C}) = 1/2$), more values of F are allowed, enabling a more detailed discussion of the impact of ΔF . As observed in the left panel, for a fixed $\Delta N = \Delta j$, the rate coefficients decrease as ΔF increases. This trend is consistent for all F_i -conserving and F_i -changing transitions.

For $\Delta j = \Delta F$ transitions (right panel), it is observed that transitions with $F, F' = j, j' \pm 1.5$ are nearly identical and slightly dominant compared to transitions with $F, F' = j, j' \pm 0.5$, which are also very similar.

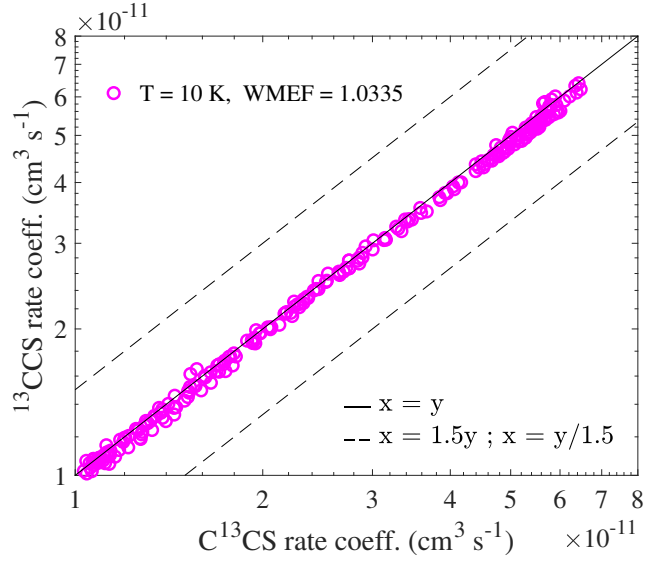


Figure 3.11: Systematic comparison of dominant de-excitation hyperfine-structure resolved rate coefficients at $T = 10$ K of the ^{13}CCS (x-axis) and C^{13}CS (y-axis) isotopologues.

Effect of the Isotopic Substitution

The hyperfine-structure resolved rate coefficients of both ^{13}CCS and C^{13}CS isotopologues are systematically compared in Figure 3.11 to discuss the isotopic effect induced by the position of the ^{13}C on the collisional rate coefficients. In the WMEF calculation, ^{13}CCS was arbitrarily considered as the reference, so $k_i^{\text{REF}} \equiv k_i^{13\text{CCS}}$ and $k_i \equiv k_i^{\text{C}^{13}\text{CS}}$.

The similarities between the datasets are quite pronounced, with overall agreement better than 10-15% for the dominant transitions and better than 40% for any transitions. This result is not surprising, as the deviation between the two sets of data appeared to be quite low when comparing the fine-structure rate coefficients. The WMEF was evaluated at 1.025 at 10 K when comparing the two sets of fine-structure rate coefficients. Therefore, the deviation slightly increased when the hyperfine-structure was taken into account, but the two sets of rate coefficients remain very similar.

3.1.5 Discussion

The effect of the peculiar fine structure of CCS was investigated, and it was found to have a significant impact on the rate coefficients. Therefore, scattering approaches that accurately account for this fine structure, described by an intermediate coupling scheme, must be employed. When comparing our datasets with those obtained in previous work,

discrepancies of up to two orders of magnitude were found, suggesting that the non-LTE modeling of CCS should be performed using the new rate coefficients provided in this work.

The effect of the isotopic substitution on the fine-structure rate coefficients was found to be weak. Thus, if the sets of rate coefficients wanted to be extended (in temperature or to other collisional partners, for example), one set of rate coefficients should suffice for the non-LTE modeling of all CCS isotopologues. However, for the hyperfine structure, the nuclear spin differs for ^{13}C isotopologues and ^{33}S , necessitating at least three sets of data: one set of fine-structure rate coefficients for all fine-structure levels, one set for all isotopologues containing one ^{13}C (and no other atoms with a nuclear spin), and one set for isotopologues containing ^{33}S with no other atoms with a nuclear spin. If doubly substituted CCS isotopologues were to be detected, their non-LTE modeling could be analyzed according to these requirements. Only $^{13}\text{CC}^{33}\text{S}$ or $\text{C}^{13}\text{C}^{33}\text{S}$ would require the calculation of a new set of data, but this could be based on the fine S-matrices computed for any of the CCS isotopologues.

3.2 Beyond Quantum Approaches to Study Heavy Collisional Systems: CS in Comets

When quantum approaches are no longer applicable due to high computational costs or memory allocation limitations in quantum scattering programs, alternative methods must be employed. In this section, the study of collisional excitation of CS induced by CO and H₂O, the most abundant molecules in cometary comae, is presented. The complexities that arise from considering such heavy colliders, and the strategies to handle them, are discussed. The accuracy of the rate coefficients obtained in this work is also discussed.

3.2.1 The Challenge of Heavy Projectiles

The CO Projectile

Usually, rate coefficients are computed for the study of the ISM where H₂ is dominant, and thus most of the collisional system involves H₂ as a projectile. Using CO adds a number of additional complexities compared to the H₂ projectile. With a rotational constant ($B_{\text{CO}} = 1.931 \text{ cm}^{-1}$, Le Floch (1991)) more than 30 times lower than that of H₂ ($B_{\text{H}_2} = 60.85 \text{ cm}^{-1}$, Huber & Herzberg (1979)), the rotational structure of CO is significantly denser than that of H₂. This density introduces a numerical challenge, as the cost of scattering calculations increases with the number of levels included in the scattering calculations.

To date, the only system of astrophysical interest studied with CO as a projectile is the CO-CO collisional system. Initially, it was studied by Ndengué et al. (2015) using the Multi-Configuration Time-Dependent Hartree (MCTDH) quantum approach, but the calculations were limited to transitions between the first four rotational levels, which is not sufficient for radiative transfer applications above 20 K. Later, it was studied by Żółtowski et al. (2022), who computed rate coefficients for transitions within the first 11 rotational levels of both colliders up to 100 K using the Coupled-States quantum approach. They reported using over 2 million CPU hours for the scattering calculations alone and encountered many problems due to memory limitations, as the calculations were performed at the edge of what current quantum scattering programs can handle (Żółtowski, 2023).

The rotational constant of CS ($B_{\text{CS}} = 0.817 \text{ cm}^{-1}$, Bustreel et al. (1979)) is half that of CO, meaning that the density of rotational levels of CS is nearly twice that of CO, as exhibited in Table 3.3. The more the temperature increases, the more the computational

CS		CO	
j_{CS}	$E_{j_{\text{CS}}}$	j_{CO}	$E_{j_{\text{CO}}}$
0	0.000	0	0.000
1	1.634	1	3.845
2	4.902	2	11.54
3	9.804	3	23.07
4	16.34	4	38.45
5	24.51	5	57.67
6	34.32	6	80.74
7	45.75	7	107.6
8	58.82	8	138.4
9	73.53	9	173.0
10	89.86	10	211.4
11	107.8	11	253.7
12	127.4	12	299.8
13	148.7	13	349.7
14	171.5	14	403.5
15	196.0	15	461.1
16	222.1	16	522.5
17	249.9		
18	279.3		
19	310.3		

Table 3.3: Energy (in cm^{-1}) of the lowest rotational levels of CS and CO. The rotational levels of CS and CO are labeled with the quantum number j_{CS} and j_{CO} .

cost of scattering calculations will increase if CS is considered as the target molecule compared to CO.

Additionally, the dipole moment of CS (1.98 D) is much larger than that of CO (0.112 D),¹ resulting in stronger interactions between the colliders, leading to a deeper potential well. As the rotational basis required to converge quantum calculations increases with potential depth, the rotational basis needed to converge CS-CO quantum calculations is expected to be much larger than for CO-CO. Combining the two factors, performing quantum calculations for the CS-CO collisional system is unlikely to be feasible, even using the Coupled-States approximation as done for the CO-CO system by Żółtowski et al. (2022).

¹<https://kida.astrochem-tools.org>

The H₂O Projectile

Considering H₂O as a collider also introduces additional complexities compared to using H₂ as a projectile in the determination of the collisional rate coefficient. H₂O is an asymmetric top molecule, so its rotational Hamiltonian is defined as

$$\hat{H}_{rot} = A\hat{j}_a^2 + B\hat{j}_b^2 + C\hat{j}_c^2, \quad (3.39)$$

where $A = 27.877 \text{ cm}^{-1}$, $B = 14.512 \text{ cm}^{-1}$, $C = 9.285 \text{ cm}^{-1}$, are the rotational constants taken from Herzberg (1966) corresponding to the moments of inertia along the a , b , and c axes, respectively, with $I_a \neq I_b \neq I_c$. The rotational levels of an asymmetric top are often labeled using $j_{k_a k_c}$, where k_a and k_c are the projections of the angular momentum on the a and c axes. This results in a complex rotational structure for H₂O, as exhibited in Table 3.4. Since the rotational constants of H₂O are larger than those of CO, its rotational structure is less dense than that of CO.

A significant advantage of H₂O over CO is that, due to the nuclear spin states ($I = \frac{1}{2}$) of its two protons and symmetry considerations, it can be separated into *para*- and *ortho*-H₂O. In *para*-H₂O (hereafter referred to as p-H₂O), the nuclear spins are antiparallel, resulting in a total nuclear spin of 0, which allows only even $|\tau| = |k_a - k_c|$ rotational levels. In *ortho*-H₂O (hereafter referred to as o-H₂O), the nuclear spins of the two hydrogen atoms are parallel, resulting in a total nuclear spin of 1, which allows only odd $|\tau|$ rotational levels. Since collisional (and radiative) transitions are forbidden between *ortho* and *para* species, o-H₂O and p-H₂O can be treated as separate species, as they are not connected through inelastic collisions. Consequently, scattering calculations are performed for two distinct systems: CS-p-H₂O and CS-o-H₂O. While this requires producing two sets of data, the density of states for each system is significantly reduced compared to a scenario where they were connected through inelastic transitions.

The PES of the CS-H₂O system is expected to be more complex than that of the CS-CO system due to an extra dimension required, necessitating more expansion coefficients and, consequently, additional memory in the scattering calculations. Therefore, for an identical rotational basis, calculations for the CS-H₂O system are expected to be more computationally demanding than for the CS-CO system. More importantly, the dipole of H₂O (1.85 D)¹ is much larger than the one of CO (0.112 D), which lead to stronger interaction with other colliders, and thus to deeper potential well. However, as already mentioned, deeper well means more channels required to converge CC calcula-

p-H ₂ O				o-H ₂ O			
j	k_a	k_c	$E_{jk_a k_c}$	j	k_a	k_c	$E_{jk_a k_c}$
0	0	0	0.000	1	0	1	23.80
1	1	1	37.16		1	0	42.39
2	0	2	70.13	2	1	2	79.53
	1	1	95.21		2	1	135.3
	2	0	136.6	3	0	3	136.9
3	1	3	142.4		1	2	173.5
	2	2	206.7		2	1	212.6
4	0	4	222.4	4	1	4	225.1
	1	3	276.0	3	3	0	287.5
3	3	1	287.3				

Table 3.4: Energy (in cm⁻¹) of the lowest rotational levels of p-H₂O and o-H₂O. The rotational levels are labeled with j , k_a , k_c quantum numbers.

tions. Therefore, the computational effort required to converge CC calculations with H₂O as the projectile is expected to be greater than when CO is used as the projectile.

3.2.2 The Collisional Excitation of CS Induced by CO

CS-CO Interaction Potential

The PES of the CS-CO system have been computed in collaboration with Pr. Richard Dawes and Dr. Ernesto Quintas-Sánchez (Missouri University of Science and Technology, USA).

The ground state of the CS-CO system being well isolated from excited states, the Born-Oppenheimer and Coupled-Clusters theories are appropriate for its description, and so for the calculation of its interaction potential. The rigid rotor approximation was employed, fixing the intramolecular distances within the two monomers. This approximation is usually adequate when low temperatures are considered, as vibrational states are expected to be closed. In this case, the first vibrational state of CS is $\nu_1 = 1,272.13$ cm⁻¹, and for CO, $\nu_1 = 2,143.53$ cm⁻¹, so the rigid rotor approximation can be safely applied. The intramolecular distances were fixed at $r_{C-O} = 2.13a_0$ (Le Floch, 1991), and $r_{C-S} = 2.90a_0$ (Bogey et al., 1982), the equilibrium geometry of the CS and CO molecules, respectively.

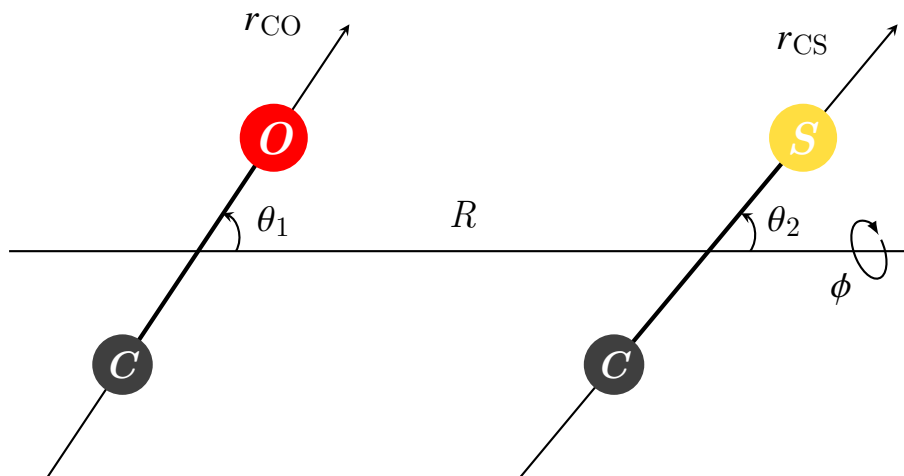


Figure 3.12: Representation of the CS-CO collisional system in Jacobi coordinates (R , θ_1 , θ_2 , and ϕ).

The description of the interaction energy between the colliders forming the complex is based on four Jacobi coordinates (R , θ_1 , θ_2 , and ϕ). The radial parameter R defines the distance between the centers of mass of each monomer, while θ_1 and θ_2 define the angles between R and the internuclear axes of CO (denoted \mathbf{r}_{CO}) and CS (denoted \mathbf{r}_{CS}), respectively. ϕ defines the out-of-plane (dihedral) torsional angle, which is the angle between the planes defined by \mathbf{R} and \mathbf{r}_{CO} , and \mathbf{R} and \mathbf{r}_{CS} . A representation of the CS-CO collisional system in Jacobi coordinates as employed in this study is shown in Figure 3.12.

The PES was computed using the AUTOSURF package, designed to assist in the creation of accurate PESs, as described by Quintas-Sánchez & Dawes (2019). This code interfaces with MOLPRO (Werner et al., 2020). The procedure starts with a sparse distribution of *ab initio* seed points, from which a fitted PES is computed over a range of energies and coordinates defined by the user. If the desired accuracy (evaluated by a RMS error) is not reached, additional data points are added in regions of low accuracy, and the procedure repeats until the desired global accuracy is achieved.

The fitting algorithms implemented in the code are based on the local interpolating moving least-squares (L-IMLS) methodology, as detailed in Dawes et al. (2010) and Dawes & Quintas-Sánchez (2018).

A total of 3,991 single-point *ab initio* energies were calculated for various geometries of the CS-CO complex, spanning the entire range of interaction. The CCSD(T)-F12b/aug-cc-pVTZ level of theory was employed, as this *ab initio* method is well-suited for accurate interaction potential calculations. The BSSE was corrected for all interaction energies at each geometry using the procedure of Boys & Bernardi (1970) [see Equation (2.46)]. The

potential was evaluated for R ranging from 1.6 Å ($\approx 3.024a_0$) to 20 Å ($\approx 37.79a_0$), and was extended by an analytic form using dispersion coefficients $\frac{C_n}{R^n}$ until the interaction energy between the monomers reaches zero. Energies were computed for θ_1 and θ_2 angles between 0° and 180°, and ϕ angle between 0° and 180° only due to symmetry considerations. Additionally, a maximum repulsive potential energy was set at approximately 2,100 cm⁻¹ in the short-range region. As long as the total energy for the study of the collisional excitation of CS induced by CO remains below this value, this restriction will not impact the validity of the results.

For an illustration of the features of the PES, contour plots and their corresponding 3D representations are shown in Figure 3.13. In Figure 3.13a, the radial dependence of the potential with respect to θ_2 at fixed θ_1 and ϕ is displayed. In this figure, the radial dependence is quite pronounced, characterized by a large energy gradient. The Global Minimum (GM) of the PES is located at $R = 9.1a_0$, $\theta_1 = 180^\circ$, $\theta_2 = 180^\circ$, $\phi = 0^\circ$, with a value of -235.57 cm⁻¹.

In Figure 3.13b, the angular dependence of the potential with respect to θ_1 and θ_2 is exhibited at fixed $R = 9.1a_0$ and $\phi = 0^\circ$. For both angles, the angular dependencies are strong with large energy gradients. The angular dependence on θ_2 is weaker, though the energy gradient remains substantial. The GM of the PES is also visible in this figure, in addition to two Local Minima (LM) for the $\theta_1 = 101^\circ$, $\theta_2 = 0^\circ$ geometry at -223.14 cm⁻¹, and for the $\theta_1 = 0^\circ$, $\theta_2 = 180^\circ$ geometry at -140.67 cm⁻¹.

From Figure 3.13, the PES of the CS-CO system appear to be highly anisotropic. For example with respect to θ_1 when the potential varies from over 1,000 cm⁻¹ to -223.14 cm⁻¹ by only a rotation of approximately $\pi/2$.

Scattering Calculations

Statistical approaches, such as the Statistical Adiabatic Channel Model (SACM) developed by Quack & Troe (1974), Quack & Troe (1975), and Loreau et al. (2018b), are particularly beneficial for the study of collisional excitation for the modeling of cometary atmospheres. Indeed, the collisional systems are too heavy for quantum approaches to be practical for this purpose, and the SACM method has demonstrated high accuracy at low temperatures [< 300 K, Loreau et al. (2018b)]. Given that comae temperature typically ranges from 10 to 150 K, this method represents a reasonable compromise between com-

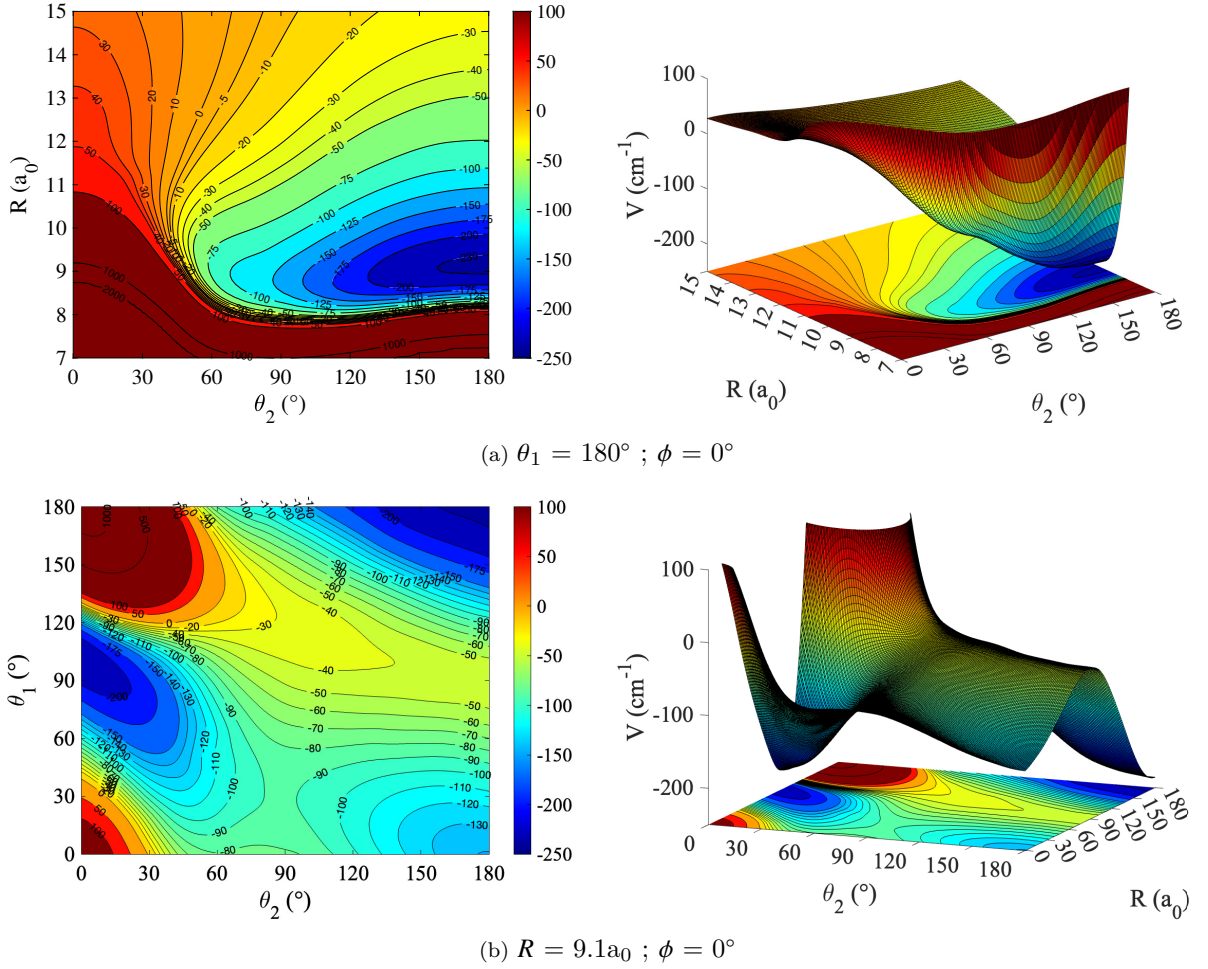


Figure 3.13: Representation of the PES for the CS-CO collisional system for (a) $\theta_1 = 180^\circ$; $\phi = 0^\circ$; (b) $R = 9.1a_0$ and $\Phi = 0^\circ$. The global minimum lays at -235.57 cm^{-1} for the $\theta_1 = \theta_2 = 180^\circ$ geometry. Two local minima lay at -223.14 cm^{-1} and -140.67 cm^{-1} , located at $\theta_1 = 101^\circ$; $\theta_2 = 0^\circ$, and $\theta_1 = 0^\circ$; $\theta_2 = 180^\circ$, respectively.

putational cost and accuracy for studying the CS-CO collisional excitation.

For the SACM approach, the first step is to compute the adiabatic channels of the complex. The basis for the adiabatic channels calculations should be chosen according to the temperature of interest. First, the most significantly populated energy levels of each monomer at the medium's temperature are identified, assuming a Maxwell-Boltzmann distribution of the populations. Then, the highest total energy for the scattering calculations is then determined by summing the energy of the last populated level of each monomer and adding the kinetic energy range corresponding to the medium's tempera-

ture, assuming a Maxwell-Boltzmann distribution for the kinetic energies. Finally, the adiabatic channels are computed by accounting for all adiabatic states with an asymptotic value lower than the highest total energy of the collision, i.e. all rotational levels of CS and CO that are open at this maximum energy.

For the CS-CO system, the adiabatic channels were computed using the OPEN MP/MPI MOLSCAT.² This version of the original MOLSCAT code allows access to more memory to support calculations with a very large number of channels N by eliminating the $v_\lambda(R)$ storage for out-of-core operation. This means the program can work with datasets that exceed the available memory capacity by breaking the data into smaller chunks that can be loaded, processed, and then written back to disk in sequence. This code also uses the F02ABF and F02AAF routines from the NAG library to diagonalize matrices more efficiently, as matrix diagonalization is a significant portion of the computational cost in adiabatic state calculations. Once the adiabatic states are computed, they are counted following the procedure described in Section 2.3.4, which I implemented in a script.

In this study, the main objective is to model CS in CO-dominated comets at large heliocentric distances where coma temperatures is below 30 K. Therefore, energy levels with internal energy lower than 75 cm^{-1} were considered, which should allow a correct distribution the population among the energy levels at this temperature. Therefore, CS levels up to $j_{\text{CS}} = 9$ should be included, corresponding to an energy of 73.54 cm^{-1} , and CO levels up to $j_{\text{CO}} = 5$, corresponding to an energy of 57.47 cm^{-1} . The maximum total energy is estimated as the sum of $E_{j_{\text{CS}}=9}$, $E_{j_{\text{CS}}=5}$ and the kinetic energy range at 30 K, so the maximum total energy of the system will be of 311 cm^{-1} . This leads to a basis of $j_{\text{CS}} \leq 19$ ($E_{j_{\text{CS}}=19} = 310.3 \text{ cm}^{-1}$), $j_{\text{CO}} \leq 12$ ($E_{j_{\text{CO}}=12} = 299.8 \text{ cm}^{-1}$) for the calculations of the adiabatic channels.

However, for this basis, the calculations were too expensive to run on the available machines, as the memory required exceeded the 200 GB memory available on the machines of the Institute of Physics of Rennes from $J = 7$. For this partial wave, 18,452 channels were required for parity $\epsilon = 1$, and 18,192 for $\epsilon = -1$. As $J \leq 6$ were insufficient to converge the scattering calculations, the basis for the adiabatic channel calculations was re-estimated by reducing the maximum total energy of the collision to the sum of $E_{j_{\text{CS}}=9}$, $E_{j_{\text{CS}}=5}$ and only 120 cm^{-1} for the kinetic energy range. This results in a maximum total energy of 250 cm^{-1} , reducing the basis to $j_{\text{CS}} \leq 16$, $j_{\text{CO}} \leq 10$. The $j_{\text{CS}} = 17$ level at 249.94

²available at: <https://ipag.osug.fr/~faurea/molscat/index.html>

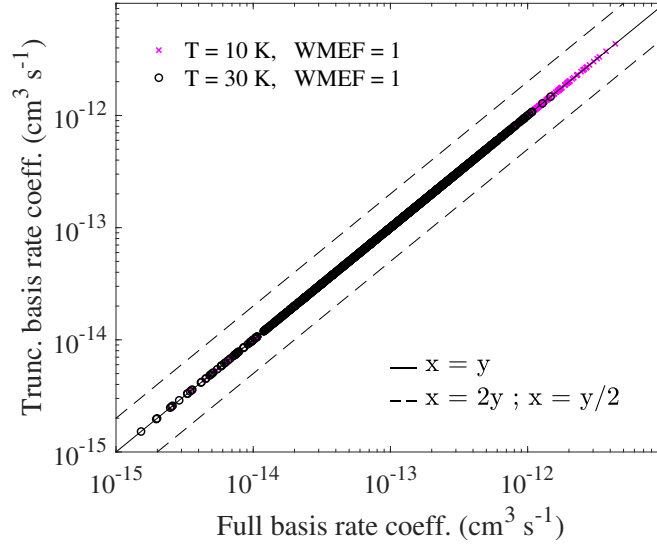


Figure 3.14: Comparison between state-to-state de-excitation rate coefficients (in $\text{cm}^3 \text{s}^{-1}$) calculated from adiabatic channels computed with full basis $j_{\text{CS}} \leq 19$, $j_{\text{CO}} \leq 12$ (x-axis), and with truncated basis $j_{\text{CS}} \leq 16$, $j_{\text{CO}} \leq 10$ (y-axis) to evaluate the impact of this basis on the rate coefficients.

cm^{-1} was ignored because the basis was still too large as the memory required exceed the 200 GB limitation. To ensure that this basis was sufficient to converge the calculations, a systematic comparison of state-to-state de-excitation rate coefficients calculated from adiabatic states computed with full and truncated bases for $J \leq 6$ is represented in Figure 3.14. For this comparison, the rate coefficients are considered for all de-excitation transitions between all energy levels that are significantly populated at 30 K for both monomers, so transitions within $j_{\text{CS}} \leq 9$ and $j_{\text{CO}} \leq 5$ levels. The rate coefficients have been computed with both basis for total energy $\leq 250 \text{ cm}^{-1}$ to ensure that the basis is the only parameter that influences the compared rate coefficients.

In this systematic comparison, no deviation is observed between the two sets of rate coefficients, suggesting that the truncated basis is sufficient to ensure a nearly perfect accuracy within the SACM method. However, the comparison is done only for low J . Nevertheless, the higher j_{CS} and j_{CO} adiabatic channels ignored in the truncated basis will be the first one to close when J increases. Therefore, if the agreement is nearly perfect at low J , it is expected to be still excellent at higher J . It can thus be safely concluded that the truncated basis employed for the adiabatic channels calculation, including all levels for $j_{\text{CS}} \leq 16$ and $j_{\text{CO}} \leq 10$, is sufficient for the calculation of state-to-state rate coefficients using the SACM approach.

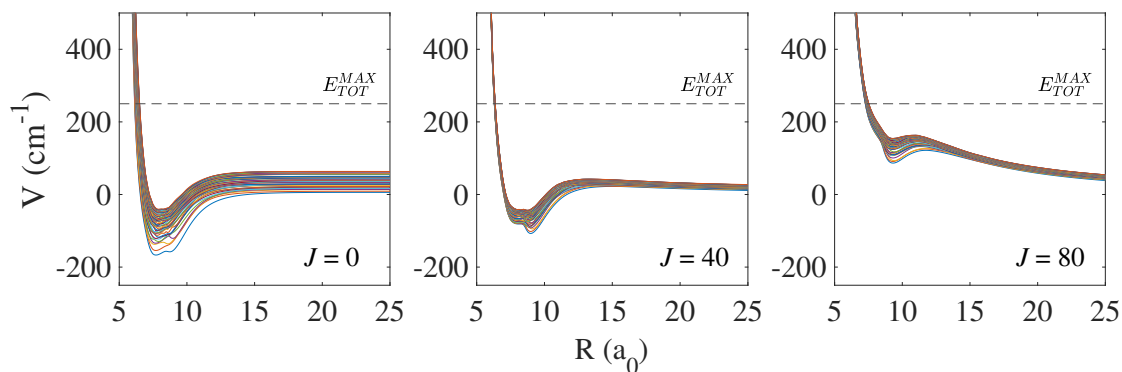


Figure 3.15: Potential energy V (in cm^{-1}) of the adiabatic states as a function of the distance R (in a_0) between CS and CO for different value of the total angular momentum J . Only the first 50 adiabatic states are represented for the sake of clarity. For $J = 0$ (left panel), 40 (center panel) and 80 (right panel), the number of adiabatic channels is of 715, 17,391 and 17,391, respectively. $E_{\text{TOT}}^{\text{MAX}} = 250 \text{ cm}^{-1}$ is the highest total energy considered in the scattering calculations.

Now that it has been ensured that the collisional rate coefficients can be computed with this basis, they were computed with an increasing number of partial waves J for both parity $\epsilon = -1, 1$, until a convergence of the cross sections is reached. The number of channels increases significantly with the total quantum number J , reaching a maximum for $J = 26$ with 17,391 and 17,578 channels for parity $\epsilon = -1$, and 1, respectively. As J increases, the centrifugal barrier will rise, causing the energy of the centrifugal barrier in the adiabatic channels to progressively exceed the total energy and thus be considered closed channels with zero probability. This is illustrated in Figure 3.15 where the first 50 adiabatic states are represented at different value of J .

The number of partial waves J included in the calculations have been increased until a convergence of the cross sections for transitions involving $j_{\text{CS}} \leq 9$ and $j_{\text{CO}} \leq 5$ is reached. The convergence criteria for inelastic transitions was set at 5%.

Finally, the cross sections were all converged at $J = 102$. Calculations of the adiabatic states with $J \geq 26$ (at which the maximum number of channels is reached) required 175 GB of memory and approximately 100 CPU hours per processor. Each calculation needed 10 to 14 processors (depending on availability). Therefore, the calculation of the adiabatic states using quantum approaches required about 100,000 CPU hours. The statistical part of the calculations was run on a MacBook Pro M1, 2020 and lasted 184 CPU seconds per J considering 1,236 points of energy. Therefore, the statistical part of the scattering

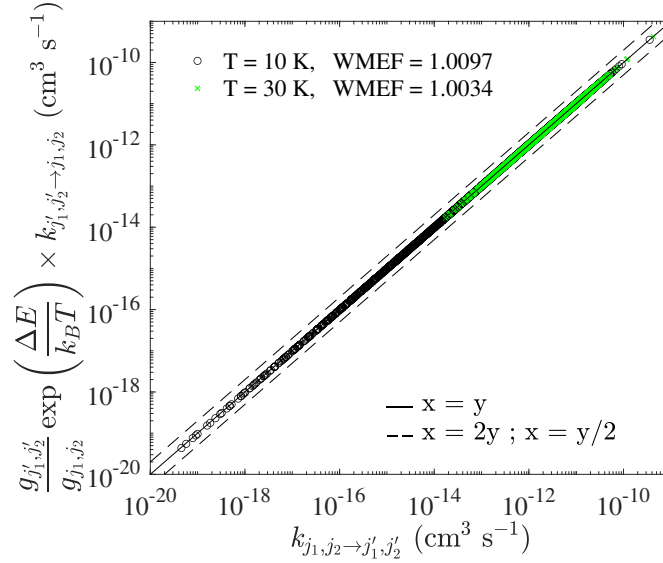


Figure 3.16: Representation of the rate coefficients $k_{j_1, j_2 \rightarrow j'_1, j'_2}$ (in cm^3) compared to their expected values according to the detailed balance principle.

calculations lasted only 5.22 CPU hours on a common laptop.

The cross sections were then averaged over the collisional energy for each transition to obtain state-to-state rate coefficients according to Equation (2.79). To verify that the thermal average over the collisional energies is accurate, i.e. enough energy points have been considered, the principle of detailed balance should be respected. In Figure 3.16, the rate coefficients $k_{j_1, j_2 \rightarrow j_1, j_2}$ for all transitions are systematically compared to their expected values according to the detailed balance principle given in Equation (2.80). In this figure, it can be observed that the detailed balance is well respected, with a deviation of less than a factor of 1.01 at both 10 K and 30 K. Therefore, the energy grid is dense enough to ensure that the thermal average is correctly done, and that the cross sections are properly averaged over the kinetic energies for the rate coefficients calculations.

Accuracy of the Rate Coefficients

To assess the accuracy of the rate coefficients produced with the SACM approach, they should be compared to rate coefficients computed with a full quantum approach. Therefore, we performed CC calculations for the CS-CO collisional system.

E (cm ⁻¹)	$j_{\text{CS}}^{\text{max}}$	$j_{\text{CO}}^{\text{max}}$	R _{max}	STEPS	DNRG
1.65 - 20	19	13	80	70	0.1
20 - 50	21	14	95	30	0.2
50 - 100	21	14	95	12	0.2
100 - 150	21	15	85	10	0.2
150 - 200	23	15	75	10	0.2

Table 3.5: MOLSCAT parameters used in the CC scattering calculations and the energy step DNRG used to span the energy grid from 1.65 cm⁻¹ to 200 cm⁻¹. The minimum value for both j_{CS} and j_{CO} was set at 0, their ground rotational level.

Considering the expensive cost of this type of calculations for the CS-CO system, the CC calculations were limited to a minimal number of partial wave, so $J = 0$. The cross sections were computed with MOLSCAT V22 (Hutson & Le Sueur, 2019). Ideally, the cross sections should be computed for total energies up to 250 cm⁻¹. However, convergence at this energy was not achieved due to memory limitations of MOLSCAT V22. Indeed, to reach convergence at 200 cm⁻¹, the $j_{\text{CO}} = 15$ and $j_{\text{CS}} = 23$ basis is required, leading to 4,784 channels (mostly closed channels). This calculation required 20 CPU hours, and 15.6 GB of memory out of the 16 GB limit of the MOLSCAT V22. As a larger basis is required to converge cross sections at 250 cm⁻¹, the energy range was cut at 200 cm⁻¹ to avoid poorly converged cross sections from 200 to 250 cm⁻¹.

Most of the inelastic cross sections between the $j_{\text{CS}} \leq 9$ and $j_{\text{CO}} \leq 5$ levels were converged at better than 5% up to 200 cm⁻¹ (the convergence for all transitions was always better than 20%). Therefore, rate coefficients were calculated from cross sections computed at $J = 0$ for total energies ranging from 1.65 to 200 cm⁻¹.

The equivalent calculation with the SACM approach has cost 0.43 CPU hours and 2.36 GB of memory, adiabatic channels and statistical counting together (the statistical part was only 2.43 CPU seconds). The set of MOLSCAT parameters employed for the CC calculations can be found in Table 3.5.

The state-to-state rate coefficients computed with the CC approach are compared to the ones obtained with the SACM approach in Figure 3.17. Only de-excitation rate coefficients are represented for the sake of clarity.

To evaluate if the deviation would affect significantly the non-LTE models in which

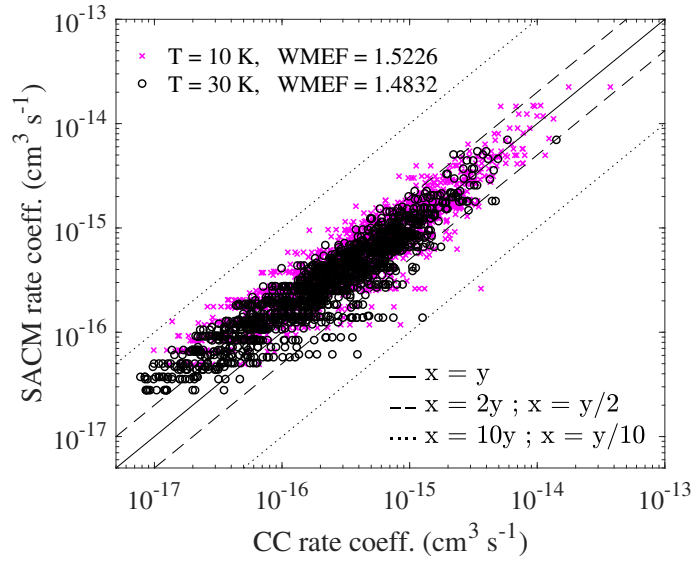


Figure 3.17: Comparison between state-to-state rate coefficients (in $\text{cm}^3 \text{s}^{-1}$) of the CS-CO collisional system computed with the CC (x-axis) and SACM (y-axis) approaches for a unique partial wave $J = 0$ at both 10 K (pink cross) and 30 K (black circles). Cross sections were computed up to 200 cm^{-1} with both method for a rigorous comparison.

these data will be employed and where dominant transitions will have more impact, the WMEF were calculated using Equation (3.28), with $k_i^{\text{REF}} \equiv k_i^{\text{CC}}$, and $k_i \equiv k_i^{\text{SACM}}$.

The two sets of data present a good agreement, especially the dominant transitions that are reproduced at better than a factor of two. At both temperature, all rate coefficients are reproduced within a factor of 10 (except one transition at 10 K).

The WMEF shows that the global deviation between the rate coefficients, weighted by the dominant transitions, is approximately a factor of 1.53 at 10 K and a factor of 1.49 at 30 K. This indicates that the rate coefficients produced by the SACM method reasonably reproduce those produced by the CC approach.

The temperature-dependent trend might seem counterintuitive, as the accuracy appears slightly better at 30 K than at 10 K. Indeed, the SACM method is expected to have better accuracy at low temperatures because the lifetime of the complex should be longer at 10 K than at 30 K. Nevertheless, quantum effects, which are significant at very low collisional energies, are neglected by statistical approaches (e.g., tunneling effects, resonances). Since low-collisional-energy cross sections contribute more at 10 K than at 30 K, this explains why the agreement slightly improves at 30 K. This behavior has also been ob-

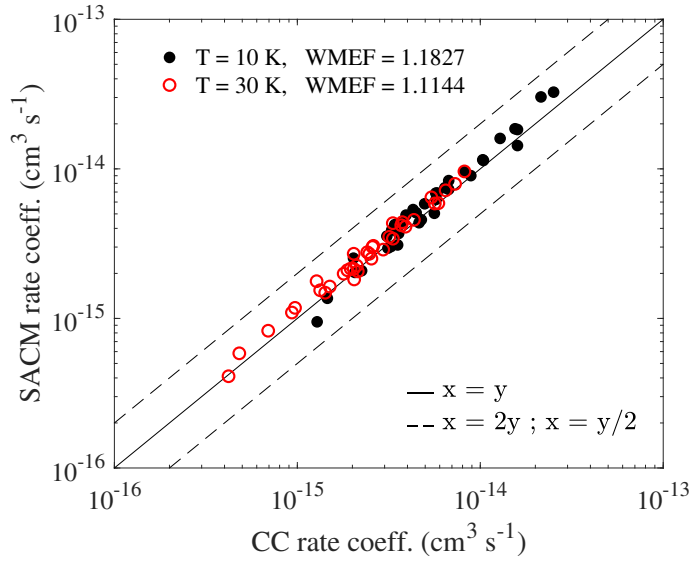


Figure 3.18: Comparison between thermalized rate coefficients (in $\text{cm}^3 \text{s}^{-1}$) of the CS-CO collisional system computed with the CC (x-axis) and SACM (y-axis) approaches at both 10 K (black bullet) and 30 K (red circles).

served in other systems where the SACM method was benchmarked (Loreau et al., 2018b).

In non-LTE models, thermalized rate coefficients are usually employed, which means that the population of the projectile is assumed to be thermalized. The thermalized rate coefficients are obtained by averaged over a thermal distribution over the projectile as

$$k_{j_1 \rightarrow j'_1}(T) = \sum_{j_2} n_{j_2}(T) \sum_{j'_2} k_{j_1 j_2 \rightarrow j'_1 j'_2}(T), \quad (3.40)$$

with

$$n_{j_2}(T) = \frac{(2j_2 + 1) \exp(-E_{j_2}/k_B T)}{\sum_{j'_2} (2j'_2 + 1) \exp(-E_{j'_2}/k_B T)}. \quad (3.41)$$

The thermalized rate coefficients for the CS-CO system were computed using Equation (3.40) based on the state-to-state rate coefficients exhibited in Figure 3.17. Thus, thermalized rate coefficients computed with the CC and the SACM approaches are compared in Figure 3.18.

The sets of thermalized rate coefficients exhibit excellent agreement at both temperatures. The WMEF is now lower than a factor of 1.19 at 10 K and about a factor of 1.12

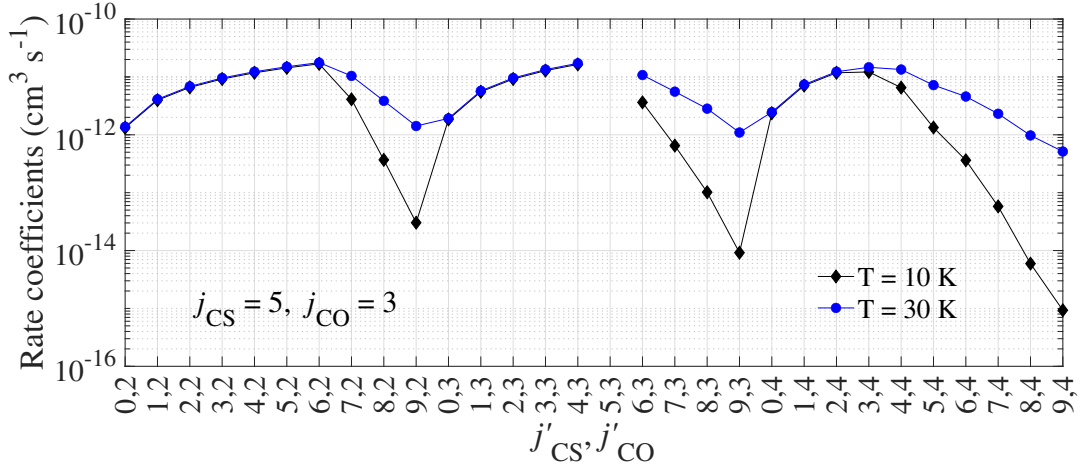


Figure 3.19: Representation of propensity rules for the CS-CO state-to-state rate coefficients (in $\text{cm}^3 \text{s}^{-1}$) from the $j_{\text{CS}}, j_{\text{CO}} = 6, 3$ level for transitions with $0 \leq j'_{\text{CS}} \leq 9$ and $j'_{\text{CO}} = 2, 3, 4$ at 10 K (black bullet) and 30 K (blue bullets).

at 30 K, indicating that the small inaccuracies due to the SACM approach are expected to have a very limited impact on non-LTE models.

From this comparison, a good accuracy for the CS-CO rate coefficients produced in this work with the SACM approach for all J values can be expected. It can thus be concluded that the rate coefficients for the CS-CO collisional system produced in this work are expected to provide a reliable tool for evaluating the abundance of CS in CO-dominated comets.

Propensity Rules

The propensity rules of the state-to-state rate coefficients obtained with the SACM approach for the CS-CO collisional system have been analyzed.

In Figure 3.19, rate coefficients from the $j_{\text{CS}}, j_{\text{CO}} = 6, 3$ rotational levels to $0 \leq j'_{\text{CS}} \leq 9$, $\Delta j_{\text{CO}} = j'_{\text{CO}} - j_{\text{CO}} = -1, 0, 1$ are analyzed at both 10 K and 30 K. The rate coefficients present a very similar behavior at both temperatures. Their values are also quite similar for low-lying levels, but become significantly larger at 30 K when higher rotational energy levels ($j'_{\text{CS}} \geq 6$ or $j_{\text{CO}} \geq 4$) are involved due to the significant energy gap compared to the temperature at 10 K.

At fixed j'_{CO} , the rate coefficients simply follow the exponential energy-gap behavior, meaning that the more energy there is between the initial and final rotational levels,

the less efficient the collisional transition will be. Therefore, $\Delta j_{CS} = j'_{CS} - j_{CS} = \pm 1$ transitions are favored. The same behavior is observed if Δj_{CS} is fixed and $0 \leq j'_{CO} \leq 5$ (not shown here).

The rate coefficients are generally following the exponential energy gap behavior. Few exceptions have been noticed for transitions involving particularly high $\Delta j_{CS} \geq 5$ and/or $\Delta j_{CO} \geq 3$, where the amplitude of the rate coefficients drops to particularly low values, lower than what exponential energy gap behavior would have predicted.

3.2.3 The Collisional Excitation of CS Induced by the H₂O Projectile

PES of the CS-H₂O Complex

As for previous systems, the study of inelastic transitions starts with evaluating the electronic interaction between the colliders. The PES has been calculated in collaboration with Dr. Dariusz Kędziera (Nicolaus Copernicus University, Toruń, Poland), and Dr. Jacek Kłos (University of Maryland, USA).

The ground electronic state is considered to be well-separated from the excited states, so the Born-Oppenheimer approximation can be used. Both species have been treated as rigid rotors, which is justified because the lowest vibrational frequency of H₂O is the bending mode, $\nu_2 = 1,595 \text{ cm}^{-1}$ (Herzberg & Herzberg, 1987). Therefore, the internuclear distances of the two monomers were fixed at their equilibrium geometries. For H₂O, the distances between the hydrogen and the oxygen atoms were fixed at $r_{O-H} = 1.81a_0$, and the angle \widehat{HOH} was set to 104.45° (Herzberg, 1966). For CS, the internuclear distance has been fixed at $r_{C-S} = 2.90a_0$ (Bogey et al., 1982), the same internuclear distance as used in the CS-CO PES.

The electronic interaction was computed for several geometries denoted by $\mathbf{R} \equiv R, \theta_1, \phi_1, \theta_2, \phi_2$, as represented in Figure 3.20. The H₂O molecule is fixed in body-fixed frame (1) and lies in the x_1z_1 plane, while the CS molecule is fixed in body-fixed frame (2) and is initially placed along the z_2 axis. The origins of these frames are placed at the centers of mass of the two molecules. Here, R defines the distance between the centers of mass of the two monomers. The angles θ_1 and ϕ_1 describe the position of CS's center of mass relative to H₂O. The rotation of CS relative to its body-fixed frame (2), which is parallel

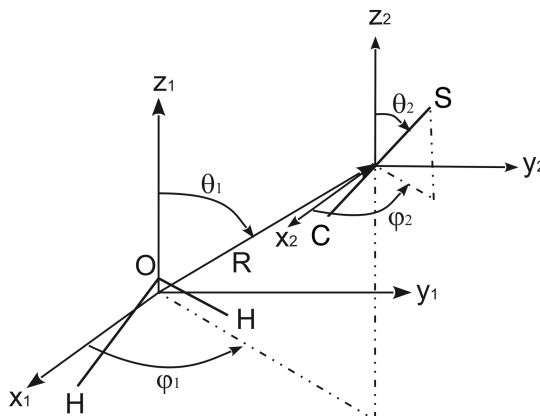


Figure 3.20: Representation of the CS-H₂O Collisional System in Jacobi Coordinates.

to body-fixed frame (1), is defined by the polar and azimuthal angles θ_2 and ϕ_2 .

The electronic energy at each geometry was computed using the Symmetry Adapted Perturbation Theory (SAPT) approach (Jeziorski et al., 1994) coupled with the Density Functional Theory (DFT) (Jansen, 2014) and an aVTZ basis set (Dunning, 1989). The accuracy of the SAPT-DFT method has recently been demonstrated to be comparable to that of CCSD(T), but with a computational cost that scales as n^5 , compared to n^7 for CCSD(T) approaches, with n the number of electrons (Taylor et al., 2016). Additionally, the SAPT approach is free of BSSE, as it is already a fragment-based method, treating each monomer individually. Consequently, at each geometry, only one calculation is required instead of three [see Equation (2.46)], reducing the computational time by an additional factor.

The AUTOPES code was employed to automatically generate the PES, as implemented according to Metz et al. (2016). The procedure used by AUTOPES is similar to that of the AUTOSURF package but interfaces with SAPT packages (Garcia et al., 2020) instead,³ and it employs a different fitting method.

The procedure begins by defining a grid of points, which is expected to represent the most important regions of interaction in the van der Waals complex. *Ab initio* points are then computed at these geometries using the chosen method. Next, *ab initio* energies at asymptotic values are calculated to model the long-range of interactions of the PES. All the *ab initio* points are combined, and a fit is performed by optimizing the parameters of

³The AUTOPES package also interfaces with the CCSD(T) method.

the PES.

The fitting approach in the AUTOPES package uses a site-site potential as (Metz et al., 2016)

$$E_{int} = \sum_{a \in A} \sum_{b \in B} v_{ab}(R_{ab})$$

$$= \sum_{a \in A} \sum_{b \in B} \left[\left(1 + \sum_{m=1}^k a_m^{ab} (R_{ab})^m \right) \exp(\alpha_{ab} - \beta_{ab} R_{ab}) \right. \quad (3.42)$$

$$\left. + \frac{A_{12}^{ab}}{(R_{ab})^{12}} + f_1(\delta_1^{ab}, R_{ab}) \frac{q_a q_b}{R_{ab}} - \sum_{n=6,8,10} f_n(\delta_n^{ab}, R_{ab}) \frac{C_n^{ab}}{(R_{ab})^n} \right], \quad (3.43)$$

where a, b are the sites on monomer A and B, respectively. The set of sites include all atoms of both monomer, and can also include off-atomic sites to improve the accuracy if needed; R_{ab} is the distance between the sites; q_a, q_b are the partial charges on each site; A_{12}^{ab} coefficients are constrained to be positive and ensure the correct repulsive behavior of the potential at short range; C_n^{ab} are $f_n(\delta_n^{ab}, R_{ab})$ is the damping function of Tang & Toennies (1984) of the form

$$f_n(\delta_n^{ab}, R_{ab}) = 1 - e^{-\delta_n^{ab} R_{ab}} \sum_{m=0}^n \frac{(\beta_n^{ab} R_{ab})^m}{m!}, \quad (3.44)$$

and a_m, α_{ab} and β_{ab} are adjustable parameters.

This fitting approach is very efficient as it is capable of producing accurate fit based on a very small number of *ab initio* points despite the highly anisotropic character of the PES. In total, only 2,209 *ab initio* points were computed to obtain the first 5-dimension PES of the CS-H₂O van der Waals complex. It is however a very technical approach, which is not easy to use. This procedure does not inherently avoid holes in the PES; therefore, the AUTOPES package includes a step to fix them. In contrast, the AUTOSURF package employs an L-IMLS procedure for fitting, which intrinsically avoids these holes. If the desired accuracy is not achieved, additional *ab initio* points are automatically added by the software, and the fit is refined until a convergence is reached.

For scattering calculations, it is however needed to expand the angular dependence of the potential into spherical harmonics. Therefore, the PES was expanded using a

bispherical harmonic expansion as defined by Phillips et al. (1994)

$$V(\mathbf{R}) = \sum_{l_1 m_1 l_2 l} v_{l_1 m_1 l_2 l}(\mathbf{R}) \bar{t}_{l_1 m_1 l_2 l}(\theta_1, \theta_2, \phi_1, \phi_2), \quad (3.45)$$

where $\bar{t}_{l_1 m_1 l_2 l}(\theta_1, \theta_2, \phi_1, \phi_2)$ is a normalized spherical tensor

$$\bar{t}_{l_1 m_1 l_2 l}(\theta_1, \theta_2, \phi_1, \phi_2) = \alpha_{l_1 m_1 l_2 l} (1 + \delta_{m_1 0})^{-1} \sum_{r_1 r_2} \begin{pmatrix} l_1 & l_2 & l \\ r_1 & r_2 & r \end{pmatrix} Y_{l_2 r_2}(\theta_2, \phi_2) \quad (3.46)$$

$$\times Y_{l r}(\theta_1, \phi_1) [\delta_{m_1 r_1} + (-1)^{l_1 + m_1 + l_2 + l} \delta_{-m_1 r_1}], \quad (3.47)$$

with the normalization of Valiron et al. (2008) as

$$\alpha_{l_1 m_1 l_2 l} = [2(1 + \delta_{m_1 0})^{-1} (2l_1 + 1)^{-1}]^{-\frac{1}{2}}, \quad (3.48)$$

with l_1 and l_2 denote the angular momenta of each monomer, while l represents the angular momentum between the monomers. The quantity m_1 is the projection of l_1 onto the z_1 axis, and Y denotes the spherical harmonics. The variables r_1 , r_2 , and r are the magnetic quantum numbers corresponding to l_1 , l_2 , and l , respectively.

For an illustration of the features of the PES, a contour plot and its corresponding 3D representation is shown in Figure 3.21, where the dependence of the potential with respect to \mathbf{R} and θ_1 is displayed at fixed θ_2 , ϕ_1 , and ϕ_2 .

The GM of the PES, visible in this figure, is located at $-1,171.82 \text{ cm}^{-1}$ for $\mathbf{R} = 7.9a_0$, $\theta_1 = 252^\circ$, $\theta_2 = 0^\circ$, $\phi_1 = 90^\circ$, $\phi_2 = 0^\circ$, which corresponds to the geometry where one hydrogen atom of H_2O faces the carbon atom of the CS molecule. A LM is also visible at -635.48 cm^{-1} for the $\mathbf{R} = 6.6a_0$, $\theta_1 = 37^\circ$, $\phi_1 = \phi_2 = 0^\circ$, $\theta_2 = 90^\circ$ geometry. The energy gradient with respect to θ_1 is quite large, and the PES exhibits strongly anisotropic behavior. Indeed, the energy can vary by about $2,000 \text{ cm}^{-1}$ with only a rotation of $\frac{\pi}{4}$.

The GM geometry of the CS- H_2O system is very similar to the one of the CO- H_2O system, suggesting comparable chemical behavior between CS and CO molecules when interacting with H_2O . However, the well depth of the CO- H_2O system is shallower, at -646 cm^{-1} , indicating a weaker interaction compared to CS- H_2O . This is expected, as the dipole moment of CO is weaker than that of CS. Consequently, the collision efficiency

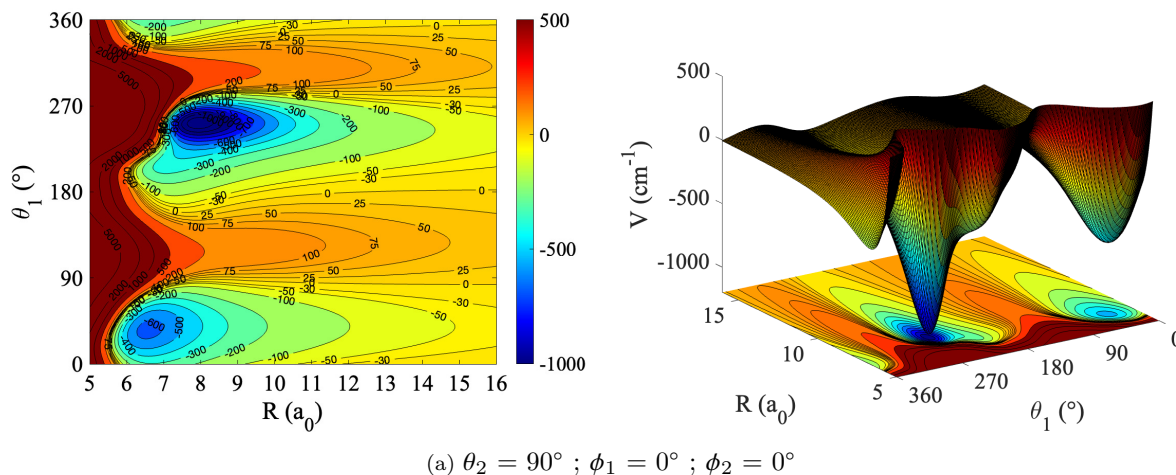


Figure 3.21: Representation of the PES for the CS-H₂O collisional system for $\theta_2 = 90^\circ$; $\phi_1 = \phi_2 = 0^\circ$. The global minimum lays at $-1,171.82 \text{ cm}^{-1}$ for the $\theta_1 = 252^\circ$, $\phi_1 = \phi_2 = 0^\circ$, $\theta_2 = 90^\circ$ geometry. A local minimum lays at -635.48 cm^{-1} for the $R = 6.6a_0$, $\theta_1 = 37^\circ$, $\phi_1 = \phi_2 = 0^\circ$, $\theta_2 = 90^\circ$ geometry.

between CS and H₂O is likely to be higher than that between CO and H₂O, which should result in larger rate coefficients for the CS-H₂O system.

For other van der Waals complexes involving linear molecules and H₂O, such as HF-H₂O (Loreau et al., 2020), H₂O-HNC, and H₂O-HCN (Żółtowski, 2023), the GM geometry occurs when the oxygen atom of H₂O faces the hydrogen atom of HF, HCN, or HNC. The GMs for these systems are deeper ($-3,059 \text{ cm}^{-1}$ vs $-2,649 \text{ cm}^{-1}$ vs $-1,814 \text{ cm}^{-1}$, respectively) due to the larger dipole moments ($\mu_{\text{HNC}} > \mu_{\text{HCN}} > \mu_{\text{CS}}$)¹, or in the case of HF, due to the significant polarization of the HF bond caused by the extremely high electronegativity of fluorine. This indicates that CS and CO do not behave chemically like HF, HCN, or HNC when interacting with H₂O, even though HCN and HNC are isoelectronic to CO. Therefore, their respective sets of rate coefficients are expected to show significant differences.

Scattering Calculations

In this work, the objective is to produce rate coefficients for the CS-H₂O collisional system from 5 K to 100 K. Given the well depth ($\approx -1,172 \text{ cm}^{-1}$) and the low rotational constant of CS ($B_{\text{CS}} = 0.817 \text{ cm}^{-1}$), employing quantum approaches to produce rate coefficients is not expected to be feasible. Therefore, the SACM method was employed as an alternative approach. This method has already been used to study collisional systems involving H₂O as a projectile, such as the collisional excitation of CO, HF, HCN, and HNC induced by

H₂O for temperatures up to 100–150 K, depending on the system (Loreau et al., 2018a; Loreau et al., 2022; Żóltowski, 2023). The same methodology has also been employed to study the collisional excitation of CS induced by CO up to 30 K in this thesis work.

The wavefunction of an asymmetric top $W_{\tau,m}^{j_1}(\alpha, \beta, \gamma)$ can be represented as a combination of the symmetric top eigenfunctions $D_{k,m}^{j_1}(\alpha, \beta, \gamma)$ (Phillips et al., 1995)

$$W_{\tau,m}^{j_1}(\alpha, \beta, \gamma) = \sum_k a_{\tau,k}^j \sqrt{\frac{2j+1}{8\pi^2}} D_{k,m}^{j_1}(\alpha, \beta, \gamma), \quad (3.49)$$

where $D_{k,m}^{j_1}(\alpha, \beta, \gamma)$ are the Wigner rotation matrices, j_1 is the rotational quantum number of the asymmetric top (here, H₂O), k is its projection on the space-fixed Z -axis, and $\tau = k_a - k_c$; the $a_{\tau,k}^j$ coefficients are obtained by diagonalization of the asymmetric top Hamiltonian (3.39) (see Phillips et al. (1995) for more details). The (α, β, γ) angles corresponds to the alignment of the body-fixed axis system with the space-fixed one.

Therefore, the angular part of the total wavefunction for the CS-H₂O collisional system, defined in Equation (2.60) for linear molecule-linear molecule collisions, becomes

$$\begin{aligned} \mathcal{Y}_{\gamma}^{JM}(\hat{\mathbf{R}}, \hat{\boldsymbol{\rho}}_2, \alpha, \beta, \gamma) = \sum_{\substack{m_1, m_2 \\ \mu, m_l}} \langle j_1 m_1 j_2 m_2 | j_{12} \mu \rangle \langle j_{12} \mu l m_l | JM \rangle \\ \times W_{\tau,m}^{j_1}(\alpha, \beta, \gamma) Y_{j_2 m_{j_2}}(\hat{\boldsymbol{\rho}}_2) Y_{l m_l}(\hat{\mathbf{R}}), \end{aligned} \quad (3.50)$$

with $\gamma \equiv j_1, \tau_1, j_2, j_{12}, \mu$; with $\mu \equiv m_{j_{12}}$ is the projection of j_{12} on the Z -axis of the space-fixed frame; $\langle \cdot \cdot | \cdot \cdot \rangle$ are Clebsch-Gordan coefficients.

Therefore, the CC equations (2.70) can be solved by replacing the total wavefunctions given in Equation (2.62) with the proper expression of its angular part given in Equation (3.50).

The HIBRIDON scattering code (Alexander et al., 2023) was used to compute the adiabatic states of the systems. As the adiabatic state calculations does not require many closed-channels, any channels with an energy larger than the highest total energy under consideration is useless, and unnecessarily increase the computational cost of the calculation. To get rid off these levels, the EMAX option was employed. Originally, this option excluded from the basis the rotational levels of monomer 1 (in this case, H₂O) that exceed EMAX. The option was thus modified to be applied on any channels of the system, not

just those of H₂O.⁴ This modification drastically reduced the number of adiabatic channels. For example, with the $j_{\text{CS}} = 36$ and $j_{k_a k_c} \geq 10_{k_a k_c}$ basis, the number of channels was reduced from nearly 15,000 channels to 4,000 for CS-p-H₂O at $J = 0$.⁵

The effort was focused on determining rate coefficients up to 100 K, although, ideally, rate coefficients up to 150 K would be necessary. Therefore, the highest rotational level of CS considered is $E_{j_{\text{CS}} = 18} = 279.41 \text{ cm}^{-1}$. For H₂O, $E_{2_{20}} = 136.56 \text{ cm}^{-1}$ for p-H₂O and $E_{3_{03}} = 136.91 \text{ cm}^{-1}$ for o-H₂O were accounted for, as they represent a significant portion of their respective populations.

In principle, more rotational levels of H₂O should be included in the rate coefficient calculations. However, due to the high computational cost, the rotational basis has to be reduced. Since mostly thermalized rate coefficients are used in non-LTE models of CS, reducing the rotational basis of H₂O is expected to have less impact on the accuracy of the modeled spectra than reducing the rotational basis of CS. Therefore, the chosen basis is expected to ensure reliable modeling of CS in comets while keeping the calculations computationally feasible.

As a result, the highest total energy was set to 817 cm^{-1} , and the EMAX parameter was adjusted accordingly. As in the previous CS-CO study, the basis for the adiabatic state calculation was reduced to fit within the memory limitations of the HIBRIDON software. The final basis set for the adiabatic states calculation included $j_{\text{CS}} \leq 31$, and $j_{k_a k_c} \leq 3_{k_a k_c}$ for CS-p-H₂O, and $j_{\text{CS}} \leq 26$, and $j_{k_a k_c} \leq 3_{k_a k_c}$.

To validate the basis set used for the adiabatic state calculations, the rate coefficients derived from cross sections calculated using the adiabatic states with the full basis ($j_{\text{CS}} = 36$, and $j_{k_a k_c} \leq 10_{k_a k_c}$) were compared to those calculated from the truncated basis ($j_{\text{CS}} = 31$, and $j_{k_a k_c} \leq 3_{k_a k_c}$ for CS-p-H₂O in Figure 3.22a, and $j_{\text{CS}} = 26$, and $j_{k_a k_c} \leq 3_{k_a k_c}$ for CS-o-H₂O in Figure 3.22b) for temperatures up to 100 K. The calculation of the cross sections was limited to a total energy of $E \leq 817 \text{ cm}^{-1}$ and $J \leq 1$ partial waves, as the number of channels for the adiabatic state calculations with the full basis was already too large to be handled by the HIBRIDON program (Alexander et al., 2023).

In this comparison, only rate coefficients of transitions between CS levels with $j_{\text{CS}} \leq 18$, and the levels of p-H₂O up to $j_{k_a k_c} = 2_{20}$, and the ones of o-H₂O up to $j_{k_a k_c} = 3_{03}$

⁴The modified code for the asymmetric top-diatom collision (basis hiba30_astp3.F90) is available at: https://github.com/AmelieGodard/EMAX_hib30.

⁵A similar reduction was observed for other J values, both parities $\epsilon = -1, 1$, and o-H₂O.

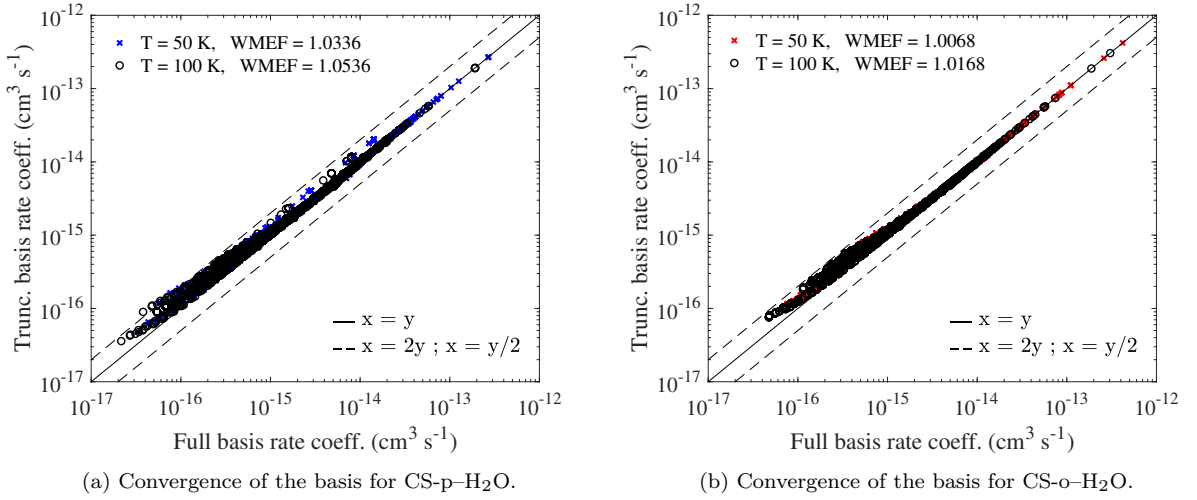


Figure 3.22: Systematic comparison between state-to-state de-excitation rate coefficients calculated from adiabatic channels computed for $J \leq 1$ with full basis $j_{\text{CS}} = 36$, and $j_{\text{H}_2\text{O}} \leq 10$ (x-axes) and truncated basis for the (a) CS-p-H₂O; $j_{\text{CS}} = 31$, and $j_{k_a k_c} \leq 3_{k_a k_c}$ (y-axis) (b) CS-o-H₂O; $j_{\text{CS}} = 26$, and $j_{k_a k_c} \leq 3_{k_a k_c}$ (y-axis).

are included.

The data sets computed with the full and truncated bases are very similar, demonstrating good agreement at both temperatures for both p-H₂O and o-H₂O projectiles. For CS-o-H₂O, all transitions are reproduced within a factor of two, with much better agreement observed for the dominant transitions. The global deviation, indicated by the WMEF, is estimated to be less than a factor of 1.02 at both temperatures. For CS-p-H₂O, almost all rate coefficients are reproduced within a factor of two, except for a few transitions with low magnitudes; however, the dominant transitions are also well reproduced. The global deviation indicated by the WMEF is less than a factor of 1.04 at 50 K and less than a factor of 1.06 at 100 K. Consequently, the overall agreement between the full and truncated bases is very good for both CS-p-H₂O and CS-o-H₂O rate coefficients.

The rate coefficients derived from the truncated basis are slightly overestimated, which is expected since some levels are omitted from the sum. This omission will cause an artificial overestimation of the weight of the remaining levels when the basis is truncated. The WMEF slightly increases with temperature, as anticipated, because the omitted levels are high-energy levels that contribute more at higher temperatures. Nevertheless, the agreement between the datasets remains very good, allowing the truncated bases to be confidently used for computing accurate rate coefficients for CS-p-H₂O and CS-o-H₂O from 5 to 100 K.

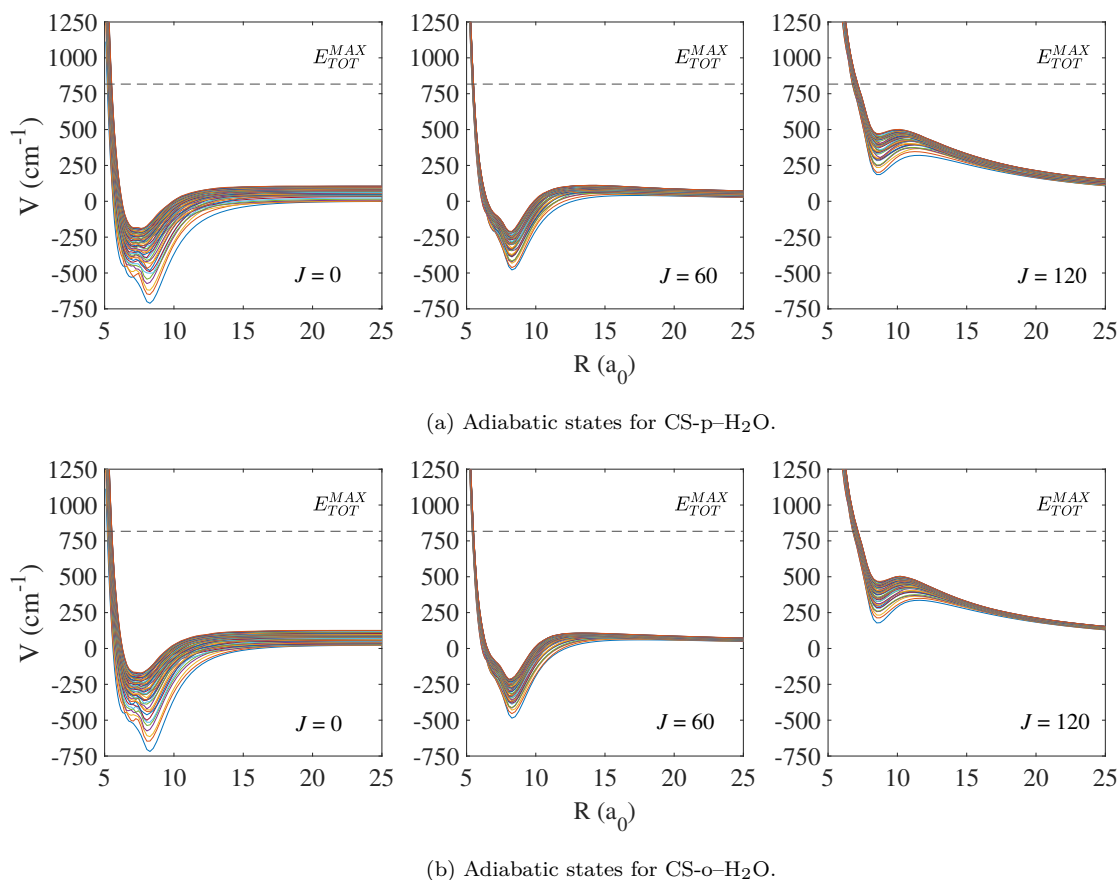


Figure 3.23: Potential energy V (in cm^{-1}) of the adiabatic states as a function of the distance R (in a_0) between CS and (a) p-H₂O (b) o-H₂O for different value of the total angular momentum J for parity $\epsilon = 1$. Only the first 50 adiabatic states are represented for the sake of clarity. For $J = 0$ (left panels), 60 (center panels), 120 (right panels), the number of adiabatic channels is of (a) 600, 16,298, and 16,298 (b) 556, 15,675 and 15,675, respectively.

Now that the bases for the adiabatic states calculation have been selected, the adiabatic states were computed with an increasing number of partial waves J for both parities $\epsilon = -1, 1$. The maximum number of channels is of 16,298 ($\epsilon = 1$) reached at $J \geq 31$ for p-H₂O, and of 15,675 ($\epsilon = 1$) reached at $J \geq 29$ for o-H₂O. The energy of the adiabatic states computed with these bases are represented as a function of the distance between the colliders R in Figure 3.23 at different J so the rising centrifugal barrier can be observed. Only the first 50 adiabatic states with $\epsilon = 1$ have been represented for the sake of clarity for the CS-p-H₂O system in Figure 3.23a and for the CS-o-H₂O in Figure 3.23b.

Based on these adiabatic states, the cross sections were calculated using the method-

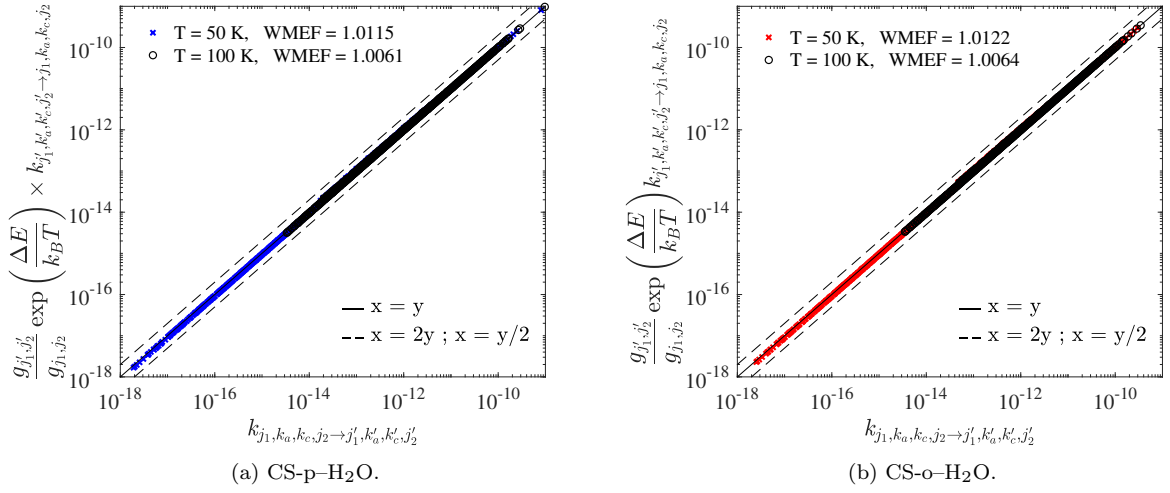


Figure 3.24: Comparison between rate coefficients $k_{j_1, k_a, k_c, j_2 \rightarrow j'_1, k'_a, k'_c, j'_2}$ (in cm^3s^{-1}) and their value obtained from $k_{j'_1, k'_a, k'_c, j'_2 \rightarrow j_1, k_a, k_c, j_2}$ (in cm^3s^{-1}) according to the detailed balance principle.

ology described in Section 2.3.4 up to $E_{\text{tot}} = 817 \text{ cm}^{-1}$. The adiabatic states and cross sections were computed for an increasing number of partial waves J until a convergence better than 5% in the inelastic cross sections is reached.

The convergence is reached for $J \leq 153$ for CS in collision with p-H₂O, and for $J \leq 149$ for o-H₂O. A total of 1,400,000 CPU hours have been used to produce adiabatic states at all partial waves for both parity $\epsilon = -1, 1$ for both CS-p-H₂O and CS-o-H₂O collisional systems. The statistical part was run a common laptop and required 2.75 CPU hours per collisional system. Based on these calculations, the first sets of rate coefficients for the CS-p-H₂O and CS-o-H₂O collisional systems were computed from 5 to 100 K.

The detailed balance has been checked to ensure that the thermalization over collisional energies has been done properly, and a WMEF lower than a factor 1.02 have been found, justifying that the energy grid was dense enough for both CS-p-H₂O and CS-o-H₂O, as illustrated in Figure 3.24.

Results

Now that a full set of rate coefficients have been obtained for the collisional excitation of CS induced by both p-H₂O and o-H₂O, the effect of the spin of H₂O is discussed. Thermalized rate coefficients calculated according to Equation (3.40) as a function of $\Delta j_{\text{CS}} = j'_{\text{CS}} - j_{\text{CS}}$ from j_{CS} are represented in Figure 3.25 for both p-H₂O and o-H₂O at

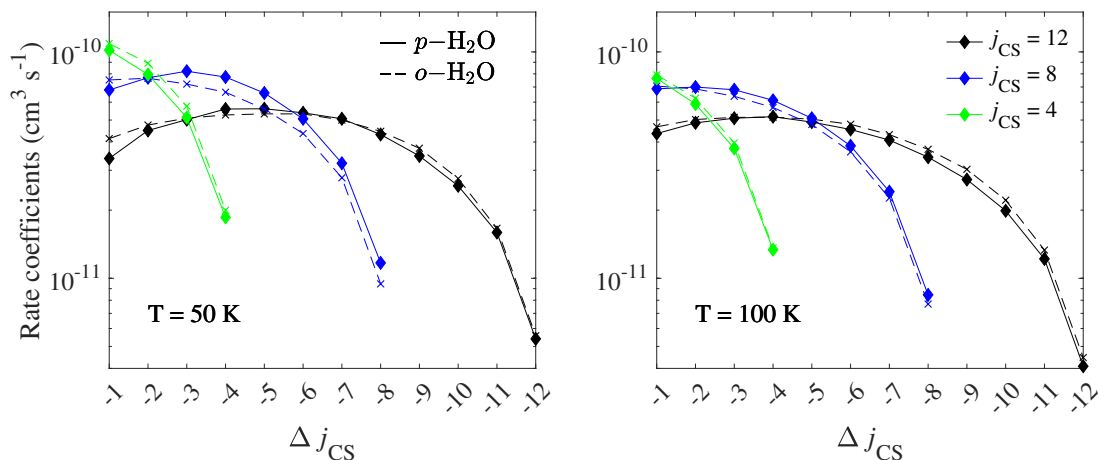


Figure 3.25: Comparison between thermalized rate coefficients (in $\text{cm}^3 \text{s}^{-1}$) computed for CS-p-H₂O (solid lines) and CS-o-H₂O (dashed lines) as functions of Δj_{CS} from $j_{\text{CS}} = 12$ (black), 8 (blue) and 4 (green) at 50 K (left panel) and 100 K (right panel).

50 K and 100 K.

The behavior of the collisional excitation of CS induced by either p-H₂O or o-H₂O is similar at both 50 K and 100 K. Their relative intensity depends on the initial level. For example, p-H₂O has slightly larger rate coefficients than o-H₂O from $j_{\text{CS}} = 8$, but it is the other way around when $j_{\text{CS}} = 4$. For $j_{\text{CS}} = 12$, it varies according to Δj_{CS} .

From $j_{\text{CS}} = 4$, the rate coefficients with both projectiles tend to decrease with increasing $|\Delta j_{\text{CS}}|$. However, for $j_{\text{CS}} = 8$ and 12, the behavior of the rate coefficients is not that straight forward. The rate coefficients starts by increasing with increasing with $|\Delta j_{\text{CS}}|$, to finally follow the usual exponential energy gap behavior by rapidly decreasing with $|\Delta j_{\text{CS}}|$ for larger $|\Delta j_{\text{CS}}|$ values (from $\Delta j_{\text{CS}} = -3$ and -5 for $j_{\text{CS}} = 8$ and 12, respectively).

The effect of the nuclear spin of H₂O appears to be weak, as the differences between the CS-p-H₂O and CS-o-H₂O datasets are rather small. When systematically comparing their sets of thermalized rate coefficients, the WMEF indicates a global deviation of a factor of 1.09 at 50 K and 1.06 at 100 K (not shown here). Therefore, the two sets of rate coefficients are very similar.

3.2.4 Discussion About the SACM Method

One objective of this work is to produce rate coefficients for systems relevant to the study of cometary atmospheres, particularly those involving heavy colliders such as CO

and H₂O. The scattering treatment of these systems is predicted to be computationally challenging using a full quantum approach due to the dense distribution of rotational levels and the large well depth of the PESs. Consequently, the SACM approach, which has proven to be very efficient for producing rate coefficients at low temperatures, was employed in this study. This discussion focuses on the SACM approach for non-reactive systems. However, it is worth mentioning that this method has also been used to study reactive systems (Konings et al., 2021; Pirlot Jankowiak, 2024).

The SACM approach, based on adiabatic channels computed with full quantum methods, was benchmarked in the work of Loreau et al. (2018b). In their study, the authors systematically compared the data produced with the SACM approach to equivalent CC data across five collisional systems: OH⁺ + H; OH⁺ + He; CN⁻ + H₂; CO + H₂; and CO + He. These systems represent different ranges of lifetimes for their intermediate complexes, with lifetimes increasing with the strength of the interaction, ranging from covalently bonded complexes (OH⁺ + H) to strongly bonded van der Waals complexes (OH⁺ + He; CN⁻ + H₂) and weakly bonded van der Waals complexes (CO + H₂; CO + He).

This study found that the accuracy of the SACM rate coefficients improves as the lifetime of the intermediate complex increases, aligning with theoretical expectations for the method. The relative lifetime of intermediate complexes can be estimated based on the well depth of their PES, which reflects the stability of the complex, and from temperatures. Higher temperatures lead to shorter lifetimes for the complexes.

For the OH⁺-H system, which features a covalent intermediate complex with a well depth of approximately 4,000 cm⁻¹, most SACM rate coefficients were reproduced with 50% accuracy at 300 K, and the WMEF deviation was less than a factor of 1.4 at 500 K, which is satisfactory for most astrophysical applications. For weaker intermediate complexes, the agreement remained good but was limited to lower temperatures. However, strong van der Waals intermediate complexes exhibited good accuracy up to 100 K.

Therefore, the substantial gains in computational time and memory achieved with the SACM approach, compared to CC or Coupled-States methods, along with its good accuracy for covalent to intermediate van der Waals complexes at temperatures below 300 K, demonstrate that the SACM approach is highly promising for the study of heavy collisional systems. In these systems, the well depth is typically large, the density of states is high, and quantum approaches are prohibitive.

In the last few years, this method have been employed to study few other non-reactive systems, such as CO-H₂O (Loreau et al., 2018a), HF-H₂O (Loreau et al., 2022), N₂H⁺-H₂ (Balança et al., 2020), and most recently, CO-CO (Żółtowski et al., 2022; Żółtowski, 2023). A summary of previously studied systems using the SACM approach is provided in Table 3.6.

For the CO-CO system, the SACM approach yielded a low WMEF of less than 1.7 up to 100 K. However, the SACM rate coefficients were compared to Coupled-States rate coefficients, not CC ones. In addition, the authors suspect that this good agreement with SACM results is due to a fortunate compensation of errors between the Coupled-States approximation and the SACM method. Thus, they expect the SACM approach to be accurate only at very low temperatures ($T < 50$ K) for this system (Żółtowski, 2023).

The CS-CO system is a weakly bound van der Waals complex, but its well depth is relatively deep compared to the temperatures under consideration in this study. Additionally, the rotational constants of both CS and CO are small, leading to a very dense distribution of energy levels. It is therefore reasonable to assume a statistical distribution among these levels, supporting the use of the SACM approach to produce accurate rate coefficients for the CS-CO system up to 30 K. Moreover, the comparison of the rate coefficients for this system with CC calculation were good, with a WMEF of approximately 1.5 at all temperatures considered. Even though this comparison was done only for $J = 0$, it is expected to realistically represent the error over all J values. However, at higher temperatures, the collision time may become too short to assume the formation of a long-lived complex, reducing the accuracy of the rate coefficients.

For the CS-H₂O rate coefficients produced in this work, a comparison with close-coupling data, even at the lowest J , seems unreasonable given the well depth and density of states. In the case of HF-H₂O, HCN-H₂O, and HNC-H₂O, SACM-derived rate coefficients could not be compared with those computed using a quantum approach due to computational expense.

The CO-H₂O system was studied by Loreau et al. (2018a), who obtained rate coefficients using the SACM approach for temperatures from 5 to 100 K, including CO levels up to $j_{\text{CO}} = 8$ and H₂O levels up to $j_{k_a k_c} = 2_{20}$. In their work, they compared their results with rate coefficients computed using a hybrid CC and Coupled-States approach at higher energies for $J \leq 2$. They reported that the deviation rarely exceeded a factor of 3, and that the SACM rate coefficients reproduced the CC results within a factor of 1.5

up to approximately 100 K.

For the CS-H₂O system, the density of states is much greater than for the CO-H₂O system, as 19 levels of CS were considered instead of nine for the same temperature range. Thus, the system is expected to behave more statistically. Additionally, the potential well of the CS-H₂O PES is deeper than that of CO-H₂O, indicating a stronger intermediate complex and a longer lifetime. Therefore, the SACM approach is expected to be more accurate for the CS-H₂O system than for the CO-H₂O system. Since Loreau et al. (2018a) estimated an accuracy within a factor of 1.5 up to 100 K, at least the same accuracy can be assumed for the CS-H₂O rate coefficients produced in this work up to 100 K.

Even if the SACM approach is assumed to be valid, a significant limitation encountered in this work—and one that will continue to be an issue if the rate coefficients for both the CS-CO and CS-H₂O systems are to be improved—is the calculation of adiabatic states using quantum approaches. As discussed in Section 3.2.2 and Section 3.2.3, one limitation is the size of the basis for the adiabatic state calculations, which can hardly exceed 20,000 channels. Due to the very dense distribution of rotational levels in the CS-CO and CS-H₂O systems, enormous basis sets are required, and the calculations were thus limited by the memory limitations of the scattering softwares MOLSCAT and HIBRIDON. Therefore, a future improvement would be to compute adiabatic states using a method that requires less memory, but without loss of accuracy.

In the future, it will be necessary to evaluate the accuracy of the SACM method for cometary systems as it seems to be one of the most promising method for getting such data. For these systems, a comparison with full CC calculations over the entire range of partial waves required to converge the calculations is impossible. Therefore, accuracy can only be definitively assessed by comparing these data with equivalent experimental results. However, since the cross sections do not reproduce resonances at low collisional energies, any comparison with crossed-beam experiments would be inconclusive, as the cross sections computed using the SACM method are not expected to exhibit the correct behavior. Nevertheless, double-resonance experiments, coupled with the CRESU technique, would enable the assessment of the accuracy of the SACM method for state-to-state rate coefficients in cometary systems, such as those computed in this work. This approach could be used to validate the SACM method for both CS-CO and possibly CS-H₂O over a wide range of temperatures, providing a benchmark for validating the SACM

method for studying the excitation of in cometary molecules.

System	Intermediate complex	Well depth (cm ⁻¹)	B (cm ⁻¹)	T (K)	WMEF	Ref.
OH ⁺ + H	Covalent	~ 4,000	$B_{\text{OH}^+} = 16.42$	50	1.18	Loreau et al. (2018b)
				200	1.14	
				1000	2.20	
OH ⁺ + He	Strong vdW	~ 730	$B_{\text{OH}^+} = 16.42$	100	2.31	Loreau et al. (2018b)
				300	3.66	
CN ⁻ + H ₂	Strong vdW	875	$B_{\text{CN}^-} = 1.87$	50	1.75	Loreau et al. (2018b)
			$B_{\text{H}_2} = 60.85$	100	1.87	
CO + H ₂	Weak vdW	94	$B_{\text{CO}} = 1.93$	20	2.40	Loreau et al. (2018b)
				300	1.60	
CO + He	Weak vdW	24	$B_{\text{CO}} = 1.93$	100	1.51	Loreau et al. (2018b)
				300	3.01	
N ₂ H ⁺ + H ₂	Strong vdW	2,531	$B_{\text{N}_2\text{H}^+} = 1.55$	100	1.28 ⁶	Balança et al. (2020)
CO-H ₂ O	Interm. vdW	646	$B_{\text{H}_2\text{O}} = 27.88$	5 - 100	NA ⁷	Loreau et al. (2018a)
HF-H ₂ O	Strong vdW	3,059	$B_{\text{HF}} = 20.56$	10 - 150	NA ⁸	Loreau et al. (2022)
CO-CO	Weak vdW	136	$B_{\text{CO}} = 1.93$	50	1.56 ⁹	Żółtowski et al. (2022)
				100	1.64 ⁹	

Table 3.6: Summary of previous studies that employed the SACM approach to treat the scattering of non-reactive systems.

⁶This has been evaluated based on Figure 4 of Balança et al. (2020). The dominant rate coefficients computed with the SACM approach have been compared to rate coefficients computed with the full CC calculations by including $0 \leq J \leq 4$ partial waves.

⁷Cross sections were computed with the CC approach at only few collisional energies. This comparison indicated an agreement better than a factor of two between CC and SACM cross sections for all transitions. Consequently, the authors predicted an agreement better than a factor 1.5 on the rate coefficients.

⁸No comparison with quantum approaches was made due to the high memory requirements of the calculations.

⁹The rate coefficients have been compared to rate coefficients computed with the Coupled-States approach, which includes an approximate treatment of the centrifugal barrier.

ASTROPHYSICAL APPLICATIONS

In this chapter, the applications and impacts of the collisional rate coefficients presented in Chapter 3 on radiative transfer modeling of CCS and CS in astrophysical media will be discussed. Section 4.1 provides a brief introduction to radiative transfer modeling, which are necessary to understand how molecular spectra are interpreted. Then, in Section 4.2, the rate coefficients computed for CCS and its isotopologues presented in Section 3.1, will be used to model emission spectra of CCS isotopologues in Dark Molecular Clouds. The new abundance ratio between ^{13}CCS and C^{13}CS led to an investigation of the ^{13}C anomaly, prompting a discussion on the chemistry of CCS. Next, Section 4.3 presents the impact of the new rate coefficients introduced in Section 3.2.1 on the modeling of CS emission spectra from comae. This includes a discussion about the sensitivity of rate coefficients regarding the colliders involved in the system, and an investigation of the sensitivity of radiative transfer models regarding these data.

4.1 Radiative Transfer

In astrophysical media, molecules can be excited by absorbing photons from external radiation fields, such as those emitted by nearby stars, from the Cosmic Microwave Background (CMB), or emitted by other molecules. They can also be (de)excited through collisions with other molecules. Moreover, these molecules can also emit photons, and the ones that escape the astrophysical medium contribute to an observable signal captured by telescopes. If this signal is properly interpreted, the physical conditions of the medium, including molecular abundances which is the ultimate goal of this study, can be derived. Finally, many conclusions can be drawn from these physical conditions, whether related to the molecule's chemistry, the evolutionary stage of the molecular clouds, or the composition of ices in cometary nuclei.

4.1.1 Radiative Transfer Equations

The journey of photons through astrophysical media is complex. When a photon is emitted by a molecule, it can either escape and be detected by observational instruments, or be absorbed by another molecule, which may re-emit it, continuing the cycle. This complicated behavior of photons makes interpreting observations highly challenging. Therefore, the first problem is understanding how photons travel through a medium to determine how many contribute to the detected signal of the observer. However, this problem will not be addressed in this work. The second challenge is that the probability of absorption and emission depends on the population of the molecules, i.e. depends on the state the molecules are in before interacting with the photon.

The transfer equation for radiation propagating over a distance ds can be expressed as

$$dI_\nu ds = j_\nu - \alpha_\nu I_\nu, \quad (4.1)$$

with I_ν the intensity of the radiation of frequency ν ; j_ν and α_ν are the local emission and extinction coefficients, respectively. These terms for the $u \rightarrow l$ transition are defined as

$$j_\nu = \frac{h\nu_{ul}}{4\pi} n_u A_{ul} \phi_\nu, \quad (4.2)$$

$$\alpha_\nu = \frac{h\nu_{ul}}{4\pi} (n_l B_{lu} \varphi_\nu - n_u B_{ul} \chi_\nu), \quad (4.3)$$

where $\nu \equiv \nu_{ul}$, the u (l) label designate the upper (lower) level; A_{ul} , B_{lu} and B_{ul} are the Einstein coefficients for the spontaneous emission, absorption and stimulated emission, respectively, and ϕ_ν , φ_ν , and χ_ν are their respective line profiles.

The source function S_ν can be defined as the ratio between local emission and extinction coefficients

$$S_\nu = \frac{j_\nu}{\alpha_\nu}, \quad (4.4)$$

and thus represents the radiation of frequency ν emitted from the source.

The optical depth of a media at a given frequency τ_ν is defined as the extinction of a line as it goes through the media, so it is equivalent to $\alpha_\nu ds$. Therefore, the intensity of the detected line, emerging from the media, is given by

$$I_\nu(\tau_\nu) = I_\nu(0)e^{-\tau_\nu} + \int_0^{\tau_\nu} S_\nu(\tau'_\nu) e^{-(\tau_\nu - \tau'_\nu)} d\tau'_\nu, \quad (4.5)$$

where $I_\nu(0)$ is the background radiation field entering the medium, and I_ν is the intensity of the radiation field that escape from the media. The difficulty in solving this equation lies in the fact that it depends on the spatial variation of S_ν , which is related to the structure of the medium. In the simplest case, the medium is assumed to be spherical and homogeneous, so S_ν remains constant throughout the space. Therefore, the intensity escaping from the medium can be expressed as

$$I_\nu(\tau_\nu) = I_\nu(0)e^{-\tau_\nu} + S_\nu(1 - e^{-\tau_\nu}). \quad (4.6)$$

The optical depth τ_ν , also called opacity, represents the optical thickness of the media. If $\tau_\nu \gg 1$, the photon will not be able to escape the media, so the medium is called optically thick; on the opposite, if $\tau_\nu \ll 1$, the photon will escape the media and be detected, in which case the medium is then called optically thin. In the optically thick case, the spectral line is difficult to interpret, as the intensity of the radiation $I_\nu \sim S_\nu$. This means that only the outer layers of the medium are probed, since photons from the inner layers are absorbed before reaching the surface. However, when the medium is optically thin, the spectral line is well-observed and ready for interpretation.

4.1.2 Statistical Equilibrium Equations

In regions where the density is high enough for Local Thermodynamic Equilibrium (LTE) conditions to prevail—where collisions dominate molecular excitation—the population of the i^{th} energy level n_i follows a Boltzmann distribution determined using

$$n_i = \frac{g_i}{Q(T)} \exp\left(-\frac{E_i}{k_B T}\right), \quad (4.7)$$

where $Q(T) = \sum_i g_i \exp(E_i/k_B T)$ is the partition function, and g_i the degeneracy of level i , given by $(2j_i + 1)$ for rotational levels with j_i being the rotational quantum number.

However, in astrophysical media, the density is generally too low to maintain LTE conditions. Consequently, the population of molecular levels is governed by the competition between collisional and radiative processes, a state known as statistical equilibrium. To accurately model the statistical equilibrium, the time-dependent equation for the population of energy levels must be solved

$$\frac{dn_i}{dt} = 0 = -n_i \left[\sum_{j<i} A_{ij} + \sum_{j\neq i} (B_{ij}J_\nu + C_{ij}) \right] + n_k \left[\sum_{k>i} A_{ki} + \sum_{k\neq i} (B_{ki}J_\nu + C_{ki}) \right], \quad (4.8)$$

where A_{ij} , B_{ij} and B_{ji} are the Einstein coefficients for spontaneous emission, stimulated emission, and absorption of photons, respectively; $C_{ij} = k_{i\rightarrow j} n_{\text{gas}}$ are the temperature-dependent collisional rates for transitions between levels i and j due to collisions with gas particles; $k_{i\rightarrow j}$ are the collisional rate coefficients as computed in Chapter 3; n_{gas} is the density of the colliding gas particles (which can be a sum if multiple gases are dominant); and J_ν is the local radiation field, encompassing all components such as CMB, gas emission, and/or solar radiation.

The radiative transfer equations must be solved to determine the local radiation field J_ν . Then, the populations are evaluated, J_ν is re-evaluated, and this process continues iteratively until convergence between the two is achieved. The complexity in solving radiative transfer problems arises from the interdependence of the population distributions and the local radiation field.

4.1.3 Escape Probability

The escape probability β is the probability that a photon escapes the medium where it was created without being absorbed. The expression of β depends on the geometry of the source and the optical depth, but is independent of the radiation field.

In methods using the escape probability formalism, the medium is assumed to be homogeneous, which allow to limit the number of free parameters, so basic physical conditions (T , $n \equiv n_{\text{gas}}$, N) can be constrained.

If the medium is assumed to be spherically symmetric and homogeneous, the escape probability β_{sphere} is given by (Osterbrock & Ferland, 2006)

$$\beta_{\text{sphere}} = \frac{1.5}{\tau_\nu} \left[1 - \frac{2}{\tau_\nu^2} + \left(\frac{2}{\tau_\nu} + \frac{2}{\tau_\nu^2} \right) e^{-\tau_\nu} \right]. \quad (4.9)$$

If the medium is assumed to be contracting or expanding such that the Doppler shifts of the emission lines are significant, the Large Velocity Gradient (LVG) model can be employed. The escape probability β_{LVG} for an expanding spherical shell can be expressed

as (Mihalas, 1978; De Jong et al., 1980)

$$\beta_{\text{LVG}} = \frac{1}{\tau_\nu} \int_0^{\tau_\nu} e^{-\tau'_\nu} d\tau'_\nu = \frac{1 - e^{-\tau_\nu}}{\tau_\nu}. \quad (4.10)$$

The optical depth in the escape probability formalism is expressed as

$$\tau_\nu = \frac{c^3}{8\pi\nu_{ul}^3} \frac{A_{ul}N_{mol}}{1.064\Delta\nu} \left[x_l \frac{g_u}{g_l} - x_u \right], \quad (4.11)$$

where N_{mol} is the column density of the molecule which represents the number of molecules along the line-of-sight in the object, $\Delta\nu$ is the half-width at half-maximum of the line profile in velocity units, x_i the fraction of the population of level i .

In practice, the populations are first obtained by solving the SE equations in the optically thin case with only the unshielded background radiation field as the external radiation field (as if the medium was empty of molecules) for a set of fixed physical conditions $\{T, N_{mol}, n_{\text{gas}}\}$. From these populations, the optical depth of the lines is calculated using Equation (4.11). The populations are then re-estimated with the new optical depth. The iteration stops once there is a convergence on the optical depth or the populations is reached.

4.1.4 Useful Quantities

Here, useful quantities are described, which can either serve as good indicators or can be compared to equivalent observational data, thus allowing to evaluate the accuracy of set of physical conditions set by the user $\{T, N_{mol}, n_{\text{gas}}\}$. For example, the excitation temperature T_{ex} is often used to highlight the non-LTE characteristics of a medium. It is defined as a 'fictional' temperature that the medium would have to reproduce the distribution of the populations among the energy levels u, l . It is defined as

$$\frac{n_u}{n_l} = \frac{g_u}{g_l} \exp \left[\frac{-(E_u - E_l)}{k_B T_{ex}} \right], \quad (4.12)$$

with n_u , and n_l are previously determined by solving the radiative transfer equations. If $T_{ex} = T_{kin}$, it indicates that the line is thermalized, meaning that the LTE assumption holds for this specific transition. It is important to note that these excitation temperatures are unique to each line, as the populations of energy levels can be thermalized under different physical conditions.

The brightness temperature T_B represents the temperature of a black body that would produce the same specific intensity I_ν . It is defined as the temperature that produces the corresponding Planck function intensity in the Rayleigh-Jeans limit ($h\nu \ll k_B T_{ex}$). In this work, T_B is determined assuming an homogeneous temperature, volume density, and column density in the medium. It is thus given by

$$T_B = \frac{c^2}{2k_B\nu^2} I_\nu. \quad (4.13)$$

This brightness temperature can be compared to the line intensity measured by telescopes, taking into account factors such as beam dilution.

4.2 The New Rate Coefficients to Study the Chemistry of CCS

As CCS is of particular interest in the study of molecular clouds, this discussion focuses on the modeling of CCS in dark molecular clouds, where the temperature is typically of about 10 K, and the volume density between 10^3 and 10^5 cm⁻³.

4.2.1 CCS in Dark Molecular Clouds: Non-LTE Effects

A way to determine if the new collisional data affects the interpretation of observations is to check the excitation temperature T_{ex} values of the observed lines. Changes in T_{ex} would reflect variations in the populations of the energy levels involved in the transitions, and consequently, in the brightness temperature T_B of the line. Since T_B can be compared to observational data, any variation in T_B is expected to lead to changes in the derived physical conditions of the medium.

Additionally, evaluating T_{ex} as a function of the density of the gas n_{gas} provides an estimate of the density range for the non-LTE domain. At very low densities, collisions are rare, and molecules can only be excited by the background radiation field, leading to $T_{ex} = T_{bg}$. At very high densities, molecular excitation is dominated by collisions, causing the population of energy levels to follow a Maxwell-Boltzmann distribution, with $T_{ex} = T_{kin}$, where the LTE assumption holds. In intermediate density ranges, the competition between collisional and radiative de-excitation must be considered. This is the non-LTE

domain, where $T_{bg} < T_{ex} < T_{kin}$.¹

Therefore, to evaluate the impact of the new data, the T_{ex} as a function of the gas density ($n_{gas} \equiv n_{H_2}$ as H_2 represents 90% of the ISM composition) is represented for the most observed lines in molecular clouds of CCS, $CC^{34}S$, ^{13}CCS and $C^{13}CS$ isotopologues.

To be used in radiative transfer models, the rate coefficients computed in this work need to be adapted. Since the most abundant molecule in the ISM is H_2 , and considering the low temperatures relevant to this study, it can be assumed that only the ground state of H_2 is populated. Therefore, the main projectile would be *para*- H_2 (hereafter, noted p- H_2) in its ground rotational state $j = 0$. To derive CCS-p- $H_2(j = 0)$ rate coefficients from the CCS-He rate coefficients computed in this work, the following relation can be applied (Schöier et al., 2005)

$$k_{X-p-H_2} \simeq \left(\frac{\mu_{X-He}}{\mu_{X-p-H_2}} \right)^{1/2} k_{X-He}, \quad (4.14)$$

with $X \equiv CCS$, CC^{34} , ^{13}CCS , or $C^{13}CS$; k_{X-p-H_2} are the rate coefficients for X in collisions with p- $H_2(j = 0)$; μ_{X-He} and μ_{X-p-H_2} are the reduced mass of the X -He and X - H_2 collisional systems, respectively.

This approach is useful because the computational cost of determining rate coefficients with He as the projectile is much lower than with p- H_2 . It is based on the idea that p- $H_2(j = 0)$ behaves similarly to a large He atom. Indeed, both species have a spherical shape, and they are isoelectronic, each having a total of two electrons. The validity of this approximation has been debated extensively, and it remains unclear under which conditions it is applicable. However, it strongly depends on the strength of the interaction between the colliders. A significant difference in the interaction strength when considering He instead of p- H_2 will induce notable changes in the PES and, consequently, in the rate coefficients. This can be evaluated based on two factors: the nature of the interaction between the colliders and the dipole moment of the target molecule.

For ions, the interaction between the dipole of the ion and the quadrupole of H_2 stabilizes the intermediate complex much more than the dipole-polarizability interaction present in ion-He interactions. It has also been observed that for light molecules, such as hydrides, this approximation is not ideal and should only be used temporarily while

¹Exceptions can occur in specific cases: $T_{ex} < T_{bg}$ can be encountered for absorption or maser emission, and $T_{ex} > T_{kin}$ can be encountered for supra-thermal effect or maser emission.

awaiting more accurate data. For heavier molecules, however, the work of Wernli et al. (2007) on HC₃N showed that the largest discrepancy between HC₃N-He and HC₃N-p-H₂($j = 0$) was a factor of 1.5, which is a reasonable agreement considering the differences in computational effort between the two systems.

Additionally, if the dipole moment of the target molecule is large, the dipole-quadrupole interaction between the target and p-H₂($j = 0$) should be significantly stronger than the dipole-polarizability interaction between the target and He. Therefore, the larger the dipole moment of the target molecule, the greater the difference between the two sets of rate coefficients is expected to be.

In the case of CCS, its dipole moment is 2.88 D (Pascoli & Lavendy, 1998), and its molecular weight is 55.97 amu. When compared to HC₃N, for which the approximation worked reasonably well, its dipole moment is 3.6 D,¹ and its molecular weight is 51.01 amu. It is therefore reasonable to assume that if the approximation worked for HC₃N, it could also work for CCS, since CCS is heavier and has a lower dipole moment. Thus, while the sets of rate coefficients for the CCS molecule should ideally be extended to the H₂ projectile, the rate coefficients provided in this work are expected to offer sufficient accuracy as a first approximation for the study of CCS in cold molecular clouds.

Therefore, the data sets produced in this thesis have been scaled by the square root of the ratio between the reduced masses of the X-He and X-H₂ collisional systems, which corresponds to approximately a factor 1.4 for all CCS isotopologues.

The radiative transfer equations were solved as implemented in the RADEX software (van der Tak et al., 2007) by assuming a homogeneous spherical medium. Only the CMB was considered as the background radiation field, with the background temperature set to $T_{\text{CMB}} = 2.73$ K. The kinetic temperature of the medium was set to 10 K to represent typical dark molecular clouds, and the line width $\Delta\nu$ was set to 1 km s⁻¹. The column density was fixed at $N = 1 \times 10^{13}$ for all isotopologues, even though, in practice, it should vary from one isotopologue to the other. However, since the focus is on collisional effects and the influence of volume density, this assumption will not impact the analysis. The Einstein coefficients were taken from the CDMS (Müller et al., 2001; Müller et al., 2005; Endres et al., 2016) and JPL (Pickett et al., 1998) databases.

In Figure 4.1, the excitation temperature T_{ex} (in K) of CCS and CC³⁴S isotopologues is shown as a function of the n_{H_2} density (in cm⁻³) for the most commonly observed $N_j \rightarrow$

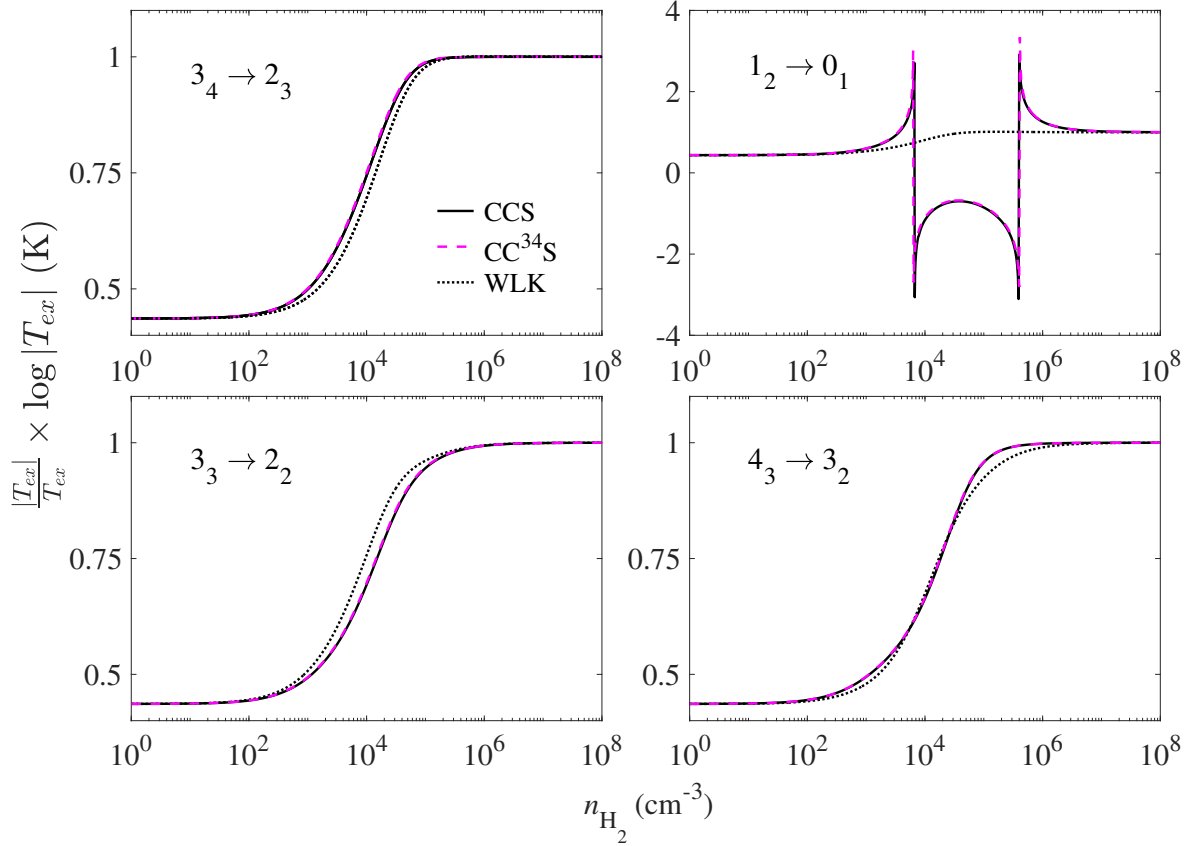


Figure 4.1: Excitation temperature (in K) as a function of the H_2 density of the gas (in cm^{-3}) for the most observed $N_j \rightarrow N'_j$ transitions of CCS in dark molecular clouds. The excitation temperatures are given for CCS (black solid lines), CC^{34}S (magenta dashed lines), and for CCS based on the rate coefficients produced by Wolkovitch et al. (1997) (black dotted lines, indicated by WLK).

N'_j transitions of these isotopologues in molecular clouds. The excitation temperatures for these transitions were also computed using the rate coefficients provided by Wolkovitch et al. (1997) for comparison. Indeed, as significant discrepancies were found between their set of rate coefficients and ours, the impact of these deviations on the excitation models—and consequently on the interpretation of observations—should be evaluated.

The excitation temperature obtained for the CCS and CC^{34}S isotopologues, based on their respective sets of rate coefficients computed in this work, are nearly identical for all transitions. This behavior was expected, as both isotopologues exhibit very similar Einstein coefficients (that differ by 11% at best, but most of the Einstein coefficients agree within 5%), and only very small variations were observed in the rate coefficients, as discussed in Section 3.1.3.

For three transitions— $3_4 \rightarrow 2_3$ (left upper panel), $3_3 \rightarrow 2_2$ (left lower panel), and $4_3 \rightarrow 3_2$ (right lower panel)—the typical behavior of the T_{ex} with n_{H_2} is followed. In the low-density regime, $T_{ex} = T_{\text{CMB}}$. As the density increases, the system enters the non-LTE regime, where T_{ex} increases until it reaches the LTE regime, where $T_{ex} = T_{kin}$. The non-LTE regime occurs between 10^3 - 10^5 cm^{-3} for the $3_4 \rightarrow 2_3$ and $4_3 \rightarrow 3_2$ transitions, and between 10^3 - 10^6 cm^{-3} for the $3_3 \rightarrow 2_2$ transition. As the typical density ranges of dark molecular clouds is of 10^3 - 10^5 cm^{-3} , interpreting observations of these emission lines in such media likely requires detailed excitation models and accurate collisional data for proper interpretation.

For the $1_2 \rightarrow 0_1$ (right upper panel), the excitation temperature exhibits a peculiar behavior within the non-LTE regime known as a maser (microwave amplification by stimulated emission of radiation) effect. This is characterized by a strong variation in the excitation temperature, which can exceed the kinetic temperature of the medium and drop to negative values over a narrow density range. This behavior is explained by a population inversion and could result in an exceptionally bright emission line. Apart from detailed excitation models with accurate collisional data, no other approach accounts for such effects. The maser effect in the $1_2 \rightarrow 0_1$ emission is expected to be observable in dark molecular clouds, as it covers the 10^3 - 10^6 cm^{-3} density range, which encompasses the typical densities of these clouds.

The excitation temperatures of CCS calculated with the rate coefficients from this work, compared to the excitation temperature computed with the data provided by Wolkovitch et al. (1997), show some deviations. For the $3_3 \rightarrow 2_2$ (left lower panel), and $4_3 \rightarrow 3_2$ (right lower panel) transitions, the deviations reach up to 1 K in the 10^4 - 10^5 cm^{-3} , which matches with typical dark molecular cloud densities. For the $3_3 \rightarrow 2_2$ transitions, the T_{ex} derived using Wolkovitch et al. (1997)'s data is higher, while the opposite tendency occurs for the $4_3 \rightarrow 3_2$ transition. Therefore, predicting how these T_{ex} differences will affect CCS modeling in molecular clouds is challenging. The most significant difference is that the maser effect in the $1_2 \rightarrow 0_1$ transition is not reproduced when using Wolkovitch et al. (1997)'s rate coefficients.

The two most commonly used lines in the radiative transfer models of CCS from previous studies are the $3_4 \rightarrow 2_3$ transition, which is very intense and systematically detected, and the $1_2 \rightarrow 0_1$ transition. For the $3_4 \rightarrow 2_3$ transition, differences in T_{ex} can be up to 0.7 K, while for the $1_2 \rightarrow 0_1$ transition, discrepancies in T_{ex} can reach up to three orders of magnitude, as the maser effect is not reproduced when using the data

from Wolkovitch et al. (1997). Since these two lines are the most frequently detected, determining CCS column densities often relies on them (Saito et al., 1987; Fuente et al., 1990; Suzuki et al., 1992; Wolkovitch et al., 1997). Therefore, due to strong discrepancies between the T_{ex} values obtained with accurate and approximate data sets, using these lines with the approximate rate coefficients may lead to inaccuracies in determining the physical conditions under which CCS is detected.

The analysis of the T_{ex} for the four most commonly observed transitions of CCS observations revealed that it is essential to model CCS spectra using detailed excitation models and accurate collisional data. Nevertheless, as discussed in Section 3.1.3, using the same set of rate coefficients for the modeling of CCS and $CC^{34}S$ is not expected to impact the accuracy of their derived column density.

The same analysis of T_{ex} as a function of the H_2 density has been conducted for the ^{13}C -bearing isotopologues to evaluate the validity of the LTE assumption. Therefore, the excitation temperature for the most observed lines of the two ^{13}CCS and $C^{13}CS$ isotopologues are presented in Figure 4.2. Unlike the main isotopologues, the spectra of ^{13}C -bearing isotopologues have typically been interpreted using the LTE assumption or the rotational diagram method, which is a pseudo-LTE approach. This is justified by the lack of collisional data for either of the CCS isotopologues before the data produced during this thesis work.

The Einstein coefficients for both isotopologues generally agree within 20%, but they can be quite different, with differences up to two orders or magnitude for a few transitions. For the observed transitions, the Einstein coefficients differ by about 15%. The Einstein coefficients of $C^{13}CS$ being generally higher than those of ^{13}CCS .

The most commonly observed lines are the hyperfine components of the $2_3 \rightarrow 1_2$ ($F = 7/2 - 5/2; 5/2 - 3/2$) (upper panels) and $1_2 \rightarrow 0_1$ ($F = 5/2 - 3/2; 3/2 - 1/2$) (lower panels) transitions. The excitation temperatures of both ^{13}CCS (in blue) and $C^{13}CS$ (in green) isotopologues are shown. As they exhibit very similar behavior and values for all transitions, which was expected given their similar sets of rate coefficients as discussed in Section 3.1.3, all following conclusions hold for both ^{13}C -bearing isotopologues.

For the two hyperfine components of the $2_3 \rightarrow 1_2$ transition ($F = 7/2 - 5/2; 5/2 - 3/2$), a small supra-thermal effect is observed. This effect is characterized by an excitation temperature that slightly exceeds the kinetic temperature before thermalization. The excitation temperature in the supra-thermal effect reaches about 11 K. This effect

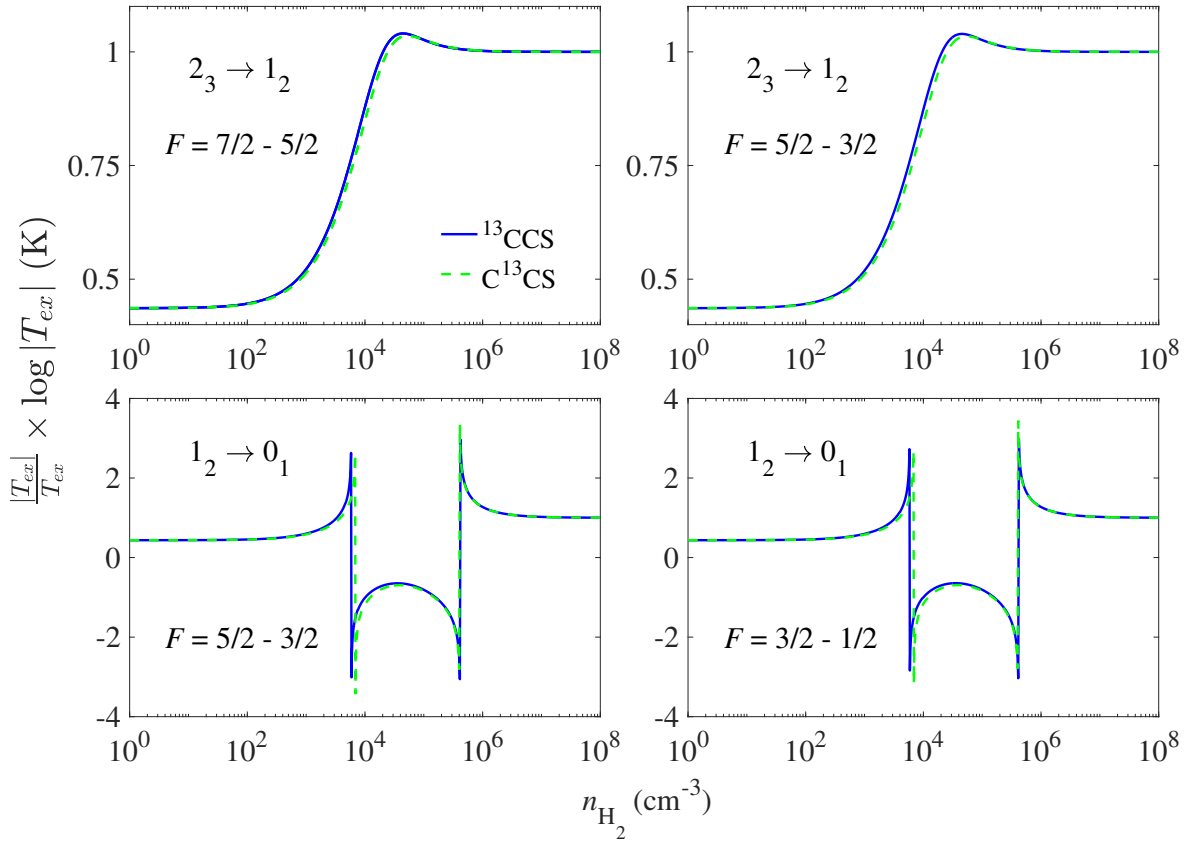


Figure 4.2: Excitation temperature (in K) as a function of the H_2 density of the gas (in cm^{-3}) for the most observed hyperfine components ($F-F'$) of the $N_j \rightarrow N'_j$ transitions of ^{13}C -bearing isotopologues of CCS in dark molecular clouds. The excitation temperatures are given for ^{13}CCS (blue solid lines), C^{13}CS (green dashed lines).

could be observed, as it occurs in the density range of $n_{\text{H}_2} \in [10^4, 10^5] \text{ cm}^{-3}$, which is the typical density range of molecular clouds. Such effects, similar to maser effects, can only be accounted for if collisional data are employed. Within the two hyperfine components, the excitation temperatures behave very similarly, with a maximum deviation of 0.1 K between the excitation temperatures of the two hyperfine components of the same fine-structure transition. Therefore, assuming the same excitation temperature for both hyperfine components is expected to be a good approximation and should not significantly impact the modeling of this transition.

More importantly, the hyperfine components of the $1_2 \rightarrow 0_1$ transition ($F = 5/2 - 3/2$; $3/2 - 1/2$) exhibit maser effects in the 10^3 - 10^6 cm^{-3} density range. This has also been observed for this fine transition in the CCS and CC^{34}S isotopologues, as shown in

Figure 4.1. These findings suggest that using the LTE approximation to model the spectra of the ^{13}C -bearing isotopologues of CCS would lead to inaccurate abundance estimates.

Therefore, for an accurate interpretation of the emission lines of the ^{13}CCS and C^{13}CS isotopologues, reliable excitation models based on accurate collisional data are required. This underscores the importance of using robust collisional rate coefficients and detailed excitation models to derive precise column densities for CCS isotopologues in molecular clouds. Nevertheless, as discussed in Section 3.1.3, using the same set of rate coefficients for the modeling of ^{13}CCS and C^{13}CS is not expected to impact the accuracy of their derived column density.

4.2.2 Impact on the Brightness Temperature

The effect of the rate coefficients produced by Wolkovitch et al. (1997) on the brightness temperature T_B of CCS lines can be investigated. As the T_B can be compared to equivalent observational data, this is the most direct way to evaluate the impact of the rate coefficients on the derived molecular column density.

In Figure 4.3, the brightness temperatures T_B of all $N_j \rightarrow N'_j$, observed emission lines by Fuentetaja et al. (in prep.), along with the $1_2 \rightarrow 0_1$ transition, are exhibited.²

The media is assumed to be a uniform homogeneous sphere, and the calculations were performed using the RADEX software (van der Tak et al., 2007). The set of physical parameters $\{T, N_{mol}, n_{gas}\}$ has been chosen as determined from the analysis of CCS emission spectra in Taurus Molecular Clouds 1 (hereafter TMC-1) at the cyanopolyne peak (noted, CP) by Fuentetaja et al. (in prep.). Thus, the kinetic temperature have been fixed at 10 K, the H_2 density at $1.3 \times 10^4 \text{ cm}^{-3}$, CCS column density at $3.4 \times 10^{13} \text{ cm}^{-2}$, and the linewidth $\Delta\nu$ at 0.6 km s^{-1} . The excitation models are based on the set of accurate rate coefficients computed in this thesis work, the set of approximate rate coefficients produced in the work of Wolkovitch et al. (1997), as well as based the LTE assumption.³

First, the agreement between the brightness temperatures calculated with LTE and non-LTE models is discussed. Generally, the agreement between brightness temperatures computed with the LTE and non-LTE models—based on either the rate coefficients

²The $1_2 \rightarrow 0_1$ @22.344 GHz emission cannot be detected by the Yebes 40m telescope due to its frequency range limitations, but it has been observed by other telescopes, such as the Green Bank Telescope (GBT) and the Nobeyama Radio Observatory (NRO).

³The LTE assumption was simulated by multiplying the set of rate coefficients by a large factor of 10^6 to ensure that collisions dominate and $T_{ex} = T_{kin}$ for all transitions.

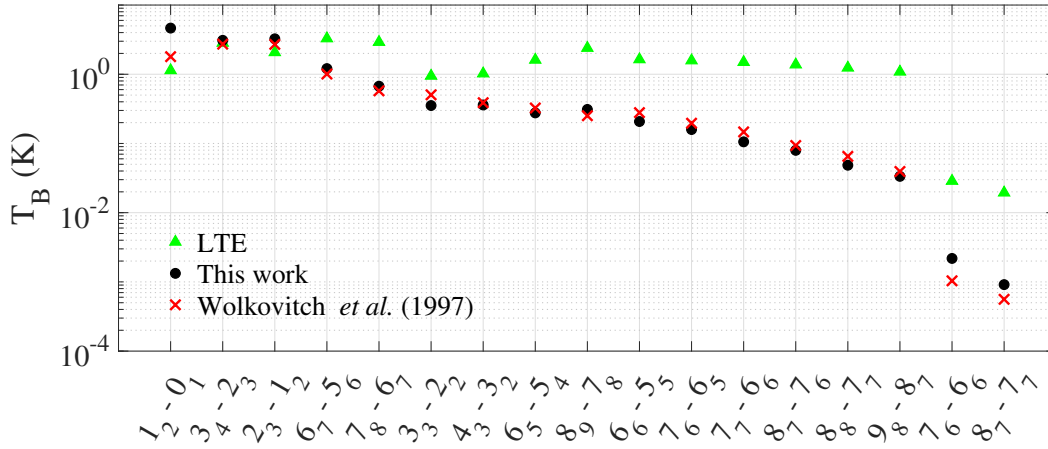


Figure 4.3: Brightness temperatures T_B (in K) as a function of the $N_j - N'_j$ observable lines. The temperatures are obtained using the LTE approximation (green triangles), based on the rate coefficients computed in this work (black circles), and based on the rate coefficients from Wolkovitch et al. (1997) (red crosses). The physical parameters used are those from the observations of TMC-1 (CP) by Fuentetaja et al. (in prep.).

produced in this work or those from Wolkovitch et al. (1997)—is better for dominant transitions, i.e., for transitions where T_B is the largest. This is explained because these lines are the closest to LTE, with excitation temperature > 6 K. Additionally, the LTE approximation tends to overestimate the brightness temperatures T_B of the lines, meaning that this approximation will tend to underestimate the abundance of CCS. Indeed, if the value computed based on our data is considered as the reference value, LTE models would need to reduce the number of CCS molecules to match the reference T_B . Furthermore, the higher the fine-structure levels involved in the transition, the larger the deviation between LTE and non-LTE brightness temperatures, with differences exceeding one order of magnitude. For all transitions, the brightness temperatures predicted by the LTE model are generally around 1 K, except for the $7_6 \rightarrow 6_6$ and $8_7 \rightarrow 7_7$ transitions for which the Einstein coefficients are particularly low ($\sim 10^{-7} \text{ s}^{-1}$). In contrast, when non-LTE models are employed, the brightness temperatures for the different lines span four orders of magnitude. This shows that LTE approximation will tend to consider a wide spread distribution among the energy levels, while the non-LTE distribution of the population will be more focused on few levels.

The agreement between the two sets of brightness temperatures calculated using non-

LTE models is significantly better than the agreement for temperatures computed under the LTE assumption. The non-LTE models exhibit similar T_B for all transitions, which usually differ by less than a factor of 1.5, except for the $1_2 \rightarrow 0_1$, $7_6 \rightarrow 6_6$ and $8_7 \rightarrow 7_7$ transitions. Additionally, the T_B based on Wolkovitch et al. (1997) data are sometimes higher and sometimes lower than those estimated from the data produced in this work, making it difficult to predict their impact on column density estimation. However, for dominant transitions, the brightness temperatures derived from Wolkovitch et al. (1997) are generally lower, suggesting a tendency to overestimate the column density of CCS. Indeed, an increased number of CCS molecules would lead to a higher brightness temperature.

As expected, the brightness temperature of the $1_2 \rightarrow 0_1$ transition, anticipated to be the brightest with $T_B = 4.7$ K, is not well reproduced by either the LTE model or the non-LTE model based on the data of Wolkovitch et al. (1997). The brightness temperature of this transition is 2.5 times higher when using the accurate collisional data produced in this work, compared to its intensity when the rate coefficients from Wolkovitch et al. (1997) are employed. It is four times lower when the LTE model is used. This discrepancy is explained by the fact that this transition, as shown in Figure 4.1, exhibits a maser effect that the rate coefficients produced by Wolkovitch et al. (1997) or the LTE approximation fail to reproduce.

For all transitions, deviations between the brightness temperatures computed with different models are observed. The use of the LTE approximation results in the most significant deviations and is expected to be insufficient for providing reliable abundances of CCS in molecular clouds. Additionally, some deviations observed between the brightness temperatures calculated using Wolkovitch et al. (1997) data and those derived from our data are quite significant, especially for the $1_2 \rightarrow 0_1$ transition, which is anticipated to be one of the brightest lines. Therefore, robust modeling of CCS in dark molecular clouds requires the use of non-LTE models that rely on detailed excitation models and accurate collisional data. Otherwise, the brightness temperature, which can then be compared to equivalent observational data, cannot be properly interpreted.

4.2.3 Revision of CCS Abundances in TMC-1 (CP)

The new CCS rate coefficients have been employed to model new observations of CCS and its isotopologues in TMC-1 in a collaboration with R. Fuentetara, Dr. Marcelino Agúndez, and Pr. José Cernicharo from the Instituto de Física Fundamental. As a result

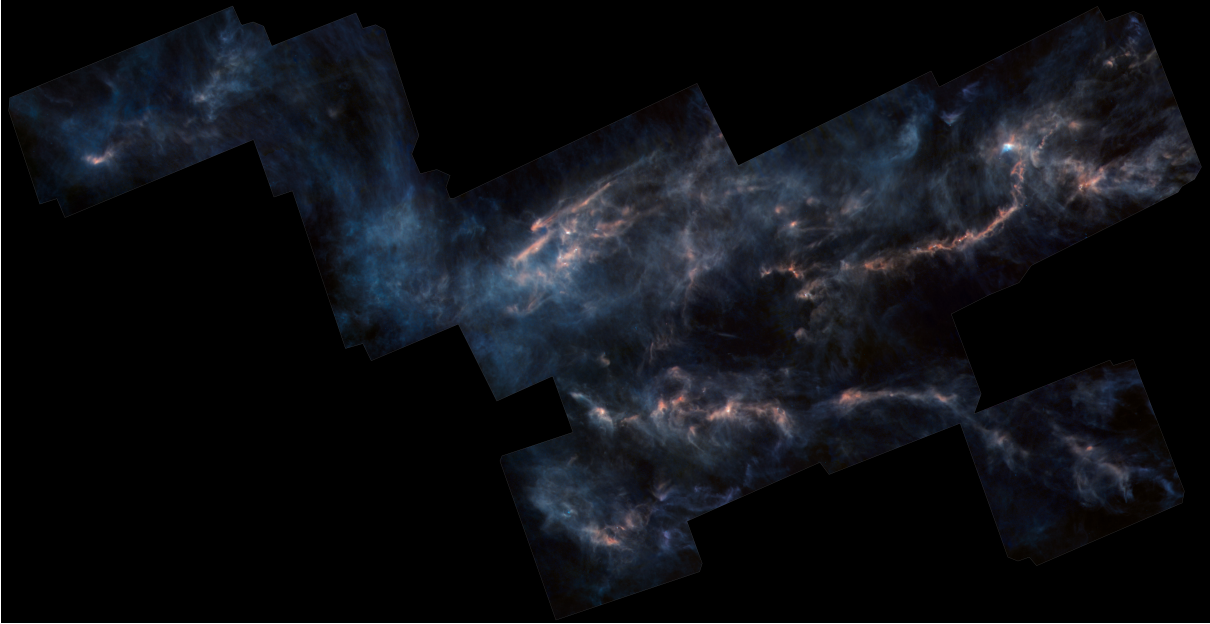


Figure 4.4: Taurus Molecular Cloud observed by ESA’s Herschel Observatory in the far-IR and sub-mm wavelengths between 2009 and 2013. The darker, blue-hued areas correspond to colder, less dense regions of the cloud, while brighter, red-hued regions are the densest environment, where the star-forming activity is the most intense. Credits: ESA/Herschel/NASA/JPL-Caltech, CC BY-SA 3.0 IGO; Acknowledgment: R. Hurt (JPL-Caltech).

of this collaboration, a paper will be submitted to a peer-reviewed journal (Fuentetaja et al., [in prep.](#)).

Dark molecular clouds are self-gravitating molecular clouds that are very opaque to visible light, which is why they are depicted as ‘dark’: visible light is completely scattered and absorbed by the dust within the cloud. Consequently, these clouds are observed using infrared and radio telescopes. To understand the processes leading to planet and star formation within these clouds, their initial physical and chemical conditions must be investigated. TMC-1, shown in Figure 4.4, is a nearby (140pc ; Onishi et al. (2002)) well studied dark molecular cloud complex located in the Taurus Constellation. It is thought to be an early stage cloud, estimated to be a few million years old.

The observational data employed in our work are part of the QUIJOTE project (Cernicharo et al., 2022), a spectral line survey of TMC-1 (CP) in the Q-band carried-out with the Yebes 40m telescope. The line identification was performed using the MADEX

	N_{mol} (in cm^{-2})	Model	Ref.
CCS	8×10^{13}	rot. diag. ($T_{rot} = 6$ K)	Saito et al. (1987)
	3.9×10^{13}	rot. diag. ($T_{rot} = 7$ K)	Fuente et al. (1990)
	1.26×10^{14}	rot. diag. ($T_{rot} = 4.19$ K)	Gratier et al. (2016)
	2.3×10^{13}	LVG	Fuente et al. (1990)
	6.6×10^{13}	LVG	Suzuki et al. (1992)
	3.4×10^{13}	LVG	Fuentetaja et al. (in prep.)
CC ³³ S	3.5×10^{11}	LVG	Fuentetaja et al. (in prep.)
CC ³⁴ S	1.5×10^{12}	LVG	Fuentetaja et al. (in prep.)
¹³ CCS	8.4×10^{10}	LVG	Fuentetaja et al. (in prep.)
C ¹³ CS	5.7×10^{11}	LVG	Fuentetaja et al. (in prep.)

Table 4.1: Column densities (in cm^{-2}) of CCS isotopologues in TMC-1 (CP) derived from interpretation of observations. The model indicated as "rot. diag." refers to the rotational diagram approach (Blake et al., 1987; Bockelee-Morvan et al., 1994), assuming a single excitation temperature for all transitions.

catalog (Cernicharo et al., 2012), and complementary data were taken from the CMDS (Müller et al., 2001; Müller et al., 2005; Endres et al., 2016), and JPL (Pickett et al., 1998) catalogs. The emission lines have been modeled using a LVG approach, which basic principle have been described in Section 4.1. A kinetic temperature of 10 K, and a linewidth $\Delta\nu$ of 0.6 km s^{-1} have been set for all emission lines of all CCS isotopologues. The rate coefficients computed for CCS isotopologues in collisions with He $k_{X-\text{He}}$ in this work were adapted using Equation (4.14) to infer the rate coefficients with the p-H₂($j = 0$) projectile.

The column densities of CCS isotopologues have been determined based on a χ^2 analysis of the fine and hyperfine emission lines detected for each isotopologue. A summary of the column densities evaluated for CCS isotopologues in TMC-1 (CP) can be found in Table 4.1. The estimated column densities of CCS from previous work are also presented. The model employed for the interpretation of observations is specified, along with the assumed excitation temperature for all transitions when applicable.

To the best of my knowledge, the column density of no secondary isotopologues of CCS has been reported to date. Therefore, the discussion about the impact of the LTE assumption and approximate collisional data on the evaluation of CCS isotopologues' column densities will solely focus on the main isotopologue. Unfortunately, the observations conducted in the work of Wolkovitch et al. (1997) were directed towards the deuterium

peak of TMC-1 [noted as TMC-1 (D)], which is a different region than the one probed during our survey. Therefore, the effect of the new data on the column densities cannot be directly assessed.

The column densities of CCS in TMC-1 (CP) can vary by over a factor of five depending on the studies (Saito et al., 1987; Fuente et al., 1990; Suzuki et al., 1992; Gratier et al., 2016; Fuentetaja et al., *in prep.*). The value deduced in this work is among the lowest and will be considered the reference for this discussion. Indeed, it is based on the most sensitive spectral survey and the accurate radiative transfer model, utilizing the LVG approach and the accurate collisional rate coefficients produced in this thesis. Therefore, the column density of CCS is evaluated as $N_{\text{CCS}} = 3.4 \times 10^{13} \text{ cm}^{-2}$ in TMC-1 (CP).

From the column density of CCS reported in Table 4.1, it can be noticed that the use of the rotational diagram approach tend to overestimate the abundance of CCS in TMC-1 (CP) (Saito et al., 1987; Fuente et al., 1990; Gratier et al., 2016). In the work of Fuente et al. (1990), they derived CCS column density based on both the rotational diagram approach and the LVG model using an approximate set of collisional rate coefficients. The column density of CCS they derived was reduced by almost a factor of two when the LVG approach was employed. However, it is interesting to note that the value derived under the LTE assumption is actually the closest to the reference, with the values differing by less than 15%.

Moreover, Gratier et al. (2016) based their analysis on the observations of Kaifu et al. (2004) and derived the excitation temperature of CCS using the rotational diagram approach based on eight transitions. However, the CCS abundance was overestimated by almost a factor of four, which shows that even using multiple lines, the rotational diagram approach fails to reproduce the accurate column densities of the CCS molecule. This discrepancy is explained by the fact that many non-LTE effects affect the emission lines of CCS, so a unique T_{ex} for all transitions cannot accurately represent the actual distribution of the populations among the energy levels. The column density they derived is, however, the suggested one by the ISA database.⁴ This highlights that this pseudo-LTE approach cannot accurately reproduce the abundance of CCS in TMC-1 (CP) and probably in other molecular clouds, as discussed in Section 4.2.1.

The column densities derived using the LVG approach vary less. The column density proposed by Suzuki et al. (1992) is almost twice as large as the one found in this work, while the one derived by Fuente et al. (1990) is lower by a factor of 1.5. However, these two

⁴<https://isa.astrochem-tools.org>

studies were expected to yield similar results, as they employ the same approach to derive the set of CCS rate coefficients using the LVG method. This discrepancy is explained by the fact that the study of Fuente et al. (1990) is based on the $3_4 \rightarrow 2_3$ line because the observations were done using the Yebes telescope 13.7 m,² while Suzuki et al. (1992) observations were done with NRO, and also included the $1_2 \rightarrow 0_1$ line in their analysis.⁵ However, this line has been found to exhibit a maser effect that is not reproduced with the approximate set of collisional data, as discussed in Section 4.2.1.

This suggests that employing accurate sets of CCS rate coefficients in future observations of CCS in other regions of TMC-1 or in other dark molecular clouds could significantly revise its abundance in these environments.

For secondary CCS isotopologues studied in this work (^{13}CCS , C^{13}CS , CC^{33}S and CC^{34}S), a comparison between column densities with previous studies was not possible. For ^{13}CCS , C^{13}CS , only abundance ratios have been reported, and the comparison is done further in the manuscript in the context of the ^{13}C -anomaly; the column density of CC^{34}S has never been documented to the best of my knowledge, and this study represents the first detection of CC^{33}S . However, CCS and its isotopologues have been found to be very sensitive to non-LTE effects, and it thus strongly recommended to employ accurate rate coefficients to interpret their emission spectra. Nevertheless, the effect of the isotopologue-specific rate coefficients on the brightness temperature has been found to be weak, as further discussed in Godard Palluet & Lique (2023b) presented in Appendix A.3.

4.2.4 Impact on the Chemistry of CCS

The Formation Paths of CCS

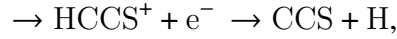
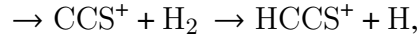
The primary formation pathway of CCS was proposed by Smith et al. (1988) to occur via acetylene (C_2H_2) following Reaction (4.15). It has since been adopted as the main mechanism in chemical models (Millar & Herbst, 1990).



Additional formation pathways were proposed by Suzuki et al. (1992) [Reaction (4.16)], and by Yamada et al. (2002), who performed *ab initio* calculations for Reactions (4.17) –

⁵They employed the NRO telescope, so they can detect the $1_2 \rightarrow 0_1$ @22.344 GHz emission line.

(4.23).



In their work, Yamada et al. (2002) emphasized on the importance of using all formation paths, as they are all possible at the low temperatures of cold molecular clouds. To date, however, the temperature-dependent rate constants and branching ratios for none of these reactions are known, so it is difficult to assess which paths are the most important.

The ^{13}C -Anomaly

The ^{13}C anomaly refers to a phenomenon where two non-equivalent ^{13}C -bearing isotopologues, such as ^{13}CCS and C^{13}CS , exhibit different abundances. This was first identified by Sakai et al. (2007), who observed significant differences between the line intensity of the two ^{13}CCS and C^{13}CS isotopologues in TM-1 (CP), as illustrated Figure 4.5a. The phenomenon has also been noted in the work of Fuentetaja et al. (in prep.) toward the same region of TMC-1, as illustrated in Figure 4.5b.

Two hypotheses have been proposed to explain the origin of the anomaly: either C^{13}CS is significantly more abundant than ^{13}CCS due to the chemistry of CCS, or the two isotopologues experience different excitation conditions, influenced by distinct sets of rate coefficients, resulting in very different line intensities. It is also possible that the reality lies somewhere between these two hypotheses.

The second hypothesis was investigated in this thesis, and it was concluded in Section 3.1.3 that the sets of rate coefficients for ^{13}CCS and C^{13}CS are very similar. Additionally, Section 4.2.1 demonstrated that both isotopologues undergo the same excitation

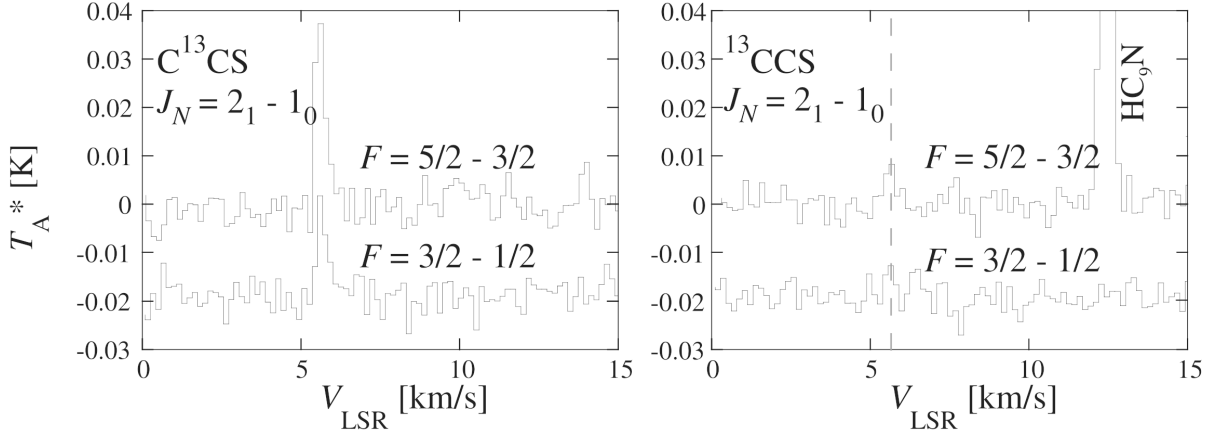
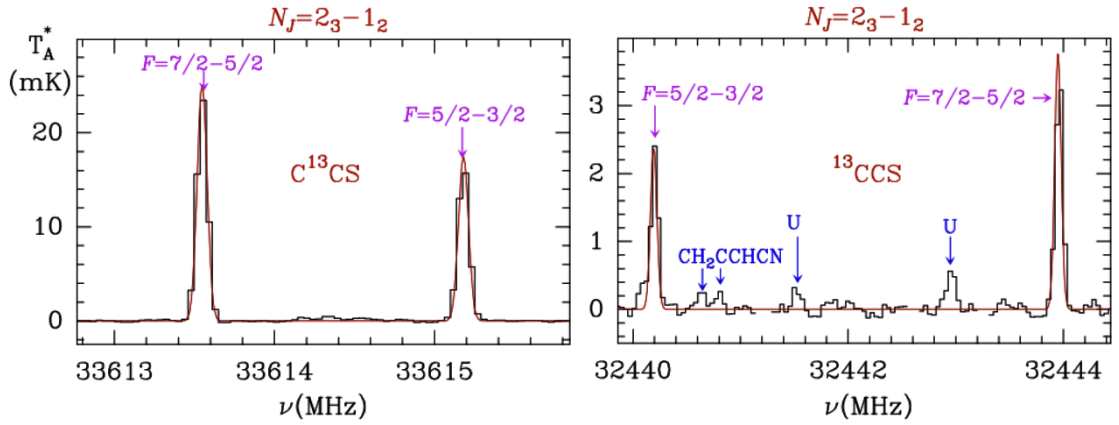

 (a) Line intensities of C^{13}CS and ^{13}CCS from Sakai et al. (2007)

 (b) Line intensities of C^{13}CS and ^{13}CCS from Fuentetaja et al. (in prep.)

 Figure 4.5: C^{13}CS (left panels) and ^{13}CCS (right panels) observed hyperfine components of the (a) $N_j = 1_2 - 0_1$ transitions by Sakai et al. (2007) (b) $N_j = 2_3 - 1_2$ transitions by Fuentetaja et al. (in prep.).

conditions. Thus, the anomaly cannot be compensated or amplified by collisional effects. Consequently, the ^{13}C anomaly likely originates from the molecule's chemistry.

To investigate the chemistry of CCS based on this anomaly, the first step is to determine the abundance ratio between the two species. Sakai et al. (2007) derived this ratio from the integrated intensities of the $N_j = 1_2 - 0_1$ hyperfine components, and they determined an abundance ratio of $[\text{C}^{13}\text{CS}]/[^{13}\text{CCS}] = 4.2 \pm 2.3$. This was the first time such a large disparity in the abundance of two ^{13}C isotopic species of the same molecule had been observed. It was particularly surprising given that the main formation path of CCS was still thought to be Reaction (4.15), which should produce both isotopologues in a 1:1 ratio, as acetylene is a symmetric molecule.

In their work, Sakai et al. (2007) reconsidered all formation pathways of CCS and ruled out any reactions that would result in a 1:1 ratio of ^{13}CCS and C^{13}CS . As a result, reactions involving symmetric molecules such as C_2H_2 or C_2 —namely Reactions (4.15), (4.18), (4.22), and (4.23)—were excluded. The remaining potential formation pathways were Reactions (4.16), (4.17), (4.19), (4.20), and (4.21). However, reactions involving HCS were also ruled out due to the low interstellar abundance of HCS, which is insufficient to be the parent molecule of a widespread species like CCS. Thus, only Reactions (4.16), (4.17), (4.19) remained.

For the reactions involving CCH, the formation of the two ^{13}C -bearing CCS isotopologues should occur as



However, since the $[\text{C}^{13}\text{CH}]/[^{13}\text{CCH}]$ abundance ratio is greater than unity [estimated as 1.6 ± 0.4 by Sakai et al. (2010)], ^{13}CCS should be favored over C^{13}CS . Thus, if Reactions (4.17) and (4.16) were to be significant formation paths for CCS, the ^{13}C -anomaly in CCH should compensate for the ^{13}C -anomaly in CCS. Therefore, only Reaction (4.19) remains, which proceeds as



leading to the two non-equivalent ^{13}C -based isotopologues of CCS.

Both CH and CS are known to be abundant in TMC-1, making this a plausible formation path for CCS. However, to explain such a large abundance ratio between ^{13}CCS and C^{13}CS , ^{13}CH needs to be significantly diluted compared to ^{13}CS , thus favoring Reaction (4.26) over Reaction (4.27).

The Interconversion Solution

To fully understand this ^{13}C -anomaly in CCS, it needs to be noticed that C^{13}CS is more stable than ^{13}CCS by 18.9 K, as illustrated in Figure 4.6.

Another possible explanation for the ^{13}C -anomaly involves exchange reactions that could swap the positions of the two carbon atoms, thereby favoring the formation of

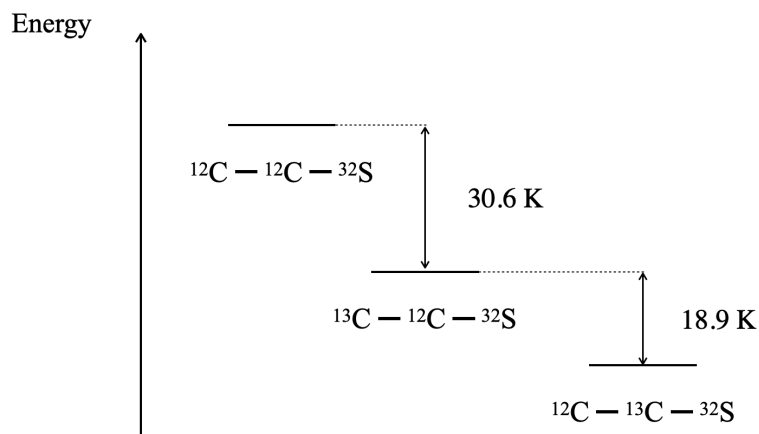


Figure 4.6: Diagram representing the relative stability of CCS, ^{13}CCS , and C^{13}CS . The relative energy are given are zero-point energy difference, accounting for anharmonic corrections, computed at the M06-2X/aug-cc-pVTZ level of theory by Talbi (2018).

C^{13}CS , the more stable isotopologue. Furuya et al. (2011) proposed an exchange reaction catalyzed by H atoms, as follows



where ΔE represents the difference in zero-point energy (hereafter, ZPE) between the two isotopologues. The ZPE represents the energy difference between the lowest energy of the electronic states and the energy of the ground vibrational state. It is evaluated as the difference between the minimum of the potential well and the dissociation energy. This concept is illustrated in Figure 4.7.

This interconversion reaction would convert the less stable isotopologue (^{13}CCS) into the more stable one (C^{13}CS), but only if no activation barrier is present. Indeed, as the media under consideration are cold dark molecular clouds, any activation barrier would be difficult to be overcome. Fortunately, Talbi (2018) studied this reaction and found that it proceeds without an activation barrier, following the path shown in Figure 4.8.

Talbi (2018) found Reaction (4.28) to be exothermic, with $\Delta E = 18.9$ K. They concluded that this reaction should consume the ^{13}CCS into C^{13}CS , thereby confirming the hypothesis of Furuya et al. (2011).

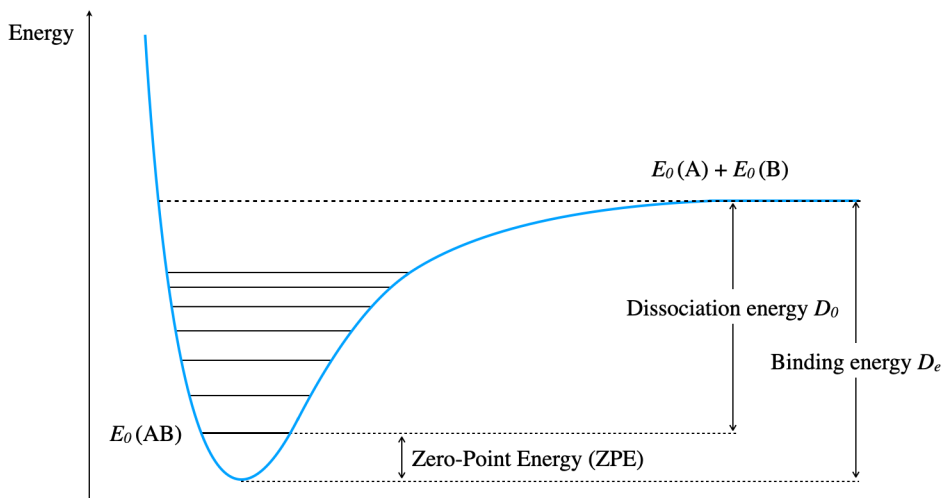


Figure 4.7: Schematic representation of the Zero-Point Energy (ZPE). $E_0(\text{AB})$ represents the energy of the AB molecule in its ground vibrational state; $E_0(\text{A})$ and $E_0(\text{B})$ represent the energy of each individual monomers A, and B. The dissociation energy is defined as $D_0 = E_0(\text{AB}) - E_0(\text{A}) - E_0(\text{B})$; the binding energy D_e is given as the energy difference between the the bottom of the potential well and the individual monomers A + B. Finally, the $\text{ZPE} = D_e - D_0$.

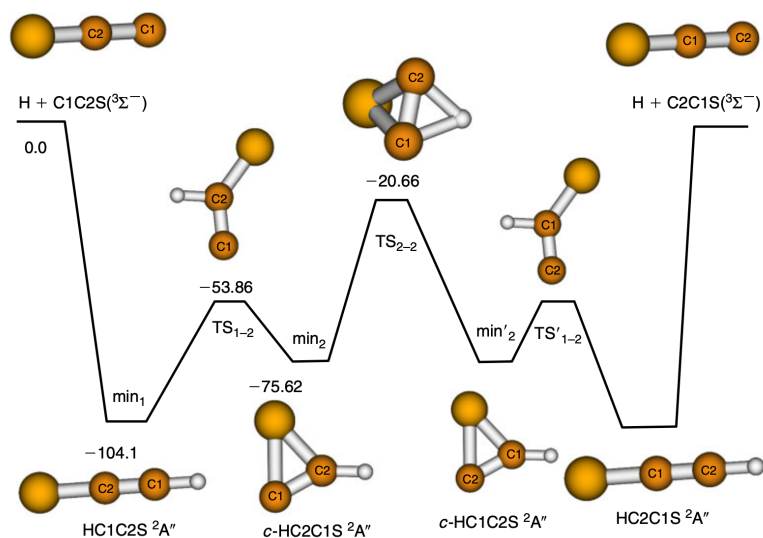


Figure 4.8: Energy profile of the H + CCS reaction calculated at the RCCSD(T)/aug-cc-pVQZ//M06-2X/aug-cc-pVTZ level of theory, taken from Talbi (2018). The relative energies corrected for the ZPE are given in kcal mol^{-1} .

The interconversion has also been suggested to occur through collisions with carbon or sulfur atoms (Sakai et al., 2007; Sakai et al., 2010). However, since hydrogen is much more

abundant, the interconversion involving CCS and H is more likely to have a significant impact on the abundances of ^{13}CCS and C^{13}CS .

If the exchange reaction (4.28) is indeed governing the chemistry of the ^{13}C -based isotopologues of CCS, it implies that thermodynamics, rather than kinetics, is driving the chemistry of CCS. Consequently, the abundance ratio between the two isotopologues should be expressed as follows

$$\frac{[\text{C}^{13}\text{CS}]}{[^{13}\text{CCS}]} = \exp\left(\frac{\Delta E}{T}\right), \quad (4.29)$$

with T the temperature of the media; $\Delta E = \text{ZPE}(^{13}\text{CCS}) - \text{ZPE}(\text{C}^{13}\text{CS})$ the energy difference between the ZPE of the two isotopologues.

Recent observations by Fuentetaja et al. (in prep.) in the same region as Sakai et al. (2007) led to a revision of the $[\text{C}^{13}\text{CS}]/[^{13}\text{CCS}]$ ratio using the column densities provided in Table 4.1. The revised abundance ratio in TMC-1 (CP) is now 6.79, significantly larger than the prediction by Sakai et al. (2007). Since both isotopologues experience the same excitation conditions, the integrated intensity method used by Sakai et al. (2007) should be equivalent to the column density method, as discussed in Appendix A of Cernicharo et al. (2021) (which is also true for the observations in Fuentetaja et al. (in prep.)). Thus, the discrepancy between the two measurements can be attributed to the substantial advancements in observational facilities over the past 15 years.

If Equation (4.29) is employed to evaluate this abundance ratio in TMC-1 (CP) where the temperature is of 10 K, then

$$\frac{[\text{C}^{13}\text{CS}]}{[^{13}\text{CCS}]} = \frac{N(\text{C}^{13}\text{CS})}{N(^{13}\text{CCS})} = 6.79 \pm 0.7; \quad \frac{[\text{C}^{13}\text{CS}]}{[^{13}\text{CCS}]} = \exp\left(\frac{\Delta E}{T}\right) = 6.62. \quad (4.30)$$

The agreement between the abundance ratio predicted by the thermodynamics of CCS chemistry and the observed abundance ratio derived from the column densities of C^{13}CS and ^{13}CCS —using a sensitive survey and a robust LVG model based on the accurate rate coefficients computed in this thesis—suggests that the ^{13}C -anomaly of the CCS isotopologues has finally found a satisfying solution.

The Anomaly in Chemical Models

The most recent model attempting to reproduce the carbon fractionation in molecular clouds was conducted by Loison et al. (2020). In their work, they developed a new gas-grain model with updated ^{13}C fractionation reactions. This model considers Reaction (4.17) as the main formation path of CCS and accounts for the ^{13}C exchange reaction catalyzed by the H atom [Reaction (4.28)], assuming $\Delta E = 18$ K.

Their chemical model predicts the $[\text{C}^{13}\text{CS}]/[^{13}\text{CCS}]$ ratio to be less than a factor of two in TMC-1 (CP); however, the observed abundance ratio between the two isotopologues is approximately a factor of seven. They expect to correct their model by reducing the efficiency of the CCH + S pathway [Reaction (4.17)] while increasing that of the CH + CS [Reaction (4.19)] formation pathway. Indeed, as mentioned earlier, the anomaly in CCH should favor ^{13}CCS over C^{13}CS , which is the opposite behavior of what is observed. However, these adjustments may not be sufficient to account for the anomaly, given that the revised $[\text{C}^{13}\text{CS}]/[^{13}\text{CCS}]$ abundance ratio provided in this work is even larger than that of Sakai et al. (2007), which they attempted to reproduce.

To correct this behavior in chemical models, a few things could be tried. First, using the $\Delta E = 18.9$ K (instead of 18 K), as computed by Talbi (2018) might help improving the observed $[\text{C}^{13}\text{CS}]/[^{13}\text{CCS}]$ abundance ratio. Also, the formation path of CCS through Reaction (4.17) is probably only a minor production path of CCS and should be much less efficient than the exchange Reaction (4.28). Considering other catalyst for the interconversion (C or S atoms or cations) are not expected to solve this issue as, even if the reactions were found to be much faster (with C^+ or S^+ ions for example), these species are significantly less abundant than H atoms, and it has not been proven that they do not occur without an activation barrier, contrary to Reaction (4.28).

4.2.5 What About Other ^{13}C -Anomaly?

While CCS is a particular case with a notably large observed abundance ratio between its two ^{13}C -bearing isotopologues, other molecules also exhibit this ^{13}C -anomaly. These include CCH, C_3S , and $c\text{-C}_3\text{H}_2$, which present the largest anomaly.⁶ If the interconversion is the solution for all these molecules, then their observed abundance ratios and estimated values based on Equation (4.29), as represented in Figure 4.9, should match perfectly.

⁶ HC_3N and C_4H could also be added to the list, but the anomaly is less significant so they are excluded from this analysis.

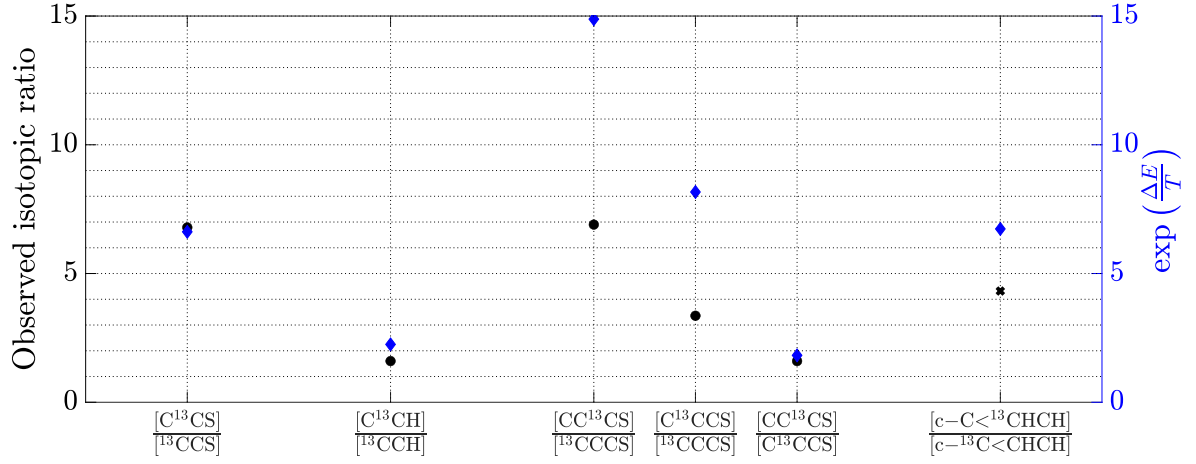


Figure 4.9: Abundance ratio of ^{13}C -based isotopologues of CCS, CCH, C_3S and $c\text{-C}_3\text{H}_2$ based on observations of TMC-1 (CP) (black circles) and L483 (black crosses) and ZPE energy differences (blue diamonds). The ΔE for CCH, CCS, C_3S and $c\text{-C}_3\text{H}_2$ have been taken from Sakai et al. (2010), Talbi (2018), Sakai et al. (2007), and Loison et al. (2020), respectively. The observed abundance ratio for CCH, CCS, C_3S , and $c\text{-C}_3\text{H}_2$ have been taken from Sakai et al. (2010), Fuentetaja et al. (in prep.), Sakai et al. (2013) and Agúndez et al. (2019). Observations made through TMC-1 (CP) are denoted by black circles, and through L483 are denoted by black crosses.

In Figure 4.9, the agreement between the observed isotopic ratio and the one evaluated from ZPE differences is good for some molecules, but large discrepancies can also be observed. For CCS, CCH, $c\text{-C}_3\text{H}_2$, and one of the isotopic ratio of C_3S , the agreement is good, so the interconversion could be the solution of the anomaly. However, for two C_3S isotopic ratio, the discrepancies indicates that the solution might be somewhere else.

CCH

In the work of Sakai et al. (2010), the abundance ratio of $[\text{C}^{13}\text{CH}]/[\text{C}^{13}\text{CCH}] = 1.6 \pm 0.4$ in TMC-1 (CP). To justify this anomaly, Sakai et al. (2010) proposed the interconversion solution as



with $\Delta E = 8.1 \text{ K}$ (Furuya et al., 2011).

The agreement between the observed abundance ratio reported by Sakai et al. (2010) and the calculated values using Equation (4.29) is quite good, with a deviation of approximately 40%. This suggests that exchange reactions could explain the ^{13}C anomaly in CCH.

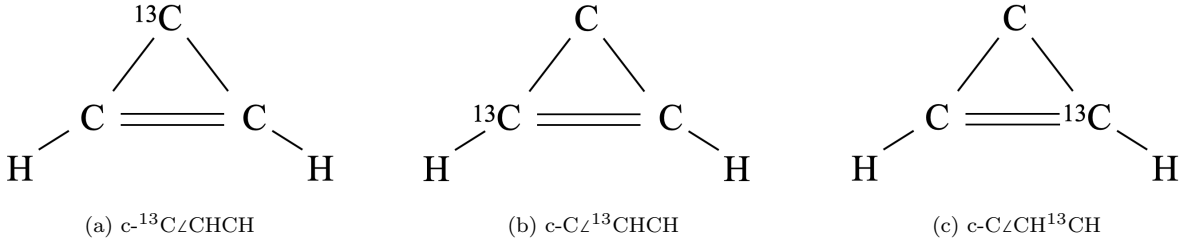


Figure 4.10: Representation of the isotopologues of $c\text{-C}_3\text{H}_2$, noted $c\text{-C}\angle\text{CHCH}$, with $\text{C}\angle$ the carbon without hydrogen atoms, namely (a) $c\text{-}^{13}\text{C}\angle\text{CHCH}$ (b) $c\text{-C}\angle^{13}\text{CHCH}$, and (c) $c\text{-C}\angle\text{CH}^{13}\text{CH}$. Note that (b) and (c) are equivalent, so only $c\text{-C}\angle^{13}\text{CHCH}$ is used in the text.

The observed abundance ratio provided by Sakai et al. (2010) was evaluated based on the assumption that ^{13}CCH and C^{13}CH were undergoing the same excitation conditions. However, new hyperfine-structure resolved rate coefficients for ^{13}CCH and C^{13}CH in collision with $p\text{-H}_2$ have been produced by Pirlo Jankowiak et al. (2023b), revealing a global deviation of about 30% in the rate coefficients between the two isotopologues. Therefore, the abundance ratio between these isotopologues is expected to be revised if these new data are employed in reliable radiative transfer models. This could lead to either improved or worsened agreement between the observed abundance ratio and the one derived from ZPE differences, making it difficult to draw strong conclusions about the origin of the ^{13}C anomaly in CCH.

$c\text{-C}_3\text{H}_2$

For $c\text{-C}_3\text{H}_2$, the three ^{13}C isotopologues are represented in Figure 4.10 and will be noted $c\text{-C}\angle\text{CHCH}$, where the carbon without hydrogen atom attached to it is indicated as $\text{C}\angle$. The two $c\text{-C}\angle^{13}\text{CHCH}$ and $c\text{-C}\angle\text{CH}^{13}\text{CH}$ isotopologues are strictly equivalent. Therefore, the $[c\text{-}^{13}\text{C}\angle\text{CHCH}]/[c\text{-C}\angle^{13}\text{CHCH}]$ obtained from Equation (4.29) was divided by two to account for the fact that the interconversion can lead to both isotopologues in an equivalent manner.

For this molecule, the observed abundance ratio in L483 $[c\text{-}^{13}\text{C}\angle\text{CHCH}]/[c\text{-C}\angle^{13}\text{CHCH}] = 4.23 \pm 0.1$ according to Agúndez et al. (2019).

In the work of Loison et al. (2020), they suggest that the ^{13}C -anomaly could be explained by an interconversion reaction occurring as



with $\Delta E = 26$ K (Loison et al., 2020).

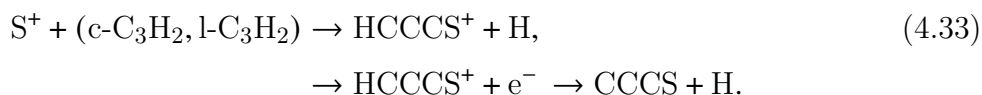
The value of the $[c\text{-C}\angle^{13}\text{CHCH}]/[c\text{-}^{13}\text{C}\angle\text{CHCH}]$ abundance ratio calculated from Equation (4.29) reproduces the observed ratio by slightly more than a factor 1.5. The difference between the observed value and the one inferred from ZPE differences is moderate, and it is possible that a revision of the isotopologue abundances using more sophisticated approaches (such as LVG with accurate collisional data) would yield to an improved agreement between the two values. Therefore, the interconversion reaction could explain the ^{13}C anomaly in $c\text{-C}_3\text{H}_2$, suggesting that the chemistry of $c\text{-C}_3\text{H}_2$ might be governed by thermodynamics. However, there is currently no evidence that Reaction (4.32) is barrierless.

C_3S

The observed abundance ratio for C_3S isotopologues have been taken from observations of Sakai et al. (2013), who detected all three isotopologues, and of Fuentetaja et al. (in prep.), which observed $^{13}\text{CCCS}$ and C^{13}CCS isotopologues only. Indeed, the CC^{13}CS isotopologue could not be detected by Fuentetaja et al. (in prep.) because of the near coincidence between the rotational constant of C_3S and CC^{13}CS . Thus, their transitions differ by less than 0.1 MHz, which is not resolved in the QUIJOTE data.

The $[\text{CC}^{13}\text{CCS}]/[\text{C}^{13}\text{CCS}]$ abundance ratio measured by Sakai et al. (2013) agrees well with the abundance ratio computed using Equation (4.29). However, the two other abundance ratio $[\text{CC}^{13}\text{CS}]/[^{13}\text{CCCS}]$, measured by Sakai et al. (2013), and $[\text{C}^{13}\text{CCS}]/[^{13}\text{CCCS}]$ measured by Fuentetaja et al. (in prep.), strongly disagree with the predictions based on the ZPE differences.

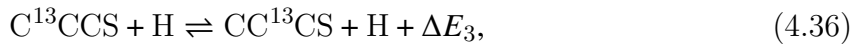
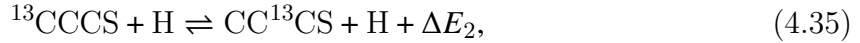
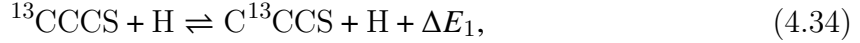
An explanation for the ^{13}C anomaly in C_3S proposed by Sakai et al. (2013) is that the anomaly in C_3 would come from the anomaly in $c\text{-C}_3\text{H}_2$ as they are chemically connected Reaction (4.33) (Millar & Herbst, 1990)



The S^+ would be more likely to attach the terminal carbon (the one without hydrogen). Therefore, if $c\text{-}^{13}\text{C}\angle\text{CHCH}$ is diluted compared to $c\text{-C}\angle^{13}\text{CHCH}$, then the CC^{13}CS isotopologues should be the less abundant, which is the opposite of what is observed. In addition, Reaction (4.33) should lead to an equivalent ratio of CC^{13}CS and C^{13}CCS as

the two non-terminal carbons (the ones with an hydrogen atom) are equivalent, which does not corresponds to observations.

Another possible explanation is that the position of the ^{13}C on the carbon chain would be exchange through interconversion reaction catalyzed by hydrogen atoms as suggested by Sakai et al. (2013)



with $\Delta E_1 = 21$ K, $\Delta E_2 = 27$ K, $\Delta E_3 = 6$ K, computed using the CCSD(T)-F12b/aug-cc-pVTZ levels of theory by Sakai et al. (2013).

There is no evidence that these interconversion paths occur without a barrier, or that they are all equivalent. Indeed, the interconversion could differ among the isotopologues: Reaction (4.36) might be barrierless, while Reactions (4.34) and (4.35) could present an activation barrier. It would explain why the $[\text{CC}^{13}\text{CCS}]/[\text{C}^{13}\text{CCS}]$ abundance ratio measured by Sakai et al. (2013) agrees well with the abundance ratio computed using Equation (4.29), but not $[\text{CC}^{13}\text{CCS}]/[^{13}\text{CCCS}]$ nor $[\text{CC}^{13}\text{CCS}]/[^{13}\text{CCCS}]$.

Furthermore, the abundance ratio obtained by Sakai et al. (2013) is based on the assumption that all isotopologues undergo the same excitation conditions, and thus could suffer from some inaccuracies. The $[\text{C}^{13}\text{CCS}]/[^{13}\text{CCCS}]$ from Fuentetaja et al. (in prep.) was evaluated based on the analysis of CCCS isotopologues column densities using the LVG approach based on the collisional rate coefficients of $\text{HC}_3\text{N-p-H}_2$ provided by Faure et al. (2016b) as the collisional data available for CCCS-He (Sahnoun et al., 2020) were not covering enough levels of C_3S . Therefore, some uncertainties remain in the observed abundance ratio derived using the LVG approach. However, it is not expected to revised the abundance ratio by over a factor of two, which would be necessary for the hypothesis of the interconversion driving ^{13}C anomaly of C_3S to hold.

Yet the ^{13}C -anomaly has been found in more and more molecules. The ^{13}C -anomaly of CCS is the first and the largest to date. Smaller abundance ratio have been observed, such as for CCH, C_3S , and it has also been suggested to be observed for longer carbon-chains like HC_nN ($n = 3, 5, 7$) and C_4H , but to a less extend. These anomaly represents

great clues on chemical models to constrain the chemistry of these molecules. However, they are not well understood. In this study, we propose a plausible solution for the ^{13}C anomaly in CCS.

Currently, the exchange reactions seem to work for molecules where the carbon chain is composed of only two carbons, like CCS or CCH, or for molecules with only two ^{13}C configurations, like *c*- C_3H_2 . For C_3S , however, these exchange reactions are not fully convincing, as they are insufficient to explain the observed ^{13}C -anomaly. Therefore, it is suggested that the ^{13}C -anomaly in C_3S more likely originates from the molecule's formation pathway. Further investigation would require a re-evaluation of the abundance ratios of these molecules by producing accurate state-to-state rate coefficients for all isotopologues and using them to reinterpret observations.

4.3 Cometary Applications: CS in Comae

In this section, the collisional data computed in Section 3.2 are analyzed in the context of modeling the emission spectra of CS in comae. First, the impact of the new sets of rate coefficients on the excitation conditions of CS in comets is investigated. Second, the differences between the sets of rate coefficients produced for CS and those for cometary applications in the literature are discussed. Finally, the sensitivity of radiative transfer models to these sets of rate coefficients is examined.

4.3.1 Impact of the Gas Composition

In this work, rate coefficients for CS in collisions with both CO and H₂O have been determined, enabling the study of CS emission spectra from cometary comae at various heliocentric distances. Comae are often composed of a mixture of CO and H₂O in different proportions, depending on the comet and its heliocentric distance. The objective of this section is to discuss how gas composition affects the population of CS energy levels. It begins with a comparison of CS-CO and CS-H₂O rate coefficients, followed by an evaluation of the populations of CS energy levels as a function of gas density, assuming different CO and H₂O mixtures in the coma.

The Rate Coefficients of CS for Cometary Applications

To assess whether CS emission spectra are sensitive to the gas composition, and whether both CS-CO and CS-H₂O rate coefficients are necessary for accurately modeling CS emission spectra in comets, a comparison of the thermalized sets of rate coefficients is presented in Figure 4.11.

From Figure 4.11a, where the thermalized rate coefficients for CS-CO are compared to those for CS-p-H₂O, it is obvious that the excitation of CS is consistently more efficient when induced by collisions with p-H₂O than with CO. The rate coefficients show a reasonably sparse distribution centered around the line $y = \frac{1}{2}x$, indicating that the data for CS-p-H₂O are approximately two times larger at both temperatures.

This trend is also observed when comparing the thermalized rate coefficients for CS-CO and CS-o-H₂O in Figure 4.11b. However, the distribution around the $y = \frac{1}{2}x$ axis is much narrower, suggesting that multiplying the CS-CO thermalized rate coefficients by a systematic factor of two could provide a good approximation for estimating the CS-o-H₂O data.

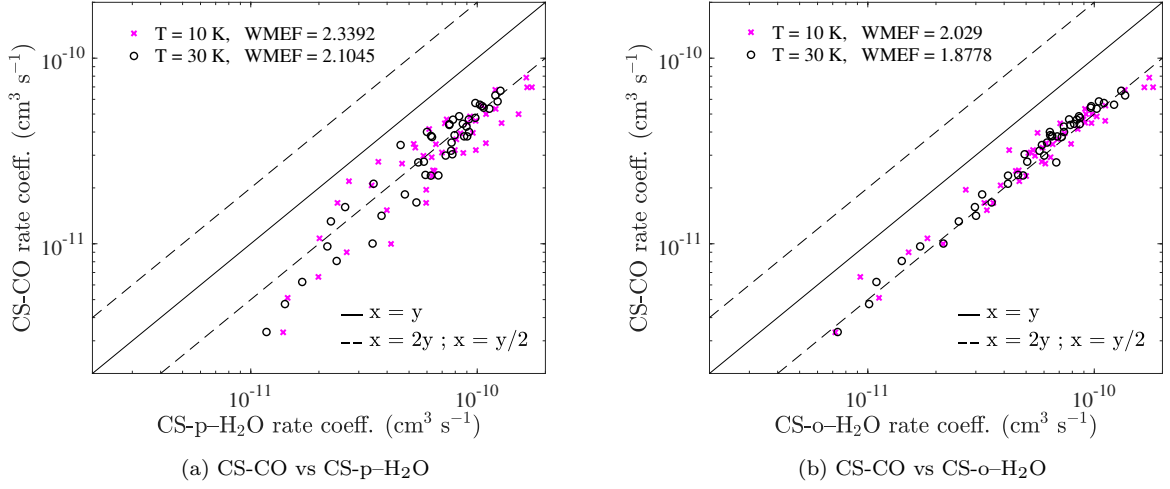


Figure 4.11: Comparison between the rate coefficients (in $\text{cm}^3 \text{s}^{-1}$) of CS in collision with H₂O (x-axis) (p-H₂O in the left panel and o-H₂O in the right panel) and CO (y-axes) at 10 K (magenta cross) and 30 K (black circles).

A common method for approximating the rate coefficients of target molecule X in collision with p-H₂ from X -He rate coefficients involves a proportional law based on the reduced mass of the systems, as shown in Equation (4.14) (Schöier et al., 2005). If this relation is adapted to estimate CS-p-H₂O or CS-o-H₂O rate coefficients from CS-CO data (or vice versa), it would be expressed as

$$k_{X-o/p-H_2O} \simeq \left(\frac{\mu_{X-CO}}{\mu_{X-o/p-H_2O}} \right)^{1/2} \times k_{X-CO}, \quad (4.37)$$

with X the target molecule, X -CO the sets of rate coefficients with CO as a projectile, and X -o/p-H₂O the sets of rate coefficients with o/p-H₂O as a projectile; μ_{X-CO} and $\mu_{X-o/p-H_2O}$ are the reduced mass of the two collisional systems.

However, the square root of the reduced mass ratio is 1.16, which is insufficient to reproduce the observed systematic deviation between the rate coefficients for CS-CO and those for CS-o/p-H₂O. Hence, this approximation is not appropriate to infer CS-CO rate coefficients based on CS-o/p-H₂O (and reciprocally).

The Population of CS Energy Levels

To assess the impact of discrepancies between the two sets of CS-CO and CS-H₂O rate coefficients on the population of CS energy levels, the coupled radiative transfer and SE equations were solved using the LVG approach implemented in the RADEX code (van der

Tak et al., 2007).

In this analysis, the volume densities are considered for pure CO, pure H₂O, and two CO:H₂O mixtures with ratios of 0.7:0.3 and 0.3:0.7.

The volume density of the gas n_{gas} was chosen according to the density range of comae $\in [10^{-3}, 10^{13}] \text{ cm}^{-3}$, which corresponds to nucleocentric distance $r \in [1; 10^6] \text{ km}$. As the column density of CS was not directly available in the literature, it was derived from the column density of CO. In their work, Lupu et al. (2007) estimated the column density of CO at $1 \times 10^{14} \text{ cm}^{-2}$ at $r \simeq 1000 \text{ km}$ for a CO abundance of 10%. As CS is typically 0.03 to 0.2% of the gas composition (Biver et al., 2023), the column density of CS was set at $1 \times 10^{12} \text{ cm}^{-2}$. The linewidth $\Delta\nu = 2\nu_{\text{exp}}$, with $\nu_{\text{exp}} = 0.51$ taken from Roth et al. (2021a) assuming an isotropic outgassing.

The background radiation field have been taken as the CMB combined with the solar radiation field. The latter was considered as a diluted blackbody of 5770 K with the dilution factor $W = \Omega_{\text{S}}/4\pi$, where Ω_{S} is the solid angle of the Sun at an heliocentric distance r_H of 1 au. Its value was set at $\simeq 6.79 \times 10^{-5} \text{ sr}$ (Faure et al., 2020). The Einstein coefficients have been taken from the CDMS database (Müller et al., 2001; Müller et al., 2005; Endres et al., 2016), and the collisional rate coefficients for CS-CO and CS-H₂O are the one computed in Section 3.2. They have been thermalized using Equation (3.40), with an o/p ratio equal to three for CS-H₂O rate coefficients.

Figure 4.12 shows the evolution of the population of the lowest and most populated CS energy levels ($j_{\text{CS}} \leq 5$) as a function of gas density (n_{gas}) for different gas compositions. Although CO₂ should ideally be included, as it is one of the main constituents of cometary comae, no rate coefficients are currently available for CS in collisions with CO₂. Therefore, this analysis only considers CO and H₂O.

The observed effects of gas composition are consistent across both temperatures, so the following conclusions apply to both 10 K and 30 K.

First, the gas composition significantly affects the population of CS energy levels in the non-LTE regime. A higher proportion of H₂O in the gas causes the LTE regime to be reached at lower densities. Conversely, a higher concentration of CO in the gas shifts the non-LTE regime to higher densities. Therefore, LTE conditions for CS will be maintained farther from the nucleus in H₂O-dominated comae, compared to CO-dominated comae. This effect can be attributed to the fact that the rate coefficients for the CS-H₂O system are approximately a factor of two higher than those for the CS-CO system, as shown in

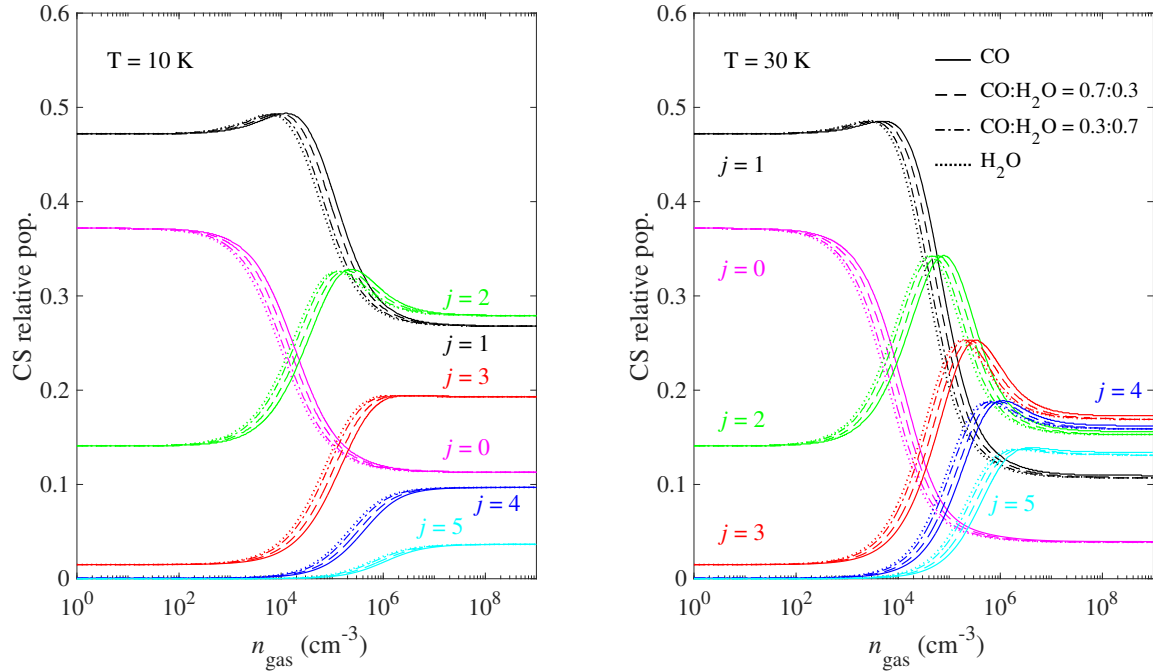


Figure 4.12: Relative population of CS energy levels as a function of the density of gas (in cm^{-3}) for different CO:H₂O composition of the gas at 10 K (left panel), and 30 K (right panel). The solid lines represent a CO:H₂O gas with a 1:0 ratio, the dashed lines represent a 70:30 ratio, the dashed-dotted lines represents a 30:70 ratio, and the dotted lines a 0:1 ratio.

Figure 4.11. As the collisions are more efficient when induced by the H₂O projectile, the LTE domain is reached at lower gas density.

It is important to note that different mixtures can be distinguished; for example, a CO-H₂O mixture with a ratio of 0.3:0.7 will affect the CS populations differently than a 0.7:0.3 ratio. Consequently, the rate coefficients could be considered as a potential tool to help constrain the gas composition in the coma.

The impact of gas composition on CO excitation has been discussed in terms of the excitation of CO across a density range of 10^2 - 10^7 cm^{-3} in Żółtowski et al. (2023), but the effects were found to be relatively small, particularly at low temperatures. For CS, however, differences can be observed even at low temperatures on the population of energy levels, and for all different gas mixture. This suggests that the sensitivity of the modeling to gas composition may vary significantly from one molecule to another. Therefore, it should be tested on additional cometary molecules by producing HCN-CO and

HF-CO collisional data to complement the existing sets of HCN-H₂O and HF-H₂O rate coefficients.

Given the significant effects of gas composition, it is important to employ rate coefficients for the CS with both CO and H₂O as projectiles to model CS emission spectra. Moreover, considering both colliders in various reliable proportions is likely necessary to derive accurate physical conditions in the coma.

The rate coefficients computed for CS-CO and CS-H₂O in this study can be employed in the modeling of emission spectra of CS in comae for various temperature and gas compositions. In this thesis work, sensitive tools for the study of CS in comets have been provided, and it is expected to lead to the accurate estimation of CS production rates in future cometary observations.

4.3.2 Sensitivity of Rate Coefficients to the Colliders

Due to the lack of state-to-state or thermalized rate coefficients for studying comae, it is important to evaluate the sensitivity of these data sets to the colliders.

Currently, only seven systems have been studied for cometary applications, including two systems computed during this work. Five of these systems involve H₂O as one of the collisional partners: HCN-H₂O (Dubernet & Quintas-Sánchez, 2019), CO-H₂O (Loreau et al., 2018a; Faure et al., 2020), HF-H₂O (Loreau et al., 2022), H₂O-H₂O (Mandal & Babikov, 2023b; Mandal & Babikov, 2023a),⁷ and finally, the CS-H₂O system studied in this work. The remaining two systems consider CO as the projectile: CO-CO (Żółtowski et al., 2022), and CS-CO, also studied in this work.

In cometary studies, collisional rate coefficients for $X\text{-H}_2$ (e.g. CS-H₂), originally computed for ISM studies, are sometimes used as a substitute for $X\text{-CO}$ and/or $X\text{-H}_2\text{O}$, where X represents the observed molecule in the coma. This approach allows molecular spectra to be modeled using accurate excitation models, albeit with approximate rate coefficients (Cordiner et al., 2023). Another common approximation, sometimes employed in ISM studies (and potentially applicable to cometary studies), is to use collisional data for a similar target molecule (Fuente et al., 1990; Fuentetaja et al., in prep.).

Since cometary data are rare because challenging to compute, evaluating the sensitivity of rate coefficients with respect to colliders is crucial. Hence, it is important to

⁷This system will not be discussed here, as the target molecule H₂O does not have the same internal structure as the others, making comparison irrelevant.

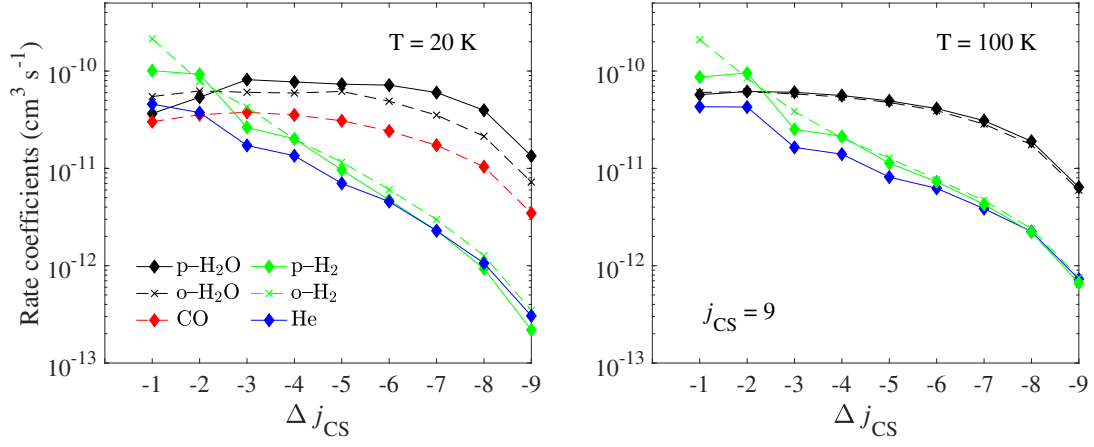


Figure 4.13: Comparison between the de-excitation rate coefficients (in $\text{cm}^3 \text{s}^{-1}$) computed for CS with different projectiles as a function of $\Delta j_{\text{CS}} = j'_{\text{CS}} - j_{\text{CS}}$ from $j_{\text{CS}} = 9$ for $T = 20 \text{ K}$ (left panel), and 100 K (right panel).

discuss whether these sets of rate coefficients differ significantly (1) from interstellar rate coefficients and (2) from each other.

In the following, only thermalized rate coefficients, computed based on Equation (3.40), will be discussed, as these are the ones most commonly employed in radiative transfer models.

Cometary vs Interstellar Data

In this work, the sets of rate coefficients for CS in collisions with CO, p-H₂O, and o-H₂O have been produced. These data complement the existing sets of rate coefficients for CS-He (Lique et al., 2006) and CS-p-H₂ and CS-o-H₂ (Denis-Alpizar et al., 2018). In these previous studies, the rate coefficients were computed using the Close-Coupling (hereafter, CC) approach. To investigate the relative behavior and magnitude of these different sets of rate coefficients, the de-excitation rate coefficients from CS ($j_{\text{CS}} = 9$) induced by collisions with these projectiles are compared in Figure 4.13 at both 20 K and 100 K.

The projectiles considered in the sets of rate coefficients can be divided into two categories: light projectiles, useful for interstellar studies (He, p-H₂, o-H₂) and heavy projectiles, useful for cometary studies (CO, p-H₂O, o-H₂O).

For small $|\Delta j_{\text{CS}}|$, the CS-He and CS-o/p-H₂ rate coefficients present significant dif-

ferences, but as $|\Delta j_{\text{CS}}|$ increases, their rate coefficients tend to become more and more similar, until they become nearly identical for $|\Delta j_{\text{CS}}| \geq 5$. The values of the rate coefficients with light projectiles decrease rapidly with increasing $|\Delta j_{\text{CS}}|$.

The magnitude of the rate coefficients involving heavy projectiles remain relatively consistent across different values of Δj_{CS} . Additionally, the rate coefficients do not systematically decrease with increasing $|\Delta j_{\text{CS}}|$, particularly for CS-CO, where the rate coefficients for $|\Delta j_{\text{CS}}| = 3$ exceed those for $|\Delta j_{\text{CS}}| = 1$ or 2. At 20 K, the behavior of the rate coefficients for CO and H₂O projectiles is very similar; however, the CO rate coefficients exhibit a lower magnitude. This has already been observed in Figure 4.11, where the rate coefficients for the CS-CO have been found approximately lower by a factor of two compared to CS-p-H₂O and CS-o-H₂O.

The differences in the sets of rate coefficients, particularly their magnitudes, can be attributed to the strength of the electronic interaction between CS and its projectiles. The stronger is the interaction, the deeper is potential well, resulting in larger rate coefficients. The deepest well is for the CS-H₂O complex, with a well depth of approximately 1,172 cm⁻¹, followed by CS-CO with a well depth of 236 cm⁻¹, CS-H₂ with a well depth of 173 cm⁻¹ (Denis-Alpizar et al., 2012), and finally, CS-He with a well depth of 22 cm⁻¹ (Lique et al., 2006). This trend in PES depths corresponds to the decreasing magnitude of the rate coefficients, with CS-o/p-H₂O data exhibiting the largest coefficients, followed by CS-CO, CS-o/p-H₂, and finally, CS-He data.

Since the rate coefficients for light projectiles exhibit different behavior compared to those for heavy projectiles, using a systematic factor to infer the rate coefficients for heavy projectiles (CO, p-H₂O, o-H₂O) from those for light projectiles (p-H₂, o-H₂, He) is unlikely to yield accurate results. This approach is expected to overestimate the rate coefficients for dominant transitions while underestimating them for weaker transitions.

To test the validity of the assumption of using the CS-H₂ collisional data to mimic CS-CO and CS-H₂O data, the sets of rate coefficients are systematically compared in Figure 4.14, and Figure 4.15.

In Figure 4.14, the thermalized rate coefficients of CS-CO and CS-p-H₂ and CS-o-H₂ collisional data are systematically compared at 10 and 20 K.

Significant deviations are observed between the sets of rate coefficients for CS in collisions with CO and o/p-H₂. The dominant transitions tend to be larger when H₂ is the

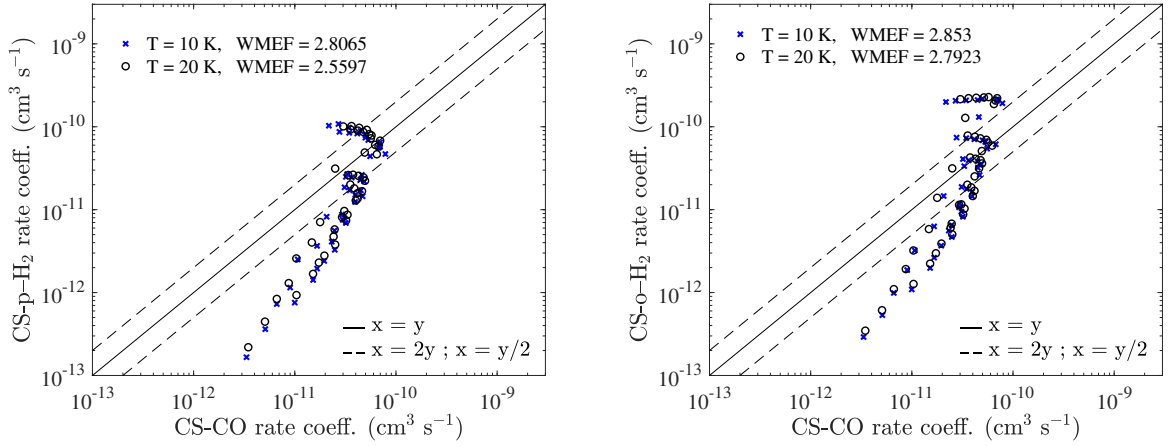


Figure 4.14: Comparison between the rate coefficients (in $\text{cm}^3 \text{s}^{-1}$) of CS in collision with CO (x-axes) and H_2 (y-axis) (p- H_2 in the left panel and o- H_2 in the right panel) at 10 K (blue crosses) and 20 K (black circles).

projectile, whereas the opposite trend is seen for weaker transitions. As illustrated Figure 4.13, the rate coefficients for CS-o/p- H_2 vary significantly with the quantum numbers, while the CS-CO data tend to vary weakly with quantum numbers. The global deviation indicated by the WMEF is approximately 2.8 at 10 K for both o/p- H_2 , slightly decreasing at 20 K to a factor 2.6 for p- H_2 , but remaining nearly constant for o- H_2 . This substantial deviation between the two sets of data suggests that using CS-o/p- H_2 rate coefficients to infer CS-CO coefficients could lead to significant inaccuracies in the modeling CS emission spectra in comae.

In Figure 4.15, the thermalized rate coefficients for CS in collision with o/p- H_2O are also compared to those computed by Denis-Alpizar et al. (2018) for the CS-o/p- H_2 systems, at 20 K and 100 K.

The deviations observed between the two sets of rate coefficients considering H_2O and H_2 as a projectile are quite significant. As for the comparison between CS-CO and CS-o/p- H_2 , the dominant transitions tend to be larger for CS-o/p- H_2 , but the weaker transitions tend to be stronger for CS-o/p- H_2O . Indeed, it was observed that for light projectile such as H_2 , the rate coefficients were rapidly decreasing with increasing Δj_{CS} , but stayed relatively stable for heavy colliders such as o/p- H_2O .

The deviations between the sets of rate coefficients are even more pronounced than

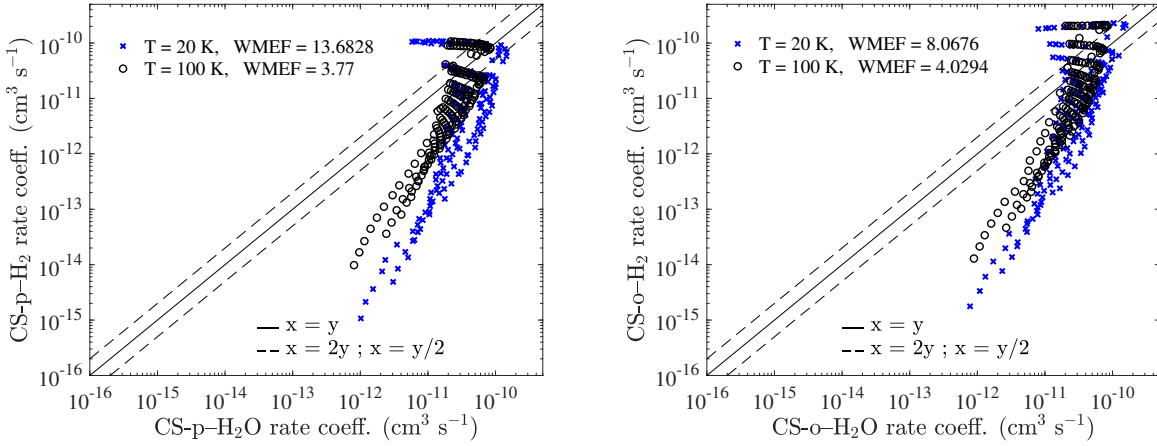


Figure 4.15: Comparison between the rate coefficients (in $\text{cm}^3 \text{s}^{-1}$) of CS in collision with H_2O (x-axes) and H_2 (y-axis) (p- H_2 /p- H_2O in the left panel and o- H_2 /o- H_2O in the right panel) at 10 K (blue crosses) and 20 K (black circles).

those observed in the comparison of CS-CO and CS-H₂ data. This trend aligns with the observations in Figure 4.13. This was expected from their PES, where the well depth differ more significantly for CS-H₂O and CS-H₂ (1,172 cm^{-1} vs 173 cm^{-1}) compared to CS-CO and CS-H₂ (236 cm^{-1} vs 173 cm^{-1}). In contrast to the comparison with CS-CO, the agreement between the two sets of data improves significantly with temperature. At 20 K, a global deviation indicated by the WMEF of about 13.7 for p- H_2O vs p- H_2 , and of 8.07 for o- H_2O vs o- H_2 is observed. These deviations decrease to approximately a factor 4 for both o/p- H_2O vs o/p- H_2 at 100 K. This improvement can be attributed to the fact that, at higher temperatures, the rate coefficients involving H_2 as a collider tend to vary less with quantum numbers, thus reducing the deviation.

However, it is obvious that the sets of o/p- H_2 rate coefficients would not be a reliable approximation for inferring CS-o/p- H_2O rate coefficients. Relying on these data instead of the appropriate ones is expected to lead to significant inaccuracies in the derived physical conditions when modeling CS emission spectra in comae.

For CS, it appears that the interstellar rate coefficients CS-H₂ and CS-He would not be a good approximation for both the CS-CO and CS-H₂O rate coefficients. However, collisional data with H_2 as the projectile are often used when data with CO or H_2O are unavailable (Cordiner et al., 2023). This analysis highlights that more accurate data sets are needed to reliably model the spectra of molecular species in cometary atmospheres.

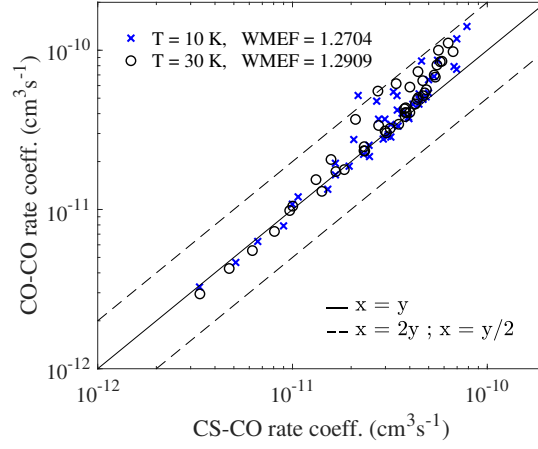


Figure 4.16: Comparison between the thermalized rate coefficients (in $\text{cm}^3 \text{s}^{-1}$) of CS (x-axes) and CO (y-axes) in collision with CO at 10 K (blue crosses) and 30 K (black circles).

Impact of the Target

Now that it has been highlighted that interstellar data cannot be safely employed to model the emission spectra of CS in comae, a discussion of the differences and similarities among the existing sets of rate coefficients for cometary studies—involving heavy projectiles like CO and H_2O —would be instructive. Therefore, the sets of collisional rate coefficients with the same projectile (CO or H_2O) but different target molecules (CS, CO, HCN, HF) are compared.

The only other collisional system of interest for cometary studies where CO has been considered as a projectile (and not as a target) is the CO-CO collisional system by Żółtowski et al. (2022) and Żółtowski (2023). The scattering calculations were performed using the Coupled-States approximation and were based on the $(\text{CO})_2$ PES of Vissers et al. (2003). In their work, they produced rate coefficients for the first 11 energy levels of both CO molecules at temperatures ranging from 5 to 100 K. In our work, the CS-CO rate coefficients were computed for the 5 - 30 K temperature range, and included the first 10 levels of CS and the first six levels of CO. Thus, the two sets of rate coefficients are compared for transitions with $j_{\text{target}} \leq 9$ and $j_{\text{projectile}} \leq 5$. The CO-CO rate coefficients were provided by the authors.

The thermalized rate coefficients, calculated according to Equation (3.40), are shown in Figure 4.16.

In Figure 4.16, the agreement between the thermalized rate coefficients of both species

is relatively good, with all transitions being reproduced at better than a factor of two. The CO-CO rate coefficients are generally higher than those for CS-CO at both temperatures, particularly for dominant transitions, contrary to expectations based on their dipole moments. Indeed, since the dipole moment of CS is larger and its potential well is deeper when interacting with CO, this would typically suggest stronger rate coefficients for CS-CO. The unexpected behavior likely comes from the homo-molecular nature of the CO-CO system, which leads to resonant effects that enhance (de)excitation probabilities, leading to higher rate coefficients for many transitions. The differences between the data sets are however relatively low, with the WMEF showing a deviation of less than a factor 1.3 at both temperatures. Nevertheless, it is important to note that both sets of rate coefficients were computed using approximate approaches (Coupled-States and SACM for the CO-CO and CS-CO systems, respectively), so the "real" deviations could vary.

The relatively small differences between the two sets of thermalized rate coefficients are not expected to influence radiative transfer models, but it will be checked in Section 4.3.3. Therefore, using CO-CO rate coefficients as an initial approximation for CS-CO rate coefficients appears to be a reasonable approach.

The rate coefficients computed for CS with the p-H₂O and o-H₂O projectiles in this work are now compared to rate coefficients using the p-H₂O and o-H₂O projectiles, but for different target molecules, such as CO, HCN, and HF.

Rate coefficients for the CO-p-/o-H₂O systems were produced by Faure et al. (2020) for temperatures from 5 to 100 K. The rate coefficients were computed with the SACM approach based on the PES of Kalugina et al. (2018). They include CO levels up to $j_{CO} = 10$, accounting for the first eight levels of both p-H₂O and o-H₂O (up to $j_{k_a k_c} = 3_{k_a k_c}$). These thermalized rate coefficients, taken from the EMAA database (Faure et al., 2021), are compared with those of CS-p-H₂O and CS-o-H₂O in Figure 4.17.

The rate coefficients of CS are generally higher than those of CO, which was expected since the dipole moment of CS is larger than that of CO. As a result of this difference between their dipole moment, the potential well of the CS-H₂O PES is much deeper than the one of the CO-H₂O PES (1,172 cm⁻¹ against 646 cm⁻¹), making the collisional excitation of CS more efficient than that of CO when induced by H₂O. This explains the overall trend seen in the data sets for both o- and p-H₂O at 50 K and 100 K.

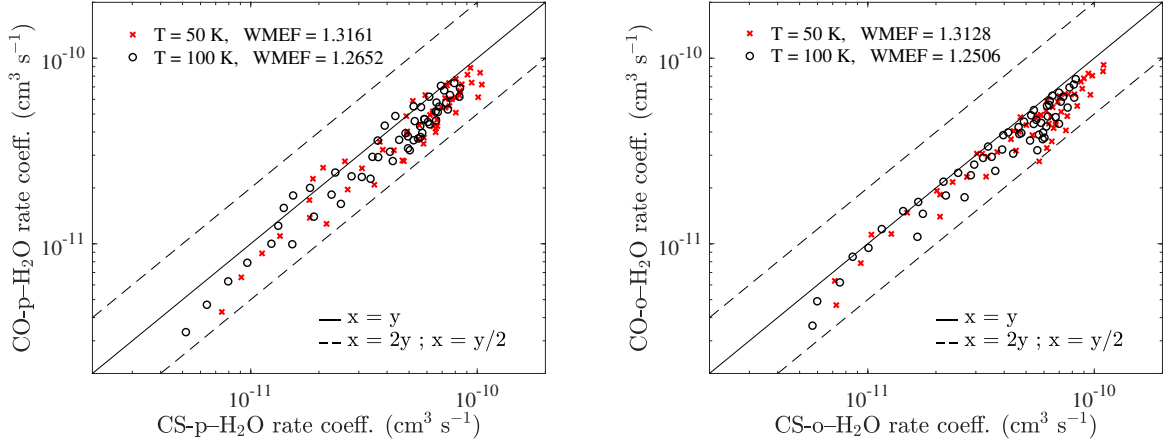


Figure 4.17: Comparison between the rate coefficients (in $\text{cm}^3 \text{s}^{-1}$) of CS (x-axes) and CO (y-axes) in collision with thermalized p-H₂O (left panel) and o-H₂O (right panel) at 50 K (red crosses) and 100 K (black circles).

The overall deviation between the thermalized rate coefficients for CO and CS in collisions with p-/o-H₂O is however moderate, and less than a factor of two for all transitions is observed. Deviations are slightly larger for dominant transitions, but tend to decrease as the temperature increases. The deviation is similar for both p-H₂O and o-H₂O which is not surprising as these sets of data are usually similar. The WMEF is around 1.3 at both 50 K and 100 K, showing slight improvement at higher temperatures, as seen with the CS-CO and CO-CO data. The global deviation between CO-H₂O and CS-H₂O data is comparable to that observed in the CO-CO and CS-CO comparison.

The good agreement between CO and CS data (with both CO and H₂O projectiles) can be explained by the fact that both species are diatomic, and have the same electronic structure. This suggests that using CO data as a first approximation for CS data is a reasonable approach (and vice-versa).

The rate coefficients of the HCN-p-H₂O system have been computed by Dubernet & Quintas-Sánchez (2019) for temperature ranging from 5 K to 150 K. This set of rate coefficients have been computed using the coupled-states approximation based on the HCN-H₂O PES of Quintas-Sánchez & Dubernet (2017). The data include transitions between the first eight levels of HCN ($j_{\text{HCN}} \leq 7$) and the p-H₂O levels up to $j_{k_a k_c} = 4_{k_a k_c}$. The thermalized rate coefficients for HCN-p-H₂O data were taken from the BASECOL database (Dubernet et al., 2024), and are compared to CS-p-H₂O data in Figure 4.18.

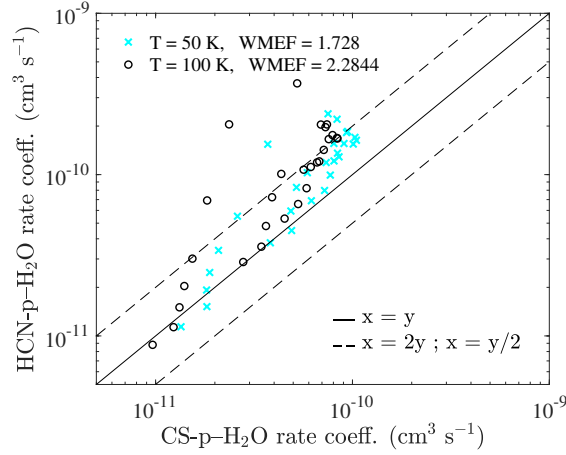


Figure 4.18: Comparison between the rate coefficients (in $\text{cm}^3 \text{s}^{-1}$) of CS (x-axes) and HCN (y-axes) in collision with thermalized p-H₂O at 50 K (cyan crosses) and 100 K (black circles).

Significant deviations are observed between the thermalized rate coefficients for the HCN-p-H₂O and CS-p-H₂O systems. Dominant transitions show deviations exceeding a factor of two, and weaker transitions are more accurately reproduced. The HCN rate coefficients are generally larger than those of CS. It was expected from their relative dipole moments ($\mu_{\text{HCN}} = 2.99 \text{ D} > \mu_{\text{CS}} = 1.98 \text{ D}$)¹, which leads to a deeper potential for the HCN-H₂O PES, compared to the one of CS-H₂O (1,814 cm^{-1} vs. 1,172 cm^{-1}). The deviations increase significantly with temperature, with a WMEF of 1.73 at 50 K and 2.28 at 100 K. It is known that the accuracy of the SACM approach decreases with increasing temperature. Nevertheless, such an increase for still relatively low temperature is surprising and may not be entirely due to the use of the SACM approach. This behavior could also be justified by the partial convergence of the HCN-p-H₂O cross sections at higher collisional energies, which are expected to have more impact in the rate coefficients at higher temperature.

In their work, Dubernet & Quintas-Sánchez (2019) achieved only partial convergence of the rate coefficients due to numerical limitations. They computed cross sections with a rotational basis that includes $j_{\text{HCN}} \leq 15$, and $j_{\text{p-H}_2\text{O}} \leq 4$. However, Żółtowski (2023) attempted to converge cross sections for the HCN-p-H₂O system with the CC approach,⁸ and did not succeed with $j_{\text{HCN}} \leq 40$, and $j_{\text{p-H}_2\text{O}} \leq 8$. It is thus surprising that Dubernet & Quintas-Sánchez (2019) concluded that the accuracy on the rate coefficients was better

⁸The rotational basis to converge cross sections is expected to be similar with both the CC approach and the Coupled-States approximation.

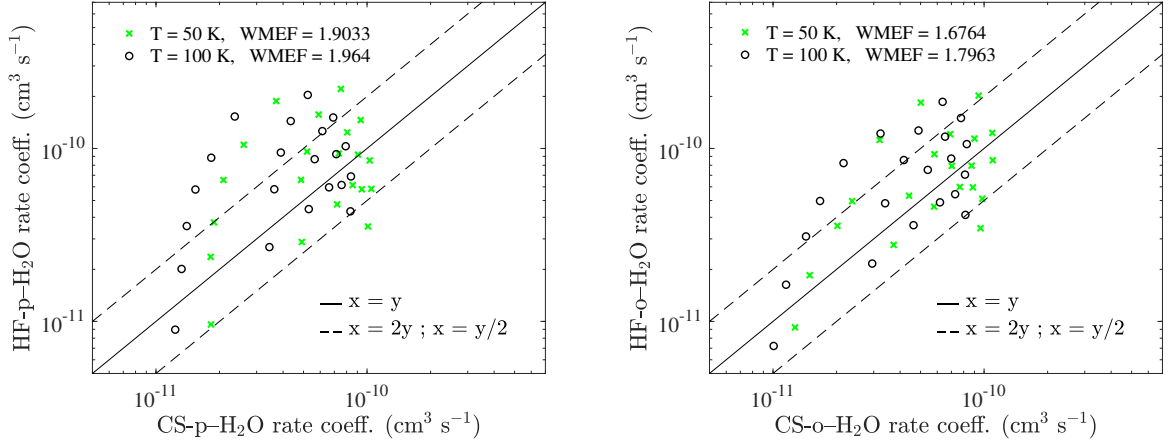


Figure 4.19: Comparison between the rate coefficients (in $\text{cm}^3 \text{s}^{-1}$) of CS (x-axes) and HF (y-axes) in collision with thermalized p-H₂O (left panel) and o-H₂O (right panel) at 50 K (green crosses) and 100 K (black circles).

than 20%. Therefore, using the present HCN-p-H₂O collisional rate coefficients to estimate CS-p-H₂O coefficients is unlikely to be a reliable approximation, but more accurate data for HCN-H₂O collisional system should be provided to confirm this preliminary result.

While the sets of CS and CO rate coefficients show great similarities, those of HCN exhibit significant discrepancies. This is surprising as CO and HCN molecules are iso-electronic, so a similar behavior in the rate coefficients could be expected. However, the geometry at the GM for the HCN-H₂O system appeared to be different than those of CO-H₂O and CS-H₂O, suggesting a different chemical behavior.

The last comparison is regarding the rate coefficients of HF in collision with p-H₂O and o-H₂O, which were produced by Loreau et al. (2022) for temperatures ranging from 5 K to 150 K. The rate coefficients were computed using the SACM approach based on the HF-H₂O PES of Loreau et al. (2020) by including HF levels up to $j_{\text{HF}} = 6$, and H₂O up to $j_{k_a k_c} = 6_{k_a k_c}$ for both p-H₂O and o-H₂O. The thermalized rate coefficients they provided, taken from the BASECOL database (Dubernet et al., 2024), are compared to the thermalized rate coefficients of CS-p-H₂O and CS-o-H₂O computed in this work in Figure 4.19.

The data distribution is quite sparse. A significant deviation is observed between the

HF-H₂O and CS-H₂O rate coefficients, with only about half of the rate coefficients agreeing within a factor of two. Rate coefficients involving HF as the target are generally higher than those for CS, due to HF's larger dipole moment, which leads to a deeper potential well (3,000 cm⁻¹ vs. 1,172 cm⁻¹). The deviations are slightly larger with p-H₂O than with o-H₂O at both temperatures, and like the trend seen with CS and HCN, the deviation increases with the temperature. The WMEF indicates a global deviation of about 1.90 at 50 K and 1.96 at 100 K for p-H₂O, and about 1.68 at 50 K and 1.80 at 100 K for o-H₂O. Therefore, using HF-H₂O rate coefficients to estimate CS-H₂O rate coefficients (or vice versa) is expected to significantly impact the modeling of these molecules in cometary comae.

From the comparison of the rate coefficients for CS with those of CO, HCN, and HF, relevant for studying cometary atmospheres, several conclusions can be drawn. First, the collisional rate coefficients between CO and CS for collisions with CO, p-H₂O, and o-H₂O showed reasonable deviations. Thus, using CO collisional data to model CS, and vice versa, is expected to be a reasonable approximation. This similarity is not surprising given that CO and CS are chemically similar.

However, larger deviations are observed when comparing the rate coefficients for HCN and CS, even though they were expected to be similar. Indeed, HCN has a similar electronic structure to both CS and CO. Moreover, it presents a similar rotational constant to CO [$B_{\text{HCN}} = 1.481 \text{ cm}^{-1}$ (Maki, 1974) vs $B_{\text{CO}} = 1.931 \text{ cm}^{-1}$ (Le Floch, 1991)]. Nevertheless, the geometry of the GM in the PES of HCN-H₂O differs from that of CS-H₂O and CO-H₂O, indicating different chemical behavior. Additionally, the scattering calculations performed for the HCN-H₂O system were only partially converged; thus, the "real" deviation between the two sets of data could differ if convergence were achieved.

In addition, the comparison between HF and CS rate coefficients exhibited that HF is not a good template for CS, and vice-versa. This can be explained by the much larger dipole of HF compared to CS, and deeper well depth. In addition, hydrides such as HF have been noticed to be peculiar species when determining their rate coefficients in interstellar studies.

Therefore, using HF or HCN collisional data to model CS is unlikely to yield accurate results and is not recommended.

4.3.3 Sensitivity of Radiative Transfer Models to Rate Coefficients

Now that the different sets of rate coefficients have been discussed, the effect of the deviations on the derived populations of CS energy levels will be investigated. Indeed, the deviations between the sets of rate coefficients employed to compute the population of CS energy levels are expected to result in discrepancies in the modeling of CS.

Therefore, the impact of using interstellar data (CS-H₂, CS-He) to model cometary observations (where CS-CO and CS-H₂O data should be employed) will be discussed. Moreover, the impact of using collisional data with another target but the same collider will also be discussed, e.g., CO-CO to infer CS-CO data, or HCN-H₂O to mimic CS-H₂O data.

Cometary vs Interstellar Data

This section tests the impact of different sets of collisional data for CS in collisions with various colliders. The objective is to determine whether using interstellar data instead of cometary data significantly affects the population of CS energy levels. Therefore, the population of CS energy levels has been evaluated using thermalized rate coefficients for CS-H₂O, CS-CO, CS-H₂, and CS-He systems. For CS-H₂O and CS-H₂ systems, the rate coefficients were thermalized assuming an o/p ratio of three. The radiative transfer equations are solved using the same approach as described in Section 4.3.1 to produce the population of CS energy levels at both 20 K and 100 K.

The populations of CS energy levels involved in the most observed transitions—namely, $j = 3 \rightarrow 2$; $5 \rightarrow 4$; and $7 \rightarrow 6$ (Roth et al., 2021a; Cordiner et al., 2023; Biver et al., 2023; Biver et al., 2024)—are represented as a function of gas density. Therefore, the deviations observed are expected to be the one affecting the most significantly the modeling of CS emission spectra from the coma.

In Figure 4.20, the population of CS energy levels as a function of density appears to be quite sensitive to the sets of rate coefficients employed. While the behavior of the CS energy level populations with volume density is relatively similar across all sets of rate coefficients, their magnitudes at a given density can exhibit significant deviations.

As indicated by the behavior of their respective rate coefficients, the population of CS reaches the LTE regime at lower densities when computed using the CS-H₂O data com-

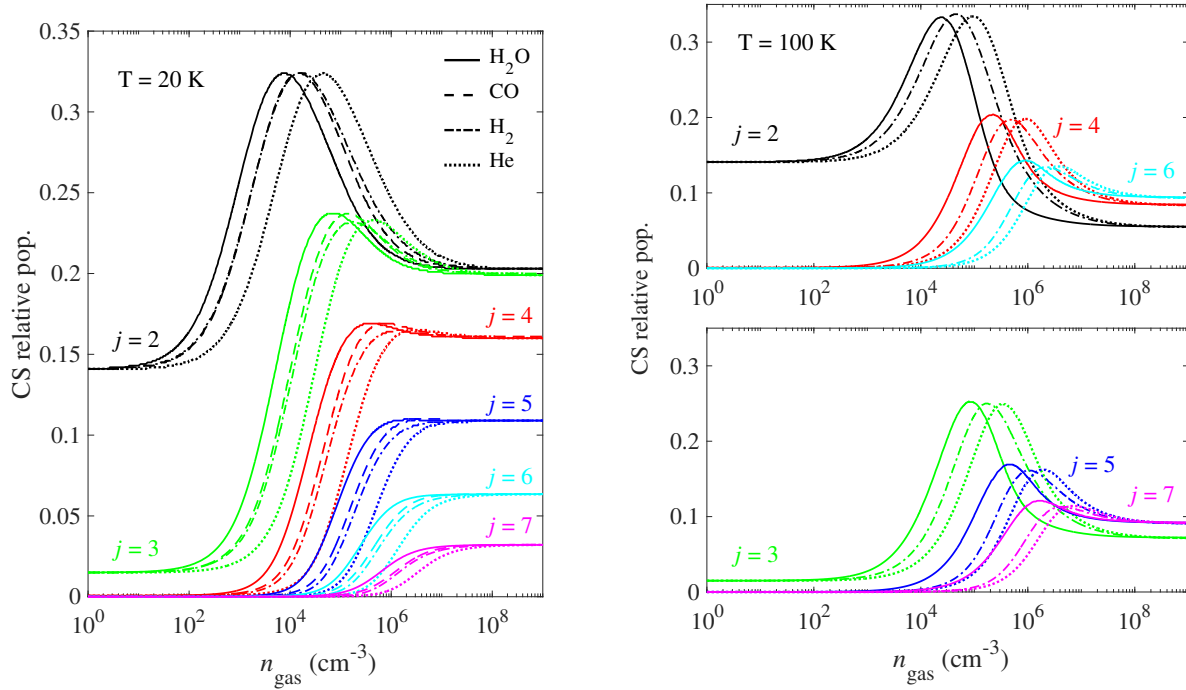


Figure 4.20: Relative population of CS energy levels as a function of the density of gas (in cm^{-3}) using different CS-H₂O (solid lines), CS-CO (dashed lines), CS-H₂ (dashed-dotted lines) and CS-He (dotted lines) thermalized rate coefficients. For H₂O and H₂, the rate coefficients have been thermalized with a fixed o/p ratio of three. At 100 K, the even (upper panel) and odd (lower panel) j levels have been separated for the sake of clarity.

pared to any other set. This observation is justified by the fact that the rate coefficients for CS-H₂O are generally higher than those for CS-H₂, which are also higher than those of CS-He. As the rate coefficients increase, the density at which the population of CS thermalizes decreases. Consequently, the LTE regime is reached at lower densities when using CS-H₂O than when employing CS-CO, CS-H₂, and CS-He data.

The substitution of CS-H₂O rate coefficients with either CS-H₂ or CS-He interstellar rate coefficients leads to significant deviations in the population of energy levels within the non-LTE density range. This outcome was anticipated due to the strong discrepancies observed between these sets of rate coefficients, as shown in Figure 4.13 and Figure 4.15. The differences are more pronounced when CS-He is used, resulting in a deviation by up to a factor of two to three in the populations of some energy levels. For CS-H₂, which is usually the one employed to substitute CS-H₂O data, the deviations remain substantial, with differences approaching nearly a factor of two in the population of some levels. The

deviations are generally larger for the lower energy levels, such as $j = 2, 3$. However, a deviation up to a factor of 1.5 is also observed on the higher levels $j = 6, 7$. This trend is consistent at both temperatures, with deviations remaining relatively constant between 20 K and 100 K. Although an improvement was anticipated at 100 K due to the decreasing deviation between the two sets of rate coefficients, this improvement is not significantly reflected in the modeling of the population of CS energy levels.

These large discrepancies between the populations calculated using CS-H₂O and CS-H₂ data were anticipated, as the WMEF indicated a global deviation of over a factor of eight at 20 K and over a factor of 3.5 at 100 K between their rate coefficients, with some transitions differing by three orders of magnitude. Therefore, the significant deviations in the population of CS energy levels when using CS-H₂ compared to CS-H₂O data are not surprising. Consequently, using CS-H₂ collision rate coefficients as a substitute for CS-H₂O data is not recommended, as it is likely to induce substantial inaccuracies in the modeling of CS emission spectra in comae.

Nevertheless, the agreement between the populations computed using CS-CO and CS-H₂ data is surprisingly good. Although some deviations are observed and the populations are still affected, the deviations between the populations are relatively small considering the significant discrepancies between the two sets of rate coefficients, as shown in Figure 4.14. Specifically, a global deviation indicated by the WMEF of nearly a factor of three was noted, but the populations only differ by about 10%. Therefore, using CS-H₂ data to infer CS-CO data represents a reasonable first approximation.

The difference between CS-H₂O and CS-CO data, as well as their impact on the population of CS energy levels, have already been discussed in Section 4.3.1, and will not be further discussed here.

In conclusion, substituting CS-H₂ rate coefficients for CS-H₂O rate coefficients in H₂O-dominated comae is expected to result in significant inaccuracies. These deviations are crucial, particularly because only a few lines of CS in comae can be detected simultaneously by observational facilities. Utilizing a χ^2 analysis based on such deviations can greatly impact the derived production rates and abundances of CS in the coma. Therefore, it is essential to use the appropriate sets of rate coefficients for CS to accurately derive the physical conditions in cometary comae where CS is observed. However, substituting CS-H₂ rate coefficients for CS-CO rate coefficients in CO-dominated comae is expected to lead to reasonably accurate results.

Impact of the Target

The sensitivity of radiative transfer models when using the proper projectile (CO or H₂O) but different target molecules (CO or HCN) is explored.⁹ For example, what if CS emission lines were interpreted using the collisional rate coefficients of CO-H₂O? Is this a better approximation than using CS-H₂ data? These are the kind of effects explored here. The population of CS energy levels has been modeled using the same methodology as the previous section, but the rate coefficients have been replaced by those of different target molecules.

The problem with this comparison is that the sets of CS-CO, CO-CO, CS-H₂O, CO-H₂O, and HCN-H₂O rate coefficients do not include the same number of levels for the target molecule. Therefore, the data sets of the two compared species have been truncated to include the same number of rotational levels, ensuring that the comparison is based solely on the deviations between the rate coefficients.

The population of CS energy levels computed using CS-CO and CO-CO rate coefficients is compared in Figure 4.21 at both 10 K and 30 K.

The deviations between the populations of CS energy levels computed with both sets of rate coefficients are moderate. The deviations are slightly larger for low j levels and tend to decrease as these levels become less populated with increasing j . The differences in the observed population are up to about 20% at 10 K, and 30 K.

Since only a few rotational levels are significantly affected by using different sets of rate coefficients, this suggests that CO-CO rate coefficients can be employed to infer those of CS-CO as a reasonable approximation. This was already suggested in Section 4.3.2, where the global deviation indicated by the WMEF was found to be better than a factor of 1.3, implying a moderate impact on the accuracy of CS modeled spectra from this approximation. Consequently, this comparison confirms that this approximation is expected to yield reliable results for modeling CS emission spectra in comae.

The comparison of the population of the rotational levels of CS as a function of gas density, using either CS-H₂O or CO-H₂O, is shown in Figure 4.22 at 50 K and 100 K.

⁹HF has not been included in the discussion because it presents no real structural similarities with CS. Therefore, it is obvious that it cannot be employed as a template for CS.

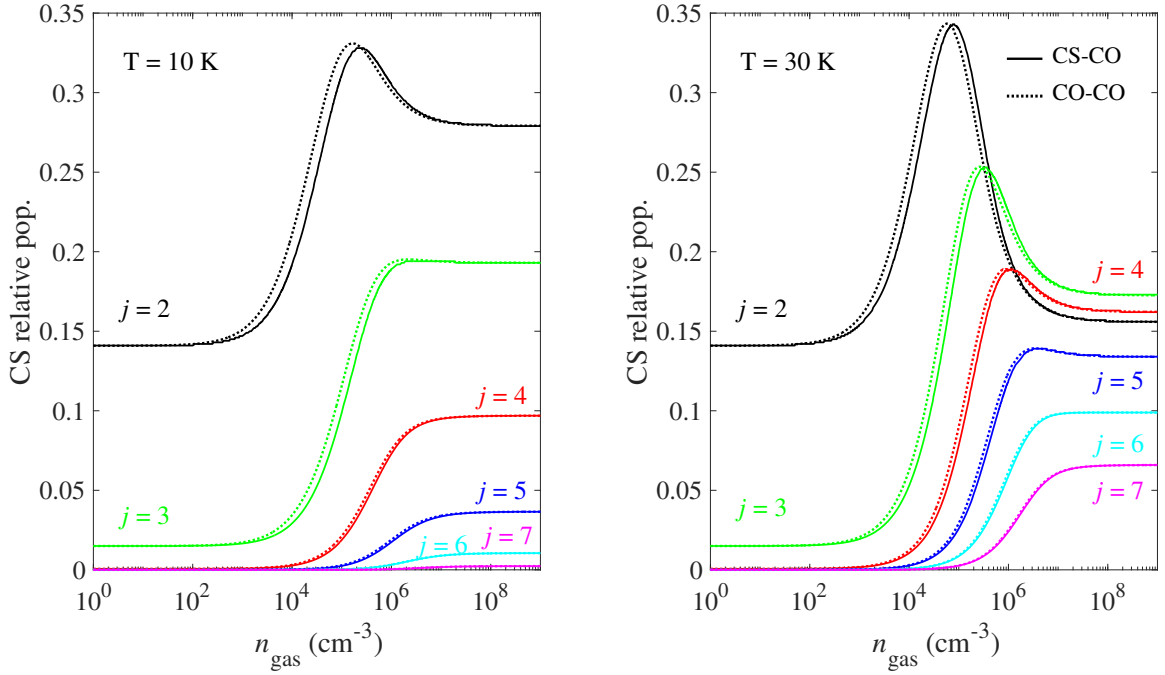


Figure 4.21: Relative population of CS energy levels ($2 \leq j_{\text{CS}} \leq 7$) as a function of the density of gas (in cm^{-3}) using CS-CO (solid lines), CO-CO (dotted lines) sets of thermalized rate coefficients.

When the populations of CS energy levels are compared using CS-H₂O or CO-H₂O rate coefficients, the deviations in the CS energy level populations are relatively small. Indeed, for all rotational levels of CS, over the entire range of densities and at both temperatures, the agreement is good. Unlike the effect observed in the comparison between CS-CO and CO-CO data, here the deviations between the sets of rate coefficients affect the population of all levels similarly. Some small deviations, of about 15%, can be observed in the non-LTE regime, but they are minor enough that they are not expected to significantly impact the modeling of CS emission spectra. This can be explained by the strong similarities between the two sets of rate coefficients, as the WMEF indicated a global deviation of about a factor of 1.3 at both temperatures. As a result, the modeling of CS populations does not appear to be sensitive to such relatively small deviations in the rate coefficients.

Consequently, the sets of CO-H₂O data could be employed to model CS-H₂O data with good confidence. However, one limiting factor is that the CO-H₂O data includes only the first eleven levels of CO, which is likely insufficient for modeling CS at 100 K. Neverthe-

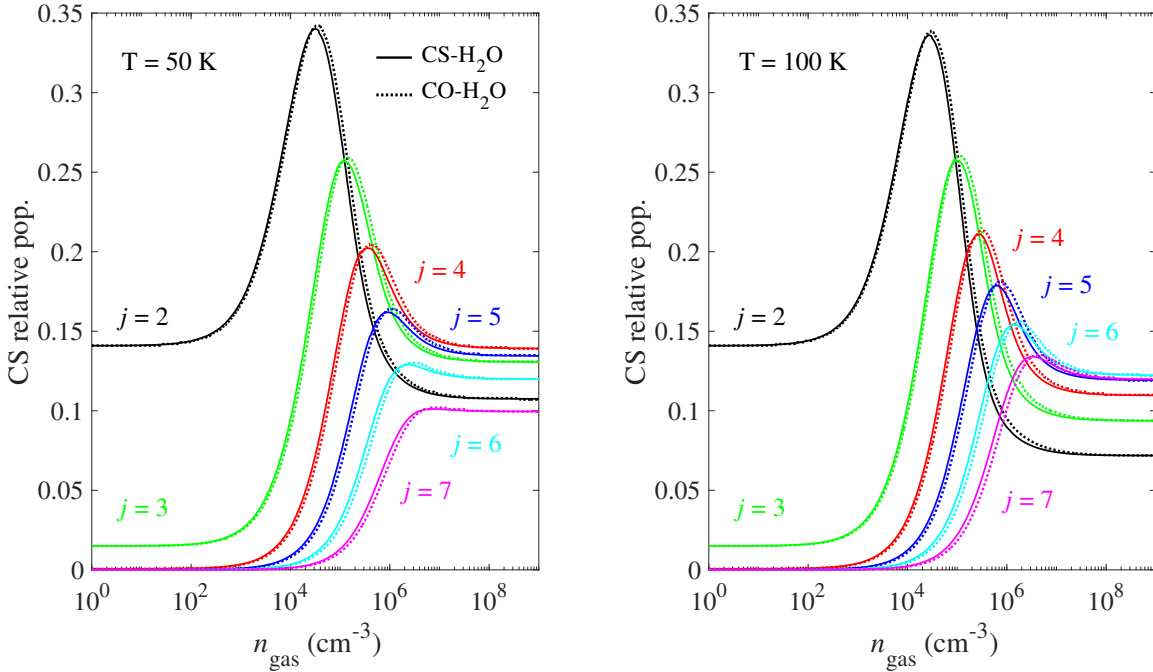


Figure 4.22: Relative population of CS energy levels ($2 \leq j_{CS} \leq 7$) as a function of the density of gas (in cm^{-3}) using CS-H₂O (solid lines), CO-H₂O (dotted lines) sets of thermalized rate coefficients.

less, this means that CS-H₂O data could be used to approximate CO-H₂O data without encountering this problem, ensuring reliable accuracy when modeling CO emission spectra in H₂O-dominated comae using CS-H₂O data.

In Figure 4.23, the populations of CS energy levels were computed at both 50 K and 100 K using the CS-H₂O and HCN-H₂O sets of thermalized rate coefficients. In the calculations by Dubernet & Quintas-Sánchez (2019), only p-H₂O was considered in their calculations so the medium was assumed to be composed solely of p-H₂O.

Significant differences between the populations of CS energy levels can be observed when computed using HCN-H₂O rate coefficients instead of CS-H₂O rate coefficients. In the non-LTE regime, the populations differ by about 15% to 40% at 50 K and by about 20% to 55% at 100 K. The increasing deviations at higher temperature is likely due to the fact that the rate coefficients for CS and HCN in collisions with H₂O differ more at 100 K than at 50 K. Indeed, the WMEF indicated a global deviation of a factor 1.7 at 50

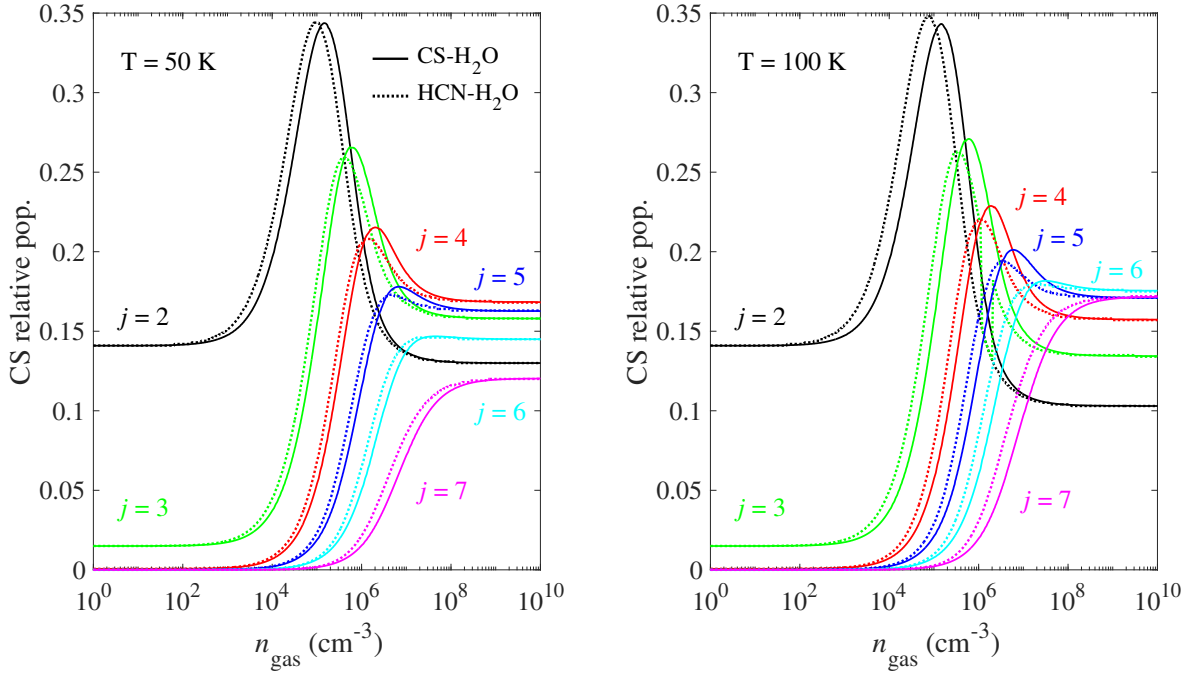


Figure 4.23: Relative population of CS energy levels ($2 \leq j_{\text{CS}} \leq 7$) as a function of the density of gas (in cm^{-3}) using CS-p-H₂O (solid lines), HCN-p-H₂O (dotted lines) sets of thermalized rate coefficients.

K, and of a factor 2.3 at 100 K in Figure 4.18. These differences between the populations of CS energy levels using CS-H₂O or HCN-H₂O rate coefficients are high enough to expect that it will impact the modeling of CS emission spectra in H₂O dominated comae. Consequently, it is not recommended to use CS-H₂O data to model HCN-H₂O data, or vice versa.

From these comparisons, several conclusions can be drawn.

It was observed that using CO as a template for CS, and vice versa, is a good approximation with both CO and H₂O as projectiles. In both cases, a good correlation between the data sets was anticipated due to the chemical similarities of CO and CS. Nevertheless, the excellent agreement between the sets of data is surprising, as the well depths of the CS-CO and CS-H₂O PESs are almost twice as deep as those of CO-CO and CO-H₂O, respectively.

The use of CO data when CS ones are unavailable is thus recommended. This could help address the temperature limitation of CS-CO data, which were computed only up to

30 K, while CO-CO data are available up to 100 K. However, it is crucial to ensure that the energy levels included in the sets of rate coefficient are sufficient to account for all significantly populated CS energy levels. Since CS has a lower rotational constant than CO, fewer rotational levels of CO are typically included in the rate coefficient calculations at the same temperature. Thus, the CO-CO data covers only eleven levels, which is insufficient for CS at this temperature. Therefore, CO-H₂O and CO-CO data would be difficult to use to compensate for a lack of CS data, but using CS-CO and CS-H₂O data to model CO-CO and CO-H₂O is feasible. Therefore, computing CS-CO₂ rate coefficients would be more interesting (but also more challenging) than CO-CO₂ if a choice had to be made.

Additionally, it was observed that using HCN-H₂O data for inferring CS-H₂O data and vice versa was not expected to be a good approximation to model CS emission spectra in H₂O-dominated comae, and is thus not recommended. In comparison with CO, it is surprising to observe such disagreement between CS and HCN data, as these species present chemical similarities. However, the HCN-H₂O data discussed in this work were obtained with the Coupled-States approximation, which is a different scattering method than the one we employed for the CS-H₂O calculations, and only partial convergence was achieved. This might justify the discrepancies observed, but calculations of HCN-H₂O rate coefficients with the SACM approach, or fully converged Coupled-States cross sections (or ideally with the CC approach) would be necessary to draw strong conclusions.

In this section, the use of interstellar data (CS-H₂, CS-He) to infer cometary data (CS-H₂O, CS-CO) for modeling CS emission spectra was also investigated. It appears that using interstellar data for the correct target molecule (like CS-H₂ or CS-He) is actually a less accurate approximation than using rate coefficients with a similar target molecule and the correct collider (as CO-CO for CS-CO, or CO-H₂O for CS-H₂O). Therefore, the sets of CS-H₂O and CS-CO data produced in this work could be used to approximate cometary data for other chemically similar linear molecules detected in comets, like OCS for example.

Regarding the sensitivity of radiative transfer models to the sets of rate coefficients, it seems that a global deviation lower than a factor of 1.5 does not lead to significant discrepancies and could be considered a sensitivity threshold. For instance, when comparing CS-CO and CO-CO data, as well as CS-H₂O and CO-H₂O data, the WMEF values for these sets of rate coefficients were lower than 1.5, and the deviations between the mod-

eled populations were relatively small. However, when comparing CS-H₂O to HCN-H₂O data, the WMEF values exceeded 1.5, and the resulting populations were quite different. Additionally, the WMEF for HCN-H₂O was significantly larger at 100 K than at 50 K (rising from 1.7 at 50 K to 2.3 at 100 K), which was reflected in larger discrepancies in the populations of energy levels.

The next step would be to investigate how uncertainties in the rate coefficients propagate through the interpretation of observations. Indeed, interpreting cometary observations is a complex task that encompasses many sources of uncertainty.

The first source of uncertainty arises from the signal-to-noise ratio, which depend on the activity of the comet.

Another source of uncertainties is coming from the different outflow components of the coma. The outgassing of ices from the nucleus is usually divided into activity regimes, as regions of the nucleus can be thermally activated or enhanced by spatially confined vents or jets, particularly on the sunward-facing side of the nucleus. To better constrain the model, only two regions are typically considered (Festou, 2001; Gunnarsson, 2003; Bockelée-Morvan et al., 2004; Cordiner et al., 2020; Roth et al., 2021a; Roth et al., 2021b; Cordiner et al., 2022). In each region, the gas is assumed to expand in a conical shape, with a constant production rate and velocity component.

Additional uncertainties arise from the kinetic temperature of the coma, which is often assumed to be constant within the delimited regions (Biver et al., 2018). This temperature is estimated from CH₃OH emission lines analyzed using either the rotational diagram approach.

Moreover, the derived production rates of molecules depend on their assumed photodissociation rates, which are not available or precisely known for all molecules.

It has been shown that radiative transfer models are sensitive to differences between sets of rate coefficients, but to what extent does this sensitivity impact the interpretation of observations? Would it lead to a significant revision of the production rates or the abundance of CS in comae? Answering these questions would require analyzing the emission spectra of CS in comae using different sets of collisional data.

CONCLUSION

This PhD thesis was devoted to the collisional excitation of sulfur-bearing molecules induced by both light and heavy colliders, with applications to the ISM and comae. The main objective was to provide rate coefficients for the study of sulfur-bearing species, enabling more accurate modeling of their abundances in astrophysical media. This work offers additional insights into sulfur chemistry in space and contributes to new perspectives on the missing-sulfur problem.

Two sulfur-bearing species were selected for this study: CCS for interstellar molecular clouds applications and CS for cometary comae applications. Both molecules are abundant in their respective environments, and significant uncertainties remain regarding their chemistry. Therefore, accurately modeling their abundances in these media would be a valuable step towards unraveling the complexities of their chemical behavior.

CCS in Dark Molecular Clouds

Summary and Conclusions

The first accurate sets of fine-structure and hyperfine-structure resolved rate coefficients were provided for the CCS-He system and four of its secondary isotopologues: ^{13}CCS , C^{13}CS , CC^{33}S , and CC^{34}S . The scattering calculations were performed using the Close-Coupling approach, which is the most accurate method for solving the scattering equations. These calculations were based on the CCS-He PES computed using state-of-the-art methods, which is the first PES calculated for the CCS molecule with any collisional partner. The fine-structure, and hyperfine-structure resolved rate coefficients for CCS and its isotopologues are now available in the BASECOL (Dubernet et al., 2024), LAMDA (Schöier et al., 2005), and EMAA (Faure et al., 2021) databases.

For the collisional excitation of CCS, the He projectile was chosen as a proxy for $\text{p-H}_2(j=0)$, the most abundant molecule in molecular clouds, where CCS is ubiquitous. This approximation, as suggested by Schöier et al. (2005), is expected to work well for CCS because of its heavy mass and moderate dipole moment. During this thesis work, many

CCS isotopologues were detected in TMC-1 (CP) with the QUIJOTE project (Cernicharo et al., 2022). As a result, our collaboration with the group of Dr. M. Agúndez and Pr. Cernicharo led to the first accurate modeling of CCS isotopologues in interstellar environments. This marks the first time CCS was modeled using radiative transfer models based on accurate collisional rate coefficients, and the first time the column densities of CC^{34}S , CC^{33}S , and ^{13}C -substituted CCS isotopologues were derived.

The study of the rate coefficients has been published in two peer-reviewed articles: Godard Palluet & Lique (2023a), which presents the PES of the CCS-He van der Waals system, scattering calculations, and a comparison with approximate rate coefficients from Wolkovitch et al. (1997), and Godard Palluet & Lique (2023b), which discusses the effect of isotopic substitution for the four CCS isotopologues— C^{13}CS , ^{13}CCS , CC^{34}S , and CC^{33}S —on rate coefficients and non-LTE radiative transfer models. These articles are presented in Appendix A.2 and Appendix A.3, respectively. A third article, Fuentetaja et al. (in prep.), will be submitted for peer review soon, focusing on the detection and modeling of CCS isotopologues in TMC-1 (CP) through the QUIJOTE survey.

Throughout this study, I had the opportunity to visit my collaborators at the Instituto de Física Fundamental in Madrid. During that stay, we worked together to investigate the ^{13}C -anomaly, using the newly modeled abundance ratios based on the updated rate coefficients. This anomaly has puzzled researchers for many molecules, but especially for CCS, where the anomaly is the most pronounced. The abundance ratio $[\text{C}^{13}\text{CS}]/[^{13}\text{CCS}]$ was evaluated at 6.8, which is larger than the previously estimated value of 4.2 ± 2.3 by Sakai et al. (2007).

For years, the formation pathway of CCS was thought to be at the origin of this anomaly. However, our preliminary study suggested that the interconversion of ^{13}CCS into C^{13}CS , catalyzed by hydrogen atoms, could perfectly explain the observed abundance ratio. This interconversion mechanism has been suggested as a likely explanation for the ^{13}C -anomaly in CCH, and $c\text{-C}_3\text{H}_2$, but it fails for the anomaly of C_3S .

Perspectives

The data produced in this work could be employed to further analyze CCS observations in many other sources. CCS has been detected in 27 dark cloud cores in the study of Suzuki et al. (1992), and has also been observed in Sagittarius B2 (Saito et al., 1987), in the outer part of the circumstellar envelope of IRC+10216 (Cernicharo et al., 1987), and in B335, a

typical example of a young protostellar core (Velusamy et al., 1995). The interpretation of observations in these media has been done using a rotational diagram method, which has proven to lead to inaccurate results for the interpretation of CCS emission spectra in TMC-1 (CP). This suggests that using these new collisional data may lead to a significant revision of CCS abundance in these environments.

To improve the accuracy of the state-to-state rate coefficients computed in this work, H_2 should be considered as a projectile instead of He. To assess the impact of this approximation on the collision rate coefficients produced, energy curves for the CCS-p- H_2 system could be computed. The closer the well depths of the two systems are, the more confidently the CCS-He rate coefficients can be used to approximate the CCS-p- H_2 collisional rate coefficients.

CCS is a ubiquitous molecule that often serves as a tracer of physical conditions. It is easily observed through many transitions, making it an excellent target for studying astrophysical environments. As it is detected in regions where temperatures can be as high as 100 K, o- H_2 can no longer be ignored, and considering only p- $\text{H}_2(j = 0)$ would be insufficient. Thus, collisional rate coefficients for CCS in collisions with both p- H_2 and o- H_2 are necessary. Consequently, a new PES must be developed using H_2 as the projectile. Furthermore, the doubly degenerate ν_2 bending level at 134 cm^{-1} should also be accounted for in both the PES and the scattering calculations. To this end, the new PES should include the bending coordinates [e.g., the vibrational excitation of HCN induced by He, Denis-Alpizar et al. (2013)]. However, the scattering equations for the collisional excitation of a bending molecule induced by another molecule are not implemented in either MOLSCAT or HIBRIDON. therefore, extending these calculations would present significant methodological and numerical challenges, as new equations would need to be developed and implemented.

Throughout this study, we learned a few things about CCS that would be useful for future studies. It has been demonstrated that the internal structure of CCS must be properly accounted for to compute accurate rate coefficients. Additionally, it has been found that the rate coefficients of the primary isotopologue $^{12}\text{C}^{12}\text{C}^{32}\text{S}$ can be applied to other isotopologues with the same structure, such as CC^{34}S . Furthermore, the S-matrices computed for the primary isotopologue can also serve for computing the hyperfine-structure rate coefficients of any CCS isotopologue presenting a nuclear spin, using the recoupling approach with minimal concern over isotopic substitution effects. This approach would

significantly reduce computational time while preserving the precision of the isotopologue datasets.

The ^{13}C -anomaly have been analyzed and it was suggested that the large discrepancies between the two ^{13}CCS and C^{13}CS isotopologues might be due to thermodynamics rather than kinetics. In previous studies, multiple pathway have been excluded because they were producing both isotopologues in equal quantities. If our hypothesis is true, then these production paths of CCS are viable again. This suggests that the chemistry of CCS might need to be re-studied. Its primary formation path was thought to be via the HCCS^+ intermediate, which was recently detected by Cabezas et al. (2022) in TMC-1 and found to be relatively abundant. The observed rotational lines of this cation are not thermalized, indicating a need for collisional rate coefficients. However, these rate coefficients are not yet available and would need to be computed. Given that the internal structure of HCCS^+ is similar to that of CCS, with a large spin-spin spectroscopic constant, its internal structure should also be treated accurately using an intermediate coupling scheme. Moreover, the approximation proposed by Schöier et al. (2005) is not effective for ions, so H_2 must be considered as the projectile. Thus, the first set of $\text{HCCS}^+\text{-H}_2$ rate coefficients should be computed to enable accurate modeling of this cation in TMC-1 and advance the investigation of CCS chemistry in molecular clouds.

Finally, further investigations of the ^{13}C -anomaly in other molecules, such as CCH, $c\text{-C}_3\text{H}_2$, and C_3S would require re-analyzing the observations revealing the anomaly based on accurate radiative transfer models that use reliable sets of collisional data. For the CCH molecule, both ^{13}CCH and C^{13}CH collisional rate coefficients with the $p\text{-H}_2$ collider have been recently provided by Pirlot Jankowiak et al. (2023b). Hence, future observations should be conclusive regarding this hypothesis. For C_3S and $c\text{-C}_3\text{H}_2$, new rate coefficients would be necessary, along with a reinterpretation of the observations of these ^{13}C -isotopologues to draw strong conclusions about the ^{13}C -anomaly and the chemistry of these molecules.

CS in Cometary Atmospheres

Summary and Conclusions

The CS molecule was studied because it is one of the most abundant S-bearing molecules in cometary atmospheres. However, the origin of CS in comae is not well understood. By accurately determining the abundance of CS, it is expected that its chemistry can be better understood. Since the chemistry in comae is highly sensitive to the heliocentric distance of the comets, the goal of this work was to provide tools that enable the study of CS in comets at both short and large heliocentric distances. To achieve this, rate coefficients for collisions between CS and CO, as well as between CS and H₂O, were necessary.

During this work, two additional sets of collisional data were added to the five existing datasets for cometary systems: CS-CO and CS-H₂O. As a result, five molecules—CO, H₂O, HCN, HF, and CS—can now be modeled in cometary comae. It also marks only the second collisional system for which CO was considered as a projectile (and not only a target, so CO-H₂O is not included). Hence, these studies represent pioneering efforts in computing collisional rate coefficients for cometary applications.

The rate coefficients for both systems studied in this work were computed using the Statistical Adiabatic Channel Model (SACM) approach, with "exact" Close-Coupling approaches used to compute the adiabatic states. These calculations were based on PESs computed for these systems using state-of-the-art quantum chemistry methods. The PES for the CS-CO system was developed in collaboration with Pr. R. Dawes and Dr. E. Quintas-Sánchez (University of Missouri, USA), and the PES of the CS-H₂O system was developed in collaboration with Dr. Dariusz Kędziera (Nicolaus Copernicus University, Toruń, Poland), and Dr. Jacek Kłos (University of Maryland, USA). The PESs and collisional rate coefficients for both systems are expected to be published in two separate peer-reviewed articles.

The accuracy of the SACM method for the CS-CO rate coefficients was evaluated. The results were compared with CC calculations, although the latter were restricted to a minimal number of partial waves. The comparison showed great accuracy in the CS-CO collisional data produced with the SACM approach. However, no comparison with CC calculations has yet been performed for the CS-H₂O system. Nevertheless, the accuracy for this system is expected to be similar to that of CS-CO, based on results from previously studied systems that also used the SACM approach that were validated

against CC calculations.

When comparing different sets of rate coefficients computed for cometary applications, the CO target molecule was found to be a reasonably good template for the CS molecule. However, using any other target molecule produced significantly different results, indicating that they cannot be used to infer CS rate coefficients, or reciprocally. The impact of the projectile was also analyzed. Interestingly, the use of CS-H₂ collisional data to approximate CS-CO data is expected to be a reasonable approximation while awaiting accurate collisional data. In contrast, using CS-H₂ data in place of CS-H₂O data is likely to lead to significant inaccuracies in the derived abundances and production rates of this molecule. Therefore, using interstellar data to infer cometary data in H₂O-dominated comae is not expected to yield reliable results.

Perspectives

The next step in this work is to use the CS-CO and CS-H₂O collisional data to interpret CS observations in comets and determine its accurate abundance. This task will be conducted in collaboration with Dr. M. Cordiner, whom I visited at the NASA Goddard Space Flight Center in Greenbelt, USA. During that visit, he introduced me to the `SUBLIME1D` code to model CS in cometary comae. Although the results are too preliminary to be presented here, this collaboration laid the groundwork for future work.

For future calculations of rate coefficients involving heavy colliders like CO or H₂O, the SACM method, as applied in this work, appears to be a good compromise. This approach can be extended to compute rate coefficients for linear target molecules, such as OCS, NS, or S₂ (the latter detected via vibrational transitions, with SACM also applicable to ro-vibrational transitions), using CO and H₂O as projectiles.

One limitation of the SACM approach lies in the computation of adiabatic states. The diagonalization of matrices with over 20,000 channels is computationally expensive and requires extreme memory resources. As demonstrated in this work, such large numbers of channels are easily exceeded when heavy colliders are involved, limiting the calculations to lower temperatures. For example, the CS-CO calculations were limited to 30 K, and extending to higher temperatures would be challenging using the same method. Moreover, the SACM approach becomes less accurate at higher temperatures, indicating the need for alternative methods. Therefore, a different approach to computing adiabatic states would be necessary for studying higher temperatures or heavier colliders, like OCS for

example.

Another promising approach to produce collisional data for cometary applications is the Mixed Quantum-Classical Trajectories (MQCT) method, developed by Semenov et al. (2020), and Mandal et al. (2024). It has been tested against full quantum calculations, showing reasonably good accuracy with agreement within a factor of two for H₂O-H₂ state-to-state rate coefficients down to 100 K (Joy et al., 2024). This suggests that the validity domains of the SACM and MQCT methods overlap around 100 K, making the two approaches complementary for producing rate coefficients to accurately interpret observational data from comae.

In this work, the effect of electrons on the excitation of CS has been neglected. However, it should be accounted for as comae exhibit large electronic fractionation, especially on molecules like CS that present a large dipole moment (Biver et al., 2022). Fortunately, rate coefficients for CS in collisions with electrons were produced by Varambhia et al. (2010) and are available for the 5 - 5000 K, so the impact of electrons on CS in CO- and H₂O-dominated comae can be investigated.

Finally, it is essential to evaluate the impact of the different sets of rate coefficients on the accuracy of CS production rates in comets. Considering the small sample of collisional rate coefficients existing for cometary applications, the conclusions drawn on this work cannot be general yet. Moreover, since only approximate methods, such as SACM or MQCT, are feasible for computing rate coefficients for cometary applications, it is crucial to assess how inaccuracies in these data propagate through radiative transfer models and affect the interpretation of observations.

What is Up in Astrochemistry

The launch of the James Webb Space Telescope (JWST), along with the operating ALMA, marks the beginning of what is often called the 'golden age' of astronomy, astrophysics, and, by extension, astrochemistry. Future observatories are also in development, such as the Square Kilometer Array (SKA) and the PRobe far-Infrared Mission for Astrophysics (PRIMA), as well as *in situ* missions like the Comet Interceptor mission. These advanced observatories will provide an unprecedented amount of data, leading to exponential growth in the detection of new molecules and in our understanding of astrophysical environments. This influx of data represents vast opportunities for astrochemical modelers and for re-

searchers who develop the laboratory and theoretical reference data needed for accurate interpretation of observations.

In the field of collisional data, there is still significant work to be done, but we are approaching the computational limits of what can be achieved with current methodologies and computational resources. Questions arise about heavy target molecules, such as COMs, heavy colliders, as CO, CO₂ and H₂O for cometary applications, but also N₂ for planetary applications. In this thesis work, only rotational excitation was considered but ro-vibrational rate coefficients will be more and more necessary with new IR observational facilities such as JWST.

Of the approximately 320 molecules currently detected in space, only about 70 have collisional data available in databases. Moreover, these data are not applicable in all environments and are often limited in their temperature range. Given the expected evolution of astrochemistry, with many more molecules likely to be detected in the coming decades, it is clear that the pace of new detections will far outstrip the speed at which collisional data can be calculated. Consequently, exploring innovative approaches for calculating collisional data should be pursued to keep up with the rapidly increasing observational data and to support astrochemical modelers.

BIBLIOGRAPHY

- A'Hearn, M. F. et al., "Deep Impact: Excavating Comet Tempel 1", *Science* **310** (2005), pp. 258–264, DOI: [10.1126/science.1118923](https://doi.org/10.1126/science.1118923).
- A'Hearn, M. F., "Deep Impact and the Origin and Evolution of Cometary Nuclei", *Space Science Reviews* **138** (2008), pp. 237–246, DOI: [10.1007/s11214-008-9350-3](https://doi.org/10.1007/s11214-008-9350-3).
- Adler, T. B., Knizia, G. & Werner, H.-J., "A Simple and Efficient CCSD(T)-F12 Approximation", *The Journal of Chemical Physics* **127** (2007), p. 221106, DOI: [10.1063/1.2817618](https://doi.org/10.1063/1.2817618).
- Agúndez, M., Marcelino, N., Cernicharo, J., Roueff, E. & Tafalla, M., "A Sensitive λ 3 Mm Line Survey of L483: A Broad View of the Chemical Composition of a Core around a Class 0 Object", *Astronomy & Astrophysics* **625** (2019), A147, DOI: [10.1051/0004-6361/201935164](https://doi.org/10.1051/0004-6361/201935164).
- Alexander, M., Dagdigian, P., Werner, H.-J., Kłos, J., Desrousseaux, B., Raffy, G. & Lique, F., "Hibridon: A Program Suite for Time-Independent Non-Reactive Quantum Scattering Calculations", *Computer Physics Communications* **289** (2023), p. 108761, DOI: [10.1016/j.cpc.2023.108761](https://doi.org/10.1016/j.cpc.2023.108761).
- Alexander, M. H., "Hybrid Quantum Scattering Algorithms for Long-Range Potentials", *The Journal of Chemical Physics* **81** (1984), pp. 4510–4516, DOI: [10.1063/1.447420](https://doi.org/10.1063/1.447420).
- Alexander, M. H. & Dagdigian, P. J., "Propensity Rules in Rotationally Inelastic Collisions of Diatomic Molecules in $^3\Sigma$ Electronic States", *The Journal of Chemical Physics* **79** (1983), pp. 302–310, DOI: [10.1063/1.445578](https://doi.org/10.1063/1.445578).
- Alexander, M. H. & Dagdigian, P. J., "Collision-Induced Transitions between Molecular Hyperfine Levels: Quantum Formalism, Propensity Rules, and Experimental Study of $\text{CaBr}(X^2\Sigma^+) + \text{Ar}$ ", *The Journal of Chemical Physics* **83** (1985), pp. 2191–2200, DOI: [10.1063/1.449311](https://doi.org/10.1063/1.449311).
- Alexander, M. H. & Manolopoulos, D. E., "A Stable Linear Reference Potential Algorithm for Solution of the Quantum Close-Coupled Equations in Molecular Scattering Theory", *The Journal of Chemical Physics* **86** (1987), pp. 2044–2050, DOI: [10.1063/1.452154](https://doi.org/10.1063/1.452154).

-
- Altwegg, K. et al., “Prebiotic Chemicals—Amino Acid and Phosphorus—in the Coma of Comet 67P/Churyumov-Gerasimenko”, *Science Advances* **2** (2016), e1600285, DOI: [10.1126/sciadv.1600285](https://doi.org/10.1126/sciadv.1600285).
- Aponte, J. C. et al., “PAHs, Hydrocarbons, and Dimethylsulfides in Asteroid Ryugu Samples A0106 and C0107 and the Orgueil (CI1) Meteorite”, *Earth, Planets and Space* **75** (2023), p. 28, DOI: [10.1186/s40623-022-01758-4](https://doi.org/10.1186/s40623-022-01758-4).
- Arthurs, A. & Dalgarno, A., “The Theory of Scattering by a Rigid Rotator”, *Proceedings of the Royal Society of London. Series A. Mathematical and Physical Sciences* **256** (1960), pp. 540–551, DOI: [10.1098/rspa.1960.0125](https://doi.org/10.1098/rspa.1960.0125).
- Balança, C., Scribano, Y., Loreau, J., Lique, F. & Feautrier, N., “Inelastic Rate Coefficients for Collisions of N_2H^+ with H_2 ”, *Monthly Notices of the Royal Astronomical Society* **495** (2020), pp. 2524–2530, DOI: [10.1093/mnras/staa1384](https://doi.org/10.1093/mnras/staa1384).
- Ball, J. A., Gottlieb, C. A., Lilley, A. E. & Radford, H. E., “Detection of Methyl Alcohol in Sagittarius”, *The Astrophysical Journal* **162** (1970), p. L203, DOI: [10.1086/180654](https://doi.org/10.1086/180654).
- Ben Khalifa, M. & Loreau, J., “Rotational Excitation of Interstellar Benzotrile by Helium Atoms”, *Monthly Notices of the Royal Astronomical Society* **527** (2023), pp. 846–854, DOI: [10.1093/mnras/stad3201](https://doi.org/10.1093/mnras/stad3201).
- Bergin, E. A. & Langer, W. D., “Chemical Evolution in Preprotostellar and Protostellar Cores”, *The Astrophysical Journal* **486** (1997), pp. 316–328, DOI: [10.1086/304510](https://doi.org/10.1086/304510).
- Berné, O., Mulas, G. & Joblin, C., “Interstellar C_{60}^+ ”, *Astronomy & Astrophysics* **550** (2013), p. L4, DOI: [10.1051/0004-6361/201220730](https://doi.org/10.1051/0004-6361/201220730).
- Bethlem, H. L., Berden, G. & Meijer, G., “Decelerating Neutral Dipolar Molecules”, *Physical Review Letters* **83** (1999), pp. 1558–1561, DOI: [10.1103/PhysRevLett.83.1558](https://doi.org/10.1103/PhysRevLett.83.1558).
- Biver, N., Bockelee-Morvan, D., Handzlik, B., Sandqvist, A., Boissier, J., Drozdovskaya, M. N., Moreno, R., Crovisier, J., Lis, D. C., Cordiner, M., Milam, S., Roth, N. X., Bonev, B. P., Russo, N. D., Vervack, R., Opitom, C. & Kawakita, H., *Chemical Composition of Comets C/2021 A1 (Leonard) and C/2022 E3 (ZTF) from Radio Spectroscopy and the Abundance of HCOOH and HNCO in Comets*, 2024, arXiv: [2408.10759](https://arxiv.org/abs/2408.10759) [[astro-ph](https://arxiv.org/abs/2408.10759)].
- Biver, N., Bockelée-Morvan, D., Colom, P., Crovisier, J., Paubert, G., Weiss, A. & Wiesemeyer, H., “Molecular Investigations of Comets C/2002 X5 (Kudo-Fujikawa), C/2002 V1 (NEAT), and C/2006 P1 (McNaught) at Small Heliocentric Distances”, *Astronomy & Astrophysics* **528** (2011), A142, DOI: [10.1051/0004-6361/201016250](https://doi.org/10.1051/0004-6361/201016250).

-
- Biver, N., Bockelée-Morvan, D., Crovisier, J., Davies, J. K., Matthews, H. E., Wink, J. E., Rauer, H., Colom, P., Dent, W. R. F., Despois, D., Moreno, R., Paubert, G., Jewitt, D. & Senay, M., “Spectroscopic Monitoring of Comet C/1996 B2 (Hyakutake) with the JCMT and IRAM Radio Telescopes”, *The Astronomical Journal* **118** (1999), pp. 1850–1872, DOI: [10.1086/301033](https://doi.org/10.1086/301033).
- Biver, N., Bockelée-Morvan, D., Crovisier, J., Lis, D. C., Moreno, R., Colom, P., Henry, F., Herpin, F., Paubert, G. & Womack, M., “Radio Wavelength Molecular Observations of Comets C/1999 T1 (McNaught-Hartley), C/2001 A2 (LINEAR), C/2000 WM₁ (LINEAR) and 153P/Ikeya-Zhang”, *Astronomy & Astrophysics* **449** (2006), pp. 1255–1270, DOI: [10.1051/0004-6361:20053849](https://doi.org/10.1051/0004-6361:20053849).
- Biver, N., Bockelée-Morvan, D., Crovisier, J., Sandqvist, A., Boissier, J., Lis, D. C., Cordiner, M., Bonev, B. P., Dello Russo, N., Moreno, R., Milam, S., Roth, N. X., Ver-
vack, R. & DiSanti, M. A., “Coma Composition of Comet 67P/Churyumov-Gerasimenko from Radio-Wave Spectroscopy,,” *Astronomy & Astrophysics* **672** (2023), A170, DOI: [10.1051/0004-6361/202245672](https://doi.org/10.1051/0004-6361/202245672).
- Biver, N., Bockelée-Morvan, D., Paubert, G., Moreno, R., Crovisier, J., Boissier, J., Bertrand, E., Boussier, H., Kugel, F., McKay, A., Dello Russo, N. & DiSanti, M. A., “The Extraordinary Composition of the Blue Comet C/2016 R2 (PanSTARRS)”, *Astronomy & Astrophysics* **619** (2018), A127, DOI: [10.1051/0004-6361/201833449](https://doi.org/10.1051/0004-6361/201833449).
- Biver, N., “Molécules Mères Cométaires : Observations et Modélisations”, PhD thesis, Université Paris VII, 1997.
- Biver, N., Russo, N. D., Opitom, C. & Rubin, M., *Chemistry of Comet Atmospheres*, 2022, DOI: [10.48550/ARXIV.2207.04800](https://doi.org/10.48550/ARXIV.2207.04800).
- Blake, G. A., Sutton, E. C., Masson, C. R. & Phillips, T. G., “Molecular Abundances in OMC-1 - The Chemical Composition of Interstellar Molecular Clouds and the Influence of Massive Star Formation”, *The Astrophysical Journal* **315** (1987), p. 621, DOI: [10.1086/165165](https://doi.org/10.1086/165165).
- Bockelee-Morvan, D., “A Model for the Excitation of Water in Comets”, *Astronomy and Astrophysics* **181** (1987), pp. 169–181, ISSN: 0004-6361.
- Bockelee-Morvan, D., Crovisier, J., Colom, P. & Despois, D., “The Rotational Lines of Methanol in Comets Austin 1990 V and Levy 1990 XX.”, *Astronomy and Astrophysics* **287** (1994), pp. 647–665, ISSN: 0004-6361.

-
- Bockelée-Morvan, D. & Biver, N., “The Composition of Cometary Ices”, *Philosophical Transactions of the Royal Society A: Mathematical, Physical and Engineering Sciences* **375** (2017), p. 20160252, DOI: [10.1098/rsta.2016.0252](https://doi.org/10.1098/rsta.2016.0252).
- Bockelée-Morvan, D., Biver, N., Colom, P., Crovisier, J., Henry, F., Lecacheux, A., Davies, J. K., Dent, W. R. & Weaver, H. A., “The Outgassing and Composition of Comet 19P/Borrelly from Radio Observations”, *Icarus* **167** (2004), pp. 113–128, DOI: [10.1016/j.icarus.2003.04.001](https://doi.org/10.1016/j.icarus.2003.04.001).
- Bøgelund, E. G. & Hogerheijde, M. R., “Exploring the Volatile Composition of Comets C/2012 F6 (Lemmon) and C/2012 S1 (ISON) with ALMA”, *Astronomy & Astrophysics* **604** (2017), A131, DOI: [10.1051/0004-6361/201629197](https://doi.org/10.1051/0004-6361/201629197).
- Bogey, M., Demuynck, C. & Destombes, J., “Millimeter and Submillimeter Wave Spectrum of CS ($^1\Sigma$) in High Vibrational States: Isotopic Dependence of Dunham Coefficients”, *Journal of Molecular Spectroscopy* **95** (1982), pp. 35–42, DOI: [10.1016/0022-2852\(82\)90234-X](https://doi.org/10.1016/0022-2852(82)90234-X).
- Boissier, J., Bockelée-Morvan, D., Biver, N., Crovisier, J., Despois, D., Marsden, B. G. & Moreno, R., “Interferometric Imaging of the Sulfur-Bearing Molecules H $_2$ S, SO, and CS in Comet C/1995 O1 (Hale-Bopp)”, *Astronomy & Astrophysics* **475** (2007), pp. 1131–1144, DOI: [10.1051/0004-6361:20078380](https://doi.org/10.1051/0004-6361:20078380).
- Boogert, A. C. A., Schutte, W. A., Helmich, F. P., Tielens, A. G. G. M. & Wooden, D. H., “Infrared Observations and Laboratory Simulations of Interstellar CH $_4$ and SO $_2$ ”, *Astronomy & Astrophysics* **317** (1997), pp. 929–941, ISSN: 0004-6361.
- Born, M. & Oppenheimer, R., “Zur Quantentheorie Der Moleküle”, *Annalen der Physik* **389** (1927), pp. 457–484, DOI: [10.1002/andp.19273892002](https://doi.org/10.1002/andp.19273892002).
- Boys, S. F., “Electronic Wave Functions - I. A General Method of Calculation for the Stationary States of Any Molecular System”, *Proceedings of the Royal Society of London. Series A. Mathematical and Physical Sciences* **200** (1950), pp. 542–554, DOI: [10.1098/rspa.1950.0036](https://doi.org/10.1098/rspa.1950.0036).
- Boys, S. & Bernardi, F., “The Calculation of Small Molecular Interactions by the Differences of Separate Total Energies. Some Procedures with Reduced Errors”, *Molecular Physics* **19** (1970), pp. 553–566, DOI: [10.1080/00268977000101561](https://doi.org/10.1080/00268977000101561).
- Buffa, G., “Hyperfine-Resolved Transition Rates of the DCO $^+$ Ion by Collisions with Helium: DCO $^+$ -He Transition Rates”, *Monthly Notices of the Royal Astronomical Society* (2012), no–no, DOI: [10.1111/j.1365-2966.2012.20347.x](https://doi.org/10.1111/j.1365-2966.2012.20347.x).

-
- Bustreel, R., Demuynck-Marliere, C., Destombes, J. & Journal, G., “Microwave Spectroscopy in an RF Plasma: Highly Excited Vibrational States of CS ($\nu \leq 14$)”, *Chemical Physics Letters* **67** (1979), pp. 178–182, DOI: [10.1016/0009-2614\(79\)87132-8](https://doi.org/10.1016/0009-2614(79)87132-8).
- Cabezas, C., Agúndez, M., Marcelino, N., Tercero, B., Endo, Y., Fuentetaja, R., Pardo, J. R., De Vicente, P. & Cernicharo, J., “Discovery of the Elusive Thioketenylum, HCCS⁺, in TMC-1”, *Astronomy & Astrophysics* **657** (2022), p. L4, DOI: [10.1051/0004-6361/202142815](https://doi.org/10.1051/0004-6361/202142815).
- Calmonte, U., Altwegg, K., Balsiger, H., Berthelier, J. J., Bieler, A., Cessateur, G., Dhooghe, F., Van Dishoeck, E. F., Fiethe, B., Fuselier, S. A., Gasc, S., Gombosi, T. I., Hässig, M., Le Roy, L., Rubin, M., Sémon, T., Tzou, C.-Y. & Wampfler, S. F., “Sulphur-Bearing Species in the Coma of Comet 67P/Churyumov–Gerasimenko”, *Monthly Notices of the Royal Astronomical Society* **462** (2016), S253–S273, DOI: [10.1093/mnras/stw2601](https://doi.org/10.1093/mnras/stw2601).
- Cami, J., Bernard-Salas, J., Peeters, E. & Malek, S. E., “Detection of C₆₀ and C₇₀ in a Young Planetary Nebula”, *Science* **329** (2010), pp. 1180–1182, DOI: [10.1126/science.1192035](https://doi.org/10.1126/science.1192035).
- Carruthers, G. R., “Rocket Observation of Interstellar Molecular Hydrogen”, *The Astrophysical Journal* **161** (1970), p. L81, DOI: [10.1086/180575](https://doi.org/10.1086/180575).
- Ceccarelli, C., Caselli, P., Bockelée-Morvan, D., Mousis, O., Pizzarello, S., Robert, F. & Semenov, D., “Deuterium Fractionation: The Ariadne’s Thread from the Precollapse Phase to Meteorites and Comets Today”, *Protostars and Planets VI*, University of Arizona Press, 2014, DOI: [10.2458/azu_uapress_9780816531240-ch037](https://doi.org/10.2458/azu_uapress_9780816531240-ch037).
- Cernicharo, J., Cabezas, C., Endo, Y., Marcelino, N., Agúndez, M., Tercero, B., Gallego, J. D. & De Vicente, P., “Space and Laboratory Discovery of HC₃S⁺”, *Astronomy & Astrophysics* **646** (2021), p. L3, DOI: [10.1051/0004-6361/202040013](https://doi.org/10.1051/0004-6361/202040013).
- Cernicharo, J., Fuentetaja, R., Agúndez, M., Cabezas, C., Tercero, B., Marcelino, N. & De Vicente, P., “Detection of Vibrationally Excited C₆H in the Cold Prestellar Core TMC-1 with the QUIJOTE Line Survey”, *Astronomy & Astrophysics* **680** (2023), p. L4, DOI: [10.1051/0004-6361/202348495](https://doi.org/10.1051/0004-6361/202348495).
- Cernicharo, J., Guélin, M., Hein, H. & Kahane, C., “Sulfur in IRC+10216”, *Astronomy & Astrophysics* **181** (1987), p. 4.
- Cernicharo, J., Marcelino, N., Roueff, E., Gerin, M., Jiménez-Escobar, A. & Muñoz Caro, G. M., “Discovery of the Methoxy Radical, CH₃O, Toward B1: Dust Grain and Gas-

-
- Phase Chemistry in Cold Dark Clouds”, *The Astrophysical Journal* **759** (2012), p. L43, DOI: [10.1088/2041-8205/759/2/L43](https://doi.org/10.1088/2041-8205/759/2/L43).
- Cernicharo, J., Agúndez, M., Cabezas, C., Marcelino, N., Tercero, B., Pardo, J. R., Fuente-taja, R. & De Vicente, P., “The QUIJOTE Line Survey of TMC-1”, *EPJ Web of Conferences* **265** (2022), ed. by L. Bouscasse, C. Kramer & F. Gueth, p. 00041, DOI: [10.1051/epjconf/202226500041](https://doi.org/10.1051/epjconf/202226500041).
- Chefdeville, S., Stoecklin, T., Naulin, C., Jankowski, P., Szalewicz, K., Faure, A., Costes, M. & Bergeat, A., “Experimental and Theoretical Analysis of Low-Energy CO + H₂ Inelastic Collisions”, *The Astrophysical Journal* **799** (2015), p. L9, DOI: [10.1088/2041-8205/799/1/L9](https://doi.org/10.1088/2041-8205/799/1/L9).
- Cheung, A. C., Rank, D. M., Townes, C. H., Thornton, D. D. & Welch, W. J., “Detection of NH₃ Molecules in the Interstellar Medium by Their Microwave Emission”, *Physical Review Letters* **21** (1968), pp. 1701–1705, DOI: [10.1103/PhysRevLett.21.1701](https://doi.org/10.1103/PhysRevLett.21.1701).
- Cheung, A. C., Rank, D. M., Townes, C. H., Thornton, D. D. & Welch, W. J., “Detection of Water in Interstellar Regions by Its Microwave Radiation”, *Nature* **221** (1969), pp. 626–628, DOI: [10.1038/221626a0](https://doi.org/10.1038/221626a0).
- Čížek, J., “On the Correlation Problem in Atomic and Molecular Systems. Calculation of Wavefunction Components in Ursell-Type Expansion Using Quantum-Field Theoretical Methods”, *The Journal of Chemical Physics* **45** (1966), pp. 4256–4266, DOI: [10.1063/1.1727484](https://doi.org/10.1063/1.1727484).
- Čížek, J., “On the Use of the Cluster Expansion and the Technique of Diagrams in Calculations of Correlation Effects in Atoms and Molecules”, *Advances in Chemical Physics*, ed. by R. LeFevbre & C. Moser, 1st ed., vol. 14, Wiley, 1969, pp. 35–89, DOI: [10.1002/9780470143599.ch2](https://doi.org/10.1002/9780470143599.ch2).
- Cordiner, M. A., Coulson, I. M., Garcia-Berrios, E., Qi, C., Lique, F., Żołtowski, M., De Val-Borro, M., Kuan, Y.-J., Ip, W.-H., Mairs, S., Roth, N. X., Charnley, S. B., Milam, S. N., Tseng, W.-L. & Chuang, Y.-L., “A SUBLIME 3D Model for Cometary Coma Emission: The Hypervolatile-rich Comet C/2016 R2 (PanSTARRS)”, *The Astrophysical Journal* **929** (2022), p. 38, DOI: [10.3847/1538-4357/ac5893](https://doi.org/10.3847/1538-4357/ac5893).
- Cordiner, M. A., Milam, S. N., Biver, N., Bockelée-Morvan, D., Roth, N. X., Bergin, E. A., Jehin, E., Remijan, A. J., Charnley, S. B., Mumma, M. J., Boissier, J., Crovisier, J., Paganini, L., Kuan, Y.-J. & Lis, D. C., “Unusually High CO Abundance of the First Active Interstellar Comet”, *Nature Astronomy* **4** (2020), pp. 861–866, DOI: [10.1038/s41550-020-1087-2](https://doi.org/10.1038/s41550-020-1087-2).

-
- Cordiner, M. A., Roth, N. X., Milam, S. N., Villanueva, G. L., Bockelée-Morvan, D., Remijan, A. J., Charnley, S. B., Biver, N., Lis, D. C., Qi, C., Bonev, B. P., Crovisier, J. & Boissier, J., “Gas Sources from the Coma and Nucleus of Comet 46P/Wirtanen Observed Using ALMA”, *The Astrophysical Journal* **953** (2023), p. 59, DOI: [10.3847/1538-4357/ace0bc](https://doi.org/10.3847/1538-4357/ace0bc).
- Corey, G. C. & McCourt, F. R., “Inelastic Differential and Integral Cross Sections for $2S+1\Sigma$ Linear Molecule- $1S$ Atom Scattering: The Use of Hund’s Case (b) Representation”, *The Journal of Chemical Physics* **87** (1983), pp. 2723–2730, DOI: [10.1021/j100238a009](https://doi.org/10.1021/j100238a009).
- Corey, G. C., Alexander, M. H. & Schaefer, J., “Quantum Studies of Inelastic Collisions of O_2 ($X^3\Sigma_g^-$) with He: Polarization Effects and Collisional Propensity Rules”, *The Journal of Chemical Physics* **85** (1986), pp. 2726–2737, DOI: [10.1063/1.451029](https://doi.org/10.1063/1.451029).
- Coulson, C. & Fischer, I., “XXXIV. Notes on the Molecular Orbital Treatment of the Hydrogen Molecule”, *The London, Edinburgh, and Dublin Philosophical Magazine and Journal of Science* **40** (1949), pp. 386–393, DOI: [10.1080/14786444908521726](https://doi.org/10.1080/14786444908521726).
- Cybulski, S. M. & Toczyłowski, R. R., “Ground State Potential Energy Curves for He_2 , Ne_2 , Ar_2 , He–Ne, He–Ar, and Ne–Ar: A Coupled-Cluster Study”, *The Journal of Chemical Physics* **111** (1999), pp. 10520–10528, DOI: [10.1063/1.480430](https://doi.org/10.1063/1.480430).
- D’Hendecourt, L. & Jourdain de Muizon, M., “The Discovery of Interstellar Carbon Dioxide”, *Astronomy & Astrophysics* **223** (1989), pp. L5–L8.
- Dagdikian, P. J., “Hyperfine Excitation of C_2H in Collisions with *Ortho*- and *Para*- H_2 ”, *Monthly Notices of the Royal Astronomical Society* **479** (2018), pp. 3227–3231, DOI: [10.1093/mnras/sty1568](https://doi.org/10.1093/mnras/sty1568).
- Dagdikian, P. J., “Rotational Excitation of Methanol in Collisions with Molecular Hydrogen”, *Monthly Notices of the Royal Astronomical Society* **527** (2023), pp. 2209–2213, DOI: [10.1093/mnras/stad3303](https://doi.org/10.1093/mnras/stad3303).
- Daly, P. W. & Oka, T., “Microwave Studies of Collision-Induced Transitions between Rotational Levels. VII Collisions between NH_3 and Nonpolar Molecules”, *The Journal of Chemical Physics* **53** (1970), pp. 3272–3278, DOI: [10.1063/1.1674477](https://doi.org/10.1063/1.1674477).
- Daniel, F., Dubernet, M.-L. & Meuwly, M., “Selective Hyperfine Excitation of N_2H^+ by He: Potential Energy Surface, Cross Sections, and Propensity Rules”, *The Journal of Chemical Physics* **121** (2004), pp. 4540–4549, DOI: [10.1063/1.1774978](https://doi.org/10.1063/1.1774978).

-
- Davison, W. D., “Rotational Energy Transfer in Molecular Collisions: Transitions in *Para*-Hydrogen”, *Discussions of the Faraday Society* **33** (1962), p. 71, DOI: [10.1039/df9623300071](https://doi.org/10.1039/df9623300071).
- Dawes, R. & Quintas-Sánchez, E., “The Construction of *Ab Initio*-Based Potential Energy Surfaces”, *Reviews in Computational Chemistry*, ed. by A. L. Parrill & K. B. Lipkowitz, 1st ed., Wiley, 2018, pp. 199–263, DOI: [10.1002/9781119518068.ch5](https://doi.org/10.1002/9781119518068.ch5).
- Dawes, R., Wang, X.-G., Jasper, A. W. & Carrington, T., “Nitrous Oxide Dimer: A New Potential Energy Surface and Rovibrational Spectrum of the Nonpolar Isomer”, *The Journal of Chemical Physics* **133** (2010), p. 134304, DOI: [10.1063/1.3494542](https://doi.org/10.1063/1.3494542).
- De Jong, T., Dalgarno, A. & Boland, W., “Hydrostatic Models of Molecular Clouds”, *Symposium - International Astronomical Union* **87** (1980), pp. 177–181, DOI: [10.1017/S0074180900072491](https://doi.org/10.1017/S0074180900072491).
- Demes, S., Bop, C. T., Ben Khalifa, M. & Lique, F., “First Close-Coupling Study of the Excitation of a Large Cyclic Molecule: Collision of *c*-C₅H₆ with He”, *Physical Chemistry Chemical Physics* **26** (2024), pp. 16829–16837, DOI: [10.1039/D4CP01380H](https://doi.org/10.1039/D4CP01380H).
- Denis-Alpizar, O., Stoecklin, T., Guilloteau, S. & Dutrey, A., “New Rate Coefficients of CS in Collision with *Para*- and *Ortho*-H₂ and Astrophysical Implications”, *Monthly Notices of the Royal Astronomical Society* **478** (2018), pp. 1811–1817, DOI: [10.1093/mnras/sty1177](https://doi.org/10.1093/mnras/sty1177).
- Denis-Alpizar, O., Stoecklin, T., Halvick, P. & Dubernet, M.-L., “The Interaction of He with Vibrating HCN: Potential Energy Surface, Bound States, and Rotationally Inelastic Cross Sections”, *The Journal of Chemical Physics* **139** (2013), p. 034304, DOI: [10.1063/1.4813125](https://doi.org/10.1063/1.4813125).
- Denis-Alpizar, O., Stoecklin, T., Halvick, P., Dubernet, M.-L. & Marinakis, S., “Potential Energy Surface and Rovibrational Energy Levels of the H₂-CS van Der Waals Complex”, *The Journal of Chemical Physics* **137** (2012), p. 234301, DOI: [10.1063/1.4771658](https://doi.org/10.1063/1.4771658).
- Despois, D., Biver, N., Bockelée-Morvan, D. & Crovisier, J., “Observations of Molecules in Comets”, *Proceedings of the International Astronomical Union* **1** (2006), p. 469, DOI: [10.1017/S1743921306007484](https://doi.org/10.1017/S1743921306007484).
- Dixon, R. N. & Field, D., “Rotational Energy Transfer in Collisions between Orbitally Non-Degenerate Open-Shell Systems”, *Proceedings of the Royal Society of London. A. Mathematical and Physical Sciences* **366** (1979), pp. 225–246, DOI: [10.1098/rspa.1979.0049](https://doi.org/10.1098/rspa.1979.0049).

-
- Douglas, A. E. & Herzberg, G., “Note on CH⁺ in Interstellar Space and in the Laboratory”, *The Astrophysical Journal* **94** (1941), p. 381, DOI: [10.1086/144342](https://doi.org/10.1086/144342).
- Draine, B. T., *Physics of the Interstellar and Intergalactic Medium*, Princeton Series in Astrophysics, Princeton, N.J: Princeton University Press, 2011, ISBN: 978-0-691-12214-4.
- Dubernet, M. L. et al., “BASECOL2023 Scientific Content”, *Astronomy & Astrophysics* **683** (2024), A40, DOI: [10.1051/0004-6361/202348233](https://doi.org/10.1051/0004-6361/202348233).
- Dubernet, M.-L. et al., “BASECOL2012: A Collisional Database Repository and Web Service within the Virtual Atomic and Molecular Data Centre (VAMDC)”, *Astronomy & Astrophysics* **553** (2013), A50, DOI: [10.1051/0004-6361/201220630](https://doi.org/10.1051/0004-6361/201220630).
- Dubernet, M. & Quintas-Sánchez, E., “First Quantum Study of the Rotational Excitation of HCN by *Para*-H₂O: Convergence of Quantum Results, Influence of the Potential Energy Surface, and Approximate Rate Coefficients of Interest for Cometary Atmospheres.”, *Molecular Astrophysics* **16** (2019), p. 100046, DOI: [10.1016/j.molap.2019.100046](https://doi.org/10.1016/j.molap.2019.100046).
- Dumouchel, F., Kłos, J., Toboła, R., Bacmann, A., Maret, S., Hily-Blant, P., Faure, A. & Lique, F., “Fine and Hyperfine Excitation of NH and ND by He: On the Importance of Calculating Rate Coefficients of Isotopologues”, *The Journal of Chemical Physics* **137** (2012), p. 114306, DOI: [10.1063/1.4753423](https://doi.org/10.1063/1.4753423).
- Dumouchel, F., Lique, F., Spielfiedel, A. & Feautrier, N., “Hyperfine Excitation of C₂H and C₂D by *Para*-H₂”, *Monthly Notices of the Royal Astronomical Society* **471** (2017), pp. 1849–1855, DOI: [10.1093/mnras/stx1707](https://doi.org/10.1093/mnras/stx1707).
- Dunham Jr., T., “Interstellar Neutral Potassium and Neutral Calcium”, *Publications of the Astronomical Society of the Pacific* **49** (1937), pp. 26–28, DOI: [10.1086/124759](https://doi.org/10.1086/124759).
- Dunning, T. H., “Gaussian Basis Sets for Use in Correlated Molecular Calculations. I. The Atoms Boron through Neon and Hydrogen”, *The Journal of Chemical Physics* **90** (1989), pp. 1007–1023, DOI: [10.1063/1.456153](https://doi.org/10.1063/1.456153).
- Eddington, A. S., “Bakerian Lecture — Diffuse Matter in Interstellar Space”, *Proceedings of the Royal Society of London. Series A, Containing Papers of a Mathematical and Physical Character* **111** (1926), pp. 424–456, DOI: [10.1098/rspa.1926.0076](https://doi.org/10.1098/rspa.1926.0076).
- Elsila, J. E., Glavin, D. P. & Dworkin, J. P., “Cometary Glycine Detected in Samples Returned by Stardust”, *Meteoritics & Planetary Science* **44** (2009), pp. 1323–1330, DOI: [10.1111/j.1945-5100.2009.tb01224.x](https://doi.org/10.1111/j.1945-5100.2009.tb01224.x).

-
- Endres, C. P., Schlemmer, S., Schilke, P., Stutzki, J. & Müller, H. S., “The Cologne Database for Molecular Spectroscopy, CDMS, in the Virtual Atomic and Molecular Data Centre, VAMDC”, *Journal of Molecular Spectroscopy* **327** (2016), pp. 95–104, DOI: [10.1016/j.jms.2016.03.005](https://doi.org/10.1016/j.jms.2016.03.005).
- Eyster, E. H., “Note on the Interpretation of Unidentified Interstellar Lines”, *The Astrophysical Journal* **86** (1937), pp. 486–488, DOI: [10.1086/143881](https://doi.org/10.1086/143881).
- Fabris, A. R. & Oka, T., “Microwave Studies of Collision-Induced Transitions Between Rotational Levels. VIII. Collisions Between NH₃ and Polar Molecules”, *The Journal of Chemical Physics* **78** (1983), pp. 3462–3466, DOI: [10.1063/1.445168](https://doi.org/10.1063/1.445168).
- Faure, A., Lique, F. & Loreau, J., “The Effect of CO-H₂O Collisions in the Rotational Excitation of Cometary CO”, *Monthly Notices of the Royal Astronomical Society* **493** (2020), pp. 776–782, DOI: [10.1093/mnras/staa242](https://doi.org/10.1093/mnras/staa242).
- Faure, A. & Lique, F., “The Impact of Collisional Rate Coefficients on Molecular Hyperfine Selective Excitation: Molecular Hyperfine Selective Excitation”, *Monthly Notices of the Royal Astronomical Society* **425** (2012), pp. 740–748, DOI: [10.1111/j.1365-2966.2012.21601.x](https://doi.org/10.1111/j.1365-2966.2012.21601.x).
- Faure, A., Bacmann, A., Boutherein, B. & Jacquot, R., “Excitation of Molecules and Atoms for Astrophysics (EMAA) Database” (2021), DOI: <https://dx.doi.org/10.17178/EMAA>.
- Faure, A., Jankowski, P., Stoecklin, T. & Szalewicz, K., “On the Importance of Full-Dimensionality in Low-Energy Molecular Scattering Calculations”, *Scientific Reports* **6** (2016a), p. 28449, DOI: [10.1038/srep28449](https://doi.org/10.1038/srep28449).
- Faure, A., Lique, F. & Remijan, A. J., “Collisional Excitation and Weak Maser Action of Interstellar Methanimine”, *The Journal of Physical Chemistry Letters* **9** (2018), pp. 3199–3204, DOI: [10.1021/acs.jpcllett.8b01431](https://doi.org/10.1021/acs.jpcllett.8b01431).
- Faure, A., Lique, F. & Wiesenfeld, L., “Collisional Excitation of HC₃N by *Para*- and *Ortho*-H₂”, *Monthly Notices of the Royal Astronomical Society* **460** (2016b), pp. 2103–2109, DOI: [10.1093/mnras/stw1156](https://doi.org/10.1093/mnras/stw1156).
- Ferrari, P., Berden, G., Redlich, B., Waters, L. B. F. M. & Bakker, J. M., “Laboratory Infrared Spectra and Fragmentation Chemistry of Sulfur Allotropes”, *Nature Communications* **15** (2024), p. 5928, DOI: [10.1038/s41467-024-50303-2](https://doi.org/10.1038/s41467-024-50303-2).
- Festou, M., “The Activity of Comet 29P/Schwassmann–Wachmann 1 Monitored through Its CO J=2→1 Radio Line”, *Icarus* **150** (2001), pp. 140–150, DOI: [10.1006/icar.2000.6553](https://doi.org/10.1006/icar.2000.6553).

-
- Festou, M. C., Keller, H. U. & Weaver, H. A., eds., *Comets II*, University of Arizona Press, 2004, DOI: [10.2307/j.ctv1v7zdzq5](https://doi.org/10.2307/j.ctv1v7zdzq5).
- Filacchione, G. et al., “Exposed Water Ice on the Nucleus of Comet 67P/Churyumov–Gerasimenko”, *Nature* **529** (2016a), pp. 368–372, DOI: [10.1038/nature16190](https://doi.org/10.1038/nature16190).
- Filacchione, G. et al., “Seasonal Exposure of Carbon Dioxide Ice on the Nucleus of Comet 67P/Churyumov–Gerasimenko”, *Science* **354** (2016b), pp. 1563–1566, DOI: [10.1126/science.aag3161](https://doi.org/10.1126/science.aag3161).
- Flower, D. R. & Lique, F., “Excitation of the Hyperfine Levels of ^{13}CN and C^{15}N in Collisions with H_2 at Low Temperatures”, *Monthly Notices of the Royal Astronomical Society* **446** (2015), pp. 1750–1755, DOI: [10.1093/mnras/stu2231](https://doi.org/10.1093/mnras/stu2231).
- Fock, V., “Näherungsmethode zur Lösung des quantenmechanischen Mehrkörperproblems”, *Zeitschrift für Physik* **61** (1930), pp. 126–148, DOI: [10.1007/BF01340294](https://doi.org/10.1007/BF01340294).
- Fortenberry, R. C., “A Vision for the Future of Astrochemistry in the Interstellar Medium by 2050”, *ACS Physical Chemistry Au* **4** (2024a), pp. 31–39, DOI: [10.1021/acspchemau.3c00043](https://doi.org/10.1021/acspchemau.3c00043).
- Fortenberry, R. C., “Quantum Chemistry and Astrochemistry: A Match Made in the Heavens”, *The Journal of Physical Chemistry A* **128** (2024b), pp. 1555–1565, DOI: [10.1021/acs.jpca.3c07601](https://doi.org/10.1021/acs.jpca.3c07601).
- Fuente, A., Cernicharo, J., Barcia, A. & Gómez-González, “Sulphur-Bearing Molecules in Dark Clouds”, *Astronomy & Astrophysics* **231** (1990), pp. 151–158.
- Fuentetaja, R., Agúndez, M., Cabezas, C., Lique, F., Godard Palluet, A., Tercero, B., Marcelino, N., Pardo, J. R., de Vicente, P. & Cernicharo, J., “Analysis of CS, CCS and CCCS Isotopologues in TMC-1 with the QUIJOTE Line Survey★” (in prep.).
- Furuya, K., Aikawa, Y., Sakai, N. & Yamamoto, S., “Carbon Isotope and Isotopomer Fractionation in Cold Dense Cloud Cores”, *The Astrophysical Journal* **731** (2011), p. 38, DOI: [10.1088/0004-637X/731/1/38](https://doi.org/10.1088/0004-637X/731/1/38).
- Garcia, J., Podeszwa, R. & Szalewicz, K., “SAPT Codes for Calculations of Intermolecular Interaction Energies”, *The Journal of Chemical Physics* **152** (2020), p. 184109, DOI: [10.1063/5.0005093](https://doi.org/10.1063/5.0005093).
- Garrod, R. T., Wakelam, V. & Herbst, E., “Non-Thermal Desorption from Interstellar Dust Grains via Exothermic Surface Reactions”, *Astronomy & Astrophysics* **467** (2007), pp. 1103–1115, DOI: [10.1051/0004-6361:20066704](https://doi.org/10.1051/0004-6361:20066704).

-
- Godard Palluet, A. & Lique, F., “Fine-Structure Excitation of CCS by He: Potential Energy Surface and Scattering Calculations”, *The Journal of Chemical Physics* **158** (2023a), p. 044303, DOI: [10.1063/5.0138470](https://doi.org/10.1063/5.0138470).
- Godard Palluet, A. & Lique, F., “The Effect of Isotopic Substitution on the Excitation of CCS Isotopologues in Molecular Clouds”, *Monthly Notices of the Royal Astronomical Society* **527** (2023b), pp. 6702–6711, DOI: [10.1093/mnras/stad3517](https://doi.org/10.1093/mnras/stad3517).
- Goldflam, R., Green, S. & Kouri, D. J., “Infinite Order Sudden Approximation for Rotational Energy Transfer in Gaseous Mixtures”, *The Journal of Chemical Physics* **67** (1977), pp. 4149–4161, DOI: [10.1063/1.435393](https://doi.org/10.1063/1.435393).
- Gordon, R. G., “New Method for Constructing Wavefunctions for Bound States and Scattering”, *The Journal of Chemical Physics* **51** (1969), pp. 14–25, DOI: [10.1063/1.1671699](https://doi.org/10.1063/1.1671699).
- Grasset, O., Dougherty, M., Coustenis, A., Bunce, E., Erd, C., Titov, D., Blanc, M., Coates, A., Drossart, P., Fletcher, L., Hussmann, H., Jaumann, R., Krupp, N., Lebreton, J.-P., Prieto-Ballesteros, O., Tortora, P., Tosi, F. & Van Hoolst, T., “JUper ICy Moons Explorer (JUICE): An ESA Mission to Orbit Ganymede and to Characterise the Jupiter System”, *Planetary and Space Science* **78** (2013), pp. 1–21, DOI: [10.1016/j.pss.2012.12.002](https://doi.org/10.1016/j.pss.2012.12.002).
- Gratier, P., Majumdar, L., Ohishi, M., Roueff, E., Loison, J. C., Hickson, K. M. & Wakelam, V., “A New Reference Chemical Composition for TMC-1”, *The Astrophysical Journal Supplement Series* **225** (2016), p. 25, DOI: [10.3847/0067-0049/225/2/25](https://doi.org/10.3847/0067-0049/225/2/25).
- Green, S., “Rotational Excitation in H₂–H₂ Collisions: Close-coupling Calculations”, *The Journal of Chemical Physics* **62** (1975), pp. 2271–2277, DOI: [10.1063/1.430752](https://doi.org/10.1063/1.430752).
- Green, S., “Collisional Excitation of Interstellar Molecules: Linear Molecules CO, CS, OCS, and HC₃N”, *The Astrophysical Journal Supplement Series* **37** (1978), p. 26.
- Gunnarsson, M., “Icy Grains as a Source of CO in Comet 29P/Schwassmann-Wachmann 1”, *Astronomy & Astrophysics* **398** (2003), pp. 353–361, DOI: [10.1051/0004-6361:20021610](https://doi.org/10.1051/0004-6361:20021610).
- Halfen, D. T., Ilyushin, V. V. & Ziurys, L. M., “Insights Into Surface Hydrogenation in the Interstellar Medium: Observations of Methanimine and Methyl Amine in Sgr B2(N)”, *The Astrophysical Journal* **767** (2013), p. 66, DOI: [10.1088/0004-637X/767/1/66](https://doi.org/10.1088/0004-637X/767/1/66).
- Hartree, D. R., “The Wave Mechanics of an Atom with a Non-Coulomb Central Field. Part I. Theory and Methods”, *Mathematical Proceedings of the Cambridge Philosophical Society* **24** (1928), pp. 89–110, DOI: [10.1017/S0305004100011919](https://doi.org/10.1017/S0305004100011919).

-
- Hays, B. M., Gupta, D., Guillaume, T., Abdelkader Khedaoui, O., Cooke, I. R., Thibault, F., Lique, F. & Sims, I. R., “Collisional Excitation of HNC by He Found to Be Stronger than for Structural Isomer HCN in Experiments at the Low Temperatures of Interstellar Space”, *Nature Chemistry* **14** (2022), pp. 811–815, DOI: [10.1038/s41557-022-00936-x](https://doi.org/10.1038/s41557-022-00936-x).
- Hegarty, D. & Robb, M. A., “Application of Unitary Group Methods to Configuration Interaction Calculations”, *Molecular Physics* **38** (1979), pp. 1795–1812, DOI: [10.1080/00268977900102871](https://doi.org/10.1080/00268977900102871).
- Herzberg, G., *Molecular Spectra and Molecular Structure. 3: Electronic Spectra and Electronic Structure of Polyatomic Molecules*, New York: van Nostrand Reinhold Comp, 1966, ISBN: 978-0-442-03387-3.
- Herzberg, G. & Herzberg, G., *Infrared and Raman Spectra of Polyatomic Molecules*, 22. print, *Molecular Spectra and Molecular Structure / by Gerhard Herzberg 2*, New York: van Nostrand, 1987, ISBN: 978-0-442-03386-6.
- Hirota, T., Ito, T. & Yamamoto, S., “L1521E: A Starless Core in the Early Evolutionary Stage?”, *The Astrophysical Journal* **565** (2002), pp. 359–363, DOI: [10.1086/324476](https://doi.org/10.1086/324476).
- Hrodmarsson, H. R. & Van Dishoeck, E. F., “Photodissociation and Photoionization of Molecules of Astronomical Interest: Updates to the Leiden Photodissociation and Photoionization Cross Section Database”, *Astronomy & Astrophysics* **675** (2023), A25, DOI: [10.1051/0004-6361/202346645](https://doi.org/10.1051/0004-6361/202346645).
- Huber, K. P. & Herzberg, G., *Molecular Spectra and Molecular Structure*, Boston, MA: Springer US, 1979, DOI: [10.1007/978-1-4757-0961-2](https://doi.org/10.1007/978-1-4757-0961-2).
- Hutson, J. & Green, S., *Molscat Computer Program, Version 14, Distributed by Collaborative Computational Project No. 6 of the UK Science and Engineering Research Council*, 1994.
- Hutson, J. & Green, S., *Molscat: A Program for Non-Reactive Quantum Scattering Calculation on Atomic and Molecular Collisions, Version 2022.0*, 2022.
- Hutson, J. M. & Le Sueur, C. R., “Molscat: A Program for Non-Reactive Quantum Scattering Calculations on Atomic and Molecular Collisions”, *Computer Physics Communications* **241** (2019), pp. 9–18, DOI: [10.1016/j.cpc.2019.02.014](https://doi.org/10.1016/j.cpc.2019.02.014).
- Ikeda, M., Sekimoto, Y. & Yamamoto, S., “Fourier Transform Microwave Spectroscopy of ^{13}C -Substituted CCS Radicals”, *Journal of Molecular Spectroscopy* **185** (1997), pp. 21–25, DOI: [10.1006/jmsp.1997.7352](https://doi.org/10.1006/jmsp.1997.7352).

-
- Irvine, W. M., Schloerb, F. P., Crovisier, J., Fegley Jr., B. & Mumma, M. J., *Comets: A Link Between Interstellar and Nebular Chemistry*, 2000, p. 1159.
- Jankowski, P., McKellar, A. R. W. & Szalewicz, K., “Theory Untangles the High-Resolution Infrared Spectrum of the *Ortho*-H₂-CO van Der Waals Complex”, *Science* **336** (2012), pp. 1147–1150, DOI: [10.1126/science.1221000](https://doi.org/10.1126/science.1221000).
- Jansen, G., “Symmetry-adapted Perturbation Theory Based on Density Functional Theory for Noncovalent Interactions”, *WIREs Computational Molecular Science* **4** (2014), pp. 127–144, DOI: [10.1002/wcms.1164](https://doi.org/10.1002/wcms.1164).
- Jenkins, E. B., “Element Abundances in the Interstellar Atomic Material”, *Interstellar Processes*, ed. by D. J. Hollenbach & H. A. Thronson, vol. 134, Dordrecht: Springer Netherlands, 1987, pp. 533–559, DOI: [10.1007/978-94-009-3861-8_20](https://doi.org/10.1007/978-94-009-3861-8_20).
- Jensen, F., *Introduction to Computational Chemistry*, 2nd ed, Chichester, England: John Wiley & Sons, 2007, ISBN: 978-0-470-05804-6.
- Jensen, P. & Bunker, P. R., eds., *Computational Molecular Spectroscopy*, Chichester ; New York: Wiley, 2000, ISBN: 978-0-471-48998-6.
- Jeziorski, B., Moszynski, R. & Szalewicz, K., “Perturbation Theory Approach to Intermolecular Potential Energy Surfaces of van Der Waals Complexes”, *Chemical Reviews* **94** (1994), pp. 1887–1930, DOI: [10.1021/cr00031a008](https://doi.org/10.1021/cr00031a008).
- Jiménez-Escobar, A. & Muñoz Caro, G. M., “Sulfur Depletion in Dense Clouds and Circumstellar Regions: I. H₂S Ice Abundance and UV-photochemical Reactions in the H₂O-matrix”, *Astronomy & Astrophysics* **536** (2011), A91, DOI: [10.1051/0004-6361/201014821](https://doi.org/10.1051/0004-6361/201014821).
- Johnson, B., “The Multichannel Log-Derivative Method for Scattering Calculations”, *Journal of Computational Physics* **13** (1973), pp. 445–449, DOI: [10.1016/0021-9991\(73\)90049-1](https://doi.org/10.1016/0021-9991(73)90049-1).
- Joy, C., Mandal, B., Bostan, D., Dubernet, M.-L. & Babikov, D., “Mixed Quantum/Classical Theory (MQCT) Approach to the Dynamics of Molecule–Molecule Collisions in Complex Systems”, *Faraday Discussions* (2024), pp. 225–248, DOI: [10.1039/D3FD00166K](https://doi.org/10.1039/D3FD00166K).
- Kaifu, N., Ohishi, M., Kawaguchi, K., Saito, S., Yamamoto, S., Miyaji, T., Miyazawa, K., Ishikawa, S.-i., Noumaru, C., Harasawa, S., Okuda, M. & Suzuki, H., “A 8.8–50 GHz Complete Spectral Line Survey toward TMC-1 I. Survey Data”, *Publications of the Astronomical Society of Japan* **56** (2004), pp. 69–173, DOI: [10.1093/pasj/56.1.69](https://doi.org/10.1093/pasj/56.1.69).
- Kalugina, Y. N., Faure, A., Van Der Avoird, A., Walker, K. & Lique, F., “Interaction of H₂O with CO: Potential Energy Surface, Bound States and Scattering Calcula-

-
- tions”, *Physical Chemistry Chemical Physics* **20** (2018), pp. 5469–5477, DOI: [10.1039/C7CP06275C](https://doi.org/10.1039/C7CP06275C).
- Kalugina, Y., Lique, F. & Klos, J., “Hyperfine Collisional Rate Coefficients of CN with $H_2(J=0)$: Rate Coefficients of CN with *Para*- $H_2(J=0)$ ”, *Monthly Notices of the Royal Astronomical Society* **422** (2012), pp. 812–818, DOI: [10.1111/j.1365-2966.2012.20660.x](https://doi.org/10.1111/j.1365-2966.2012.20660.x).
- Kendall, R. A., Dunning, T. H. & Harrison, R. J., “Electron Affinities of the First-Row Atoms Revisited. Systematic Basis Sets and Wave Functions”, *The Journal of Chemical Physics* **96** (1992), pp. 6796–6806, DOI: [10.1063/1.462569](https://doi.org/10.1063/1.462569).
- King, L. V., “The Density of Molecules in Interstellar Space”, *Nature* **95** (1915), pp. 701–703, DOI: [10.1038/095701b0](https://doi.org/10.1038/095701b0).
- Knauth, D. C., Andersson, B.-G., McCandliss, S. R. & Warren Moos, H., “The Interstellar N_2 Abundance Towards HD 124314 from Far-Ultraviolet Observations”, *Nature* **429** (2004), pp. 636–638, DOI: [10.1038/nature02614](https://doi.org/10.1038/nature02614).
- Knizia, G., Adler, T. B. & Werner, H.-J., “Simplified CCSD(T)-F12 Methods: Theory and Benchmarks”, *The Journal of Chemical Physics* **130** (2009), p. 054104, DOI: [10.1063/1.3054300](https://doi.org/10.1063/1.3054300).
- Knowles, P. J., Hampel, C. & Werner, H.-J., “Coupled Cluster Theory for High Spin, Open Shell Reference Wave Functions”, *The Journal of Chemical Physics* **99** (1993), pp. 5219–5227, DOI: [10.1063/1.465990](https://doi.org/10.1063/1.465990).
- Knowles, P. J., Hampel, C. & Werner, H.-J., “Erratum: “Coupled Cluster Theory for High Spin, Open Shell Reference Wave Functions [*J. Chem. Phys.* **99** , 5219 (1993)]””, *The Journal of Chemical Physics* **112** (2000), pp. 3106–3107, DOI: [10.1063/1.480886](https://doi.org/10.1063/1.480886).
- Konings, M., Desrousseaux, B., Lique, F. & Loreau, J., “Benchmarking an Improved Statistical Adiabatic Channel Model for Competing Inelastic and Reactive Processes”, *The Journal of Chemical Physics* **155** (2021), p. 104302, DOI: [10.1063/5.0062388](https://doi.org/10.1063/5.0062388).
- Labiad, H., Fournier, M., Mertens, L. A., Faure, A., Carty, D., Stoecklin, T., Jankowski, P., Szalewicz, K., Le Picard, S. D. & Sims, I. R., “Absolute Measurements of State-to-State Rotational Energy Transfer between CO and H_2 at Interstellar Temperatures”, *Physical Review A* **105** (2022), p. L020802, DOI: [10.1103/PhysRevA.105.L020802](https://doi.org/10.1103/PhysRevA.105.L020802).
- Le Floch, A., “Revised Molecular Constants for the Ground State of CO”, *Molecular Physics* **72** (1991), pp. 133–144, DOI: [10.1080/00268979100100081](https://doi.org/10.1080/00268979100100081).

-
- Lique, F., Spielfiedel, A. & Cernicharo, J., “Rotational Excitation of Carbon Monosulfide by Collisions with Helium”, *Astronomy & Astrophysics* **451** (2006), pp. 1125–1132, DOI: [10.1051/0004-6361:20054363](https://doi.org/10.1051/0004-6361:20054363).
- Lique, F., Spielfiedel, A., Dubernet, M.-L. & Feautrier, N., “Rotational Excitation of Sulfur Monoxide by Collisions with Helium at Low Temperature”, *The Journal of Chemical Physics* **123** (2005), p. 134316, DOI: [10.1063/1.2004994](https://doi.org/10.1063/1.2004994).
- Lique, F., Bulut, N. & Roncero, O., “Hyperfine Excitation of OH⁺ by H”, *Monthly Notices of the Royal Astronomical Society* **461** (2016), pp. 4477–4481, DOI: [10.1093/mnras/stw1638](https://doi.org/10.1093/mnras/stw1638).
- Liszt, H. S. & Turner, B. E., “Microwave Detection of Interstellar NO”, *The Astrophysical Journal* **224** (1978), p. L73, DOI: [10.1086/182762](https://doi.org/10.1086/182762).
- Loison, J.-C., Wakelam, V., Gratier, P. & Hickson, K. M., “Gas-Grain Model of Carbon Fractionation in Dense Molecular Clouds”, *Monthly Notices of the Royal Astronomical Society* **498** (2020), pp. 4663–4679, DOI: [10.1093/mnras/staa2700](https://doi.org/10.1093/mnras/staa2700).
- Loreau, J., Faure, A. & Lique, F., “The Effect of Water and Electron Collisions in the Rotational Excitation of HF in Comets”, *Monthly Notices of the Royal Astronomical Society* **516** (2022), pp. 5964–5971, DOI: [10.1093/mnras/stac2378](https://doi.org/10.1093/mnras/stac2378).
- Loreau, J., Faure, A. & Lique, F., “Scattering of CO with H₂O: Statistical and Classical Alternatives to Close-Coupling Calculations”, *The Journal of Chemical Physics* **148** (2018a), p. 244308, DOI: [10.1063/1.5036819](https://doi.org/10.1063/1.5036819).
- Loreau, J., Kalugina, Y. N., Faure, A., Van Der Avoird, A. & Lique, F., “Potential Energy Surface and Bound States of the H₂O–HF Complex”, *The Journal of Chemical Physics* **153** (2020), p. 214301, DOI: [10.1063/5.0030064](https://doi.org/10.1063/5.0030064).
- Loreau, J., Lique, F. & Faure, A., “An Efficient Statistical Method to Compute Molecular Collisional Rate Coefficients”, *The Astrophysical Journal Letters* **853** (2018b), p. L5, DOI: [10.3847/2041-8213/aaa5fe](https://doi.org/10.3847/2041-8213/aaa5fe).
- Lupu, R. E., Feldman, P. D., Weaver, H. A. & Tozzi, G.-P., “The Fourth Positive System of Carbon Monoxide in the *Hubble Space Telescope* Spectra of Comets”, *The Astrophysical Journal* **670** (2007), pp. 1473–1484, DOI: [10.1086/522328](https://doi.org/10.1086/522328).
- Maki, A. G., “Microwave Spectra of Molecules of Astrophysical Interest VI. Carbonyl Sulfide and Hydrogen Cyanide”, *Journal of Physical and Chemical Reference Data* **3** (1974), pp. 221–244, DOI: [10.1063/1.3253139](https://doi.org/10.1063/1.3253139).

-
- Mandal, B. & Babikov, D., “Improved Temperature Dependence of Rate Coefficients for Rotational State-to-State Transitions in H₂O + H₂O Collisions”, *Astronomy & Astrophysics* **678** (2023a), A51, DOI: [10.1051/0004-6361/202346895](https://doi.org/10.1051/0004-6361/202346895).
- Mandal, B. & Babikov, D., “Rate Coefficients for Rotational State-to-State Transitions in H₂O + H₂O Collisions for Cometary and Planetary Applications, as Predicted by Mixed Quantum-Classical Theory”, *Astronomy & Astrophysics* **671** (2023b), A51, DOI: [10.1051/0004-6361/202245699](https://doi.org/10.1051/0004-6361/202245699).
- Mandal, B., Zoltowski, M., Cordiner, M., Lique, F. & Babikov, D., “Rotational State-to-State Transition Rate Coefficients for H₂O + H₂O Collisions at Nonequilibrium Conditions”, *Astronomy & Astrophysics* (2024), DOI: [10.1051/0004-6361/202450738](https://doi.org/10.1051/0004-6361/202450738).
- Manolopoulos, D. E., “An Improved Log Derivative Method for Inelastic Scattering”, *The Journal of Chemical Physics* **85** (1986), pp. 6425–6429, DOI: [10.1063/1.451472](https://doi.org/10.1063/1.451472).
- McGuire, B. A., “2021 Census of Interstellar, Circumstellar, Extragalactic, Protoplanetary Disk, and Exoplanetary Molecules”, *The Astrophysical Journal Supplement Series* **259** (2022), p. 30, DOI: [10.3847/1538-4365/ac2a48](https://doi.org/10.3847/1538-4365/ac2a48).
- McGuire, B. A., Martin-Drumel, M.-A., Lee, K. L. K., Stanton, J. F., Gottlieb, C. A. & McCarthy, M. C., “Vibrational Satellites of C₂S, C₃S, and C₄S: Microwave Spectral Taxonomy as a Stepping Stone to the Millimeter-Wave Band”, *Physical Chemistry Chemical Physics* **20** (2018), pp. 13870–13889, DOI: [10.1039/C8CP01102H](https://doi.org/10.1039/C8CP01102H).
- McGuire, B. A. & mcguiregroup, *Astromol*, 2021.
- McGuire, P. & Kouri, D. J., “Quantum Mechanical Close Coupling Approach to Molecular Collisions. J_z -Conserving Coupled States Approximation”, *The Journal of Chemical Physics* **60** (1974), pp. 2488–2499, DOI: [10.1063/1.1681388](https://doi.org/10.1063/1.1681388).
- McKellar, A., “Evidence for the Molecular Origin of Some Hitherto Unidentified Interstellar Lines”, *Publications of the Astronomical Society of the Pacific* **52** (1940), p. 187, DOI: [10.1086/125159](https://doi.org/10.1086/125159).
- Meier, R., Owen, T. C., Matthews, H. E., Jewitt, D. C., Bockelée-Morvan, D., Biver, N., Crovisier, J. & Gautier, D., “A Determination of the HDO/H₂O Ratio in Comet C/1995 O1 (Hale-Bopp)”, *Science* **279** (1998), pp. 842–844, DOI: [10.1126/science.279.5352.842](https://doi.org/10.1126/science.279.5352.842).
- Metz, M. P., Piszczatowski, K. & Szalewicz, K., “Automatic Generation of Intermolecular Potential Energy Surfaces”, *Journal of Chemical Theory and Computation* **12** (2016), pp. 5895–5919, DOI: [10.1021/acs.jctc.6b00913](https://doi.org/10.1021/acs.jctc.6b00913).

-
- Mihalas, D., *Stellar Atmospheres*, 2. ed, A Series of Books in Astronomy and Astrophysics, San Francisco: Freeman, 1978, ISBN: 978-0-7167-0359-4.
- Mihelcic, D. & Schindler, R. N., “ESR-spektroskopische Untersuchung Der Reaktion von Atomarem Wasserstoff Mit H₂S”, *Berichte der Bunsengesellschaft für physikalische Chemie* **74** (1970), pp. 1280–1288, DOI: [10.1002/bbpc.19700741213](https://doi.org/10.1002/bbpc.19700741213).
- Millar, T. J. & Herbst, E., “Organo-Sulfur Chemistry in Dense Interstellar Clouds”, *Astronomy & Astrophysics* **231** (1990), pp. 466–472.
- Müller, H. S. P., Thorwirth, S., Roth, D. A. & Winnewisser, G., “The Cologne Database for Molecular Spectroscopy, CDMS”, *Astronomy & Astrophysics* **370** (2001), pp. L49–L52, DOI: [10.1051/0004-6361:20010367](https://doi.org/10.1051/0004-6361:20010367).
- Müller, H. S., Schlöder, F., Stutzki, J. & Winnewisser, G., “The Cologne Database for Molecular Spectroscopy, CDMS: A Useful Tool for Astronomers and Spectroscopists”, *Journal of Molecular Structure* **742** (2005), pp. 215–227, DOI: [10.1016/j.molstruc.2005.01.027](https://doi.org/10.1016/j.molstruc.2005.01.027).
- Mumma, M. J. & Charnley, S. B., “The Chemical Composition of Comets—Emerging Taxonomies and Natal Heritage”, *Annual Review of Astronomy and Astrophysics* **49** (2011), pp. 471–524, DOI: [10.1146/annurev-astro-081309-130811](https://doi.org/10.1146/annurev-astro-081309-130811).
- Murakami, A., “A Quantum Chemical Study on the Linear C₂S and C₃S Molecules”, *The Astrophysical Journal* **357** (1990), p. 288, DOI: [10.1086/168916](https://doi.org/10.1086/168916).
- Murphy, J. S. & Boggs, J. E., “Collision Broadening of Rotational Absorption Lines. V. Pressure Broadening of Microwave Absorption Spectra Involving Asymmetric-Top Molecules”, *The Journal of Chemical Physics* **51** (1969), pp. 3891–3901, DOI: [10.1063/1.1672608](https://doi.org/10.1063/1.1672608).
- Naulin, C. & Costes, M., “Experimental Search for Scattering Resonances in Near Cold Molecular Collisions”, *International Reviews in Physical Chemistry* **33** (2014), pp. 427–446, DOI: [10.1080/0144235X.2014.957565](https://doi.org/10.1080/0144235X.2014.957565).
- Navarro-Almaida, D., Bop, C. T., Lique, F., Esplugues, G., Rodríguez-Baras, M., Kramer, C., Romero, C. E., Fuente, A., Caselli, P., Rivière-Marichalar, P., Kirk, J. M., Chacón-Tanarro, A., Roueff, E., Mroczkowski, T., Bhandarkar, T., Devlin, M., Dicker, S., Lowe, I., Mason, B., Sarazin, C. L. & Sievers, J., “Linking the Dust and Chemical Evolution: Taurus and Perseus: New Collisional Rates for HCN, HNC, and Their C, N, and H Isotopologues”, *Astronomy & Astrophysics* **670** (2023), A110, DOI: [10.1051/0004-6361/202245000](https://doi.org/10.1051/0004-6361/202245000).

-
- Ndaw, D., Bop, C. T., Dieye, G., Faye, N. A. B. & Lique, F., “The Excitation of CNCN in the Interstellar Medium: Hyperfine Resolved Rate Coefficients and Non-LTE Modelling”, *Monthly Notices of the Royal Astronomical Society* **503** (2021), pp. 5976–5983, DOI: [10.1093/mnras/stab775](https://doi.org/10.1093/mnras/stab775).
- Ndengué, S. A., Dawes, R. & Gatti, F., “Rotational Excitations in CO–CO Collisions at Low Temperature: Time-Independent and Multiconfigurational Time-Dependent Hartree Calculations”, *The Journal of Physical Chemistry A* **119** (2015), pp. 7712–7723, DOI: [10.1021/acs.jpca.5b01022](https://doi.org/10.1021/acs.jpca.5b01022).
- Neugebauer, M., Gloeckler, G., Gosling, J. T., Rees, A., Skoug, R., Goldstein, B. E., Armstrong, T. P., Combi, M. R., Makinen, T., McComas, D. J., Von Steiger, R., Zurbuchen, T. H., Smith, E. J., Geiss, J. & Lanzerotti, L. J., “Encounter of the *Ulysses* Spacecraft with the Ion Tail of Comet McNaught”, *The Astrophysical Journal* **667** (2007), pp. 1262–1266, DOI: [10.1086/521019](https://doi.org/10.1086/521019).
- Noga, J. & Bartlett, R. J., “Erratum: The Full CCSDT Model for Molecular Electronic Structure [J. Chem. Phys. **86**, 7041 (1987)]”, *The Journal of Chemical Physics* **89** (1988), pp. 3401–3401, DOI: [10.1063/1.455742](https://doi.org/10.1063/1.455742).
- Noga, J. & Bartlett, R. J., “The Full CCSDT Model for Molecular Electronic Structure”, *The Journal of Chemical Physics* **86** (1987), pp. 7041–7050, DOI: [10.1063/1.452353](https://doi.org/10.1063/1.452353).
- Öberg, K. I. & Bergin, E. A., “Astrochemistry and Compositions of Planetary Systems”, *Physics Reports* **893** (2021), pp. 1–48, DOI: [10.1016/j.physrep.2020.09.004](https://doi.org/10.1016/j.physrep.2020.09.004).
- Oka, T., “Microwave Studies of Collision-Induced Transitions between Rotational Levels. IV. Steady-State Measurements in NH₃”, *The Journal of Chemical Physics* **48** (1968a), pp. 4919–4928, DOI: [10.1063/1.1668157](https://doi.org/10.1063/1.1668157).
- Oka, T., “Microwave Studies of Collision-Induced Transitions between Rotational Levels. V. “Selection Rules” in NH₃–Rare-Gas Collisions”, *The Journal of Chemical Physics* **49** (1968b), pp. 3135–3145, DOI: [10.1063/1.1670561](https://doi.org/10.1063/1.1670561).
- Onishi, T., Mizuno, A., Kawamura, A., Tachihara, K. & Fukui, Y., “A Complete Search for Dense Cloud Cores in Taurus”, *The Astrophysical Journal* **575** (2002), pp. 950–973, DOI: [10.1086/341347](https://doi.org/10.1086/341347).
- Orlikowski, T., “Theoretical Studies of Rotationally Inelastic Collisions of Molecules in ³Σ Electronic States: O₂ (*X*³Σ_g⁻) + He”, *Molecular Physics* **56** (1985), pp. 35–46, DOI: [10.1080/00268978500102141](https://doi.org/10.1080/00268978500102141).
- Osterbrock, D. E. & Ferland, G. J., *Astrophysics of Gaseous Nebulae and Active Galactic Nuclei*, 2006.

-
- Pack, R. T., “Space-Fixed vs Body-Fixed Axes in Atom-Diatomic Molecule Scattering. Sudden Approximations”, *The Journal of Chemical Physics* **60** (1974), pp. 633–639, DOI: [10.1063/1.1681085](https://doi.org/10.1063/1.1681085).
- Palumbo, M. E., Geballe, T. R. & Tielens, A. G. G. M., “Solid Carbonyl Sulfide (OCS) in Dense Molecular Clouds”, *The Astrophysical Journal* **479** (1997), pp. 839–844, DOI: [10.1086/303905](https://doi.org/10.1086/303905).
- Pascoli, G. & Lavendy, H., “Structures and Energies of C_nS ($1 \leq n \leq 20$) Sulphur Carbide Clusters”, *International Journal of Mass Spectrometry* **181** (1998), pp. 11–25, DOI: [10.1016/S1387-3806\(98\)14126-X](https://doi.org/10.1016/S1387-3806(98)14126-X).
- Percival, I. C. & Seaton, M. J., “The Partial Wave Theory of Electron-Hydrogen Atom Collisions”, *Mathematical Proceedings of the Cambridge Philosophical Society* **53** (1957), pp. 654–662, DOI: [10.1017/S0305004100032722](https://doi.org/10.1017/S0305004100032722).
- Phillips, T. R., Maluendes, S. & Green, S., “Collision Dynamics for an Asymmetric Top Rotor and a Linear Rotor: Coupled Channel Formalism and Application to H_2O-H_2 ”, *The Journal of Chemical Physics* **102** (1995), pp. 6024–6031, DOI: [10.1063/1.469337](https://doi.org/10.1063/1.469337).
- Phillips, T. R., Maluendes, S., McLean, A. D. & Green, S., “Anisotropic Rigid Rotor Potential Energy Function for H_2O-H_2 ”, *The Journal of Chemical Physics* **101** (1994), pp. 5824–5830, DOI: [10.1063/1.467297](https://doi.org/10.1063/1.467297).
- Pickett, H., Poynter, R., Cohen, E., Delitsky, M., Pearson, J. & Müller, H., “Submillimeter, Millimeter, and Microwave Spectral Line Catalog”, *Journal of Quantitative Spectroscopy and Radiative Transfer* **60** (1998), pp. 883–890, DOI: [10.1016/S0022-4073\(98\)00091-0](https://doi.org/10.1016/S0022-4073(98)00091-0).
- Pirlot Jankowiak, P., Lique, F. & Dagdigan, P. J., “Collisional Excitation of C_2H and C_2D by Molecular Hydrogen”, *Monthly Notices of the Royal Astronomical Society* **526** (2023a), pp. 885–894, DOI: [10.1093/mnras/stad2821](https://doi.org/10.1093/mnras/stad2821).
- Pirlot Jankowiak, P., Lique, F. & Dagdigan, P. J., “Hyperfine Excitation of ^{13}CCH and $C^{13}CH$ by Collisions with *Para*- H_2 ”, *Monthly Notices of the Royal Astronomical Society* **523** (2023b), pp. 3732–3740, DOI: [10.1093/mnras/stad1646](https://doi.org/10.1093/mnras/stad1646).
- Pirlot Jankowiak, P., “Collisional Excitation of Radicals of Astrophysical Interest”, PhD thesis, 2024.
- Purvis, G. D. & Bartlett, R. J., “A Full Coupled-Cluster Singles and Doubles Model: The Inclusion of Disconnected Triples”, *The Journal of Chemical Physics* **76** (1982), pp. 1910–1918, DOI: [10.1063/1.443164](https://doi.org/10.1063/1.443164).

-
- Quack, M. & Troe, J., “Specific Rate Constants of Unimolecular Processes II. Adiabatic Channel Model”, *Berichte der Bunsengesellschaft für physikalische Chemie* **78** (1974), pp. 240–252, DOI: [10.1002/bbpc.19740780306](https://doi.org/10.1002/bbpc.19740780306).
- Quack, M. & Troe, J., “Complex Formation in Reactive and Inelastic Scattering: Statistical Adiabatic Channel Model of Unimolecular Processes III”, *Berichte der Bunsengesellschaft für physikalische Chemie* **79** (1975), pp. 170–183, DOI: [10.1002/bbpc.19750790211](https://doi.org/10.1002/bbpc.19750790211).
- Quintas-Sánchez, E. & Dawes, R., “AUTOSURF: A Freely Available Program To Construct Potential Energy Surfaces”, *Journal of Chemical Information and Modeling* **59** (2019), pp. 262–271, DOI: [10.1021/acs.jcim.8b00784](https://doi.org/10.1021/acs.jcim.8b00784).
- Quintas-Sánchez, E. & Dubernet, M.-L., “Theoretical Study of HCN–Water Interaction: Five Dimensional Potential Energy Surfaces”, *Physical Chemistry Chemical Physics* **19** (2017), pp. 6849–6860, DOI: [10.1039/C6CP07894J](https://doi.org/10.1039/C6CP07894J).
- Raghavachari, K., Trucks, G. W., Pople, J. A. & Head-Gordon, M., “A Fifth-Order Perturbation Comparison of Electron Correlation Theories”, *Chemical Physics Letters* **157** (1989), pp. 479–483, DOI: [10.1016/S0009-2614\(89\)87395-6](https://doi.org/10.1016/S0009-2614(89)87395-6).
- Rivilla, V. M., Sanz-Novo, M., Jiménez-Serra, I., Martín-Pintado, J., Colzi, L., Zeng, S., Megías, A., López-Gallifa, Á., Martínez-Henares, A., Massalkhi, S., Tercero, B., De Vicente, P., Martín, S., Andrés, D. S., Requena-Torres, M. A. & Alonso, J. L., “First Glycine Isomer Detected in the Interstellar Medium: Glycolamide (NH₂C(O)CH₂OH)”, *The Astrophysical Journal Letters* **953** (2023), p. L20, DOI: [10.3847/2041-8213/ace977](https://doi.org/10.3847/2041-8213/ace977).
- Rohlfs, K. & Wilson, T. L., *Tools of Radio Astronomy*, Astronomy and Astrophysics Library, Berlin, Heidelberg: Springer Berlin Heidelberg, 2004, DOI: [10.1007/978-3-662-05394-2](https://doi.org/10.1007/978-3-662-05394-2).
- Roos, B. O., *Lecture Notes in Quantum Chemistry. 2*, Lecture Notes in Chemistry 64, Berlin Heidelberg: Springer, 1994, ISBN: 978-3-540-58620-3.
- Roth, N. X., Milam, S. N., Cordiner, M. A., Bockelée-Morvan, D., Biver, N., Boissier, J., Lis, D. C., Remijan, A. J. & Charnley, S. B., “Leveraging the ALMA Atacama Compact Array for Cometary Science: An Interferometric Survey of Comet C/2015 ER61 (PanSTARRS) and Evidence for a Distributed Source of Carbon Monosulfide”, *The Astrophysical Journal* **921** (2021a), p. 14, DOI: [10.3847/1538-4357/ac0441](https://doi.org/10.3847/1538-4357/ac0441).
- Roth, N. X., Milam, S. N., Cordiner, M. A., Bockelée-Morvan, D., DiSanti, M. A., Boissier, J., Biver, N., Crovisier, J., Russo, N. D., Bonev, B. P., Qi, C., Remijan, A. J., Charn-

-
- ley, S. B., Gibb, E. L., Val-Borro, M. D. & Jehin, E., “Rapidly Varying Anisotropic Methanol (CH₃OH) Production in the Inner Coma of Comet 46P/Wirtanen as Revealed by the ALMA Atacama Compact Array”, *The Planetary Science Journal* **2** (2021b), p. 55, DOI: [10.3847/PSJ/abdd3a](https://doi.org/10.3847/PSJ/abdd3a).
- Rothenberg, S. & Schaefer, H. F., “Methane as a Numerical Experiment for Polarization Basis Function Selection”, *The Journal of Chemical Physics* **54** (1971), pp. 2764–2766, DOI: [10.1063/1.1675248](https://doi.org/10.1063/1.1675248).
- Roueff, E. & Lique, F., “Molecular Excitation in the Interstellar Medium: Recent Advances in Collisional, Radiative, and Chemical Processes”, *Chemical Reviews* **113** (2013), pp. 8906–8938, DOI: [10.1021/cr400145a](https://doi.org/10.1021/cr400145a).
- Rowe, B. & Marquette, J., “CRESU Studies of Ion/Molecule Reactions”, *International Journal of Mass Spectrometry and Ion Processes* **80** (1987), pp. 239–254, DOI: [10.1016/0168-1176\(87\)87033-7](https://doi.org/10.1016/0168-1176(87)87033-7).
- Rubin, M., Altwegg, K., Balsiger, H., Berthelier, J.-J., Combi, M. R., De Keyser, J., Drozdovskaya, M., Fiethe, B., Fuselier, S. A., Gasc, S., Gombosi, T. I., Hänni, N., Hansen, K. C., Mall, U., Rème, H., Schroeder, I. R. H. G., Schuhmann, M., Sémon, T., Waite, J. H., Wampfler, S. F. & Wurz, P., “Elemental and Molecular Abundances in Comet 67P/Churyumov-Gerasimenko”, *Monthly Notices of the Royal Astronomical Society* **489** (2019), pp. 594–607, DOI: [10.1093/mnras/stz2086](https://doi.org/10.1093/mnras/stz2086).
- Ruffle, D. P., Hartquist, T. W., Caselli, P. & Williams, D. A., “The Sulphur Depletion Problem”, *Monthly Notices of the Royal Astronomical Society* **306** (1999), pp. 691–695, DOI: [10.1046/j.1365-8711.1999.02562.x](https://doi.org/10.1046/j.1365-8711.1999.02562.x).
- Sahnoun, E., Ben Khalifa, M., Khadri, F. & Hammami, K., “Rotational De-Excitation of Tricarbon Monosulfide (C₃S) in Collision with He: Potential Energy Surface and Rates”, *Astrophysics and Space Science* **365** (2020), p. 183, DOI: [10.1007/s10509-020-03892-5](https://doi.org/10.1007/s10509-020-03892-5).
- Saito, S., Kawaguchi, K., Yamamoto, S., Ohishi, M., Suzuki, H. & Kaifu, N., “Laboratory Detection and Astronomical Identification of a New Free Radical, CCS(³Σ⁻)”, *Astronomy & Astrophysics* **317** (1987), pp. L115–L119.
- Sakai, N., Saruwatari, O., Sakai, T., Takano, S. & Yamamoto, S., “Abundance Anomaly of the ¹³C Species of CCH”, *Astronomy & Astrophysics* **512** (2010), A31, DOI: [10.1051/0004-6361/200913098](https://doi.org/10.1051/0004-6361/200913098).

-
- Sakai, N., Ikeda, M., Morita, M., Sakai, T., Takano, S., Osamura, Y. & Yamamoto, S., “Production Pathways of CCS and CCCS Inferred from Their ^{13}C Isotopic Species”, *The Astrophysical Journal* **663** (2007), pp. 1174–1179, DOI: [10.1086/518595](https://doi.org/10.1086/518595).
- Sakai, N., Takano, S., Sakai, T., Shiba, S., Sumiyoshi, Y., Endo, Y. & Yamamoto, S., “Anomalous ^{13}C Isotope Abundances in C_3S and C_4H Observed toward the Cold Interstellar Cloud, Taurus Molecular Cloud-1”, *The Journal of Physical Chemistry A* **117** (2013), pp. 9831–9839, DOI: [10.1021/jp3127913](https://doi.org/10.1021/jp3127913).
- Sandford, S. A. et al., “Organics Captured from Comet 81P/Wild 2 by the Stardust Spacecraft”, *Science* **314** (2006), pp. 1720–1724, DOI: [10.1126/science.1135841](https://doi.org/10.1126/science.1135841).
- Scappini, F. & Codella, C., “Radio Observations in NH_3 and C_2S towards Small Molecular Clouds and around Pre-Main-Sequence Stars”, *Monthly Notices of the Royal Astronomical Society* **282** (1996), pp. 587–596, DOI: [10.1093/mnras/282.2.587](https://doi.org/10.1093/mnras/282.2.587).
- Scharfenberg, L., Van De Meerakker, S. Y. T. & Meijer, G., “Crossed Beam Scattering Experiments with Optimized Energy Resolution”, *Physical Chemistry Chemical Physics* **13** (2011), p. 8448, DOI: [10.1039/c0cp02405h](https://doi.org/10.1039/c0cp02405h).
- Schöier, F. L., van der Tak, F. F. S., van Dishoeck, E. F. & Black, J. H., “An Atomic and Molecular Database for Analysis of Submillimetre Line Observations”, *Astronomy & Astrophysics* **432** (2005), pp. 369–379, DOI: [10.1051/0004-6361:20041729](https://doi.org/10.1051/0004-6361:20041729).
- Schrödinger, E., “An Undulatory Theory of the Mechanics of Atoms and Molecules”, *Physical Review* **28** (1926), pp. 1049–1070, DOI: [10.1103/PhysRev.28.1049](https://doi.org/10.1103/PhysRev.28.1049).
- Semenov, A., Mandal, B. & Babikov, D., “MQCT: User-ready Program for Calculations of Inelastic Scattering of Two Molecules”, *Computer Physics Communications* **252** (2020), p. 107155, DOI: [10.1016/j.cpc.2020.107155](https://doi.org/10.1016/j.cpc.2020.107155).
- Sendt, K., Jazbec, M. & Haynes, B., “Chemical Kinetic Modeling of the H/S System: H_2S Thermolysis and H_2 Sulfidation”, *Proceedings of the Combustion Institute* **29** (2002), pp. 2439–2446, DOI: [10.1016/S1540-7489\(02\)80297-8](https://doi.org/10.1016/S1540-7489(02)80297-8).
- Shavitt, I. & Bartlett, R. J., *Many-Body Methods in Chemistry and Physics: MBPT and Coupled-Cluster Theory*, Cambridge Molecular Science, Cambridge ; New York: Cambridge University Press, 2009, ISBN: 978-0-521-81832-2.
- Shingledecker, C. N., Lamberts, T., Laas, J. C., Vasyunin, A., Herbst, E., Kästner, J. & Caselli, P., “Efficient Production of S_8 in Interstellar Ices: The Effects of Cosmic-Ray-driven Radiation Chemistry and Nondiffusive Bulk Reactions”, *The Astrophysical Journal* **888** (2020), p. 52, DOI: [10.3847/1538-4357/ab5360](https://doi.org/10.3847/1538-4357/ab5360).

-
- Slater, J. C., “Atomic Shielding Constants”, *Physical Review* **36** (1930), pp. 57–64, DOI: [10.1103/PhysRev.36.57](https://doi.org/10.1103/PhysRev.36.57).
- Smith, A. M., Stecher, T. P. & Casswell, L., “Production of Carbon, Sulfur, and CS in Comet West”, *The Astrophysical Journal* **242** (1980), p. 402, DOI: [10.1086/158473](https://doi.org/10.1086/158473).
- Smith, D., Adams, N. G., Giles, K. & Herbst, E., “Organo-Sulfur Chemistry in Dense Interstellar Clouds via S⁺-Hydrocarbon Reactions”, *Astronomy & Astrophysics* **200** (1988), pp. 191–194.
- Smith, R. G., “A Search for Solid H₂S in Dense Clouds”, *Monthly Notices of the Royal Astronomical Society* **249** (1991), pp. 172–176, DOI: [10.1093/mnras/249.1.172](https://doi.org/10.1093/mnras/249.1.172).
- Snyder, L. E., Buhl, D., Zuckerman, B. & Palmer, P., “Microwave Detection of Interstellar Formaldehyde”, *Physical Review Letters* **22** (1969), pp. 679–681, DOI: [10.1103/PhysRevLett.22.679](https://doi.org/10.1103/PhysRevLett.22.679).
- Suzuki, H., Yamamoto, S., Ohishi, M., Kaifu, N., Ishikawa, S.-I., Hirahara, Y. & Takano, S., “A Survey of CCS, HC₃N, HC₅N, and NH₃ toward Dark Cloud Cores and Their Production Chemistry”, *Astronomy & Astrophysics* **392** (1992), p. 551, DOI: [10.1086/171456](https://doi.org/10.1086/171456).
- Swings, P. & Rosenfeld, L., “Considerations Regarding Interstellar Molecules”, *The Astrophysical Journal* **86** (1937), pp. 483–486, DOI: [10.1086/143880](https://doi.org/10.1086/143880).
- Takano, S., Masuda, A., Hirahara, Y., Suzuki, H., Ohishi, M., Ishikawa, S.-i., Kaifu, N., Kasai, Y., Kawaguchi, K. & Wilson, T. L., “Observations of ¹³C Isotopomers of HC₃N and HC₅N in TMC-1: Evidence for Isotopic Fractionation”, *Astronomy & Astrophysics* **329** (1998), pp. 1156–1169.
- Talbi, D., “A Theoretical Study of the Astrochemical ¹³C¹²CS + H → ¹²C¹³CS + H Reaction”, *Australian Journal of Chemistry* **71** (2018), p. 311, DOI: [10.1071/CH17582](https://doi.org/10.1071/CH17582).
- Tang, K. T. & Toennies, J. P., “An Improved Simple Model for the van Der Waals Potential Based on Universal Damping Functions for the Dispersion Coefficients”, *The Journal of Chemical Physics* **80** (1984), pp. 3726–3741, DOI: [10.1063/1.447150](https://doi.org/10.1063/1.447150).
- Taniguchi, K., Ozeki, H., Saito, M., Sakai, N., Nakamura, F., Kamenno, S., Takano, S. & Yamamoto, S., “Implication of Formation Mechanisms of HC₅N in TMC-1 as Studied by ¹³C Isotopic Fractionation”, *The Astrophysical Journal* **817** (2016), p. 147, DOI: [10.3847/0004-637X/817/2/147](https://doi.org/10.3847/0004-637X/817/2/147).
- Tatum, J. B. & Watson, J. K. G., “Rotational Line Strengths in ³Σ[±]–³Σ[±] Transitions with Intermediate Coupling”, *The Canadian Journal of Physics* **49** (1971), pp. 2693–2703, DOI: [10.1139/p71-325](https://doi.org/10.1139/p71-325).

-
- Taylor, D. E., Ángyán, J. G., Galli, G., Zhang, C., Gygi, F., Hirao, K., Song, J. W., Rahul, K., Anatole Von Lilienfeld, O., Podeszwa, R., Bulik, I. W., Henderson, T. M., Scuseria, G. E., Toulouse, J., Peverati, R., Truhlar, D. G. & Szalewicz, K., “Blind Test of Density-Functional-Based Methods on Intermolecular Interaction Energies”, *The Journal of Chemical Physics* **145** (2016), p. 124105, DOI: [10.1063/1.4961095](https://doi.org/10.1063/1.4961095).
- Ten-no, S., “Initiation of Explicitly Correlated Slater-type Geminal Theory”, *Chemical Physics Letters* **398** (2004), pp. 56–61, DOI: [10.1016/j.cplett.2004.09.041](https://doi.org/10.1016/j.cplett.2004.09.041).
- Tonolo, F., “Collisional Excitation in Space: From the Interstellar Medium to Planetary Atmospheres”, PhD thesis, Scuola Normale Superiore, 2024.
- Townes, C. H., “Microwave and Radio-Frequency Resonance Lines of Interest to Radio Astronomy”, *Symposium - International Astronomical Union* **4** (1957), pp. 92–103, DOI: [10.1017/S0074180900048919](https://doi.org/10.1017/S0074180900048919).
- Townes, C. H. & Schawlow, A. L., *Microwave Spectroscopy*, New York: Dover publications, 1975, ISBN: 978-0-486-61798-5.
- Valiron, P., Wernli, M., Faure, A., Wiesenfeld, L., Rist, C., Kedžuch, S. & Noga, J., “R12-Calibrated H₂O–H₂ Interaction: Full Dimensional and Vibrationally Averaged Potential Energy Surfaces”, *The Journal of Chemical Physics* **129** (2008), p. 134306, DOI: [10.1063/1.2988314](https://doi.org/10.1063/1.2988314).
- van der Tak, F. F. S., Black, J. H., Schöier, F. L., Jansen, D. J. & van Dishoeck, E. F., “A Computer Program for Fast Non-LTE Analysis of Interstellar Line Spectra: With Diagnostic Plots to Interpret Observed Line Intensity Ratios”, *Astronomy & Astrophysics* **468** (2007), pp. 627–635, DOI: [10.1051/0004-6361:20066820](https://doi.org/10.1051/0004-6361:20066820).
- van der Tak, F. F. S., Boonman, A. M. S., Braakman, R. & van Dishoeck, E. F., “Sulphur Chemistry in the Envelopes of Massive Young Stars”, *Astronomy & Astrophysics* **412** (2003), pp. 133–145, DOI: [10.1051/0004-6361:20031409](https://doi.org/10.1051/0004-6361:20031409).
- van Dishoeck, E. F., Jansen, D. J., Schilke, P. & Phillips, T. G., “Detection of the Interstellar NH₂ Radical”, *The Astrophysical Journal* **416** (1993), p. L83, DOI: [10.1086/187076](https://doi.org/10.1086/187076).
- Vanhaecke, N., Meier, U., Andrist, M., Meier, B. H. & Merkt, F., “Multistage Zeeman Deceleration of Hydrogen Atoms”, *Physical Review A* **75** (2007), p. 031402, DOI: [10.1103/PhysRevA.75.031402](https://doi.org/10.1103/PhysRevA.75.031402).
- Varambhia, H. N., Faure, A., Graupner, K., Field, T. A. & Tennyson, J., “Electron-Impact Rotational Excitation of the Carbon Monosulphide (CS) Molecule”, *Monthly Notices*

-
- of the *Royal Astronomical Society* **403** (2010), pp. 1409–1412, DOI: [10.1111/j.1365-2966.2010.16207.x](https://doi.org/10.1111/j.1365-2966.2010.16207.x).
- Velusamy, T., Kuiper, T. B. H. & Langer, W. D., “CCS Observations of the Protostellar Envelope of B335”, *The Astrophysical Journal* **451** (1995), pp. L75–L78.
- Vidal, T. H. G. & Wakelam, V., “A New Look at Sulphur Chemistry in Hot Cores and Corinos”, *Monthly Notices of the Royal Astronomical Society* **474** (2018), pp. 5575–5587, DOI: [10.1093/mnras/stx3113](https://doi.org/10.1093/mnras/stx3113).
- Vidal, T. H. G., Loison, J.-C., Jaziri, A. Y., Ruaud, M., Gratier, P. & Wakelam, V., “On the Reservoir of Sulphur in Dark Clouds: Chemistry and Elemental Abundance Reconciled”, *Monthly Notices of the Royal Astronomical Society* **469** (2017), pp. 435–447, DOI: [10.1093/mnras/stx828](https://doi.org/10.1093/mnras/stx828).
- Vissers, G. W. M., Wormer, P. E. S. & Van Der Avoird, A., “An *Ab Initio* CO Dimer Interaction Potential and the Computation of the Rovibrational Spectrum of (CO)₂”, *Physical Chemistry Chemical Physics* **5** (2003), p. 4767, DOI: [10.1039/b309468e](https://doi.org/10.1039/b309468e).
- Vogels, S. N., Gao, Z. & Van De Meerakker, S. Y., “Optimal Beam Sources for Stark Decelerators in Collision Experiments: A Tutorial Review”, *EPJ Techniques and Instrumentation* **2** (2015), p. 12, DOI: [10.1140/epjti/s40485-015-0021-y](https://doi.org/10.1140/epjti/s40485-015-0021-y).
- Wakelam, V., Caselli, P., Ceccarelli, C., Herbst, E., Mascetti, J. & Castets, A., “Searching for Sulphur Polymers in Young Protostars with Herschel and ALMA”, **577** (2005), pp. 435–436.
- Weinreb, S., Barrett, A. H., Meeks, M. L. & Henry, J. C., “Radio Observations of OH in the Interstellar Medium”, *Nature* **200** (1963), pp. 829–831, DOI: [10.1038/200829a0](https://doi.org/10.1038/200829a0).
- Werner, H.-J. et al., *Molpro*, 2015.
- Werner, H.-J., Follmeg, B. & Alexander, M. H., “Adiabatic and Diabatic Potential Energy Surfaces for Collisions of CN($X^2\Sigma^+$, $A^2\Pi$) with He”, *The Journal of Chemical Physics* **89** (1988), pp. 3139–3151, DOI: [10.1063/1.454971](https://doi.org/10.1063/1.454971).
- Werner, H.-J., Follmeg, B., Alexander, M. H. & Lemoine, D., “Quantum Scattering Studies of Electronically Inelastic Collisions of CN ($X^2\Sigma^+$, $A^2\Pi$) with He”, *The Journal of Chemical Physics* **91** (1989), pp. 5425–5439, DOI: [10.1063/1.457570](https://doi.org/10.1063/1.457570).
- Werner, H.-J., Knowles, P. J., Knizia, G., Manby, F. R. & Schütz, M., “Molpro: A General-purpose Quantum Chemistry Program Package”, *WIREs Computational Molecular Science* **2** (2012), pp. 242–253, DOI: [10.1002/wcms.82](https://doi.org/10.1002/wcms.82).
- Werner, H.-J., Knowles, P. J., Manby, F. R., Black, J. A., Doll, K., Heßelmann, A., Kats, D., Köhn, A., Korona, T., Kreplin, D. A., Ma, Q., Miller, T. F., Mitrushchenkov,

-
- A., Peterson, K. A., Polyak, I., Rauhut, G. & Sibae, M., “The Molpro Quantum Chemistry Package”, *The Journal of Chemical Physics* **152** (2020), p. 144107, DOI: [10.1063/5.0005081](https://doi.org/10.1063/5.0005081).
- Wernli, M., Wiesenfeld, L., Faure, A. & Valiron, P., “Rotational Excitation of HC₃N by H₂ and He at Low Temperatures”, *Astronomy & Astrophysics* **464** (2007), pp. 1147–1154, DOI: [10.1051/0004-6361:20066112](https://doi.org/10.1051/0004-6361:20066112).
- Wilson, R. W., Jefferts, K. B. & Penzias, A. A., “Carbon Monoxide in the Orion Nebula”, *The Astrophysical Journal* **161** (1970), p. L43, DOI: [10.1086/180567](https://doi.org/10.1086/180567).
- Wolkovitch, D., Langer, W. D., Goldsmith, P. F. & Heyer, M., “Physical Conditions in Quiescent Dark Cloud Cores Determined from Multitransition Observations of CCS”, *The Astrophysical Journal* **477** (1997), pp. 241–264, DOI: [10.1086/303677](https://doi.org/10.1086/303677).
- Woon, D. E. & Dunning, T. H., “Gaussian Basis Sets for Use in Correlated Molecular Calculations. III. The Atoms Aluminum through Argon”, *The Journal of Chemical Physics* **98** (1993), pp. 1358–1371, DOI: [10.1063/1.464303](https://doi.org/10.1063/1.464303).
- Xie, Y. & Schaefer, H. F., “Naked Organosulfur Clusters: The Infrared Spectrum of the C₂S Molecule”, *The Journal of Chemical Physics* **96** (1992), p. 3751.
- Yamada, M., Osamura, Y. & Kaiser, R. I., “A Comprehensive Investigation on the Formation of Organo-Sulfur Molecules in Dark Clouds via Neutral-Neutral Reactions”, *Astronomy & Astrophysics* **395** (2002), pp. 1031–1044, DOI: [10.1051/0004-6361:20021328](https://doi.org/10.1051/0004-6361:20021328).
- Yamamoto, S., *Introduction to Astrochemistry*, Astronomy and Astrophysics Library, Tokyo: Springer Japan, 2017, DOI: [10.1007/978-4-431-54171-4](https://doi.org/10.1007/978-4-431-54171-4).
- Yamamoto, S., Saito, S., Kawaguchi, K., Chikada, Y., Suzuki, H., Kaifu, N., Ishikawa, S.-I. & Ohishi, M., “Rotational Spectrum of the CCS Radical Studied by Laboratory Microwave Spectroscopy and Radio-Astronomical Observations”, *The Astrophysical Journal* **361** (1990), p. 318, DOI: [10.1086/169197](https://doi.org/10.1086/169197).
- Yang, X. J., Hua, L. & Li, A., “Where Have All the Sulfur Atoms Gone? Polycyclic Aromatic Hydrocarbon as a Possible Sink for the Missing Sulfur in the Interstellar Medium. I. The C–S Band Strengths”, *The Astrophysical Journal* **974** (2024), p. 30, DOI: [10.3847/1538-4357/ad6dd7](https://doi.org/10.3847/1538-4357/ad6dd7).
- Żółtowski, M., Lique, F., Loreau, J., Faure, A. & Cordiner, M., “The Excitation of CO in CO-dominated Cometary Comae”, *Monthly Notices of the Royal Astronomical Society* **520** (2023), pp. 3887–3894, DOI: [10.1093/mnras/stad268](https://doi.org/10.1093/mnras/stad268).

Żółtowski, M., “Collisional Excitation of Astrophysical Molecules Induced by H₂O and CO Molecules”, PhD thesis, Université Le Havre Normandie, 2023.

Żółtowski, M., Loreau, J. & Lique, F., “Collisional Energy Transfer in the CO–CO System”, *Physical Chemistry Chemical Physics* **24** (2022), pp. 11910–11918, DOI: [10.1039/D2CP01065H](https://doi.org/10.1039/D2CP01065H).

PEER-REVIEWED ARTICLES

A.1 Rotational Excitation of CO₂ Induced by He: New Potential Energy Surface and Scattering Calculations

The work on the collisional excitation of CO₂ induced by He began during my master's studies. During a three-month internship, I joined the COLLEXISM team led by François Lique at the Laboratory of Waves and Complex Media in Le Havre, France. I computed the PES of the CO₂-He collisional system using the CCSD(T) method and an extrapolation of the basis set.

The following year, I returned for a second internship of five months in François's group, which had moved to the Institute of Physics of Rennes, to continue the work I started in Le Havre. During that internship, I ran scattering calculations using the Close-Coupling approach to produce state-to-state rate coefficients for CO₂ collisions with He at temperatures ranging from 5 to 300 K.

Finally, in the early months of my thesis, we collaborated with Dr. Franck Thibault from the Institute of Physics of Rennes on calculating pressure broadening cross sections that can be compared to experimental measurements. This work was published in a peer-reviewed journal during the first year of my thesis. The CO₂-He rate coefficients are currently available in the BASECOL database (Dubernet et al., 2024).

During this work, I learned to use various tools that will be applied in my PhD research, such as the quantum chemistry software MOLPRO (Werner et al., 2015) and the quantum scattering code MOLSCAT (Hutson & Green, 1994). Consequently, this experience has been very valuable for my future thesis work.

Rotational excitation of CO₂ induced by He: New potential energy surface and scattering calculations

Cite as: J. Chem. Phys. **156**, 104303 (2022); <https://doi.org/10.1063/5.0085094>

Submitted: 12 January 2022 • Accepted: 14 February 2022 • Accepted Manuscript Online: 14 February 2022 • Published Online: 11 March 2022

 A. Godard Palluet,  F. Thibault and  F. Lique



View Online



Export Citation



CrossMark

ARTICLES YOU MAY BE INTERESTED IN

[Do not forget the Rydberg orbitals](#)

The Journal of Chemical Physics **156**, 100901 (2022); <https://doi.org/10.1063/5.0084574>

[High-resolution vibronic spectroscopy of a single molecule embedded in a crystal](#)

The Journal of Chemical Physics **156**, 104301 (2022); <https://doi.org/10.1063/5.0081297>

[Perturbation theories for fluids with short-ranged attractive forces: A case study of the Lennard-Jones spline fluid](#)

The Journal of Chemical Physics **156**, 104504 (2022); <https://doi.org/10.1063/5.0082690>

[Learn More](#)

The Journal of Chemical Physics **Special Topics** Open for Submissions

Rotational excitation of CO₂ induced by He: New potential energy surface and scattering calculations

Cite as: J. Chem. Phys. 156, 104303 (2022); doi: 10.1063/5.0085094

Submitted: 12 January 2022 • Accepted: 14 February 2022 •

Accepted Manuscript Online: 14 February 2022 • Published Online: 11 March 2022



View Online



Export Citation



CrossMark

A. Godard Palluet,^{a),b)}  F. Thibault,^{c)}  and F. Lique^{b),d)} 

AFFILIATIONS

Université de Rennes 1, CNRS, IPR (Institut de Physique de Rennes)—UMR 6251, F-35000 Rennes, France

^{a)} Author to whom correspondence should be addressed: amelie.godard@univ-rennes1.fr

^{b)} Also at: LOMC (Laboratoire des ondes et milieux complexes), Université du Havre and CNRS, Normandie Université, F-76063 Le Havre, France.

^{c)} Electronic mail: franck.thibault@univ-rennes1.fr

^{d)} Electronic mail: francois.lique@univ-rennes1.fr

ABSTRACT

The CO₂ molecule is of great interest for astrophysical studies since it can be found in a large variety of astrophysical media where it interacts with the dominant neutral species, such as He, H₂, or H₂O. The CO₂–He collisional system was intensively studied over the last two decades. However, collisional data appear to be very sensitive to the potential energy surface (PES) quality. Thus, we provide, in this study, a new PES of the CO₂–He van der Waals complex calculated with the coupled-cluster method and a complete basis set extrapolation in order to provide rotational rate coefficients that are as accurate as possible. The PES accuracy was tested through the calculations of bound state transition frequencies and pressure broadening coefficients that were compared to experimental data. An excellent agreement was globally found. Then, revised collisional data were provided for the 10–300 K temperature range. Rate coefficients were compared to previously computed ones and are found to be up to 50% greater than previously provided ones. These differences can induce non-negligible consequences for the modeling of CO₂ abundance in astrophysical media.

Published under an exclusive license by AIP Publishing. <https://doi.org/10.1063/5.0085094>

I. INTRODUCTION

Interacting systems that include the CO₂ molecule are of great interest for astrophysical studies. Indeed, CO₂ can be found in various astrophysical media, such as the interstellar medium (ISM),¹ protoplanetary disks,² and planetary and cometary atmospheres.³ It is also a major component of interstellar and cometary ice mantles.⁴

In these media, *in situ* measurements are very complicated if not impossible. Therefore, the analysis of their chemical compositions and physical conditions is made through the interpretation of spectra captured by telescopes.

The spectral analysis requires knowledge of the population of the molecular energy levels.⁵ Most of the astrophysical media are not at the local thermodynamic equilibrium (LTE) so the population of molecular energy levels is no longer following a Maxwell–Boltzmann distribution. It is then evaluated by a radiative transfer model

analysis, taking into account both radiative and collisional (de)excitations. Radiative processes are characterized by Einstein coefficients, for which an analytical formula exists, and collisional processes are characterized by the so-called rate coefficients, which are collisional-system-specific.⁵ Such rate coefficients are obtained from scattering calculations based on a potential energy surface (PES) describing the interactions between the two colliders.

The CO₂ molecule is detected through rovibrational transitions due to its lack of dipole moment.⁴ Since a non-LTE distribution of the rovibrational energy levels is expected to occur in cold astrophysical media, collisional data for both rotational and rovibrational transitions are needed. Note that, despite the absence of electric dipole moment, non-LTE effects are still predicted to occur at low density ($n < 10^4 \text{ cm}^{-3}$) for the lowest rotational states in the fundamental vibrational level.² As a first estimate, rovibrational data can be estimated from pure rotational ones.⁶ It is then crucial to provide accurate collisional data for the CO₂ molecule.

Helium is an important collider in astrophysical media and rate coefficients involving helium can be used to infer those for para- H_2 ($j = 0$) through an adequate scaling factor involving the reduced mass.⁵

CO_2 -He rate coefficients were provided for only five rotational levels (up to $j = 8$) by Yang and Stancil⁷ based on the PES described by Ran and Xie.⁸ The latter computed their PES with the coupled-cluster single double and perturbative triple excitations method [hereafter CCSD(T)] and the augmented correlation-consistent quadruple-zeta (hereafter aVQZ) basis set with additional mid-bond functions. Despite an already accurate PES, larger basis sets are now reachable in terms of computational times. Moreover, mid-bond functions as used for the computation of the PES of Ran and Xie⁸ can introduce an overestimation of the potential energy and an inhomogeneous accuracy.⁹ As collisional data are very sensitive to the PES, especially at low energy,^{7,10,11} it is of the utmost importance to provide a PES as accurate as possible. Therefore, we decided to compute a new one with the gold standard CCSD(T) method and an extrapolation to the complete basis set (CBS).¹²

This new PES was then used to run scattering calculations using a full close-coupling (CC) approach in order to provide new highly accurate rotational state-to-state rate coefficients involving 21 rotational levels (up to $j = 40$) for the 10–300 K range of temperature of great interest for astrophysical modeling of the CO_2 molecule.

The presentation of this work starts in Sec. II by a summary of the previous studies on the CO_2 -He collisional system from a theoretical and experimental point of view. Section III presents the computational methods used to obtain the PES (Sec. III A), bound states (Sec. III B), and scattering data (Sec. III C).

In Sec. IV, a description of the PES is included and its comparison with previously computed PESs will be discussed. The accuracy of the surface is then validated in Sec. V through a comparison between computed and experimental bound state transition frequencies and pressure broadening coefficients in Secs. V A and V B, respectively. New collisional data, such as inelastic cross sections and rate coefficients, are presented in Sec. VI A. In addition, the sensitivity of collisional data with respect to the PES will be discussed through the comparison of rate coefficients previously published by Yang and Stancil⁷ based on the PES of Ran and Xie.⁸ Furthermore, the cross sections described in this work will be compared (see Sec. VI B) to the ones described by al-Qady *et al.*,¹³ who studied cold collisions between helium and highly rotationally excited CO_2 . Finally, conclusions are drawn.

II. PREVIOUS WORK ON CO_2 -He INTERACTING SYSTEM

During the 1970s, the success of the simple electron gas model^{14–16} renewed the interest in interaction energy calculations in vdW complexes. In order to investigate the angular dependence on such energies in these systems, Parker *et al.*¹⁷ used this method to obtain the earliest realistic 2D-PES of the CO_2 -He collisional system, where vibrational motions were ignored.

Based on this surface, Parker and Pack¹⁸ performed vibrational close-coupling rotational infinite order sudden (VCC-IOS) scattering calculations. They obtained rate coefficients that were assumed to be accurate for temperatures above 300 K.

The empirical PES for the CO_2 -He system was then established by Keil *et al.*¹⁹ It was obtained through central field and anisotropic parameterizations based on deconvolution of molecular-beam total differential cross sections.

Later, Stroud and Raff²⁰ provided a full *ab initio* PES computed with the self-consistent field (SCF) method. The CO_2 molecule was considered as a rigid rotor with a C–O bond set to $2.1942a_0$. This PES was in reasonable agreement with the two former ones. In order to study its accuracy, Stroud and Raff²⁰ computed rate coefficients, state-to-state cross sections, and differential cross sections with about 28 500 quasiclassical trajectories on their *ab initio* PES, and the ones of Parker *et al.*¹⁷ and Keil *et al.*¹⁹ It was then highlighted that long-range attractive forces are of crucial importance on scattering processes at low collisional energy. However, at high energy, the potential well is no longer an important topological feature, unlike the curvature and slope of the repulsive wall.

In 1982, Clary²¹ provided the first PES taking into account the symmetric and asymmetric stretch and the bending normal vibrational mode. Based on this surface computed with the SCF method, vibrational relaxation rate coefficients for the 50–373 K temperature range were obtained with the VCC-IOS approach.

With increasing quality of experimental collisional data along the years, new and improved (semi)empirical PESs were provided, such as the two-dimensional ones of Keil *et al.*^{22,23} and of Beneventi *et al.*,²⁴ which were obtained by simultaneous analysis of different scattering properties.

In 1994, Weida *et al.*²⁵ provided the very first infrared spectra of the CO_2 -He vdW complex and, thus, strong validation criteria for the PESs. It was recorded in the region of the ν_3 asymmetric stretch on the $^{12}\text{C}^{16}\text{O}_2$ isotopologue. Later, studies by Xu and Jäger²⁶ and McKellar²⁷ were also devoted to experimental spectra of this system. Xu and Jäger²⁶ reported experimental spectra of pure rotational transitions for seven CO_2 isotopologues, including $^{12}\text{C}^{16}\text{O}_2$, $^{13}\text{C}^{16}\text{O}_2$, $^{12}\text{C}^{18}\text{O}_2$, and $^{13}\text{C}^{18}\text{O}_2$. McKellar²⁷ presented experimental infrared spectra obtained on three CO_2 isotopologues in the ν_3 band, including $^{13}\text{C}^{16}\text{O}_2$ and $^{13}\text{C}^{18}\text{O}_2$.

In order to interpret the recently obtained IR spectra, new PESs were established, such as the one of Yan *et al.*²⁸ in 1998 and the one of Negri *et al.*²⁹ in 1999. Both these surfaces were computed using the fourth-order Møller–Plesset (MP4) perturbational theory with a large basis set containing mid-bond functions.

The so-called mid-bond functions are functions centered at half distance of the vdW bond, i.e., between the molecule and the rare gas atom. Such functions are often used since it has been shown to improve the accuracy of the potential well when limited basis sets are used. However, these orbitals have no physical meaning, and thus, they can also introduce an overestimation of the interaction energy in some regions of the PES.⁹

In the work of Thibault *et al.*,¹⁰ experimental pressure broadening coefficients were provided for various R and Q spectroscopic lines in the 123–760 K temperature range. They also computed such coefficients using the PESs of Negri *et al.*,²⁹ Beneventi *et al.*,²⁴ and Yan *et al.*²⁸ in order to evaluate the quality of these PESs. After running scattering calculations with the CC and the coupled-state (CS) approaches, they deduced that the PES of Negri *et al.*²⁹ was the most accurate of the three.

In 2001, Korona *et al.*³⁰ published a new PES computed with a symmetry-adapted perturbational theory (SAPT). The CO_2

molecule was considered as a rigid rotor and its bond length was set to $2.1944a_0$. The rovibrational energy levels computed from variational calculations on their SAPT potential lead to an excellent agreement with experimental data of Weida *et al.*,²⁵ indicating that the potential well is well described. The pressure broadening coefficients that they obtained with scattering calculations are also in the experimental error bars of the measurements of Boissoles *et al.*³¹ and Thibault *et al.*,¹⁰ suggesting the great quality of this PES.

Li and Le Roy³² and Ran and Xie⁸ included the effect of the antisymmetric-stretch Q_3 normal mode in the 3D-PESs that they computed with the CCSD(T) method in conjunction with an aVQZ basis set and additional mid-bond functions. Potential wells of both surfaces were validated through a comparison between computed spectroscopic values and experimental measurements.

In 2009, two additional CO₂-He studies were published. Deng *et al.*¹¹ provided new experimental pressure broadening coefficients for the R(10) and P(2) lines in the ν_3 band at several temperatures between 100 and 300 K. They compared them to the ones they obtained by scattering calculations performed on the PES described by Korona *et al.*³⁰ These coefficients were found between experimental error bars for almost all temperatures, which prove the accuracy of the repulsive wall on the PES of Korona *et al.*³⁰ Yang and Stancil⁷ provided relaxation cross sections and quenching rate coefficients for rotational levels $j = 2, 4, 6$, and 8 in the temperature range from 10^{-5} K up to 3000 K using the PES of Ran and Xie.⁸

Two years later, al-Qady *et al.*¹³ published a study of cold collisions of highly rotationally excited CO₂ with helium. Based on the PES of Ran and Xie⁸ with a mix of the CC and the CS approaches, they computed cross sections for j up to 200.

Recently, Selim *et al.*³³ presented a new computational method to compute state-to-state rate coefficients of rovibrational transitions within this vdW complex. It is based on the CC approach for rotational transitions and a multi-channel distorted-wave Born approximation for vibrational ones. They computed *ab initio* three-dimensional PES, including Q_1 and Q_3 , the normal modes corresponding, respectively, to the symmetric and asymmetric CO₂ stretching ν_1 and ν_3 . They used a CCSD(T) method and an aVQZ basis set with additional mid-bond functions.

III. METHODS

A. *Ab initio* calculations

CO₂ is considered here as a rigid rotor. Its internuclear C–O distance is taken at $2.1944a_0$, the experimental average length over the ground vibrational wavefunction.³⁴ The interaction potential between CO₂ and He was described using Jacobi coordinates (R, θ) as presented in Fig. 1.

The major attractive contributions to the PES in rare-gas-neutral-molecule complexes are dispersion energies.^{28,29} Hence, a correlated method and a large basis set must be used to compute the intermolecular interaction of such systems.³⁵ The PES was thus calculated using the CCSD(T) method with an empirical extrapolation to the complete basis set (CBS) limit. This extrapolation is based on calculations using an augmented correlation-consistent X zeta basis set (hereafter aVXZ), where $X = T, Q$, and 5. Thus, the basis is noted CBS(T,Q,5). The extrapolated energy E_{CBS} is obtained by solving the following set of equations:³⁶

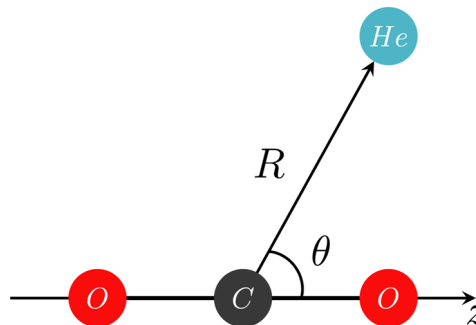


FIG. 1. CO₂-He collisional system in Jacobi coordinates.

$$E_X = E_{CBS} + Ae^{-(X-1)} + Be^{-(X-1)^2}, \quad (1)$$

where A and B are adjustable fitting parameters.

The basis set superposition error was corrected at every geometry (R, θ) with the counterpoise procedure of Boys and Bernardi,³⁷

$$V(R, \theta) = E_{\text{CO}_2-\text{He}}(R, \theta) - E_{\text{CO}_2}(R, \theta) - E_{\text{He}}(R, \theta), \quad (2)$$

where $V(R, \theta)$ is the interaction potential, and all energies E are computed with full basis set.

Calculations have been performed for $R \in [4, 20]a_0$ with a step depending on the short/intermediate/long-range regions of interactions and for $\theta \in [0^\circ, 90^\circ]$ with a regular step of 10° . In total, 260 *ab initio* points were calculated with the MOLPRO software.³⁸

A global fit of the potential was performed using an expansion over Legendre polynomials $P_\lambda(\cos \theta)$,³⁸

$$V(R, \theta) = \sum_{\lambda=0}^{\lambda_{\max}} v_\lambda(R) P_\lambda(\cos \theta), \quad (3)$$

where λ_{\max} was taken equal to 18 according to the numbers of θ angles chosen for the *ab initio* calculations. In fact, given the CO₂ symmetry, only even Legendre polynomials appear in the sum. The radial coefficients $v_\lambda(R)$ have been fitted as³⁸

$$v_\lambda(R) = e^{-a_1^\lambda R} \left(a_2^\lambda + a_3^\lambda R + a_4^\lambda R^2 + a_5^\lambda R^3 \right) - \frac{1}{2} \left[1 + \tanh R/R_{\text{ref}} \right] \left(\frac{C_6^\lambda}{R^6} + \frac{C_8^\lambda}{R^8} + \frac{C_{10}^\lambda}{R^{10}} \right), \quad (4)$$

where a_n^λ are the expansion coefficients, and the coefficients of the R^{-n} terms are symbolized by C_n^λ . The latter are then used for the long-range extrapolation. The hyperbolic tangent factor provided a smooth transition between the short-range ($\theta < R < R_{\text{ref}}$) and the long-range regions ($R > R_{\text{ref}}$). The fitted potential reproduces all *ab initio* points with an error inferior to 1%. The root-mean-square error of the fitted potential is of 0.0149 cm^{-1} and is mostly due to deviation at short distances.

In Fig. 2, we compare the long-range of interactions of the PES of this work to the one of Li and Le Roy.³² The latter used a multipolar expansion to determine the C_n^λ coefficients, so their long-range of interactions are trustworthy. The agreement is excellent over the full range of angles and distances presented here, so we can be confident

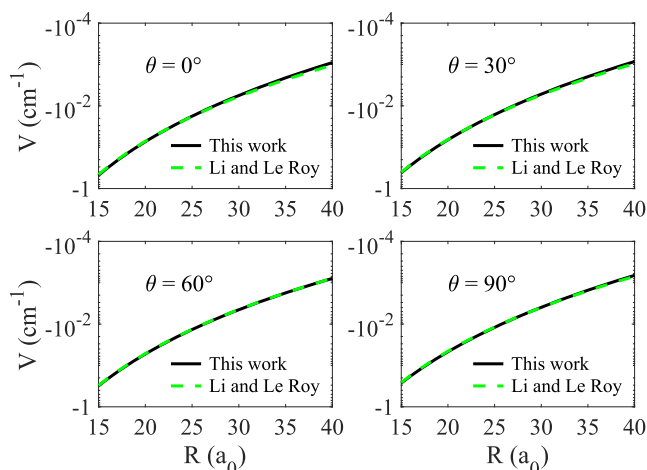


FIG. 2. Comparison(s) of the long-range of interactions of the PES of this work and that of Li and Le Roy³² for $\theta = 0^\circ, 30^\circ, 60^\circ,$ and 90° .

in the accuracy of the PES of this work for low-temperature collisions.

B. Bound states calculations

Bound states were computed in the ground vibrational state with the BOUND software.³⁹ Calculations were performed with the CC approach. The coupled equations were solved with the log-derivative method of Manolopoulos.⁴⁰ The propagation step was set to $0.01a_0$, the rotational basis included the first 16 rotational levels (up to $j = 30$ since only rotational levels with even j exist due to nuclear spin statistics), and the maximum distance of propagation was set at $30a_0$. These parameters were converged in order to get an error lower than 0.001% on bound state energies.

Transition frequencies were computed for the different carbon dioxide isotopologues: $^{12}\text{C}^{16}\text{O}_2$, $^{13}\text{C}^{16}\text{O}_2$, $^{12}\text{C}^{18}\text{O}_2$, and $^{13}\text{C}^{18}\text{O}_2$. Their respective rotational constants were set at $B_0 = 0.390\,219, 0.390\,237, 0.346\,817,$ and $0.346\,834\text{ cm}^{-1}$.^{25,41,42}

C. Scattering calculations

As introduced earlier, CO_2 is an interesting molecule for cometary and planetary atmospheres, ISM, and protoplanetary disks. Such media generally exhibit temperature between 10 and 300 K.^{2,3,43} At 300 K, assuming a Boltzmann distribution of the population on the energy levels, levels with internal energy lower than 500 cm^{-1} can be significantly populated. Hence, we performed scattering calculations for rotational levels up to $j = 40$, which corresponds to over 96% of the population assuming a Maxwell-Boltzmann distribution over the rotational energy levels.

In order to ensure the accuracy of our results up to this j for this temperature range, calculations were carried out for a range of total energy E from 2.4 up to 2500 cm^{-1} . The grid of energy is really dense at low energies to correctly describe resonances, and as the energy increases, the energy step also increases.

The scattering matrix, also called the S-matrix, is obtained through a CC approach with the log-derivative method of Manolopoulos⁴⁰ implemented in the MOLSCAT program.⁴⁴

Propagation parameters and maximum total angular momentum J_{max} were automatically converged by the MOLSCAT code. The rotational basis set fixed by j_{max} , the rotational quantum number of CO_2 , the number of Legendre polynomials used, fixed by λ_{max} , and the STEPS of propagation were set after a series of convergence tests in order to ensure the convergence of the S-matrix over all the energy interval considered with an error lower than 1%. These parameters are presented in Table I.

1. Rate coefficients

From the S-matrix, noted $S^J(j'l',jl)$ hereafter (with J being the total angular momentum quantum number, and l and j being the relative angular and rotational quantum numbers, respectively), state-to-state cross sections $\sigma_{j' \leftarrow j}$ are obtained as⁴⁵

$$\sigma_{j' \leftarrow j} = \frac{\pi}{(2j+1)k_j^2} \sum_{J=0}^{\infty} \sum_{l=|j-j'|}^{J+j} \sum_{l'=|j-j'|}^{J+j'} (2J+1) \times |\delta_{jj'} \delta_{ll'} - S^J(j'l',jl)|^2, \quad (5)$$

with the squared wavenumber $k_j^2 = \frac{2\mu}{\hbar^2} [E - E_j]$ (where E is the total energy of the system and E_j is the energy of the j th rotational level of the rigid rotor).

Rate coefficients $k_{j' \leftarrow j}$ are the Maxwellian average of these collisional cross sections at a given temperature T , such as⁴⁵

$$k_{j' \leftarrow j}(T) = \sqrt{\frac{8k_B T}{\pi\mu}} \left(\frac{1}{k_B T} \right)^2 \times \int_0^{\infty} E_{kin} \sigma_{j' \leftarrow j}(E_{kin}) e^{-(E_{kin}/k_B T)} dE_{kin}, \quad (6)$$

where k_B is the Boltzmann constant and $E_{kin} = E - E_j$ is the kinetic energy of the collision.

2. Pressure broadening (PB) coefficients

Pressure broadening (PB) coefficients, which are by-products of S-matrices, were computed for the R(0), R(10), and P(2) lines corresponding to the ν_3 band ($00^0_0 \rightarrow 00^0_1$).

Only rotational levels with even values of j exist in the vibrational ground state (00^0_0), and only the ones with odd j values exist

TABLE I. MOLSCAT parameters j_{max} , J_{max} , λ_{max} , STEPS depending on the energy, and the energy step DNRG used to span the energy grid.

E (cm^{-1})	j_{max}	J_{max}	STEPS	λ_{max}	DNRG
2.4–10	12	12–17	74	14	0.1
10–20	12	17–21	74	14	0.2
20–50	16	21–28	24	14	0.2
50–100	20	28–36	19	14	0.2
100–150	24	36–41	15	14	0.2
150–200	28	41–45	13	14	0.5
200–300	32	45–53	12	18	0.5
300–500	40	53–65	22	18	1
500–1000	54	65–84	10	16	2
1000–2500	54	84–117	6	14	50

in $\nu_3(00^01)$ due to nuclear spins statistics.²⁷ Since the PES of this work was computed only for the ground vibrational state, we made the assumption that both these vibrational states have the same PES, which means that we neglected the vibrational dependence of the PES. In addition, the vibrational coupling was also neglected, and thus, it is equivalent to consider all rotational states, with even and odd j , on the same PES.

PB coefficients γ^0 designate the *half-width-at-half-maximum* (HWHM) of the Lorentzian-shape spectroscopic line. Its normalized per helium atmosphere expression is^{10,30}

$$\gamma^0 = n_p \bar{v} \langle \sigma^{(n)}(jj'; E_{kin}) \rangle = \frac{56.6915}{\sqrt{\mu T}} \bar{\sigma}, \quad (7)$$

where γ^0 unit is $10^{-3} \text{ cm}^{-1} \text{ atm}^{-1}$, n_p is the density of perturbers, $\bar{v} = \sqrt{8k_B T / \pi \mu}$ is the mean velocity, μ is the reduced mass of the $\text{CO}_2\text{-He}$ complex, and $\bar{\sigma}$ is the thermally averaged PB cross sections in \AA^2 . These PB cross sections are expressed as follows:¹⁰

$$\begin{aligned} \sigma^{(n)}(jj'; E_{kin}) &= \left(\frac{\pi}{k_j^2} \right) \sum_{jj'l'l'} (2J+1)(2J'+1) \\ &\times \begin{Bmatrix} j & n & j' \\ J' & l & J \end{Bmatrix} \begin{Bmatrix} j & n & j' \\ J' & l' & J \end{Bmatrix} \\ &\times \left[\delta_{ll'} - \langle j'l'|S^l(E_{kin} + E_j)|jl \rangle \right. \\ &\left. \times \langle j'l'l'|S^{l'}(E_{kin} + E_{j'})|j'l \rangle^* \right], \end{aligned} \quad (8)$$

where n is the tensor order of the radiative transition ($0 = \text{isotropic Raman}$, $1 = \text{infrared}$, and $2 = \text{anisotropic Raman}$).

IV. PES

The PES of this work, computed at the CCSD(T)/CBS(T,Q,5) level of theory, has a global minimum $V = -49.22 \text{ cm}^{-1}$ for the T-shape complex ($\theta = 90^\circ$) at $R = 5.78a_0$ and a local minimum

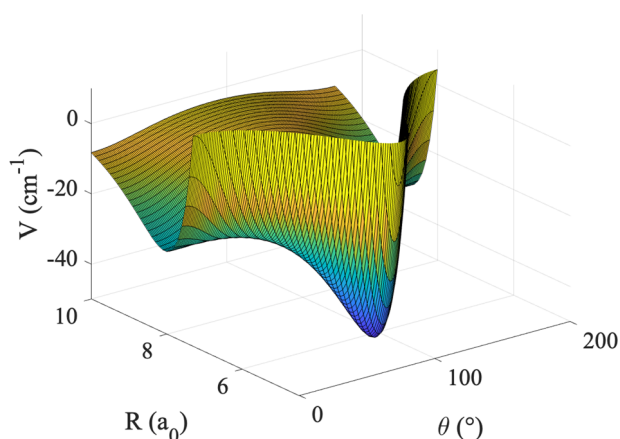


FIG. 3. PES in 3D of the $\text{CO}_2\text{-He}$ collisional system.

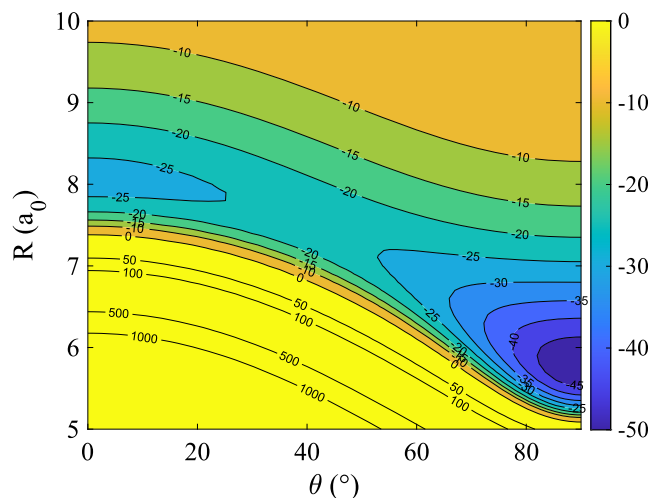


FIG. 4. Isocontours of the PES of the $\text{CO}_2\text{-He}$ collisional system.

$V = -26.51 \text{ cm}^{-1}$ for the linear geometry ($\theta = 0^\circ$) at $R = 8.05a_0$. A representation of this PES is given in 3D in Fig. 3, and its isocontours are presented in Fig. 4.

The PES of this work is compared to the PES of some of the most recently published studies by Negri *et al.*,²⁹ Korona *et al.*,³⁰ Ran and Xie,⁸ and Li and LeRoy³² (see Table II that lists the positions and well depths of the global and local minima). In this study and previous studies, minima are at the same geometry (T-shape and linear-shape).

As found in previous studies, the interaction around the global minimum is highly anisotropic. Positions and well depths of all PESs are in really good agreement. The PES of Negri *et al.*²⁹ has the least deep potential wells, followed by the PES of this work. The potential wells obtained by Korona *et al.*³⁰ for both the T-shape and the linear-shaped complex are the deepest ones. Their global minimum is over 2% deeper than that obtained in this work and almost 10% deeper than that obtained in the work of Negri *et al.*²⁹ Ran and Xie,⁸ Li and LeRoy,³² and this work have very similar PESs, which is not surprising since we used a similar theoretical approach.

As we did not use any mid-bond functions and used a highly correlated method with an extrapolation to the complete basis set, we are confident in the accuracy of the PES of this work for the

TABLE II. Properties of global ($\theta = 90^\circ$) and local ($\theta = 0^\circ$) minima for the present and previously computed PESs of the $\text{CO}_2\text{-He}$ vdW complex.

References	Global minimum		Local minimum	
	$R (a_0)$	$V (\text{cm}^{-1})$	$R (a_0)$	$V (\text{cm}^{-1})$
This work	5.78	-49.22	8.05	-26.51
Negri <i>et al.</i> ²⁹	5.86	-45.98	8.13	-26.31
Korona <i>et al.</i> ³⁰	5.81	-50.38	8.03	-28.94
Ran and Xie ⁸	5.79	-49.39	8.06	-26.70
Li and LeRoy ³²	5.78	-49.57	8.06	-26.69

short-, intermediate-, and long-range of interactions. It will be demonstrated by a comparison between theoretical data computed based on the PES of this work and experimental measurements, such as bound state transition frequencies and pressure broadening coefficients.

V. TEST OF THE NEW CO₂-He PES ACCURACY

A. Bound states

We have computed the energies of the bound states supported by the CO₂-He vdW well. The transition frequencies in the CO₂-He complex were deduced from the computed bound state energies. Frequencies of $\Delta(0_{00}-1_{01})$, $\Delta(0_{00}-1_{11})$, $\Delta(0_{00}-2_{02})$, and $\Delta(0_{00}-3_{03})$ transitions were computed for 4 CO₂ isotopologues: ¹²C¹⁶O₂, ¹³C¹⁶O₂, ¹²C¹⁸O₂, and ¹³C¹⁸O₂. Bound states are labeled with the rigid asymmetric rotor quantum numbers $J_{K_a K_c}$, where K_a and K_c are projections of J over the inertia moment axis. The frequencies of this work and previous theoretical ones from Korona *et al.*,³⁰ Li and LeRoy,³² and Ran and Xie⁸ are presented in Table III. This table contains also the absolute relative error = $|v_{th.} - v_{expt.}|/v_{expt.}$ with experimental values, which are obtained from the work of Xu and Jäger²⁶ for ¹²C isotopologues and from McKellar²⁷ for ¹³C ones.

Computed frequencies of the $\Delta(0_{00}-1_{01})$ transition for the ¹²C¹⁶O₂ isotopologue are very similar for all theoretical studies^{8,30,32} and in good agreement with the experimental measurement, the relative errors being lower than 0.6%. Additionally, Li and LeRoy³² and this work computed other transition frequencies, such as $\Delta(0_{00}-1_{01})$ for the ¹³C¹⁶O₂ isotopologue and $\Delta(0_{00}-1_{11})$ for both ¹²C¹⁸O₂ and ¹³C¹⁸O₂ isotopologues. Again, the results are similar and in excellent agreement with experimental values. We also provide further transition frequencies $\Delta(0_{00}-2_{02})$ and $\Delta(0_{00}-3_{03})$ for ¹³C-based isotopologues. They are in very good agreement with experimental values, the highest absolute error for these transitions being ~0.3%.

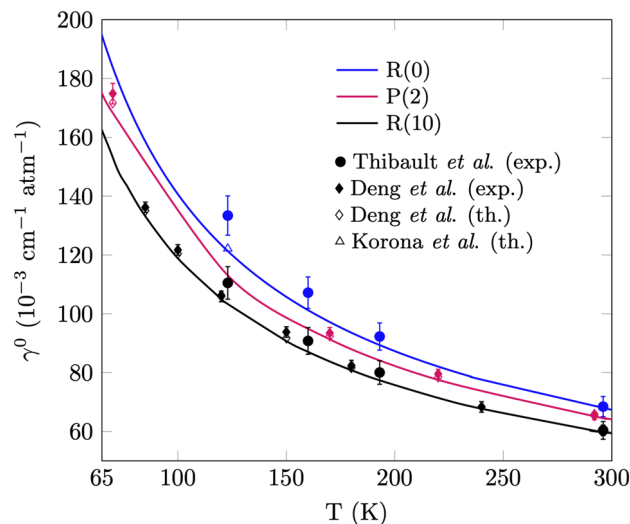


FIG. 5. HWHM γ^0 for R(0), R(10), and P(2) lines from our theoretical study (lines); experimental studies of Thibault *et al.*¹⁰ (●) and Deng *et al.*¹¹ (◆); theoretical results of Deng *et al.*¹¹ (◇) and Korona *et al.*³⁰ (△); which are obtained based on Korona *et al.*³⁰ PES for both studies. The marks are color-coded for the lines investigated. Some of the experimental values overlay theoretical ones.

Thus, the accuracy of the shape and the depth of the potential well is validated.

B. Pressure broadening coefficients

The PB coefficients that we obtained with the PES of this work for the ¹²C¹⁶O₂ isotopologue were compared to experimental ones provided by Thibault *et al.*¹⁰ and Deng *et al.*¹¹ in Fig. 5. The latter

TABLE III. Frequencies of several bound state transitions within v_0 for different isotopologues and theoretical studies.^{8,30,32}

$\Delta(J_{K_a K_c} - J'_{K'_a K'_c})$	Isotopologues		This work	Ran and Xie ⁸	Korona <i>et al.</i> ³⁰	Li and LeRoy ³²
$\Delta(0_{00}-1_{01})$	¹² C ¹⁶ O ₂	ν (cm ⁻¹)	0.589	0.589	0.592	0.588
		abs. error (%) ²⁶	0.436	0.436	0.072	0.588
	¹³ C ¹⁶ O ₂	ν (cm ⁻¹)	0.588			0.587
		abs. error (%) ²⁷	0.508			0.677
$\Delta(0_{00}-1_{11})$	¹² C ¹⁸ O ₂	ν (cm ⁻¹)	0.576			0.575
		abs. error (%) ²⁶	0.472			0.645
	¹³ C ¹⁸ O ₂	ν (cm ⁻¹)	0.575			0.575
		abs. error (%) ²⁷	0.519			0.519
$\Delta(0_{00}-2_{02})$	¹³ C ¹⁶ O ₂	ν (cm ⁻¹)	1.577			
		abs. error (%) ²⁷	0.316			
	¹³ C ¹⁸ O ₂	ν (cm ⁻¹)	1.482			
		abs. error (%) ²⁷	0.202			
$\Delta(0_{00}-3_{03})$	¹³ C ¹⁶ O ₂	ν (cm ⁻¹)	2.919			
		abs. error (%) ²⁷	0.311			

made their measurements with the $^{13}\text{CO}_2$ isotopologue and indicated that the substitution of $^{12}\text{CO}_2$ by $^{13}\text{CO}_2$ includes an error smaller than 0.1% on calculated PB cross sections.¹¹ Our results are also compared to theoretical ones provided by Deng *et al.*¹¹ for the R(10) and P(2) lines and by Korona *et al.*³⁰ for the R(0) line. Both these calculations were performed based on the PES of Korona *et al.*³⁰

As expected from Eq. (7) (in particular, at room temperature), the HWHM for all considered lines is decreasing with increasing temperature. Our results and the ones theoretically obtained based on the PES of Korona *et al.*³⁰ show an overall good agreement with experimental measurements for all the present lines. At lower temperatures, there is slightly less agreement with the data of Thibault *et al.*¹⁰ but they pointed out that their experimental values for this temperature range may suffer an unexplained bias.¹⁰ However, at a temperature above 200 K, our results are within the error bars, indicating that the accuracy of the PES is good. In addition, we note that both the experimental setup and the line shape analysis used by Deng *et al.*¹¹ are more accurate than the ones used by Thibault *et al.*¹⁰ Thus, the very good agreement between our calculated values for the P(2) and R(10) HWHM, and the experimental results of Deng *et al.*¹¹ give us confidence in the quality of the PES of this work.

The temperature range investigated is above the dissociation limit of the bound complex, and thus, this comparison with experimental data is mainly a test of the repulsive wall.¹¹ Therefore, the repulsive wall of the surface considered in this work is validated.

VI. COLLISIONAL DATA AND DISCUSSION

A. Inelastic cross sections and rate coefficients

In Fig. 6, cross sections resulting from scattering calculations detailed in Sec. III C are provided for excitations from the rotational level $j = 0$ for various $\Delta j = |j' - j|$ as a function of kinetic energy.

At low collisional energy ($E_{\text{kin}} \sim 50 \text{ cm}^{-1}$), Feshbach and shape resonances⁴⁶ can be observed. These are due to a temporary formation of the $\text{CO}_2\text{-He}$ vdW complex when the energy corresponds to a (quasi)bound state energy in the potential well. It

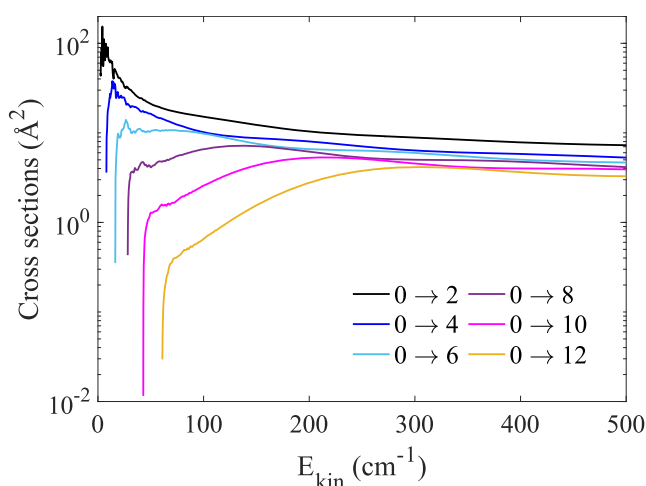


FIG. 6. Cross sections for $j = 0$ at various Δj as a function of kinetic energy.

explains why such resonances disappear when kinetic energy is large compared to the well depth. Thus, in order to correctly represent such phenomena, the grid of energy needs to be really dense at low energy.

The general propensity rule is, as expected, favoring excitation with the lowest Δj (here equal to 2 since rotational levels with odd j do not exist), in agreement with the exponential energy-gap behavior.⁷ Hence, as Δj increases, so does the energy gap and thus cross sections decrease. However, for cross sections with a $\Delta j \geq 6$, this propensity rule vanishes at particular collisional energy, and cross sections for this Δj are similar to cross sections for $\Delta j \pm 2$, for example, $\sigma_{0 \rightarrow 4} \sim \sigma_{0 \rightarrow 6}$ at $E_{\text{kin}} \sim 110 \text{ cm}^{-1}$, $\sigma_{0 \rightarrow 6} \sim \sigma_{0 \rightarrow 8}$ at $E_{\text{kin}} \sim 170 \text{ cm}^{-1}$, and $\sigma_{0 \rightarrow 8} \sim \sigma_{0 \rightarrow 10}$ at $E_{\text{kin}} \sim 240 \text{ cm}^{-1}$. It is also the case for $\sigma_{0 \rightarrow 10}$, which is almost equal to $\sigma_{0 \rightarrow 12}$ at $E_{\text{kin}} \sim 340 \text{ cm}^{-1}$. The small difference between the cross sections at higher kinetic energies can be explained by the fact that the rotational constant of the CO_2 molecule is low, and thus, the energy spacing between rotational states becomes negligible compared to the kinetic energy.

Rate coefficients presented in Fig. 7 were obtained from thermal averaging of the above-mentioned state-to-state cross sections.

The propensity rule is still favoring (de-)excitation with the lowest Δj . These rate coefficients decrease as the initial rotational quantum number j increases because of the increasing energy gap to reach the next levels. However, contrary to cross sections of Fig. 6, this rule does not vanish over the temperature range explored in this work. It is explained by the high weight given to low kinetic energy behavior in the Maxwellian average of the cross sections. In addition, we can observe that an asymptotical value is reached for rate coefficients with $\Delta j \leq 6$.

In order to observe the sensitivity of the rate coefficients to the PES, relaxation rate coefficients obtained in this work from $j = 8$ to $j' = 6, 4, 2$, and 0 are compared in Fig. 8 to the ones obtained by Yang and Stancil,⁷ which were computed on the PES of Ran and Xie.⁸ Their dynamical calculations were performed with the CC approach for collisional energies lower than 500 cm^{-1} and with the CS approximation for energies up to 10^4 cm^{-1} . The rotational level considered

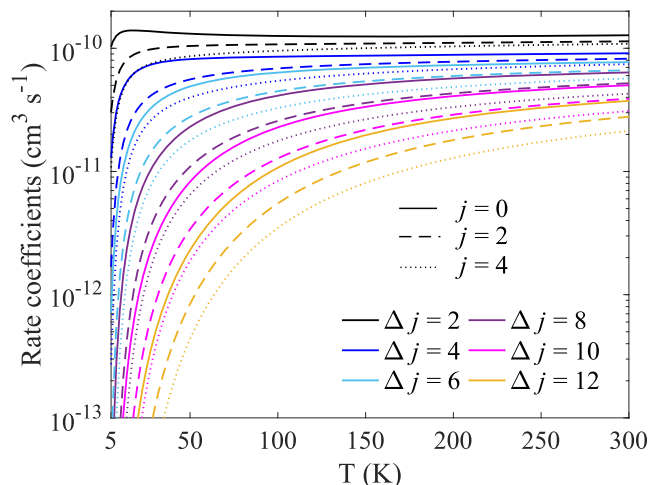


FIG. 7. Excitation rate coefficients from $j = 0, 2$, and 4 for various Δj as a function of temperature.

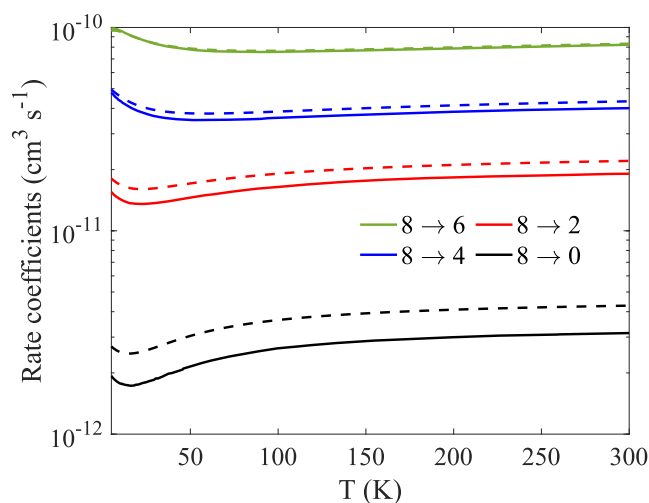


FIG. 8. Relaxation rate coefficients from Yang and Stancil⁷ (dashed lines) and our study (solid lines) from $j = 8$ to various j' as a function of temperature.

here is $j = 8$, which states at 28.096 cm^{-1} , and thus, we consider that we are comparing here rate coefficients obtained with very similar dynamical calculations and then that the observed differences are almost exclusively due to the different PESs used.

The rate coefficients of this work (solid lines) and the ones obtained by Yang and Stancil⁷ (dashed lines) have the same behavior, and the agreement for low Δj is very good. However, for larger Δj transitions, the new rate coefficients can be 1.5 times higher than the former ones. In fact, the bigger Δj is, the larger the difference is.

In the present case, we can suspect that their radial coefficients for $l \geq 6$ are smaller than the ones obtained in this work (v_8 in particular), a consequence of a slightly lower anisotropy of their PES. In this temperature range, the rate coefficients are more sensitive to the short/intermediate-range of interaction on the PES. Thus, it is the anisotropy in the PES well and on the repulsive wall that must differ and leads to non-negligible differences in the scattering calculations.

Despite the use of similar approaches and *ab initio* methods leading to a difference on the global minimum of the surface inferior to 1% and a similar dynamical method (CC), the difference between the rate coefficients can be up to 50%. Indeed, the magnitude of the cross sections is determined by both the well depth and the global anisotropy of the PES. Therefore, it is of primary importance to use a PES as accurate as possible.

B. CO₂: A super-rotor in helium-buffer-gas

In the aim of checking the effect of different PESs on cross sections for this collisional system, we compared cross sections of this work to the ones of al-Qady *et al.*¹³ in Fig. 9. Our results are in solid lines, and the results of al-Qady *et al.* are in dashed lines.

The main purpose of the study of al-Qady *et al.*¹³ was the demonstration of the feasibility of producing CO₂ super-rotors, i.e., highly rotationally excited CO₂ in a cold helium-buffer-gas. Producing this kind of systems can be useful in order to study intramolecular forces, inelastic collisions, and cold chemistry.¹³

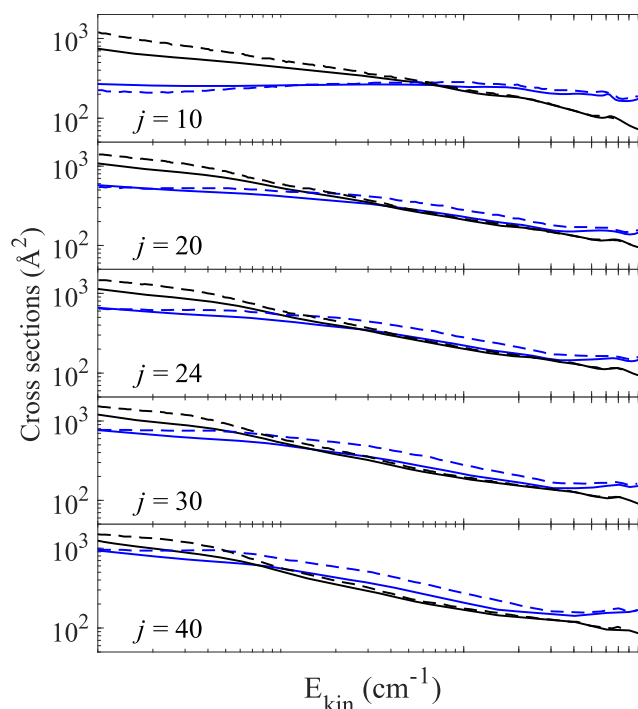


FIG. 9. Elastic (blue) and quenching (black) cross sections for CO₂ and He collisions at $j = 10, 20, 24, 30,$ and 40 in al-Qady *et al.*¹³ (dashed lines) and our study (solid lines).

To produce such a stable system, the elastic cross section of a rotational level j must be larger than the downward cross sections at the cryogenic temperature of the buffer-gas, which is 4.2 K in the case of helium at atmospheric pressure. To provide cross sections from $j = 10, 20, 24, 30,$ and 40 , al-Qady *et al.*¹³ used the PES of Ran and Xie⁸ and performed CC scattering calculations.

The crossing between lines represents the physical conditions from which rotationally excited CO₂ is stable in a buffer-gas of helium despite collisions occur. Both studies give similar results, tendency, and crossing energies. In both, we observe that the higher the j is, the lower the kinetic energy is at the crossing between the lines so the wider is the temperature range of stability for the super-rotor. It suggests that producing a stable CO₂ super-rotor in a helium-buffer-gas is feasible.

However, the stability of such super-rotors may have been overestimated. In fact, elastic cross sections of this work are lower than the ones obtained by al-Qady *et al.*¹³ Furthermore, crossing energies of this work are slightly shifted to higher values of energy, indicating a decreasing stability of the system compared to the previous results. Therefore, a stable CO₂ super-rotor in a helium-buffer-gas appears to be possible, even though a bit more difficult to generate than previously predicted.

Moreover, another point needs to be highlighted: There is up to almost 30% of difference on the quenching cross sections at low energy. It exhibits that at low collisional energies, cross sections (and thus rate coefficients) are really sensitive to the PES. Yang and Stancil⁷ also emphasized this point by comparing state-to-state cross sections obtained with the PESs of Negri *et al.*,²⁹ Korona *et al.*,³⁰ and

Ran and Xie⁸ for collisional energies between 5×10^{-4} and 100 cm^{-1} . They exhibited that even the behavior of these cross sections can be different depending on the PES used.

The potential well depth of both surfaces are really similar, and the repulsive wall is not a topological feature of importance at such low collisional energy,²² contrary to the long-range of interactions. We can thus confirm that rotational inelastic cross sections are highly sensitive to the global anisotropy of the system (along all the radial coordinates), as suggested by Benvenuti *et al.*,²⁴ and specifically to the anisotropy of the long-range of interactions in the present case.

VII. CONCLUSIONS

This work presented a new potential energy surface of the $\text{CO}_2\text{-He}$ van der Waals complex. It was computed with the highly correlated CCSD(T) method and an extrapolation to the complete basis set, noted CBS(T, Q, 5). The PES accuracy was tested through a comparison between theoretical and experimental bound state transition frequencies and pressure broadening coefficients. The very good agreement with experimental results certified that the computed PES is homogeneously accurate.

After the validation of the PES of this work, collisional cross sections, which exhibited characteristic resonances, were calculated with the CC approach. Using the Maxwellian average of these cross sections, revised rate coefficients for this system in the 10–300 K temperature range were obtained.

The rate coefficients of this work exhibit up to 50% differences with the ones computed by Yang and Stancil⁷ based on the PES of Ran and Xie,⁸ even though a similar dynamical approach was used. Based on this same PES and with the same dynamical approach, al-Qady *et al.*¹³ computed cross sections at low temperature, which are up to 30% lower than those obtained in this work. It was thus highlighted that small discrepancies on the short- and long-range anisotropy of the PES can induce significant differences in collisional data, which need to be as accurate as possible for astrophysical modeling.

$\text{CO}_2\text{-He}$ rate coefficients can be used as a first approximation⁵ to model more complex CO_2 -bearing collisional systems, such as $\text{CO}_2\text{-H}_2$ or $\text{CO}_2\text{-H}$, which are useful systems for interstellar molecular clouds and planetary atmospheres. Knowing that the new rates can be up to 1.5 times higher than the old ones suggests that the use of improved scattering data can lead to non-negligible consequences on the modeling of the CO_2 abundance in a large variety of astrophysical media. In addition, measuring the CO_2 abundances is also a test of astrochemical models, since this molecule is at the end of reaction chains, implying the CO molecule and the OH radical, or the O_2 molecule and CH_2 or HCCO .⁴⁷

SUPPLEMENTARY MATERIAL

See the [supplementary material](#) for a Fortran subroutine of the potential energy surface.

ACKNOWLEDGMENTS

We acknowledge financial support from the European Research Council (Consolidator Grant COLLEXISM, Grant Agreement No. 811363) and the Programme National “Physique et Chimie du

Milieu Interstellaire” (PCMI) of CNRS/INSU with INC/INP co-funded by CEA and CNES.

F.L. acknowledges the Institut Universitaire de France.

A.G. thanks B. Desrousseaux, C. Bop, S. Demes, and M. Zóltowski for their help and support during this work. This work was supported by Rennes Metropole.

AUTHOR DECLARATIONS

Conflict of Interest

The authors have no conflicts to disclose.

DATA AVAILABILITY

The data that support the findings of this study are available from the corresponding author upon reasonable request.

REFERENCES

- L. D'Hendecourt and M. Jourdain de Muizon, *Astron. Astrophys.* **223**, L5 (1989).
- A. D. Bosman, S. Bruderer, and E. F. van Dishoeck, *Astron. Astrophys.* **601**, A36 (2017).
- D. Despois, N. Biver, D. Bockelée-Morvan, and J. Crovisier, *Proc. Int. Astron. Union* **1**, 469 (2006).
- E. F. van Dishoeck, *Annu. Rev. Astron. Astrophys.* **42**, 119 (2004).
- E. Roueff and F. Lique, *Chem. Rev.* **113**, 8906 (2013).
- J. Cernicharo, J. R. Goicoechea, and E. Caux, *Astrophys. J.* **534**, L199 (2000).
- B. Yang and P. C. Stancil, *J. Chem. Phys.* **130**, 134319 (2009).
- H. Ran and D. Xie, *J. Chem. Phys.* **128**, 124323 (2008).
- R. Matveeva, M. Falck Erichsen, H. Koch, and I. M. Høyvik, *J. Comput. Chem.* **43**, 121 (2021).
- F. Thibault, B. Calil, J. Boissoles, and J. M. Launay, *Phys. Chem. Chem. Phys.* **2**, 5404 (2000).
- W. Deng, D. Mondelain, F. Thibault, C. Camy-Peyret, and A. W. Mantz, *J. Mol. Spectrosc.* **256**, 102 (2009).
- As it can be seen in Sec. II, all recent $\text{CO}_2\text{-He}$ PES were computed with mid-bond functions so we wanted to provide the first highly accurate PES without them.
- W. H. al-Qady, R. C. Forrey, B. H. Yang, P. C. Stancil, and N. Balakrishnan, *Phys. Rev. A* **84**, 054701 (2011).
- V. K. Nikulin and Yu. N. Tsarev, *Chem. Phys.* **10**, 433 (1975).
- R. G. Gordon and Y. S. Kim, *J. Chem. Phys.* **56**, 3122 (1972).
- Y. S. Kim and R. G. Gordon, *J. Chem. Phys.* **60**, 1842 (1974).
- G. A. Parker, R. L. Snow, and R. T. Pack, *J. Chem. Phys.* **64**, 1668 (1976).
- G. A. Parker and R. T. Pack, *J. Chem. Phys.* **68**, 1585 (1978).
- M. Keil, G. A. Parker, and A. Kuppermann, *Chem. Phys. Lett.* **59**, 443 (1978).
- C. L. Stroud and L. M. Raff, *J. Chem. Phys.* **72**, 5479 (1980).
- D. C. Clary, *Chem. Phys.* **65**, 247 (1982).
- M. Keil and G. A. Parker, *J. Chem. Phys.* **82**, 1947 (1985).
- M. Keil, L. J. Rawluk, and T. W. Dingle, *J. Chem. Phys.* **96**, 6621 (1992).
- L. Beneventi, P. Casavecchia, F. Vecchiocattivi, G. G. Volpi, U. Buck, C. Lauenstein, and R. Schinke, *J. Chem. Phys.* **89**, 4671 (1988).
- M. J. Weida, J. M. Sperhac, D. J. Nesbitt, and J. M. Hutson, *J. Chem. Phys.* **101**, 8351 (1994).
- Y. Xu and W. Jäger, *J. Mol. Struct.* **599**, 211 (2001).
- A. R. W. McKellar, *J. Chem. Phys.* **125**, 114310 (2006).
- G. Yan, M. Yang, and D. Xie, *J. Chem. Phys.* **109**, 10284 (1998).
- F. Negri, F. Ancilotto, G. Mistura, and F. Toigo, *J. Chem. Phys.* **111**, 6439 (1999).
- T. Korona, R. Moszynski, F. Thibault, J.-M. Launay, B. Bussery-Honvault, J. Boissoles, and P. E. S. Wormer, *J. Chem. Phys.* **115**, 3074 (2001).
- J. Boissoles, F. Thibault, R. Le Doucen, V. Menoux, and C. Boulet, *J. Chem. Phys.* **101**, 6552 (1994).

- ³²H. Li and R. J. Le Roy, *Phys. Chem. Chem. Phys.* **10**, 4128 (2008).
- ³³T. Selim, A. Christianen, A. van der Avoird, and G. C. Groenenboom, *J. Chem. Phys.* **155**, 034105 (2021).
- ³⁴G. Guelachvili, *J. Mol. Spectrosc.* **79**, 72 (1980).
- ³⁵G. Chałasiński, J. Rak, M. M. Szczyński, and S. M. Cybulski, *J. Chem. Phys.* **106**, 3301 (1997).
- ³⁶K. A. Peterson, D. E. Woon, and T. H. Dunning, *J. Chem. Phys.* **100**, 7410 (1994).
- ³⁷S. F. Boys and F. Bernardi, *Mol. Phys.* **19**, 553 (1970).
- ³⁸H.-J. Werner, MOLPRO, a package of *ab initio* programs, version 2010.1, 2010.
- ³⁹J. Hutson, BOUND computer code, version 5, distributed by Collaborative Computational Project No. 6 of the Science and Engineering Research Council, 1993.
- ⁴⁰D. E. Manolopoulos, *J. Chem. Phys.* **85**, 6425 (1986).
- ⁴¹L. S. Rothman and L. D. G. Young, *J. Quant. Spectrosc. Radiat. Transfer* **25**, 505 (1981).
- ⁴²G. Graner, C. Rossetti, and D. Bailly, *Mol. Phys.* **58**, 627 (1986).
- ⁴³T. L. Wilson, *Annu. Rev. Astron. Astrophys.* **32**, 191 (1994).
- ⁴⁴J. Hutson and S. Green, Molscat computer program, version 14, distributed by Collaborative Computational Project No. 6 of the UK Science and Engineering Research Council, 1994.
- ⁴⁵A. M. Arthurs and A. Dalgarno, *Proc. R. Soc. London, Ser. A* **256**, 540 (1960).
- ⁴⁶M. Costes and C. Naulin, *Chem. Sci.* **7**, 2462 (2016).
- ⁴⁷J. A. Miller, R. J. Kee, and C. K. Westbrook, *Annu. Rev. Phys. Chem.* **41**, 345 (1990).

A.2 Fine-Structure Excitation of CCS by He: Potential Energy Surface and Scattering Calculations

Fine-structure excitation of CCS by He: Potential energy surface and scattering calculations

Cite as: J. Chem. Phys. **158**, 044303 (2023); <https://doi.org/10.1063/5.0138470>

Submitted: 12 December 2022 • Accepted: 08 January 2023 • Accepted Manuscript Online: 11 January 2023 • Published Online: 30 January 2023

 A. Godard Palluet and  F. Lique



View Online



Export Citation



CrossMark

ARTICLES YOU MAY BE INTERESTED IN

Rotational excitation of CO₂ induced by He: New potential energy surface and scattering calculations

The Journal of Chemical Physics **156**, 104303 (2022); <https://doi.org/10.1063/5.0085094>

Rotational excitation of NS⁺ by H₂ revisited: A new global potential energy surface and rate coefficients

The Journal of Chemical Physics **156**, 204311 (2022); <https://doi.org/10.1063/5.0089745>

Collisional excitation of NH by H₂: Potential energy surface and scattering calculations

The Journal of Chemical Physics **155**, 134303 (2021); <https://doi.org/10.1063/5.0066161>

Learn More

The Journal
of Chemical Physics **Special Topics** Open for Submissions

Fine-structure excitation of CCS by He: Potential energy surface and scattering calculations

Cite as: J. Chem. Phys. 158, 044303 (2023); doi: 10.1063/5.0138470

Submitted: 12 December 2022 • Accepted: 8 January 2023 •

Published Online: 30 January 2023



View Online



Export Citation



CrossMark

A. Godard Palluet^{a)}  and F. Lique^{a)} 

AFFILIATIONS

Université de Rennes 1, CNRS, IPR (Institut de Physique de Rennes)—UMR 6251, F-35000 Rennes, France

^{a)} Authors to whom correspondence should be addressed: amelie.godard@univ-rennes1.fr and francois.lique@univ-rennes1.fr

ABSTRACT

The fine structure excitation of the interstellar CCS radical induced by collisions with He is investigated. The first potential energy surface (PES) for the CCS–He van der Waals complex is presented. It was obtained from a highly correlated spin unrestricted coupled cluster approach with single double and perturbative triple excitations. The PES presents two shallow minima of 31.85 and 37.12 cm⁻¹ for the linear (He facing S) and the nearly T-shaped geometries, respectively. The dissociation energy of the complex was calculated and found to be $D_0 = 14.183$ cm⁻¹. Inelastic scattering calculations were performed using the close-coupling approach. Cross-sections for transitions between the 61 first fine structure levels of CCS were obtained for energy up to 600 cm⁻¹ and rate coefficients for the 5–50 K temperature range were derived. This set of collisional data can be used to model CCS emission spectra in dark molecular interstellar clouds and circumstellar envelopes and enable an accurate determination of CCS abundance in these astrophysical media.

Published under an exclusive license by AIP Publishing. <https://doi.org/10.1063/5.0138470>

I. INTRODUCTION

In 1984, a new emission line at 45.379 GHz was detected in TMC-1, TMC-2, and SgrB2 by Suzuki *et al.*¹ but remains unidentified due to its atypical shape explained by an extraordinary large spin-splitting.¹ At that time, it was the most intense unassigned line among radio lines,^{1,2} suggesting that the observed molecule is one of the most abundant species in molecular clouds.³ This mysterious line was finally assigned to the CCS(³Σ⁻) radical a few years later by Saito *et al.*³

After this detection, astronomers started to look for longer carbon chains containing sulfur, now convinced that they exist in space.⁴ Hence, C_nS ($n = 3, 4, 5$) chains were detected in several astronomical sources.^{2,5–9} Researchers also started to investigate the formation processes of these carbon chains. Different mechanisms were discussed for decades,^{10–20} and still are. Their main production pathways are thought to involve ion–neutral reactions forming HC_nS⁺, followed by its dissociative recombination.^{10–14,17,20} It was also proposed that these carbon-chains can be formed and can grow through neutral–neutral reactions involving C_nS or H_mC_nS ($m, n = 1, 2$) molecules.^{15–20} In addition, proofs were reported that sulfur-containing carbon chains chemistry is related to the one of the nitrogen-containing carbon-chains.^{14,21}

After its first assignment, CCS was widely observed in dark molecular clouds, including TMC-1.^{2,4,14,21–28} It was also seen in the circumstellar envelope of IRC+10216,^{6,29} in the protostellar envelope of B335,²⁵ and in Bok globules.³⁰

The CCS molecule is a key to understand the physical and chemical evolution of molecular clouds.^{14,20,24,25} Its abundance is highly sensitive to physical conditions and, thus, reflects some properties that are hidden by other tracers.²⁴ Indeed, it is produced in dense gas as a result of the collapse of the core, and it is rapidly destroyed in the densest material of the central region. Its distribution will thus describe the variation of physical conditions of the observed molecular clouds.²⁴ Therefore, its abundance ratio with NH₃, which will be desorbed from the grain surfaces during star formation, indicates evolution stages of dense cores^{14,23,27} and Bok globules.³⁰ In addition, the CCS lines are intense enough to investigate physical structures of dense cores,²³ such as clumps and dense filaments, which are suggested to play a dominant role in the formation of prestellar cores.^{26,28} Finally, due to its fine structure, CCS can also be used to estimate the magnetic field in molecular clouds by measuring the Zeeman splitting of its lines.^{31,32}

A reliable modeling of chemical species abundances from emission spectra requires accurate collisional data.³³ Collisional excitation in molecular clouds and circumstellar envelopes (astrophysical

media where CCS molecules are mostly detected) is mainly induced by H_2 and He. Such accurate collisional data do not exist yet for CCS to the best of our knowledge. In fact, due to the presence of an electronic spin, and a large spin-splitting, CCS very peculiar internal structures (see Sec. II B) can only be described with the intermediate coupling scheme as presented by Alexander and Dagdigan,³⁴ which makes the accurate collisional data quite difficult to compute.²⁵

In radiative transfer models involving CCS, three sets of approximate collisional data were used. Fuente *et al.*²¹ and Suzuki *et al.*¹⁴ computed CCS– H_2 rate coefficients using the OCS– H_2 rotational rate coefficients of Green and Chapman,³⁵ to which they reintroduced the spin dependence with the Infinite Order Sudden (IOS) approximation. Wolkovitch *et al.*²⁵ computed CCS– H_2 rotational rate coefficients based on OCS– H_2 potential energy surface (PES) of Green and Chapman³⁵ with the Close-Coupling (CC) approach. The spin dependence was also reintroduced with the IOS approximation. However, the IOS approximation, used to compute all these sets of collisional data, is considered not to be suitable for molecules presenting large spin-splitting such as CCS.^{21,25,36,37} Note that in all these calculations, H_2 was considered as a structureless projectile.

The aim of this work is to overcome this lack of accurate CCS collisional data by providing the first state-to-state rate coefficients for the CCS–He collisional system considering explicitly the fine structure levels of CCS.

To this end, a new highly correlated PES of the CCS–He system was computed. It was then used in scattering calculations using the close-coupling (CC) approach to provide the dissociation energy of the complex and fine structure resolved rate coefficients for the 5–50 K temperature range. The collisional data that we provide here could be used to derive accurate abundances of the CCS molecule in dark molecular clouds and circumstellar envelopes such as TMC-1 and IRC+10 216, respectively.

Section II presents the computational methods used to obtain the PES (Sec. II A), a description of the peculiar fine structure of the CCS ($^3\Sigma^-$) radical (Sec. II B), the methods used to compute the dissociation energy of the complex (Sec. II C), and scattering data (Sec. II D).

In Sec. III, the results of the calculations are presented. The new PES is described in Sec. III A. The dissociation energy D_0 of the complex and the effect of the fine structure on its computed value are discussed in Sec. III B. Accurate fine-structure resolved collisional rate coefficients based on cross-sections are presented in Sec. III C. Finally, the rate coefficients are compared to the latest set of CCS– H_2 data provided by Wolkovitch *et al.*²⁵ in Sec. III D.

II. METHODS

A. CCS–He potential energy surface (PES)

1. *Ab initio* calculations

In its ground electronic ($^3\Sigma^-$) and vibrational states, the CCS molecule is linear.^{38,39} The interaction potential between CCS and He was described using Jacobi coordinates (R, θ), where R is the distance between the center of mass of the CCS radical and the He atom and θ describes the angle between \mathbf{R} and CCS internuclear axis (see Fig. 1). The internuclear distances in the CCS radical were set at their experimental equilibrium distances $r_{\text{C-S}} = 2.96a_0$ and $r_{\text{C-C}} = 2.47a_0$.⁴

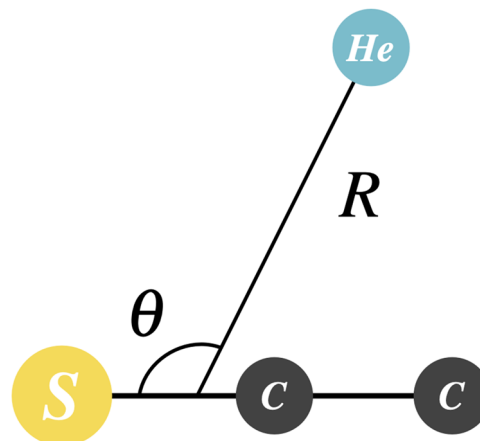


FIG. 1. Representation of the CCS–He collisional system in Jacobi coordinates.

The potential energy surface (PES) was computed with the spin unrestricted coupled-cluster single double and perturbative triple excitations *ab initio* method [UCCSD(T)]⁴⁰ and the augmented correlation consistent quadruple-zeta basis set (hereafter, aVQZ) augmented by additional mid-bond functions of Cybulski and Toczyłowski.⁴¹

The *ab initio* calculations have been performed for 32 values of θ between 0° and 180° with an unregular step. For each value of θ , 44 values of R were chosen between 4.5 and $30a_0$ with various steps in order to accurately describe the different range of interactions. All *ab initio* points were computed with the MOLPRO package.⁴²

The basis set superposition error was corrected at every geometry (R, θ) with the counterpoise procedure of Boys and Bernardi,⁴³

$$V(R, \theta) = E_{\text{CCS-He}}(R, \theta) - E_{\text{CCS}}(R, \theta) - E_{\text{He}}(R, \theta), \quad (1)$$

where $V(R, \theta)$ is the interaction potential, and all energies E are computed with the full basis set.

2. Analytical representation

A global fit of the interaction potential $V(R, \theta)$ was performed based on the 1351 *ab initio* points using an expansion over Legendre polynomials $P_\lambda(\cos \theta)$,⁴⁴

$$V(R, \theta) = \sum_{\lambda=0}^{\lambda_{\text{max}}} v_\lambda(R) P_\lambda(\cos \theta), \quad (2)$$

where λ_{max} was taken equal to 31 according to the number of θ angles calculated. The radial coefficients $v_\lambda(R)$ have been fitted following the procedure of Werner *et al.*⁴⁴ The long-range of interaction was fitted and extrapolated using a multipolar expansion with $\frac{C_n}{R^n}$ ($n = 6, 8, \text{ and } 10$) coefficients. The fitted potential reproduces all of our *ab initio* points with an error inferior to 1.7%. The root mean square (rms) deviation is equal to 3.51 cm^{-1} but is mostly due to deviations at short distances for angles between 140° and 180° where the PES is highly repulsive. The rms is about 0.016 cm^{-1} in the potential well regions [$V(R, \theta) < -1 \text{ cm}^{-1}$] and about 9.3×10^{-4} in the long-range of interactions [$0 \leq V(R, \theta) \leq -1 \text{ cm}^{-1}$].

B. Fine structure of CCS

In $^3\Sigma^-$ open-shell molecules, as CCS in its electronic ground state, a coupling between the electronic spin S and the rotational angular momentum of the radical N occurs. This so-called spin-rotation coupling will split the rotational levels into fine structure levels. CCS energy levels are described with an intermediate coupling representation.

The total angular momentum j is then expressed as

$$\mathbf{j} = \mathbf{N} + \mathbf{S}. \quad (3)$$

In the intermediate coupling scheme for $S = 1$, the rotational wavefunction can take three expressions for each $j \geq 1$ as^{34,45,46}

$$\begin{aligned} |F_1jm\rangle &= \cos \alpha |N = j - 1, Sjm\rangle + \sin \alpha |N = j + 1, Sjm\rangle, \\ |F_2jm\rangle &= |N = j, Sjm\rangle, \\ |F_3jm\rangle &= -\sin \alpha |N = j - 1, Sjm\rangle + \cos \alpha |N = j + 1, Sjm\rangle, \end{aligned} \quad (4)$$

where $|N, Sjm\rangle$ denotes pure Hund's case (b) basis functions and α is the mixing angle. This angle is obtained by diagonalization of the molecular Hamiltonian. It depends on j , on the rotational constant B_0 , on the spin-rotation constant γ_0 , and on the spin-spin constant λ_0 .

In pure Hund's case (b) limit, $\alpha \rightarrow 0$ and the F_1 , F_2 , and F_3 fine structure levels will correspond to $N = j - 1$, $N = j$, and $N = j + 1$, respectively.

Hereafter, each fine structure energy level will be labeled as for pure Hund's case (b) by the couple of quantum numbers N_j according to the astrophysical notation.

The rotational and fine energy levels of the CCS radical were computed with the use of McGuire *et al.*⁴⁷ spectroscopic constants: $B_0 = 0.216\,074\text{ cm}^{-1}$; $D = 5.760\,985 \times 10^{-8}\text{ cm}^{-1}$; $\gamma_0 = -4.907\,061 \times 10^{-4}\text{ cm}^{-1}$; $\lambda_0 = 3.242\,098\text{ cm}^{-1}$. Fine structure levels of CCS are represented in Fig. 2. For CCS, the fine structure levels are ordered by their rotational quantum number N only from $N_j \geq 10$. For N values from 1 to 10, α decreases from 41° to 17° , exhibiting the decreasing degree of coupling between pure Hund's case (b) basis as N increases.

C. Dissociation energy calculations

The dissociation energy D_0 of the $^{12}\text{C}^{12}\text{C}^{32}\text{S}$ -He complex was obtained from the new highly correlated PES using the coupled-channel approach. The coupled-equations were solved with the log-derivative method of Manolopoulos⁴⁸ as implemented in the BOUND software.⁴⁹

Calculations were performed both with only the rotational structure of CCS (e.g., neglecting the spin-rotation and spin-spin couplings) and then considering the fine structure of CCS. As the fine structure of CCS is peculiar, it might be expected to observe some impact on the bound state energies and, thus, on the dissociation energy, if the fine structure is taken into account or not.

The parameters were adjusted in order to converge the dissociation energy to better than 0.0001%. For the calculations with the rotational structure alone, the rotational basis contains the first 23 rotational levels (up to $N = 22$). The propagation parameter R_{max} and DR were set to $56a_0$ and 0.004, respectively. To accurately include

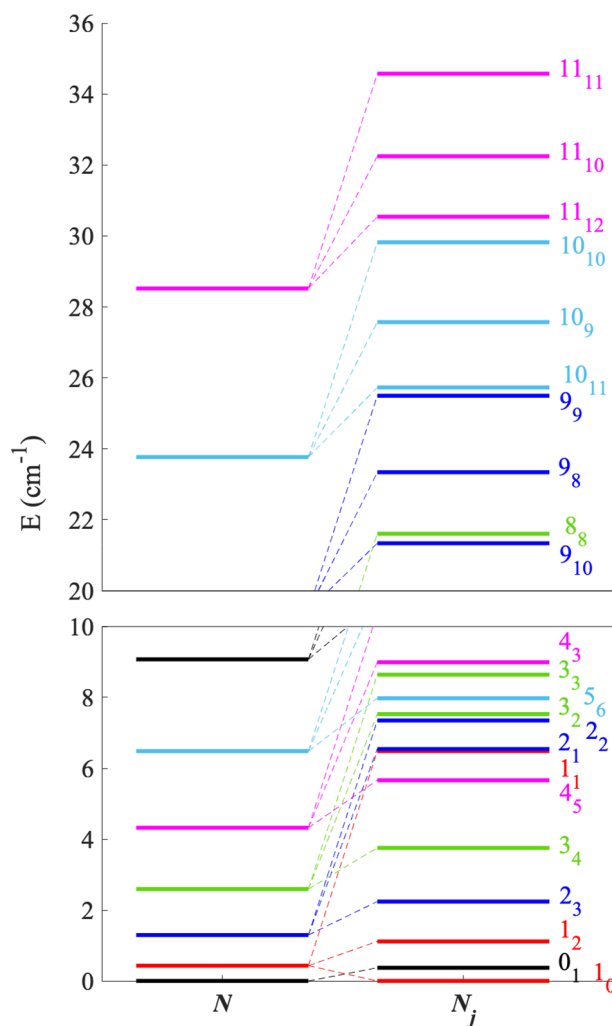


FIG. 2. Representation of the rotational (top) and fine structure (bottom) energy levels of the CCS($^3\Sigma^-$) radical.

the fine structure of CCS, a modified version of the BOUND software was used.⁴⁹ The basis contains the first 64 fine structure levels (up to $N_j = 21_j$). The propagation parameter R_{max} and DR were set to $36a_0$ and 0.014, respectively.

D. Scattering calculations

1. Cross sections and rate coefficients calculations

As previously mentioned, the CCS radical is often found in cold molecular clouds. The temperature in these astrophysical media varies from few to a few tenths of K.⁵⁰ CCS was also detected in the outer part of the B335 circumstellar envelope, where the temperature is about 25 K,²⁴ and in the outer part of the IRC+10 216 circumstellar envelope, in which the temperature is typically around 50 K.²⁹

In astrophysical media, only levels with an internal energy $\leq 100\text{ cm}^{-1}$ can be considered as significantly populated at 50 K.

TABLE I. MOLSCAT parameters used in the scattering calculations. The energy step DNRG used to span the energy grid is also given.

E (cm ⁻¹)	N_{max}	J_{max}	R_{max}	STEPS	DNRG
0.5–30	18	26	30	65	0.5
30–50	21	31	20	40	0.5
50–100	27	40	20	25	0.5
100–150	29	46	20	20	0.5
150–200	31	51	14	16	1
200–300	32	59	14	12	1
300–400	35	64	14	12	2
400–500	37	71	14	12	2
500–600	39	76	14	11	2

Scattering calculations were thus performed for fine structure levels up to $N_j = 20_j$, with the 20_{20} fine structure level at 96.79 cm⁻¹.

To ensure the convergence of the cross-sections for the range of temperature of interest, the scattering calculations were performed for transitions between the first 61 fine structure levels for a total energy E of up to 600 cm⁻¹ with a various energy step in order to accurately describe their resonances.

Accordingly, all calculations reported in the present paper were carried out by taking into account the exact energy splitting of the levels as well as rotational wavefunction that are linear combination of pure Hund's case (b). Inelastic cross-sections from an initial state N_j to a final one N'_j , are given by³⁴

$$\sigma_{N_j \rightarrow N'_j} = \frac{\pi}{(2j+1)k_{N_j}^2} \sum_{J, J'} (2J+1) |\delta_{N_j N'_j} \delta_{JJ'} - S^J(N_j; N'_j, J)|^2 \quad (5)$$

with $k_{N_j}^2 = \frac{2\mu}{\hbar^2} [E - E_{N_j}]$, where E is the total energy of the system, E_{N_j} is the energy of the N_j level, and J is the total angular momentum.

The scattering matrices $S^J(N_j; N'_j, J)$ were computed for each total energy E with the Close-Coupling (CC) approach and the log-derivative propagator of Manolopoulos⁴⁸ implemented in the MOLSCAT code.⁵¹

Some parameters were constrained by the fit of the PES. Hence, the minimum distance of propagation of the wavefunction $R_{min} = 4.36a_0$, allowing the calculations up to 1500 cm⁻¹, and $\lambda_{max} = 31$, the number of radial coefficients used to describe the PES. Some of the parameters were obtained through convergence tests. Hence, STEPS related to the step of propagation of the wavefunction, R_{max} the largest distance of propagation of the wavefunction and N_{max} the highest rotational quantum number of CCS included in the basis, were adjusted. The total angular momentum J_{max} of the system was automatically converged by the MOLSCAT code. These parameters, which can be found in Table I, were converged to ensure less than 2% of uncertainties on the cross-sections.

Rate coefficients are computed assuming a Maxwell-Boltzmann distribution of kinetic energies as:

$$k_{N_j \rightarrow N'_j}(T) = \left(\frac{8k_B T}{\pi\mu} \right)^{1/2} \left(\frac{1}{k_B T} \right)^2 \int_0^\infty E_k \sigma_{N_j \rightarrow N'_j}(E_k) e^{-E_k/k_B T} dE_k, \quad (6)$$

with k_B being the Boltzmann constant.

III. RESULTS AND DISCUSSIONS

A. PES

The isocontours of the PES produced in this work are presented in Fig. 3. It was computed with the UCCSD(T)/aVQZ level of theory with additional mid-bond functions, as described in Sec. II A. The PES has one local minimum $V = -31.85$ cm⁻¹ for the linear complex ($\theta = 0^\circ$), with the He atom facing the sulfur of the CCS radical at $R = 8.35a_0$, and a global minimum at $V = -37.12$ cm⁻¹ for the nearly T-shaped complex ($\theta = 97.72^\circ$) at $R = 6.70a_0$. These two minima are separated by a low barrier of about 16 cm⁻¹ with respect to the global minimum.

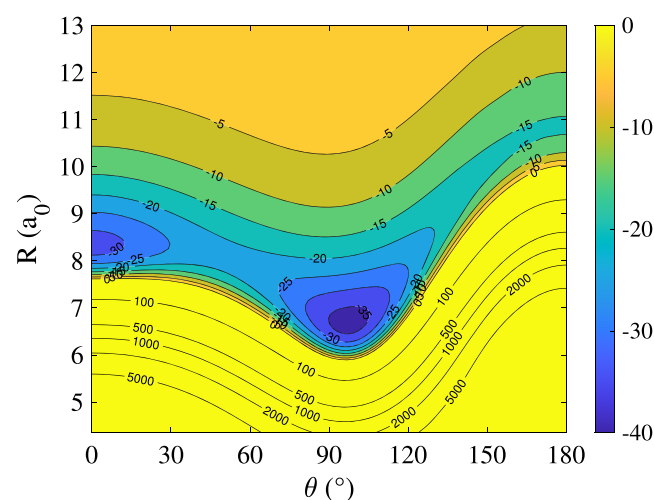
The PES is globally highly anisotropic with respect to the θ coordinate, which explains why 32 angular coefficients were needed to obtain its correct analytical fit. Nonetheless, if θ is considered only between 0° and $\sim 100^\circ$, i.e., when the He atom is attracted by the sulfur side of CCS, then the anisotropy is not very pronounced. On the contrary, if θ is considered between 100° and 180° , the He is approaching CCS while facing the terminal carbon and the interaction is highly repulsive.

B. Dissociation energy calculations

The dissociation energies, with only the rotational structure of CCS included and with the fine structure of CCS taken into account, were computed based on the methodology described in Sec. II C.

If the fine structure is neglected, then the computed dissociation energy D_0 is 14.159 cm⁻¹. If the fine structure is taken into account, then $D_0 = 14.183$ cm⁻¹. In both cases, the dissociation energy is found above the barrier between the two minima of the complex.

The good agreement between these two results, different by less than 0.2%, demonstrates that the fine structure, even if peculiar, does not have a strong influence on D_0 , the dissociation energy of the complex, contrarily to what could have been anticipated. This agreement shows that the coupling between the electronic spin of CCS and the rotation of the whole complex is weak. However, this

**FIG. 3.** Isocontours (in cm⁻¹) of the CCS-He PES.

difference is not negligible and could be probed by experimental measurements. Thus, the impact of the fine structure on the dissociation energy D_0 value is moderated, but still, the fine structure needs to be taken into account for calculations of spectroscopical accuracy.

To the best of our knowledge, no measurements of the dissociation energy for the CCS–He complex have been reported. However, the comparison between theoretical and future experimental measurements could help us in evaluating the quality of the PES. The PES could also be used to study the spectroscopy of the complex. Indeed, such calculations are sensitive to the shape and the depth of the potential wells since it is where bound states are located and can also be another probe of the PES quality.

C. Cross-sections and rate coefficients

In this section, cross-sections obtained from the scattering calculations performed as detailed in Sec. II D 1 are presented. Rate coefficients, which are derived from averaging these cross-sections over a Boltzmann distribution of the velocities, are also described.

In Figs. 4 and 5, cross-sections as a function of kinetic energy are presented in the upper panels, and their associated rate coefficients as a function of temperature are in the lower panels. These collisional data are represented for $\Delta N = \Delta j$ (F_i conserving) transitions, which are the dominant ones.

In the cross-sections of both figures, Feshbach and shape resonances are observed when the kinetic energy is lower or similar to the well depth, so when $E_k \lesssim 37 \text{ cm}^{-1}$. These are explained by the temporary formation of (quasi)bound states.⁵² These resonances have to be taken into account in order to obtain correct values and behaviors of the rate coefficients, especially at low temperatures, and it justifies why the energy step needed to be smaller when the collisional energy is small or similar to the well depth of the PES.

As one can see, the same type of transitions are represented within the lowest N_j levels (from the $N_j = 1_j$ levels) in Fig. 4, so when fine structure levels are not ordered by increasing N values, and within $N_j \geq 10_j$ levels (from the $N_j = 10_j$ levels) in Fig. 5, so when they are ordered by increasing N values. If low- N_j fine structure levels are considered (Fig. 4), then the rate coefficients with the same ΔN but with different j (different F_i) have very different magnitudes. In fact, they can differ by up to two orders of magnitude. At the opposite, if high- N_j transitions are considered (Fig. 5), then, the rate coefficients for transitions with the same ΔN are very similar. Therefore, it is suspected that the strength of the mixing between Hund's case (b) basis has a huge influence on the rate coefficients and on the propensity rules.

To discuss this hypothesis, propensity rules are investigated in Fig. 6 where rate coefficients from $N_{j=N+1} = 1_2, 6_7,$ and 10_{11} levels as a function of ΔN are represented at 30 K. Different initial levels were considered since, according to Figs. 4 and 5, the propensity rules are expected to change with respect to the initial N_j levels.

For all transitions, rate coefficients globally decrease with increasing ΔN . However, the general propensity rule is in favor of transitions with even ΔN compared to transitions with odd ΔN . It was already observed in other ($X^3\Sigma^-$) systems, for which it was justified by the even anisotropy of the PES.^{36,46,53–56} The propensity rule favoring even ΔN fades with increasing ΔN , and it tends to

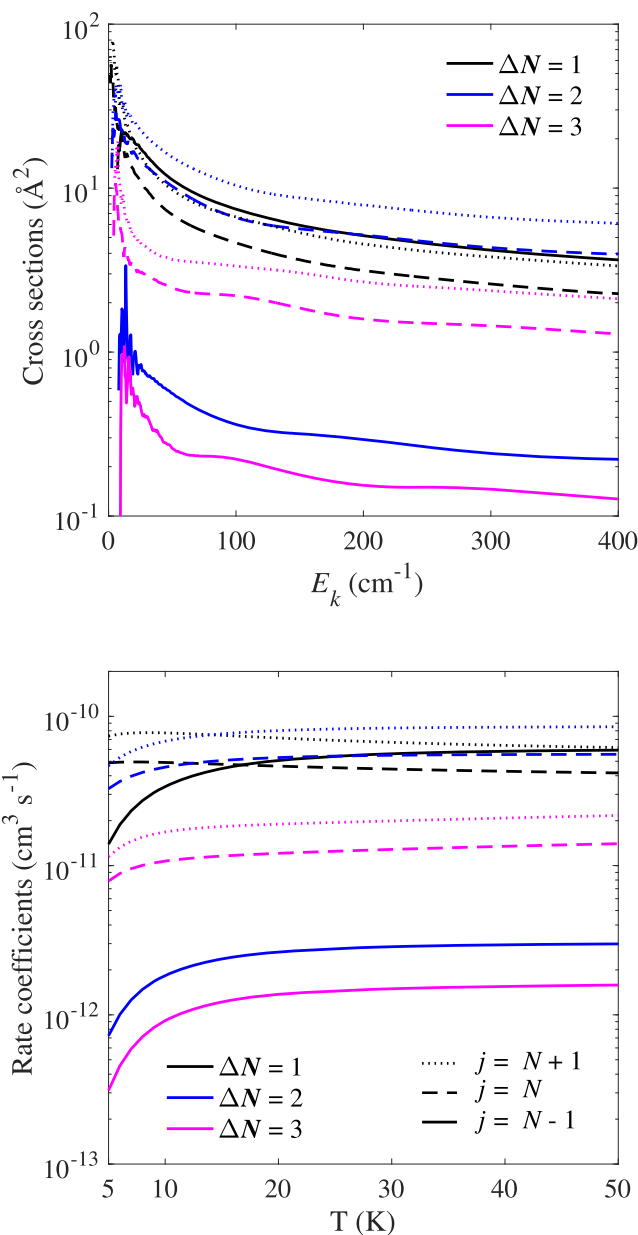


FIG. 4. Cross-sections as a function of kinetic energy (upper panel) and rate coefficients as a function of temperature (lower panel) for $\Delta N = \Delta j$ transitions from the 1_j levels.

vanish when $\Delta N \geq 10$, where the magnitude of the rate coefficients then only decrease with increasing ΔN following the exponential energy-gap behavior.

As previously mentioned, $\Delta N = \Delta j$ transitions are dominant compared to other types of transitions. This behavior is frequently observed in molecules in the ($X^3\Sigma^-$) electronic state,^{36,46,53,54,57–59} and was also predicted theoretically by Alexander and Dagdigian.³⁴ The latter study also mentioned that this propensity rule is indepen-

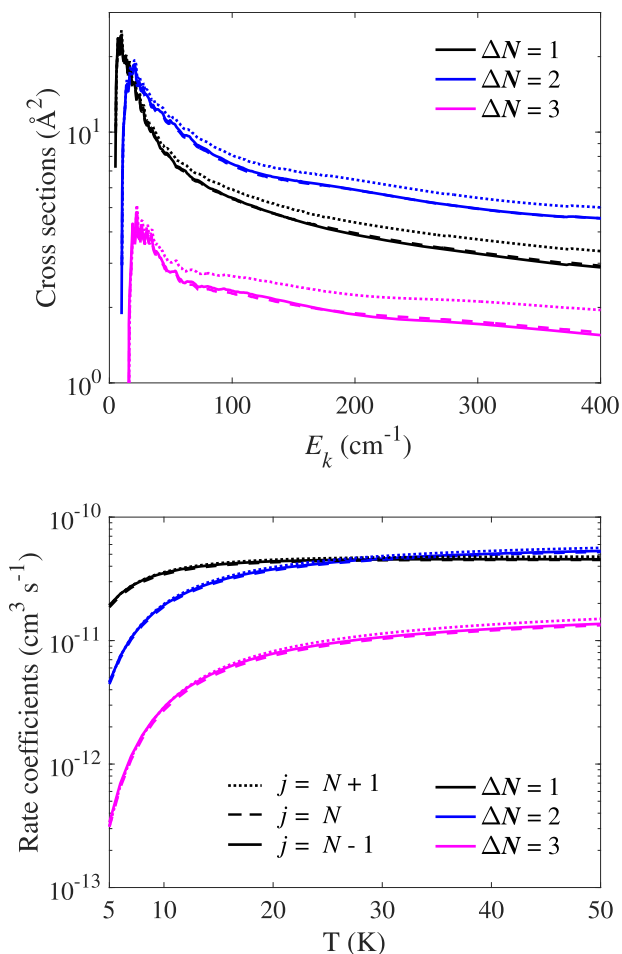


FIG. 5. Cross-sections as a function of kinetic energy (upper panel) and rate coefficients as a function of temperature (lower panel) for $\Delta N = \Delta j$ transitions from the 10_j levels.

dent of the degree of intermediate coupling. However, a competition between $1_2 \rightarrow N_{j=N+1}$ (F_1 conserving) and $1_2 \rightarrow N_{j=N-1}$ ($F_1 \rightarrow F_3$) transitions for $\Delta N \geq 10$ is observed in the left panel and is in conflict with Alexander and Dagdigian³⁴ prediction.

To understand this surprising behavior, the wavefunctions of the different 1_2 , 6_7 , and 10_{11} initial states considered here are presented according to Eq. (4),

$$\begin{aligned} 1_2 &\equiv 0.75|1_2\rangle + 0.66|3_2\rangle \\ 6_7 &\equiv 0.92|6_7\rangle - 0.40|8_7\rangle \\ 10_{11} &\equiv 0.96|10_{11}\rangle - 0.29|12_{11}\rangle. \end{aligned}$$

With regard of the wavefunction expressions, it can be observed that the level hitherto named 1_2 is actually a linear combination of the $|1_2\rangle$ and the $|3_2\rangle$ Hund's case (b) basis with similar weight. As N increases, for an $N_{j=N+1}$ (F_1) level, the weight of the $|N = j - 1, Sjm\rangle$ basis increases, and the weight of the $|N = j + 1, Sjm\rangle$ basis decreases. Thus, as N increases, the internal structure of the system tends to be closer to a pure Hund's case (b) description.

Therefore, when one of the state involved in the transition cannot be represented within a pure Hund's case (b) (as for the 1_2 level), then usual Hund's case (b) propensity rules are not valid anymore. At the opposite, when the levels can be reasonably described by a pure Hund's case (b) approach (as for the 10_{11} level), the expected propensity rules for pure Hund's case (b) are then valid.

Alexander and Dagdigian³⁴ also predicted $\Delta N = \Delta j$ for $j = N$ (F_2 conserving) transitions to be dominant, and $\Delta N = \Delta j$ for $j = N + 1$ (F_1 conserving) and for $j = N - 1$ (F_3 conserving) to be equal. However, for CCS-He rate coefficients, $\Delta N = \Delta j$ for $j = N + 1$ (F_1 conserving) transitions are the most dominant ones for low N_j levels, and all $\Delta N = \Delta j$ transitions tend to be equivalent for high N_j levels, as shown in Fig. 5.

The relative magnitude of $N_{j=N+1} \rightarrow N_{j=N}$ ($F_1 \rightarrow F_2$) and $N_{j=N+1} \rightarrow N_{j=N-1}$ ($F_1 \rightarrow F_3$) transitions depends here on the N_j initial level. Indeed, when transitions from the 10_{11} fine structure level are considered (right panel), rate coefficients for transitions to final $N_{j=N}$ (F_2) levels are stronger than transitions to final $N_{j=N-1}$ (F_3) levels. This propensity rule corresponds to Hund's case (b) limit, in agreement with the previous observation that levels with $N_j \geq 10$ are well described within pure Hund's case (b). However, this propensity rule reverses when N of the initial level decreases. For transitions from the 6_7 (F_1) fine structure level (center panel), transitions to final $N_{j=N-1}$ (F_3) and $N_{j=N}$ (F_2) are in competition. For transitions from the 1_2 (F_1) fine structure level (left panel), rate coefficients for transitions to final $N_{j=N-1}$ (F_3) levels are stronger than rate coefficients to final $N_{j=N}$ (F_2) levels. This propensity rules do not correspond to Hund's case (b) limit³⁴ and can be explained by the fact that the mixing between Hund's case (b) basis is significant for low N_j levels. Such findings clearly confirm that the mixing between pure Hund's case (b) levels is not negligible for the CCS($^3\Sigma^-$) molecule and, thus, that a pure Hund's case (b) approach will not be suitable for this system.

D. Comparison with previous data

In this part, our rate coefficients are compared to the most recent ones provided by Wolkovitch *et al.*,²⁵ in order to evaluate the potential impact of the new collisional data on the modeling of CCS observations.

Wolkovitch *et al.*²⁵ rate coefficients were obtained for fine structure levels up to $N_j = 12_j$ based on OCS- H_2 PES of Green and Chapman.³⁵ This PES was adapted from an OCS-He interaction potential computed with the electron gas model. As mentioned in the Introduction, the H_2 collider is thus considered as a structureless particle, as done for the He atom in this work. Based on this PES, Wolkovitch *et al.*²⁵ computed rotational rate coefficients with the CC approach, to which they reintroduced the spin-dependence with the IOS approximation within the pure Hund's case (b), as developed by Corey and McCourt.⁶⁰

In Fig. 7, a comparison between fine-structure rate coefficients computed by Wolkovitch *et al.*²⁵ and in the present work is done at 10 and 20 K.

A difference of a factor of 2–10 is globally found between the two sets of rate coefficients at both temperatures considered. The distribution around the $x = y$ axis is very sparse, and differences up to two orders of magnitude are observed for some transitions at both 10 and 20 K.

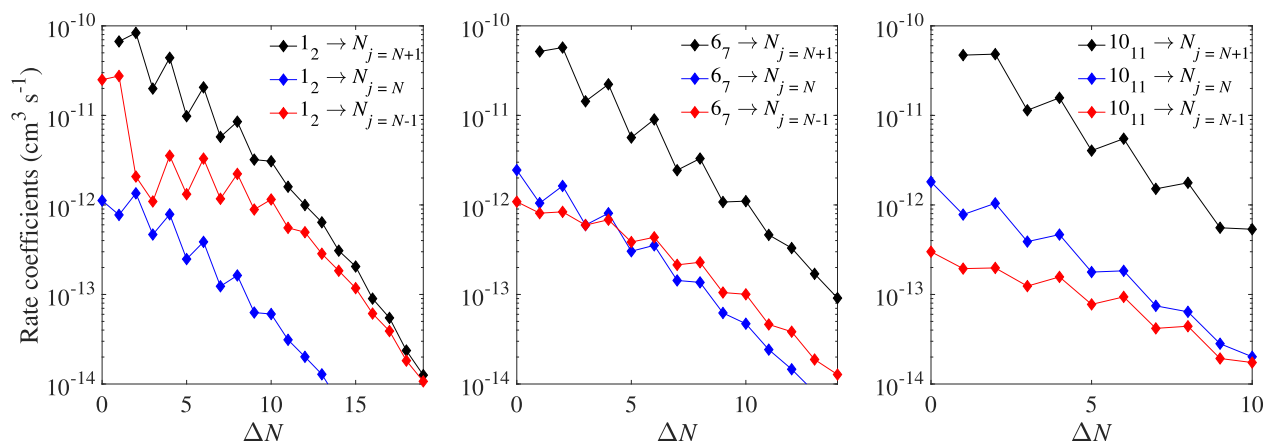


FIG. 6. Propensity rules for transitions out of the 1_2 (left panel), 6_7 (center panel), and 10_{11} (right panel) levels for a temperature of 30 K.

For astrophysical modeling, it was found that an order of magnitude of difference in collisional excitation rate coefficients can induce up to a factor of 2–5 in the abundance determinations.³³ Therefore, the differences between the two sets of rate coefficients are very significant and should impact the determination of CCS abundances in astrophysical media.

The discrepancies between the Wolkovitch *et al.*²⁵ set of data and the one presented in this work are the results of the different projectiles, of the different PESs, and of the use of different scattering approaches (the IOS approximation within pure Hund's case (b) description of the levels was used in Wolkovitch *et al.*²⁵ work).

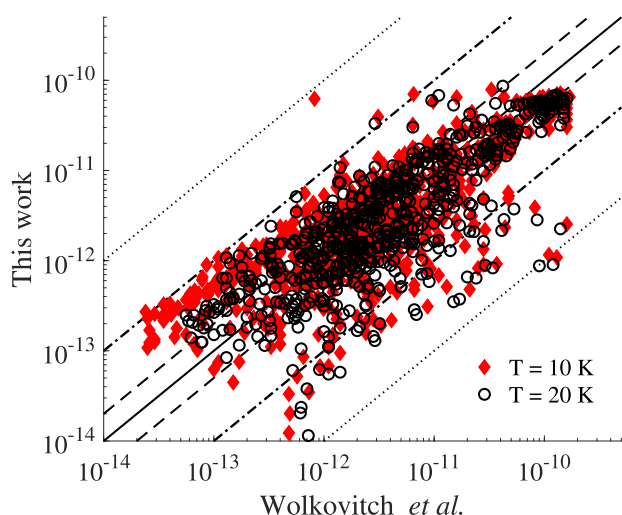


FIG. 7. Direct comparison of Wolkovitch *et al.*²⁵ CCS–H₂ fine-structure resolved rate coefficients and CCS–He ones provided in this work at 10 K (red diamonds) and 20 K (black open circles). The solid line represents a perfect agreement between the two sets of data; dashed, dashed-dotted, and dotted lines delimit the regions where the rate coefficients differ by less than a factor of 2, 10, and 100, respectively.

In order to investigate the influence of the PES and of the different colliders, pure rotational rate coefficients were computed from the new CCS–He PES presented in Sec. III A. The scattering calculations were performed with the CC approach to obtain converged cross-sections for the first 13 rotational CCS energy levels for temperatures up to 20 K. Rotational rate coefficients from the ground rotational state are compared in Table II to the ones used by Wolkovitch *et al.*²⁵ to derive their fine-structure resolved rate coefficients.

For the dominant transitions, i.e., for transitions with even ΔN , the agreement between these rates is better than a factor of 2, especially at 10 K where the agreement for these transitions for $\Delta N \leq 6$ is better than 20%. The differences between the rotational rate coefficients increase as the ΔN increases, in particular at 10 K, where it reaches almost two orders of magnitudes for $\Delta N = 12$. However, such small rate coefficients do not significantly contribute to the fine structure rate coefficients within the IOS approach used by Wolkovitch *et al.*²⁵ At 20 K, the discrepancies stay under a factor of 2 for all transitions with $\Delta N \leq 10$. If the discrepancies between rotational rate coefficients for high ΔN at 10 K were the source of the differences on the fine structure-resolved rate coefficients exhibited in Fig. 7, then they should vanish or at least decrease at 20 K, where the discrepancies between rotational rate coefficients stay reasonable (below a factor of 5 for all considered transitions). However, the distribution of the fine rate coefficients is very similar at both 10 and 20 K, so this hypothesis is disproved.

Such a similarity between the two sets of rotational rate coefficients is not surprising because the PES for both molecular systems (CCS–He vs OCS–H₂) is similar. Indeed, only the long-range of Green³⁵ OCS–H₂ PES was actually computed with H₂, and all other features of the PES, i.e., the repulsive wall and the potential wells, were computed for the OCS–He system. Therefore, no significant differences were expected between the two sets of rotational rate coefficients for CCS–H₂ and CCS–He. Therefore, the remarkable differences between the fine structure rate coefficients highlighted in Fig. 7 do not seem to originate from the colliders, or from the PES considered. It suggests that the scattering approach is the main reason for such differences.

TABLE II. Comparison of rotational rate coefficients from the ground rotational state computed by Wolkovitch *et al.*²⁵ and in this work.

$N \rightarrow N'$	T = 10 K		T = 20 K	
	Wolkovitch <i>et al.</i> ²⁵	This work	Wolkovitch <i>et al.</i> ²⁵	This work
0 → 1	4.8×10^{-11}	9.82×10^{-11}	4.5×10^{-11}	8.90×10^{-11}
0 → 2	1.1×10^{-10}	9.77×10^{-11}	1.1×10^{-10}	1.08×10^{-10}
0 → 3	2.2×10^{-11}	2.41×10^{-11}	2.0×10^{-11}	2.59×10^{-11}
0 → 4	5.8×10^{-11}	5.90×10^{-11}	5.8×10^{-11}	7.21×10^{-11}
0 → 5	1.5×10^{-11}	7.96×10^{-12}	1.4×10^{-11}	1.10×10^{-11}
0 → 6	2.0×10^{-11}	1.92×10^{-11}	1.8×10^{-11}	3.41×10^{-11}
0 → 7	1.3×10^{-11}	3.40×10^{-12}	1.0×10^{-11}	7.03×10^{-12}
0 → 8	1.1×10^{-11}	4.14×10^{-12}	9.5×10^{-12}	1.31×10^{-11}
0 → 9	7.6×10^{-12}	8.79×10^{-13}	6.1×10^{-12}	3.65×10^{-12}
0 → 10	8.4×10^{-12}	5.80×10^{-13}	6.9×10^{-12}	3.95×10^{-12}
0 → 11	7.6×10^{-12}	1.97×10^{-13}	7.6×10^{-12}	1.75×10^{-12}
0 → 12	3.8×10^{-12}	4.34×10^{-14}	3.3×10^{-12}	8.97×10^{-13}

With the IOS approximation, the exact energy of the fine structure levels is not taken into account in the scattering calculations. Indeed, the later approximation uses rotational cross-sections from the ground state to infer fine structure resolved cross-sections for all levels considered.²⁵ However, if the CCS energetic structure is not explicitly taken into account, some transitions will be considered as excitations, when, in fact, they are de-excitations such as the $0_1 \rightarrow 1_0$ transition, or all transitions between the 1_1 level and any N_j levels with $N \leq 4$ and $j = N + 1$.

According to these results, the IOS approximation within pure Hund's case (b) for the CCS molecule is failing at reproducing accurate fine-structure resolved rate coefficients at (least at) low temperature. It also suggests that it may fail for other systems with a large spin-splitting as it was already discussed in previous studies.^{21,25,36,37} Therefore, the conclusions drawn from the astrophysical model based on Wolkovitch *et al.*²⁵ data may need to be reconsidered.

IV. CONCLUSIONS

State-to-state rate coefficients for the $\text{CCS}(^3\Sigma^-)$ -He system were obtained for the 5–50 K temperature range, by explicitly taking into account the CCS fine structure. For that purpose, the first PES of the CCS-He van der Waals complex was computed. It exhibits a strong anisotropy, and thus, a great number of *ab initio* points and $v_\lambda(R)$ coefficients were required to correctly describe it. The dissociation energy of the complex was computed with and without considering explicitly the CCS fine-structure in the close-coupling calculations, and the effect of such a peculiar structure on this dissociation energy appears to be not huge although not negligible.

Based on the PES, cross-sections were computed with the close-coupling approach within the intermediate coupling scheme, and rate coefficients for temperatures from 5 to 50 K were derived by integration of the cross-sections over kinetic energies. Propensity rules were discussed, and the degree of mixing between pure Hund's case (b) basis was found to have a strong influence on them.

Therefore, it was concluded that CCS collisional data could only be properly described with the intermediate coupling scheme.

The obtained rate coefficients were compared at 10 and 20 K to previous ones provided by Wolkovitch *et al.*,²⁵ and a global difference of a factor of 2–10 was observed. Some transitions exhibited discrepancies up to 2 orders of magnitudes. Thus, the derived abundances of CCS and extended conclusions might need to be reconsidered.

For now, CCS abundances in astrophysical media were derived within the local thermodynamic approximation (LTE) approximation, which is known to not be accurate in many astrophysical media (such as molecular clouds, where CCS is widely detected) or with the data of Wolkovitch *et al.*²⁵ With the new set of data provided here, the CCS abundances may be significantly revised, and then, its correlated abundance with HC_3N and carbon chains, in general, can be further investigated and may decipher on the formation path of such molecules.

SUPPLEMENTARY MATERIAL

A Fortran subroutine of the potential energy surface is available in the [supplementary material](#).

ACKNOWLEDGMENTS

The authors acknowledge financial support from the European Research Council (Consolidator Grant COLLEXISM, Grant No. 811363) and the Program National "Physique et Chimie du Milieu Interstellaire" (PCMI) of CNRS/INSU with INC/INP cofunded by CEA and CNES. The authors also acknowledge Rennes Metropole for financial support. F.L. acknowledges the Institut Universitaire de France.

AUTHOR DECLARATIONS

Conflict of Interest

The authors have no conflicts to disclose.

Author Contributions

A. Godard Palluet: Data curation (lead); Writing – original draft (lead); Writing – review & editing (equal). **F. Lique:** Conceptualization (lead); Supervision (lead); Writing – original draft (supporting); Writing – review & editing (equal).

DATA AVAILABILITY

The data that support the findings of this study are available from the corresponding author upon reasonable request.

REFERENCES

- H. Suzuki, N. Kaifu, T. Miyaji, M. Morimoto, M. Ohishi, and S. Saito, *Astrophys. J.* **282**, 197 (1984).
- N. Kaifu, H. Suzuki, M. Ohishi, T. Miyaji, S.-I. Ishikawa, T. Kasuga, M. Morimoto, and S. Saito, *Astrophys. J.* **317**, L111 (1987).
- S. Saito, K. Kawaguchi, S. Yamamoto, M. Ohishi, and H. Suzuki, *Astron. Astrophys.* **317**, L115 (1987).
- S. Yamamoto, S. Saito, K. Kawaguchi, Y. Chikada, H. Suzuki, N. Kaifu, S.-I. Ishikawa, and M. Ohishi, *Astrophys. J.* **361**, 318 (1990).
- S. Yamamoto, S. Saito, K. Kawaguchi, N. Kaifu, and H. Suzuki, *Astrophys. J.* **317**, L119 (1987).
- J. Cernicharo, M. Guélin, H. Hein, and C. Kahane, *Astron. Astrophys.* **181**, L9 (1987).
- J. Cernicharo, C. Cabezas, M. Agúndez, B. Tercero, J. R. Pardo, N. Marcelino, J. D. Gallego, F. Tercero, J. A. López-Pérez, and P. de Vicente, *Astron. Astrophys.* **648**, L3 (2021).
- M. Agúndez, J. Cernicharo, and M. Guélin, *Astron. Astrophys.* **570**, A45 (2014).
- M. B. Bell, L. W. Avery, and P. A. Feldman, *Astrophys. J.* **417**, L37 (1993).
- D. Smith, N. G. Adams, K. Giles, and E. Herbst, *Astron. Astrophys.* **200**, 191 (1988).
- H. Suzuki, M. Ohishi, N. Kaifu, T. Kasuga, S.-i. Ishikawa, and T. Miyaji, *Vistas Astron.* **31**, 459 (1988).
- T. J. Millar and E. Herbst, *Astron. Astrophys.* **231**, 466 (1990).
- D. A. Howe and T. J. Millar, *Mon. Not. R. Astron. Soc.* **244**, 444 (1990).
- H. Suzuki, S. Yamamoto, M. Ohishi, N. Kaifu, S.-I. Ishikawa, Y. Hirahara, and S. Takano, *Astron. Astrophys.* **392**, 551 (1992).
- S. Petrie, *Mon. Not. R. Astron. Soc.* **281**, 666 (1996).
- J. R. Flores, C. M. Estévez, L. Carballeira, and I. P. Juste, *J. Chem. Phys.* **105**, 4716 (2001).
- T. J. Millar, J. R. Flores, and A. J. Markwick, *Mon. Not. R. Astron. Soc.* **327**, 1173 (2001).
- R. I. Kaiser, M. Yamada, and Y. Osamura, *J. Chem. Phys.* **106**, 4825 (2002).
- M. Yamada, Y. Osamura, and R. I. Kaiser, *Astron. Astrophys.* **395**, 1031 (2002).
- N. Sakai, M. Ikeda, M. Morita, T. Sakai, S. Takano, Y. Osamura, and S. Yamamoto, *Astrophys. J.* **663**, 1174 (2007).
- A. Fuente, J. Cernicharo, A. Barcia, and J. Gómez-González, *Astron. Astrophys.* **231**, 151 (1990).
- W. M. Irvine, L. W. Avery, P. Friberg, H. E. Matthews, and L. M. Ziurys, *Astro. Lett. Commun.* **26**, 167 (1988).
- Y. Hirahara, H. Suzuki, S. Yamamoto, K. Kawaguchi, N. Kaifu, M. Ohishi, S. Takano, S.-I. Ishikawa, and A. Masuda, *Astrophys. J.* **394**, 539 (1992).
- T. Velusamy, T. B. H. Kuiper, and W. D. Langer, *Astrophys. J.* **451**, L75 (1995).
- D. Wolkovitch, W. D. Langer, P. F. Goldsmith, and M. Heyer, *Astrophys. J.* **477**, 241 (1997).
- R. Peng, W. D. Langer, T. Velusamy, T. B. H. Kuiper, and S. Levin, *Astrophys. J.* **497**, 842 (1998).
- P. J. Benson, P. Caselli, and P. C. Myers, *Astrophys. J.* **506**, 743 (1998).
- K. Dobashi, T. Shimoikura, T. Ochiai, F. Nakamura, S. Kameno, I. Mizuno, and K. Taniguchi, *Astrophys. J.* **879**, 88 (2019).
- J. H. He, Dinh-V-Trung, S. Kwok, H. S. P. Müller, Y. Zhang, T. Hasegawa, T. C. Peng, and Y. C. Huang, *Astrophys. J., Suppl. Ser.* **177**, 275 (2008).
- F. Scappini and C. Codella, *Mon. Not. R. Astron. Soc.* **282**, 587 (1996).
- S. M. Levin, W. D. Langer, T. Velusamy, T. B. H. Kuiper, and R. M. Crutcher, *Astrophys. J.* **555**, 850 (2001).
- K. I. Uchida, D. Fiebig, and R. Güsten, *Astron. Astrophys.* **371**, 274 (2001).
- E. Roueff and F. Lique, *Chem. Rev.* **113**, 8906 (2013).
- M. H. Alexander and P. J. Dagdigian, *J. Chem. Phys.* **79**, 302 (1983).
- S. Green, S. Chapman, *Astrophys. J., Suppl. Ser.* **37**, 169 (1978).
- F. Lique, A. Spielfiedel, M.-L. Dubernet, and N. Feautrier, *J. Chem. Phys.* **123**, 134316 (2005).
- F. Lique, M.-L. Dubernet, A. Spielfiedel, and N. Feautrier, *Astron. Astrophys.* **450**, 399 (2006).
- A. Murakami, *Astrophys. J.* **357**, 288 (1990).
- Y. Xie and H. F. Schaefer III, *J. Chem. Phys.* **96**, 3714 (1992).
- M. J. O. Deegan and P. J. Knowles, *Chem. Phys. Lett.* **227**, 321 (1994).
- S. M. Cybulski and R. R. Toczyłowski, *J. Chem. Phys.* **111**, 10520 (1999).
- H.-J. Werner, MOLPRO, a package of *ab initio* programs, version 2015.1, 2015.
- S. F. Boys and F. Bernardi, *Mol. Phys.* **19**, 553 (1970).
- H.-J. Werner, B. Follmeg, and M. H. Alexander, *J. Chem. Phys.* **89**, 3139 (1988).
- J. B. Tatum and J. K. G. Watson, *Can. J. Phys.* **49**, 2693 (1971).
- G. C. Corey, M. H. Alexander, and J. Schaefer, *J. Chem. Phys.* **85**, 2726 (1986).
- B. A. McGuire, M.-A. Martin-Drumel, K. L. K. Lee, J. F. Stanton, C. A. Gottlieb, and M. C. McCarthy, *Phys. Chem. Phys. Chem.* **20**, 13870 (2018).
- D. E. Manolopoulos, *J. Chem. Phys.* **85**, 6425 (1986).
- J. Hutson, BOUND Computer Code, Version 5, Distributed by Collaborative Computational Project No. 6 of the Science and Engineering Research Council, 1993.
- E. A. Bergin and M. Tafalla, *Annu. Rev. Astron. Astrophys.* **45**, 339 (2007).
- J. Hutson and S. Green, Molscat Computer Program, Version 14, Distributed by Collaborative Computational Project No. 6 of the UK, Science and Engineering Research Council, 1994.
- M. Costes and C. Naulin, *Chem. Sci. J.* **7**, 2462 (2016).
- T. Orlikowski, *Mol. Phys.* **56**, 35 (1985).
- F. Lique, M.-L. Senent, A. Spielfiedel, and N. Feautrier, *J. Chem. Phys.* **126**, 164312 (2007).
- F. Lique, *J. Chem. Phys.* **132**, 044311 (2010).
- R. Ramachandran, J. Klos, and F. Lique, *J. Chem. Phys.* **148**, 084311 (2018).
- S. Green, *Astron. Astrophys.* **434**, 188 (1994).
- R. Toboła, F. Dumouchel, J. Klos, and F. Lique, *J. Chem. Phys.* **134**, 024305 (2011).
- F. Dumouchel, J. Klos, R. Toboła, A. Bacmann, S. Maret, P. Hily-Blant, A. Faure, and F. Lique, *J. Chem. Phys.* **137**, 114306 (2012).
- G. C. Corey and F. R. McCourt, *J. Chem. Phys.* **87**, 2723 (1983).

A.3 The Effect of Isotopic Substitution on the Excitation of CCS Isotopologues in Molecular Clouds

The effect of isotopic substitution on the excitation of CCS isotopologues in molecular clouds

Amélie Godard Palluet   and François Lique 

Université de Rennes, CNRS, IPR (Institut de Physique de Rennes) - UMR 6251, F-35000 Rennes, France

Accepted 2023 November 13. Received 2023 November 12; in original form 2023 September 30

ABSTRACT

CCS($^3\Sigma^-$) is one of the few molecules which presents many observable isotopologues, with the reported detection of ^{13}CCS , C^{13}CS , CC^{34}S , and CC^{33}S . The accurate determination of CCS isotopologues abundances enables the study of the isotopic fraction in media where they are detected, and gives insights into their formation pathways. The availability of collisional rate coefficients, that are prerequisite for accurate determination of their abundances in astrophysical media under non-local thermodynamic equilibrium (LTE) conditions, allows drawing reliable conclusions on their abundances. In this study, fine and hyperfine-structure resolved excitation rate coefficients induced by collisions with helium are produced with a quantum approach for all detected CCS isotopologues for the 5–50 K temperature range. Radiative transfer models have been performed with the new data to discuss their impact on the excitation conditions of these species. The effect of the isotopic substitution appears to be weak between fine-structure rate coefficients. The observed lines of CCS, ^{13}CCS , C^{13}CS , and CC^{34}S are found to be out of LTE conditions, and therefore, the proper determination of the abundance of CCS isotopologues in molecular clouds requires the use of the data produced in this work.

Key words: molecular data – molecular processes – radiative transfer – scattering.

1 INTRODUCTION

The CCS ($^3\Sigma^-$) radical was detected in many astronomical sources, especially in molecular clouds where it is known to be a good tracer of physical conditions and evolution stages (Suzuki et al. 1992; Velusamy, Kuiper & Langer 1995). However, an accurate determination of its abundance in these media, which does not satisfy local thermodynamic equilibrium (LTE) conditions, requires the use of inelastic rate coefficients.

Due to the presence of an electronic spin and a large spin-splitting, CCS very peculiar internal structure is difficult to take into account in rate coefficients calculations. Up to now, the analysis of CCS observations has been done, either under LTE assumption, either with approximated rate coefficients derived from OCS- H_2 rotational rate coefficients (Fuente et al. 1990; Suzuki et al. 1992), or obtained from OCS- H_2 potential energy surface (PES) (Wolkovitch et al. 1997). To overcome this lack of data, Godard Palluet & Lique (2023) (hereafter Paper I) performed full quantum scattering calculations based on the first CCS-He PES computed from highly correlated methods. In this work, He is used as a template for H_2 , the dominant collisional partner in molecular clouds and circumstellar envelopes. The use of He as a substitute for H_2 could lead to significant uncertainties in case of collisions with light hydrides but is expected to be reasonably accurate for heavy molecules (Wernli et al. 2007) such as CCS.

In Paper I, the authors derived the first accurate set of CCS-He fine-structure resolved rate coefficients for the 5–50 K temperature range. These new rate coefficients have been shown to be in strong disagreement with previous data suggesting significant inaccuracies on former non-LTE models of CCS.

Four secondary isotopologues of CCS have been currently detected in molecular clouds: ^{13}CCS ; C^{13}CS ; CC^{34}S (Ikeda, Sekimoto & Yamamoto 1997) and CC^{33}S (Fuentetaja et al., in preparation). It is one of the few molecules to present many observable isotopologues.

The isotopic fraction $^{12}\text{C}/^{13}\text{C}$, $^{32}\text{S}/^{33}\text{S}$, and $^{32}\text{S}/^{34}\text{S}$ is one of the best tool to follow the chemical evolution of molecular clouds and planetary systems bodies (Hily-Blant et al. 2018; Loison et al. 2020). The abundance ratio between ^{13}C -bearing isotopologues can also be used to constrain the production path of interstellar molecules, as done for HC_3N and HC_5N by Takano et al. (1998) and Taniguchi et al. (2016), and also for CCH and CCS by Sakai et al. (2007). The later study found an abundance ratio $[\text{C}^{13}\text{CS}]/[\text{C}^{12}\text{CS}]$ of 4.2 in TMC-1, which cannot be explained by zero-point energy differences. However, it was derived based on LTE assumptions so it might be over(under)estimated.

No rate coefficients have been reported for any of the isotopologues of CCS. Indeed, in addition to the complex fine structure of CCS radicals, ^{13}C ($I = \frac{1}{2}$) and ^{33}S ($I = \frac{3}{2}$) present a nuclear spin from which hyperfine structures arise, making the rate coefficients even more complicated to compute. Therefore, the abundance of CCS secondary isotopologues have always been derived assuming LTE conditions. It is known, however, that this assumption does not hold in molecular clouds where these isotopologues have been detected.

* E-mail: amelie.godard@univ-rennes.fr (AGP); francois.lique@univ-rennes.fr (FL)

Previous works of Dumouchel et al. (2012), Faure & Lique (2012), Flower & Lique (2015), and Navarro-Almaida et al. (2023) demonstrated the need of isotopologue-specific rate coefficients.

The isotopic substitution of one ^{12}C by one ^{13}C in rate coefficients calculations have been studied for CN (Flower & Lique 2015), CO (Dagdikian 2022), CCH (Pirlot Jankowiak, Lique & Dagdigian 2023a), and HCN/HNC (Navarro-Almaida et al. 2023). These studies report an effect of about 20–30 percent on the magnitude of collisional rate coefficients, with no predictable pattern however. Given that such deviation could have an impact on radiative transfer analysis, it might be important to compute isotopologue-specific rate coefficients and not to derive them from CCS data. To the best of our knowledge, rate coefficients for a molecule where the ^{32}S have been substituted by either ^{33}S or ^{34}S have never been reported.

In this paper, we present the first accurate state-to-state inelastic rate coefficients for $^{13}\text{C}^{12}\text{C}^{12}\text{S}$; $^{12}\text{C}^{13}\text{C}^{32}\text{S}$; $^{12}\text{C}^{12}\text{C}^{34}\text{S}$; $^{12}\text{C}^{12}\text{C}^{33}\text{S}$ in collision with He and we test the impact of CCS isotopologue-specific rate coefficients on non-LTE models.

The five isotopologues discussed here have a $^3\Sigma^-$ ground electronic state, from which a fine structure arise (Section 2.2.2). ^{13}CCS , C^{13}CS , and CC^{33}S isotopologues add an hyperfine structure to this fine structure due to non-zero nuclear spin of ^{13}C ($I = \frac{1}{2}$), and ^{33}S ($I = \frac{3}{2}$) (see Section 2.2.3).

The potential energy surface (PES) provided in Paper I was adapted for each isotopologue to perform scattering calculations with the close-coupling (CC) approach. On this basis, fine-structure resolved rate coefficients for the 5–50 K temperature range were provided and the recoupling approach was then applied to obtain hyperfine-structure resolved rate coefficients in the 5–15 K temperature range for ^{13}CCS , C^{13}CS , and CC^{33}S isotopologues (see Sections 2.1 and 2.2). Fine and hyperfine inelastic rate coefficients as well as the effect of the isotopic substitution on these data are presented in Sections 3.1 and 3.2. The impact of the rate coefficients on radiative transfer models are discussed in Section 3.3. Finally, Section 4 presents concluding remarks.

2 METHODS

2.1 Potential energy surfaces

The potential energy surface (PES) used to model the collision between CCS isotopologues and helium is the one computed in Paper I. In the later, the PES have been computed for the $^{12}\text{C}^{12}\text{C}^{32}\text{S}$ -He collisional system. It was described using Jacobi coordinates with a radial parameter R , the distance between G , the centre-of-mass (noted hereafter c.o.m.) of CCS and the He atom, and an angular parameter θ , the angle between the internuclear axis and R , as represented in Fig. 1. CCS internuclear distances were fixed at experimental equilibrium geometry $r_{\text{C-S}} = 2.96a_0$ and $r_{\text{C-C}} = 2.47a_0$.

The interaction potential was computed assuming CCS as a rigid rotor, using the unrestricted coupled cluster single double and perturbative triple excitation [UCCSD(T)] ab initio method (Deegan & Knowles 1994), along with the augmented correlation consistent quadruple-zeta basis set (aug-cc-pVQZ) including additional mid-bond functions as defined by Cybulski & Toczyłowski (1999). The basis set superposition error was corrected at each geometry with the counterpoise procedure of Boys & Bernardi (1970). Further details about the PES can be found in Paper I.

Within the Born–Oppenheimer approximation, the PES is valid for all CCS isotopologues which are all linear in their ground electronic state, assuming that the isotopic substitution will not affect the

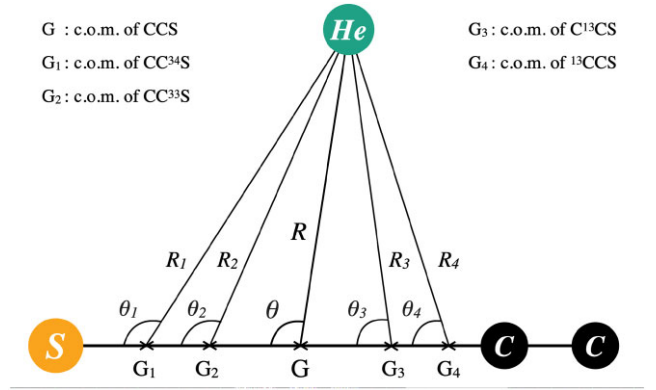


Figure 1. Representation of CCS isotopologues in collision with He in Jacobi coordinates.

internuclear distances. However, a correction to the position of the c.o.m. must be applied. Indeed, in the Jacobi coordinate system, the origin of the frame is on the c.o.m. of the target molecule, which is not the same for all CCS isotopologues. Thus, the coordinate system of the PES is corrected according to the c.o.m. position, as represented in Fig. 1. When the ^{32}S is substituted by ^{34}S or ^{33}S , the c.o.m., G_1 and G_2 respectively, are shifted closer to the sulphur atom according to G . On the contrary, if one of the ^{12}C is substituted by ^{13}C , the c.o.m. is shifted closer to the centred carbon according to G . The proper Jacobi coordinates for the n^{th} CCS isotopologue are then R_n , and θ_n .

As required for scattering calculations, the PES for each CCS isotopologues is expressed in terms of Legendre polynomials as:

$$V(R_n, \theta_n) = \sum_{\lambda=0}^{\lambda_{\text{max}}} v_{\lambda}(R_n) P_{\lambda}(\cos \theta_n), \quad (1)$$

where R_n is the distance between the centre-of-mass G_n of the n^{th} CCS isotopologues and the He atom, and θ_n is the angle between the axis of the molecule and R_n , as shown in Fig. 1.

2.2 Scattering calculations

2.2.1 Fine and hyperfine structure of CCS isotopologues

This study aims at producing accurate state-to-state rate coefficients for CCS isotopologues in collisions with He. Therefore, the proper structure of each CCS isotopologue needs to be taken into account. This is even more true for CCS isotopologues which present a large spin-splitting, leading to a peculiar fine structure. Indeed, accurately taking into account the structure of CCS in the scattering calculations have been proven to have a significant impact on the rate coefficients in Paper I.

All CCS isotopologues are $^3\Sigma^-$ in their electronic ground state. Therefore, a coupling between the electronic spin S and the rotational angular momentum of the radical N occurs. This so-called spin-rotation coupling will split the rotational levels into fine structure levels.

The total angular momentum j of the molecule is then expressed as

$$j = N + S \quad (2)$$

Table 1. Spectroscopic constants of CCS, ^{13}CCS , C^{13}CS , and CC^{34}S isotopologues from McGuire et al. (2018), and of CC^{33}S from Fuentetaja et al. (in preparation). The values in brackets are theoretical values.

Spectroscopic constants (cm^{-1})	CCS	^{13}CCS	C^{13}CS	CC^{34}S	CC^{33}S
B	0.216074	0.206412	0.215048	0.211342	0.213630
$D \times 10^8$	5.760985	5.243628	5.710284	5.518151	[5.763988]
$\gamma_0 \times 10^4$	-4.907061	-4.689911	-4.880043	-4.798653	[-4.916]
λ_0	3.242098	3.242376	3.243134	3.242080	3.242934

The molecular Hamiltonian H included in the scattering calculations is

$$H = H_{\text{rot}} + H_{\text{sr}} + H_{\text{ss}}, \quad (3)$$

where H_{rot} , H_{sr} , and H_{ss} denote for the rotational, spin-rotation, and spin-spin terms, respectively. They are given by

$$\begin{aligned} H_{\text{rot}} &= BN^2 - DN^4 \\ H_{\text{sr}} &= \gamma_0(N \cdot S) \\ H_{\text{ss}} &= \frac{2}{3}\lambda_0(3S_z - S), \end{aligned}$$

where B is the rotational constant of the molecule, D the centrifugal distortion constant, γ_0 the spin-rotation interaction constant, and λ_0 the spin-spin interaction constant.

The fine-structure energy levels are described with the intermediate coupling representation. The rotational wavefunctions for CCS isotopologues for $j \geq 1$ within the intermediate coupling scheme is written as (Alexander & Dagdigian 1983)

$$\begin{aligned} |F_1 jm\rangle &= \cos\alpha|N = j - 1, Sjm\rangle + \sin\alpha|N = j + 1, Sjm\rangle, \\ |F_2 jm\rangle &= |N = j, Sjm\rangle, \\ |F_3 jm\rangle &= -\sin\alpha|N = j - 1, Sjm\rangle + \cos\alpha|N = j + 1, Sjm\rangle, \end{aligned} \quad (4)$$

where α described the mixing angle between pure Hund's case (b) basis functions $|N, Sjm\rangle$. In pure Hund's case (b) limit, $\alpha \rightarrow 0$ and the F_1 , F_2 , and F_3 fine structure levels will correspond to $N = j - 1$, $N = j$, and $N = j + 1$, respectively. Hereafter, each fine structure energy level will be labelled as for pure Hund's case (b) by the couple of quantum numbers N_j according to the usual astrophysical notation.

The spectroscopic constants used here, presented in Table 1, were taken from McGuire et al. (2018) for CCS, ^{13}CCS , C^{13}CS , and CC^{34}S isotopologues, and from Fuentetaja et al. (in preparation) for the CC^{33}S isotopologue.

These constants are quite similar for all isotopologues, leading to very similar fine structure, as one can see in Table A1. What matters is that the order of levels remains consistent between all isotopologues since it could have affected the rate coefficients if the transition is an excitation in some isotopologues and de-excitations in others.

If one of the atom of the molecule presents a non-zero nuclear spin, then a coupling will occur between the nuclear spin I of the atom and the angular momentum j , leading to a splitting of the fine structure energy levels into hyperfine structure energy levels. In that case, the correct quantum number F is now defined as:

$$F = j + I \quad (5)$$

In this study, three of the five isotopologues considered present an hyperfine structure: ^{13}CCS , C^{13}CS , and CC^{33}S . The nuclear spin I of the ^{13}C atom being equal to $\frac{1}{2}$, each fine structure level with $j \geq 1$ will be splitted into two hyperfine levels. The nuclear spin of the ^{33}S atom $I = \frac{3}{2}$, so each fine structure level with $j \geq 2$ energy levels will be splitted into four hyperfine energy levels (and only in three hyperfine structure energy levels for $j = 1$).

2.2.2 Fine structure resolved rate coefficients

In astrophysical media, only levels with an internal energy $\leq 100 \text{ cm}^{-1}$ can be considered as significantly populated at 50 K. Scattering calculations were performed for all isotopologues to produce converged fine structure excitation cross-sections between levels up to $N_j = 20_j$, which are below the first excited bending mode $\nu_2 = 134 \text{ cm}^{-1}$. Thus, rate coefficients are obtained for all transitions between the first 61 fine structure levels of the isotopologues.

Calculations for all CCS isotopologues reported in this paper were carried out by taking into account the exact energy splitting of the levels as well as rotational wavefunction that are linear combination of pure Hund's case (b), as defined in equation (4). Inelastic cross-sections from an initial state N_j to a final one N'_j are given by the following formula (Alexander & Dagdigian 1983)

$$\begin{aligned} \sigma_{N_j \rightarrow N'_j} &= \frac{\pi}{(2j+1)k_{N_j}^2} \\ &\times \sum_{j'l'} (2J+1) |\delta_{NN'} \delta_{jj'} \delta_{ll'} - S^J(N_j l; N'_j l')|^2 \end{aligned} \quad (6)$$

where l is the angular momentum of the whole complex, $k_{N_j}^2 = \frac{2\mu}{\hbar^2} [E - E_{N_j}]$ with E is the total energy of the system, and E_{N_j} is the energy of the N_j level.

The scattering matrices $S^J(N_j l; N'_j l')$ were computed for each total energy E with the close-coupling (CC) approach and the log-derivative propagator of Manolopoulos (1986) as implemented in the MOLSCAT code from Hutson & Green (1994). To ensure the convergence of the rate coefficients, cross-sections were computed for a total energy from 0.5 up to 600 cm^{-1} with a various energy step in order to accurately describe their resonances.

Some parameters are constrained by the analytical representation of the PES, as the minimum distance of propagation R_{min} set at $4.36a_0$ and the number of radial coefficients used to describe the PES λ_{max} set at 31. Other parameters were converged to guarantee that the cross-sections are converged to better than 2 per cent. The total angular momentum J_{max} of the system was automatically converged by the MOLSCAT code. More details about the scattering calculations can be found in Paper I since the strategy used for all isotopologues was very similar to that used for the $^{12}\text{C}^{12}\text{C}^{32}\text{S}$ -He collisional system.

Rate coefficients are then computed from the cross-sections assuming a Maxwell-Boltzmann distribution of kinetic energies, as

$$\begin{aligned} k_{N_j \rightarrow N'_j}(T) &= \left(\frac{8k_B T}{\pi \mu}\right)^{1/2} \left(\frac{1}{k_B T}\right)^2 \\ &\int_0^\infty E_k \sigma_{N_j \rightarrow N'_j}(E_k) e^{-E_k/k_B T} dE_k, \end{aligned} \quad (7)$$

with k_B the Boltzmann constant.

2.2.3 Hyperfine-structure resolved rate coefficients

^{13}CCS , C^{13}CS , and CC^{33}S isotopologues have been detected only in molecular clouds, and thus to limit the CPU cost, we decided to restrict our calculations to the 5–15 K temperature range. Thus the highest hyperfine level taken into account is the 10_{10} , F_i level at $\sim 30 \text{ cm}^{-1}$.

In order to take into account the hyperfine structure of the ^{13}CCS , C^{13}CS , and CC^{33}S isotopologues into the rate coefficients calculations, the recoupling method was used. In this approximation, the hyperfine cross-sections will be inferred from the nuclear spin free S-matrices $S^J(N_j l; N'_j l')$, that were here obtained from the full quantum CC approach. This approximation holds if the splitting between hyperfine energy levels is small compared to the splitting between fine energy levels. In the case of CCS isotopologues, the typical splitting between hyperfine levels is of the order of $\sim 10^{-3} \text{ cm}^{-1}$. Consequently, this approach can be considered valid.

The hyperfine cross-sections are then obtained based on the S-matrices $S^J(N_j l; N'_j l')$ given by equation (6), as defined by Alexander & Dagdigian (1985)

$$\sigma_{N_j F \rightarrow N'_j F'}^{\text{REC}} = \frac{\pi}{k_{N_j F}^2} (2F' + 1) \sum_K \left\{ \begin{matrix} j & j' & K \\ F' & F & I \end{matrix} \right\}^2 P^K(N_j \rightarrow N'_j) \quad (8)$$

with

$$P^K(N_j \rightarrow N'_j) = \frac{1}{2K + 1} \sum_{l'l'} |T^K(N_j l; N'_j l')|^2 \quad (9)$$

and

$$T^K(N_j l; N'_j l') = (-1)^{-j-l'} (2K + 1) \sum_J (-1)^J (2J + 1) \quad (10)$$

$$\times \left\{ \begin{matrix} l' & j' & J \\ j & l & K \end{matrix} \right\} (\delta_{N N'} \delta_{j j'} \delta_{l l'} - S^J(N_j l; N'_j l')), \quad (11)$$

where $|F - F'| \leq K \leq F + F'$.

Once the cross-sections are defined, the associated rate coefficients can be inferred by averaging these cross-sections over the collisional energies, as in equation (7).

2.3 Radiative transfer calculations

Rate coefficients are key ingredients to interpret astrophysical observations of molecules through radiative transfer models.

In order to discuss the impact of the rate coefficients produced in this work on the interpretation of observations, non-LTE radiative transfer calculations were performed with the RADEX code (van der Tak et al. 2007) to derive astrophysically relevant quantities, such as excitation temperature T_{ex} , and radiance temperature T_r . It is based on the escape probability formalism. It assumes an isothermal and homogeneous medium, which is fully contained in the antenna beam.

For such modelling, it was assumed that the background radiation field was the cosmic microwave background (CMB) of 2.73 K. The line width was set at 1.0 km s^{-1} , and the kinetic temperature of the gas at 10 K, the typical temperature of dense molecular clouds (McGuire 2022).

To properly model CCS isotopologues, rate coefficients for CCS in collisions with both He and H_2 are required. A well-known approximation to infer rate coefficients with H_2 collider from rate coefficients with He collider is to multiply the data sets by a factor of ~ 1.39 , the square-root of the reduced mass ratio.

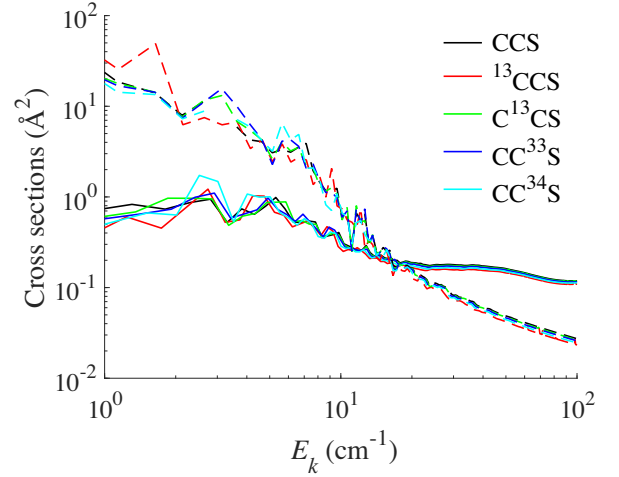


Figure 2. Fine-structure resolved cross-sections of CCS, ^{13}CCS , C^{13}CS , CC^{33}S , and CC^{34}S for the 6_7-5_4 (solid lines) and the 0_1-1_0 (dashed lines) de-excitation transitions.

The Einstein coefficients used were those available in CDMS (Müller et al. 2001, 2005; Endres et al. 2016), and JPL (Pickett et al. 1998) databases.

3 RESULTS AND DISCUSSION

3.1 Fine structure resolved cross-sections and rate coefficients

Fine structure resolved cross-sections were produced according to the methodology described in Section 2.2.2.

Fig. 2 shows the collisional energy dependence of the de-excitation fine-structure resolved cross-sections for the 6_7-5_4 and the 0_1-1_0 transitions for all 5 CCS isotopologues.

At low kinetic energy, one observe Feshbach and shape resonances that are typical when the collisional energy is lower than the well depth (here about 37 cm^{-1}). They are due to the temporary formation of (quasi)bound states before the complex dissociates (Costes & Naulin 2016).

The behaviour and values of the cross-sections for all isotopologues are very similar. Some differences can be seen in the resonances area that are by nature very sensitive to the shape of the potential and to the spectroscopic constants. However, the overall isotopic substitution effect is rather small even in the resonance part due to similar spectroscopic constants (see Table 1), and small shift in the c.o.m. positions induced by the isotopic substitution ($\delta_{G/G_1} = -0.06395a_0$ and $\delta_{G/G_2} = -0.0205a_0$, $\delta_{G/G_3} = 0.03155a_0$; $\delta_{G/G_4} = 0.06193a_0$). When the resonances disappear ($E_k > 37 \text{ cm}^{-1}$), the cross-sections are almost identical.

Fine-structure resolved rate coefficients for ^{13}CCS , C^{13}CS , CC^{34}S , and CC^{33}S in collision with He have been provided for the 5–50 K temperature range based on the fine-structure resolved cross-sections. The fine-structure resolved rate coefficients of $^{12}\text{C}^{12}\text{C}^{32}\text{S}$ -He have already been provided in Paper I in the same temperature range.

In Paper I, the propensity rules governing CCS-He fine-structure resolved rate coefficients were investigated, with a particular emphasis on the impact of CCS's peculiar fine structure on these rules. The following propensity rules were determined:

- (i) Rate coefficients generally decrease with increasing ΔN , which is the usual behaviour for rotational rate coefficients

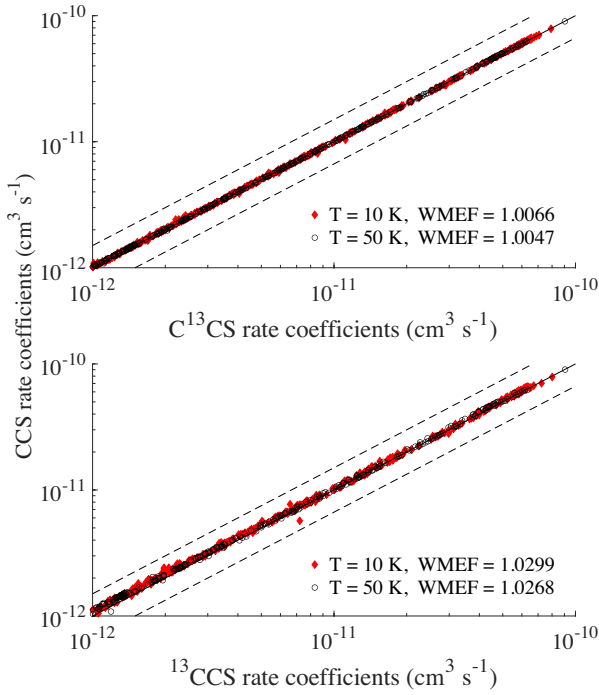


Figure 3. Systematic comparison of de-excitation fine-structure resolved rate coefficients at $T = 10$ K and 50 K of $^{12}\text{C}^{13}\text{C}^{32}\text{S}$ (upper panel) and $^{13}\text{C}^{12}\text{C}^{32}\text{S}$ (lower panel) isotopologues with respect to the fine rate coefficients of the main isotopologue $^{12}\text{C}^{12}\text{C}^{32}\text{S}$. The solid line represents a perfect agreement, and the dashed line a deviation of 50 per cent.

(ii) Even ΔN transitions are favoured compared to odd ΔN due to larger even anisotropy in the PES

(iii) $\Delta N = \Delta j$ transitions are strongly favoured, as generally observed in molecules in $^3\Sigma^-$ electronic state

These propensity rules have been found for all CCS isotopologues addressed in this work.

In order to evaluate the influence of the isotopic substitution on CCS isotopologues rate coefficients, a systematic comparison of CCS fine-structure resolved rate coefficients and with those of its secondary isotopologues is presented in Figs 3 and 4 for the isotopic substitution of one of the ^{12}C and of the ^{32}S , respectively. Only de-excitation rate coefficients are considered to prevent bias arising from threshold effects. Transitions between the first 31 levels are represented for the sake of clarity, but the weighted mean error factor (WMEF) calculated takes into account the de-excitation rate coefficients between all 61 fine-structure levels included in the scattering calculations. The WMEF, defined as in equation (12), represents the deviation between the rate coefficients of the main isotopologue and those of the secondary isotopologues, pondered by the highest rate coefficients. This indicator is important to estimate the relevance of the deviation between the two sets of data on non-LTE models, where dominant transitions have more impact.

$$\text{WMEF} = \frac{\sum_i k_i^{\text{main}} r_i}{\sum_i k_i^{\text{main}}}, \quad (12)$$

where $r_i = \max(k_i^{\text{main}}/k_i^{\text{sec}}; k_i^{\text{sec}}/k_i^{\text{main}}) \geq 1$, with k_i^{main} and k_i^{sec} rate coefficients for the i -th transition of the main isotopologue $^{12}\text{C}^{12}\text{C}^{32}\text{S}$ and of the secondary isotopologue considered, respectively.

In Fig. 3, rate coefficients of ^{13}C -bearing isotopologues reproduce the rate coefficients of the main isotopologue at better than 10 per cent for C^{13}CS , and at better than 30 per cent for ^{13}CCS at both 10 K (red

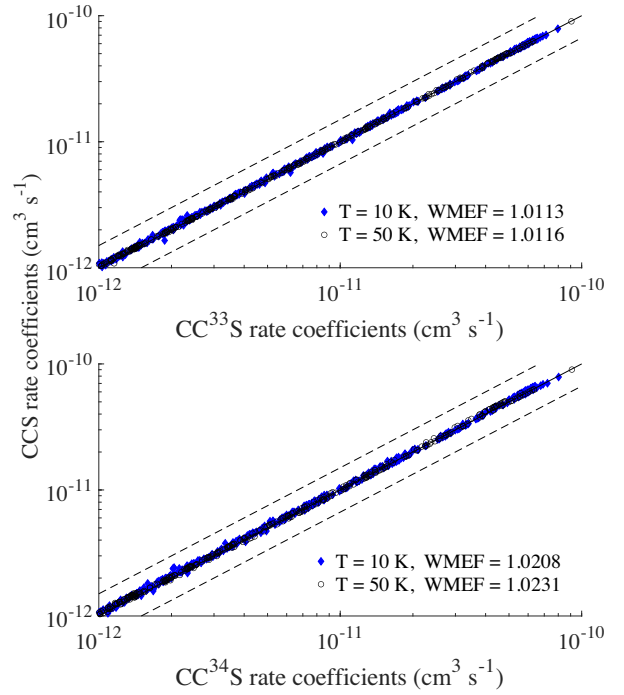


Figure 4. Systematic comparison of de-excitation fine-structure resolved rate coefficients at $T = 10$ K and 50 K of $^{12}\text{C}^{12}\text{C}^{33}\text{S}$ (upper panel) and $^{12}\text{C}^{12}\text{C}^{34}\text{S}$ (lower panel) isotopologues with respect to the fine rate coefficients of the main isotopologue $^{12}\text{C}^{12}\text{C}^{32}\text{S}$. The plain line represents a perfect agreement, the dashed line represents a deviation of 50 per cent.

diamonds) and 50 K (black circles). The discrepancies are larger for the ^{13}CCS isotopologue, for which the shift of the c.o.m. is larger than for the C^{13}CS isotopologue.

In Fig. 4, the overall agreement between the fine-structure resolved rate coefficients induced by the substitution of ^{32}S with either ^{33}S (upper panel) or ^{34}S (lower panel) in the rate coefficients is better than 20 per cent for all transitions at both temperatures considered. The WMEF for both isotopologues is small, but is slightly larger for CC^{34}S than for CC^{33}S . The fact that the data sets are similar is justified by comparable reduced mass, spectroscopic constants, and PES shift. This observation is consistent with previous conclusions drawn for the ^{12}C substitution.

For both ^{12}C and ^{32}S isotopic substitution, the overall effect of isotopic substitution on the fine-structure resolved rate coefficients appears to be weak, with $\text{WMEF} < 1.05$ for all isotopologues. No temperature effect on the WMEF is reported for all isotopologues. Also, the sets of fine rate coefficients for ^{13}CCS and CC^{34}S were also compared (not shown here) since they both exhibit the largest deviations compared to the reference. However, even in that case, the discrepancies exhibited were small, and the WMEF values are of about 1.01 and 1.02 at 10 K and 50 K, respectively. One can conclude that the effect of isotopic substitution in CCS molecule is weak and much lower than previously found for non-hydrides molecules (Faure & Lique 2012; Flower & Lique 2015; Navarro-Almaida et al. 2023).

3.2 Hyperfine-structure resolved cross-sections and rate coefficients

Hyperfine structures of ^{13}CCS , C^{13}CS , and CC^{33}S induced by the nuclear spin of ^{13}C ($I = \frac{1}{2}$) and of ^{33}S ($I = \frac{3}{2}$) were taken into ac-

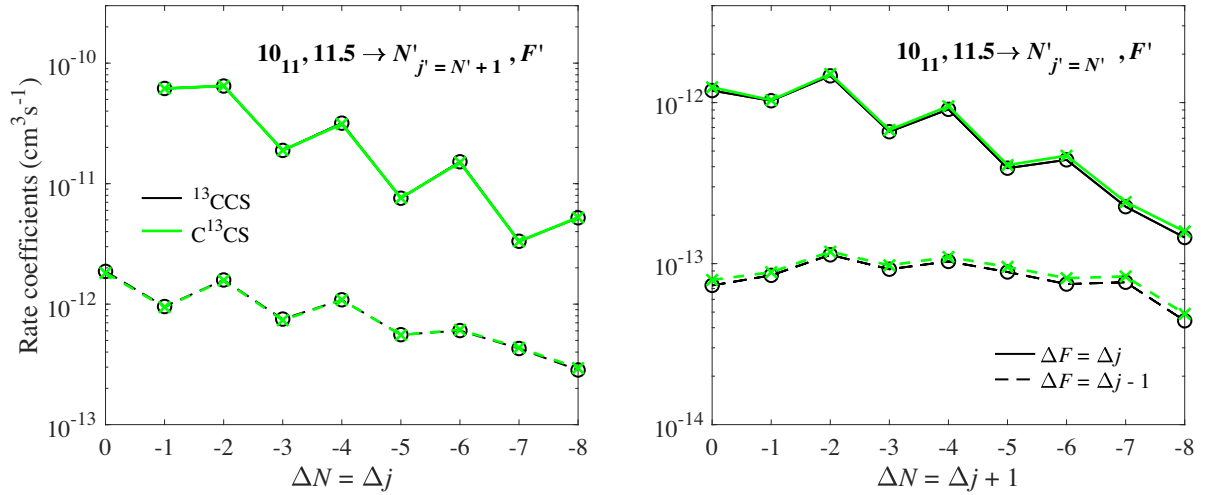


Figure 5. Propensity rules for hyperfine-structure resolved rate coefficients at 10 K for ^{13}CCS and C^{13}CS isotopologues from the $10_{11}, 11.5$ level. Rate coefficients for $\Delta F = \Delta j$ (solid lines) and $\Delta F \neq \Delta j$ (dashed lines) are presented for both $\Delta N = \Delta j$ (right panel) and $\Delta N \neq \Delta j$ (left panel) transitions.

count to compute hyperfine-structure resolved cross-sections and rate coefficients according to the methodology presented in Section 2.2.3.

The propensity rules of the hyperfine-structure resolved rate coefficients for ^{13}CCS (black) and C^{13}CS (green) are presented at 10 K in Fig. 5. The influence of ΔF value is investigated for $\Delta N = \Delta j$ (left panel) and $\Delta N \neq \Delta j$ (right panel) transitions.

Fig. 5 exhibits that both ^{13}CCS (black) and C^{13}CS (green) do respect the same propensity rules, so all following conclusions hold for both these isotopologues.

A clear propensity is in favour of $\Delta F = \Delta j$ transitions for both $\Delta N = \Delta j$ (left panel) and $\Delta N \neq \Delta j$ (right panel) transitions. This is typical of systems with hyperfine structure, due to 6- j Wigner's symbol used in the recoupling technique and has been predicted by Dixon & Field (1979) and Alexander & Dagdigian (1985) and confirmed experimentally by Alexander & Dagdigian (1985). It has been already observed in other systems (Daniel, Dubernet & Meuwly 2004; Buffa 2012; Dumouchel et al. 2012; Kalugina, Lique & Klos 2012; Lique, Bulut & Roncero 2016; Dumouchel et al. 2017; Dagdigian 2018; Ndaw et al. 2021; Pirlot Jankowiak, Lique & Dagdigian 2023a, b). In addition, the dominance of $\Delta F = \Delta j$ over $\Delta F \neq \Delta j$ is greater for $\Delta N = \Delta j$ transitions than for $\Delta N \neq \Delta j$.

Propensity rules of CC^{33}S isotopologues are presented in Fig. 6. The propensity rules regarding the impact of ΔF on $\Delta N = \Delta j$ (left panel) and $\Delta N \neq \Delta j$ (right panel) rate coefficients are presented.

As for ^{13}CCS and C^{13}CS , the dominant transitions in CC^{33}S are $\Delta F = \Delta j$ transitions for both $\Delta N = \Delta j$ and $\Delta N \neq \Delta j$ transitions. The greater the difference between ΔF and Δj is, the more the magnitude of the rate coefficients decrease. Therefore, rate coefficients with $\Delta F = \Delta j + 1$ are larger than those with $\Delta F = \Delta j + 2$, and similarly, those with $\Delta F = \Delta j + 2$ are larger than those with $\Delta F = \Delta j + 3$ transitions.

To discuss the isotopic effect induced by the position of the ^{13}C on the collisional rate coefficients, hyperfine-structure resolved de-excitation rate coefficients of ^{13}CCS and C^{13}CS isotopologues are systematically compared at 10 K in Fig. 7. In the WMEF calculation, ^{13}CCS was considered as the reference, so $k_i^{\text{main}} \equiv k_i^{^{13}\text{CCS}}$ and $k_i^{\text{sec}} \equiv k_i^{\text{C}^{13}\text{CS}}$.

The similarities between the data sets are quite pronounced with an overall agreement better than 10–15 per cent over the dominant transitions, and better than 40 per cent for any transitions. The WMEF

is small and comparable to what have been observed when comparing fine-structure resolved rate coefficients of CCS isotopologues.

3.3 Astrophysical modelling

In this section, the isotopologues are treated separately according to their structure. First, astrophysical application for fine-structure transitions in CCS and CC^{34}S are considered, and then hyperfine-structure transitions in ^{13}CCS and C^{13}CS are examined. Since the Einstein coefficients for CC^{33}S are not available, no astrophysical applications have been conducted for this isotopologue.

3.3.1 CCS and CC^{34}S

The excitation temperature is useful to check the validity of the LTE approximation at a given volume density, i.e. if the population of the energy levels involve in the transition are following a Boltzmann distribution.

In Fig. 8, excitation temperatures (higher panels) of three transitions of CCS (black lines) and CC^{34}S (red lines) are plotted against the volume density of the gas at 10 K. The column density for both isotopologues have been set at $1 \times 10^{13} \text{ cm}^{-2}$ in order to discuss collisional effect. Even though this value will be different for all isotopologues in practice (probably underestimated for the main isotopologue, and overestimated for secondary ones), it is not suppose to influence much the value of T_{ex} as long as the opacity is weak.

Typically, the excitation temperature behaves as follows: at very low volume density, the radiative processes are dominant so $T_{\text{ex}} = T_{\text{CMB}}$. As the volume density of the medium increases, radiative and collisional processes come into competition, thus characterizing the non-LTE domain where $T_{\text{CMB}} < T_{\text{ex}} < T_{\text{kin}}$. This is typically the domain of densities where inelastic rate coefficients are required to proper model molecular abundances. When collisions dominate, the LTE domain starts, so that $T_{\text{ex}} = T_{\text{kin}}$, and the population of energy levels are following a Boltzmann distribution, and will only depend on the kinetic temperature of the gas.

The 3_4-2_3 transition follows the general behaviour as described above. The 1_2-0_1 transition presents a maser effect (microwave amplification by stimulated emission of radiation) due to a population

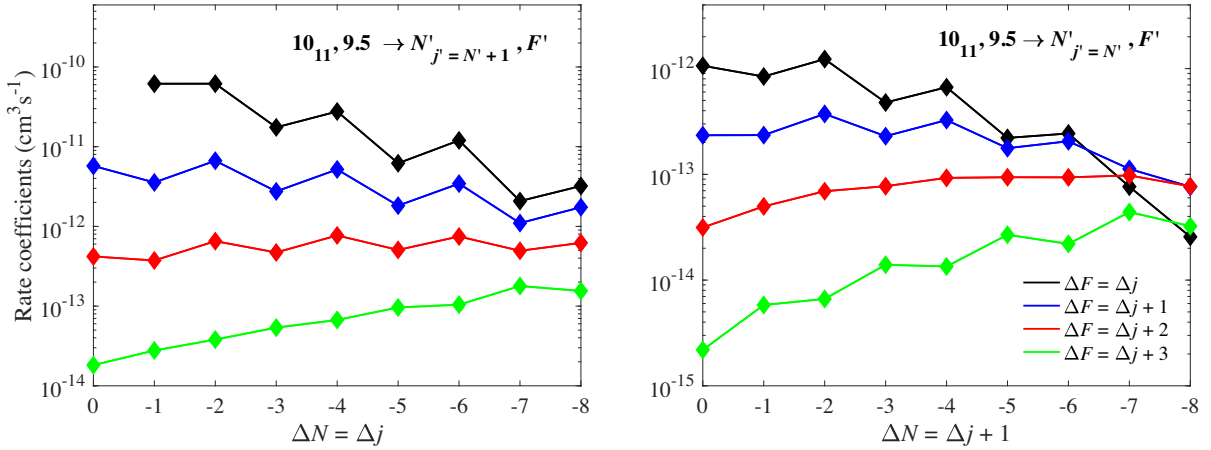


Figure 6. Propensity rules for hyperfine-structure resolved rate coefficients of CC^{33}S isotopologue at 10 K from the $10_{11}, 9.5$ level. Rate coefficients for $\Delta F = \Delta j$ (solid lines) and $\Delta F \neq \Delta j$ (dashed lines) are presented for both $\Delta N = \Delta j$ (right panel) and $\Delta N \neq \Delta j$ (left panel) transitions.

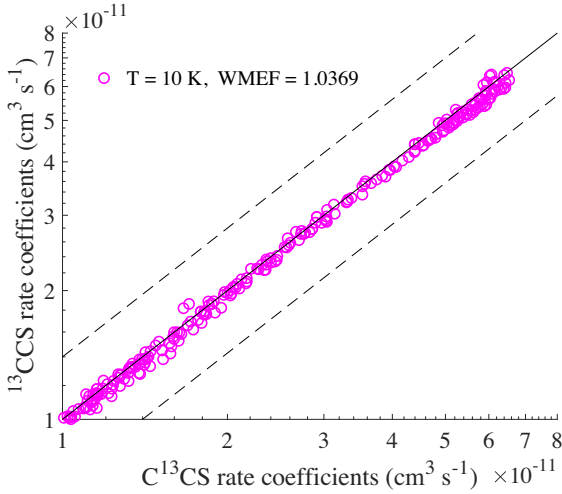


Figure 7. Systematic comparison of dominant de-excitation hyperfine-structure resolved rate coefficients at $T = 10$ K of the $^{13}\text{C}^{12}\text{C}^{32}\text{S}$ (x-axis) and $^{12}\text{C}^{13}\text{C}^{32}\text{S}$ (y-axis) isotopologues. The plain line represents a perfect agreement between the two data sets and the dashed line a deviation of 50 percent.

inversion. This maser covers a large range of volume densities, from 10^3 to 10^6 cm^{-3} , and might be observable in several molecular clouds. The 3_2-2_1 transition presents a so-called subthermal effect for volume density ranging from 10^3 to 10^5 cm^{-3} , which means that its excitation temperature is lower than T_{CMB} in this density range. Consequently, this transition might be observable in absorption, contrary to other lines presented here. Such effect is also present at a lower scale in the 1_0-0_1 transition.

None of these lines are thermalized at the typical volume density of molecular clouds (10^4 – 10^5 cm^{-3}), and reach LTE from volume density of about 10^5 – 10^6 cm^{-3} . Therefore, accurate determination of CCS and CC^{34}S abundances in molecular clouds would require the use of the fine-structure resolved rate coefficients produced in this work in non-LTE models.

The radiance temperature T_r is of the upmost importance since it can be directly compared to what is measured by telescopes. In the lower panels of Fig. 8, the variation of T_r for CCS (black line) and CC^{34}S (red lines) transitions across column densities ranging from

between 10^{12} and 10^{15} cm^{-2} is presented at two different volume densities: $n = 10^4$ cm^{-3} (dashed lines) and $n = 10^5$ cm^{-3} (dotted lines).

Radiance temperature for the transitions under discussion here generally increases with the increasing column density of the molecule at both volume densities (as expected for optically thin lines) and reaches a plateau when the lines become optically thick. The exception is the 3_2-2_1 transition, which exhibits a negative radiance temperature at a volume density of 10^4 cm^{-3} , characteristic of absorption lines.

The radiance temperature tend to be higher at increased volume density, except for the 1_2-0_1 maser emission when the column density of the molecule is lower than 10^{14} cm^{-2} .

The excitation conditions of the two isotopologues are similar and the effect of isotopic substitution is weak. The excitation temperature for the transitions under consideration here are very similar, even though some differences for the 3_2-2_1 transition can be observed within the typical density of molecular clouds. The same remarks hold for the radiance temperature.

3.3.2 ^{13}CCS and C^{13}CS

The excitation temperature of two observed lines of ^{13}CCS (black lines) and C^{13}CS (green lines) are presented in the upper panels of Fig. 9 against the volume density of the gas at 10 K. Here also, the column density of both isotopologues have been set at 10^{13} cm^{-2} .

The $2_{3,3.5}-1_{2,2.5}$ transition presents a weak suprathemal effect ($T_{\text{ex}} > T_{\text{kin}}$) for a volume density 10^4 – 10^5 cm^{-3} . The $1_{2,2.5}-0_{1,1.5}$ transition presents a maser effect for volume density ranging from 10^3 to 10^6 cm^{-3} . Therefore, the use of the rate coefficients provided in this work is recommended for a reliable determination of ^{13}CCS and C^{13}CS abundances in molecular clouds.

The excitation temperatures of both isotopologues have the same behaviour and very similar values, even though some slight discrepancies can be observed. The excitation temperatures of the C^{13}CS are slightly shifted towards higher volume densities compared to the excitation temperatures of ^{13}CCS .

The radiance temperatures for transitions of ^{13}CCS (black lines) and C^{13}CS (green lines) as a function of their column density ranging from 10^{10} and 10^{14} cm^{-2} is represented in the lower panels of Fig. 9 at two volume densities of the gas: $n = 10^4$ cm^{-3} (dashed lines) and $n = 10^5$ cm^{-3} (dotted lines).

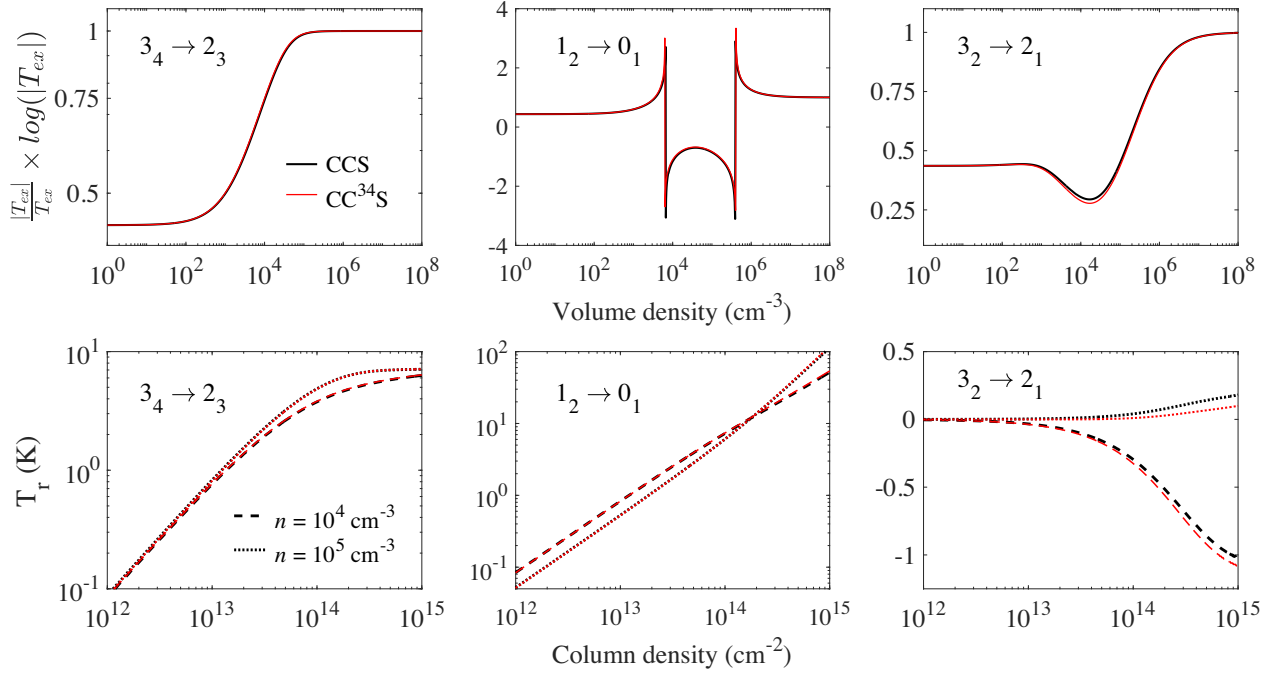


Figure 8. In the upper panels, excitation temperatures of two observed transitions of CCS (black lines) and CC^{34}S (red lines) against the volume density of the gas. In the lower panels, radiance temperature for the same transitions as a function of the column density of the isotopologues at two volume densities of the gas: $n = 10^4 \text{ cm}^{-3}$ (dashed lines) and $n = 10^5 \text{ cm}^{-3}$ (dotted lines). The kinetic temperature of the gas was set at 10 K.

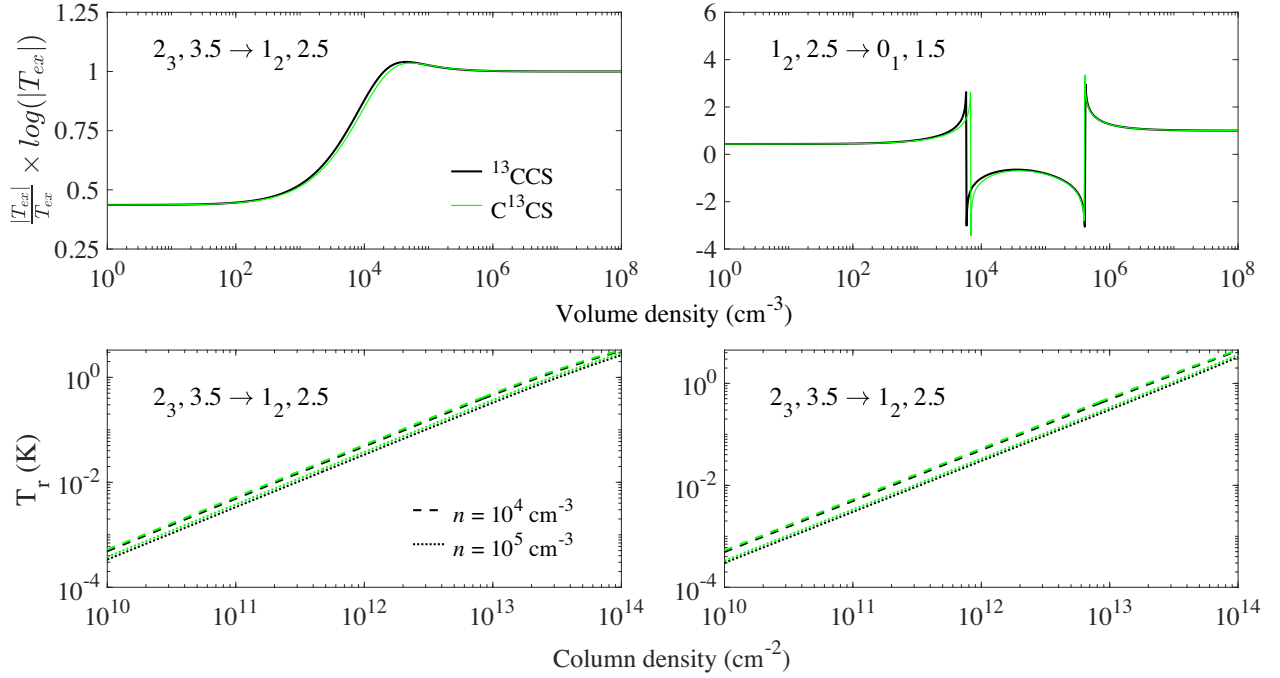


Figure 9. In the upper panels, excitation temperatures of two observed transitions of ^{13}CCS (black lines) and C^{13}CS (green lines) against the volume density of the gas. In the lower panels, radiance temperature for the same transitions as a function of the column density of the isotopologues at two volume densities of the gas: $n = 10^4 \text{ cm}^{-3}$ (dashed lines) and $n = 10^5 \text{ cm}^{-3}$ (dotted lines). The kinetic temperature of the gas was set at 10 K.

The radiance temperatures are generally higher at lower gas densities (dashed lines), likely due to suprathermal and maser effects.

In the work of Sakai et al. (2007), C^{13}CS abundance has been found to be 4.2 times larger than that of ^{13}CCS based on LTE modelling. The production mechanism of CCS was assumed to be the cause of

such differences between C^{13}CS and ^{13}CCS isotopologues. Another possible explanation would have been to consider that the levels of C^{13}CS involved in the observed transitions were more efficiently populated by collisions. However, the weak effect for the isotopic substitution in the collisional data observed between the two ^{13}C -

bearing isotopologues is not strong enough to explain such anomaly. Thus, the formation and destruction paths of the isotopologues are probably the source of the discrepancies in ^{13}CCS and C^{13}CS abundances.

4 CONCLUSIONS

In this work, the very first state-to-state rate coefficients were provided for detectable CCS isotopologues: ^{13}CCS , C^{13}CS , CC^{34}S , and CC^{33}S . Scattering calculations were performed with the CC approach for all four isotopologues in collision with He explicitly accounting for their fine structure, to derive rate coefficients for the 5–50 K temperature range. The hyperfine structures induced by the nuclear spin of ^{13}C ($I = \frac{1}{2}$) and ^{33}C ($I = \frac{3}{2}$) were considered to provided hyperfine-structure resolved rate coefficients using the recoupling approach for the 5–15 K temperature range for ^{13}CCS , C^{13}CS , and CC^{33}S isotopologues.

The sets of rate coefficients of CCS , ^{13}CCS , C^{13}CS , and CC^{34}S isotopologues have been used in radiative transfer calculations, and all commonly observed transitions have been found to have a population not following a Boltzmann distribution at typical volume density of molecular clouds (10^4 – 10^5 cm^{-3}), showing that the data provided in this work must be used to properly model CCS isotopologues observations in molecular clouds.

For such models, rate coefficients for CCS isotopologues in collision with H_2 ($j = 0$) are required. Here, they have been inferred by scaling the rate coefficients of CCS isotopologues in collision with He computed in this work. Performing calculations for the CCS-H_2 ($j = 0$), however difficult regarding the complexity of the internal structure of CCS isotopologues, would be interesting to confirm the results obtained here.

The effect of the isotopic substitution on the fine and hyperfine structure rate coefficients have been studied and was found to be weak for all isotopic substitutions but stronger for ^{13}CCS and CC^{34}S , which exhibit larger shifts of the c.o.m. in the PES representation. The differences between hyperfine-structure rate coefficients of ^{13}CCS and C^{13}CS isotopologue appear to be stronger than on the fine-structure resolved rate coefficients only.

The effect of the deviation in the sets of rate coefficients on the excitation and radiance temperature have been found to be weak for all transitions. Therefore, according to the precision requested to interpret observations, the fine-structure resolved rate coefficients of CCS could be used to model CC^{34}S ; the hyperfine-structure resolved rate coefficients of ^{13}CCS could be used to model C^{13}CS , and vice-versa. Therefore, it is then possible to limit the number of isotopologues under consideration if one wants to extend the temperature range of CCS isotopologues collisional data.

The anomaly between ^{13}CCS and C^{13}CS abundances reported in the work of Sakai et al. (2007) cannot be explained by collisional excitation effects, and need to be further discussed based on reliable abundances of the two ^{13}C -based isotopologues derived by using the hyperfine-structure rate coefficients provided in this work.

ACKNOWLEDGEMENTS

We acknowledge Professor Cernicharo and Marcelino Agúndez for initiating this project and for fruitful discussions.

We acknowledge financial support from the European Research Council (Consolidator Grant COLLEXISM, Grant Agreement No. 811363). We wish to acknowledge the support from the CEA/GENCI (Grand Equipement National de Calcul Intensif) for awarding us access to the TGCC (Très Grand Centre de Calcul) Joliot Curie/IRENE

supercomputer within the A0110413001 project. We also acknowledge Rennes Metropole for financial support. FL acknowledges the Institut Universitaire de France.

DATA AVAILABILITY

The computed collisional data for the 5 CCS isotopologues studied here (CCS , ^{13}CCS , C^{13}CS , CC^{33}S , and CC^{34}S) in collision with He will be available on the following data bases: BASECOL (Dubernet et al. 2013), LAMDA (Schoier et al. 2005), and EMAA (Faure et al. 2021).

REFERENCES

- Alexander M. H., Dagdigian P. J., 1983, *J. Chem. Phys.*, 79, 302
 Alexander M. H., Dagdigian P. J., 1985, *J. Chem. Phys.*, 83, 2191
 Boys S., Bernardi F., 1970, *Mol. Phys.*, 19, 553
 Buffa G., 2012, *MNRAS*, 421, 719
 Costes M., Naulin C., 2016, *Chem. Sci. J.*, 7, 2462
 Cybulski S. M., Toczyłowski R. R., 1999, *J. Chem. Phys.*, 111, 10520
 Dagdigian P. J., 2018, *MNRAS*, 479, 3227
 Dagdigian P. J., 2022, *MNRAS*, 514, 2214
 Daniel F., Dubernet M.-L., Meuwly M., 2004, *J. Chem. Phys.*, 121, 4540
 Deegan M. J., Knowles P. J., 1994, *Chem. Phys. Lett.*, 227, 321
 Dixon R. N., Field D., 1979, *Proc. R. Soc. Lon. A. Math. Phys. Sci.*, 366, 225
 Dubernet M.-L. et al., 2013, *A&A*, 553, A50, available at: <https://basecol.vmdc.eu>
 Dumouchel F., Klos J., Toboła R., Bacmann A., Maret S., Hily-Blant P., Faure A., Lique F., 2012, *J. Chem. Phys.*, 137, 114306
 Dumouchel F., Lique F., Spielfiedel A., Feautrier N., 2017, *MNRAS*, 471, 1849
 Endres C. P., Schlemmer S., Schilke P., Stutzki J., Müller H. S., 2016, *J. Mol. Spectrosc.*, 327, 95, available at: <https://cdms.astro.uni-koeln.de/cdms/portal/>
 Faure A., Bacmann A., Bouthier B., Jacquot R., 2021, *UGA, CNRS, CNRS-INSU, OSUG*, available at: <https://emaa.osug.fr>
 Faure A., Lique F., 2012, *MNRAS*, 425, 740
 Flower D. R., Lique F., 2015, *MNRAS*, 446, 1750
 Fuente A., Cernicharo J., Barcia A., Gómez-González, 1990, *A&A*, 231, 151
 Godard Palluet A., Lique F., 2023, *J. Chem. Phys.*, 158, 044303 (Paper I)
 Hily-Blant P., Faure A., Vastel C., Magalhaes V., Lefloch B., Bachiller R., 2018, *MNRAS*, 480, 1174
 Hutson J., Green S., 1994, Molscat Computer Program, Version 14, Distributed by Collaborative Computational Project No. 6 of the UK Science and Engineering Research Council.
 Ikeda M., Sekimoto Y., Yamamoto S., 1997, *J. Mol. Spectrosc.*, 185, 21
 Kalugina Y., Lique F., Klos J., 2012, *MNRAS*, 422, 812
 Lique F., Bulut N., Roncero O., 2016, *MNRAS*, 461, 4477
 Loison J.-C., Wakelam V., Gratier P., Hickson K. M., 2020, *MNRAS*, 498, 4663
 Manolopoulos D. E., 1986, *J. Chem. Phys.*, 85, 6425
 McGuire B. A., 2022, *ApJS*, 259, 30
 McGuire B. A., Martin-Drumel M.-A., Lee K. L. K., Stanton J. F., Gottlieb C. A., McCarthy M. C., 2018, *Phys. Chem. Phys. Chem.*, 20, 13870
 Müller H. S. P., Thorwirth S., Roth D. A., Winniewisser G., 2001, *A&A*, 370, L49, available at: <https://cdms.astro.uni-koeln.de/cdms/portal/>
 Müller H. S., Schlöder F., Stutzki J., Winniewisser G., 2005, *J. Mol. Struct.*, 742, 215, available at: <https://cdms.astro.uni-koeln.de/cdms/portal/>
 Navarro-Almáida D. et al., 2023, *A&A*, 670, A110
 Ndaw D., Bop C. T., Dieye G., Faye N. A. B., Lique F., 2021, *MNRAS*, 503, 5976
 Pickett H. M., Poynter R. L., Cohen E. A., Delitsky M. L., Pearson J. C., Muller H. S. P., 1998, *J. Quant. Spectrosc. Radiat. Transfer*, 60, 883, available at: <https://spec.jpl.nasa.gov>
 Pirlot Jankowiak P., Lique F., Dagdigian P. J., 2023a, *MNRAS*, 523, 3732
 Pirlot Jankowiak P., Lique F., Dagdigian P. J., 2023b, *MNRAS*, 526, 885

- Sakai N., Ikeda M., Morita M., Sakai T., Takano S., Osamura Y., Yamamoto S., 2007, *ApJ*, 663, 1174
- Schoïer F. L., van der Tak F. F. S., van Dishoeck E. F., Black J. H., 2005, *A&A*, 432, 369, available at: <https://home.strw.leidenuniv.nl/~moldata/>
- Suzuki H., Yamamoto S., Ohishi M., Kaifu N., Ishikawa S.-I., Hirahara Y., Takano S., 1992, *A&A*, 392, 551
- Takano S. et al., 1998, *A&A*, 329, 1156
- Taniguchi K., Ozeki H., Saito M., Sakai N., Nakamura F., Kameno S., Takano S., Yamamoto S., 2016, *ApJ*, 817, 147
- van der Tak F. F. S., Black J. H., Schöier F. L., Jansen D. J., van Dishoeck E. F., 2007, *A&A*, 468, 627
- Velusamy T., Kuiper T. B. H., Langer W. D., 1995, *ApJ*, 451, L75
- Wernli M., Wiesenfeld L., Faure A., Valiron P., 2007, *A&A*, 464, 1147
- Wolkovitch D., Langer W. D., Goldsmith P. F., Heyer M., 1997, *ApJ*, 477, 241

APPENDIX A: FINE STRUCTURE ENERGY LEVELS OF CCS ISOTOPOLOGUES

Table A1. List of fine structure energy levels of the CCS, ^{13}CCS , C^{13}CS , CC^{34}S , and CC^{33}S isotopologues based on the spectroscopic constants from McGuire et al. (2018) and Fuentetaja et al. (in preparation).

Label N_j	Energy (cm^{-1})				
	CCS	^{13}CCS	C^{13}CS	CC^{34}S	CC^{33}S
1 ₀	0.00000	0.00000	0.00000	0.00000	0.00000
0 ₁	0.37091	0.35707	0.36947	0.36416	0.36744
1 ₂	1.11623	1.07412	1.11184	1.09568	1.10568
2 ₃	2.24205	2.15627	2.23311	2.20018	2.22054
3 ₄	3.75574	3.6098	3.74048	3.68447	3.71909
4 ₅	5.66470	5.4412	5.64129	5.55549	5.60851
1 ₁	6.48371	6.48428	6.48578	6.48368	6.48537
2 ₁	6.54495	6.54004	6.54641	6.54220	6.5451
2 ₂	7.34800	7.30993	7.34597	7.32905	7.33989
3 ₂	7.52821	7.474279	7.52441	7.50141	7.51599
5 ₆	7.97567	7.65654	7.94217	7.81964	7.89535
3 ₃	8.64444	8.54840	8.63625	8.59709	8.62167
4 ₃	8.99525	8.86905	8.98370	8.93300	8.96467
4 ₄	10.3730	10.1997	10.3566	10.2878	10.3307
6 ₇	10.6944	10.2610	10.6488	10.4824	10.5852
5 ₄	10.9387	10.7181	10.9171	10.8302	10.8841
5 ₅	12.5337	12.2638	12.5071	12.4012	12.4670
6 ₅	13.3512	13.0148	13.3172	13.1859	13.2673
7 ₈	13.8256	13.2589	13.7659	13.5483	13.6827
6 ₆	15.1266	14.7407	15.0876	14.9373	15.0305
7 ₆	16.2259	15.7533	16.1773	15.9939	16.1075

Table A1 – continued

Label N_j	Energy (cm^{-1})				
	CCS	^{13}CCS	C^{13}CS	CC^{34}S	CC^{33}S
8 ₉	17.3730	16.6538	17.2971	17.0210	17.1916
7 ₇	18.1515	17.6304	18.0982	17.8960	18.0212
8 ₇	19.5570	18.9282	19.4918	19.2485	19.3991
9 ₁₀	21.3395	20.4486	21.2455	20.9035	21.1147
8 ₈	21.6086	20.9329	21.5388	21.2773	21.4392
9 ₈	23.3400	22.5353	23.2561	22.9453	23.1375
9 ₉	25.4978	24.6481	25.4095	25.0813	25.2843
10 ₁₁	25.7276	24.6456	25.6133	25.1980	25.4545
10 ₉	27.5709	26.5709	27.4662	27.0806	27.3190
10 ₁₀	29.8190	28.7761	29.7103	29.3079	29.5567
11 ₁₂	30.5391	29.2465	30.4025	29.9063	30.2127
11 ₁₀	32.2468	31.0322	32.1193	31.6513	31.9405
11 ₁₁	34.5723	33.3169	34.4410	33.9572	34.2563
12 ₁₃	35.7755	34.2529	35.6145	35.0300	35.3909
12 ₁₁	37.3654	35.9167	37.2130	36.6553	36.9999
12 ₁₂	39.7577	38.2705	39.6018	39.0290	39.3830
13 ₁₄	41.4378	39.6658	41.2504	40.5702	40.9902
13 ₁₂	42.9246	41.2228	42.7453	42.0906	42.4951
13 ₁₃	45.3751	43.6367	45.1925	44.5234	44.9369
14 ₁₅	47.5272	45.4863	47.3112	46.5279	47.0115
14 ₁₃	48.9231	46.9490	48.7148	47.9557	48.4246
14 ₁₄	51.4246	49.4156	51.2132	50.4404	50.9179
15 ₁₆	54.0442	51.7150	53.7976	52.9037	53.4555
15 ₁₄	55.3596	53.0939	55.1203	54.2494	54.7873
15 ₁₅	57.9060	55.6073	57.6639	56.7799	57.3259
16 ₁₇	60.9895	58.3527	60.7103	59.6983	60.3230
16 ₁₅	62.2331	59.6567	61.9608	60.9708	61.5823
16 ₁₆	64.8194	62.2116	64.5445	63.5419	64.1612
17 ₁₈	68.3637	65.3997	68.0497	66.9122	67.6144
17 ₁₆	69.5429	66.6366	69.2356	68.1190	68.8086
17 ₁₇	72.1648	69.2286	71.8550	70.7265	71.4235
18 ₁₉	76.1670	72.8565	75.8162	74.5459	75.3300
18 ₁₇	77.2883	74.0329	76.9439	75.6935	76.4657
18 ₁₈	79.9421	76.6582	79.5954	78.3335	79.1128
19 ₂₀	84.3998	80.7235	84.0103	82.5995	83.4703
19 ₁₈	85.4688	81.8451	85.0852	83.6936	84.5529
19 ₁₉	88.1513	84.5004	87.7656	86.3630	87.2292
20 ₂₁	93.0626	89.0009	92.6321	91.0735	92.0355
20 ₁₉	94.0839	90.0727	93.6592	92.1189	93.0700
20 ₂₀	96.7924	92.7552	96.3658	94.8149	95.7725

This paper has been typeset from a $\text{T}_{\text{E}}\text{X}/\text{L}_{\text{A}}\text{T}_{\text{E}}\text{X}$ file prepared by the author.


A.4 Navigating in the Dark

During my thesis, I had the opportunity to work with Dr. Marie Gueguen from the Institute of Physics of Rennes. As a philosopher of science, she brings a different perspective to scientific inquiry and is particularly interested in research fields that present many uncertainties, such as astrochemistry.

During the Philosophy of Science 2022 Meeting, I presented a talk titled 'Collisional Excitation of Interstellar Molecules: Methodology and Uncertainties.' From this session, we published a proceeding paper titled 'Navigating in the Dark,' which presents an indirect validation process used to assess the accuracy of a methodology applied to a given system when the data cannot be compared to equivalent experimental data. This approach, which we call the Snap-Hook method, posits that methodologies can be extended from one system to another based on sufficient similarities. While this method was not 'invented' by us, it is often used implicitly, and we believe that a proper formulation could enhance interdisciplinary collaboration, which is essential to astrochemistry.

SYMPOSIA PAPER

Navigating in the Dark

Amélie Godard Palluet and Marie Gueguen 

Institut de physique de Rennes, Université de Rennes, Rennes, France

Corresponding author: Marie Gueguen; Email: mgueguen@uwo.ca

(Received 20 April 2023; revised 28 August 2023; accepted 04 December 2023)

Abstract

This article introduces the snap hook methodology, a method used notably in astrochemistry as a way to indirectly validate and assess the accuracy of computational calculations in the absence of experimental or observational data. We argue that this methodology has tremendous potential for all computationally intensive scientific fields as a substitute for traditional verification and validation standards when those are not accessible and estimating the reliability of numerical predictions becomes a real difficulty. The goal of this article is to give to this method, which seems to be implicitly relied upon in many areas, a proper formulation, in order for philosophers of science to enter the debate and to highlight its undeniable potential in terms of interdisciplinary facilitation and knowledge transmission.

1. Introduction

Astrochemistry studies the formation and destruction of molecules in the interstellar medium (ISM). As a young science, it is characterized by an accelerating influx of new observations, made possible by the development of high-resolution observational facilities: 297 molecules have been detected in the ISM since 1937,¹ 74 during the last two years only. As possible probes of the physical conditions of the environment hosting them, molecules can offer irreplaceable insights from an astrophysical point of view but can do so only if the observed molecular spectra are interpreted on the basis of complex theoretical calculations that require important computational resources and methodological innovations. The latter include approximate methods like statistical approaches, to replace computationally expensive exact quantum calculations. The performance and impact of these approximations are not always well established, given how difficult it is to perform experimental measures reproducing the extreme conditions observed in the ISM.² To complicate the problem even further, the lack of experimental results often overlaps with the impossibility of cross-checking numerical programs to assess their different strengths and

¹ According to the Cologne Database for Molecular Spectroscopy (<https://cdms.astro.uni-koeln.de/classic/>).

² Temperature can go down to a few kelvin, and the density can be even lower than that of the best vacuum chambers.

weaknesses, as in most cases, only one numerical method is available for a given system. This epistemic scenario makes it challenging to validate theoretical results³ and thus to assess the reliability of astrophysical inferences made on their basis. This produces an interesting epistemic situation in which astrochemists produce data “in the dark,” that is, without knowing *if* and *when* experimental measures will be performed or whether numerical methods will be developed that will allow the evaluation of their results’ accuracy—a situation becoming increasingly common in computationally intensive sciences.

In this article, we describe a method, to which we refer as the *snap hook methodology* (SHM), implicitly used by astrochemists to validate their methodologies in the absence of experimental results. It consists of a three-step procedure: after a computational methodology has been traditionally validated and secured for a well-understood system, the latter is used as a “validation proxy”—that is, a snap hook—for partially validating the methodology used for a more complicated target, on the basis of structural similarities considered sufficient to warrant extrapolation. Finally, the target is embedded into a web of partially validated systems that together complete the puzzle and permit full validation. As progress is made, the network is extended to new target and proxy systems that together strengthen and reinforce this notion of validation.

Our intention in this article is not to defend or criticize this method but to initiate a broader discussion among scientists in fields facing sparse or lacking empirical data. This method could be instrumental in computationally heavy sciences facing similar epistemic challenges and should thus be given a general formulation. Here is the trick, however: if not discussed from the point of view of a specific case study, the notion of validation upon which it relies can quickly become an empty shell. Thus we chose to write a technical article, considering a minimal level of technicality necessary to do justice to the method, while at the same time trying to ensure that its general features emerge clearly from the discussion.

In section 2, we introduce astrochemistry and what constitutes a “methodology” herein. We then explore how validating the results for a well-known system can be extended through the SHM to validate the methodology applied to systems without available experimental results. Section 3 delves into the specifics of our case study, focusing on validating collisional rate coefficients for the CO₂-He and CCS-He systems. We conclude by highlighting the philosophical significance of the SHM, including its potential for interdisciplinary facilitation and knowledge transmission. The philosophical literature on verification and validation (V&V) has grown rapidly over the last years but has focused primarily on the challenges posed by the complexity of computational models (Lenhard and Winsberg 2010; Lenhard 2018, 2019; Jebeile and Ardourel 2019). Analyzing what scientists do when studying systems without clear validation domains is an area to which philosophers of science must and can significantly contribute.

³ According to Oberkampf and Trucano (2002), comparisons among different numerical methods do not constitute verification or validation methods. In practice, however, they are often considered as such. We follow the practice for simplicity here.

2. Understanding the collisional excitation of interstellar molecules

2.1. Why do we need collisional data at all?

Astrophysical media, such as molecular clouds, are extremely difficult, if not impossible, to probe: they are too far, too wide, and usually at very extreme conditions of temperature and density. Besides rare exceptions (i.e., a few nearby comets and asteroids that represent a tiny part of the possible astrophysical richness), their chemical composition can be characterized only by analyzing the light spectrum unique to each molecule registered by telescopes.

Molecules offer unprecedented insights into the physical conditions characterizing their environment, making them powerful tools for understanding, for example, star formation or the evolution of molecular clouds. Theoretical calculations play a crucial role in inferring such information from the spectra, but they do so by modeling the population of energy levels, influenced by radiative and collisional processes. Radiative processes, corresponding to the spontaneous emission or absorption of photons, are well understood. But obtaining accurate inelastic rate coefficients for the collisional processes that characterize how a molecule can be (de)excited by a partner is extremely challenging. Only 69 of these rate coefficients have been calculated for detected molecules,⁴ and even those tend to be incomplete because of multiple possible collisional partners (the dominant astrophysical species He, H, H₂, and e⁻) and the temperature range that must be explored.

This is explained by the fact that exact rate quantum calculations are often not reachable in terms of computational memory and time, which can go from hundreds of CPU hours to millions of hours for large systems with big colliders. Thus a tractable methodology with approximations is necessary, but the impact of these approximations needs to be quantified to determine the extent to which astrophysical inferences drawn from these can be trusted.

2.2. Some vocabulary: What do astrochemists call a “methodology”?

Some vocabulary is first necessary: calculations of rate coefficients require numerical *methods*, based on quantum chemistry. Such methods are implemented into numerical *programs* through a *code*, meaning that several programs can implement a unique method through different code. By *methodology*, we refer to the ensemble of steps, requiring multiple numerical programs, that permits calculation of inelastic rate coefficients, as developed in the following pages.

The first step consists in calculating the interaction potential energy between the colliders to obtain a potential energy surface (PES). This involves choosing a computational method, implemented in a quantum chemistry program like molpro.⁵ Among the possible methods available, the coupled-cluster method (hereinafter CCSD[T]) is the gold standard but is expensive and as such only feasible for small systems (up to six to ten atoms). Even for this method, a number of approximations or

⁴ According to the BASECOL (<https://basecol.vamdc.eu>) database. Unfortunately, this database is underused by astronomers, probably because it does not generate files in the format required by modeling software. To fill this gap, the database E_{MAA} (<https://emaa.osug.fr>) was launched in 2021, but it gathers inelastic rate coefficients for only twenty-five molecules today.

⁵ MOLPRO is a package of ab initio programs for electronic structure calculations.

simplifications are needed. An indispensable approximation to make the calculations tractable is the Born–Oppenheimer (BO) approximation, which permits decoupling of the electronic and nucleus motions by assuming a very small electron mass compared to that of the nuclei. Thus it ensures that the Schrödinger equation can be solved separately for each.⁶ Likewise, a basis set, that is, a set of functions used to model the molecular orbitals, must be chosen. A realistic basis would have to include an infinite set of functions, something obviously not doable. Calculations are thus on a finite basis, ranging from double (aVDZ) to sextuple (aV6Z) perturbative excitations. Whenever possible, an empirical relationship between energies calculated for three basis sets (say, double, triple, and quadruple excitations), called the complete basis set (CBS) extrapolation, is used to mimic the interaction energy that would have been obtained with an infinite number of functions. Using the CCSD(T) method with a CBS reconstruction of the basis set represents the best of what can currently be done. Mid-bond functions, consisting of adding physically meaningless empty orbitals halfway between the colliders to mimic a bigger basis set, are another widely used trick to save computational time. Their use permits one to reach the accuracy of a given aVXZ basis set by using a much cheaper aV(X-1)Z set. Additional approximations may be needed, depending on the system's complexity.

The second step consists in deriving a fitting formula from the ab initio points of the PES to extrapolate the energy values at short and long distances. The fit error is estimated by comparing predictions to ab initio energy values, and the root-mean-square (RMS) error, which expresses the cumulative error, indicates the reliability of the PES. Anisotropic PESs can be tricky to fit, as generating nonphysical behavior (e.g., oscillations, holes) where no ab initio points were computed. Various formulas may be attempted and additional ab initio points added, if necessary. An accurate PES is crucial for inelastic rate coefficients, so the RMS error of the fit must be well understood.

Then, the dynamics of the nuclei is studied by solving the nuclear Schrödinger equation within the theory of collisions. The “exact” (full quantum) method to solve them is the close-coupling approach, developed by Arthurs and Dalgarno (1960) for a closed-shell linear molecule in collision with an atom. Modern calculations based on this approach exhibit a typical accuracy of 20–30 percent as compared to experimental measures. This accuracy represents important progress but is only a decent minimum to make the most of recent sensitivity improvements in ground-based and space telescopes. Solving the coupled equations results in S-matrices containing all transition probabilities, for each total energy, from which cross sections are derived. Then, assuming that the velocities are thermally distributed, cross sections are averaged over these velocities, resulting finally in rate coefficients.

Our term *methodology* refers to this whole process, from the construction of a PES from ab initio points to its full reconstruction using an analytic fitting formula to the dynamical calculations that lead finally to rate coefficients. The “gold standard” methodology has been validated against experimental results for various systems. However, as systems become more complex, new approximations and numerical methods are needed that are increasingly difficult to validate, as experimental

⁶ For this approximation to hold, the ground electronic state needs to be well separated in energy from other electronic states.

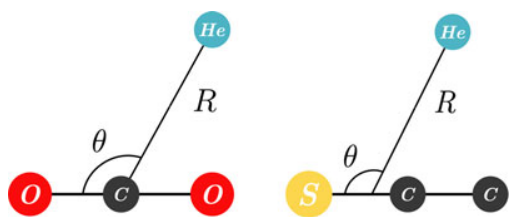


Figure 1. Representations of the (left) CO₂-He and (right) CCS-He collisional systems in (R, θ) coordinates.

measures are less likely to be available. As Oberkampf and Trucano (2002) emphasized, V&V procedures are crucial to comprehensive accuracy assessment, including the identification of numerical errors. Without them, scientists are navigating in the dark, unable to determine the reliability of their numerical results. What can be done, then, to exploit the tools and means that scientists have, while minimizing the impact of those they do not have?

3. Can the CO₂-He system serve as a validation proxy for the CCS-He system?

This section shows how the SHM fills this gap, using CO₂-He and CCS-He as examples of inelastic rate coefficient calculations. We describe our first snap hook, the CO₂-He, and how it serves as a validation proxy for CCS-He before explaining how a growing network of systems can be built that completes the validation puzzle.

3.1. The snap hook CO₂-He system

Constructing the PES for the CO₂-He system required the “rigid rotor” approximation, which neglects the vibration of the molecule and fixes the internuclear distances, thus leaving only two coordinates to consider: R and θ . As CO₂ is symmetric, θ angles between 0° and 90° are equivalent to θ angles between 90° and 180° (see figure 1), allowing for the use of expensive methods on a limited number of points. This resulted in the best accuracy possible for the PES, based on CCSD(T) with a CBS extrapolation.

We fitted the 260 ab initio points for this system thanks to an analytic formula based on Legendre polynomials, with an accuracy better than 1 percent. Rate coefficients were calculated using the molscat program and validated through different methods. First, the RMS error is only 0.0149 cm⁻¹, sufficient for astrochemistry scattering calculations. The PES was also validated by computing spectroscopic data, such as bound-state transition frequencies and pressure-broadening coefficients (PBCs), and comparing them to experimental data. Bound states are located within the potential well of the PES. Transition frequencies between these states are highly sensitive to the shape and depth of the well. The agreement between the seven computed and measured transition frequencies, better than 0.6 percent, validates the accuracy of the PES’s well. PBCs evaluate the accuracy of the PES at short-range distances, where it is repulsive. Their values can be computed based on the same S-matrices used for the cross section calculations and thus permit an indirect validation of the rate coefficients provided for astrophysical applications. As seen in Godard Palluet, Thibault, and Lique (2022, figure 5), PBCs measured experimentally by Deng et al. (2009) and Thibault et al. (2000) are in agreement with our

theoretical values for the three targeted spectroscopic lines and validate the accuracy of the PES and collisional rate coefficients, as well as the methodology used to obtain these results. The latter is the validation that we will extend to other systems.

CO₂ is a very stable molecule, which explains why bound states and PBCs could be acquired experimentally, even at very low temperatures and densities. In addition, its symmetry induces a dimension-limited problem for the PES and the scattering calculations. Such ideal features, unfortunately, no longer apply to the CCS-He system, thus greatly increasing the complexity of the calculations.

3.2. The snap hook and its target: The CCS-He system

CCS is a highly detected molecule in various astrophysical environments and serves as an important tracer of the physical conditions and evolutionary stages of molecular clouds—an ideal target for the SHM. Its abundance, however, has been modeled using inappropriate methods, given the complexity of theoretical calculations and the fact that no experimental measure is possible. Given that CCS-He and CO₂-He share many features, the questions arise, To what extent can the methodology used for CCS-He be validated through CO₂-He, considered as a snap hook for CCS-He? Which parts of the methodology are validated that way, and which other hooks would be needed?

CCS-He (Godard Palluet and Lique 2023) and CO₂-He have many similarities. Both involve collisions with helium, a structureless atom that makes high-level-theory quantum calculations feasible. In both cases, the BO approximation and the rigid rotor approximation apply unambiguously, and the same fit formula can be used given their geometry. Given that this PES methodology has been validated for CO₂-He, in turn, it validates its use for CCS-He, meaning that the accuracy of the results can be quantified and considered understood on the basis of those obtained for the former. Such a statement requires clear differentiation between two kinds of error. Contrary to CO₂-He, CCS-He is not symmetric, with a highly anisotropic PES and a subsequent difficult fit, evidenced by the need for 1,351 points. Likewise, the computational cost was such that a smaller and less accurate aVQZ (“Q” for “quadruple excitations”) basis set was needed, without the CBS extrapolation and with additional mid-bond functions. Such differences are not negligible. However, they do not introduce new *systematic* errors into the calculations but only a well-defined and quantifiable loss of accuracy. Comparing PESs obtained with different basis sets is a traditional verification step whenever doable, used as a tracer to exclude gross anomalies in the PES’s behavior.⁷ The complexity of the fit also entails a loss of accuracy, accounting for a larger RMS error of 3.51130 cm⁻¹. A quantified accuracy loss is not tantamount to using a new approximation or numerical method, the impact on the results of which is not known and which could introduce systematic errors or artificial effects that must be identified, neutralized, or quantified. As long as one is confident that the loss of accuracy is well defined and understood, the methodology used for the CCS-He PES can be considered validated through CO₂-He.

This is not the case for the dynamical part of the methodology, however. Unlike CO₂-He, CCS-He has a fine structure that requires supplementary theoretical

⁷ Oberkamp and Trucano (2002) mention as a verification procedure tracer variables, that is, variables the behavior of which is known and that are thus used to ensure that the system behaves as expected.

development.⁸ The intermediate coupling scheme (ICS), proposed by Alexander and Dagdigian (1983), offers a proper representation of the fine-structure energy levels that neither of the basic versions of molscat and hibridon, the two main numerical programs for exact quantum scattering calculations, include in their molecule–atom collision calculations. A modified and nonpublic version of molscat incorporating ICS has been reported (Lique et al. 2005), but it must be tested and validated. Thus the methodology used for CCS-He is only partially validated through CO₂, as molscat-ics remains a missing piece of the puzzle. To make the need for validating the ICS module even more pressing, CCS-He has an unusual spin splitting of its energy levels, resulting in a messy fine structure. Tracers guaranteeing that known transition rules are respected are thus more difficult to find, making detection of possible code anomalies more difficult.

Thus we had to dive into the literature to find out whether molscat-ics had been previously validated on other systems. We found five potentially relevant examples in the literature but decided to focus on systems with a similar electronic configuration and colliding with He to maintain a safe level of comparability. This left us with three options: SO-He (Lique et al. 2005), NH-He (Toboła et al. 2011), and O₂-He (Bishwakarma et al. 2016). No experimental measures exist to this day for SO-He. Experimental data exist for NH-He (Toboła et al. 2011), but significant differences to theoretical state-to-state individual collisional transitions were found, and the source of the disagreement is difficult to interpret. The BO approximation could not be appropriate for NH-He and an electronic state thus caught by mistake. But the authors also have good reason to challenge the experimental results, inasmuch as these do not satisfy well-established theoretical predictions (or “propensity rules”) used as tracers of rate coefficients for ³Σ systems. However, for O₂-He, a PES based on the CCSD(T) method with an aVTZ basis with additional mid-bond functions was constructed, dynamical calculations were performed on these grounds using molscat-ics, and the results were successfully matched to experimental differential cross sections (DCSs). This makes O₂-He an ideal secondary snap hook for the missing part of the CCS-He methodology:

In summary, the theoretical predictions of Lique for rotationally inelastic collisions between O₂ and helium have been confirmed by measurements of DCSs, which provide the most sensitive test of scattering and PESs. The O₂-He collisional data can now be used with confidence to derive the interstellar O₂ abundance from astronomical observations. (Bishwakarma et al. 2016)

Even better, studying O₂-He made us realize its extraordinary capacity as a snap hook, first because validating MOLSCAT-ICS through O₂-He validates the (dynamical part of the) methodology not only of CCS-He but also of SO-He and NH-He. Moreover, this validation extends to the two systems we had previously excluded, O₂-Ar (Bop et al. 2021) and C₄-He (Bishwakarma et al. 2016). The case of C₄-He makes particularly

⁸ A fine structure corresponds to the splitting of the spectral lines of an atom due to electron spin and relativistic effects.

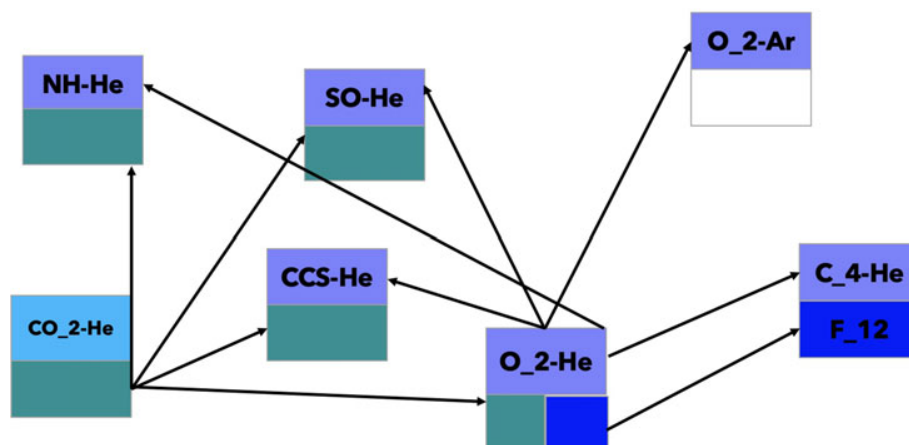


Figure 2. An example of a validation network. The bottom part corresponds to the PES and fit calculations, the top part to scattering calculations. Arrows go from the snap hooks to the validated parts of the target systems.

clear what constitutes a good snap hook. Indeed, the high symmetries of O_2 -He's PES allow the exploration of a wide range of numerical methods and approximations, the varying accuracy of which can be compared and quantified (Lique, Kłos, and Hochlaf 2010). These symmetries and the existence of experimental data of high quality turn O_2 -He into a “test case for generating of $^3\Sigma$ molecular species in collision with rare gas” (Bishwakarma et al. 2016, 15674), thus highlighting its potential in terms of building a network of mutually validating systems (see figure 2).

Consider the case of C_4 -He. Given that the cost of a PES strongly depends on the basis set size, attempts to circumvent this problem have notably explored the introduction of terms into the wave function ansatz that depend explicitly on the interelectronic coordinates—the so-called explicitly correlated CCSD(T)-F12 methods. A PES for C_4 -He cannot be built without F12 methods, hence the idea of building different PESs for O_2 -He, to systematically compare and quantify the accuracies of different basis sets in CCSD(T) and CCSD(T)-F12 methods. As the F12-based PES is in good agreement with the former, and the domain of performance of this approximation has been thoroughly analyzed, this allowed for full validation of the C_4 -He methodology. One can see in figure 2 how the validation of O_2 -He was thus extremely rewarding from a theoretical point of view, regarding the number of systems the methodologies of which were validated and the possible extension of the network to rare gases other than helium (e.g., argon), but also in terms of reinforcing the interconnections within the network. Experimental results for O_2 -Ar and NH-He, for instance, are possible and would greatly reinforce the network connections. Note how the graph permits identifying advantageous future snap hooks and where experimental results would be most beneficial.

4. Philosophical takeaways and concluding remarks

In a nutshell, the SHM allows for indirectly validating a methodology through snap hook systems that progressively build a network of interconnected and mutually validating systems. A snap hook such as CO_2 -He serves as a starting point for

validating a target system such as CCS-He, the full validation of which requires an additional hook, O₂-He, thus knitting a web of systems that together will enable the validation of more and more systems with varying degrees of complexity.

One important feature of the SHM is that it assumes modularity, that is, that individual components of a methodology can be evaluated independently. This assumption has been challenged in contexts like astrophysical or climate science simulations (Lenhard and Winsberg 2010; Lenhard 2018; Jebeile and Ardourel 2019), where couplings between different parts of the model tend to undermine their individual assessments. Here modularity is not jeopardized: parts evaluated separately correspond to autonomous steps of the methodology. The question here is rather that of entrenchment, that is, the sensitivity of a step to the former, in terms of accuracy loss.

Among the important characteristics of the SHM deserving a thorough philosophical analysis, we emphasize the following three, hoping to generate broader discussion:

- Tools like the network graph of figure 2 can potentially encode a great amount of information, including (nonexhaustively) the details of the approximations, of the numerical programs and basis set used, and of the systems for which experimental measures are possible or already done. Recovering this information usually requires a tedious literature search and contacting authors for missing information. Given that choosing the systems on which astrochemists should focus is considered the most pressing challenge for the field, such tools would greatly facilitate the identification of maximally rewarding potential hooks and thus support a systematized strategy for approaching the question of identifying the systems deserving the most attention. Note that such graphs might also help to support a confidence analysis, where the degree of confidence that one can have in rate coefficients could be evaluated based on the network size and its structure. All of these tasks could definitely benefit from a philosophical perspective.
- Finding systems of common interest to experimenters and theoreticians is tricky, due to different research interests, constraints, and associated costs. Within the SHM, a strategic choice of systems validates, not a unique target, but an entire network, making the time and cost that experimenters spend much more rewarding, while at the same time providing tools to facilitate mutual understanding and thus to foster fruitful interdisciplinary collaboration.
- Finally, the notion of validation grounding the SHM might seem controversial or weakened, as based on indirect comparison with experimental results. Yet, such a notion of validation accounts for the knowledge and acquaintance with numerical tools that theoreticians develop in practice through their careers and that often remain nontransmissible. It is not rare, to say the least, to see a senior scholar predict the performance of a given method applied to a new system without necessarily being able to determine where this intuition comes from and to account for it. We argue that this “intuitive” knowledge is grounded in implicit SHM reasoning, developed through the scholar’s career but not given a

concrete formulation. Making it explicit, for example, through network graphs, would constitute a remarkable opportunity to store, transmit, and exploit this knowledge to its fullest.

Acknowledgments. This project received funding from the European Research Council(ERC) under the European Union Horizon 2020 research and innovation program (Grant Agreement No. 811363) and from the European Union Horizon 2020 research and innovation program under the Marie Slodowska-Curie grant agreement No.101026214. The authors would like to thank François Lique for his time and feedback, the members of the COLLEXISM team and of the Molecular Physics Department of the Institute of Physics of Rennes.

References

- Alexander, Millard H., and Paul J. Dagdigian. 1983. "Propensity Rules in Rotationally Inelastic Collisions of Diatomic Molecules in $^3\Sigma$ Electronic States." *Journal of Chemical Physics* 79 (1):302–10. <https://doi.org/10.1063/1.445578>.
- Arthurs, A. M., and A. Dalgarno. 1960. "The Theory of Scattering by a Rigid Rotator." *Proceedings of the Royal Society of London, Series A* 256 (1287):540–51. <https://doi.org/10.1098/rspa.1960.0125>.
- Bishwakarma, Chandan Kumar, George van Oevelen, Roy Scheidsbach, David H. Parker, Yulia Nikolaevna Kalugina, and François Lique. 2016. "State-to-State Inelastic Scattering of O₂ with Helium." *Journal of Physical Chemistry A* 120 (6):868–74. <https://doi.org/10.1021/acs.jpca.6b00817>.
- Bop, Cheikh T., Ernesto Quintas-Sánchez, Sangeeta Sur, Mathurin Robin, François Lique, and Richard Dawes. 2021. "Inelastic Scattering in Isotopologues of O₂-Ar: The Effects of Mass, Symmetry, and Density of States." *Physical Chemistry Chemical Physics* 23 (10):5945–55. <https://doi.org/10.1039/D1CP00326G>.
- Deng, Wenping, Didier Mondelain, Franck Thibault, Claude Camy-Peyret, and Arlan W. Mantz. 2009. "Experimental He-Pressure Broadening for the R(10) and P(2) Lines in the ν_3 Band of $^{13}\text{CO}_2$, and Experimental Pressure Shifts for R(10) Measured at Several Temperatures between 300K and 100K." *Journal of Molecular Spectroscopy* 256 (1):102–8. <https://doi.org/10.1016/j.jms.2009.02.021>.
- Godard Palluet, Amélie, and François Lique. 2023. "Fine-Structure Excitation of CCS by He: Potential Energy Surface and Scattering Calculations." *Journal of Chemical Physics* 158 (4):044303. <https://doi.org/10.1063/5.0138470>.
- Godard Palluet, Amélie, Franck Thibault, and François Lique. 2022. "Rotational Excitation of CO₂ Induced by He: New Potential Energy Surface and Scattering Calculations." *Journal of Chemical Physics* 156 (10):104303. <https://doi.org/10.1063/5.0085094>.
- Jebeile, Julie, and Vincent Ardourel. 2019. "Verification and Validation of Simulations against Holism." *Minds and Machines* 29 (1):149–68. <https://doi.org/10.1007/s11023-019-09493-8>.
- Lenhard, Johannes. 2018. "Holism, or the Erosion of Modularity: A Methodological Challenge for Validation." *Philosophy of Science* 85 (5):832–44. <https://doi.org/10.1086/699675>.
- Lenhard, Johannes. 2019. "How Does Holism Challenge the Validation of Computer Simulation?" In *Computer Simulation Validation: Fundamental Concepts, Methodological Frameworks, and Philosophical Perspectives*, edited by Claus Beisbart and Nicole J. Saam, 943–60. Berlin: Springer. https://doi.org/10.1007/978-3-319-70766-2_39.
- Lenhard, Johannes, and Eric Winsberg. 2010. "Holism, Entrenchment, and the Future of Climate Model Pluralism." *Studies in History and Philosophy of Science, Part B* 41 (3):253–62. <https://doi.org/10.1016/j.shpsb.2010.07.001>.
- Lique, François, J. Klos, and M. Hochlaf. 2010. "Benchmarks for the Generation of Interaction Potentials for Scattering Calculations: Applications to Rotationally Inelastic Collisions of C₄($\chi^3\Sigma_g^-$) with He." *Physical Chemistry Chemical Physics* 12 (48):15672–80. <https://doi.org/10.1039/C004945J>.
- Lique, F., A. Spielfiedel, M.-L. Dubernet, and N. Feautrier. 2005. "Rotational Excitation of Sulfur Monoxide by Collisions with Helium at Low Temperature." *Journal of Chemical Physics* 123 (13):134316. <https://doi.org/10.1063/1.2004994>.
- Oberkampf, William L., and Timothy G. Trucano. 2002. "Verification and Validation in Computational Fluid Dynamics." *Progress in Aerospace Sciences* 38 (3):209–72.

- Thibault, F., B. Calil, J. Boissoles, and J. M. Launay. 2000. "Experimental and Theoretical CO₂-He Pressure Broadening Cross Sections." *Physical Chemistry Chemical Physics* 2 (23):5404–10. <https://doi.org/10.1039/b006224n>.
- Toboła, Robert, Fabien Dumouchel, Jacek Kłos, and François Lique. 2011. "Calculations of Fine-Structure Resolved Collisional Rate Coefficients for the NH₃(Σ^-)-He System." *Journal of Chemical Physics* 134 (2):024305. <https://doi.org/10.1063/1.3524311>.

Cite this article: Godard Palluet, Amélie and Marie Gueguen. 2024. "Navigating in the Dark." *Philosophy of Science*. <https://doi.org/10.1017/psa.2023.175>

A.5 BASECOL2023 Scientific Content

Great efforts from the Laboratory Astrophysics community are dedicated to producing inelastic rate coefficients. To maximize the impact of these data, they should be collected and made available in databases.

The BASECOL database plays an important role in this regard. The data produced in my thesis ($\text{CO}_2\text{-He}$, CCS-He , and their isotopologues) are currently available in this database, while data for CS-CO and $\text{CS-H}_2\text{O}$ will be added soon. A peer-reviewed paper has been published to present the recent updates to the database, along with recommendations for usage and challenges to be addressed in the coming decades. In this work, I contributed by preparing and submitting datasets ready for use by astronomers, which were produced in this thesis, to the Scientific Leaders of the project.

BASECOL2023 scientific content

M. L. Dubernet¹, C. Boursier¹, O. Denis-Alpizar³, Y. A. Ba¹, N. Moreau¹, C. M. Zwölf¹, M. A. Amor⁴, D. Babikov⁵, N. Balakrishnan⁶, C. Balança¹, M. Ben Khalifa⁷, A. Bergeat², C. T. Bop⁸, L. Cabrera-González⁹, C. Cárdenas^{10,11}, A. Chefai⁴, P. J. Dagdigan¹², F. Dayou¹, S. Demes⁸, B. Desrousseaux⁸, F. Dumouchel¹³, A. Faure¹⁴, R. C. Forrey¹⁵, J. Franz¹⁶, R. M. García-Vázquez^{2,26}, F. Gianturco¹⁷, A. Godard Palluet⁸, L. González-Sánchez¹⁹, G. C. Groenenboom²⁰, P. Halvick², K. Hammami⁴, F. Khadri⁴, Y. Kalugina⁸, I. Kleiner²¹, J. Kłos^{22,23}, F. Lique⁸, J. Loreau⁷, B. Mandal⁵, B. Mant¹⁷, S. Marinakis¹⁸, D. Ndaw²⁴, P. Pirlot Jankowiak⁸, T. Price¹⁵, E. Quintas-Sánchez²⁷, R. Ramachandran^{13,28}, E. Sahnoun⁴, C. Santander³, P. C. Stancil²⁵, T. Stoecklin², J. Tennyson²⁹, F. Tonolo^{30,31}, R. Urzúa-Leiva³, B. Yang²⁵, E. Yurtsever³², and M. Żóltowski^{8,13}

(Affiliations can be found after the references)

Received 11 October 2023 / Accepted 5 November 2023

ABSTRACT

Context. The global context of making numerous data produced by researchers available requires collecting and organising the data, assigning meaningful metadata, and presenting the data in a meaningful and homogeneous way. The BASECOL database, which collects inelastic rate coefficients for application to the interstellar medium and to circumstellar and cometary atmospheres, meets those requirements.

Aims. We aim to present the scientific content of the BASECOL2023 edition.

Methods. While the previous versions relied on finding rate coefficients in the literature, the current version is populated with published results sent by the producers of data. The paper presents the database, the type of data that can be found, the type of metadata that are used, and the Virtual Atomic and Molecular Data Centre (VAMDC) standards that are used for the metadata. Finally, we present the different datasets species by species.

Results. As the BASECOL database, interconnected with the VAMDC e-infrastructure, uses the VAMDC standards, the collisional data can be extracted with tools using VAMDC standards and can be associated with spectroscopic data extracted from other VAMDC connected databases such as the Cologne database for molecular spectroscopy (CDMS), the jet propulsion laboratory molecular spectroscopy database (JPL), and the high-resolution transmission molecular absorption database (HITRAN).

Key words. standards – astrochemistry – molecular data – molecular processes – astronomical databases: miscellaneous

1. Introduction

The paper presents the scientific content of the BASECOL2023 edition¹. BASECOL provides state-to-state inelastic atomic and molecular collisional rate coefficients with energy transfer in both the target and the projectile, in a temperature range suitable for radiative transfer modelling in the interstellar medium (ISM) or circumstellar atmospheres and cometary atmospheres, where local thermodynamic equilibrium (LTE) conditions are not fulfilled. In addition, the BASECOL format provides effective and thermalised rate coefficients, as stated below (Sect. 2.4). BASECOL provides a wide overview of the field of rate coefficient calculations for the above applications, and it follows the VAMDC standards (Albert et al. 2020; Dubernet et al. 2016). BASECOL is therefore accessible from VAMDC applications such as the VAMDC portal², the species database service³, and other user tools that use VAMDC standards. One of the tools is the SPECTCOL tool⁴, the latest edition of which will be published in 2024.

¹ <https://basecol.vamdc.org>

² <https://portal.vamdc.eu>

³ <https://species.vamdc.eu>

⁴ <https://vamdc.org/activities/research/software/spectcol/>

Other databases, such as the Leiden atomic and molecular database (LAMDA; van der Tak et al. 2020)⁵ and the excitation of molecules and atoms for astrophysics database (EMAA)⁶, provide ready-to-use ASCII data files that combine selected rate coefficients and spectroscopic datasets. EMAA in particular allows the user to select the projectile(s) of interest, and a digital object identifier (DOI) is provided as a persistent identifier for each dataset.

Contents of the BASECOL2012 edition (Dubernet et al. 2013) were created by the scientific maintainer using rate coefficients mostly extracted from the literature. It was recently underlined by Dubernet et al. (2023) that this method is no longer sustainable. Therefore, the producers of rate coefficients are now invited to send their data formatted in a requested template. The current scientific content of the BASECOL database, called BASECOL2023, corresponds to the efforts of the various co-authors in providing their data with that template; in doing so, they contribute to the long-term preservation of the data and to the data indexation with relevant and community standard metadata for atomic and molecular data, that is VAMDC

⁵ <https://home.strw.leidenuniv.nl/~moldata/>

⁶ <https://emaa.osug.fr>

standards (Albert et al. 2020; Dubernet et al. 2016, 2010)⁷. From surveys of the literature, we know that there are still missing rate coefficient datasets, and producers are welcome to contact the next BASECOL scientific leader, Dr Otoniel Denis-Alpizar, in order to include their data.

We would like to emphasise that BASECOL2023 provides an environment where the numerical data are not manipulated prior to their ingestion in the database, and if inconsistencies are noticed, the producers of the data are invited to provide new numerical data. In addition, prior to public access, the producers of the data privately visualise the display of their numerical and text data, and can ask that the BASECOL maintainer changes the text data. Finally, the references to the main papers for both the rate coefficients and the potential energy surfaces are provided, and the BASECOL home page emphasises that users must cite the original papers. The BASECOL technical design has been entirely updated: in particular, a versioning feature that allows accessibility to all versions has been added, and the dataset ingestion procedure has been reviewed in order to directly include the VAMDC metadata and to check the consistency of the datasets. A full description of the new BASECOL technical infrastructure is provided in Ba et al. (2020). From a scientific point of view, BASECOL2023 has been intensively updated in the past three years, and this paper provides the current status. BASECOL2023 contains a total of 491 collisional datasets of which 358 datasets correspond to the last version of the recommended datasets. It includes information on the collisional inelastic de-excitation of 103 atomic and molecular, neutral, and ionic species colliding mainly with projectiles such as H, He, H₂, and H₂O.

2. Description of the datasets found in BASECOL

2.1. Composition and display of datasets

The BASECOL data are organised and displayed in a collisional dataset. A dataset corresponds to a collision between two colliding species: the target and the projectile species. As the product species are formally the same as the colliding species (target and the projectile), BASECOL can handle elastic, inelastic, and possibly rearrangement processes if the product species are the same as the colliding species.

The species can either be neutral or charged and atomic or molecular in nature. It is described by its usual chemical formula and is internally uniquely identified by its InChIkey and InChI number⁸, possibly supplemented by the nuclear spin symmetry (ortho, para, meta, etc.). The species database website⁹ makes it possible to find the VAMDC species including the InChIkey and InChI number expressions.

Once the colliding species are identified, a dataset corresponds to three numerical tables: one table containing the process rate coefficients of the state-to-state energy level transitions of the two colliding species (in cm³ s⁻¹) as a function of temperature (in kelvin), and one table per species containing the energy levels whose labels characterise the transitions in the rate coefficient table (see Sect. 2.4 for the specific issues of labelling the energy levels transitions for effective and thermalised rate coefficients).

⁷ <https://vamdc.org/activities/research/documents/standards/>

⁸ <https://iupac.org/who-we-are/divisions/division-details/inchi/>

⁹ <https://species.vamdc.eu>

The unique dataset is associated with its ‘main’ publication, that is, the one in which it was published¹⁰, and it is complemented by a short description of the methodologies used in the potential energy surface (PES) and the dynamical calculations wherever relevant. The PES’s references are systematically cited, as well as references linked to the energy levels (for the latter it depends on the availability of the information provided by the data producer). Additional references – such as references linked to methodologies or to a historical review of the collisional system – that might be associated with the dataset are also cited. Additional information about precision or review of data is sometimes included. In particular, datasets are labelled as ‘outdated’ whenever this is the case, or are labelled ‘not recommended’ when the datasets have errors either mentioned in a published erratum or mentioned privately by the authors.

As part of the newly designed BASECOL structure (Ba et al. 2020), the versioning of the dataset has been introduced. A new version is created when the rate coefficient table and/or the associated energy table are changed, and BASECOL provides access to the previous versions of the datasets in order to guarantee traceability of data and reproducibility of usage. We comment on the modifications between versions.

2.2. Discussion on BASECOL recommendation

The BASECOL interfaces, which display the list of available datasets corresponding to a query, indicate the status, ‘Recommended: yes or no’. ‘Recommended: no’ corresponds both to outdated datasets and to datasets with errors (see previous paragraph). It should be noted that VAMDC accesses the last version of the recommended datasets only to avoid confusing users. The current choice of BASECOL2023 is to provide access to ‘recommended sets’ only, but this paradigm could be changed upon a user’s request.

A priori, all datasets are recommended when they are first included in the BASECOL database. The outdated datasets are ‘non-recommended’ for the following reasons: 1) new calculations are performed with a clearly more sophisticated potential energy surface, 2) new calculations are performed with more sophisticated scattering methodologies (e.g. the basis set is larger, the scattering method has less approximation). Nevertheless, some datasets are still recommended even if they do not fit the above criteria, as they offer alternative realistic datasets that can be used to test the influence of rate coefficients in radiative transfer studies.

The detailed description of the datasets given in the following paragraphs explains the choices.

2.3. BASECOL2023 molecular quantum number description

The description of BASECOL2023 quantum numbers follows the VAMDC standards¹¹. Within VAMDC standards the molecules are classified by fourteen so-called cases¹². Each case corresponds to a specific type of molecule: diatomic, linear triatomic, non-linear triatomic, linear polyatomic, symmetric top, spherical, and asymmetric molecules, combined with its electronic state separated into closed-shell and open-shell states. Diatomic open-shell molecules can be described in two possible

¹⁰ The main publication is marked in red on the BASECOL website.

¹¹ <https://standards.vamdc.eu/#data-model>

¹² <https://amdis.iaea.org/cbc/>

cases: *hunda* (Hund's a coupling) and *hundb* (Hund's b coupling). Table A.1 indicates the BASECOL2023 molecules and their cases.

Currently, three molecules have issues with the VAMDC cases because the energy tables provided by the authors cannot be described with the current VAMDC cases. The *hundb* case has been assigned to the C₄ (X³Σ_g⁻) energy table (ID = 127) because the SpinComponentLabel label does not exist in the linear polyatomic open shell (lpos) case. The *hunda* has been assigned to the C₆H (X²Π) energy tables (ID = 154, 155) because the authors used (J,Ω) quantum numbers and the lpos case does not include Ω. This is a temporary solution while the VAMDC standards evolve. The CH₃OH molecule is described with a spherical top closed shell (stcs) case, in which the label ro vibSym is used for the symmetry of the torsional function (see Sect. 9.9 for more information).

2.4. Rate coefficients

The collisional rate coefficients provided by BASECOL are state-to-state rate coefficients, effective rate coefficients, and thermalised rate coefficients, each of which is defined below. In most cases, state-to-state (de-)excitation rate coefficients ($R(T)$) are obtained at a given temperature from Boltzmann thermal averages of the calculated state-to-state inelastic cross-sections obtained on a grid of kinetic energies E :

$$R(\alpha \rightarrow \alpha'; \beta \rightarrow \beta')(T) = \left(\frac{8}{\pi\mu}\right)^{1/2} \frac{1}{(k_B T)^{3/2}} \int_0^\infty \sigma_{\alpha \rightarrow \alpha'; \beta \rightarrow \beta'}(E) E e^{-E/k_B T} dE, \quad (1)$$

where k_B is the Boltzmann constant, μ is the reduced mass of the colliding system, and (α, β) , (α', β') represent the initial and final levels of the target (α) and projectile (β). Therefore, a typical BASECOL rate coefficient table is composed of the following items: Cols. 1 and 2 contain the initial α and final α' levels of the target, Cols. 3 and 4 contain the initial β and final β' levels of the projectile, the subsequent columns give the state-to-state rate coefficients (Eq. (1)) at different temperatures (in kelvin).

These state-to-state collisional rate coefficients follow the principle of detailed balance, and reverse rate coefficients $R(\alpha' \rightarrow \alpha; \beta' \rightarrow \beta)(T)$ can be obtained from forward rate coefficients by the usual formula:

$$g_{\alpha'} g_{\beta'} e^{-\frac{E_{\text{int}}(\alpha')}{k_B T}} e^{-\frac{E_{\text{int}}(\beta')}{k_B T}} R(\alpha' \rightarrow \alpha; \beta' \rightarrow \beta) = g_\alpha g_\beta e^{-\frac{E_{\text{int}}(\alpha)}{k_B T}} e^{-\frac{E_{\text{int}}(\beta)}{k_B T}} R(\alpha \rightarrow \alpha'; \beta \rightarrow \beta'), \quad (2)$$

where g_α and g_β are the statistical weights related to the ro-vibrational levels of the target and projectile, respectively, and the different E_{int} are the ro-vibrational energies of the species. When the projectile is an electron or an atom whose internal energy does not change during the collision, the state-to-state (de-)excitation rate coefficient is Eq. (1) with $\beta = \beta' = 1$.

When the projectile is a molecule, such as H₂ or H₂O, transitions are possible in the projectile molecule. Nevertheless, most published calculations with H₂ do not allow excitation of H₂, thereby fixing H₂ in its lowest para (-p) ($j = 0$) and ortho (-o) ($j = 1$) states. Within this approximation, the state-to-state (de-)excitation rate coefficient is Eq. (1) with $\beta = \beta' = 1$, similarly to atoms.

BASECOL allows the inclusion of the so-called effective rate coefficients $\hat{R}_\beta(\alpha \rightarrow \alpha')$ that are given by the sum of the state-to-state rate coefficients (Eq. (1)) over final projectile states, β' for

a given initial β :

$$\hat{R}_\beta(\alpha \rightarrow \alpha')(T) = \sum_{\beta'} R(\alpha \rightarrow \alpha'; \beta \rightarrow \beta')(T). \quad (3)$$

In BASECOL the effective rate coefficients are identified as 'effective' in the title of the dataset, and the table's entry for the projectile initial level indicates the β level of Eq. (3), while the projectile's final level is meaningless and is currently set equal to the initial level for convenience. It should be mentioned that these effective rate coefficients do not follow the principle of detailed balance, so both excitation and de-excitation rate coefficients should be calculated explicitly.

Finally, thermalised de-excitation rate coefficients can be obtained by averaging over the initial ro-vibrational levels of the projectile:

$$\bar{R}(\alpha \rightarrow \alpha')(T) = \sum_{\beta} \rho(\beta) \hat{R}_\beta(\alpha \rightarrow \alpha')(T), \quad (4)$$

with $\rho(\beta) = g_\beta e^{-\frac{E_{\text{int}}(\beta)}{k_B T}} / Z(T)$, where $Z(T)$ is the partition function obtained as a sum over the β states. Such rate coefficients follow the principle of detailed balance automatically if an accurate quantum scattering methodology – such as the close-coupling (CC) or coupled states (CS) method – is employed. If the approximate scattering methodology is employed (such as classical, semi-classical, or mixed quantum/classical), the values of computed rate coefficients for excitation and quenching may need to be 'symmetrised' first to ensure that they satisfy the principle of detailed balance. The examples of such a symmetrisation procedure can be found in Boursier et al. (2020) and Mandal & Babikov (2023a).

For projectiles with ortho and para species such as H₂ or H₂O, the datasets can be calculated considering the two nuclear symmetries as independent. For example, the quasi-classical calculations (QCT) calculations by Faure et al. (2007b) directly calculate the rotational de-excitation rate coefficients of H₂O by thermalised ortho and para H₂ considered as separate species (labelled o/p-t-H₂ in the tables of the Appendix). Another example is the quantum de-excitation of HCN by a thermalised para-H₂O dataset (Dubernet & Quintas-Sánchez 2019; labelled p-t-H₂O in the tables of the Appendix).

In some cases, the calculations are provided for a thermalisation over both the para- and ortho-projectile species. An example is the ro-vibrational de-excitation (Faure & Josselin 2008) of o/p-H₂O with thermalised H₂ over the two nuclear species (labelled t-H₂ in the tables of the Appendix) and the calculations for the de-excitation of o/p-H₂O by H₂O (Boursier et al. 2020; Mandal & Babikov 2023a) thermalised over both para- and ortho-H₂O projectiles (labelled t-H₂O in the tables of the Appendix). The user is referred to the papers to see how the thermalisation was performed.

In BASECOL, the thermalised rate coefficients are identified as thermalised in the title of the dataset, and the entries for the projectile's initial and final levels are meaningless. They are always denoted as the $\beta = \beta' = 1$ level for convenience.

2.5. Fitting information of the datasets

BASECOL2012 had fitting features that made it possible to download and to visualise fitting functions for rate coefficient datasets; those fits were either provided in the authors publications (mainly for electron impact collisions), or were mostly calculated by one of the former BASECOL maintainers (F. Daniel)

for collisions with the heavy projectiles. The list of fitted datasets is indicated in Table A.1 of our previous publication (Dubernet et al. 2013).

No additional set has been fitted since 2013 as the astrophysical users prefer to use their own fitting functions, but BASECOL2023 has been upgraded with a new graphical display of fits that allows us to visualise the quality of the fits.

The electron impact rate coefficients for D₂O, H₂O, and HDO datasets (Faure et al. 2004); HCN, HNC, DCN, and DNC datasets (Faure et al. 2007b); SiO (Varambhia et al. 2009); the HC₃N–p-H₂ dataset (Wernli et al. 2007a,b); and the o-H₂CO–o/p-H₂ datasets (Troscompt et al. 2009) use the following fitting equation introduced by Balakrishnan et al. (1999a):

$$\log(R(T)) = \sum_{k=0}^4 a_k \left[\frac{1}{T^{(1/6)}} \right]^k, \quad (5)$$

where $R(T)$ is the rate coefficient in cm³ s⁻¹, T the temperature in kelvin, and a_k the fitted coefficients.

The electron impact rate coefficients for the CO⁺, HCO⁺, NO⁺, o/p-H₂⁺ (Faure & Tennyson 2001), o/p-H₃⁺, and o/p-H₃O⁺ datasets (Faure & Tennyson 2003) used the following fitting function with $T_0 = 300$ K:

$$\log(R(T)) = a \left[\frac{T}{T_0} \right]^b \exp(-c/T), \quad (6)$$

where $R(T)$ is the rate coefficient in cm³ s⁻¹, T the temperature in kelvin, and a , b , c the fitted coefficients. The electron-H₂⁺ rate coefficients dataset of Sarpal & Tennyson (1993) is fitted with the latter formula where $T_0 = 1$ K (in BASECOL we used $\exp(c/T)$, so the coefficient c is negative for that particular dataset). The dataset (Lim et al. 1999) for the collision of CH⁺ with electrons is fitted with

$$\log(R(T)) = a [T]^{[b+c \ln(T)]}, \quad (7)$$

where $R(T)$ is the rate coefficient in cm³ s⁻¹, T is the temperature in kelvin, and a , b , c are the fitted coefficients.

Apart from the above cited datasets, BASECOL2012 datasets for collisions with heavy projectiles have been internally fitted with the so-called common fit equation⁷ (please note that there was a typo in the formula for this equation in Ba et al. (2020), which is corrected below):

$$\log(R(T)) = \sum_{k=1}^{N-1} a_k \left[\log \left(\frac{T}{\epsilon T_0} \right) \right]^{k-1} + a_N \left(\frac{1}{\frac{T}{\epsilon T_0} + \epsilon} - 1 \right), \quad (8)$$

where $R(T)$ is the rate coefficient in cm³ s⁻¹, T is the temperature in kelvin, and ϵ , a_k are the fitted coefficients (in addition $T_0 = 1$ K is formally introduced for homogeneity purposes).

2.6. Search for the datasets

The search feature has evolved since the description of Ba et al. (2020). The ‘collision’ search of Ba et al. (2020) has been renamed ‘browse collision’, and a ‘search collision’ has been added. The latter search requires clicking on the fields in order to perform the selection, as can be seen in Fig. 1. This search collisions interface is extremely useful for rapidly querying the content of the database as one can access all datasets for a single or several target species, or for a single or several projectile species. One can find all datasets related to a given collisional

Fig. 1. Query interface for collisional rate coefficients for HCN-He with hyperfine selection. This interface is accessible from the ‘search collisions’ item in the black band.

process (rotation, vibration, ro-vibration, fine, and hyperfine). One can select a given range of years, the name of an author, or part of the name of an author. The implicit rule of selection between the year, target, target symmetry, collider (i.e. projectile), and collider symmetry (i.e. projectile symmetry) fields is an ‘and’ rule, and the explicit rule for a given field is an ‘or’ rule.

3. Bibliographic database

The 2023 bibliographic database can be independently searched in the search articles section (see Fig. 1). The bibliographic database includes the references attached to the collisional datasets only. The references are classified in five categories: category 1 corresponds to the main publication where the data are published, category 2 corresponds to the references of the potential energy surfaces used to calculate the rate coefficients, category 3 corresponds to references linked to the spectroscopy of the molecules (energy tables), category 4 is used whenever a methodology or a code is mentioned, and category 5 corresponds to the context. This category index selects which references are sent to VAMDC. Currently, we transfer all references up to and including category 3.

Each reference is indexed with keywords that allow us to narrow the search of references in the database, for example with respect to the target or projectile species, the type of data that can be found (cross-sections, rate coefficients, potential energy surfaces), the type of transitions (rotation, fine, hyperfine, etc.), or even the programs used (this can be found via the key term miscellaneous: program). The outputs of the bibliographic database are in BibTeX and in BASECOL internal format.

4. BASECOL policies

When the data producer submits the paper related to the datasets to a journal, he/she should contact the BASECOL scientific leader whose credentials are in the contact section of the

BASECOL website. In return, the data producer receives the instructions and a directory containing examples of the files to be sent. We prefer not to provide the information online as items might change over time, and we stress the importance of following the instructions in order to speed up the procedure. Once the publication is accepted by a journal, the data producer sends the package of information that includes numerical data and text data. The numerical data are composed of the rate coefficients table and the energy table that allows to identify the transitions in the rate coefficients table. To this effect, the producer is invited to follow VAMDC standards for the quantum numbers' designation. The text data are composed of a description of the main features of the methodology used in the calculations and a file containing the references cited in the methodology. The producer includes the relevant publications linked to the dataset in the package. The text data, references, energy table values, and additional metadata are included in the original producers' file, which contains the numerical values of the rate coefficients, and a so-called ingestion file is created. The BASECOL manager uploads this ingestion file to the database through a script that parses the file. The parsing procedure checks the consistency of the numerical data. Many items related to the structure of the ingestion file and to the ingestion procedure are already described in the BASECOL technical paper by Ba et al. (2020). During the process of creating the entries for BASECOL, the scientific maintainer interacts with the producer in order to verify any issues that might be raised in the various data. At the end, the producer verifies the data on a password-protected private website and gives his/her agreement for publication on the public website. From 2021 the BASECOL business model relies on the data producers sending data to the maintainer and following the above described policies. The data producer is informed and agrees that his/her mail credentials are kept so that the person who prepared the initial numerical data can be contacted.

5. Collisions with electrons

Table B.1 provides the collisional systems with electrons as projectiles; no new dataset has been added since BASECOL2012, indeed no authors sent their data in the requested format. BASECOL2023 datasets have been upgraded with VAMDC standards for the description of quantum numbers, and the energy levels unit has been changed to wavenumbers whenever it was necessary. The electron impact rate coefficients are labelled 'recommended' in BASECOL, even if newer datasets can be found in the literature. For more recent information on electron impact collision for astrophysical applications, a review can be found in Tennyson & Faure (2019). In addition, several academic and open science databases, mainly aimed at plasma application, contain rate coefficients for the collisional excitation of atoms and molecules by electrons (see VAMDC; Albert et al. 2020; and the LAMDA; van der Tak et al. 2020¹³; and EMAA¹⁴ databases for astrophysical applications).

6. Atoms and atomic ions with heavy partners (H, He, o/p-H₂)

Table B.2 provides the list of datasets for the excitation of the fine structure of C and C⁺ (sometimes referred to as C I and C II, respectively), of O (OI), of S (S I), and of Si and Si⁺ (Si I and Si II, respectively). We say that an atomic species has

a complete collisional panel when datasets are available for the four projectiles: H, He, o/p-H₂.

The carbon atom C has a complete collisional panel. BASECOL2023 has been updated with a dataset (Bergeat et al. 2018) for the de-excitation of C(³P_{*j*}) by He for temperatures up to 350 K. We consider that this dataset supersedes the dataset by Staemmler & Flower (1991) as the theoretical cross-sections reproduce most of the resonances found in the experimental results well; thus, we assume that the theoretical potential energy surfaces (PES) are accurate enough to provide reliable cross-sections and rate coefficients. BASECOL2012 already included the dataset from Abrahamsson et al. (2007) for C(³P_{*j*}) in collision with H that superseded the non-recommended dataset of Launay & Roueff (1977) and a dataset (Schröder et al. 1991) for C(³P_{*j*}) impacted by o/p-H₂ for temperatures up to 1000 K/1200 K.

The carbon C⁺(²P_{1/2}) ion has an incomplete collisional panel. The dataset C⁺(²P_{1/2})-H comes from Barinovs et al. (2005) for temperatures up to $T = 2000$ K. BASECOL2023 has been updated with two datasets (Kłos et al. 2020a) for the quenching of the spin-orbit transition of C⁺(²P_{1/2}) by o/p-H₂ for temperature up to 500 K; those datasets have been calculated with a newly calculated PES (Kłos et al. 2020a) and with CC calculations using a basis set that includes rotational levels of ortho-H₂ up to $j=15$ or of para-H₂ up to $j = 16$. The dataset with ortho-H₂ corresponds to state-to-state rate coefficients restrained to o-H₂ remaining in its lowest rotational level ($j = 1$), while the dataset for para-H₂ corresponds to thermalised rate coefficients (see Eq. (4)) calculated with state-to-state rate coefficients involving transitions between para-H₂ rotational levels.

The oxygen atom O(³P_{*j*}) has a complete collisional panel. The quenching of the spin-orbit transition of O(³P_{*j*}) by H has been revisited by two groups (Lique et al. 2017; Vieira & Krems 2017), and new calculations for the de-excitation of O(³P_{*j*}) by o/p-H₂ (Lique et al. 2017) and by He (Lique et al. 2017) have been performed. BASECOL2023 has been updated with these five recommended datasets. Therefore, the old datasets for O-H (Abrahamsson et al. 2007; Launay & Roueff 1977) and O-o/p-H₂ (Jaquet et al. 1992) are now obsolete and labelled as non-recommended.

For the quenching of the oxygen atom O(³P_{*j*}) by H, the competing datasets (Lique et al. 2017; Vieira & Krems 2017) calculated the same year, use different potential energy surfaces, but identical spin-coupling terms (Parlant & Yarkony 1999): the calculation of Lique et al. (2017) uses the recent PES from Dagdigian et al. (2016), and the calculations of Vieira & Krems (2017) use the PES from Parlant & Yarkony (1999). Vieira & Krems (2017) mentioned that they corrected some errors made by Abrahamsson et al. (2007), and with the help of machine learning techniques they provide error bars on the rate coefficients.

For the S(³P), Si(³P) atoms and the Si⁺(²P_{1/2}) ion, the collisional panel is incomplete since only one projectile is available: either H or He. The dataset (Barinovs et al. 2005) for the quenching of the spin-orbit transition of Si⁺ by H for temperatures up to 2000 K was already in BASECOL2012. BASECOL2023 has been updated with two recent datasets (Lique et al. 2018) for the de-excitation of S(³P) by He and of Si(³P) by He for temperatures up to 1000 K.

7. Diatomic molecules with heavy partners

The diatomic species Table B.3 includes neutral molecules, cations and anions in collision with He, H and H₂ for

¹³ <https://home.strw.leidenuniv.nl/~moldata/>

¹⁴ <https://emaa.osug.fr>

astrophysical applications, as well as some collisional datasets concerning excitation by Ar and Ne.

7.1. Anions and cations

BASECOL2012 had three ionised species only. It included the rotational de-excitation of CH^+ by He with two recommended datasets: one dataset (Turpin et al. 2010) for transitions among six rotational levels ($T = 1\text{--}200$ K) and another dataset (Hammami et al. 2009) for transitions among 11 levels ($T = 20\text{--}2000$ K). The latter dataset already superseded an older dataset (Hammami et al. 2008a) marked as non-recommended. BASECOL2012 also included the rotational de-excitation among eleven rotational levels of CN^- by o/p- H_2 (Kłos & Lique 2011) and among eleven levels of SiH^+ by He (Nkem et al. 2009). BASECOL2023 has been updated with nine additional datasets concerning the rotational and vibrational excitation of C_2^- (Mant et al. 2020a,c,b) in collision with He, Ar, and Ne, and of CN^- (González-Sánchez et al. 2020, 2021; Mant et al. 2021) in collision with He and Ar. As far as cations are concerned, the new additions mainly concern rotational de-excitation of the following species: AlO^+ by He (Denis-Alpizar et al. 2018c); $^{36}\text{ArH}^+$ by He (Bop et al. 2016); $^{36}\text{ArD}^+$ by He (García-Vázquez et al. 2019); CF^+ by He (Denis-Alpizar et al. 2018a), by p- H_2 (Denis-Alpizar & Rubayo-Soneira 2019; Desrousseaux et al. 2021), and by o- H_2 (Desrousseaux et al. 2021); HeH^+ by H (Desrousseaux & Lique 2020); NeH^+ by He (Bop et al. 2017); NO^+ by He (Denis-Alpizar & Stoecklin 2015) and by p- H_2 (Cabrera-González et al. 2020); and NS^+ by He (Cabrera-González et al. 2018).

In the case of the collisional rotational excitation of CF^+ with p- H_2 (Denis-Alpizar & Rubayo-Soneira 2019; Desrousseaux et al. 2021), a good agreement was found between the two new sets of data despite the use of a less accurate PES by Denis-Alpizar & Rubayo-Soneira (2019). The dataset of Denis-Alpizar & Rubayo-Soneira (2019) provides rate coefficients for roughly the same transitions, but for temperatures between $T = 10$ K and $T = 300$ K, while Desrousseaux et al. (2021) provide data between $T = 5$ K and $T = 150$ K.

The de-excitation among rotational levels of NS^+ cation by H_2 has been included with several datasets: a first dataset (Bop 2019; 24 levels; $T = 5\text{--}100$ K) of NS^+ in collision with p- H_2 ($j = 0$) that was calculated with a PES spherically averaged over the H_2 directions, and two datasets (Bop et al. 2022a; 15 levels; $T = 5\text{--}50$ K) in collision with p- H_2 ($j = 0$) and with o- H_2 ($j = 1$); both datasets were calculated with a 4D PES (Bop et al. 2022a). For these datasets, the authors (Bop et al. 2022a) performed some interesting precision tests related to the dimension of the H_2 rotational basis in the dynamical calculations. They found that the neglect of higher H_2 rotational levels induced differences up to 30% in the rate coefficients.

The rate coefficients among hyperfine levels, obtained via IOS recoupling techniques, are added for CF^+ by He (Denis-Alpizar et al. 2018a), for NS^+ by He (Cabrera-González et al. 2018), and for NS^+ by p- H_2 ($j = 0$) (Bop 2019). The rovibrational excitation of $^{36}\text{ArH}^+$ by He (García-Vázquez et al. 2019) has been added as well.

7.2. CH

BASECOL2023 is enriched with the CH species with two datasets: the fine structure resolved excitation of $\text{CH}(^2\Pi)$ by He (Marinakos et al. 2015) and the hyperfine structure resolved excitation for $\text{CH}(^2\Pi)\text{--He}$ (Marinakos et al. 2019). The hyperfine

results are obtained with a recoupling technique using the data from Marinakis et al. (2015).

7.3. CN, ^{13}CN , C^{15}N

The current CN data (Table B.3) include collisions with He and H_2 and tackle rotational, fine and hyperfine resolved de-excitation processes. Nine recommended datasets are available for CN, one for ^{13}CN and one for C^{15}N .

7.3.1. CN–He

BASECOL2012 included the CN–He system with two datasets: one for transitions among the lowest 41 fine levels of CN for temperatures between 5 and 350 K (Lique et al. 2010b) and for transitions among the lowest 37 hyperfine levels of CN for temperatures between 5 and 30 K (Lique & Kłos 2011).

7.3.2. CN and isotopologues with H_2

BASECOL2023 has been enriched with collisional processes involving the H_2 projectile for CN, ^{13}CN , and C^{15}N . The CN– H_2 saga includes a first publication by Kalugina et al. (2012b), where they calculated a 4D PES and then reduced the dimensionality to a 3D PES in order to calculate rate coefficients among hyperfine levels of CN in collision with p- H_2 ($j = 0$). This dataset, included in BASECOL2012, is now superseded by the new calculations cited thereafter and marked as non-recommended. In a subsequent publication, Kalugina et al. (2013) calculated a 4D PES, and using this 4D PES they calculated rate coefficients among rotational and fine resolved structure of CN in collision with o- H_2 ($j = 1$) and with para- H_2 ($j = 0, 2$); for the fine resolved structure calculations they used a recoupling technique. For para- H_2 they provided state-to-state rate coefficients that include transitions $j(\text{H}_2) = 0\text{--}0, 2\text{--}2$ and $2\text{--}0$ (note that separate fine structure datasets are provided for $j(\text{H}_2) = 0\text{--}0$ and $j(\text{H}_2) = 2\text{--}0, 2\text{--}2$ as the $0\text{--}0$ dataset includes 25 transitions among 25 fine levels of CN, while the $j(\text{H}_2) = 2\text{--}0, 2\text{--}2$ datasets involve 17 fine levels). Finally, Kalugina & Lique (2015) used the PES from Kalugina et al. (2013) to calculate rate coefficients among hyperfine levels of CN using a recoupling technique. The hyperfine rates from Kalugina & Lique (2015) are within a factor of two of those reported in Kalugina et al. (2012b) due primarily to the use of a reduced PES in the latter case. Two new datasets have been added for the hyperfine excitation of ^{13}CN and of C^{15}N by para- H_2 (Flower & Lique 2015), where the PES of Kalugina et al. (2013) is used.

7.4. CO

The current CO data (Table B.3) include collisions with H, He, H_2 , and H_2O , and tackle rotational, vibrational, and rovibrational de-excitation processes. 17 recommended datasets are available.

7.4.1. CO–He

BASECOL2012 already had datasets (Cecchi-Pestellini et al. 2002) for the de-excitation of 15 rotational levels of CO ($T = 5\text{--}500$ K) and of seven vibrational levels of CO ($T = 500\text{--}5000$ K).

7.4.2. CO–H

BASECOL2012 had a dataset by Balakrishnan et al. (2002) for the de-excitation of five vibrational levels of CO in the

temperature range from 100 K to 3000 K. BASECOL2012 also included two datasets (Balakrishnan et al. 2002) calculated with the CC method; they span the low-temperature range ($T = 5\text{--}100$ K) among eight rotational levels and the high-temperature range ($T = 100\text{--}3000$ K) among 17 rotational levels. These three datasets were calculated with the PES of Keller et al. (1996); they are kept as recommended in order to provide meaningful comparisons with the more recent data cited below. New datasets for the CO-H system have been added to BASECOL2023 for rotational de-excitation (Walker et al. 2015) and for ro-vibrational de-excitation (Song et al. 2015b,a); both datasets use the PES of Song et al. (2013).

The rotational de-excitation rate coefficients (Walker et al. 2015) for temperatures ranging from 2 K to 3000 K are obtained for CO ($v = 0, j$) quenching from $j = 1\text{--}45$ to all lower j' levels, where j is the rotational quantum number. CC and CS calculations were performed in full dimension for $j = 1\text{--}5, 10, 15, 20, 25, 30, 35, 40,$ and 45 , while scaling approaches were used to estimate rate coefficients for all other intermediate rotational states.

For the ro-vibrational de-excitation process in the temperature range from 2 to 3000 K, the dataset (Song et al. 2015b) provides the rate coefficients from initial states ($v = 1\text{--}5, j = 0\text{--}30$) to (v', j'), where $v' = 0, 1, \dots, v - 1$, and $j' = 0, 1, \dots$, the highest final $j' = 27\text{--}42$, depending on the initial j . The transitions for larger final j' are not reported, either because they are negligibly small, or because they were not completely converged. It should be noted that the rate coefficients for ro-vibrational ($v = 1, j = 0\text{--}30$) \rightarrow ($v' = 0, j'$) transitions were obtained from scattering cross-sections previously computed with the CC method by Song et al. (2015a). Combining these with the rate coefficients for vibrational $v = 1\text{--}5 \rightarrow v' < v$ quenching obtained with the infinite-order sudden approximation, Song et al. (2015b) used an extrapolation scheme that yields the rate coefficients for ro-vibrational $v = 2\text{--}5, j = 0\text{--}30$, de-excitation.

7.4.3. CO-H₂

BASECOL2012 already contained datasets (Yang et al. 2010) calculated with the PES of Jankowski & Szalewicz (1998), which provided the rotational de-excitation of CO by o/p-H₂ among the lowest 41 rotational CO levels and for temperature between 1 K and 3000 K. The above datasets provide a larger number of transitions for a larger temperature range than previous datasets (Wernli et al. 2006; Flower 2001a) calculated with the same PES (Jankowski & Szalewicz 1998). All datasets are kept as recommended, as no strong argument can distinguish between the methodologies.

New datasets for the ro-vibrational de-excitation of CO by o/p-H₂ have been added to BASECOL2023 (Yang et al. 2016): the ro-vibrational de-excitation rate coefficients for all transitions from CO ($v = 1, j = 1\text{--}5$) to ($v' = 0, j' = 0\text{--}22$) in collisions with para-H₂ ($j = 0$) and ortho-H₂ ($j = 1$) are provided. In addition, the state to state rate coefficients for vibrational transitions of CO from ($v = 2, j = 0$) to ($v' = 1$ and $0, j' = 0\text{--}20$) are also provided for para-H₂ remaining in its ground rotational state ($j = 0$) and for para-H₂ excited from $j = 0$ to $j = 2$. Those calculations are based on the PES of Yang et al. (2015b).

7.4.4. CO-H₂O

For cometary applications, BASECOL2023 has been updated with two datasets (Faure et al. 2020) with thermalised rate

coefficients for the de-excitation of CO by o/p-H₂O (11 levels; $T = 5\text{--}100$ K). The calculations use a new 5D PES (Kalugina et al. 2018) and the statistical approach of Loreau et al. (2018). The thermalised rate coefficients are obtained from the state-to-state rate coefficients summing over the final states of o/p-H₂O and averaging over the initial rotational states of o/p-H₂O where p-H₂O and o-H₂O are independent species.

7.5. CS

The CS data (Table B.3) include collisions with He and H₂, and tackle rotational and ro-vibrational processes; six recommended datasets are available.

7.5.1. CS-He

BASECOL2012 already included collisions of CS with He that are still recommended: one dataset (Lique et al. 2006b) for the de-excitation among the lowest 31 rotational levels of CS ($T = 10\text{--}300$ K) and another one (Lique & Spielfiedel 2007) for the de-excitation among the lowest 114 ro-vibrational levels ($T = 300\text{--}1500$ K).

7.5.2. CS-H₂

BASECOL2023 has been updated with collisional processes with the H₂ molecule. The recent rotational de-excitation datasets for CS by o/p-H₂ of Denis-Alpizar et al. (2018b) have been added and supersede previous results (Turner et al. 1992; Green & Chapman 1978) calculated with an old PES (Green & Chapman 1978).

Two new datasets by Yang et al. (2018a) have been included for the ro-vibrational de-excitation of CS by o/p-H₂. Those datasets cover the ro-vibrational de-excitation rate coefficients from the CS ro-vibrational states ($v = 1, j = 1\text{--}5$) to the ($v' = 0, j' = 0\text{--}35$) levels in collision with para-H₂ ($j = 0$) and with ortho-H₂ ($j = 1$). In addition, the state-to-state rate coefficients for ro-vibrational transitions of CS from ($v = 1, j = 1\text{--}5$) to ($v' = 0, j' = 0\text{--}33$) are also provided for para-H₂ excited from $j = 0$ to $j = 2$, as well as the state-to-state rate coefficients for ro-vibrational transitions of CS from ($v = 1, j = 1\text{--}5$) to ($v' = 0, j' = 0\text{--}28$) for ortho-H₂ excited from $j = 1$ to $j = 3$. Within those two datasets, the rotational de-excitation rate coefficients among the first six rotational levels of CS are also provided for $v = 0$ for collisions with both para-H₂ ($j = 0$) and ortho-H₂ ($j = 1$).

7.6. HCl

The current HCl data (Table B.3) include collisions with He, H₂, and H, and tackle rotational and hyperfine resolved de-excitation processes. Six recommended datasets are available.

7.6.1. HCl-He

BASECOL2023 has been updated with three datasets: two datasets for the de-excitation among rotational levels of HCl, those sets have been calculated by Lanza & Lique (2012) (11 levels; $T = 10\text{--}300$ K) and by Yang & Stancil (2014) (21 levels; $T = 1\text{--}3000$ K), and a dataset for the de-excitation from hyperfine resolved transitions (40 levels; $T = 10\text{--}300$ K; Lanza & Lique 2012) obtained by a recoupling technique. The rotational datasets of Lanza & Lique (2012) and of Yang & Stancil (2014) are of comparable quality and are both recommended; in addition, the hyperfine rate coefficients could be obtained from the

latter dataset (Yang & Stancil 2014) using the usual recoupling techniques (Lanza & Lique 2012). These datasets supersede the previous rotational and hyperfine datasets of Neufeld & Green (1994) as Lanza & Lique (2012) and Yang & Stancil (2014) use more recent PES and better methodologies for the scattering calculations. The datasets of Neufeld & Green (1994) are now marked as non-recommended.

7.6.2. HCl–H₂

BASECOL2023 has been updated with two rotational datasets (Lanza et al. 2014a) for the de-excitation among the eleven lowest rotational levels of HCl ($T = 10\text{--}300\text{ K}$) with o/p-H₂. Those rotational state-to-state rate coefficients were obtained with rotational basis sets that include, respectively, the $j_2 = 3$ and $j_2 = 2$ levels of H₂. It should be mentioned that the dataset with para-H₂ includes transitions among the $j_2 = 0, 2$ levels of H₂ projectile.

7.6.3. HCl–H

More recently, calculations including dissociation were performed by Lique & Faure (2017) for the rotational excitation of HCl–H system. Their rotational de-excitation rate coefficients (Lique & Faure 2017; 11 levels; $T = 10\text{--}500\text{ K}$) are now in BASECOL2023.

7.7. HF

The current HF data (Table B.3) include collisions with He, H₂, H, and H₂O, and tackle rotational de-excitation processes. Seven recommended datasets are available.

7.7.1. HF–He

BASECOL2023 has been updated with a dataset (Yang et al. 2015a) for the rotational de-excitation of HF by He (21 levels and $T = 1\text{--}3000\text{ K}$), this dataset is calculated with the PES of Moszynski et al. (1994). BASECOL2012 already included the dataset (10 levels; $T = 0.1\text{--}300\text{ K}$) of Reese et al. (2005) that was calculated with the more recent PES of Stoecklin et al. (2003). Yang et al. (2015a) presented a comparison with the results obtained by Reese et al. (2005); they indicate a percentage difference from 20% to 75% at 50 K for most of the strongest transitions. As no objective quality arguments can be put forward, the two datasets are kept as recommended.

7.7.2. HF–H₂

BASECOL2023 has also been updated with two datasets (Guillon & Stoecklin 2012) for the de-excitation of six rotational levels of HF in collision with o/p-H₂ ($T = 0.1\text{--}150\text{ K}$): these datasets include some transitions within the H₂ rotational levels.

7.7.3. HF–H

A recent dataset (Desrousseaux & Lique 2018) for the rotational de-excitation of HF by H (9 levels $T = 10\text{--}500\text{ K}$) has been added to BASECOL2023; it uses the PES of Li et al. (2007).

7.7.4. HF–H₂O

For cometary applications, BASECOL2023 has been updated with two datasets (Loreau et al. 2022) with thermalised rate

coefficients for the de-excitation of HF by o/p-H₂O (7 levels; $T = 5\text{--}150\text{ K}$). The calculations use a new 5D PES (Loreau et al. 2020) and the statistical approach of Loreau et al. (2018). The thermalised rate coefficients are obtained from the state-to-state rate coefficients summing over the final states of o/p-H₂O and averaging over the initial rotational states of o/p-H₂O where p-H₂O and o-H₂O are independent species.

7.8. HD

The current HD data (Table B.3) include collisions with He, H₂, and H, and tackle rotational and ro-vibrational de-excitation processes. Ten recommended datasets are available.

7.8.1. HD–He

All the BASECOL datasets concerning HD in collision with He had been calculated using the PES of Muchnick & Russek (1994). BASECOL2012 already had the rotational de-excitation of HD by He (10 levels; $T = 80\text{--}2000\text{ K}$) by Roueff & Zeippen (1999). BASECOL2023 has been updated with two datasets from Nolte et al. (2011) for the ro-vibrational de-excitation of HD by He: those two datasets span different temperature range and transitions. In those calculations, Nolte et al. (2011) extended the calculations of Roueff & Zeippen (2000) to include transitions with $j = 0$ and 1 for $v = 0\text{--}17$, and for which $\Delta v = 0, -1, -2$. Compared to Roueff & Zeippen (2000), significant discrepancies were found for the highest previously considered vibrational state of $v = 3$, but for $v = 0, 1, 2$, the new results are very close to previous results. The ro-vibrational data from Roueff & Zeippen (2000) were never provided to BASECOL.

7.8.2. HD with H₂ projectile

Two new datasets, calculated with the PES of Patkowski et al. (2008), have been included in BASECOL2023 for the de-excitation of nine rotational levels of HD by o/p-H₂ (Wan et al. 2019) for temperatures up to 10 000 K. These results supersede the results (9 levels; $T = 50\text{--}500\text{ K}$) of Flower (1999a) as the latter calculations used on older PES (Schwenke 1988) and did not take into account the excitation of the H₂ molecule in the rotational basis set. Therefore, the rotational dataset from Flower (1999a) is now indicated as non-recommended. The BASECOL2012 datasets for the ro-vibrational de-excitation of HD by o/p-H₂ by Flower & Roueff (1999a) with the PES of Schwenke (1988) have not been revisited and to our knowledge are currently the only available datasets.

7.8.3. HD–H

A new dataset for the rotational de-excitation of eleven rotational levels of HD by H (Desrousseaux et al. 2018) was added to BASECOL2023 in the temperature range between 10 K and 1000 K; calculations were performed with the PES of Mielke et al. (2002). BASECOL2012 already included the rotational de-excitation of HD by H for ten rotational levels and a temperature range from 100 K to 2000 K (Roueff & Flower 1999) where the PES of Boothroyd et al. (1996) was used. The rotational dataset of Roueff & Flower (1999) is kept as recommended to keep the coherence with the ro-vibrational de-excitation rate coefficients of HD by H (Flower & Roueff 1999a) calculated with the same PES (Boothroyd et al. 1996). In addition, there is no strong argument about the difference of quality of the PES of Boothroyd et al. (1996) and the one of Mielke et al. (2002).

7.9. H₂

The current H₂ data (Table B.3) include collisions with He, H₂, and H, and they tackle rotational and ro-vibrational de-excitation processes. Eleven recommended datasets are available.

BASECOL2023 was updated with one new dataset for the collision of H₂ with H (Lique et al. 2012), where the ortho-para conversion was tackled. All the other datasets were already included in BASECOL2012, and they form a very complete manifold of datasets calculated at the end of the last century.

7.9.1. H₂ with He projectile

The ro-vibrational de-excitation datasets of o/p-H₂ by He calculated with the PES of Muchnick & Russek (1994) are currently the only available datasets (Flower et al. 1998) in BASECOL. These results can be used for the rotational de-excitation of o/p-H₂ by He. Flower et al. (1998) provided ro-vibrational rate coefficients for all transitions among levels below ($v = 3, j \leq 8, E = 15228.88 \text{ cm}^{-1}$) for para-H₂ and below ($v = 3, j \leq 7, E = 14495.46 \text{ cm}^{-1}$) for ortho-H₂ ($T = 100\text{--}6000 \text{ K}$). It should be noted that for para-H₂ the rate coefficients had not been calculated for transitions involving the 27th level of para-H₂, (i.e. $v = 1, j = 14$), but they were available for transitions involving the 28th level ($v = 3, j = 8$); so, in BASECOL2023 we decided to limit the data set at the 26th level. For ortho-H₂, the rate coefficients had not been calculated for transitions involving level 24 (i.e. $v = 2, j = 11$), but they were calculated for transitions involving level 25 ($v = 3, j = 7$), so in BASECOL2023 we limited the dataset at level 23. In BASECOL2012, the rate coefficients for the missing transitions were set to zero. Nevertheless, another work has been carried out for this system. Balakrishnan et al. (1999b) calculated ro-vibrational de-excitation rate coefficients from $v = 2$ to 6, with $\Delta v = -1$, for temperatures between 100 K and 4000 K. For ortho-H₂ the transitions involve de-excitation from ($v, j = 1\text{--}7$) to ($v - 1, j = 1\text{--}11$) and to ($v, j = 1\text{--}5$). For para-H₂ the transitions involve de-excitation from ($v, j = 0\text{--}6$) to ($v - 1, j = 0\text{--}10$) and to ($v, j = 0\text{--}4$). These calculations are an extension for $v = 4, 5, 6$ of the work of Flower et al. (1998) using the same PES (Muchnick & Russek 1994). It should be noted that the calculations of Balakrishnan et al. (1999b) are an extension of the calculations by Balakrishnan et al. (1999a), but with a larger ro-vibrational basis set. Ro-vibrational results of Balakrishnan et al. (1999b) and Flower et al. (1998) show discrepancies for ro-vibrational results with large Δj transitions, but there is no conclusion about the respective quality of results. As far as pure rotational calculations are concerned, Flower et al. (1998) and Balakrishnan et al. (1999a) agree well at the published temperature (100 K and higher). For unknown reasons, those data have never been included in BASECOL, and if the authors (Balakrishnan et al. 1999a) provide their data in the BASECOL format, we are happy to include them.

7.9.2. H₂ with o/p-H₂ projectile

BASECOL2023 includes four datasets (Flower & Roueff 1998a, 1999b) with the o/p-H₂ projectile; those datasets have been obtained with the PES of Schwenke (1988). With the p-H₂ projectile kept in its ground state ($v = 0, j = 0$), two datasets (Flower & Roueff 1998a) provide ro-vibrational rate coefficients between 100 K and 6000 K for the de-excitation from the 26 lowest target para-H₂ levels, and from the 23 lowest target ortho-H₂ levels. Flower & Roueff (1998a) calculated more levels: for para-H₂ such that $j \leq 16$ in $v = 0$, $j \leq 12$ in $v = 1$, and $j \leq 8$ in $v = 2$ and for target ortho-H₂ levels such that $j \leq 15$ in $v = 0$, $j \leq 13$ in

$v = 1, j \leq 9$ in $v = 2$, and $j \leq 7$ in $v = 3$. For the reasons developed above for H₂-He, BASECOL2023 truncates the datasets.

With the ortho-H₂ projectile kept in its ground state ($v = 0, j = 1$), two datasets (Flower & Roueff 1999b) provide ro-vibrational rate coefficients between 100 K and 6000 K for the de-excitation from the 19 lowest target para-H₂ levels, and from the 17 lowest target ortho-H₂ levels. Flower & Roueff (1999b) calculated ro-vibrational rate coefficients for more levels in the case of ortho-H₂ such that $j \leq 15$ in $v = 0$, $j \leq 13$ in $v = 1$ and $j \leq 9$ in $v = 2$. But rate coefficients have not been calculated for transitions involving the 18th and 20th levels of the ortho-H₂ target (i.e. $v = 3, j = 1; v = 3, j = 3$). Therefore, BASECOL2023 provides the data set up to level 17 of the ortho-H₂ target. We are aware of the recent calculations by Hernández et al. (2021) of rotational H₂-H₂ de-excitation rate coefficients and we invite the authors to provide the data in our format.

7.9.3. H₂ with H projectile

Currently, BASECOL2023 includes two datasets (Flower & Roueff 1998b) for the ro-vibrational de-excitation of o/p-H₂ by H; those datasets have been calculated with the PES of Boothroyd et al. (1996) and provide rate coefficients from 100 K to 6000 K: one dataset for p-H₂ with 26 ro-vibrational levels and another one for o-H₂ with 23 ro-vibrational levels (see the paragraph on H₂-He above for explanations on the number of levels in the datasets).

The above results could be used for the rotational excitation of o/p-H₂ by H, but the pure rotational rate coefficients have differences as much as a factor of 2 compared to the results of Forrey et al. (1997) and the contribution of the reactive channel to the inelastic rate coefficients is not included as been done in Lique et al. (2012).

BASECOL includes the two datasets calculated by Forrey et al. (1997) that provide rotational de-excitation among the lowest three rotational levels of either p-H₂ or o-H₂ between 100 K and 1000 K. These datasets have been calculated with the same 3D PES (Boothroyd et al. 1996) as the ro-vibrational datasets of Flower & Roueff (1998b), but an exact wave function for H₂ is used instead of a harmonic approximation. This approximation is likely to explain the difference of factor of two between the two types of calculations. Indeed, Forrey et al. (1997) compared various ways to reduce a 3D PES to a 2D PES: a rigid rotor approximation, an average of 3D PES over the harmonic oscillator approximation, an average of 3D PES over the exact ro-vibrational wave function. They found that the rigid rotor approximation and the harmonic oscillator wave function strongly underestimate the rotational cross-sections (about a factor of two).

Finally, the combination of inelastic scattering of H₂ by H and ortho-para conversion of H₂ via H exchange has been studied by Lique et al. (2012) using the PES of Mielke et al. (2002). BASECOL2023 has been updated with the corresponding dataset of collisional rate coefficients among the first nine rotational levels of H₂ in collision with H for temperatures between 300 K and 1500 K (Lique et al. 2012). The differences between the data-sets of Forrey et al. (1997), Flower & Roueff (1998b), and Lique et al. (2012) are given in Fig. C.1 and show the importance of considering the exchange channel for this collision.

7.10. KCl

BASECOL2023 was updated with the KCl molecule and with a single dataset (Sahnoun et al. 2018) concerning the de-excitation

of KCl by p-H₂ ($j = 0$) among the 16 lowest rotational levels of KCl ($T = 2\text{--}50$ K).

7.11. NaH

Another new molecule is NaH, and the current unique dataset (Bop et al. 2019b) concerns the rotational de-excitation of NaH by He (11 levels; $T = 5\text{--}200$ K) calculated with a PES averaged over the ground vibrational wave function of NaH (Bop et al. 2019b).

7.12. NH

The NH($X^3\Sigma^+$) data (Table B.3) include collisions with He and tackle the rotational fine structure process; two recommended datasets are available, and no strong arguments could be used to distinguish between them. BASECOL2023 has been updated with a new dataset (Ramachandran et al. 2018) for the fine structure rotational excitation of NH by He (25 levels; $T = 10\text{--}350$ K). This dataset has been calculated with a 2D PES averaged over a 3D PES that included the vibrational coordinate of NH when the previous dataset of Toboła et al. (2011), already in BASECOL2012, had been calculated with a 2D PES. It should be noted that both datasets agree reasonably well with the experimental rate coefficients of Rinnenthal & Gericke (2002); they both provide transitions among the lowest 25 rotational levels and in the same temperature range up to 350 K. Figure C.2 displays the differences between the two calculated rate coefficient datasets: as it appears that they do not show any significant differences (the average percentage difference between the two data sets is less than 40% for the $\Delta N = \Delta F$ transition), and it is worth noting that the differences are not homogeneous. Both datasets are marked as recommended in BASECOL2023.

7.13. NO

The NO data (Table B.3) include collisions with He and H₂ and tackle fine and hyperfine processes; two recommended datasets are available. BASECOL2012 already had the dataset (Kłos et al. 2008) for the rotational de-excitation of the fine structure levels of NO by He (98 levels; $T = 10\text{--}500$ K). On that dataset (Kłos et al. 2008), BASECOL2023 has updated the notation for the Kronig parity labels in order for them to agree with VAMDC standards, and the energy levels have been put in increasing order, but the scientific content is not changed; the final version of the dataset has changed to v4. BASECOL2023 has been updated with a dataset (Ben Khalifa & Loreau 2021) for the rotational de-excitation of the hyperfine structure of NO by p-H₂ (100 levels; $T = 7\text{--}100$ K), the authors use the new PES of Kłos et al. (2017a).

7.14. OH, OD

The OH data (Table B.3) include collisions with He, H₂, and H, and tackle rotational fine and hyperfine structure resolved processes. Ten recommended datasets are available.

7.14.1. OH–He

The oldest dataset (Kłos et al. 2007), already in BASECOL2012, includes fine structure de-excitation rate coefficients of OH by He using the 2D PES of Lee et al. (2000). BASECOL2023 has been updated with a more recent dataset (Kalugina et al. 2014) that provides rate coefficients for the same system and process.

This is for the same number of transitions (roughly 44) and for the same temperature range ($T = 5\text{--}350$ K), but the authors used the new vibrationally averaged 3D PES of Kalugina et al. (2014). The discussions of Kalugina et al. (2014) seem to show that a vibrationally averaged PES provides some theoretical results in closer agreement with the experimental results. Nevertheless, other tests (Kalugina et al. 2014) show no difference in using either a 2D or an averaged 3D PES. For all the above reasons, the two datasets are indicated as recommended. We checked both sets of rate coefficients at 5, 10, 50, and 300 K. For the transitions up to level 9.5e, the agreement is good, with averaged percentage differences of 28.3, 19, 18.4, and 10.9, respectively. However, for transitions from level 9.5e up to level 10.5e, the averaged percentage differences are 172.2, 130.1, 64.3, and 101, respectively.

BASECOL2023 is further updated with a dataset (Marinakos et al. 2019) that provides hyperfine resolved collisional de-excitation rate coefficients of OH by He. The authors used a recoupling technique together with the nuclear spin-free S matrices of Kalugina et al. (2014).

7.14.2. OH/OD–H₂

The OH–H₂ system has been investigated by Offer et al. (1994), the corresponding datasets can be found on the LAMDA database (LAMDA; van der Tak et al. 2020). BASECOL2023 was updated with two datasets (Kłos et al. 2017b) for the fine structure de-excitation of OH by o/p-H₂ (20 levels; $T = 10\text{--}150$ K) and two datasets (Kłos et al. 2020b) for the hyperfine resolved structure de-excitation of OH by o/p-H₂ (24 levels; $T = 10\text{--}150$ K), the four datasets were obtained with the PES of Ma et al. (2014). The OH–H₂ fine structure rate coefficients for collisions with both para-H₂($j = 0$) and ortho-H₂($j = 1$) differ by a factor of less than three from the older rates by Offer et al. (1994), and the new hyperfine resolved rate coefficients (Kłos et al. 2020b) are found to increase the hyperfine intensities by a factor of about 1–3 in comparison to previous rates of Offer et al. (1994). The new OH–H₂ rate coefficients (Kłos et al. 2017b, 2020b) are expected to be more precise than the previous ones (Offer et al. 1994), as the new datasets were obtained with the recent PES (Ma et al. 2014) that performed fairly well in comparison of theoretical calculations with scattering experiments (Schewe et al. 2015). The OD molecule is new in BASECOL, and two datasets (Dagdikian 2021a) provide hyperfine resolved structure de-excitation of OD by o/p-H₂ (40 levels; $T = 5\text{--}200$ K); they were obtained with the same PES (Ma et al. 2014) as above.

7.14.3. OH–H

BASECOL2023 was updated with a dataset (Dagdikian 2022a) that provides hyperfine resolved collisional de-excitation rate coefficients of OH by H atoms calculated with a recoupling technique and with fine resolved structure excitation results of OH by H (Dagdikian 2022b). These calculations used the potential energy curves of Alexander et al. (2004).

7.15. O₂

The O₂ data (Table B.3) include collisions with He and o/p-H₂, and tackle rotational and fine structure resolved processes; three recommended datasets are available. BASECOL2012 already had the dataset for the rotational fine structure resolved de-excitation of O₂ by He (36 fine levels; $T = 5\text{--}350$ K; Lique 2010), which was calculated using the PES of

Groenenboom & Struniewicz (2000). BASECOL20023 was updated with two datasets from Kalugina et al. (2012a) concerning the rotational de-excitation of O₂ by o/p-H₂ (7 rotational levels; $T = 5\text{--}150\text{ K}$).

7.16. PN

The PN data (Table B.3) include collisions with He and p-H₂ and tackle the rotational process; two recommended datasets are available. BASECOL2012 already had the dataset for the rotational de-excitation of PN by He (31 levels; $T = 10\text{--}300\text{ K}$; Toboła et al. 2007). BASECOL20023 was updated with a dataset from Najar et al. (2017) concerning the rotational de-excitation of PN by p-H₂ (40 levels; $T = 10\text{--}300\text{ K}$).

7.17. SH

BASECOL2012 already had the dataset for the rotational de-excitation of the fine structure levels of SH by He (Kłos et al. 2009; 60 levels; $T = 5\text{--}350\text{ K}$). On that dataset (Kłos et al. 2009), BASECOL2023 updated the notation for the Kronig parity labels in order for them to agree with VAMDC standards; the scientific content is not changed, but the version of the dataset has changed to v2 and is recommended.

7.18. SiO

The SiO data (Table B.3) include collisions with He and H₂, and tackle the rotational and ro-vibrational processes; eight recommended datasets are available.

7.18.1. SiO–He

BASECOL2023 has been updated with two datasets: a low temperature dataset for rotational de-excitation (Dayou & Balança 2006) among 27 rotational levels ($T = 10\text{--}300\text{ K}$) and a more approximate high temperature dataset for ro-vibrational de-excitation (Balança & Dayou 2017) among 246 levels ($T = 250\text{--}10\,000\text{ K}$).

7.18.2. SiO–H₂

BASECOL2023 was updated with two very rich datasets by Yang et al. (2018b) for collisions with o/p-H₂: the ro-vibrational and rotational de-excitation rate coefficients for SiO ro-vibrational states ($v = 1, j = 1\text{--}10$) to ($v' = 0, j' = 0\text{--}35$) in collisions with ortho-H₂ ($j = 1$) and para-H₂ ($j = 0$). The rate coefficients for rotational transition of SiO from ($v = 1, j = 1\text{--}10$) to ($v' = 1, j' < j$) and among the first six rotational levels in the ground vibrational state are also included in both the para-H₂ and ortho-H₂ datasets. In addition, the para-H₂ dataset provides the ro-vibrational de-excitation rate coefficients for SiO ro-vibrational states ($v = 1, j = 1\text{--}10$) to ($v' = 0, j' = 0\text{--}34$) when para-H₂ is excited from $j(\text{H}_2) = 0$ to $j(\text{H}_2) = 2$.

In addition, BASECOL2023 was updated with four datasets (Balança et al. 2018) for the rotational de-excitation of SiO with o/p-H₂: two low temperature datasets (21 levels; $T = 5\text{--}300\text{ K}$) calculated with the CC method, and two high temperature datasets (30 levels; $T = 5\text{--}1000\text{ K}$) obtained with the more approximate CS method (the sets are identified, respectively, as CC and CS in Table B.3). The above CC and CS SiO–H₂ datasets are recommended as they could be used to test the influence of different datasets on the radiative transfer results. The user should prefer the CC results over the CS or the infinite

order sudden (IOS) approximation results in the relevant temperature range and contact the authors if any doubt. However, the older datasets (Dayou & Balança 2006; Turner et al. 1992) have been set to non-recommended.

7.19. SiS

The SiS data (Table B.3) include collisions with He and H₂ and tackle the rotational and ro-vibrational processes; four recommended datasets are available. BASECOL2012 already included a dataset (Vincent et al. 2007) for the rotational de-excitation of SiS by He (26 levels; $T = 10\text{--}200\text{ K}$), two datasets (Kłos et al. 2008) for the rotational de-excitation of SiS by o/p-H₂ (41 levels; $T = 5\text{--}300\text{ K}$), and one dataset (Toboła et al. 2008) for the ro-vibrational de-excitation of SiS by He (505 levels corresponding to vibration up to $v = 4$ and to rotation up to $j = 100$ with $T = 100\text{--}1500\text{ K}$).

7.20. SO

The SO data (Table B.3) include collisions with He and H₂ and tackle the rotational fine structure and ro-vibrational fine structure processes. Six recommended datasets are available.

7.20.1. SO–He

BASECOL2012 already included two datasets for the rotational fine structure de-excitation of SO by He: one dataset (Lique et al. 2005) for 31 fine levels ($T = 5\text{--}50\text{ K}$) and another one (Lique et al. 2006a) for 91 fine levels ($T = 60\text{--}300\text{ K}$). It also included a dataset (Lique et al. 2006c) for the ro-vibrational fine structure de-excitation of SO by He (236 levels; $T = 300\text{--}800\text{ K}$).

7.20.2. SO–H₂

Recently, new extensive calculations have been performed for the ro-vibrational fine structure de-excitation of SO by o/p-H₂ (Price et al. 2021), where a new 6D PES by Yang et al. (2020) was used. BASECOL2023 has been updated with the corresponding two datasets (Price et al. 2021) that span 273 ro-vibrational transitions up to $v = 2$ for temperatures between 10 K and 3000 K. BASECOL2012 already included the smaller dataset of Lique et al. (2007) for the rotational fine structure de-excitation of SO by p-H₂ (31 levels; $T = 5\text{--}50\text{ K}$), which already superseded an older dataset from Green (1994) as the 1994 calculations used a CS-H₂ PES.

8. Triatomic molecules with heavy partners

BASECOL2023 contains 31 triatomic species (Table B.4) aside from the para-ortho symmetries.

8.1. AICN, AINC

One recommended set is available for AICN and two for AINC. BASECOL2023 was updated with two datasets (Hernández Vera et al. 2013) concerning the de-excitation by He among the 30 rotational levels of AICN and of AINC in the 5 K to 100 K temperature range. A dataset for the rotational de-excitation of AINC by p-H₂ (Urzúa-Leiva & Denis-Alpizar 2020) where H₂ is treated as a spherical atom was also added (27 levels; $T = 5\text{--}105\text{ K}$).

8.2. C_3

Four recommended datasets are available for the C_3 molecule. BASECOL2012 included the dataset (Ben Abdallah et al. 2008) for the de-excitation among six rotational levels of C_3 by impact with He ($T = 5\text{--}15$ K). BASECOL2023 was enriched with three additional datasets: a dataset (Stoecklin et al. 2015) for the rovibrational excitation of C_3 by He (23 levels; $T = 10\text{--}155$ K) and two datasets (Santander et al. 2022) for the rotational de-excitation of C_3 by o/p- H_2 (11 levels; $T = 5\text{--}50$ K).

8.3. C_2H , C_2D , ^{13}CCH , $C^{13}CH$

Five recommended datasets are available for the $C_2H(X^2\Sigma^+)$ molecule: four datasets for $C_2D(X^2\Sigma^+)$, one for $^{13}CCH(X^2\Sigma^+)$, and one for $C^{13}CH(X^2\Sigma^+)$.

8.3.1. $C_2H\text{--}He$

BASECOL2023 has been upgraded with a new version of the dataset (Spielfiedel et al. 2013; version 2, 46 levels; $T = 5\text{--}100$ K) for the de-excitation of the hyperfine levels of C_2H by He, this dataset replaces the previous dataset (version 1, 34 levels; $T = 5\text{--}100$ K; Spielfiedel et al. 2012) which had flaws in the calculations and is not recommended.

8.3.2. $C_2H\text{--}H_2$

This system has been updated with a series of datasets of increasing reliability. BASECOL2023 had been updated with a dataset (Dumouchel et al. 2017) for the de-excitation of the first 17 fine levels of C_2H by p- H_2 , and the corresponding dataset (Dumouchel et al. 2017) for the de-excitation of the first 34 hyperfine levels of C_2H by p- H_2 ($T = 2\text{--}80$ K). These datasets were obtained with a 2D PES (Najar et al. 2014) where H_2 is taken as spherical, and where the PES is averaged over H_2 orientations. Those datasets are now labelled as non-recommended as the PES is crude compared to the calculations of Pirlot Jankowiak et al. (2023b).

BASECOL2023 had also been updated with two datasets (Dagdigian 2018a) for the de-excitation from the first 30 hyperfine levels of C_2H by o/p- H_2 ($T = 10\text{--}300$ K); they were obtained with a newly calculated 4D PES (Dagdigian 2018b). Pirlot Jankowiak et al. (2023b) found an error in those calculations and re-did the dynamical calculations with the same 4D PES (Dagdigian 2018b). BASECOL keeps a trace of the data, and therefore the datasets of Dagdigian (2018a) are kept, but they are labelled as non-recommended. Keeping those datasets of Dagdigian (2018b) is very important, as they were publicly available on both the BASECOL and the LAMDA databases for a certain period of time.

BASECOL2023 was updated with the two recent datasets (Pirlot Jankowiak et al. 2023b) for the de-excitation of 41 fine rotational levels of C_2H by o/p- H_2 ($T = 5\text{--}500$ K) and the two corresponding datasets (Pirlot Jankowiak et al. 2023b) for the de-excitation of the first 38 hyperfine levels of C_2H by o/p- H_2 ($T = 5\text{--}100$ K). Those datasets were obtained with the 4D PES of Dagdigian (2018b). The dynamical calculations with p- H_2 include the first two rotational levels of p- H_2 , but the state-to-state rate coefficients concern the j(p- H_2) 0-0 transition only.

8.3.3. $C_2D\text{--}p\text{--}H_2$

BASECOL2023 had been updated with two datasets (Dumouchel et al. 2017) for the de-excitation from the first

49 hyperfine levels and the first 17 fine levels of C_2D by p- H_2 have been added ($T = 2\text{--}80$ K); these datasets were obtained with the 2D PES of Najar et al. (2014) averaged over H_2 orientations and shifted to take into account the D isotope. Those datasets have been superseded by the datasets of Pirlot Jankowiak et al. (2023b), and they are labelled as non-recommended.

BASECOL2023 had been updated with two datasets (Pirlot Jankowiak et al. 2023b) for the state-to-state de-excitation from the 31 fine structure levels of C_2D with o/p- H_2 ($T = 5\text{--}200$ K), and the corresponding two datasets (Pirlot Jankowiak et al. 2023b) for the state-to-state de-excitation from the first 55 hyperfine levels of C_2D by o/p- H_2 ($T = 5\text{--}100$ K). The dynamical calculations with p- H_2 include the first two rotational levels of p- H_2 , but the state-to-state rate coefficients concern the j(p- H_2) 0-0 transition only.

8.3.4. ^{13}CCH , $C^{13}CH$ with p- H_2

BASECOL2023 has been updated with two datasets (Pirlot Jankowiak et al. 2023a) for the hyperfine and fine resolved rotational de-excitation of $C^{13}CH$ and ^{13}CCH by p- H_2 . Both datasets involve transitions among 98 hyperfine levels for temperatures between 5 K and 100 K. The hyperfine couplings include a first coupling with the ^{13}C nuclear spin leading to the F_1 quantum number and then a coupling to the hydrogen nuclear spin leading to the F quantum number.

8.4. C_2H^-

Two recommended datasets are available for the C_2H^- molecule. BASECOL2023 was updated with two datasets for the rotational de-excitation of C_2H^- by He; one dataset (Gianturco et al. 2019) involves nine rotational levels ($T = 5\text{--}100$ K), and the other dataset (Dumouchel et al. 2012) involves 13 rotational levels ($T = 5\text{--}100$ K). Both datasets were calculated with the same PES (Dumouchel et al. 2012); the cross-sections were obtained over the same range of energies up to 1000 cm^{-1} with the close coupling method; therefore, the rate coefficients should be equivalent, as shown in Fig. C.3.

8.5. C_2N^-

One recommended dataset is available for the open shell $C_2N^- (X^3\Sigma^-)$ molecule. BASECOL2023 was updated with a dataset (Franz et al. 2020) for the de-excitation among rotational levels of C_2N^- in collision with He (16 levels; $T = 5\text{--}100$ K). In that calculation, the electronic structure of C_2N^- has been ignored, and the energy levels are labelled with the spin free quantum number N ; they also calculated a new PES for the C_2N^- -He system.

8.6. C_2O

One recommended dataset is available for the open shell $C_2O(X^3\Sigma^-)$ molecule. BASECOL2023 was upgraded with a dataset (Khadri et al. 2022b) concerning the de-excitation of C_2O in collision with He (31 levels; $T = 2\text{--}80$ K); this dataset was obtained with a newly developed PES (Khadri et al. 2022b). This is part of a series of calculations that explore the excitation of long carbon chains (see below).

8.7. CH_2

Four recommended datasets are available for the asymmetric open shell $CH_2 (X^3B_1)$ molecule.

BASECOL2023 was upgraded with four new datasets (Dagdikian 2021b) for the CH₂ molecule in its para and ortho symmetries: datasets for the de-excitation from the first 69 hyperfine levels of o-CH₂ by o/p-H₂ and from the first 27 rotational levels of p-CH₂ by o/p-H₂ were added for temperatures between 5 K and 300 K. Those four datasets were obtained with a newly calculated PES (Dagdikian 2021c), and the splittings due to the electron spin were treated using a recoupling method. For o-CH₂ the splittings due to the nuclear spin were treated with the M_J randomisation approximation (Alexander & Dagdikian 1985).

8.8. CO₂

One recommended dataset is available for the CO₂ molecule. BASECOL2023 was upgraded with a collisional dataset (Godard Palluet et al. 2022) for the rotational de-excitation of CO₂ by He (21 levels; $T = 4\text{--}300$ K); this dataset was calculated with a newly developed PES (Godard Palluet et al. 2022).

8.9. HCN

Six recommended datasets are available for the HCN molecule.

8.9.1. HCN–He

BASECOL2012 already contained the dataset for the excitation of the 26 rotational levels of HCN by He (Dumouchel et al. 2010; Sarrasin et al. 2010). This dataset uses the sophisticated PES of Toczyłowski et al. (2001) and therefore supersedes the calculations by Green & Thaddeus (1974). When hyperfine resolved lines are observed, the dataset of Monteiro & Stutzki (1986) could be used in the absence of other data, though it is not reliable because of the poor PES used in the dynamical calculations. This dataset is currently indicated as non-recommended, and additional calculations of hyperfine rate coefficients should be performed. As an alternative, the rotational rate coefficients of Dumouchel et al. (2010); Sarrasin et al. (2010) could be used to produce hyperfine levels transitions using an IOS approach (Corey & McCourt 1983).

8.9.2. HCN–H₂

The excitation of HCN by para and ortho-H₂ has led to the two datasets (Hernández Vera et al. 2017) of BASECOL2023, that include the excitation of 26 rotational levels of HCN up to 500 K, with calculations based on the PES of Denis-Alpizar et al. (2013). Part of this work is an extension of the work of Hernández Vera et al. (2014), where the excitation of 13 levels by para H₂ below 100 K was calculated, and the data are identical in the overlapping region. The latter dataset (Hernández Vera et al. 2014) is kept in BASECOL2023, as one objective of BASECOL is to curate data published in journals.

Using those highly accurate rate coefficients and an IOS recoupling method, Goicoechea et al. (2022) calculated the hyperfine resolved rate coefficients for HCN in collision with o/p-H₂, the two corresponding datasets (34 levels; $T = 5\text{--}500$ K; Goicoechea et al. 2022) are in BASECOL2023. Those datasets supersede the hyperfine HCN-p-H₂ dataset by Ben Abdallah et al. (2012) calculated with a simpler PES averaged over three orientations of H₂. It was mentioned in Hernández Vera et al. (2014) that the HCN-p-H₂ calculations of Ben Abdallah et al. (2012) led to significant inaccuracies,

in particular at low temperatures. Therefore, the dataset of Ben Abdallah et al. (2012) is labelled as non-recommended.

Finally, for cometary applications, BASECOL2023 was updated with a dataset (Dubernet & Quintas-Sánchez 2019) with thermalised rate coefficients for the de-excitation of HCN (8 levels; $T = 5\text{--}150$ K) by p-H₂O. The calculations use a new 5D PES (Quintas-Sánchez & Dubernet 2017) and the CS method, where the basis sets are not fully converged (about 20%). The thermalised rate coefficients are obtained from the state-to-state rate coefficients summing over the final states of para-H₂O and averaging over the initial rotational states of para-H₂O.

8.10. HNC

Five recommended datasets are available for the HNC molecule for collisions with He and o/p-H₂. BASECOL2012 already included the dataset (Dumouchel et al. 2010; Sarrasin et al. 2010) for the excitation among the 26 rotational levels of HNC by He calculated with the new PES of Sarrasin et al. (2010; $T = 5\text{--}500$ K), and two datasets (Dumouchel et al. 2010) for the rotational de-excitation among eleven rotational levels of HNC by o/p-H₂ ($T = 5\text{--}100$ K). The p-H₂ dataset included the excitation between the ground level and the first excited state of p-H₂, as well as de-excitation of HCN rotational levels for $j = 2$ of p-H₂. The o-H₂ dataset was calculated with an extended basis for H₂ ($j = 1, 3$).

BASECOL2023 has been updated with two datasets (Hernández Vera et al. 2017) for the de-excitation of HNC by p-H₂ ($j = 0$) and o-H₂ ($j = 1$) (26 levels; $T = 5\text{--}500$ K). The p-H₂ dataset was calculated with an extended basis set for p-H₂ ($j = 0, 2$), but the o-H₂ dataset was calculated with o-H₂ ($j = 1$) only. The new datasets (Hernández Vera et al. 2017) are identical or similar for the 11 lowest transitions and for temperatures below 100 K to the previous datasets of Dumouchel et al. (2010) when H₂ stays, respectively, in its lowest level, $j = 0$ or $j = 1$. The datasets of Dumouchel et al. (2010) are recommended as the quality of the data is identical to those of Hernández Vera et al. (2017) for collision with both p-H₂ and o-H₂; in addition, the dataset of Dumouchel et al. (2010) provides information on the behaviour of rate coefficients with $j(\text{H}_2) = 2$.

8.11. HCO⁺, DCO⁺, HC¹⁷O⁺

Three recommended datasets are available for HCO⁺: one for DCO⁺ and one for HC¹⁷O⁺. BASECOL2023 was upgraded with a dataset (Tonolo et al. 2021) for the de-excitation of six rotational levels of HCO⁺ in collision with He ($T = 5\text{--}100$ K) calculated with their new PES (Tonolo et al. 2021) and with two datasets (Denis-Alpizar et al. 2020) for the rotational de-excitation of HCO⁺ by o/p-H₂ (22 levels; $T = 10\text{--}200$ K), calculated with their new 4D PES (Denis-Alpizar et al. 2020). The previous dataset for the de-excitation of HCO⁺ by p-H₂ ($j=0$) from Flower (1999b), which used an old PES (Monteiro 1985), is now outdated because of the quality of the PES, and it is indicated as non-recommended.

A new dataset (Denis-Alpizar et al. 2020) was added for the rotational de-excitation of DCO⁺ in collision with p-H₂ (22 levels; $T = 10\text{--}200$ K) calculated with the same 4D PES (Denis-Alpizar et al. 2020) as HCO⁺-H₂. BASECOL2012 included a low-quality dataset (Pagani et al. 2012) for the hyperfine structure resolved de-excitation of DCO⁺ by p-H₂ obtained with an IOS recoupling technique using the HCO⁺-p-H₂ rotational rate coefficients of Flower (1999b), the latter being now

superseded. Nevertheless, the dataset of [Pagani et al. \(2012\)](#) is left as recommended as it is the only available dataset. However, we would recommend using the newly calculated rotational dataset of $\text{DCO}^+ - \text{p-H}_2$ ([Denis-Alpizar et al. 2020](#)) to calculate new hyperfine rate coefficients for this system. Finally, we have added a dataset ([Tonolo et al. 2022](#)) for the de-excitation among the 33 first hyperfine levels of HC^{17}O^+ with p-H_2 ; in these calculations, the H_2 projectile has been treated as a spherical body and an average of the potential based on five orientations of H_2 has been employed for the scattering calculations.

8.12. HCO

Two recommended datasets are available for the HCO asymmetric open shell molecule. BASECOL2023 was upgraded with two datasets ([Dagdigian 2020b](#)) for the de-excitation among hyperfine resolved rotational levels of HCO by o/p-H_2 (86 levels; $T = 5\text{--}200$ K). Those rate coefficients were obtained with a new PES ([Dagdigian 2020d](#)), the splittings due to the electron spin was treated using a recoupling method, while the splittings due to the nuclear spin was treated with the M_J randomisation approximation ([Alexander & Dagdigian 1985](#)).

8.13. HCP

Two recommended datasets are available for the HCP molecule. BASECOL2012 already had a dataset ([Hammami et al. 2008b](#)) for the rotational de-excitation of HCP by He (16 levels; $T = 20\text{--}200$ K) and a dataset ([Hammami et al. 2008c](#)) for the rotational de-excitation of HCP by p-H_2 (11 levels; $T = 10\text{--}70$ K). In both systems, a new PES was calculated; for the HCP- p-H_2 system, the H_2 projectile was treated as a spherical body and an average of the potential based on five orientations of H_2 was employed for the scattering calculations.

8.14. HCS^+

Two recommended datasets are available for the HCS^+ molecule. BASECOL2023 was updated with a dataset ([Dubernet et al. 2015](#)) for the rotational de-excitation of HCS^+ by He (20 levels; $T = 5\text{--}100$ K) calculated with a new PES ([Dubernet et al. 2015](#)). This dataset supersedes the dataset of [Monteiro \(1984\)](#) because of better quality of the PES and of the dynamical calculations, the dataset of [Monteiro \(1984\)](#) is indicated as non-recommended.

A new dataset ([Denis-Alpizar et al. 2022](#)) for the rotational de-excitation of HCS^+ by p-H_2 has been added; this dataset has been obtained with a new PES ([Quintas-Sánchez et al. 2021](#)). The authors mention that this dataset can be used for collisions with o-H_2 to a good approximation.

8.15. H_2O

Twenty-two recommended datasets are currently available for the H_2O molecule.

8.15.1. $\text{H}_2\text{O-He}$

BASECOL2023 was updated with two datasets ([Yang et al. 2013](#)) for the de-excitation of rotational levels of $\text{o/p-H}_2\text{O}$ by He (10 levels; $T = 2\text{--}3000$ K); these calculations have used the PES from [Patkowski et al. \(2002\)](#). BASECOL2012 already had the two datasets (45 levels; $T = 20\text{--}2000$ K) from [Green et al. \(1993\)](#) that had been calculated with the PES of

[Maluendes et al. \(1992\)](#). Those datasets are still marked as recommended as they span more transitions, and the agreement between both sets are reasonably good, see Fig. C.4. However, at low temperatures, the data of [Yang et al. \(2013\)](#) show significant differences with the previous rates.

8.15.2. H_2O with o/p-H_2 and thermalised H_2

There are three types of calculation for the rotational de-excitation of H_2O with H_2 : highly accurate quantum calculations (mostly CC calculations; [Daniel et al. 2011, 2010](#); [Dubernet et al. 2009](#)), quasi-classical calculations (QCT; [Faure et al. 2007a](#)), and more approximate quantum CS calculations ([Żóltowski et al. 2021](#)) that provide rate coefficients among twice the number of rotational levels than the two other sets of calculations.

BASECOL2012 contained the four state-to-state rate coefficients datasets ([Daniel et al. 2011, 2010](#); [Dubernet et al. 2009](#)) for the rotational de-excitation of $\text{o/p-H}_2\text{O}$ by $\text{o/p-H}_2(j)$ (45 levels; $T = 5\text{--}1500$ K) where the transitions among H_2 levels have been considered up to $j(\text{H}_2) = 4$ for some water transitions; those datasets have been obtained with a 5D average of the 9D PES of [Valiron et al. \(2008\)](#) and quantum calculations (mostly close coupling) for the dynamics of the nuclei. [Daniel et al. \(2011\)](#) completed calculations of respectively [Dubernet et al. \(2009\)](#) and [Daniel et al. \(2010\)](#). A package is distributed in the ‘tools’ section of the BASECOL website in order to calculate effective and thermalised rate coefficients. Those results superseded the four datasets (5 levels; $T = 20\text{--}140$ K) of [Phillips et al. \(1996\)](#) calculated with the PES of [Phillips et al. \(1994\)](#), which are now marked as non-recommended.

BASECOL2012 contained four datasets ([Faure et al. 2007a](#)) calculated with a 5D average of the 9D PES of [Valiron et al. \(2008\)](#) and with quasi-classical trajectories (45 levels; $T = 20\text{--}2000$ K). Though those data have been obtained with a less precise method than the results of [Daniel et al. \(2011, 2010\)](#); [Dubernet et al. \(2009\)](#), and though they might show differences of as much as a factor of three, they are still marked as recommended as an alternative choice for users.

BASECOL2023 was updated with two datasets ([Żóltowski et al. 2021](#)) for the rotational de-excitation of $\text{o/p-H}_2\text{O}$ by p-H_2 (97 levels; $T = 10\text{--}2000$ K). The authors used the 5D average of the 9D PES of [Valiron et al. \(2008\)](#), but this potential was further approximated using the adiabatic hinder rotor approximation proposed by [Scribano et al. \(2012\)](#), reducing its dimensionality to 3D, where the H_2 molecule is treated as a pseudo-atom. The authors indicate that the precision of the rate coefficients can be between a factor of two and three compared to quantum close coupling calculations using a full 5D PES. The datasets are nevertheless marked recommended, as they provide a very large extension in the number of transitions. BASECOL2012 contained two datasets ([Faure et al. 2007a](#)) calculated with the 9D PES of [Valiron et al. \(2008\)](#) for the ro-vibrational de-excitation of $\text{o/p-H}_2\text{O}$ with fully thermalised H_2 (411 levels; $T = 200\text{--}5000$ K).

8.15.3. $\text{H}_2\text{O-H}$

BASECOL2023 was updated with two datasets ([Daniel et al. 2015](#)) for the rotational de-excitation of $\text{o/p-H}_2\text{O}$ by H (45 levels; $T = 5\text{--}1500$ K). These datasets were obtained with the PES of [Dagdigian & Alexander \(2013\)](#).

8.15.4. H₂O–H₂O

BASECOL2023 has been updated with four datasets for the rotational de-excitation of o/p-H₂O by thermalised H₂O; those datasets are intended for cometary and planetary atmospheres applications. Two datasets (Boursier et al. 2020) for transitions among 59 o/p-H₂O levels ($T = 100\text{--}800\text{ K}$) have been obtained with a crude PES and with semi-classical calculations; two other datasets (Mandal & Babikov 2023a) for transitions among 21/22 o/p-H₂O levels ($T = 5\text{--}1000\text{ K}$) were obtained with the MQCT method (Mandal & Babikov 2023b; Mandal et al. 2022), a truncated expansion of the PES of Jankowski & Szalewicz (2005) and extrapolations of cross-sections at low and high collision energy. All of these datasets were obtained using approximate scattering methods that involve the symmetrisation of cross-sections computed for excitation and quenching to ensure that the final data satisfy the principle of detailed balance, as explained in detail in the references cited (Boursier et al. 2020; Mandal & Babikov 2023a).

8.16. D₂O, HDO

Two recommended datasets are currently available for the D₂O molecule, and three are available for the HDO molecule. BASECOL2023 was updated with two datasets (Faure et al. 2012) for the rotational de-excitation of o/p-D₂O by p-H₂ (6 levels; $T = 5\text{--}100\text{ K}$); these datasets were obtained with the PES of Valiron et al. (2008) and with quantum calculations for the dynamics of the nuclei.

BASECOL2012 already included a dataset (Green 1989) for the rotational de-excitation of HDO by He (34 levels; $T = 50\text{--}500\text{ K}$). BASECOL2023 has been updated with two datasets (Faure et al. 2012); one dataset provides thermalised rotational de-excitation rate coefficients of HDO by p-H₂ (30 levels; $T = 5\text{--}300\text{ K}$) and the other includes rotational de-excitation rate coefficients of HDO by o-H₂ ($j = 1$). These datasets were obtained with the PES of Valiron et al. (2008) and with quantum calculations for the dynamics of the nuclei.

8.17. H₂S

Four recommended datasets are available for the closed-shell asymmetric H₂S molecule. BASECOL2023 was updated with four datasets (Dagdigian 2020a) for the rotational de-excitation of o/p-H₂S by o/p-H₂ (19 levels; $T = 5\text{--}500\text{ K}$). These datasets were calculated with a new 4D PES (Dagdigian 2020c).

8.18. MgCN, MgNC

Two recommended datasets are available for MgCN, and there are two for MgNC. BASECOL2023 was updated with two datasets (Hernández Vera et al. 2013) concerning the rotational de-excitation by He among the 36 rotational levels of MgCN and of MgNC ($T = 5\text{--}100\text{ K}$) and with two datasets (Hernández Vera et al. 2013) for the de-excitation among the fine resolved structures of MgCN and MgNC ($T = 5\text{--}100\text{ K}$). The de-excitation among fine levels uses a recoupling technique based on the IOS approximation (Corey & McCourt 1983).

8.19. NH₂

Four recommended datasets are available for the asymmetric open shell NH₂ (X^2B_1) molecule.

The NH₂ (X^2B_1) molecule presents a fine and hyperfine structure, but presently no collisional studies including either the electronic or the nuclear spins have been performed. BASECOL2023 was updated with four datasets (Bouhafs et al. 2017a) for the de-excitation among 15 spin free rotational levels of p-NH₂ and o-NH₂ by o/p-H₂ ($T = 10\text{--}150\text{ K}$); these datasets were obtained with a 4D PES (Bouhafs et al. 2017a) constructed from the 9D global PES of the ground electronic state of NH₄ (Li & Guo 2014).

8.20. N₂H⁺

Four recommended datasets are available for the N₂H⁺ molecule. BASECOL2012 already included two datasets (Daniel et al. 2005) calculated with a new PES (Daniel et al. 2004) for the de-excitation among seven rotational and among 55 hyperfine levels of N₂H⁺ by He. The dataset of Green (1975) was superseded and is labelled as non-recommended.

BASECOL2023 was updated with a dataset (Balança et al. 2020) for the de-excitation among 26 rotational levels of N₂H⁺ by p-H₂ ($T = 5\text{--}500\text{ K}$). The data were obtained with the adiabatic hindered rotor (AHR) approach (Li et al. 2010; Zeng et al. 2011), which reduced the 4D PES of Spielfiedel et al. (2015) to a 2D PES, and thus did not take into account the structure of the H₂ projectile. In addition, BASECOL2023 was updated with a dataset (Lique et al. 2015) for the de-excitation among 64 hyperfine levels of N₂H⁺ by p-H₂. This dataset was obtained with the same AHR approach, the same PES (Spielfiedel et al. 2015), and with a recoupling technique (Daniel et al. 2004).

8.21. OCS

Three recommended datasets are available for the OCS molecule. New work is certainly needed for this molecule. BASECOL2012 already included a dataset (Green & Chapman 1978) for the rotational de-excitation of OCS by p-H₂ (13 levels; $T = 10\text{--}100\text{ K}$), and a dataset (Flower 2001b) for the rotational de-excitation of OCS by He (27 levels; $T = 10\text{--}150\text{ K}$). The dataset with p-H₂ was obtained with a very crude PES and the CS method. BASECOL2023 was updated with a dataset (Chefai et al. 2018) for the de-excitation of OCS by Ar, for which a new PES was calculated (Chefai et al. 2018).

8.22. o-SiC₂

One recommended dataset is available for the o-SiC₂ molecule. BASECOL2012 already included a dataset (Chandra & Kegel 2000) for the rotational de-excitation of o-SiC₂ by He (40 levels; $T = 25\text{--}125\text{ K}$). The authors used an infinite order sudden approximation method, extended the work of Palma & Green (1987), and claimed that their results applied to the H₂ projectile. We re-did the calculations, and it is clear that their results correspond to a collision with He.

8.23. SO₂

Three recommended datasets are available for the SO₂ molecule. BASECOL2012 already included a dataset (Green 1995) for the rotational de-excitation of SO₂ by He (50 levels; $T = 25\text{--}125\text{ K}$) with the PES of Palma (1987) and an IOS method. BASECOL2012 included two datasets (Cernicharo et al. 2011) for the de-excitation of SO₂ by o/p-H₂ (31 levels; $T = 5\text{--}30\text{ K}$). These datasets were obtained with a 5D PES from Spielfiedel et al. (2009) and with the close coupling method.

9. Molecules with more than three atoms with heavy partners

The general table (Table B.5) presents collisional datasets for 26 molecules with more than three atoms.

9.1. C_3H_2

Two recommended datasets are available for the C_3H_2 molecule. BASECOL2012 already included a dataset (Chandra & Kegel 2000) for the rotational de-excitation of o/p- C_3H_2 by He (47/48 levels; $T = 30$ –120 K). The authors used the IOS method, extended the work of Green et al. (1987), and claimed that their excitation rate coefficients applied to the H_2 projectile. We re-did the calculations and it is clear that their results correspond to a collision with He. The current datasets provide the de-excitation rate coefficients obtained by detailed balance using the JPL database (Pearson et al. 2010) spectroscopic data. It should be noted that more precise datasets were calculated by Avery & Green (1989), but for fewer levels. They provided CS rate coefficients among the 16 lowest ortho levels and the 17 lowest para levels for three temperatures ($T = 10, 20, 30$ K); they used the same PES (Green et al. 1987). The latter calculation is not in BASECOL.

9.2. C_3O, C_3S

One recommended dataset is available for C_3O and one for C_3S . BASECOL2023 was updated with a dataset (Bop et al. 2022b) for the rotational de-excitation of C_3O by He (31 levels; $T = 5$ –150 K) calculated with the PES of Khadri & Hammami (2019), and a dataset (Sahnoun et al. 2020) for the rotational de-excitation of C_3S by He (11 levels; $T = 2$ –25 K); in the latter calculation the authors calculated a new PES.

9.3. C_4

One recommended dataset is available for the C_4 ($X^3\Sigma_g^-$) molecule. BASECOL2012 already included a dataset (Lique et al. 2010a) for the fine structure resolved rotational de-excitation of C_4 by He (30 levels; $T = 5$ –50 K). The authors calculated a new PES.

9.4. C_4H^-

Two recommended datasets are available for the C_4H^- molecular ion. BASECOL2023 was updated with two datasets (Balança et al. 2021) for the rotational de-excitation of C_4H^- by o/p- H_2 (30 levels; $T = 5$ –100 K). A new PES was calculated by the authors.

9.5. C_5, C_5O, C_5S

One recommended dataset is available for C_5 , one is available for C_5O , and one is available for C_5S . BASECOL2023 was updated with a dataset (Chefai et al. 2021) for the rotational de-excitation of C_5 by He (15 levels; $T = 5$ –300 K) and a dataset (Khadri et al. 2020) for the rotational de-excitation of C_5S by He (51 levels; $T = 2$ –100 K). In both cases the respective authors calculated a new PES. In addition, it has been updated with a dataset (Bop et al. 2022b) for the rotational de-excitation of C_5O by He (31 levels; $T = 5$ –150 K). These calculations were performed with the PES of Khadri et al. (2022a).

9.6. C_5H^+

One recommended dataset is available for the C_5H^+ molecular ion. BASECOL2023 has been updated with a dataset (Khadri et al. 2023) for the rotational de-excitation of C_5H^+ by He (16 levels; $T = 5$ –100 K). The authors calculated a new 2D PES. This calculation follows the recent discovery of this new molecule in TMC-1 (Cernicharo et al. 2022).

9.7. C_6H^-, C_6H

Two recommended datasets are available for C_6H ($^2\Pi$) and three for C_6H^- . BASECOL2023 was updated with two datasets (Walker et al. 2018): one for the fine resolved rotational de-excitation of C_6H by He (122 levels; $T = 5$ –100 K) and one for the hyperfine resolved de-excitation for the same system (52 levels; $T = 5$ –100 K). The authors calculated a new PES.

Three new datasets (Walker et al. 2017) for the excitation of the close-shell anion C_6H^- were added: one dataset for the rotational de-excitation of C_6H^- by He (11 levels; $T = 5$ –100 K) and two datasets for the rotational de-excitation of C_6H^- by o/p- H_2 (31 levels; $T = 5$ –100 K). The three datasets were obtained with a new PES (Walker et al. 2016).

9.8. CH_3CN, CH_3NC

Two recommended datasets are available for CH_3CN and two are available for CH_3NC . BASECOL2023 was updated with four datasets (Ben Khalifa et al. 2023) for the rotational de-excitation of o/p- CH_3CN (52/75 levels; $T = 7$ –100 K) and of o/p- CH_3NC (66/63 levels; $T = 7$ –100 K) by He. These collisional datasets were calculated with the PES of Ben Khalifa et al. (2022).

9.9. CH_3OH

Fourteen recommended datasets are available for CH_3OH ; they handle rotational processes for three torsional states and for ro-torsional processes. The datasets existed in BASECOL2012, but they were very recently imported to BASECOL2023 as we needed to take decisions about the labelling of the energy levels.

The current BASECOL labelling of levels is J, K ($=K_a$), v_t the torsional quantum number, and the ro-torsional symmetry of the wave function (A or E). In addition, for A states the pseudo-parity is indicated by a + or – symbol; this pseudo-parity comes from the two possible linear combinations of basis set functions as explained in Herbst et al. (1984) and Hougen et al. (1994). Therefore, the VAMDC rovibSym label is used as a ro-torsional symmetry label and follows the convention $A+, A-, E1$ (equivalent to “ E with positive K -sign”) and $E2$ (equivalent to “ E with negative K -sign”) with the symmetric quantum numbers J and K (>0). CH_3OH is currently identified by the stcs VAMDC case (see Table A.1), as no other case can fit this description.

Those notations are implicitly used in the traditional output of the JPL (Pearson et al. 2010) database, and both in the traditional and the VAMDC access of the HITRAN database (Gordon et al. 2022). It should be noted that the JPL quantum numbers are incomplete. The rovibSym label is omitted, and the pseudo-parity quantum number is included for the A -symmetry states only. By deduction, the levels without pseudo-parity belong to the E -symmetry, and JPL uses the K -signed notation.

It is possible to use the usual labelling of the C_{3v} symmetry group, that is the asymmetric rotational quantum numbers (J, K_a ($=K$), K_c), the v_t quantum number, and the ro-torsional A or E symmetry. An example of these notations is provided in

the CDMS (Müller et al. 2005) database; these notations imply that their VAMDC output uses an asymmetric top closed shell (asymcs) case.

Hougen et al. (1994) explained how to transform notations from one label to the other. In addition, the supplementary material of Xu et al. (2008) identifies the energy levels with notations that allow to find the two ways of labelling. For A-symmetry the states are identified with $J, K_a = K, K_c, v_t$ and the pseudo-parity; for the E-symmetry, the states are identified with J, K -signed, and K_c, v_t .

9.9.1. CH₃OH-He

Two datasets (Rabli & Flower 2011) are available for the torsional de-excitation of A-CH₃OH and E-CH₃OH by He (150 levels; $T = 10$ –400 K). The authors used the PES of Pottage et al. (2002). Six datasets (Rabli & Flower 2010b) are available for the rotational de-excitation of A/E-CH₃OH by He, with A/E-CH₃OH in respectively the ground, the $v_t = 1$ and the $v_t = 2$ torsional states (256 levels; $T = 10$ –200 K); the authors used the PES of Pottage et al. (2002). It should be noted that those calculations were carried out with a maximum value of $j = 15$, which means that there are missing higher j rotational levels for energy levels lying above 200 cm^{-1} .

9.9.2. CH₃OH-p-H₂

Six datasets (Rabli & Flower 2010a) are available for the rotational de-excitation of A/E-CH₃OH by p-H₂, with A/E-CH₃OH in the ground, the $v_t = 1$, and the $v_t = 2$ torsional states, respectively (256 levels; $T = 10$ –200 K); the authors used the PES of Pottage et al. (2004). Again, it should be noted that those calculations are carried out with a maximum value of $j = 15$, which means that there are missing higher j rotational levels for energy levels lying above 200 cm^{-1} .

9.10. CNCN

One recommended dataset is available for CNCN. BASECOL2023 was updated with a dataset (Ndaw et al. 2021) for the rotational de-excitation of CNCN by He (30 levels; $T = 5$ –150 K); the authors calculated a new PES.

9.11. H₂CO

Four recommended datasets are available for the H₂CO molecule. BASECOL2012 already included two datasets (Green 1991) for the rotational de-excitation of o/p-H₂CO by He (40/41 levels; $T = 10$ –300 K) that used the PES of Garrison & Lester (1975) and two datasets (Troscmidt et al. 2009) for the rotational de-excitation of o-H₂CO by o/p-H₂ (10 levels; $T = 5$ –100 K), where the authors calculated a new PES.

9.12. H₃O⁺

Four recommended datasets are available for the H₃O⁺ molecular ion. BASECOL2023 has been updated with four datasets (Demes et al. 2022) for the rotational de-excitation of the lowest 11 rotation-inversion levels of o-H₃O⁺ with o/p-H₂ and of the 21 lowest rotation-inversion levels of p-H₃O⁺ with o/p-H₂, for temperatures between 10 K and 300 K. The collisional datasets with p-H₂ include calculations described in Demes et al. (2021, 2022), and all four datasets were calculated with the PES of Demes et al. (2020).

9.13. HC₃N

Seven recommended datasets are available for the HC₃N molecule. BASECOL2012 already included a dataset (Wernli et al. 2007a) for the rotational de-excitation of HC₃N by He (11 levels; $T = 10$ –40 K). This dataset is considered to supersede the dataset (21 levels; $T = 10$ –80 K) of Green & Chapman (1978) as the authors (Green & Chapman 1978) used a Gordon-Kim PES (Gordon & Kim 1972) and the dynamics of the collision is treated with the quasi-classical trajectory approach. Therefore, the dataset of Green & Chapman (1978) is marked as non-recommended.

BASECOL2012 included a dataset (Wernli et al. 2007a) for the rotational de-excitation of HC₃N by p-H₂ ($j = 0$) (51 levels; $T = 10$ –100 K). This dataset suffered from errors in the calculations, and the authors (Wernli et al. 2007b) indicated that the uncertainties on rate coefficients might be around 20%. This dataset is now indicated as non-recommended, as new calculations are available.

BASECOL2023 was updated with three datasets (Faure et al. 2016) for the rotational de-excitation of HC₃N by p-H₂ and o-H₂ (38 levels; $T = 10$ –300 K). One dataset presents the state-to-state rate coefficients of HC₃N by p-H₂ in its ground rotational state $j = 0$; a second dataset presents the thermalised rate coefficients of HC₃N by p-H₂; the third dataset corresponds to the state-to-state rate coefficients of HC₃N by o-H₂ ($j = 1$) that can be used as thermalised rate coefficients. The calculations were not performed for $j(\text{H}_2)$ larger than 1; thus, assumptions were performed in order to obtain the thermalised rate coefficients (see Faure et al. 2016 for the methodology used for the thermalisation). It should be noted that close coupling calculations were used below $j(\text{HC}_3\text{N}) = 30$. For HC₃N levels between $j(\text{HC}_3\text{N}) = 31$ and 37, only QCT rate coefficients for para-H₂ ($j = 0$) were available, and this set was employed directly for both para-H₂ and ortho-H₂ (no thermal averaging).

In addition, BASECOL2023 was updated with three datasets (Faure et al. 2016) for the de-excitation among hyperfine resolved rotational levels of HC₃N by p-H₂ and o-H₂ (61 levels; $T = 10$ –100 K). Those datasets were obtained from the above-mentioned three rotational rate coefficient datasets using the scaled-infinite-order-sudden-limit method (Neufeld & Green 1994; Lanza & Lique 2014), which was checked against recoupling calculations.

9.14. HNCCC, HCCNC

Two recommended datasets are available for the HNCCC molecule, and two are available for HCCNC. BASECOL2023 was updated with two datasets (Bop et al. 2021) for the rotational de-excitation of HNCCC by o/p-H₂ (30 levels; $T = 5$ –80 K) and with two datasets (Bop et al. 2021) for the rotational de-excitation of HCCNC by o/p-H₂ (30 levels; $T = 5$ –80 K). The datasets were obtained with a new PES (Bop et al. 2019a).

9.15. HMgNC

One recommended dataset is available for the HMgNC molecule. BASECOL2023 was updated with a dataset (Amor et al. 2021) for the rotational de-excitation of HMgNC by He (14 levels; $T = 5$ –200 K); the authors calculated a new PES.

9.16. HOCO⁺

One recommended dataset is available for the HOCO⁺ molecule. BASECOL2012 already included a dataset (Hammami et al. 2007) for the rotational de-excitation of HOCO⁺ by He

(25 levels; $T = 10\text{--}30\text{ K}$); the dataset was calculated with the PES of Hammami et al. (2004).

9.17. NCCNH^+

One recommended dataset is available for the NCCNH^+ molecule. BASECOL2023 was updated with a dataset (Bop et al. 2018) for the rotational de-excitation of NCCNH^+ by He (11 levels; $T = 5\text{--}100\text{ K}$); the authors calculated a new PES.

9.18. NH_3

Sixteen recommended datasets are available for the NH_3 molecule.

9.18.1. $\text{NH}_3\text{-He}$

BASECOL 2012 already included two datasets (Machin & Roueff 2005) for the rotational de-excitation of o/p- NH_3 by He (22/16 levels; $T = 5\text{--}300\text{ K}$). Those datasets were obtained with the PES of Hodges & Wheatley (2001).

9.18.2. $\text{NH}_3\text{-H}_2$

The first calculations for the excitation of o/p- NH_3 by para- H_2 were performed by Danby et al. (1986, 1987) in the temperature range from 15 K to 300 K, subsequently improved and extended to 17 levels for ortho- NH_3 and to 24 levels for para- NH_3 by Danby et al. (1988). Therefore, the datasets of Danby et al. (1986, 1987) are marked as non-recommended.

The next set of calculations for the excitation of o/p- NH_3 by p- H_2 were performed by Maret et al. (2009) using their newly calculated PES for ten levels of p- NH_3 and six levels of ortho- NH_3 in the temperature range from 5 K to 100 K; those datasets were already in BASECOL2012.

BASECOL2023 was updated with four datasets (Bouhafs et al. 2017b) for the rotational de-excitation of o/p- NH_3 by o/p- H_2 . The work of Bouhafs et al. (2017b) used the same PES (Maret et al. 2009), extended the number of transitions to 17 o- NH_3 and 34 p- NH_3 levels, and increased the temperature range up to 200 K. The calculations of Bouhafs et al. (2017b) are of better quality than those of Danby et al. (1988), as their basis set included the $j(\text{H}_2) = 2$ level for collision with p- H_2 . However, the calculations of Bouhafs et al. (2017b) did not include the temperature $T = 5\text{ K}$.

Very recently and using the same PES (Maret et al. 2009), close coupling calculations were performed up to 500 K by Demes et al. (2023), where most of the rotation-inversion levels of ammonia were considered below the first vibrational excitation threshold, leading to a total of 33 ortho- and 62 para- NH_3 states. Those calculations were carried out with a basis set that includes $j(\text{H}_2) = 0, 2$ for p- H_2 and $j(\text{H}_2) = 1$ for o- H_2 .

Therefore, BASECOL2023 was updated with four datasets (Demes et al. 2023) for the state-to-state rotational de-excitation of o(33 levels)/p(62 levels)- NH_3 by o/p- H_2 between 100 K and 500 K. It should be noted that the two datasets for o/p- NH_3 with p- H_2 include the state-to-state rate coefficients involving all transitions between $j(\text{p-H}_2) = 0$ and $j(\text{p-H}_2) = 2$ (i.e. 0-0, 0-2, 2-0 and 2-2 transitions). In addition, two datasets (Demes et al. 2023) for thermalised rate coefficients of o(33 levels)/p(62 levels)- NH_3 with p-t- H_2 , built upon the previously mentioned state-to-state rate coefficients ($j(\text{H}_2) = 0, 2$), are included.

As a conclusion, we choose to remove the recommendation of the results of Danby et al. (1988), and we kept the datasets of Maret et al. (2009), of Bouhafs et al. (2017b), and of Demes et al. (2023), as recommended. These should overlap and agree in some regions of temperature and transitions. We did this so that the user can access all those data through VAMDC.

9.18.3. $\text{NH}_3\text{-H}$

BASECOL2023 was updated with two datasets (Bouhafs et al. 2017b) for the de-excitation of 34 levels of p- NH_3 by H and for the de-excitation of 17 levels of o- NH_3 by H. They are calculated with the PES of Li & Guo (2014).

9.19. NH_3 isotopologues

Four recommended datasets are available for the NH_2D , four are available for ND_2H , and three are available for ND_3 . BASECOL2012 already included two datasets (Machin & Roueff 2006) for the rotational de-excitation of o/p- NH_2D by He (9 levels; $T = 5\text{--}100\text{ K}$) and two datasets (Machin & Roueff 2007) for the rotational de-excitation of o/p- ND_2H by He (9 levels; $T = 5\text{--}100\text{ K}$). The four datasets were calculated with a modified version of the PES of Hodges & Wheatley (2001) to account for isotopic shift.

BASECOL2023 was updated with two datasets (Daniel et al. 2014) for the rotational de-excitation of o/p- NH_2D by p- H_2 (79 levels; $T = 5\text{--}300\text{ K}$), two datasets (Daniel et al. 2016) for the rotational de-excitation of o/p- ND_2H by p- H_2 (16 levels; $T = 5\text{--}50\text{ K}$), and three datasets (Daniel et al. 2016) for the rotational de-excitation of o/p/meta- ND_3 by p- H_2 (16/9/9 levels; $T = 5\text{--}50\text{ K}$). The seven new datasets were calculated with a modified version of the PES of Maret et al. (2009) to account for isotopic shift. It should be noted that the collisional treatment ignored the para or meta specificity of ND_3 , so the theoretical results for the para and meta spin isomers are identical. However, specific calculations were performed for the ortho- ND_3 spin isomer.

10. Other information displayed on the BASECOL website

Two other sections are displayed on the BASECOL website: the contacts section, which provides the information about the maintainers of the BASECOL, and the tools section, where tools sent by producers and by other teams are provided. Currently, there is a package called the water rate package, which makes it possible to use the fitting functions of the $\text{H}_2\text{O-H}_2$ rate coefficients (Daniel et al. 2011, 2010; Dubernet et al. 2009) in order to obtain state to state, effective and thermalised rate coefficients; the package contains an option to create outputs in the RADEX format¹⁵.

A link to the VAMDC SPECTCOL tool is also provided; the aim of the client tool SPECTCOL¹⁶ is to associate spectroscopic data extracted from spectroscopic databases through VAMDC, with collisional data provided by collisional databases. It can also be used to display the extracted spectroscopic data (transitions, energy levels, etc.) and the extracted collisional data. The current features of the SPECTCOL tool are described in a forthcoming publication.

¹⁵ <https://personal.sron.nl/~vdtak/radex/index.shtml>

¹⁶ <https://vamdc.org/activities/research/software/spectcol/>

11. Conclusions

BASECOL2023 gives a wide overview of the field of inelastic rate coefficients, mostly for collisions with heavy projectiles and in the temperature range relevant to the ISM, circumstellar atmospheres, and cometary atmospheres. The numerical data sent by the producers of data are not modified. The producers of data have the right to modify the entries prior to their publication, and even later, as the BASECOL versioning system allows us to keep track of the changes at a fine granularity. BASECOL is one of the 40 interconnected databases of the VAMDC e-infrastructure, which ensures that the data can be easily identified and combined, for example by the SPECTCOL tool, with spectroscopic data from other databases such as the CDMS database (Endres et al. 2016) in order to produce ready-to-use outputs for the modelling of non-LTE media. Users can use the VAMDC standards and the java or python libraries in order to create their own access to BASECOL and to other databases in VAMDC.

From a scientific point of view, our main plan for the future is to maintain and further expand this database including new datasets, which is a challenge in itself. In addition, we plan to introduce technical changes that will, for example, allow the user to select data formats when exporting data and make it easier for data producers to prepare files. However, this idea is still in the making, and once implemented, it will be communicated to the astronomical community.

Finally, we stress that the BASECOL database is an international database that is open to all data producers who have published inelastic rate coefficients that fit within the database format. As mentioned in the introduction, Dr O. Denis-Alpizar is the next manager of the BASECOL database.

Acknowledgements. BASECOL has been supported by the VAMDC consortium and by Paris Astronomical Data Center (PADC) from Paris Observatory. For this paper and for the scientific update of BASECOL2023 M.L.D. thanks her collaborator and co-author Corinne Boursier (CB) for her scientific contributions and support, she has been a key motor for the completion of this work. M.L.D. thanks Otoniel Denis-Alpizar for his decision to take over the scientific leadership of BASECOL, and Yaye Awa Ba and Nicolas Moreau for the long term collaboration and their continuous support to the technical platforms. M.L.D. thanks two post-docs who contributed to the maintenance of the database: Dr Sarandis Marinakis and Dr Fabien Daniel, the latter has left the field of research. We are grateful to one of our co-author, Dr Isabelle Kleiner, for very helpful discussions on the spectroscopy of CH₃OH. The list of co-authors includes the scientific team who maintains the database content, the technical team who designed and maintains the technical platforms, the data providers who provided their data in the requested format, thus contributing to the numerical and text information of the BASECOL database and paper.

References

- Abrahamsson, E., Krems, R. V., & Dalgarno, A. 2007, *ApJ*, 654, 1171
- Albert, D., Antony, B. K., Ba, Y. A., et al. 2020, *Atoms*, 8, 76
- Alexander, M. H., & Dagdigian, P. J. 1985, *J. Chem. Phys.*, 83, 2191
- Alexander, M. H., Rackham, E. J., & Manolopoulos, D. E. 2004, *J. Chem. Phys.*, 121, 5221
- Amor, M. A., Hammami, K., & Wiesenfeld, L. 2021, *MNRAS*, 506, 957
- Avery, L. W., & Green, S. 1989, *ApJ*, 337, 306
- Ba, Y.-A., Dubernet, M.-L., Moreau, N., & Zwölf, C. M. 2020, *Atoms*, 8, 69
- Balakrishnan, N., Forrey, R. C., & Dalgarno, A. 1999a, *ApJ*, 514, 520
- Balakrishnan, N., Vieira, M., Babb, J. F., et al. 1999b, *ApJ*, 524, 1122
- Balakrishnan, N., Yan, M., & Dalgarno, A. 2002, *ApJ*, 568, 443
- Balança, C., & Dayou, F. 2017, *MNRAS*, 469, 1673
- Balança, C., Dayou, F., Faure, A., Wiesenfeld, L., & Feautrier, N. 2018, *MNRAS*, 479, 2692
- Balança, C., Scribano, Y., Loreau, J., Lique, F., & Feautrier, N. 2020, *MNRAS*, 495, 2524
- Balança, C., Quintas-Sánchez, E., Dawes, R., et al. 2021, *MNRAS*, 508, 1148
- Barinovs, G., & van Hemert, M. 2004, *Chem. Phys. Lett.*, 399, 406
- Barinovs, G., van Hemert, M. C., Krems, R., & Dalgarno, A. 2005, *ApJ*, 620, 537
- Ben Abdallah, D., Hammami, K., Najar, F., et al. 2008, *ApJ*, 686, 379
- Ben Abdallah, D., Najar, F., Jaidane, N., Dumouchel, F., & Lique, F. 2012, *MNRAS*, 419, 2441
- Ben Khalifa, M., & Loreau, J. 2021, *MNRAS*, 508, 1908
- Ben Khalifa, M., Dagdigian, P. J., & Loreau, J. 2022, *J. Phys. Chem. A*, 126, 9658
- Ben Khalifa, M., Dagdigian, P., & Loreau, J. 2023, *MNRAS*, 523, 2577
- Bergeat, A., Chefdeville, S., Costes, M., et al. 2018, *Nat. Chem.*, 10, 519
- Bian, W., & Werner, H.-J. 2000, *J. Chem. Phys.*, 112, 220
- Boothroyd, A. I., Keogh, W. J., Martin, P. G., & Peterson, M. R. 1996, *J. Chem. Phys.*, 104, 7139
- Bop, C. T. 2019, *MNRAS*, 487, 5685
- Bop, C. T., Hammami, K., Niane, A., Faye, N. A. B., & Jaidane, N. 2016, *MNRAS*, 465, 1137
- Bop, C. T., Hammami, K., & Faye, N. A. B. 2017, *MNRAS*, 470, 2911
- Bop, C. T., Faye, N. A. B., & Hammami, K. 2018, *MNRAS*, 478, 4410
- Bop, C. T., Batista-Romero, F. A., Faure, A., et al. 2019a, *ACS Earth Space Chem.*, 3, 1151
- Bop, C. T., Faye, N., & Hammami, K. 2019b, *Chem. Phys.*, 519, 21
- Bop, C. T., Lique, F., Faure, A., Quintas-Sánchez, E., & Dawes, R. 2021, *MNRAS*, 501, 1911
- Bop, C., Kalugina, Y., & Lique, F. 2022a, *J. Chem. Phys.*, 156, 204311
- Bop, C. T., Khadri, F., & Hammami, K. 2022b, *MNRAS*, 518, 3533
- Bouhafs, N., Lique, F., Faure, A., et al. 2017a, *J. Chem. Phys.*, 146, 064309
- Bouhafs, N., Rist, C., Daniel, F., et al. 2017b, *MNRAS*, 470, 2204
- Boursier, C., Mandal, B., Babikov, D., & Dubernet, M. L. 2020, *MNRAS*, 498, 5489
- Cabrera-González, L., Mera-Adasme, R., Páez-Hernández, D., & Denis-Alpizar, O. 2018, *MNRAS*, 480, 4969
- Cabrera-González, L., Páez-Hernández, D., & Denis-Alpizar, O. 2020, *MNRAS*, 494, 129
- Cecchi-Pestellini, C., Bodo, E., Balakrishnan, N., & Dalgarno, A. 2002, *ApJ*, 571, 1015
- Cernicharo, J., Spielfiedel, A., Balança, C., et al. 2011, *A&A*, 531, A103
- Cernicharo, J., Agúndez, M., Cabezas, C., et al. 2022, *A&A*, 657, A16
- Chandra, S., & Kegel, W. H. 2000, *A&AS*, 142, 113
- Chefai, A., Jellali, C., Hammami, K., & Aroui, H. 2018, *Astrophys. Space Sci.*, 363, 265
- Chefai, A., Ben Khalifa, M., Khadri, F., & Hammami, K. 2021, *Phys. Chem. Chem. Phys.*, 23, 23741
- Corey, G. C., & McCourt, F. R. 1983, *J. Chem. Phys.*, 87, 2723
- Cybulski, S. M., Toczyłowski, R. R., Lee, H.-S., & McCoy, A. B. 2000, *J. Chem. Phys.*, 113, 9549
- Cybulski, S. M., Krems, R. V., Sadeghpour, H. R., et al. 2005, *J. Chem. Phys.*, 122, 094307
- Dagdigian, P. 2018a, *MNRAS*, 479, 3227
- Dagdigian, P. 2018b, *J. Chem. Phys.*, 148, 024304
- Dagdigian, P. J. 2020a, *MNRAS*, 494, 5239
- Dagdigian, P. J. 2020b, *MNRAS*, 498, 5361
- Dagdigian, P. J. 2020c, *J. Chem. Phys.*, 152, 074307
- Dagdigian, P. J. 2020d, *J. Chem. Phys.*, 152, 224307
- Dagdigian, P. J. 2021a, *MNRAS*, 505, 1987
- Dagdigian, P. J. 2021b, *MNRAS*, 508, 118
- Dagdigian, P. J. 2021c, *Mol. Phys.*, 119, 21
- Dagdigian, P. J. 2022a, *MNRAS*, 518, 5976
- Dagdigian, P. J. 2022b, *J. Chem. Phys.*, 157, 104305
- Dagdigian, P. J., & Alexander, M. H. 2013, *J. Chem. Phys.*, 139, 194309
- Dagdigian, P. J., Klos, J., Warehime, M., & Alexander, M. H. 2016, *J. Chem. Phys.*, 145, 164309
- Danby, G., Flower, D. R., Kochanski, E., Kurdi, L., & Valiron, P. 1986, *J. Phys. B: At. Mol. Opt. Phys.*, 19, 2891
- Danby, G., Flower, D. R., Valiron, P., Kochanski, E., & Kurdi, L. 1987, *J. Phys. B: At. Mol. Opt. Phys.*, 20, 1039
- Danby, G., Flower, D. R., Valiron, P., Schilke, P., & Walmsley, C. M. 1988, *MNRAS*, 235, 229
- Daniel, F., Dubernet, M.-L., & Meuwly, M. 2004, *J. Chem. Phys.*, 121, 4540
- Daniel, F., Dubernet, M.-L., Meuwly, M., Cernicharo, J., & Paganì, L. 2005, *MNRAS*, 363, 1083
- Daniel, F., Dubernet, M.-L., Pacaud, F., & Grosjean, A. 2010, *A&A*, 517, A13
- Daniel, F., Dubernet, M.-L., & Grosjean, A. 2011, *A&A*, 536, A76
- Daniel, F., Faure, A., Wiesenfeld, L., et al. 2014, *MNRAS*, 444, 2544
- Daniel, F., Faure, A., Dagdigian, P. J., et al. 2015, *MNRAS*, 446, 2312
- Daniel, F., Rist, C., Faure, A., et al. 2016, *MNRAS*, 457, 1535
- Dayou, F., & Balança, C. 2006, *A&A*, 459, 297
- Demes, S., Lique, F., Faure, A., & Rist, C. 2020, *J. Chem. Phys.*, 153, 094301
- Demes, S., Lique, F., Faure, A., et al. 2021, *MNRAS*, 509, 1252

- Demes, S., Lique, F., Faure, A., & van der Tak, F. F. S. 2022, *MNRAS*, 518, 3593
- Demes, S., Lique, F., Loreau, J., & Faure, A. 2023, *MNRAS*, 524, 2368
- Denis-Alpizar, O., & Rubayo-Soneira, J. 2019, *MNRAS*, 486, 1255
- Denis-Alpizar, O. & Stoecklin, T. 2015, *MNRAS*, 451, 2986
- Denis-Alpizar, O., Stoecklin, T., Halvick, P., Dubernet, M.-L., & Marinakis, S. 2012, *J. Chem. Phys.*, 137, 234301
- Denis-Alpizar, O., Kalugina, Y., Stoecklin, T., Vera, M. H., & Lique, F. 2013, *J. Chem. Phys.*, 139, 224301
- Denis-Alpizar, O., Stoecklin, T., & Halvick, P. 2014, *J. Chem. Phys.*, 140, 084316
- Denis-Alpizar, O., Inostroza, N., & Castro Palacio, J. 2018a, *MNRAS*, 473, 1438
- Denis-Alpizar, O., Stoecklin, T., Guilloteau, S., & Dutrey, A. 2018b, *MNRAS*, 478, 1811
- Denis-Alpizar, O., Trabelsi, T., Hochlaf, M., & Stoecklin, T. 2018c, *MNRAS*, 475, 783
- Denis-Alpizar, O., Stoecklin, T., Dutrey, A., & Guilloteau, S. 2020, *MNRAS*, 497, 4276
- Denis-Alpizar, O., Quintas-Sánchez, E., & Dawes, R. 2022, *MNRAS*, 512, 5546
- Desrousseaux, B., & Lique, F. 2018, *MNRAS*, 476, 4719
- Desrousseaux, B., & Lique, F. 2020, *J. Chem. Phys.*, 152, 074303
- Desrousseaux, B., Coppola, C. M., Kazandjian, M. V., & Lique, F. 2018, *J. Phys. Chem. A*, 122, 8390
- Desrousseaux, B., Quintas-Sánchez, E., Dawes, R., & Lique, F. 2019, *J. Phys. Chem. A*, 123, 9637
- Desrousseaux, B., Lique, F., Goicoechea, J. R., Quintas-Sánchez, E., & Dawes, R. 2021, *A&A*, 645, A8
- Dubernet, M.-L., & Quintas-Sánchez, E. 2019, *Mol. Astrophys.*, 16, 100046
- Dubernet, M.-L., Daniel, F., Grosjean, A., & Lin, C. Y. 2009, *A&A*, 497, 911
- Dubernet, M. L., Boudon, V., Culhane, J. L., et al. 2010, *JQSRT*, 111, 2151
- Dubernet, M.-L., Alexander, M. H., Ba, Y. A., et al. 2013, *A&A*, 553, A50
- Dubernet, M.-L., Quintas-Sánchez, E., & Tuckey, P. 2015, *J. Chem. Phys.*, 143
- Dubernet, M. L., Antony, B. K., Ba, Y. A., et al. 2016, *J. Phys. B: At. Mol. Opt. Phys.*, 49
- Dubernet, M., Berriman, G., Barklem, P., et al. 2023, in *Proceedings IAU Symposium No. 371*, Busan, Korea, 9–11 August 2022, eds. D. Soderblom, & G. Nave, Honoring Charlotte Moore Sitterly: Astronomical Spectroscopy in the 21st century, S371 (Cambridge University Press, International Astronomical Union), 72
- Dumouchel, F., Faure, A., & Lique, F. 2010, *MNRAS*, 406, 2488
- Dumouchel, F., Klos, J., & Lique, F. 2011, *Phys. Chem. Chem. Phys.*, 13, 8204
- Dumouchel, F., Spielfiedel, A., Senent, M., & Feautrier, N. 2012, *Chem. Phys. Lett.*, 533, 6
- Dumouchel, F., Lique, F., Spielfiedel, A., & Feautrier, N. 2017, *MNRAS*, 471, 1849
- Endres, C. P., Schlemmer, S., Schilke, P., Stutzki, J., & Mueller, H. S. P. 2016, *J. Mol. Spectrosc.*, 327, 95
- Faure, A., & Josselin, E. 2008, *A&A*, 492, 257
- Faure, A., & Tennyson, J. 2001, *MNRAS*, 325, 443
- Faure, A., & Tennyson, J. 2003, *MNRAS*, 340, 468
- Faure, A., Gorfinkiel, J. D., & Tennyson, J. 2004, *MNRAS*, 347, 323
- Faure, A., Crimier, N., Ceccarelli, C., et al. 2007a, *A&A*, 472, 1029
- Faure, A., Varambhia, H. N., Stoecklin, T., & Tennyson, J. 2007b, *MNRAS*, 382, 840
- Faure, A., Wiesenfeld, L., Scribano, Y., & Ceccarelli, C. 2012, *MNRAS*, 420, 699
- Faure, A., Lique, F., & Wiesenfeld, L. 2016, *MNRAS*, 460, 2103
- Faure, A., Lique, F., & Loreau, J. 2020, *MNRAS*, 493, 776
- Flower, D. R. 1999a, *J. Phys. B: At. Mol. Opt. Phys.*, 32, 1755
- Flower, D. R. 1999b, *MNRAS*, 305, 651
- Flower, D. R. 2001a, *J. Phys. B: At. Mol. Opt. Phys.*, 34, 2731
- Flower, D. R. 2001b, *MNRAS*, 328, 147
- Flower, D. R., & Lique, F. 2015, *MNRAS*, 446, 1750
- Flower, D. R., & Roueff, E. 1998a, *J. Phys. B: At. Mol. Opt. Phys.*, 31, 2935
- Flower, D. R., & Roueff, E. 1998b, *J. Phys. B: At. Mol. Opt. Phys.*, 31, L955
- Flower, D. R., & Roueff, E. 1999a, *MNRAS*, 309, 833
- Flower, D. R., & Roueff, E. 1999b, *J. Phys. B: At. Mol. Opt. Phys.*, 32, 3399
- Flower, D. R., Roueff, E., & Zeippen, C. J. 1998, *J. Phys. B: At. Mol. Opt. Phys.*, 31, 1105
- Forrey, R. C., Balakrishnan, N., Dalgarno, A., & Lepp, S. 1997, *ApJ*, 489, 1000
- Franz, J., Mant, B. P., González-Sánchez, L., Wester, R., & Gianturco, F. A. 2020, *J. Chem. Phys.*, 152, 234303
- García-Vázquez, R. M., Márquez-Mijares, M., Rubayo-Soneira, J., & Denis-Alpizar, O. 2019, *A&A*, 631, A86
- Garrison, B. J., & Lester, W. A. 1975, *J. Chem. Phys.*, 63, 1449
- Gianturco, F. A., González-Sánchez, L., Mant, B. P., & Wester, R. 2019, *J. Chem. Phys.*, 151, 144304
- Godard Palluet, A., Thibault, F., & Lique, F. 2022, *J. Chem. Phys.*, 156, 104303
- Goicoechea, J. R., Lique, F., & Santa-Maria, M. G. 2022, *A&A*, 658, A28
- González-Sánchez, L., Mant, B. P., Wester, R., & Gianturco, F. A. 2020, *ApJ*, 897, 75
- González-Sánchez, L., Yurtsever, E., Mant, B. P., Wester, R., & Gianturco, F. A. 2021, *Phys. Chem. Chem. Phys.*, 23, 7703
- Gordon, R. G., & Kim, Y. S. 1972, *J. Chem. Phys.*, 56, 3122
- Gordon, I., Rothman, L., Hargreaves, R., et al. 2022, *JQSRT*, 277, 107949
- Green, S. 1975, *ApJ*, 201, 366
- Green, S. 1989, *ApJS*, 70, 813
- Green, S. 1991, *ApJS*, 76, 979
- Green, S. 1994, *ApJ*, 434, 188
- Green, S. 1995, *ApJS*, 100, 213
- Green, S., & Chapman, S. 1978, *ApJS*, 37, 169
- Green, S., & Thaddeus, P. 1974, *ApJ*, 191, 653
- Green, S., Defrees, D. J., & McLean, A. D. 1987, *ApJS*, 65, 175
- Green, S., Maluendes, S., & McLean, A. D. 1993, *ApJS*, 85, 181
- Groenenboom, G. C., & Struniewicz, I. M. 2000, *J. Chem. Phys.*, 113, 95621
- Guillon, G., & Stoecklin, T. 2012, *MNRAS*, 420, 579
- Hammami, K., Jaidane, N., Spielfiedel, A., & Feautrier, N. 2004, *J. Chem. Phys.*, 121, 1325
- Hammami, K., Lique, F., Jaidane, N., et al. 2007, *A&A*, 462, 789
- Hammami, K., Owono Owono, L., Jaidane, N., & Ben Lakhdar, Z. 2008a, *J. Mol. Struct.: THEOCHEM*, 853, 18
- Hammami, K., Owono Owono, L. C., Jaidane, N. J., & Ben Lakhdar, Z. 2008b, *J. Mol. Struct.: THEOCHEM*, 860, 45
- Hammami, K., Nkem, C., Owono Owono, L. C., Jaidane, N., & Ben Lakhdar, Z. 2008c, *J. Chem. Phys.*, 129, 204305
- Hammami, K., Owono Owono, L. C., & Stäuber, P. 2009, *A&A*, 507, 1083
- Heijmen, T. G. A., Moszynski, R., Wormer, P. E. S., & van der Avoird, A. 1997, *J. Chem. Phys.*, 107, 9921
- Herbst, E., Messer, J., De Lucia, F., & Helminger, P. 1984, *J. Mol. Spectrosc.*, 108, 42
- Hernández, M. I., Tejada, G., Fernández, J. M., & Montero, S. 2021, *A&A*, 647, A155
- Hernández Vera, M., Lique, F., Dumouchel, F., et al. 2013, *MNRAS*, 432, 468
- Hernández Vera, M., Kalugina, Y., Denis-Alpizar, O., Stoecklin, T., & Lique, F. 2014, *J. Chem. Phys.*, 140, 224302
- Hernández Vera, M., Lique, F., Dumouchel, F., Hily-Blant, P., & Faure, A. 2017, *MNRAS*, 468, 1084
- Higgins, K., & Klemperer, W. 1999, *J. Chem. Phys.*, 110, 1383
- Hodges, M. P., & Wheatley, R. J. 2001, *J. Chem. Phys.*, 114, 8836
- Hougen, J., Kleiner, I., & Godefroid, M. 1994, *J. Mol. Spectrosc.*, 163, 559
- Jankowski, P., & Szalewicz, K. 1998, *J. Chem. Phys.*, 108, 3554
- Jankowski, P., & Szalewicz, K. 2005, *J. Chem. Phys.*, 123, 104301
- Jaquet, R., Staemmler, V., Smith, M. D., & Flower, D. R. 1992, *J. Phys. B: At. Mol. Opt. Phys.*, 25, 285
- Kalamos, A., Mavridis, A., & Metropoulos, A. 1999, *J. Chem. Phys.*, 111, 9536
- Kalugina, Y., & Lique, F. 2015, *MNRAS*, 446, L21
- Kalugina, Y., Alpizar, O. D., Stoecklin, T., & Lique, F. 2012a, *Phys. Chem. Chem. Phys.*, 14, 16458
- Kalugina, Y., Lique, F., & Klos, J. 2012b, *MNRAS*, 2545
- Kalugina, Y., Klos, J., & Lique, F. 2013, *J. Chem. Phys.*, 139, 074301
- Kalugina, Y., Lique, F., & Marinakis, S. 2014, *Phys. Chem. Chem. Phys.*, 16, 13500
- Kalugina, Y. N., Faure, A., van der Avoird, A., Walker, K., & Lique, F. 2018, *Phys. Chem. Chem. Phys.*, 20, 5469
- Keller, H.-M., Floethmann, H., Dobbyn, A. J., et al. 1996, *J. Chem. Phys.*, 105, 4983
- Khadri, F., & Hammami, K. 2019, *Phys. Chem. Chem. Phys.*, 21, 4606
- Khadri, F., Chefai, A., & Hammami, K. 2020, *MNRAS*, 498, 5159
- Khadri, F., Chefai, A., & Hammami, K. 2022a, *MNRAS*, 513, 4573
- Khadri, F., Hachani, L., Elabidi, H., & Hammami, K. 2022b, *MNRAS*, 513, 6152
- Khadri, F., Elabidi, H., & Hammami, K. 2023, *MNRAS*, 522, 4038
- Klos, J., & Lique, F. 2008, *MNRAS*, 390, 239
- Klos, J., & Lique, F. 2011, *MNRAS*, 418, 271
- Klos, J., Chalasinski, G., Berry, M. T., Bukowski, R., & Cybulski, S. M. 2000, *J. Chem. Phys.*, 112, 2195
- Klos, J., Lique, F., & Alexander, M. H. 2007, *Chem. Phys. Lett.*, 445, 12
- Klos, J., Lique, F., & Alexander, M. H. 2008, *Chem. Phys. Lett.*, 455, 1
- Klos, J., Lique, F., & Alexander, M. H. 2009, *Chem. Phys. Lett.*, 476, 135
- Klos, J., Ma, Q., Alexander, M. H., & Dagdigian, P. J. 2017a, *J. Chem. Phys.*, 146, 114301
- Klos, J., Ma, Q., Dagdigian, P. J., et al. 2017b, *MNRAS*, 471, 4249
- Klos, J., Dagdigian, P., & Lique, F. 2020a, *MNRAS*, 501, L38
- Klos, J., Dagdigian, P. J., Alexander, M. H., Faure, A., & Lique, F. 2020b, *MNRAS*, 493, 3491
- Lanza, M., & Lique, F. 2012, *MNRAS*, 424, 1261
- Lanza, M., & Lique, F. 2014, *J. Chem. Phys.*, 141, 164321

- Lanza, M., Kalugina, Y., Wiesenfeld, L., Faure, A., & Lique, F. 2014a, *MNRAS*, **443**, 3351
- Lanza, M., Kalugina, Y., Wiesenfeld, L., & Lique, F. 2014b, *J. Chem. Phys.*, **140**, 064316
- Launay, J. M., & Roueff, E. 1977, *A&A*, **56**, 289
- Lee, H., McCoy, A. B., Toczylowski, R. R., & Cybulski, S. M. 2000, *J. Chem. Phys.*, **113**, 5736
- Li, J., & Guo, H. 2014, *Phys. Chem. Chem. Phys.*, **16**, 6753
- Li, G., Werner, H.-J., Lique, F., & Alexander, M. H. 2007, *J. Chem. Phys.*, **127**, 174302
- Li, H., Roy, P. N., & Le Roy, R. J. 2010, *J. Chem. Phys.*, **133**, 104305
- Lim, A. J., Rabadán, I., & Tennyson, J. 1999, *MNRAS*, **306**, 473
- Lique, F. 2010, *J. Chem. Phys.*, **132**, 044311
- Lique, F., & Faure, A. 2017, *MNRAS*, **472**, 738
- Lique, F., & Klos, J. 2011, *MNRAS*, **413**, L20
- Lique, F., & Spielfiedel, A. 2007, *A&A*, **462**, 1179
- Lique, F., Spielfiedel, A., Dubernet, M.-L., & Feautrier, N. 2005, *J. Chem. Phys.*, **123**, 134316
- Lique, F., Dubernet, M.-L., Spielfiedel, A., & Feautrier, N. 2006a, *A&A*, **450**, 399
- Lique, F., Spielfiedel, A., & Cernicharo, J. 2006b, *A&A*, **451**, 1125
- Lique, F., Spielfiedel, A., Dhont, G., & Feautrier, N. 2006c, *A&A*, **458**, 331
- Lique, F., Senent, M.-L., Spielfiedel, A., & Feautrier, N. 2007, *J. Chem. Phys.*, **126**, 164312
- Lique, F., Klos, J., & Hochlaf, M. 2010a, *Phys. Chem. Chem. Phys.*, **12**, 15672
- Lique, F., Spielfiedel, A., Feautrier, N., et al. 2010b, *J. Chem. Phys.*, **132**, 024303
- Lique, F., Honvault, P., & Faure, A. 2012, *J. Chem. Phys.*, **137**, 154303
- Lique, F., Daniel, F., Pagani, L., & Feautrier, N. 2015, *MNRAS*, **446**, 1245
- Lique, F., Klos, J., Alexander, M. H., Le Picard, S. D., & Dagdigan, P. J. 2017, *MNRAS*, **474**, 2313
- Lique, F., Klos, J., & Le Picard, S. D. 2018, *Phys. Chem. Chem. Phys.*, **20**, 5427
- Loreau, J., Lique, F., & Faure, A. 2018, *ApJ*, **853**, L5
- Loreau, J., Kalugina, Y. N., Faure, A., van der Avoird, A., & Lique, F. 2020, *J. Chem. Phys.*, **153**, 214301
- Loreau, J., Faure, A., & Lique, F. 2022, *MNRAS*, **516**, 5964
- Ma, Q., Klos, J., Alexander, M. H., van der Avoird, A., & Dagdigan, P. J. 2014, *J. Chem. Phys.*, **141**, 174309
- Machin, L., & Roueff, E. 2005, *J. Phys. B: At. Mol. Opt. Phys.*, **38**, 1519
- Machin, L., & Roueff, E. 2006, *A&A*, **460**, 953
- Machin, L., & Roueff, E. 2007, *A&A*, **465**, 647
- Maluendes, S., McLean, A. D., & Green, S. 1992, *J. Chem. Phys.*, **96**, 8150
- Mandal, B., & Babikov, D. 2023a, *A&A*, **678**, A51
- Mandal, B., & Babikov, D. 2023b, *A&A*, **671**, A51
- Mandal, B., Joy, C., Bostan, D., Eng, A., & Babikov, D. 2022, *J. Phys. Chem. Lett.*, **14**, 817
- Mant, B. P., Gianturco, F. A., González-Sánchez, L., Yurtsever, E., & Wester, R. 2020a, *J. Phys. B: At. Mol. Opt. Phys.*, **53**, 025201
- Mant, B. P., Gianturco, F. A., Wester, R., Yurtsever, E., & González-Sánchez, L. 2020b, *Phys. Rev. A*, **102**, 062810
- Mant, B. P., Gianturco, F. A., Wester, R., Yurtsever, E., & González-Sánchez, L. 2020c, *J. Int. Mass Spectrom.*, **457**, 116426
- Mant, B. P., Yurtsever, E., González-Sánchez, L., Wester, R., & Gianturco, F. A. 2021, *J. Chem. Phys.*, **154**, 084305
- Maret, S., Faure, A., Scifoni, E., & Wiesenfeld, L. 2009, *MNRAS*, **399**, 425
- Marinakakis, S., Dean, I. L., Klos, J., & Lique, F. 2015, *Phys. Chem. Chem. Phys.*, **17**, 21583
- Marinakakis, S., Kalugina, Y., Klos, J., & Lique, F. 2019, *A&A*, **629**, A130
- Mielke, S. L., Garrett, B. C., & Peterson, K. A. 2002, *J. Chem. Phys.*, **116**, 4142
- Monteiro, T. 1984, *MNRAS*, **210**, 1
- Monteiro, T. S. 1985, *MNRAS*, **214**, 419
- Monteiro, T. S., & Stutzki, J. 1986, *MNRAS*, **221**, 33P
- Moszynski, R., Wormer, P. E. S., Jeziorski, B., & van der Avoird, A. 1994, *J. Chem. Phys.*, **101**, 2811
- Muchnick, P., & Russek, A. 1994, *J. Chem. Phys.*, **100**, 4336
- Müller, H. S. P., Schlöder, F., Stutzki, J., & Winnewisser, G. 2005, *J. Mol. Struct.*, **742**, 215
- Murdachaw, G., Szalewicz, K., Jiang, H., & Bačić, Z. 2004, *J. Chem. Phys.*, **121**, 11839
- Najar, F., Ben Abdallah, D., Spielfiedel, A., et al. 2014, *Chem. Phys. Lett.*, **614**, 251
- Najar, F., Nouai, M., ElHanini, H., & Jaidane, N. 2017, *MNRAS*, **472**, 2919
- Ndaw, D., Bop, C. T., Dieye, G., Faye, N. B., & Lique, F. 2021, *MNRAS*, **503**, 5976
- Neufeld, D. A., & Green, S. 1994, *ApJ*, **432**, 158
- Nkem, C., Hammami, K., Manga, A., et al. 2009, *J. Mol. Struct.: THEOCHEM*, **901**, 220
- Nolte, J. L., Stancil, P. C., Lee, T.-G., Balakrishnan, N., & Forrey, R. C. 2011, *ApJ*, **744**, 62
- Offer, A. R., van Hemert, M. C., & van Dishoeck, E. F. 1994, *J. Chem. Phys.*, **100**, 362
- Pagani, L., Bourgoïn, A., & Lique, F. 2012, *A&A*, **548**, A4
- Palma, A. 1987, *ApJS*, **64**, 565
- Palma, A., & Green, S. 1987, *ApJ*, **316**, 830
- Palma, A., Green, S., Defrees, D. J., & McLean, A. D. 1988, *J. Chem. Phys.*, **89**, 1401
- Parlant, G., & Yarkony, D. R. 1999, *J. Chem. Phys.*, **110**, 363
- Patkowski, K., Brudermann, J., Steinbach, C., Buck, U., & Moszynski, R. 2002, *J. Chem. Phys.*, **117**, 11166
- Patkowski, K., Cencek, W., Jankowski, P., et al. 2008, *J. Chem. Phys.*, **129**, 094304
- Pearson, J. C., Mueller, H. S. P., Pickett, H. M., Cohen, E. A., & Drouin, B. J. 2010, *JQSRT*, **111**, 1614
- Phillips, T. R., Maluendes, S., McLean, A. D., & Green, S. 1994, *J. Chem. Phys.*, **101**, 5824
- Phillips, T. R., Maluendes, S., & Green, S. 1996, *ApJS*, **107**, 467
- Pirlot Jankowiak, P., Lique, F., & Dagdigan, P. 2023a, *MNRAS*, **523**, 3732
- Pirlot Jankowiak, P., Lique, F., & Dagdigan, P. J. 2023b, *MNRAS*, **526**, 885
- Pottage, J. T., Flower, D. R., & Davis, S. L. 2002, *J. Phys. B: At. Mol. Opt. Phys.*, **35**, 2541
- Pottage, J. T., Flower, D. R., & Davis, S. L. 2004, *MNRAS*, **352**, 39
- Price, T. J., Forrey, R. C., Yang, B., & Stancil, P. C. 2021, *J. Chem. Phys.*, **154**, 034301
- Quintas-Sánchez, E., & Dubernet, M.-L. 2017, *Phys. Chem. Chem. Phys.*, **19**, 6849
- Quintas-Sánchez, E., Dawes, R., & Denis-Alpizar, O. 2021, *Mol. Phys.*, **119**, e1980234
- Rabadan, I., Sarpal, B. K., & Tennyson, J. 1998, *MNRAS*, **299**, 171
- Rabli, D., & Flower, D. R. 2010a, *MNRAS*, **406**, 95
- Rabli, D., & Flower, D. R. 2010b, *MNRAS*, **403**, 2033
- Rabli, D., & Flower, D. R. 2011, *MNRAS*, **411**, 2011
- Ramachandran, C., De Fazio, D., Cavalli, S., Tarantelli, F., & Aquilanti, V. 2009, *Chem. Phys. Lett.*, **469**, 26
- Ramachandran, R., Klos, J., & Lique, F. 2018, *J. Chem. Phys.*, **148**, 084311
- Reese, C., Stoecklin, T., Voronin, A., & Rayez, J. C. 2005, *A&A*, **430**, 1139
- Rinnenthal, J. L., & Gericke, K.-H. 2002, *J. Chem. Phys.*, **116**, 9776
- Roueff, E., & Flower, D. R. 1999, *MNRAS*, **305**, 353
- Roueff, E., & Zeippen, C. J. 1999, *A&A*, **343**, 1005
- Roueff, E., & Zeippen, C. J. 2000, *A&AS*, **142**, 475
- Sahnoun, E., Nkem, C., Naindouba, A., et al. 2018, *Astrophys. Space Sci.*, **363**, 195
- Sahnoun, E., Ben Khalifa, M., Khadri, F., & Hammami, K. 2020, *ApJS*, **365**, 1
- Santander, C., Denis-Alpizar, O., & Cárdenas, C. 2022, *A&A*, **657**, A55
- Sarpal, B. K., & Tennyson, J. 1993, *MNRAS*, **263**, 909
- Sarrasin, E., Abdallah, D. B., Wernli, M., et al. 2010, *MNRAS*, **404**, 518
- Schewe, H. C., Ma, Q., Vanhaecke, N., et al. 2015, *J. Chem. Phys.*, **142**, 204310
- Schröder, K., Staemmler, V., Smith, M. D., Flower, D. R., & Jaquet, R. 1991, *J. Phys. B: At. Mol. Opt. Phys.*, **24**, 2487
- Schwenke, D. W. 1988, *J. Chem. Phys.*, **89**, 2076
- Scribano, Y., Faure, A., & Lavergnat, D. 2012, *J. Chem. Phys.*, **136**, 094109
- Song, L., van der Avoird, A., & Groenenboom, G. C. 2013, *J. Phys. Chem. A*, **117**, 7571
- Song, L., Balakrishnan, N., van der Avoird, A., Karman, T., & Groenenboom, G. C. 2015a, *J. Chem. Phys.*, **142**, 204303
- Song, L., Balakrishnan, N., Walker, K. M., et al. 2015b, *ApJ*, **813**, 96
- Spielfiedel, A., Senent, M.-L., Dayou, F., et al. 2009, *J. Chem. Phys.*, **131**, 014305
- Spielfiedel, A., Feautrier, N., Najar, F., et al. 2012, *MNRAS*, **421**, 1891
- Spielfiedel, A., Feautrier, N., Najar, F., et al. 2013, *MNRAS*, **429**, 923
- Spielfiedel, A., Senent, M. L., Kalugina, Y., et al. 2015, *J. Chem. Phys.*, **143**, 024301
- Staemmler, V., & Flower, D. R. 1991, *J. Phys. B: At. Mol. Opt. Phys.*, **24**, 2343
- Stoecklin, T., & Voronin, A. 2011, *J. Chem. Phys.*, **134**, 204312
- Stoecklin, T., Voronin, A., & Rayez, J. C. 2003, *Chem. Phys.*, **294**, 117
- Stoecklin, T., Denis-Alpizar, O., & Halvick, P. 2015, *MNRAS*, **449**, 3420
- Tennyson, J., & Faure, A. 2019, in *Gas-phase Chemistry in Space: From Elementary Particles to Complex Organic Molecules*, eds. F. Lique, & A. Faure (AAS-IOP Astronomy)
- Toboła, R., Klos, J., Lique, F., Chałasiński, G., & Alexander, M. H. 2007, *A&A*, **468**, 1123
- Toboła, R., Lique, F., Klos, J., & Chałasiński, G. 2008, *J. Phys. B: At. Mol. Opt. Phys.*, **41**, 155702
- Toboła, R., Dumouchel, F., Klos, J., & Lique, F. 2011, *J. Chem. Phys.*, **134**, 024305
- Toczylowski, R. R., Doloresco, F., & Cybulski, S. M. 2001, *J. Chem. Phys.*, **114**, 851
- Tonolo, F., Bizzocchi, L., Melosso, M., et al. 2021, *J. Chem. Phys.*, **155**, 234306

- Tonolo, F., Lique, F., Melosso, M., Pizzarini, C., & Bizzocchi, L. 2022, *MNRAS*, **516**, 2653
- Troscompt, N., Faure, A., Wiesenfeld, L., Ceccarelli, C., & Valiron, P. 2009, *A&A*, **493**, 687
- Turner, B. E., Chan, K.-W., Green, S., & Lubowich, D. A. 1992, *ApJ*, **399**, 114
- Turpin, F., Stoecklin, T., & Voronin, A. 2010, *A&A*, **511**, A28
- Urzúa-Leiva, R., & Denis-Alpizar, O. 2020, *ACS Earth Space Chem.*, **4**, 2384
- Valiron, P., Wernli, M., Faure, A., et al. 2008, *J. Chem. Phys.*, **129**, 134306
- van der Tak, F. F. S., Lique, F., Faure, A., Black, J. H., & van Dishoeck, E. F. 2020, *Atoms*, **8**, 15
- Varambhia, H. N., Gupta, M., Faure, A., Baluja, K. L., & Tennyson, J. 2009, *J. Phys. B: At. Mol. Opt. Phys.*, **42**, 095204
- Vieira, D., & Krems, R. V. 2017, *ApJ*, **835**, 255
- Vincent, L. F. M., Spielfiedel, A., & Lique, F. 2007, *A&A*, **472**, 1037
- Walker, K. M., Song, L., Yang, B. H., et al. 2015, *ApJ*, **811**, 27
- Walker, K. M., Dumouchel, F., Lique, F., & Dawes, R. 2016, *J. Chem. Phys.*, **145**, 024314
- Walker, K. M., Lique, F., Dumouchel, F., & Dawes, R. 2017, *MNRAS*, **466**, 831
- Walker, K. M., Lique, F., & Dawes, R. 2018, *MNRAS*, **473**, 1407
- Wan, Y., Balakrishnan, N., Yang, B. H., Forrey, R. C., & Stancil, P. C. 2019, *MNRAS*, **488**, 381
- Wernli, M., Valiron, P., Faure, A., et al. 2006, *A&A*, **446**, 367
- Wernli, M., Wiesenfeld, L., Faure, A., & Valiron, P. 2007a, *A&A*, **464**, 1147
- Wernli, M., Wiesenfeld, L., Faure, A., & Valiron, P. 2007b, *A&A*, **475**, 391
- Xu, L.-H., Fisher, J., Lees, R. M., et al. 2008, *J. Mol. Spectrosc.*, **251**, 305
- Yang, B., & Stancil, P. C. 2014, *ApJ*, **783**, 92
- Yang, B., Stancil, P. C., Balakrishnan, N., & Forrey, R. C. 2010, *ApJ*, **718**, 1062
- Yang, B., Stancil, P. C., Kimura, M., Satomi, W., & Nagao, M. 2013, *ApJ*, **765**, 77
- Yang, B., Walker, K. M., Forrey, R. C., Stancil, P. C., & Balakrishnan, N. 2015a, *A&A*, **578**, A65
- Yang, B. H., Zhang, P., Wang, X. H., et al. 2015b, *Nat. Commun.*, **6**, 6629
- Yang, B. H., Zhang, P., Wang, X. H., et al. 2016, *J. Chem. Phys.*, **145**, 034308
- Yang, B., Zhang, P., Qu, C., et al. 2018a, *Phys. Chem. Chem. Phys.*, **20**, 28425
- Yang, B., Zhang, P., Qu, C., et al. 2018b, *J. Phys. Chem. A*, **122**, 1511
- Yang, B., Zhang, P., Qu, C., et al. 2020, *Chem. Phys.*, **532**, 110695
- Yau, A. W., & Dalgarno, A. 1976, *ApJ*, **206**, 652
- Zeng, T., Li, H., Le Roy, R. J., & Roy, P. N. 2011, *J. Chem. Phys.*, **135**, 094304
- Żóltowski, M., Lique, F., Karska, A., & Żuchowski, P. S. 2021, *MNRAS*, **502**, 5356
- ⁸ Univ. Rennes, CNRS, IPR (Institut de Physique de Rennes) – UMR 6251, 35000 Rennes, France
- ⁹ Department of Chemistry, The University of Manchester, Oxford Road, Manchester M13 9PL, UK
- ¹⁰ Departamento de Física, Facultad de Ciencias, Universidad de Chile, Av. Las Palmeras 3425, Ñuñoa, Santiago, Chile
- ¹¹ Centro para el Desarrollo de la Nanociencia y la Nanotecnología (CEDENNA), Av. Ecuador 3493, Santiago 9170124, Chile
- ¹² Department of Chemistry, The Johns Hopkins University, Baltimore, MD 21218-2685, USA
- ¹³ LOMC – UMR 6294, CNRS-Université du Havre, 25 rue Philippe Lebon, BP 1123, 76063 Le Havre Cedex, France
- ¹⁴ IPAG, Université Grenoble Alpes & CNRS, CS 40700, 38058 Grenoble, France
- ¹⁵ Department of Physics, Penn State University, Berks Campus, Reading, PA 19610, USA
- ¹⁶ Department of Theoretical Physics and Quantum Informatics, Faculty of Applied Physics and Mathematics, Gdansk University of Technology, ul. Narutowicza 11/12, 80-233 Gdansk, Poland
- ¹⁷ Institute for Ion Physics and Applied Physics, University of Innsbruck, Technikerstr. 25/3, 6020 Innsbruck, Austria
- ¹⁸ Department of Chemistry, University of Patras, Patras 26504, Greece
- ¹⁹ Departamento de Química Física, University of Salamanca, Plaza de los Caídos s/n, 37008 Salamanca, Spain
- ²⁰ Theoretical Chemistry, Institute for Molecules and Materials, Radboud University, Heyendaalseweg 135, 6525 AJ Nijmegen, The Netherlands
- ²¹ Université Paris Cité and Univ. Paris Est Creteil, CNRS, LISA, 75013 Paris, France
- ²² Joint Quantum Institute, Department of Physics, University of Maryland, College Park, MD 20742, USA
- ²³ Department of Physics, Temple University, Philadelphia, PA 19122, USA
- ²⁴ Laboratoire Atomes Lasers, Département de Physique, Faculté des Sciences et Techniques, Université Cheikh Anta Diop, Dakar 5005, Senegal
- ²⁵ Depart. of Physics and Astronomy and Center for Simulation Physics, The University of Georgia, Athens, Georgia 30602-2451, USA
- ²⁶ Departamento de Física Atómica y Molecular, Instituto Superior de Tecnologías y Ciencias Aplicadas, Universidad de La Habana, Ave. Salvador Allende No. 1110, 10400 Plaza de la Revolución, La Habana, Cuba
- ²⁷ Department of Chemistry, Missouri University of Science and Technology, Rolla, MO 65409, USA
- ²⁸ Physical Research Laboratory, Ahmedabad, India
- ²⁹ Department of Physics and Astronomy, University College London, London WC1E 6BT, UK
- ³⁰ Scuola Normale Superiore, Piazza dei Cavalieri 7, 56126 Pisa, Italy
- ³¹ Department of Chemistry “Giacomo Ciamician,” University of Bologna, Via F. Selmi 2, 40126 Bologna, Italy
- ³² Department of Chemistry, Koç University, Rumelifeneri Yolu, Sariyer, 34450, Istanbul, Turkey
- ¹ Observatoire de Paris, PSL University, Sorbonne Université, CNRS, LERMA, Paris, France
e-mail: marie-lise.dubernet@observatoiredeparis.obspm.fr
- ² Univ. Bordeaux, CNRS, Bordeaux INP, ISM, UMR 5255, 33400 Talence, France
- ³ Facultad de Ingeniería, Universidad Autónoma de Chile, Av. Pedro de Valdivia 425, 7500912 Providencia, Santiago, Chile
e-mail: otonieldenialpizar@gmail.com
- ⁴ LSAMA, Department of Physics, Faculty of Sciences, Université Tunis El-Manar, 1060 Tunis, Tunisia
- ⁵ Marquette University, Chemistry Department, Milwaukee, WI 53233, USA
- ⁶ Department of Chemistry and Biochemistry, University of Nevada, Las Vegas, NV 89154, USA
- ⁷ KU Leuven, Department of Chemistry, Celestijnenlaan 200F, 3001 Leuven, Belgium

Appendix A: List of VAMDC cases and BASECOL associated molecules

Table A.1. List of BASECOL2023 molecules with the associated cases.

Cases	Description	Molecules
des	Diatomic cs	$^{36}\text{ArH}^+$, $^{36}\text{ArD}^+$, AlO^+ , CF^+ , CH^+ , CN^- , CO , CS H_2 , HD , HeH^+ , HCl , HF , KCl , NaH , NeH^+ , NO^+ , NS^+ , PN , SiH^+ , SiO , SiS
hunda	Diatomic os: hund's case a	CH ($X^2\Pi$), OH ($X^2\Pi$), OD ($X^2\Pi$), NO ($X^2\Pi$), SH ($X^2\Pi$), C_6H ($X^2\Pi$)
hundb ^(a)	Diatomic os: hund's case b	C_2^- ($X^2\Sigma_g^+$), CN ($X^2\Sigma^+$), ^{13}CN ($X^2\Sigma^+$), C^{15}N ($X^2\Sigma^+$), CO^+ ($X^2\Sigma^+$) C_4 ($X^3\Sigma_g^-$), H_2^+ ($X^2\Sigma_g^+$), NH ($X^3\Sigma^+$), O_2 ($X^3\Sigma_g^-$), SO ($X^3\Sigma^-$)
ltcs	linear triatomic cs	AlCN , AlNC , C_3 , C_2H^- , CO_2 , HCN , HNC , DCN , DNC , HCO^+ , HC^{17}O^+ , DCO^+ , HCP , HCS^+ , N_2H^+ , OCS
nlts	non-linear triatomic cs	D_2O , HDO , H_2O , H_2S , SiC_2 , SO_2
stcs	symmetric top cs	H_3^+ , H_3O^+ , NH_3 , ND_3 , CH_3CN , CH_3NC , CH_3OH
lpcs	linear polyatomic cs	CNCN , C_6H^- , HC_3N , HCCNC , HNCCC , HMgNC , NCCNH^+ , C_3O , C_3S , C_4H^- , C_5 , C_5O , C_5S
asymcs	asymmetric cs	H_2CO , HOCO^+ , C_3H_2 , NH_2D , ND_2H
asymos	asymmetric os	none
sphcs	spherical cs	none
sphos	spherical os	none
ltos	linear triatomic os	C_2H ($X^2\Sigma^+$), C_2D ($X^2\Sigma^+$), C_2N^- ($X^3\Sigma^-$), C_2O ($X^3\Sigma^-$), MgCN ($X^2\Sigma^+$), MgNC ($X^2\Sigma^+$)
lpos	linear polyatomic os	none
nlts	non-linear triatomic os	NH_2 (X^2B_1), CH_2 (X^3B_1), HCO

Notes. cs and os denote closed shell and open shell molecules. The molecules in blue have issues with the case assignment; this is explained in the text (see Sect. 2.3). ^(a) The hundb case includes intermediate coupling based on Hund's case b.

Appendix B: Tables of collisional datasets

This appendix provides tables describing the content of the BASECOL database. The names of the columns are self-explanatory, and each line in the sections corresponds to collisional dataset(s), as described in our technical publication. The current tables display some differences compared to Table 1 of the BASECOL2012 publication. The internal ID is not provided anymore because BASECOL2023 stores the successive versions of a given collisional dataset, and each version has a different ID. It is still possible to navigate through BASECOL with the IDs if the user keeps them in memory, as one ID corresponds to a unique couple collisional dataset/version. To date, we have removed the output flat files corresponding to the combination of collisional and spectroscopic data from the BASECOL interface; therefore, the tables do not include information related to those output files. In the following tables, the columns provide the following information: (1) the atomic or molecular target; (2) the perturbing projectile; (3) the energy levels for which rate coefficients are available: the symbols r, f, v, rv, rt, and h are used to denote rotational, fine, vibrational, ro-vibrational, ro-torsional, and hyperfine transitions, respectively (for example, r7 means that rate coefficients are available for the 7 lowest rotational levels); (4) temperature range in kelvin for which the rates have been calculated; (5 & 6) references to the papers describing, respectively, the collisional calculations and the potential energy surfaces; and (7) the year of publication. For Sect. 5, columns (2) and (6) have been removed. In the tables, the notation o/p-H₂ is a synthetic notation that corresponds to two datasets that have the same characteristics: number (except if marked otherwise) and type of levels, temperature range, and references; however one dataset is for a collision with ortho-H₂, and the other one with para-H₂.

Appendix B.1. Collisional data with electrons

Table B.1. List of collisional data with electrons.

Target	Levels	T (K)	Ref	Year
RECOMMENDED				
CH ⁺	r8	100-15000	Lim et al. (1999)	1999
H ₂ ⁺	v3	100-20000	Sarpal & Tennyson (1993)	1993
o/p-H ₂ ⁺	r2	100-10000	Faure & Tennyson (2001)	2001
o/p-H ₃ ⁺	r2/r4	100-10000	Faure & Tennyson (2003)	2003
o/p-H ₃ O ⁺	r4/r8	100-10000	Faure & Tennyson (2003)	2003
HeH ⁺	r3	100-20000	Rabadan et al. (1998)	1998
HeH ⁺	v3	100-20000	Rabadan et al. (1998)	1998
CO ⁺	r5	100-10000	Faure & Tennyson (2001)	2001
HCO ⁺	r3	100-10000	Faure & Tennyson (2001)	2001
NO ⁺	r5	100-10000	Faure & Tennyson (2001)	2001
o/p-H ₂ O	r18	100-8000	Faure et al. (2004)	2004
o/p-D ₂ O	r18	100-8000	Faure et al. (2004)	2004
o-H ₂ O	rv411	200 - 5000	Faure & Josselin (2008)	2008
p-H ₂ O	rv413	200 - 5000	Faure & Josselin (2008)	2008
HDO	r36 (a-type)	100-8000	Faure et al. (2004)	2004
HDO	r36 (b-type)	100-8000	Faure et al. (2004)	2004
HCN	r9	5-2000	Faure et al. (2007b)	2007
HCN	h10	10-100-1000	Faure et al. (2007b)	2007
HNC	r9	5-2000	Faure et al. (2007b)	2007
HNC	h10	10-1000	Faure et al. (2007b)	2007
DCN	r9	5-2000	Faure et al. (2007b)	2007
DCN	h10	10-100-1000	Faure et al. (2007b)	2007
DNC	r9	5-2000	Faure et al. (2007b)	2007
DNC	h10	10-100-1000	Faure et al. (2007b)	2007
SiO	r41	5-5000	Varambhia et al. (2009)	2009

Notes. This list of datasets has not changed since 2012 (see text).

Appendix B.2. Collisional data of atoms excited by heavy projectiles

Table B.2. List of collisional datasets of atoms and atomic ions/cations excited by heavy projectiles.

Target	Projectile	Levels	T (K)	Ref	PES Ref	Year
RECOMMENDED						
C	H	f3	5-1000	Abrahamsson et al. (2007)	Kalamos et al. (1999)	2007
C	o/p-H₂	f3	10-1200	Schröder et al. (1991)	Schröder et al. (1991)	1991
C	He	f3	5-350	Bergeat et al. (2018)	Bergeat et al. (2018)	2018
C⁺	H	f2	20-2000	Barinovs et al. (2005)	Barinovs & van Hemert (2004)	2005
C⁺	o/p-H₂	f2	5-500	Kłos et al. (2020a)	Kłos et al. (2020a)	2020
O	H	f3	50-1000	Vieira & Krems (2017)	Parlant & Yarkony (1999)	2017
O	H	f3	10-1000	Lique et al. (2017)	Dagdigian et al. (2016)	2017
O	He	f3	10-1000	Lique et al. (2017)	Lique et al. (2017)	2017
O	o/p-H₂	f3	10-1000	Lique et al. (2017)	Dagdigian et al. (2016)	2017
Si	He	f3	5-1000	Lique et al. (2018)	Lique et al. (2018)	2018
S	He	f3	5-1000	Lique et al. (2018)	Lique et al. (2018)	2018
Si ⁺	H	f2	20-2000	Barinovs et al. (2005)	Barinovs et al. (2005)	2005
NOT RECOMMENDED (outdated)						
O	H	f3	50-1000	Launay & Roueff (1977)	Launay & Roueff (1977)	1977
O	H	f3	50-1000	Abrahamsson et al. (2007)	Parlant & Yarkony (1999)	2007
O	o/p-H ₂	f3	20-1500	Jaquet et al. (1992)	Jaquet et al. (1992)	1992
C	H	f3	4-1000	Launay & Roueff (1977)	Yau & Dalgarno (1976)	1977
C	He	f3	10-150	Staemmler & Flower (1991)	Staemmler & Flower (1991)	1991

Notes. The species in bold correspond to the systems added since 2012.

Appendix B.3. Collisional data of diatomic species excited by heavy projectiles

Table B.3. List of neutral and ionic diatomic collisional data.

Target	Coll.	Levels	T (K)	Ref	PES Ref	Year
RECOMMENDED						
AlO⁺	He	r16	10-1005	Denis-Alpizar et al. (2018c)	Denis-Alpizar et al. (2018c)	2018
³⁶ArH⁺	He	r11	5-300	Bop et al. (2016)	Bop et al. (2016)	2016
³⁶ArH⁺	He	rv33	10-500	García-Vázquez et al. (2019)	García-Vázquez et al. (2019)	2019
³⁶ArD⁺	He	r13	10-500	García-Vázquez et al. (2019)	García-Vázquez et al. (2019)	2019
C₂⁻	He	r9	5-100	Mant et al. (2020a)	Mant et al. (2020a)	2020
C₂⁻	Ar	r5	5-100	Mant et al. (2020c)	Mant et al. (2020c)	2020
C₂⁻	Ne	r5	5-100	Mant et al. (2020c)	Mant et al. (2020c)	2020
C₂⁻	He	v3	5-100	Mant et al. (2020b)	Mant et al. (2020b)	2020
C₂⁻	Ne	v3	5-100	Mant et al. (2020b)	Mant et al. (2020b)	2020
C₂⁻	Ar	v3	5-100	Mant et al. (2020b)	Mant et al. (2020b)	2020
CF⁺	He	r22	5-155	Denis-Alpizar et al. (2018a)	Denis-Alpizar et al. (2018a)	2019
CF⁺	He	h29	5-155	Denis-Alpizar et al. (2018a)	Denis-Alpizar et al. (2018a)	2019
CF⁺	p-H₂	r21	10-300	Denis-Alpizar & Rubayo-Soneira (2019)	Denis-Alpizar & Rubayo-Soneira (2019)	2019
CF⁺	p-H₂	r22	5-150	Desrousseaux et al. (2021)	Desrousseaux et al. (2019)	2021
CF⁺	o-H₂	r22	5-150	Desrousseaux et al. (2021)	Desrousseaux et al. (2019)	2021
CH⁺	He	r11	20-2000	Hammami et al. (2009)	Hammami et al. (2008a)	2009
CH⁺	He	r6	0.1-200	Turpin et al. (2010)	Turpin et al. (2010)	2010
CH	He	f30	10-300	Marinakis et al. (2015)	Marinakis et al. (2015)	2015
CH	He	h60	10-300	Marinakis et al. (2019)	Marinakis et al. (2015)	2019
CN⁻	o/p-H₂^(c)	r11	5-100	Klos & Lique (2011)	Klos & Lique (2011)	2011
CN⁻	He	r11	5-100	González-Sánchez et al. (2020)	González-Sánchez et al. (2020)	2020
CN⁻	Ar	r11	5-100	González-Sánchez et al. (2021)	González-Sánchez et al. (2021)	2021
CN⁻	He	v3	5-100	Mant et al. (2021)	Mant et al. (2021)	2021
CN	He	f41	5 - 350	Lique et al. (2010b)	Lique et al. (2010b)	2010
CN	He	h37	5 - 30	Lique & Klos (2011)	Lique et al. (2010b)	2011
CN^(a)	p-H₂	r18	5 - 300	Kalugina et al. (2013)	Kalugina et al. (2013)	2013
CN	o-H₂	r16	5 - 300	Kalugina et al. (2013)	Kalugina et al. (2013)	2013
CN^(b)	p-H₂	f25	5 - 100	Kalugina et al. (2013)	Kalugina et al. (2013)	2013
CN^(c)	p-H₂	f17	5 - 100	Kalugina et al. (2013)	Kalugina et al. (2013)	2013
CN	o-H₂	f17	5 - 100	Kalugina et al. (2013)	Kalugina et al. (2013)	2013
CN	o/p-H₂	h73	5 - 100	Kalugina & Lique (2015)	Kalugina et al. (2013)	2015
¹³CN	p-H₂	h146	5 - 80	Flower & Lique (2015)	Kalugina et al. (2013)	2015
C¹⁵N	p-H₂	h34	5 - 150	Flower & Lique (2015)	Kalugina et al. (2013)	2015
CO	He	r15	5-500	Cecchi-Pestellini et al. (2002)	Heijmen et al. (1997)	2002
CO	He	v7	500-5000	Cecchi-Pestellini et al. (2002)	Heijmen et al. (1997)	2002
CO	H	r77	2-3000	Walker et al. (2015)	Song et al. (2013)	2015
CO	H	r8	5-100	Balakrishnan et al. (2002)	Keller et al. (1996)	2002
CO	H	r17	100-3000	Balakrishnan et al. (2002)	Keller et al. (1996)	2002
CO	H	rv350	2-3000	Song et al. (2015b)	Song et al. (2013)	2015
CO	H	v5	100-3000	Balakrishnan et al. (2002)	Keller et al. (1996)	2002
CO	o/p-H₂	r41	1-3000	Yang et al. (2010)	Jankowski & Szalewicz (1998)	2010
CO	o/p-H₂	r6	5-70	Wernli et al. (2006)	Jankowski & Szalewicz (1998)	2006
CO	o-H₂	r20	5-400	Flower (2001a)	Jankowski & Szalewicz (1998)	2001
CO	p-H₂	r29	5-400	Flower (2001a)	Jankowski & Szalewicz (1998)	2001
CO	p-H₂	rv45	1-300	Yang et al. (2016)	Yang et al. (2015b)	2016
CO	o-H₂	rv29	1-300	Yang et al. (2016)	Yang et al. (2015b)	2016
CO	o/p-t-H₂0	r11	10-100	Faure et al. (2020)	Kalugina et al. (2018)	2020
CS	He	r31	10-300	Lique et al. (2006b)	Lique et al. (2006b)	2006
CS	He	rv114	300-1500	Lique & Spielfiedel (2007)	Lique & Spielfiedel (2007)	2007
CS	o/p-H₂	rv42	5-1000	Yang et al. (2018a)	Yang et al. (2018a)	2018
CS	o/p-H₂	r30	5-305	Denis-Alpizar et al. (2018b)	Denis-Alpizar et al. (2012)	2018
HCl	He	r21	1-3000	Yang & Stancil (2014)	Murdachaew et al. (2004)	2014
HCl	He	r11	10-300	Lanza & Lique (2012)	Lanza & Lique (2012)	2012
HCl	He	h40	10-300	Lanza & Lique (2012)	Lanza & Lique (2012)	2012
HCl^(a)	p-H₂	r11	10-300	Lanza et al. (2014a)	Lanza et al. (2014b)	2014
HCl	o-H₂	r11	10-300	Lanza et al. (2014a)	Lanza et al. (2014b)	2014

Continued on next page.

Table B.3 – Continued from previous page.

Target	Coll.	Levels	T (K)	Ref	PES Ref	Year
HCl	<i>o/p</i> -H ₂	h20	10-300	Lanza & Lique (2014)	Lanza et al. (2014b)	2014
HCl	H	r11	10-500	Lique & Faure (2017)	Bian & Werner (2000)	2017
HF	He	r21	1-3000	Yang et al. (2015a)	Moszynski et al. (1994)	2015
HF	He	r10	0.1-300	Reese et al. (2005)	Stoecklin et al. (2003)	2005
HF	<i>o/p</i> -H ₂	r6	0.1-150	Guillon & Stoecklin (2012)	Guillon & Stoecklin (2012)	2012
HF	H	r9	10-500	Desrousseaux & Lique (2018)	Li et al. (2007)	2018
HF	<i>o/p-t</i> -H ₂ 0	r7	10-150	Loreau et al. (2022)	Loreau et al. (2020)	2022
HD	He	r10	80-2000	Roueff & Zeppen (1999)	Muchnick & Russek (1994)	1999
HD	He	rv94	2-100	Nolte et al. (2011)	Muchnick & Russek (1994)	2011
HD	He	rv223	2-1000	Nolte et al. (2011)	Muchnick & Russek (1994)	2011
HD	<i>o/p</i> -H ₂	r9	1-10000	Wan et al. (2019)	Patkowski et al. (2008)	2019
HD	<i>o/p</i> -H ₂	rv24	100-1940	Flower & Roueff (1999a)	Schwenke (1988)	1999
HD	H	r11	10-1000	Desrousseaux et al. (2018)	Mielke et al. (2002)	2018
HD	H	r10	100-2000	Roueff & Flower (1999)	Boothroyd et al. (1996)	1999
HD	H	rv30	100-2080	Flower & Roueff (1999a)	Boothroyd et al. (1996)	1999
<i>o</i> -H ₂	He	rv23	100-6000	Flower et al. (1998)	Muchnick & Russek (1994)	1998
<i>p</i> -H ₂	He	rv26	100-6000	Flower et al. (1998)	Muchnick & Russek (1994)	1998
<i>o</i> -H ₂	<i>o</i> -H ₂	rv17	100-6000	Flower & Roueff (1999b)	Schwenke (1988)	1999
<i>p</i> -H ₂	<i>o</i> -H ₂	rv19	100-6000	Flower & Roueff (1999b)	Schwenke (1988)	1999
<i>o</i> -H ₂	<i>p</i> -H ₂	rv23	100-6000	Flower & Roueff (1998a)	Schwenke (1988)	1998
<i>p</i> -H ₂	<i>p</i> -H ₂	rv26	100-6000	Flower & Roueff (1998a)	Schwenke (1988)	1998
H ₂	H	r9	300-1500	Lique et al. (2012)	Mielke et al. (2002)	2012
<i>o/p</i> -H ₂	H	r3	100-1000	Forrey et al. (1997)	Boothroyd et al. (1996)	1997
<i>o</i> -H ₂	H	rv23	100-6000	Flower & Roueff (1998b)	Boothroyd et al. (1996)	1998
<i>p</i> -H ₂	H	rv26	100-6000	Flower & Roueff (1998b)	Boothroyd et al. (1996)	1998
HeH ⁺	H	r10	5-500	Desrousseaux & Lique (2020)	Ramachandran et al. (2009)	2020
KCl	<i>p</i> -H ₂	r16	2-50	Sahnoun et al. (2018)	Sahnoun et al. (2018)	2018
NaH	He	r11	5-200	Bop et al. (2019b)	Bop et al. (2019b)	2019
NeH ⁺	He	r11	5-300	Bop et al. (2017)	Bop et al. (2017)	2017
NH	He	f25	5- 350	Toboła et al. (2011)	Cybulski et al. (2005)	2011
NH	He	f25	10- 350	Ramachandran et al. (2018)	Ramachandran et al. (2018)	2018
NO ⁺	He	r8	1-205	Denis-Alpizar & Stoecklin (2015)	Stoecklin & Voronin (2011)	2015
NO ⁺	<i>p</i> -H ₂	r19	5-300	Cabrera-González et al. (2020)	Cabrera-González et al. (2020)	2020
NO	He	f98	10-500	Kłos et al. (2008)	Kłos et al. (2000)	2008
NO	<i>p</i> -H ₂	h100	7-100	Ben Khalifa & Loreau (2021)	Kłos et al. (2017a)	2021
NS ⁺	He	r28	10-305	Cabrera-González et al. (2018)	Cabrera-González et al. (2018)	2018
NS ⁺	He	h40	10-305	Cabrera-González et al. (2018)	Cabrera-González et al. (2018)	2018
NS ⁺	<i>o/p</i> -H ₂	r15	5-50	Bop et al. (2022a)	Bop et al. (2022a)	2019
NS ⁺	<i>p</i> -H ₂	r24	5-100	Bop (2019)	Bop (2019)	2019
NS ⁺	<i>p</i> -H ₂	h67	10-100	Bop (2019)	Bop (2019)	2019
OH	He	f46	5-350	Kłos et al. (2007)	Lee et al. (2000)	2007
OH	He	f44	5-350	Kalugina et al. (2014)	Kalugina et al. (2014)	2014
OH	He	h56	5-350	Marinakakis et al. (2019)	Kalugina et al. (2014)	2019
OH	<i>o/p</i> -H ₂	f20	10-150	Kłos et al. (2017b)	Ma et al. (2014)	2017
OH	<i>o/p</i> -H ₂	h24	10-150	Kłos et al. (2020b)	Ma et al. (2014)	2020
OD	<i>o/p</i> -H ₂	h40	5-200	Dagdigian (2021a)	Ma et al. (2014)	2021
OH	H	h24	5-500	Dagdigian (2022a)	Alexander et al. (2004)	2022
O ₂	He	f36	5-350	Lique (2010)	Groenenboom & Struniewicz (2000)	2010
O ₂	<i>o/p</i> -H ₂	r7	5-150	Kalugina et al. (2012a)	Kalugina et al. (2012a)	2012
PN	He	r31	10-300	Toboła et al. (2007)	Toboła et al. (2007)	2007
PN	<i>p</i> -H ₂	r40	10-300	Najar et al. (2017)	Najar et al. (2017)	2017
SH	He	f60	5-350	Kłos et al. (2009)	Cybulski et al. (2000)	2009
SiH ⁺	He	r11	5-200	Nkem et al. (2009)	Nkem et al. (2009)	2009
SiO	He	r27	10-300	Dayou & Balança (2006)	Dayou & Balança (2006)	2006
SiO	He	rv246	250-10000	Balança & Dayou (2017)	Balança & Dayou (2017)	2017
SiO	<i>o/p</i> -H ₂	rv47	5-1000	Yang et al. (2018b)	Yang et al. (2018b)	2018
SiO ^(d)	<i>o/p</i> -H ₂	r21	5-300	Balança et al. (2018)	Balança et al. (2018)	2018
SiO ^(e)	<i>o/p</i> -H ₂	r30	5-1000	Balança et al. (2018)	Balança et al. (2018)	2018
SiS	He	r26	10-200	Vincent et al. (2007)	Vincent et al. (2007)	2007
SiS	He	rv505	100-1500	Toboła et al. (2008)	Toboła et al. (2008)	2008
SiS	<i>o/p</i> -H ₂	r41	5-300	Kłos & Lique (2008)	Kłos & Lique (2008)	2008

Continued on next page.

Table B.3 – Continued from previous page.

Target	Coll.	Levels	T (K)	Ref	PES Ref	Year
SO	He	f31	5-50	Lique et al. (2005)	Lique et al. (2005)	2005
SO	He	f91	60-300	Lique et al. (2006a)	Lique et al. (2005)	2006
SO	He	rv236	300-800	Lique et al. (2006c)	Lique et al. (2006c)	2006
SO	o/p-H ₂	rv273	5-3000	Price et al. (2021)	Yang et al. (2020)	2021
SO	p-H ₂	r31	5-50	Lique et al. (2007)	Lique et al. (2007)	2007
NOT RECOMMENDED (outdated)						
CH ⁺	He	r11	20-200	Hammami et al. (2008a)	Hammami et al. (2008a)	2008
CN	p-H ₂	h73	5 - 100	Kalugina et al. (2012b)	Kalugina et al. (2012b)	2012
CS	p-H ₂	r21	20-300	Turner et al. (1992)	Green & Chapman (1978)	1992
CS	p-H ₂	r13	10-100	Green & Chapman (1978)	Green & Chapman (1978)	1978
HCl	He	r8	10-300	Neufeld & Green (1994)	Neufeld & Green (1994)	1994
HCl	He	h28	10-300	Neufeld & Green (1994)	Neufeld & Green (1994)	1994
HD	o/p-H ₂	r9	50-500	Flower (1999a)	Schwenke (1988)	1999
SiO	p-H ₂	r21	20-300	Turner et al. (1992)	Turner et al. (1992)	1992
SiO	p-H ₂	r20	10-300	Dayou & Balança (2006)	Dayou & Balança (2006)	2006
SO	p-H ₂	f70	50-350	Green (1994)	Green (1994)	1994

Notes. The species in bold correspond to the systems added since 2012.^(a) The transitions among the first two levels of the projectile are provided.^(b) In this dataset the projectile remains in its ground state.^(c) The projectile's transitions $j=2-2$ and $j=2-0$ are provided.^(d) This SiO dataset from Balança et al. (2018) uses the CC method.^(e) This SiO dataset from Balança et al. (2018) uses the CS method.

Appendix B.4. Collisional data of triatomic species excited by heavy projectiles

Table B.4. List of triatomic collisional data.

Target	Coll.	Levels	T (K)	Ref	PES Ref	Year
RECOMMENDED						
AICN	He	r30	5-100	Hernández Vera et al. (2013)	Hernández Vera et al. (2013)	2013
AINC	He	r30	5-100	Hernández Vera et al. (2013)	Hernández Vera et al. (2013)	2013
AINC	p-H₂	r27	5-105	Urzúa-Leiva & Denis-Alpizar (2020)	Urzúa-Leiva & Denis-Alpizar (2020)	2020
C ₃	He	r6	5-15	Ben Abdallah et al. (2008)	Ben Abdallah et al. (2008)	2008
C₃	He	rv23	10-155	Stoeklin et al. (2015)	Denis-Alpizar et al. (2014)	2015
C₃	o/p-H₂	r11	5-50	Santander et al. (2022)	Santander et al. (2022)	2022
C₂H	He	h46	5-100	Spielfiedel et al. (2013)	Spielfiedel et al. (2013)	2013
C₂H	o/p-H₂	f41	5-500	Pirlot Jankowiak et al. (2023b)	Dagdgian (2018b)	2023
C₂H	o/p-H₂	h38	5-100	Pirlot Jankowiak et al. (2023b)	Dagdgian (2018b)	2023
C₂D	o/p-H₂	f31	5-200	Pirlot Jankowiak et al. (2023b)	Dagdgian (2018b)	2023
C₂D	o/p-H₂	h55	5-100	Pirlot Jankowiak et al. (2023b)	Dagdgian (2018b)	2023
C¹³CH	p-H₂	h98	5-100	Pirlot Jankowiak et al. (2023a)	Dagdgian (2018b)	2023
¹³CCH	p-H₂	h98	5-100	Pirlot Jankowiak et al. (2023a)	Dagdgian (2018b)	2023
C₂H⁻	He	r13	5-100	Dumouchel et al. (2012)	Dumouchel et al. (2012)	2012
C₂H⁻	He	r9	5-100	Gianturco et al. (2019)	Dumouchel et al. (2012)	2019
C₂N⁻	He	r16	5-100	Franz et al. (2020)	Franz et al. (2020)	2020
C₂O	He	f31	2-80	Khadri et al. (2022b)	Khadri et al. (2022b)	2022
o-CH₂	o/p-H₂	h69	5-300	Dagdgian (2021b)	Dagdgian (2021c)	2021
p-CH₂	o/p-H₂	r27	5-300	Dagdgian (2021b)	Dagdgian (2021c)	2021
CO₂	He	r21	4-300	Godard Palluet et al. (2022)	Godard Palluet et al. (2022)	2022
HCN	He	r26	5-500	Dumouchel et al. (2010)	Toczyłowski et al. (2001)	2010
HCN	p-H₂	r13	5-100	Hernández Vera et al. (2014)	Denis-Alpizar et al. (2013)	2014
HCN	o/p-H₂	r26	5-500	Hernández Vera et al. (2017)	Denis-Alpizar et al. (2013)	2017
HCN	o/p-H₂	h34	5 - 500	Goicoechea et al. (2022)	Denis-Alpizar et al. (2013)	2022
HCN	p-t-H₂0	r8	5 - 150	Dubernet & Quintas-Sánchez (2019)	Quintas-Sánchez & Dubernet (2017)	2019
HNC	He	r26	5-500	^c Dumouchel et al. (2010)	Sarrasin et al. (2010)	2010
HNC	o/p-H ₂	r11	5-100	Dumouchel et al. (2011)	Dumouchel et al. (2011)	2011
HNC	o/p-H₂	r26	5-500	Hernández Vera et al. (2017)	Dumouchel et al. (2011)	2017
HCO⁺	He	r6	5-100	Tonolo et al. (2021)	Tonolo et al. (2021)	2021
HCO⁺	o/p-H₂	r22	10-200	Denis-Alpizar et al. (2020)	Denis-Alpizar et al. (2020)	2020
DCO⁺	p-H₂	r22	10-200	Denis-Alpizar et al. (2020)	Denis-Alpizar et al. (2020)	2020
DCO ⁺	p-H ₂	h31	5-300	Pagani et al. (2012)	Monteiro (1985)	2012
HC¹⁷O⁺	p-H₂	h33	5-100	Tonolo et al. (2022)	Tonolo et al. (2022)	2022
HCO	o/p-H₂	h86	5-200	Dagdgian (2020b)	Dagdgian (2020d)	2020
HCP	p-H ₂	r11	10-70	Hammami et al. (2008c)	Hammami et al. (2008c)	2008
HCP	He	r16	20-200	Hammami et al. (2008b)	Hammami et al. (2008b)	2008

Continued on next page.

Table B.4 – Continued from previous page.

Target	Coll.	Levels	T (K)	Ref	PES Ref	Year
HCS⁺	He	r20	5-100	Dubernet et al. (2015)	Dubernet et al. (2015)	2015
HCS⁺	p-H₂	r31	5-100	Denis-Alpizar et al. (2022)	Quintas-Sánchez et al. (2021)	2022
o/p-H₂O	He	r10	2-3000	Yang et al. (2013)	Patkowski et al. (2002)	1993
o/p-H ₂ O	He	r45	20-2000	Green et al. (1993)	Maluendes et al. (1992)	1993
p-H ₂ O	o/p-H ₂	r45	5-1500	Daniel et al. (2011)	Valiron et al. (2008)	2011
o-H ₂ O	o-H ₂	r45	5-1500	Daniel et al. (2011)	Valiron et al. (2008)	2011
o-H ₂ O	p-H ₂	r45	5-1500	Dubernet et al. (2009)	Valiron et al. (2008)	2011
o/p-H₂O	p-H₂	r97	10-2000	Żółtowski et al. (2021)	Valiron et al. (2008)	2021
o/p-H ₂ O	o/p-t-H ₂	r45	20-2000	Faure et al. (2007a)	Valiron et al. (2008)	2007
o/p-H ₂ O	t-H ₂	rv411	200 - 5000	Faure & Josselin (2008)	Valiron et al. (2008)	2008
o/p-H₂O	H	r45	5-1500	Daniel et al. (2015)	Dagdikian & Alexander (2013)	2015
o/p-H₂O	t-H₂O	r59	100 - 800	Boursier et al. (2020)	Boursier et al. (2020)	2020
o/p-H₂O	t-H₂O	r21/r22	5 - 1000	Mandal & Babikov (2023a)	Jankowski & Szalewicz (2005)	2023
o/p-D₂O	p-H₂	r6	5-100	Faure et al. (2012)	Valiron et al. (2008)	2012
HDO	He	r34	50-500	Green (1989)	Palma et al. (1988)	1989
HDO	p-t-H₂	r30	5 - 300	Faure et al. (2012)	Valiron et al. (2008)	2012
HDO	o-H₂	r30	5 - 300	Faure et al. (2012)	Valiron et al. (2008)	2012
o/p-H₂S	o/p-H₂	r19	5 - 500	Dagdikian (2020a)	Dagdikian (2020c)	2020
MgCN	He	r36	5-100	Hernández Vera et al. (2013)	Hernández Vera et al. (2013)	2013
MgCN	He	f41	5-100	Hernández Vera et al. (2013)	Hernández Vera et al. (2013)	2013
MgNC	He	r36	5-100	Hernández Vera et al. (2013)	Hernández Vera et al. (2013)	2013
MgNC	He	f41	5-100	Hernández Vera et al. (2013)	Hernández Vera et al. (2013)	2013
o/p-NH₂	o/p-H₂	r15	10-150	Bouhafs et al. (2017a)	Li & Guo (2014)	1978
N ₂ H ⁺	He	r7	5-50	Daniel et al. (2005)	Daniel et al. (2004)	2005
N ₂ H ⁺	He	h55	5-50	Daniel et al. (2005)	Daniel et al. (2004)	2005
N₂H⁺	p-H₂	r26	5-500	Balança et al. (2020)	Spielfiedel et al. (2015)	2020
N₂H⁺	p-H₂	h64	5-70	Lique et al. (2015)	Spielfiedel et al. (2015)	2015
OCS	p-H ₂	r13	10-100	Green & Chapman (1978)	Green & Chapman (1978)	1978
OCS	He	r27	10-150	Flower (2001b)	Higgins & Klemperer (1999)	2001
OCS	Ar	r21	5-400	Chefai et al. (2018)	Chefai et al. (2018)	2018
o-SiC ₂	He	r40	25-125	Chandra & Kegel (2000)	Palma & Green (1987)	2000
SO ₂	He	r50	25-125	Green (1995)	Palma (1987)	1995
SO ₂	o/p-H ₂	r31	5-30	Cernicharo et al. (2011)	Spielfiedel et al. (2009)	2011
NON-RECOMMENDED (mostly outdated)						
C₂H	o/p-H₂	h30	10-300	Dagdikian (2018a)	Dagdikian (2018b)	2018
C₂H	p-H₂	f17	5-80	Dumouchel et al. (2017)	Najar et al. (2014)	2017
C₂H	p-H₂	h34	2-80	Dumouchel et al. (2017)	Najar et al. (2014)	2017
C₂D	p-H₂	h49	2-80	Dumouchel et al. (2017)	Najar et al. (2014)	2017
C₂D	p-H₂	f17	5-80	Dumouchel et al. (2017)	Najar et al. (2014)	2017
HCN	He	h13	10-30	Monteiro & Stutzki (1986)	Green & Thaddeus (1974)	1986
HCN	He	r8	5-100	Green & Thaddeus (1974)	Green & Thaddeus (1974)	1974
HCN	p-H ₂	h31	5 - 100	Ben Abdallah et al. (2012)	Ben Abdallah et al. (2012)	2012
HCO ⁺	p-H ₂	r21	5-390	Flower (1999b)	Monteiro (1985)	1999
HCS ⁺	He	r11	10-60	Monteiro (1984)	Monteiro (1984)	1984
o/p-H ₂ O	o/p-H ₂	r5	20-140	Phillips et al. (1996)	Phillips et al. (1994)	1996
N ₂ H ⁺	He	r7	5-40	Green (1975)	Green (1975)	1975

Notes. For H₂O collisional data: t-H₂, t-H₂O means that H₂, H₂O are thermalised over para and ortho species (you should refer to the papers to see how this is done); o/p-t-H₂ or o/p-t-H₂O means that H₂ or H₂O is thermalised over para-species only or ortho-species only. The species in bold correspond to the systems added since 2012.

Appendix B.5. Collisional data of species with more than 3 atoms excited by heavy projectiles

Table B.5. List of collisional datasets for molecules with more than three atoms.

Target	Coll.	Levels	T (K)	Ref	PES Ref	Year
RECOMMENDED						
o/p c-C ₃ H ₂	He	r47/48	30-120	Chandra & Kegel (2000)	Green et al. (1987)	2000
C ₃ O	He	r31	5-150	Bop et al. (2022b)	Khadri & Hammami (2019)	2022
C ₃ S	He	r11	2-25	Sahnoun et al. (2020)	Sahnoun et al. (2020)	2020
C ₄	He	f30	5-50	Lique et al. (2010a)	Lique et al. (2010a)	2010
C ₄ H ⁻	o/p-H ₂	r30	5-100	Balança et al. (2021)	Balança et al. (2021)	2021
C ₅	He	r15	5-300	Chefai et al. (2021)	Chefai et al. (2021)	2021
C ₅ H ⁺	He	r16	5-100	Khadri et al. (2023)	Khadri et al. (2023)	2023
C ₅ O	He	r31	5-150	Bop et al. (2022b)	Khadri et al. (2022a)	2022
C ₅ S	He	r51	2-100	Khadri et al. (2020)	Khadri et al. (2020)	2020
C ₆ H	He	f122	5-100	Walker et al. (2018)	Walker et al. (2018)	2018
C ₆ H	He	h52	5-100	Walker et al. (2018)	Walker et al. (2018)	2018
C ₆ H ⁻	He	r11	5-100	Walker et al. (2017)	Walker et al. (2016)	2017
C ₆ H ⁻	o/p-H ₂	r31	5-100	Walker et al. (2017)	Walker et al. (2016)	2017
p-CH ₃ CN	He	r75	7-100	Ben Khalifa et al. (2023)	Ben Khalifa et al. (2022)	2023
o-CH ₃ CN	He	r52	7-100	Ben Khalifa et al. (2023)	Ben Khalifa et al. (2022)	2023
p-CH ₃ NC	He	r63	7-100	Ben Khalifa et al. (2023)	Ben Khalifa et al. (2022)	2023
o-CH ₃ NC	He	r66	7-100	Ben Khalifa et al. (2023)	Ben Khalifa et al. (2022)	2023
A/E-CH ₃ OH	He	rt150	10-400	Rabli & Flower (2011)	Pottage et al. (2002)	2011
A-CH ₃ OH	He	r256, vt=0	10-200	Rabli & Flower (2010b)	Pottage et al. (2002)	2010
A-CH ₃ OH	He	r256, vt=1	10-200	Rabli & Flower (2010b)	Pottage et al. (2002)	2010
A-CH ₃ OH	He	r256, vt=2	10-200	Rabli & Flower (2010b)	Pottage et al. (2002)	2010
E-CH ₃ OH	He	r256, vt=0	10-200	Rabli & Flower (2010b)	Pottage et al. (2002)	2010
E-CH ₃ OH	He	r256, vt=1	10-200	Rabli & Flower (2010b)	Pottage et al. (2002)	2010
E-CH ₃ OH	He	r256, vt=2	10-200	Rabli & Flower (2010b)	Pottage et al. (2002)	2010
A-CH ₃ OH	p-H ₂	r256, vt=0	10-200	Rabli & Flower (2010a)	Pottage et al. (2004)	2010
A-CH ₃ OH	p-H ₂	r256, vt=1	10-200	Rabli & Flower (2010a)	Pottage et al. (2004)	2010
A-CH ₃ OH	p-H ₂	r256, vt=2	10-200	Rabli & Flower (2010a)	Pottage et al. (2004)	2010
E-CH ₃ OH	p-H ₂	r256, vt=0	10-200	Rabli & Flower (2010a)	Pottage et al. (2004)	2010
E-CH ₃ OH	p-H ₂	r256, vt=1	10-200	Rabli & Flower (2010a)	Pottage et al. (2004)	2010
E-CH ₃ OH	p-H ₂	r256, vt=2	10-200	Rabli & Flower (2010a)	Pottage et al. (2004)	2010
CNCN	He	r30	5-150	Ndaw et al. (2021)	Ndaw et al. (2021)	2021
o/p-H ₂ CO	He	r40/r41	10-300	Green (1991)	Garrison & Lester (1975)	1991
o-H ₂ CO	o/p-H ₂	r10	5-100	Troscompt et al. (2009)	Troscompt et al. (2009)	2009
p-H ₃ O ⁺	o/p-H ₂	r21	10-300	Demes et al. (2022)	Demes et al. (2020)	2022
o-H ₃ O ⁺	o/p-H ₂	r11	10-300	Demes et al. (2022)	Demes et al. (2020)	2022
HC ₃ N	He	r11	10-40	Wernli et al. (2007a,b)	Wernli et al. (2007a,b)	2007
HC ₃ N	o/p-H ₂	r38	10-300	Faure et al. (2016)	Wernli et al. (2007a)	2016
HC ₃ N	t-p-H ₂	r38	10-300	Faure et al. (2016)	Wernli et al. (2007a)	2016
HC ₃ N	o/p-H ₂	h61	10-100	Faure et al. (2016)	Wernli et al. (2007a)	2016
HC ₃ N	t-p-H ₂	h61	10-100	Faure et al. (2016)	Wernli et al. (2007a)	2016
HNCCC	o/p-H ₂	r30	5-80	Bop et al. (2021)	Bop et al. (2019a)	2021
HCCNC	o/p-H ₂	r30	5-80	Bop et al. (2021)	Bop et al. (2019a)	2021
HMgNC	He	r14	5-200	Amor et al. (2021)	Amor et al. (2021)	2021
HOCO ⁺	He	r25	10-30	Hammami et al. (2007)	Hammami et al. (2004)	2007
HNCCN ⁺	He	r11	5-100	Bop et al. (2018)	Bop et al. (2018)	2018
o/p-NH ₃	He	r22/16	5-300	Machin & Roueff (2005)	Hodges & Wheatley (2001)	2005
o/p-NH ₃	o/p-H ₂	r33/62	100-500	Demes et al. (2023)	Maret et al. (2009)	2023
o/p-NH ₃	p-t-H ₂	r33/62	100-500	Demes et al. (2023)	Maret et al. (2009)	2023
o/p-NH ₃	o/p-H ₂	r17/34	10-200	Bouhafs et al. (2017b)	Maret et al. (2009)	2017
o/p-NH ₃	p-H ₂	r6/10	5-100	Maret et al. (2009)	Maret et al. (2009)	2009
o/p-NH ₃	H	r17/34	10-200	Bouhafs et al. (2017b)	Li & Guo (2014)	2017
o/p-NH ₂ D	He	r9	5-100	Machin & Roueff (2006)	Hodges & Wheatley (2001) ^(a)	2006
o/p-NH ₂ D	p-H ₂	r79	5-300	Daniel et al. (2014)	Maret et al. (2009)	2014
o/p-ND ₂ H	He	r9	5-100	Machin & Roueff (2007)	Hodges & Wheatley (2001) ^(a)	2007
o/p-ND ₂ H	p-H ₂	r16	5-50	Daniel et al. (2016)	Maret et al. (2009)	2016
o/p/meta-ND ₃	p-H ₂	r16/r9/r9	5-50	Daniel et al. (2016)	Maret et al. (2009)	2016

NON-RECOMMENDED (mostly outdated)

Continued on next page.

Table B.5 – Continued from previous page.

Target	Coll.	Levels	T (K)	Ref	PES Ref	Year
HC ₃ N	He	r21	10-80	Green & Chapman (1978)	Green & Chapman (1978)	1978
HC ₃ N	p-H ₂	r51	10-100	Wernli et al. (2007a,b)	Wernli et al. (2007a,b)	2007
o-NH ₃	p-H ₂	r9	15-300	Danby et al. (1986)	Danby et al. (1986)	1986
p-NH ₃	p-H ₂	r16	15-300	Danby et al. (1987)	Danby et al. (1986)	1987
o/p-NH ₃	p-H ₂	r17/24	15-300	Danby et al. (1988)	Danby et al. (1986)	1988

Notes. The species in bold correspond to the systems added since 2012. ^(a)The PES of [Hodges & Wheatley \(2001\)](#) was adapted by [Machin & Roueff \(2006\)](#) and [Machin & Roueff \(2007\)](#) to account for the isotopic shift.

Appendix C: Figures

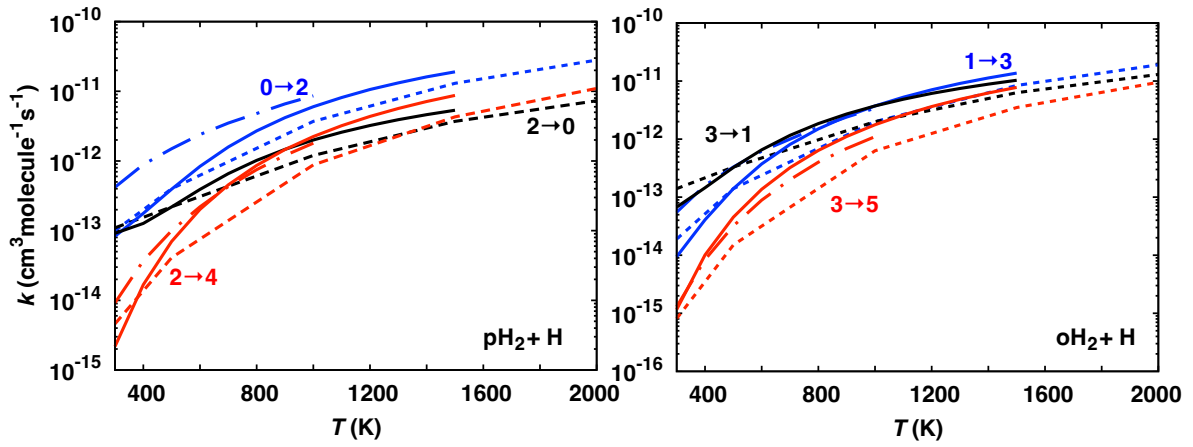


Fig. C.1. Rotational rate coefficients of para-H₂ and ortho-H₂ by H reported by [Forrey et al. \(1997\)](#) (dash-dotted lines), [Flower & Roueff \(1998b\)](#) (dashed lines), and [Lique et al. \(2012\)](#) (solid lines). Rotational transitions of H₂ are labelled as $j_i \rightarrow j_f$.

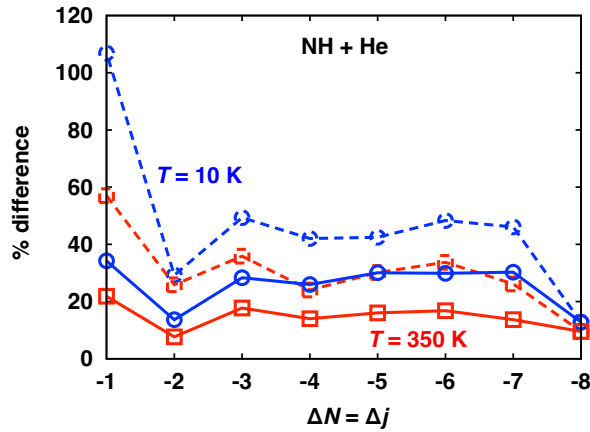


Fig. C.2. Average percentage difference (solid lines) and maximum percentage difference (dashed lines) between the rate coefficients reported by [Tobola et al. \(2011\)](#) and [Ramachandran et al. \(2018\)](#) for the $\Delta N = \Delta j$ transitions in the NH+He collision at 10 K (circles) and 350 K (squares).

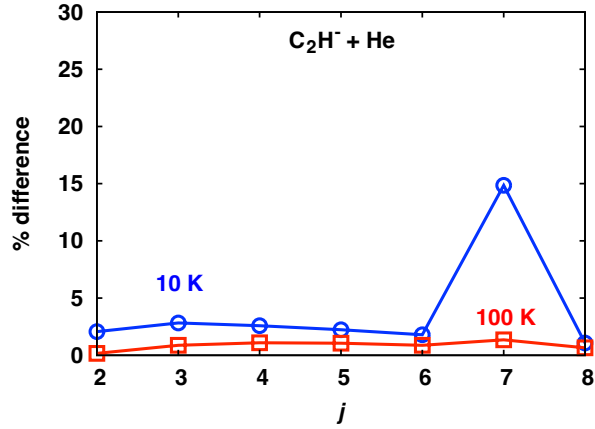


Fig. C.3. Percentage difference between rate coefficients reported by Dumouchel et al. (2012) and Gianturco et al. (2019) for the $\Delta j = 2$ transitions (strong propensity was found for this transition) in the $\text{C}_2\text{H}^+ + \text{He}$ collision at 10 K (circles) and 100 K (squares).

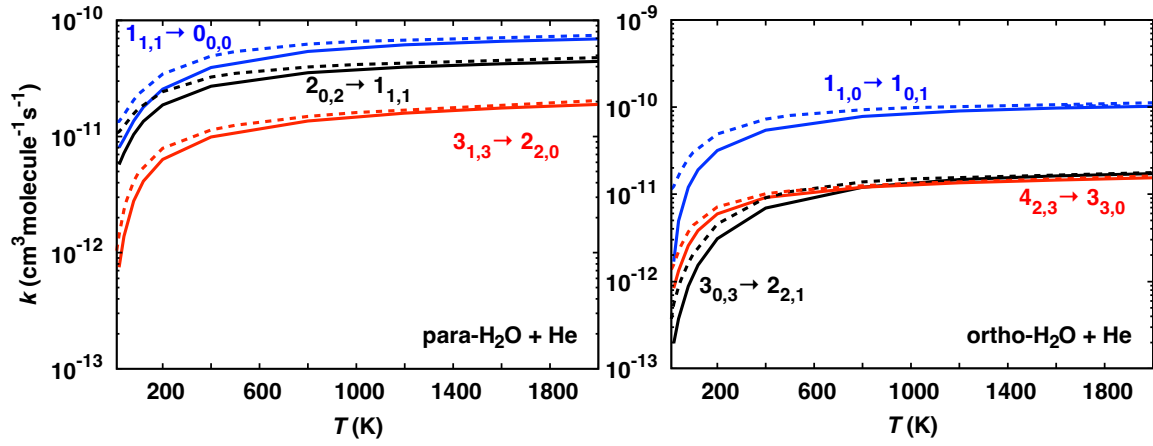


Fig. C.4. Rotational rate coefficient of para- H_2O and ortho- H_2O by He reported by Green et al. (1993) (solid lines), and Yang et al. (2013) (dashed lines). Rotational transitions of H_2O are labelled as $j_{K_a, K_c}^i \rightarrow j_{K_a, K_c}^f$.



Titre : Excitation collisionnelle des molécules soufrées par des projectiles légers et lourds pour des applications interstellaires et cométaires

Mot clés : Astrochimie - Taux de collisions - Milieu Interstellaire - Comètes - Soufre

Résumé : La connaissance des milieux astrophysiques provient principalement des spectres moléculaires capturés par les télescopes. Leur interprétation repose souvent sur les taux de collisions, qui font défaut pour de nombreuses molécules, limitant ainsi l'exploitation des observations. La chimie du soufre restant énigmatique, modéliser précisément les abondances des espèces soufrées peut apporter des pistes sur le problème du soufre manquant. Dans ce but, des taux de collisions pour CCS et ses isotopologues en collision avec He ont été calculés via une approche quantique, permettant de réviser leurs abondances dans le milieu interstellaire et

d'apporter de nouvelles perspectives sur leur chimie. En parallèle, des taux de collisions pour CS en collision avec CO et H₂O ont été calculés, permettant d'interpréter les spectres d'émission de CS dans les atmosphères cométaires à grandes et courtes distances héliocentriques. Une nouvelle approche statistique a été employée et s'est avérée prometteuse pour les futures études de systèmes collisionnels d'intérêt cométaire. L'interprétation de futures observations à l'aide des données calculées dans ce travail de thèse devrait offrir de nouvelles perspectives sur la chimie de ces molécules et, ainsi, sur le problème du soufre manquant.

Title: Collisional Rate Coefficients of Sulfur-Bearing Molecules Induced by Light and Heavy Colliders for Interstellar and Cometary Applications

Keywords: Astrochemistry - Rate Coefficients - Interstellar Medium - Comets - Sulfur

Abstract: The main knowledge gathered from astrophysical media comes from molecular spectra captured by telescopes. The interpretation of these spectra often relies on collisional rate coefficients, which are lacking for many molecules, thus limiting the full exploitation of these observations. Since sulfur chemistry remains a puzzling issue in astrochemistry, accurately modeling the abundances of key sulfur-bearing species can provide new insights into what is known as the missing sulfur problem. To this end, rate coefficients for CCS and its isotopologues in collisions with He were produced using quantum approaches to model their abundances in the interstellar medium, allowing for a revision of their

abundance and offering new insights into their chemistry. In parallel, rate coefficients for the excitation of CS due to collisions with both CO and H₂O were produced, enabling the interpretation of CS emission spectra in cometary atmospheres at both large and short heliocentric distances. A newly developed statistical approach was employed for this task and has proven to be a promising method for future studies of collisional systems of cometary interest. The interpretation of future observations using the data computed in this thesis is expected to provide further insights into the chemistry of these molecules and, consequently, into the missing sulfur problem.